Single-molecule imaging with upconverting nanoparticles

Oleksii Dukhno

UNIVERSITÉ DE STRASBOURG

ÉCOLE DOCTORALE DES SCIENCES DE LA VIE ET DE LA SANTÉ

UMR CNRS 7021 Laboratoire de Bioimagerie et Pathologies

THÈSE présentée par:

Oleksii DUKHNO

soutenue le : **13 novembre 2018**

pour obtenir le grade de: **Docteur de l'université de Strasbourg**

Discipline/ Spécialité: Biophysique

Microscopie de molécules uniques avec des nanoparticules à conversion ascendante

THÈSE dirigée par :

[M. MELY Yves]	Professeur, université de Strasbourg

RAPPORTEURS :

[Mme RESCH-GENGER Ute]	Directeur de division Biophotonique, Bundesanstalt für Materialforschung und -prüfung (l'Institut Federal pour le recherche et les essais des materiaux), Berlin, Allemagne
[M. COGNET Laurent]	Directeur de recherche CNRS, université de Bordeaux

---

AUTRES MEMBRES DU JURY :

[M. CHARBONNIERE Loïc]	Directeur de recherche CNRS, université de Strasbourg

Preface

Fluorescence microscopy is an indispensable tool in biology, which allows direct visualisation of a plethora of structures and processes in organisms. In particular, single-molecule microscopy (SMM) is an especially powerful set of techniques for molecular and cell biology. It is based on attachment of light-emissive luminophore moieties to biological molecules or their assemblies and allows visualizing their movement, probing their interactions, or precisely pinpointing their location with high resolution. However, SMM has strict requirements towards the utilized luminophores, especially concerning the homogeneity of their luminescence, resistance against light and chemical degradation, and brightness.

Recently, a new luminophore called upconverting particles (UCNPs) gained attention of the research community due to their efficient emission of visible light upon excitation with infrared light. This property makes UCNPs a valuable luminophore for biological applications due to the elimination of autofluorescence background, commonly associated with regular visible light excitation. Extreme photostability of UCNPs and absence of sporadic photoswitching are also valuable for SMM experiments.

The objective of this thesis was to adapt UCNPs to SMM applications, with the ultimate goal of exploiting their unique properties towards superior performance of SMM experiments.

As this project is highly multidisciplinary, an ample amount of introduction is provided for the fields of fluorescence microscopy in biology, SMM, and UCNPs. Readers who are thoroughly familiar with either of these fields are advised to skip the corresponding parts of the introduction.

The main results of the work are presented in two published research articles about UCNP-dye FRET and UCNP dissolution in water, and one article manuscript under development about single-particle tracking of UCNPs. Each article is provided with a brief preface that summarizes the work performed in it and provides the context for the work relative to the thesis project.

Table of contents

Acknowledgements

This work is the largest project I have undertook so far in my life, one that will leave many memories and that has given me a lot of experience in multiple fields of research I wouldn't even think I would work in.

I would like to thank my supervisor, Prof. Yves Mely, for providing me the opportunity to pursue my studies in Strasbourg. Yves is one of the brightest people I have ever met, and his skillful management, multidisciplinary knowledge and relentless optimism have successfully guided this project towards its objectives. My thanks to Dr. Frederic Przybilla, with whom I have worked together for more than three years, and who is one of the best coworkers I have ever had pleasure to work with. Fred's deep knowledge of optics and can-do attitude were immensely helpful during these years.

I would like to thank the jury members Dr. Ute Resch-Genger, Dr. Laurent Cognet and Dr. Loïc Charbonniere for accepting my request to evaluate this work.

I am grateful to Dr. Guy Duportail for his advice and guidance during my first years in France, to Dr. Andrey Klymchenko, Dr. Mayeul Collot, and Dr. Andreas Reisch for their insights in all fields of chemistry and nanoparticles, to Dr. Ludovic Richert, Dr. Pascal Didier, Dr. Julien Godet, Dr. Romain Vauchelles and Dr. Philippe Carl for their help with microscopy, to Dr. Nicholas Humbert, Dr. Halina Anton, Dr. Manuel Boutant and Dr. Eleonore Real for sharing their knowledge of biology. My thanks to Marlyse Wernert, Ingrid Barthel and Michel Morciano for providing the infrastructure and help.

I am thankful to our collaborators, Dr. Thomas Hirsch and (now both also Drs.) Verena Muhr and Markus Buchner. Thomas has provided us with a lot of fruitful discussions and deep insight into peculiarities of behavior of nanomaterials. I am grateful to Prof. Vasyl Pivovarenko, my former supervisor, for guiding my first steps in academic research, and to my school teacher Natalia Druzhinina, who has single-handedly propelled many other students and myself into the world of chemistry.

I thank all my colleagues from the Laboratory of Biophotonics and Pharmacology, for being an endless source of help, discussions, great moments and good memories. Sasha, Lesia, Iryna, Vasia, Marianna, Bogdan, Taras, Redouane, Rajhans, Katya, Yevgen, Manu,

Kamal, Krishna, Yosuke, Hassan, Waseem, Faisal, Tanveer, Doriane, Anne, Nina, Dima, Caterina, Kyong, Lilia, Tania, Sylvie, Raphael, Maaz, Vanille, and everybody.

I would like to thank my family and my friends in Ukraine and abroad, for providing me with support during these years.

Finally, I would like to thank Ecole Doctorale des Sciences de la Vie et Sante, especially Melanie Muser and Geraldine Schverer, for providing me with support and the financial backing to pursue my PhD project, and Campus France and Ministere de la Recherche for providing me with the Eiffel Scholarship, which has started this journey.

Thank you all!

--Alex

List of abbreviations

AFM – atomic force microscopy
APD – avalanche photodiode
CCD – charge-coupled device
CMOS – complementary metal oxide semiconductor
DCM – dichloromethane
DIPEA – diisopropylethylamine
DLS – dynamic light scattering
DNA – deoxyribonucleic acid
DMF – dimethylformamide
DMSO – dimethylsulfoxide
ESA – excited state absorption
ETU – energy transfer upconversion
FTIR – Fourier transfer infrared spectroscopy
FLIM – fluorescence lifetime imaging microscopy
FRET – Förster resonance energy transfer
FWHM – full width at half maximum
GFP – green fluorescent protein
GNP – gold nanoparticle
IgE – immunoglobulin, type E
IR – infrared
LSFM – light sheet fluorescence microscopy
MSD – mean square displacement
MRI – magnetic resonance imaging
NA– numerical aperture
NHS – N-hydroxysuccinimide
NIR – near-infrared
NMR – nuclear magnetic resonance
NP – nanoparticle
NSOM – near-field scanning optical microscopy
OA – oleic acid
PA – photon avalanche
PAFP – photoactivated fluorescent protein
PAINT – point accumuation for imaging in nanoscale topography
PALM – photoactivated localization microscopy
PDT – photodynamic therapy
PEG – polyethyleneglycol
PMT – photomultiplier tube
PTT – photothermal therapy
PSF – point spread function
QD – quantum dot
QY – quantum yield
RBL-2H3 – rat basophilic leukemia, line 2H3
RhB – rhodamine B
RNA – ribonucleic acid
ROI – region of interest
SIM – structured illumination microscopy
smFRET – single-molecule Förster resonance energy transfer
SHG – second harmonic generation
SMM – single-molecule microscopy
SMLM – single-molecule localization microscopy
SNR – signal-to-noise ratio
SOFI – super-resolution optical fluctuation imaging
SPM – spectral precision microscopy
SPT – single-particle tracking
STED(M) – stimulated emission depletion (microscopy)
STORM – stochastic optical reconstruction microscopy
TCSPC – time-correlated single photon counting
TEM – transmission electron microscopy
TIRF(M) – total internal reflection (microscopy)
TTA – triplet-triplet annihilation
TTET – triplet-triplet energy transfer
TPA – two-photon absorption
UC – upconversion
UCNP – upconversion nanoparticle
UCQY – upconversion quantum yield
UV – ultraviolet
XRD – X-ray diffraction

The best that most of us can hope to achieve in physics is simply to misunderstand at a deeper level.

– Wolfgang Pauli

Chapter 1. Bibliographical review.

Part 1. Fluorescence microscopy.

1.1.1. Basics of optical microscopy.

Since its invention in the XVII century, the optical microscope remains an indispensable tool in physics, chemistry and especially life sciences. The ability to directly see the microstructure of living objects has yielded over the centuries a plethora of information that led to numerous discoveries and breakthroughs in biology and medicine.

First, let us consider the naked human eye (Fig. 1.1.1.1A). This organ by itself already allows researchers to resolve objects down to ~100 μm in size in good lighting conditions (*Yanoff and Duker, 2008*). While its structure is quite complicated, from a purely optical point of view it can be reduced to four elements (Fig. 1.1.1.1B): a thin refracting layer (cornea), an aperture (pupil), a lens, and a liquid-filled reservoir. Together, these elements focus the image of the observed object onto the retina, a detector surface consisting of multiple types of photosensitive cells. Eye muscle contractions allow to change the shape of the lens to focus on closer or farther objects (*accommodation*), and also change the size of the pupil to increase or reduce the amount of light falling on the retina.

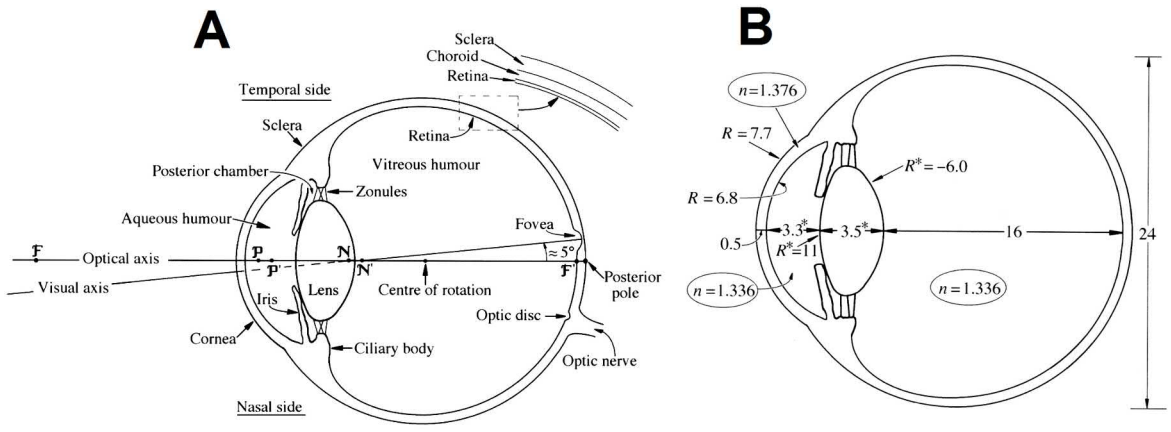

Fig. 1.1.1.1. A: Structure of a human eye, with the components labeled. B: Simplified optical system of a typical relaxed human eye. Distance and radii of curvature are given in millimeters. Starred values depend on accommodation. Image adapted from (Atchison and

Smith, 2000).

The relaxed human eye has a lower limit on the distance at which the object stays in focus ("near point", typically ~25 cm (*Hecht, 2002*)). Accommodation of the eye allows to view objects even closer, however even with accommodation there is still a lower limit on the distance at which objects stay in focus, after wahich the object's image becomes blurred and the fine details cannot be seen.

A simplest microscope can be built by putting a single lens in front of the human eye, known as *magnifying glass* (Fig. 1.1.1.2B). The angular magnification power (MA) of such a system is defined by the focal distance of a single lens (*f*) and the near point distance. In the case of the object being close to the lens it is equal to:

$$MA = (\ 25\ cm\ /\ f\ ) + 1 \qquad \textit{(Eq. 1.1.1.1)}$$

Imaging objects with a magnifying lens was perfected by Antonie van Leeuwenhoek in late XVII century, with reported magnification of up to ~125x using custom-made lenses, used for discovery of microorganisms. However, limits of human eyesight, issues with reliable production of such lenses, and difficulties in recording images from such setups ultimately required more advanced experimental setups than the magnifying glass.

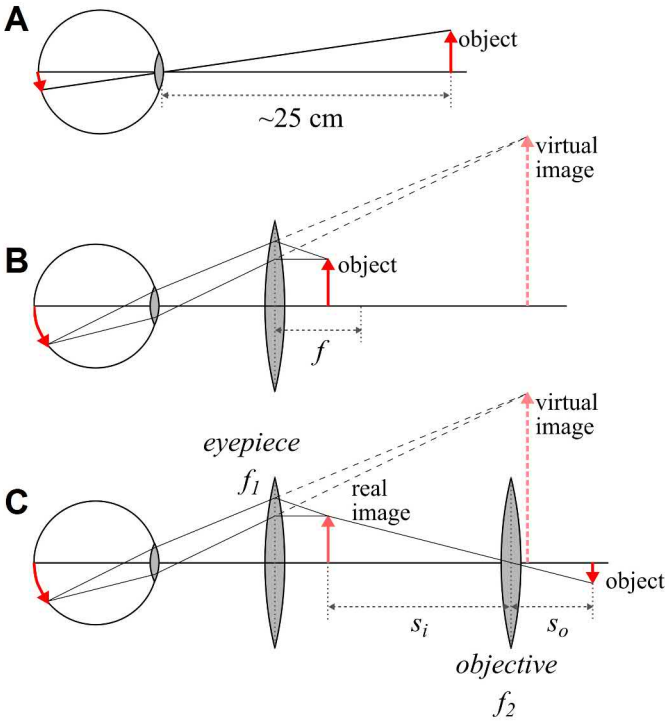

Fig. 1.1.1.2. Principles of image magnification by magnifying glass and a compound microscope. A: Formation of an image on the retina of a human eye. B: Formation of an image using a magnifying glass. C: Formation of an image using a compound microscope.

Adding a second lens into this system produces a *compound microscope* (Fig. 1.1.1.2C). The lens closer to the object is defined as *objective*, and the one closer to the eye is called an *eyepiece*. The magnification power of such system is defined as a product of magnification of an image by the objective and the eyepiece:

$$M = M_{objective}\, M_{eyepiece} = (\, s_i / s_o \,)(\, (25\ cm / f\,) + 1\,) \quad \textit{(Eq. 1.1.1.2)}$$

where s_i is the distance of the real image from the objective and s_o is the distance of the object from the objective (has to be higher than the focal distance of the objective).

This system allows for much higher magnification powers (>100x) and provides much more flexibility in regards to changing the magnification, imaging modality, etc. Also, both the objective and the eyepiece can be replaced by sets of lenses and other optical elements designed to correct for image distortions (*aberrations*) produced by manufacturing imperfections as well as fundamental physical effects, e.g. unequal refraction of different wavelengths of light.

Meanwhile, the size of the objective lens and its focal distance determine the *numerical aperture* (NA), a dimensionless value that characterizes the angle of the most tilted ray from the optical axis that can still be collected:

$$NA = n \sin \theta \quad \textit{(Eq. 1.1.1.3)}$$

, where n is the refraction index of the medium between the sample and the lens, and θ is the half-angle for the cone of light that can enter or exit the lens. Higher NA values allow to collect more light from the sample, but require the objective to be positioned closer to the sample.

After having passed through all optical elements of the microscope, light that carries information about the object is eventually perceived by the detector. There is a wide variety of detectors used in optical microscopy, ranging from the researcher's eye retina to point detectors like avalanche photodiodes (APDs), photomultiplier tubes (PMTs), to semiconductor detector arrays like CMOS and CCD sensors.

The response of the detector after collecting light is a sum of the following components:

- **Signal:** the value of the measurement which contains information about the sample.
- **Background:** the systematic error in the measurement. In microscopy, sources of background usually include stray light, uneven surface of optical components (e.g. dust or scratches), uneven response of the detector, and the response from out-of-focus parts of sample.
- **Noise:** the random error in the measurement. In microscopy, noise can arise due to imperfections in the experimental setup (e.g. electronic noise or thermal fluctuations in the detector) and fundamental phenomena (e.g. particle nature of light).

All in all, the aforementioned parameters ultimately define the performance of an optical microscopy experimental setup. It is typically expressed through the parameters that characterize its performance in regards to the information that can be extracted from the experiment:

- **Signal-to-noise ratio (SNR),** that describes the contrast between **t**he useful information-carrying *signal* and the useless *noise* in the measurement (Fig. 1.1.1.3A)**.** SNR characterizes the sensitivity of the setup and is defined as the ratio of signal amplitude to standard deviation of noise. High SNR is a desirable parameter. However, at high values, increasing SNR has diminishing (logarithmic) returns. The Shannon-Hartley theorem predicts that at high SNR values, increasing SNR by a factor of 10 increases the information content of the image by approximately a factor of 2 (*Shannon, 1949a; Cox and Sheppard 1986*).
- **Resolution,** that describes the minimum distance between two point sources of light at which they are distinguishable from one another. Increasing resolution gives more information about smaller features in the sample (Fig. 1.1.1.3B). The resolution depends on multiple parts of the microscopy setup, most notably the objective and the detector.
- **Readout time/imaging frequency** that describes the minimum time/maximum frequency at which the observation can be made. Lower readout time / higher imaging frequency gives information about fast processes in the sample. Readout time is usually synonymous to *exposure* – the amount of time the detector is open to

accumulate light, although in some experimental setups those parameters can be different. Per Nyquist-Shannon theorem, the imaging frequency should be at least twice as high as the frequency of the fastest process to be investigated (*Shannon, 1949b*).

These three parameters are locked in a tradeoff between each other. For example, consider a simple microscope setup consisting of two lenses and a detector array. Resolution can be increased by using a more finely divided detector array with more individual sensing elements. However, this means that each sensing element will collect less light due to its lower surface area, thus lowering the signal-to-noise ratio. One can then increase the readout time, illuminate the detector for longer amounts of time and compensate for loss in SNR. However, this will make the setup unable to resolve fast processes that happen during the readout time.

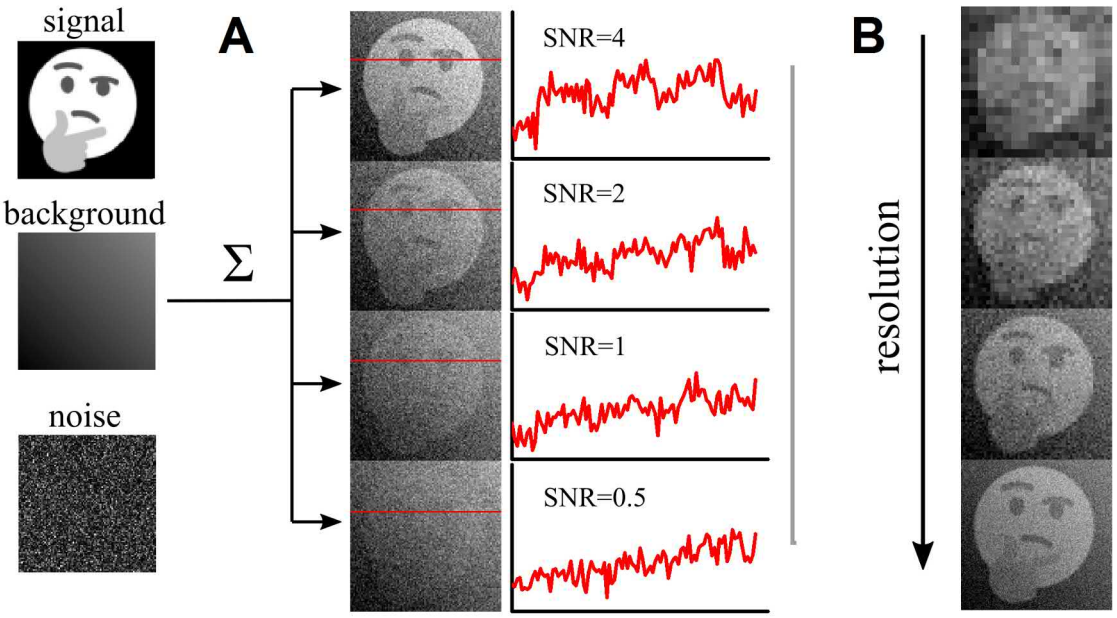

Fig. 1.1.1.3. Signal-to-noise ratio and resolution. A: A microscopy image is a sum of signal, background, and noise. With lower SNR, image quality becomes lower and the finer details eventually become indistinguishable from noise. Red graphs correspond to red-highlighted sections in corresponding images. B: with increase in resolution, smaller features and edges can be observed with more precision. Initial "signal" image adapted from Twitter, Inc.

Another very important aspect of optical microscopy is that at a certain point any further magnification does not improve the details in the image. This limit of resolution in conventional optical microscopy is known as the diffraction limit (Abbe limit). In brief, in an ideal optical system with a spherical objective lens, an infinitely small point source of light will yield a spherical wavefront entering the objective (Fig. 1.1.1.4A). As they exit the objective, the waves diffract on the objective aperture and eventually arrive at the image plane. Depending on the position in image plane, the wavefront may perform constructive or destructive interference, resulting in a formation of a distinct pattern with a central peak and multiple progressively weaker concentric circles around it, called an Airy pattern (Fig. 1.1.1.4B). The width of the peak depends only on the NA and the wavelength of light (λ) collected from the sample:

$$FWHM \approx 0.51\,\lambda / NA \qquad \textit{(Eq. 1.1.1.4)}$$

where *FWHM* is full width at half maximum of the peak. In practice, typical objectives used for biological imaging have NA values up to 1.4. This means that for green light (530 nm) the peak width would be roughly 190 nm. Thus, at a certain point, increasing the magnification of an objective stops improving the resolution, as point sources at a distance lower than the diffraction limit are indistinguishable (Fig. 1.1.1.4C). Also, in non-ideal systems, the resulting shape of a single-spot image can deviate from Airy pattern due to optical aberrations. The shape of the image of an infinitesimal single point source is generally known as instrumental point spread function (PSF). Overall, this effect is unfortunate for many biological studies, as a number of the features on molecular and cellular levels are smaller than the diffraction limit (Fig. 1.1.1.4D).

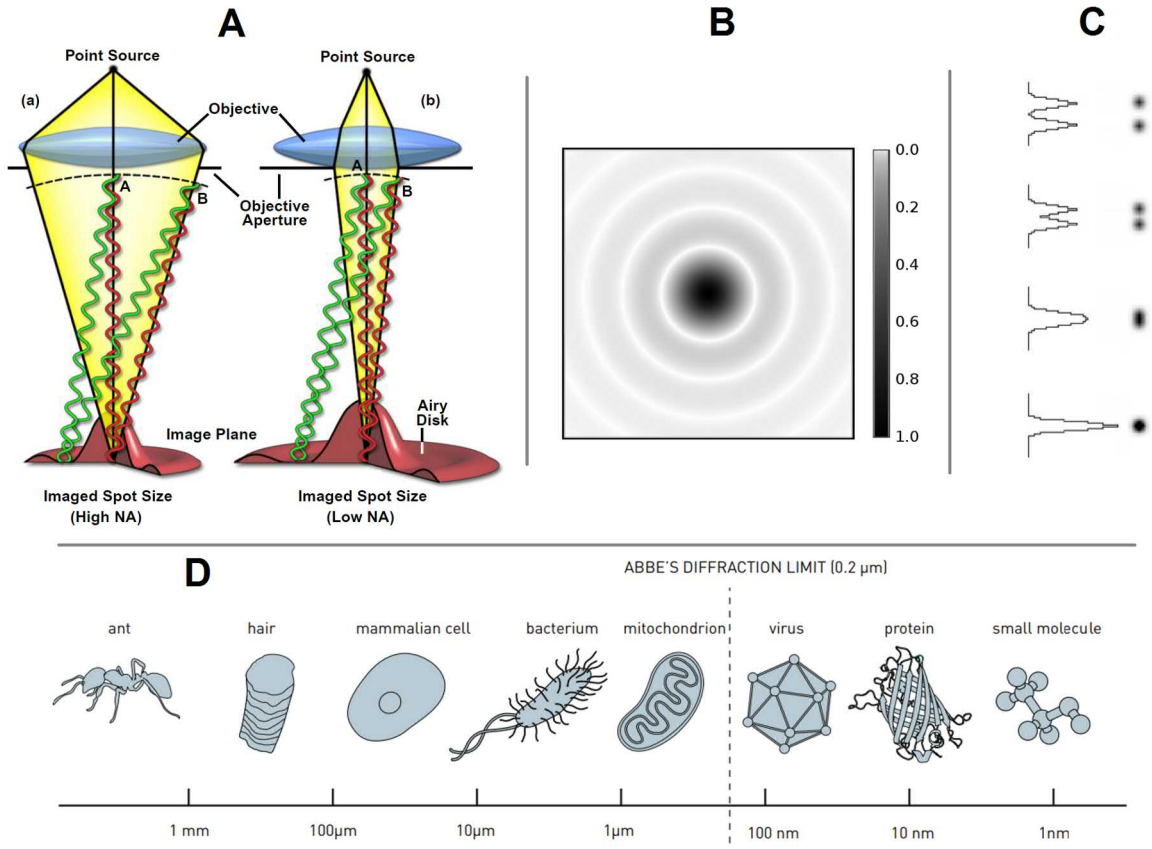

Fig. 1.1.1.4. Diffraction limit in optical microscopy. A: Formation of a point spread function on a 2D plane by objectives with high or low NA. B: Airy pattern. C: as two point sources come closer to each other, their Airy patterns start overlapping, preventing the possibility to distinguish them. D: Comparison of sizes of biological objects with Abbe limit (logarithmic scale). Images adapted from Nikon Instruments Inc., (Patterson, 2009) and Royal Swedish Academy of Sciences.

Nevertheless, for the larger features, optical microscopy remains one of the main tools in biologist's arsenal. It can be performed in a wide variety of modes. Light can be collected after being transmitted through the sample (bright-field microscopy), reflected from the sample (reflected light microscopy), after being scattered by the sample (dark-field microscopy), after being emitted by the sample (luminescence microscopy), etc. The illumination and collection pathways can be modified to observe the differences in rotation of light polarization by the sample (polarized light microscopy), the differences in phase shift when light passes through the sample (phase contrast and differential interference contrast

microscopy), the three-dimensional topology of the sample by simultaneously collecting light through two slightly angled optical pathways (stereomicroscopy), etc (*Murphy, 2002*).

Among this cornucopia of optical microscopy modes, one set of techniques has become particularly prominent in molecular, cellular and tissue biology over the last three decades. These techniques are called *fluorescence microscopy*, a subset of luminescence microscopy, in which the sample is illuminated by a high-energy, low-wavelength light and then reemits low-energy, high-wavelength light through a process known as fluorescence. The advantages of fluorescence microscopy for biological imaging include non-invasiveness, fast readout times, high contrast, resolution down to hundreds of nanometers (or even lower with certain techniques), ability to work both *in vitro* and *in vivo*, possibility to selectively label and image particular features of the specimen, extraction of microscale information and interactions within the specimen, and possibility for combination with other imaging modes or techniques (*Combs, 2010*).

1.1.2. Principles of fluorescence

As a phenomenon, fluorescence is a type of photoluminescence (emission of light by a material after absorption of light). There are multiple definitions of fluorescence. Most commonly, when referring to fluorescence, researchers mean "emission of light from excited singlet state of a molecule after light absorption in ground singlet state". In this context, the fluorescing molecule is called a *fluorophore*.

Fluorescence and other processes related to the electronic transitions from and to low excited states of molecules are usually represented together with their timescales via a Jablonski diagram (Fig. 1.1.2.1) (*Lakowicz, 2011*). The process of fluorescence starts from absorption of light from the ground singlet electronic state (S_0) of the fluorophore and its transition to one of the vibrational sub-levels of one of the excited singlet states (S_1 or S_2). This transition and the change of the shape of molecular orbitals occurs extremely quick (on the order of femtoseconds). This amount of time is too small for significant changes in the positions of atom nuclei. This is known as *Franck-Condon principle*. As the position of nuclei immediately after excitation usually does not match their equilibrium position for the new molecular orbital, the nuclei start moving to accommodate themselves to the new electronic structure. This process is known as *vibrational relaxation*.

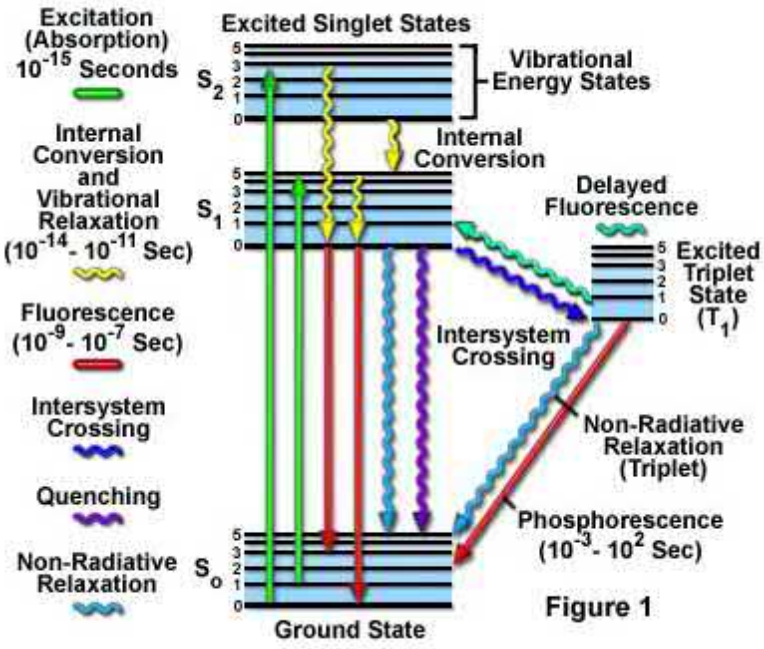

Fig. 1.1.2.1. Jablonski diagram and timescales of fluorescence and related processes. Figure adapted from the website of Florida State University.

From the S_2 state, the molecule performs a transition into a high vibrational sub-level of S_1 state through a process known as *internal conversion*. Afterwards, through vibrational relaxation, the fluorophore decays to the lowest sublevels of excited singlet state (S_1), with the energy transformed into vibrations of the molecule. From the S_1 state, the fluorophore can decay to one of the vibrational sub-states of the S_0 state, with the emission of a photon (*fluorescence*) or with dissipation of energy into vibrations of the molecule through internal conversion to high vibrational sub-levels of S_0 state. The fluorophore can also perform *intersystem crossing* – a transition to the excited triplet state (T_1), from which it then can relax to the ground state with emission of light (*phosphorescence*) or non-radiatively through internal conversion.

All of these processes have different, sometimes comparable timescales. One of the important parameters of fluorophores is fluorescence lifetime – the average time that the fluorophore spends in the excited state. Typical fluorescence lifetimes are ranged from 100 ps

to 100 ns. This time can be defined as the inverse of the sum of radiative and all non-radiative relaxation rate constants from the S_1 state:

$$\tau = 1 / (k_r + \Sigma k_{nr}) \qquad (Eq.\ 1.1.2.1)$$

Due to the losses associated with vibrational relaxation, the energy of the emitted photons is lower than the energy of absorbed ones. This difference between the wavelengths of absorption and emission is known as *Stokes shift* (Fig. 1.1.2.1B). The efficiency of the fluorescence process can be defined by *quantum yield* (QY) – the ratio of the quantity of emitted photons to the quantity of absorbed ones:

$$QY = N_{emitted} / N_{absorbed} \quad (Eq.\ 1.1.2.2)$$

As fluorophores are more prone to chemical reactions in excited state, eventually most fluorophores undergo irreversible chemical reactions, in a process known as *bleaching*. Conversely, the resistance of fluorophores to bleaching is termed *photostability*.

Absorption and emission wavelength ranges, fluorescence quantum yield, lifetime and photostability are the main parameters for any fluorescent molecule. A large variety of fluorophores exist and are being developed for a multitude of applications, including fluorescence microscopy.

Fluorescence microscopy can be done with biological samples without any labeling, through visualizing the natural fluorescence (autofluorescence) of certain molecules (e.g. tryptophan aminoacids in proteins, NADPH and some others) (*Billinton and Knight, 2001*). However, their fluorescence isn't particularly efficient and gives information only on their own localization. Thus, the objects to be visualised are typically selectively labeled with fluorescent labels and probes. Those include organic dyes, fluorescent proteins, fluorescent nucleosides, quantum dots and other nanoparticles. Labeling strategies for fluorescence microscopy are discussed more thoroughly in the part 1.2.4.

1.1.3. Brief overview of fluorescence microscopy techniques and modalities

There is a vast range of techniques and modalities for fluorescence microscopy for biological imaging, and new ones are still being invented today. The most distinct and well-known types of microscopy are described in this section, however this list is not exhaustive,

and most of these techniques can be combined and modified to produce unique imaging modalities.

Wide-field epifluorescence microscopy is the simplest and most popular technique used in biological imaging (Fig. 1.1.3.1). The microscopy setup for this mode involves illuminating the sample with excitation light through an objective and then collecting its fluorescence signal. A point of fundamental importance is the optical separation of the excitation and emission beams. Typically, such setups rely on interference filters, with the use of band-pass filters in conjunction with *dichroic mirrors* that can transmit light in a fixed range of wavelengths and reflect all other light. Excitation is typically performed either by filtering the light from a white lamp or using lasers, while emitted light is typically being detected by a digital camera.

Due to the ease of setting it up, fast readout frequencies (up to 100 frames per second dependent on the camera), simultaneous sampling of a large area (typically from 10x10 μm^2 upwards, although smaller areas can be imaged as well), and a number of possible modifications, epifluorescence microscopy remains one of the most prominent techniques in routine biological experiments. However, epifluorescence microscopy is limited by low signal-to-noise ratio and difficulty in observing the three-dimensional structure of the specimen due to collection of light from out-of-focus parts of the sample.

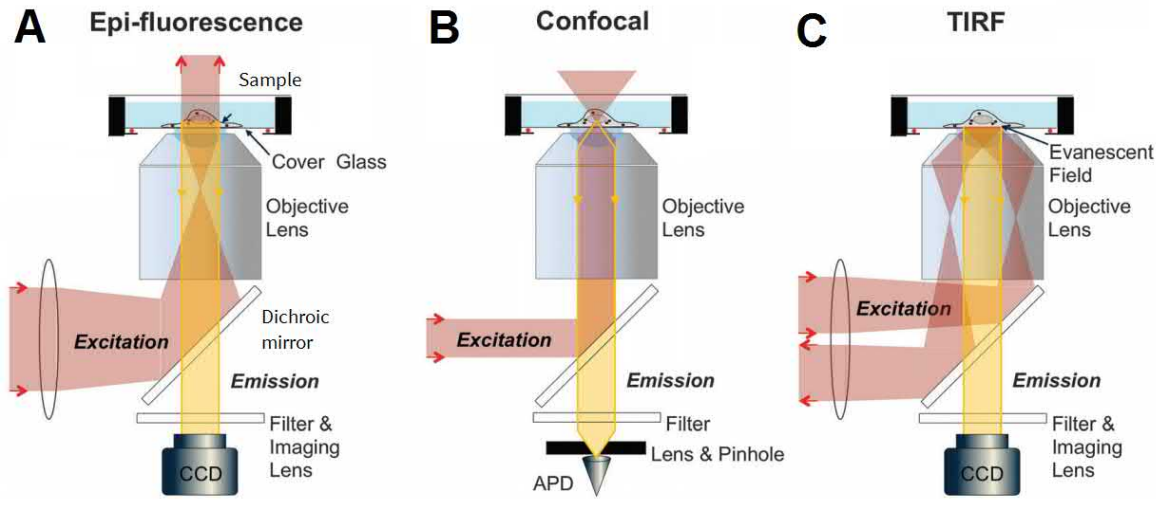

Fig. 1.1.3.1. Basic fluorescence microscopy illumination modes. A: Epifluorescence mode. B: Confocal microscopy mode. C: Total internal reflection. Image adapted from (Park et al.,

2015).

In **confocal microscopy** the excitation beam (typically a laser) is focused in a small spot in the sample. Fluorescence from the focal volume is collected by a point detector. In order to reconstruct an image, the focal point is scanned over the sample typically by deviating the excitation beam with galvanometric mirrors. Thus in contrast to wide field microscopy where one full field of view is snapped at a time, the image is collected pixel by pixel in the confocal geometry. The advantage of confocal microscopy stems from the presence of a pinhole positioned in front of the point detector (usually a photomultiplier tube, PMT, or avalanche photodiode, APD). As a result, only the light from the focal volume is being collected whereas all out-of-focus signal is being rejected (Fig. 1.1.3.1B).

Higher signal-to-noise ratio, ability to resolve finer details in the sample, the possibility to image thicker sections of a specimen, and large amounts of additional imaging modalities are the main advantages of confocal microscopy. However, scanning is usually slower than imaging with a camera, resulting in longer readout times than wide-field microscopy.

In **total internal reflection wide-field fluorescence microscopy (TIRFM)**, the excitation beam illuminates the sample with a sharp angle so that total internal reflection occurs at the interface between the thin coverglass (on which the sample resides) and the medium containing the sample (typically water or buffer). This reflection produces an *evanescent field*, which is a non-propagating electromagnetic field that concentrates the energy in the vicinity of the interface. Typically the excitation intensity close the surface can be increased by up to a factor of 4-6 (*Axelrod, 2001*) and it decreases exponentially away from the interface (characteristic thickness of ~100-300 nm). Fluorophores can interact with this field as they would with a regular electromagnetic wave; for example, they can absorb energy from it and subsequently fluoresce (Fig. 1.1.3.1C).

This mode of imaging allows selective excitation of fluorophores in very close proximity to the reflecting surface. This permits to perform wide-field microscopy with much higher signal-to-noise ratio due to the absence of out-of-focus background light. The main disadvantage of TIRFM is the inability to image fluorophores farther than ~1 μm away from glass surface.

Light sheet fluorescence microscopy (LSFM) uses a separate objective to illuminate a small section of the sample through its side by an excitation beam (*Voie et al. 1993*). A variety of beam shaping methods can be used for this purpose, most commonly passing the beam through a cylindrical lens. An example of a setup for LSFM is provided on Fig. 1.1.3.2.

LSFM allows to drastically reduce the background fluorescence coming from the sample, by avoiding illuminating the parts of the sample that are not in focus. This facilitates imaging of three-dimensional structure of the sample. Reducing the amount of incident light also has the advantage of reducing *phototoxicity* – damage of the biological sample by light-induced chemical reactions. However, LSFM has higher instrumental setup costs and requires more calibration compared to epifluorescence setups.

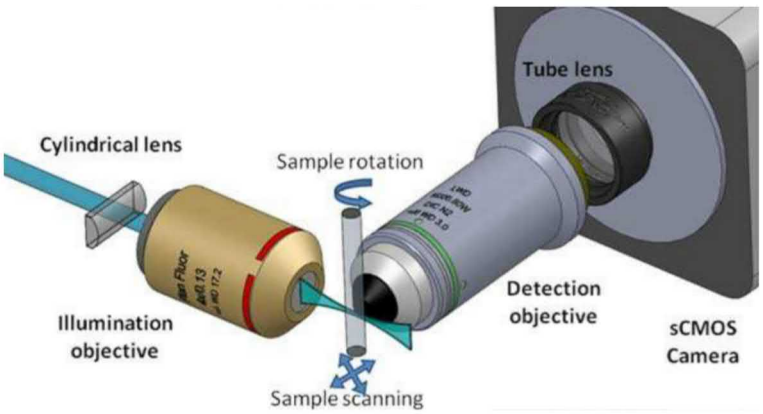

Fig. 1.1.3.2. An example of a setup for light sheet fluorescence microscopy. Image adapted from (Gualda et al., 2017).

In **near-field scanning optical microscopy (NSOM)** (*Synge 1928; Ash and Nicholls 1972*) the excitation and collection pathways are coupled to an optical fiber with a very small exit aperture (<1 μm), which is positioned on a controllable piezoelectric scanning stage very close to the sample, at distances lower than a single wavelength of light (Fig. 1.1.3.3) In these *near field* conditions an evanescent field is formed in the immediate proximity of the fiber aperture, and can excite the sample. Correspondingly, the evanescent field produced by the fluorescing sample can then get detected back through the same optical fiber. By scanning the surface of the sample with the optical fiber probe, an image can be reconstructed.

The regular laws of diffraction do not apply to evanescent fields. Thus, the key advantage of the NSOM is the ability to improve the image resolution past the diffraction barrier and achieve what is known as *super-resolution imaging*, a feat that is not achievable by aforementioned conventional microscopy techniques. Also, NSOM allows correlating the physical topology of the sample with its luminescence. The major disadvantages of NSOM are its inability to access the deeper parts of the sample, costly instrumental setups, long scanning times, and its potential to influence and/or damage the sample due to a very small working distance.

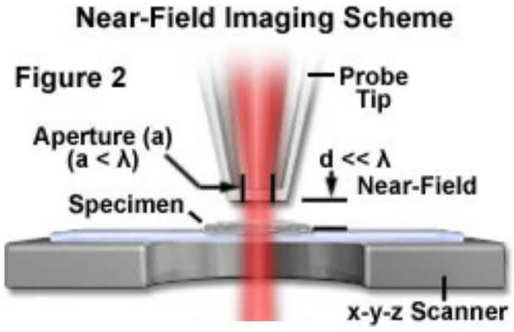

Fig. 1.1.3.3. Near-field optical microscopy. Image adapted from Olympus Corporation website.

Structured illumination microscopy (SIM) techniques involve an uneven excitation beam forming an uneven illumination pattern on the sample with a defined structure (typically a grid) (Fig. 1.1.3.4 A). High-frequency features in the sample lost in conventional microscopy form Moire patterns with the illumination profile and can be recovered (Fig. 1.1.3.4 B). By acquiring a sequence of images by rotating the excitation pattern by small incremental steps it is possible to recover many spatial frequencies (and henceforth, finer details). Moire patterns are very sensitive to phase and/or angle shift and their changes can be easily resolved. By processing the set of images, the fluorescent structures can be resolved with higher precision (typically down to ~150 nm) (Fig. 1.1.3.4 C, D) (*Gustafsson et al., 2008*).

The main advantage of this method is achievement of super-resolution, usually lowering the diffraction limit by a factor of ~2 compared to conventional microscopy. However, it

needs complicated experimental setups with multiple potential sources of error, longer readout times compared to wide-field microscopy and computation-intensive post-processing steps, complicating investigation of the fast processes in the sample.

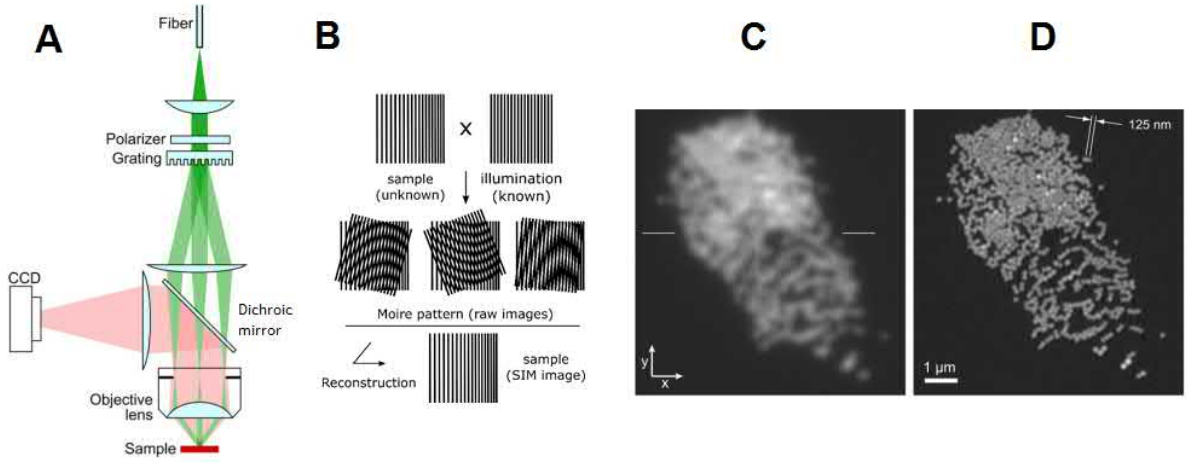

Fig. 1.1.3.4. Structured illumination microscopy. A: an example of a SIM setup. B: Principle of reconstruction. C and D: a regular wide-field microscopy image and a SIM reconstruction of the same sample of fluorescent spheres. Images adapted from (Gustafsson et al., 2008) and the website of Andor Technology Ltd.

Stimulated emission depletion fluorescence microscopy (STED) is based upon *stimulated emission,* a fundamental phenomenon where a photon can interact with a fluorophore in excited state, forcing it to emit another photon (*Hell and Wichmann, 1994*). STED operates in a confocal configuration, but requires a second laser beam, with a doughnut-shaped PSF that is superimposed with the excitation beam. The wavelength of the so-called depletion beam is chosen in such a way that it forces the fluorophores to relax to ground state through stimulated emission. Therefore only the fluorophores in the middle of the depletion doughnut remained excited and their fluorescence can be collected afterwards. The net result of this process is a reduction of the effective excitation volume (Fig. 1.1.3.5).

By scanning the sample with a smaller excitation PSF, super-resolution imaging can be achieved, providing unique information about the fine structure of the sample with a much simpler setup compared to NSOM. The disadvantage of STED is the high excitation power required for stimulated emission, leading to fast bleaching of fluorophores and high phototoxicity in live samples.

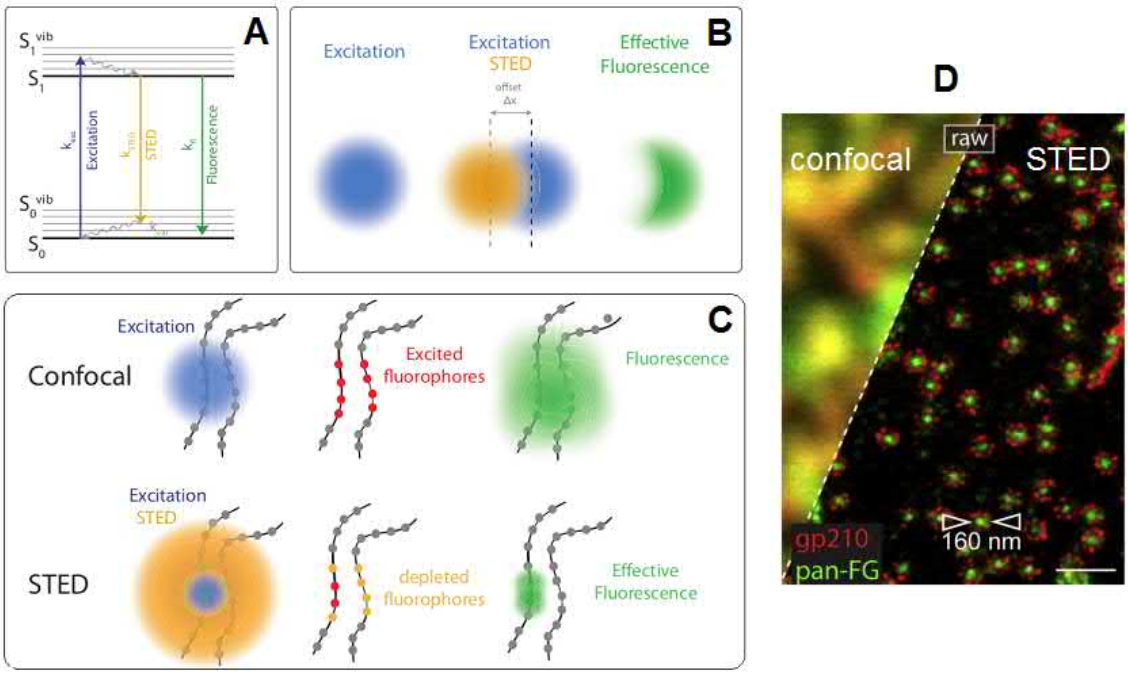

Fig. 1.1.3.5. STED microscopy. A: Simplified Jablonski diagram for the case of STED. The transition from S_1 to S_0 state can be induced (stimulated) if the excited molecule is illuminated with light at a correct wavelength. B: STED can be used to decrease the effective fluorescence PSF. C: Principle of STED microscopy with a doughnut depletion profile. A smaller effective excitation PSF can excite fluorophores in a small region and make them distinguishable from their nearby neighbors. D: Example of two combined STED images of nuclear pore complexes. STED allows to resolve the spatial configuration and directly visualize the stoichiometry of protein complexes (Göttfert et al., 2013). Images adapted from (Göttfert et al., 2013) and Scientific Volume Imaging, b.v.

Another type of super-resolution microscopy, **single-molecule localization microscopy (SMLM)** and its variations, is more thoroughly discussed in part 1.2.1.

The importance and necessity of super-resolution techniques was underlined by the 2014 Nobel Prize in Chemistry awarded to Hell, Betzig and Moerner for their development of STED, SMLM and PALM/STORM. SMLM and PALM/STORM are described in much higher detail in Part 2.

For some of the aforementioned techniques, the excitation and detection pathways can be modified to observe particular behaviors of fluorophores. Frequently these modifications are performed in confocal microscopy mode, as it allows a lot of flexibility due to the simplicity of its collection pathway.

In **multichannel imaging**, the dichroic mirror, filters and/or excitation sources are sequentially changed during imaging. This allows to observe the response of several different types of fluorophores in the same sample. The method can be modified to be performed simultaneously, by splitting the collection beam with a dichroic mirror and passing the separate beams through a set of filters, and collecting them afterwards by multiple detectors (or a single detector split in several parts). A subtype of multichannel imaging, *ratiometric imaging* observes the different spectral responses of the same fluorophore dependent on its interactions with the sample. In a similar fashion, in **spectral imaging** the collection pathway contains a diffraction grating or another dispersive element that allows to spatially separate the emission with different wavelengths. By using a line of detectors (or by moving the dispersive element), the emission spectrum can be reconstructed (*Zimmermann et al. 2003*).

In **two-photon imaging**, the excitation is performed by pulsed lasers (typically femtosecond laser) with high peak intensity and a long wavelength, usually in red or near-infrared region. Under high excitation intensity, molecules can undergo a nonlinear process called *two-photon absorption* (TPA), in which they are excited to the S_1 state by simultaneous absorption of two photons. While the process is very inefficient, its high dependency on illumination intensity ensures excitation only in the center of the focused beam. Also, biological samples are more transparent to long-wavelength light, allowing deeper penetration for tissue imaging. The disadvantage of this imaging mode is mainly associated with the high cost of the experimental setup and inefficiency of TPA process, requiring quite high excitation powers, which can be detrimental to the sample and/or fluorescent labels.

In **fluorescence lifetime imaging microscopy (FLIM)**, a short-pulsed excitation source is used. Fluorophores exhibiting different lifetimes will fluoresce at different delay after excitation, which can be measured by using time-gated detection, time-correlated single photon counting (TCSPC) or phase-modulation techniques. This can be used to reconstruct a spatial map of fluorophore lifetimes in the sample (*Becker, 2012*).

1.1.4. Biological applications of fluorescence microscopy

In modern biology and medicine, fluorescence microscopy techniques are an indispensable tool. Frequently microscopy is performed with *chemically fixed* samples, in which the whole sample is permeated with chemical agents (commonly formaldehyde or glutaraldehyde) that link and polymerize the proteins in the sample to make it resistant to short-term degradation while retaining its microstructure. This procedure results in a solid or gel-like specimen that can be imaged for extensive periods of time. Some fluorescent microscopy techniques are adapted to work in living specimens, although those usually have more stringent demands to the experimental setup.

On the **tissue level**, fluorescence microscopy is performed typically in experiments investigating the structure of the tissue. For this, the tissues are stained with fluorescent labels which are selectively uptaken into specific types of cells. As fluorescence microscopy allows to observe multiple labels with different excitation and emission spectra, different types of cells or extracellular elements can be stained. This allows to investigate overall morphology of the tissue, differences between tissues exposed to different conditions, relative quantities of different cells in tissue, and many more parameters. Imaging can be performed either on thin tissue sections, thicker tissue slabs, or even living organisms (Fig. 1.1.4.1). As light scattering and out-of-focus background adversely affect the image quality, usually confocal and two-photon techniques are preferred for tissue imaging.

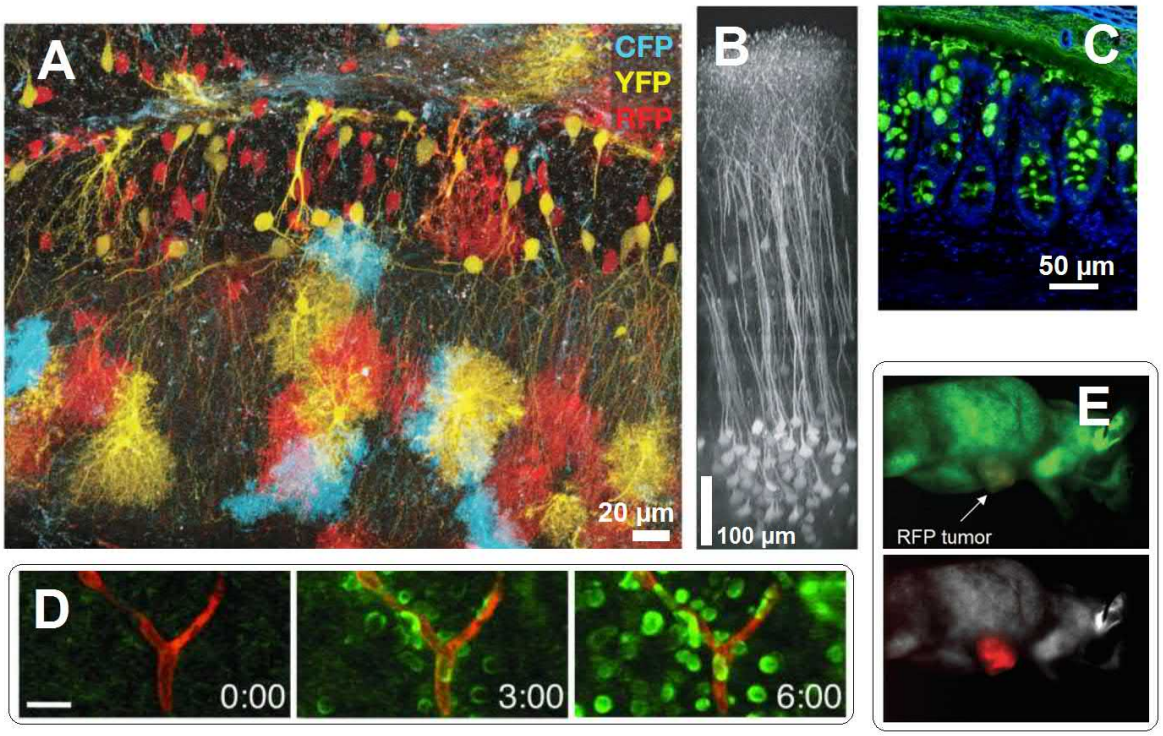

Fig. 1.1.4.1. Examples of tissue imaging. A: Confocal microscopy image of a section of a fixed section of dental gyrus of mouse brain from a mouse stochastically expressing red, yellow and cyan fluorescent proteins (so-called "Brainbow" strategy) (Livet et al., 2007). B: Two-photon microscopy image of the neocortex of a living mouse expressing a fluorescent protein (Helmchen and Denk, 2005). C: confocal microscopy image of a fixed section of mouse distal colon, with a protein (Muc2, green) labeled by a fluorescent antibody and DNA (blue) labeled by an organic dye, DAPI (Ermund et al., 2013). D: Time-lapse two-photon microscopy of Hoechst dye permeation into nuclei (green) of salivary glands of a live rat. Vasculature was highlighted by Texas Red-dextran injected systemically. E: Full-body imaging of a green fluorescence protein (GFP) expressing mouse with a red fluorescent protein (RFP) expressing tumor (Ntziachristos et al., 2005). Images are adapted from corresponding references.

On the **cellular level**, fluorescence microscopy is used for observing the structure of the sample and its internal interactions. Simplest cell experiments involve labeling of organelles or specific biomolecules to observe their cellular localization and elucidate their function (Fig. 1.1.4.2A). Multiple dyes emitting in separate spectral regions can be used for *colocalization*

experiments, which can shed light on interactions between different biomolecules (Fig. 1.1.4.2B). Fluorescent probes that change their response according to their local environment can be used to elucidate the spatial structure of the internal parameters of the sample like local analyte concentration, hydrophobicity, and many other properties (*Johnson, 2010*) (Fig. 1.1.4.2C).

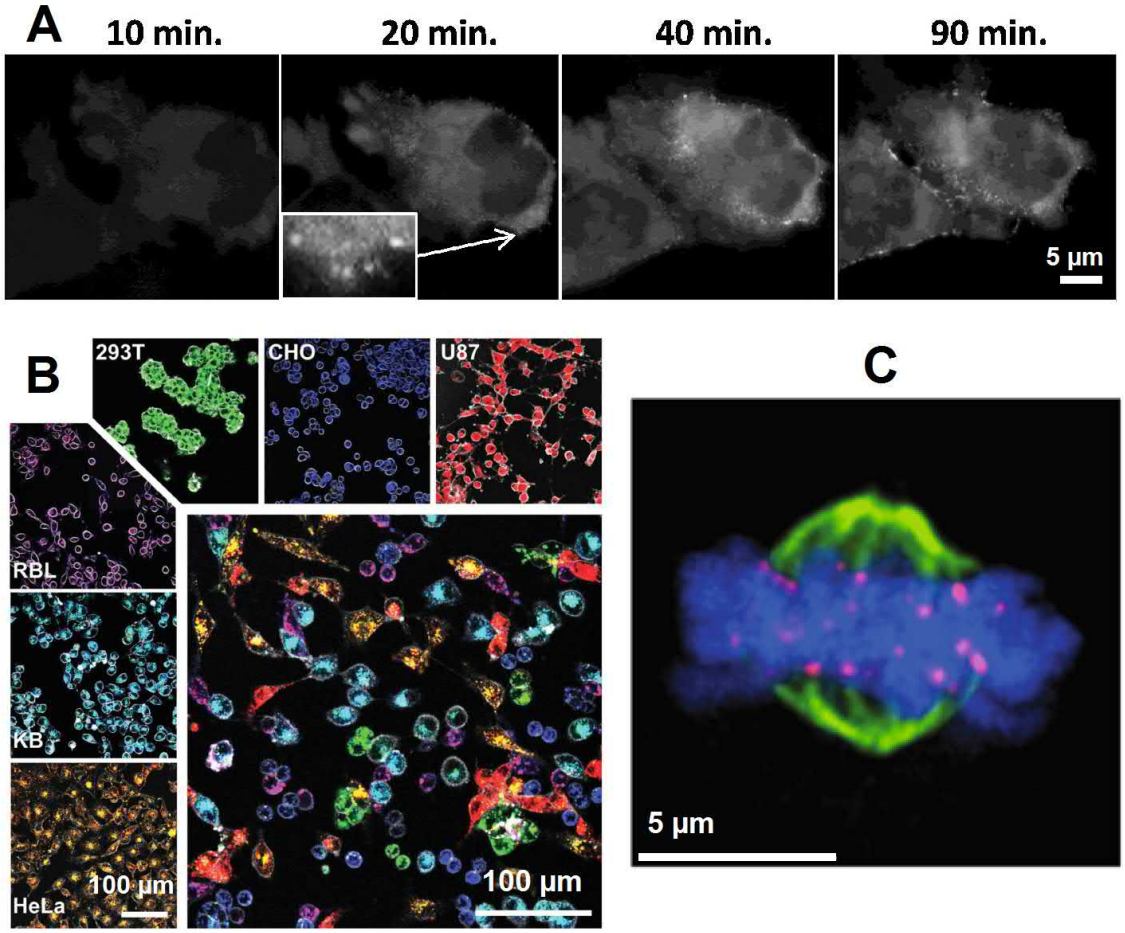

Fig. 1.1.4.2. Examples of cell imaging. A: Wide-field time-lapse microscopy of self-assembly of Gag, a HIV-1 protein, in live HeLa cells microinjected with DNA encoding a mixture of Gag and Gag with GFP tag (El Meshri et al., 2015). B: Confocal microscopy image of a co-culture of multiple mammal cell lines pre-labeled with fluorescent nanoparticles with different spectral responses (shown in pseudocolor) (Andreiuk et al., 2017). C: Confocal microscopy of tubulin (green), DNA (blue) and CREST protein (red) in a dividing cell (Shrestha et al., 2017). Images are adapted from corresponding references.

On the **molecular level**, fluorescence microscopy is primarily used to observe inter- or intramolecular interactions of biomolecules. This typically involves observation of the response of individual environment-sensitive fluorophores coupled to individual biomolecules. Depending on the interactions of the biomolecules, the fluorophores can change their positions, brightness, spectral response, lifetimes (e.g. through various energy transfer processes), fluorescence anisotropy, or other luminescence parameters. This permits to elucidate the mechanisms by which the biomolecules perform their functions.

The molecular-level fluorescence microscopy experiments usually involve observation of individual fluorophores. Such techniques are dubbed single-molecule microscopy techniques, or SMM.

Part 2. Single-molecule microscopy techniques (SMM).

1.2.1. Single-molecule localization microscopy (SMLM)

In a labeled sample, the diffraction limit precludes distinguishing fluorophores that are close to each other. There are several methods (Rayleigh, Abbe and Sparrow) to quantify this limit (Fig. 1.2.1.1 A). All three are based on the width of the PSF for a microscopy setup, which is an Airy pattern in the idealized case.

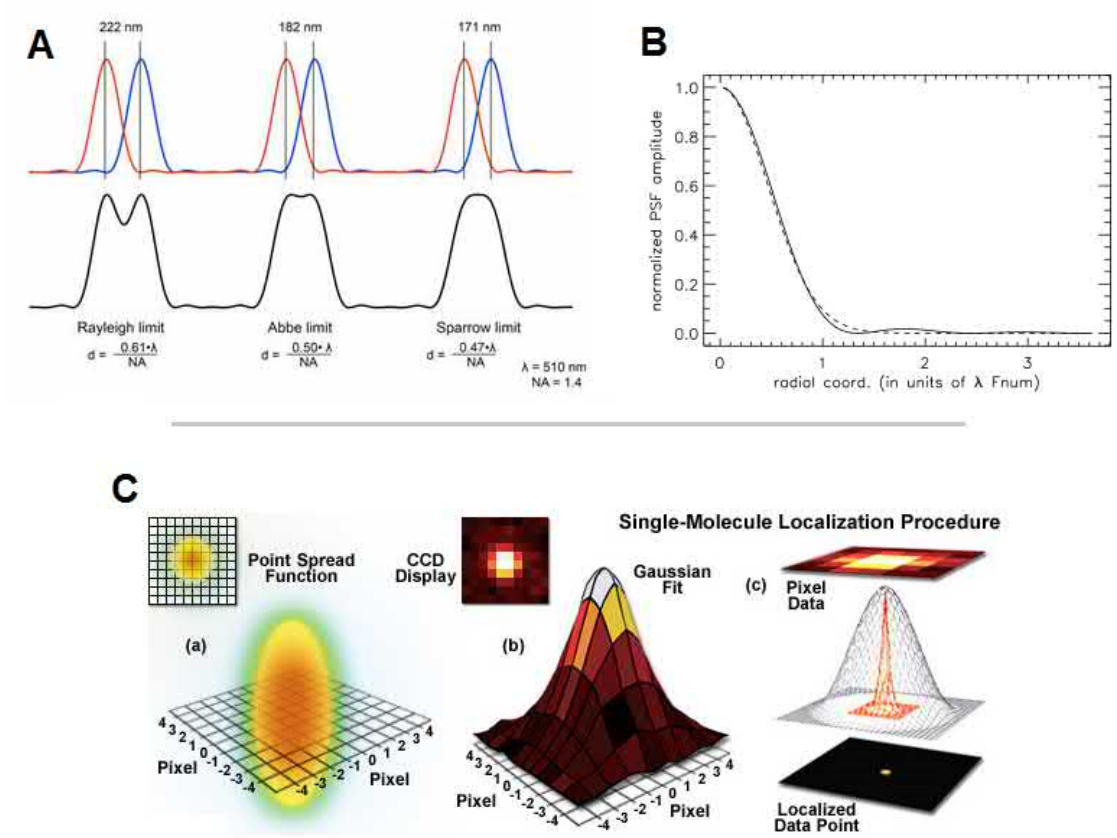

Fig. 1.2.1.1. Distinguishing separate fluorophores. A: Rayleigh, Abbe and Sparrow limits. B: Comparison of the shape of the Airy disk PSF and the Gaussian fit of its central peak. C: Single-molecule localization procedure. An image of the PSF in presence of noise is fitted by a Gaussian curve. By finding the center of the peak, the precise position of the fluorophore can be found. Images adapted from the website of the University of Utah ("Super-Resolution Tutorial - Education - Advanced Microscopy," n.d.), Wikimedia Foundation and Florida State University ("ZEISS Microscopy Online Campus | Introduction to Superresolution

Microscopy," n.d.).

However, if a single fluorophore is observed with no other fluorophores in its vicinity, its position can be derived much more precisely. This is known as *localizing* the fluorophore (Bobroff 1986,). The simplest way to do it is finding the position of the peak maximum, either by finding the center of mass of several bright pixels (*centroid*) or by fitting the peak with a Gaussian curve, which is a very good first approximation for the main peak in the Airy pattern (Fig. 1.2.1.1 B). This concept is core for single-molecule localization microscopy techniques (SMLM), which achieve super-resolution imaging by separating the response of individual, single fluorophores (Fig. 1.2.1.1 C).

To localize individual fluorophores that are in close proximity to each other, there are several possible approaches:

- Distinguish their luminescence spectrally. A sample can be labeled with several fluorophores with identical labeling specificity, but different spectral response. If two labels with different spectral response are close to each other, the intensity profile of their combined emission peaks will look differently through different emission filters. This is the base for techniques called spectral precision microscopy and spectral precision distance microscopy (SPM and SPDM, Fig. 1.2.1.2) (*Cremer et al., 2011*). This approach works best at moderate labeling densities. With a high labeling density there is a high probability that two labels with the same spectral response will be close to each other.

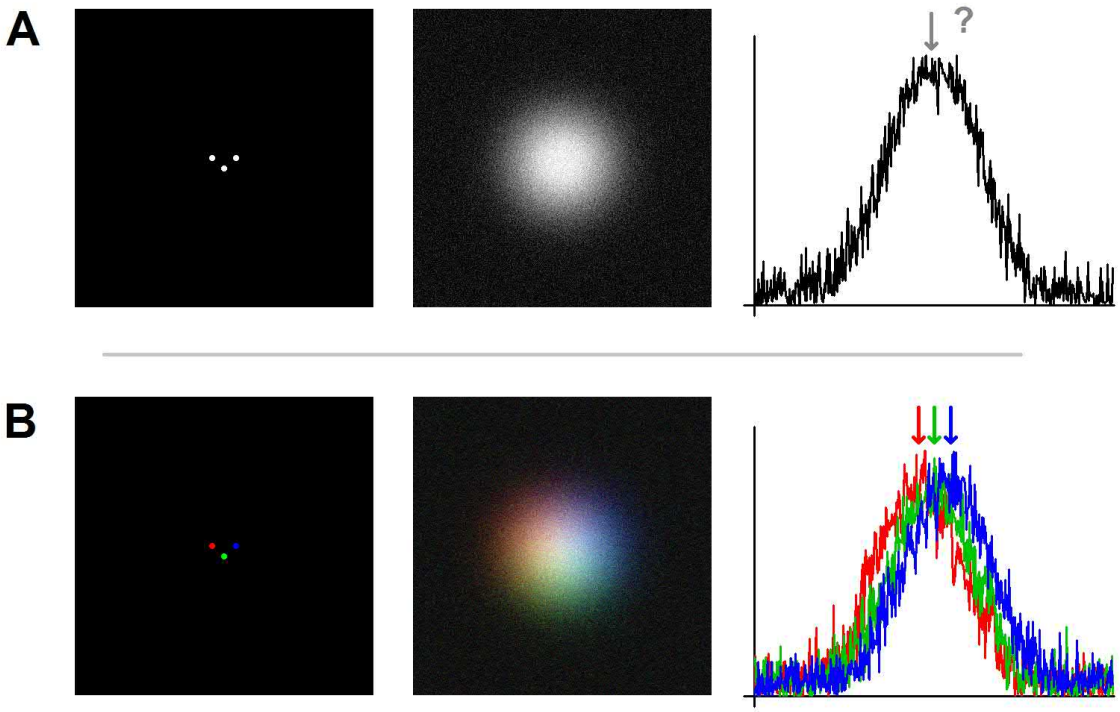

Fig. 1.2.1.2. Principle of SPM. A: Three fluorophores are located in close proximity. Even at very high magnification, their PSFs overlap too strongly for the positions to be resolvable. B: Three fluorophores with different spectral signatures are located in close proximity. If they are imaged on a multichannel microscope with good band separation, emission belonging to different fluorophores can be separated, and the fluorophores can be localized.

- Distinguish their luminescence temporally. If two neighboring fluorophores perform emission sequentially, their positions can be extracted from the images where only one of them is emitting. Taking multiple images (making a video) yields a high probability of capturing the positions of multiple individual fluorophores with high precision. This is a base for techniques known as stochastic super-resolution microscopy (Fig. 1.2.1.3) (*Hell et al., 2015; Patterson et al., 2010*). This approach trades the readout time for resolution improvement; thus, stochastic super-resolution techniques are best used for immobile samples, or samples where only sufficiently slow processes are imaged. Also, special fluorophores have to be used, that can either spontaneously or controllably be switched on and off.

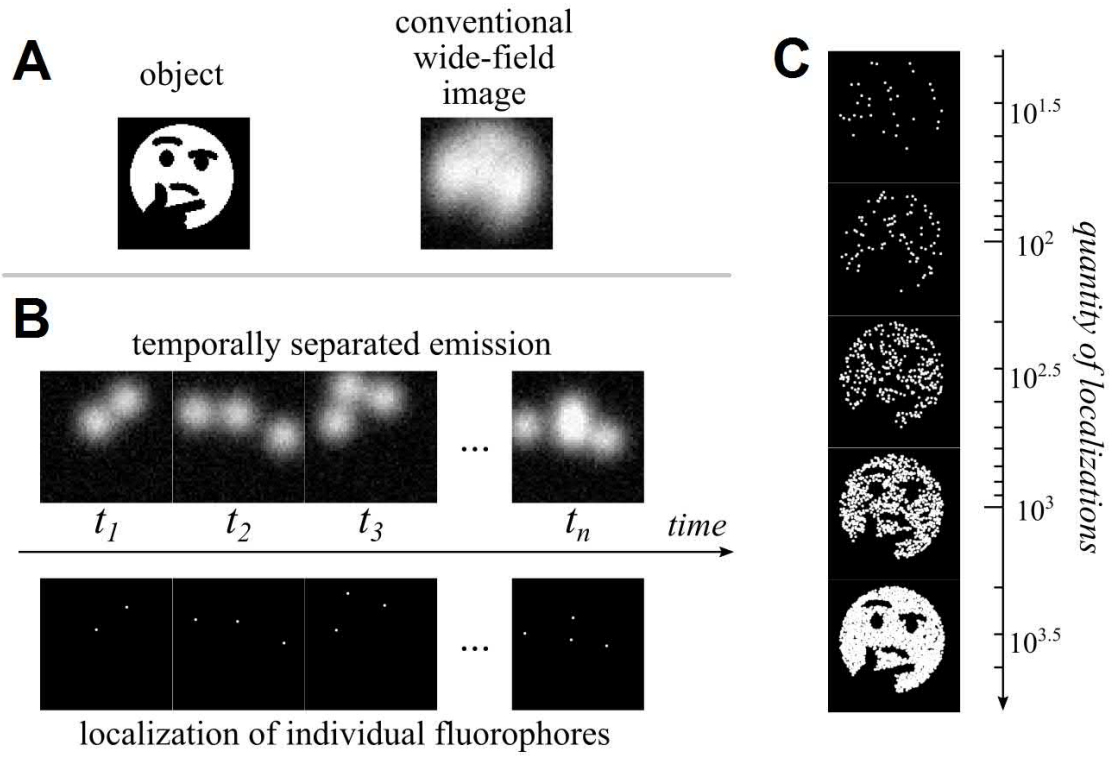

Fig. 1.2.1.3. Principle of stochastic super-resolution microscopy. A: An object is stained by fluorophores. If the wide-field image of the object is taken, the fluorescence PSFs from individual fluorophores overlap, and the finer features in the object become unrecognizable. B: If only a few fluorophores emit at the same time, they can be precisely localized. This can be repeated multiple times to accumulate a lot of fluorophore positions. C: By combining together the accumulated localizations, the object can be reconstructed. More localizations yield more information about the features in the object.

- Distinguish their luminescence fluctuations. If two identical labels exhibit a fluctuating fluorescence intensity, the shape of their combined intensity peaks will fluctuate slightly over time. From the autocorrelation of the combined peak intensity profile, the fluorophore positions can be located. This is the base for a method called super-resolution optical fluctuation imaging (SOFI, Fig. 1.2.1.4) (*Dertinger et al., 2009; Girsault et al., 2016*). The advantage of this method relies on its lower instrumental requirement and the ability to work with samples even when the

PSFs of the emitters heavily overlap. Its disadvantages include a low resolution improvement factor (usually about 2) and the potential formation of artifacts.

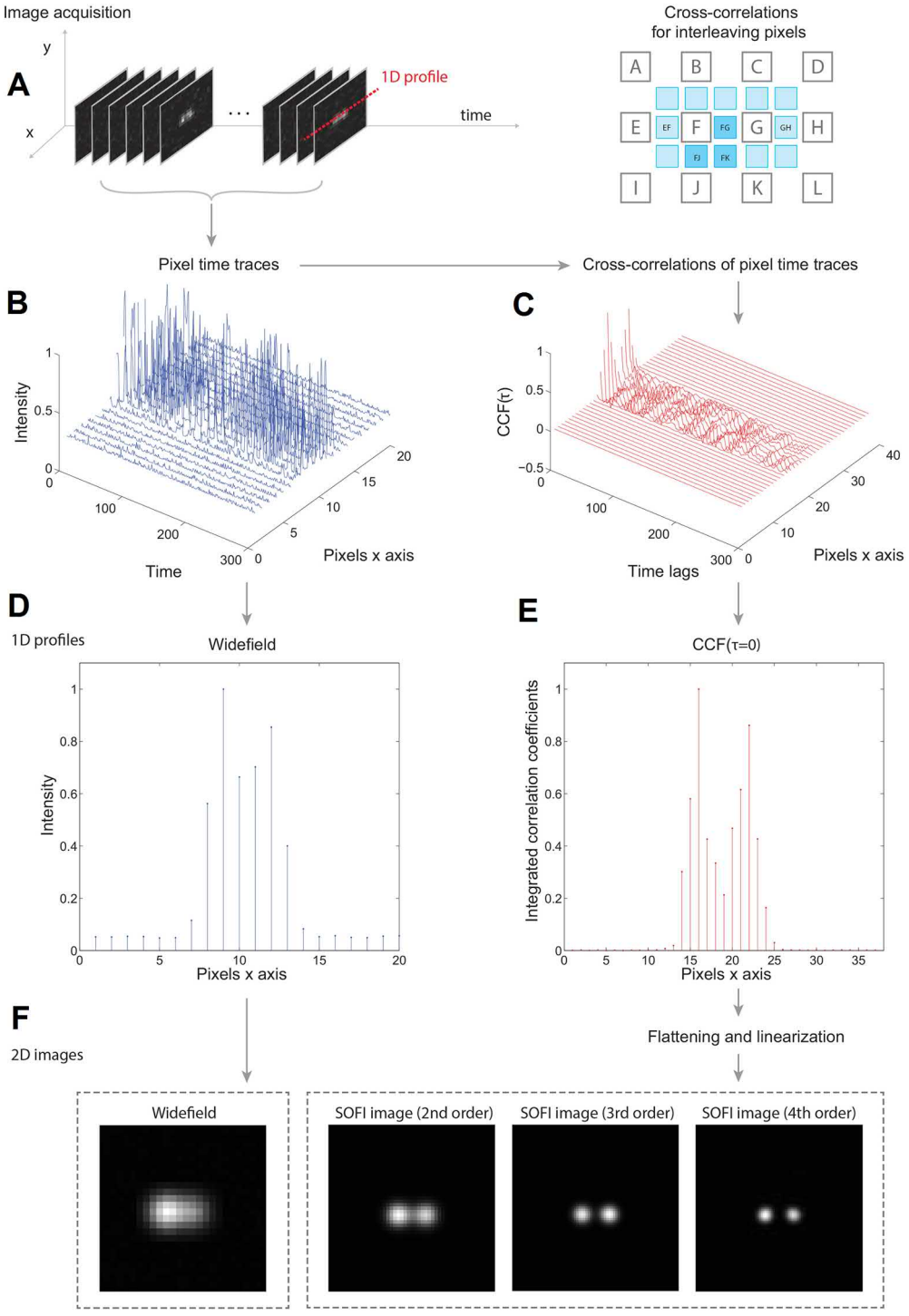

Fig. 1.2.1.4. Principle of SOFI. A: a wide-field video is taken, and the images are upscaled, with extra virtual pixels corresponding to cross-correlations of interleaving pixels. B: Time

trace of a 1D profile of the upscaled video. C: Cross-correlation function with different time lags for the 1D profile. D and E: Comparison of the average 1D profile and the cross-correlation 1D profile at zero time lag. F: Average wide-field image and its comparison with reconstructed images calculated from cross-correlations. The order of cross-correlation functions yields the SOFI image of respective order. Image taken from (Girsault et al., 2016).

- Mix the aforementioned approaches to yield more information and thus improve the resolution. For instance, SPM can be combined with stochastic super-resolution to achieve a further increase in resolution (*Zhang et al., 2015*).

In SMLM, the second (stochastic) approach is by far more common due to lower requirements for instrumental setups and higher reliability. Commonly several methods are distinguished for achieving temporal separation of fluorophore emission:

- **Photoactivated localization microscopy (PALM)**. In PALM, photoactivatable fluorescent proteins (PAFPs) are used. By themselves, these proteins fluoresce inefficiently. However, upon absorption of short-wavelength light (typically with wavelength of ~400-500 nm), they perform a chemical reaction which transforms them into a highly fluorescent molecule. Using a short burst of UV light, only a few fluorophores can be activated in the sample, with high probability of being spatially well-separated. Afterwards, fluorescence microscopy is performed and their positions are localized. Then, if the reaction is irreversible, the excitation is left on until these fluorophores are photobleached; otherwise, the fluorophores are switched back into non-emissive form (if the reaction is reversible). These three steps are repeated to sequentially localize all fluorophores in the sample and reconstruct its structure (Fig. 1.2.1.5) (*Betzig et al., 2006; Hess et al., 2006; Sengupta et al., 2014*).

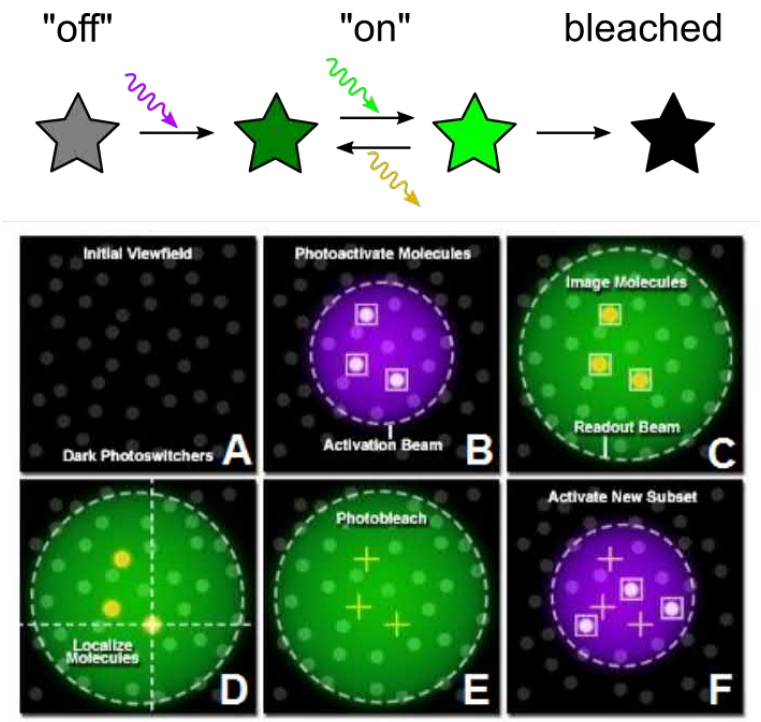

Fig. 1.2.1.5. Principle of PALM. A PAFP in "off" state can be transformed (photoactivated) into a fluorescent "on" state by absorbing high-energy light. After multiple cycles of fluorescence, it eventually photobleaches. A: A sample contains multiple PAFPs. B: Using a short pulse of high-energy light, a few PAFPs can be activated. C: Their fluorescence can be then observed as in usual wide-field microscopy. D: PAFPs are localized and their positons are recorded. E: After a period of illumination PAFPs eventually photobleach. F: a new subset of PAFPs can then be activated to repeat the process. Image adapted from Carl Zeiss AG website.

The main advantage of PALM is the usage of fluorescent proteins, which allows to generate fluorophores intrinsically in cells, typically by transfecting cells with plasmids encoding the target protein together with the PAFP. The usage of fluorescent proteins is also a disadvantage, as cell transfection protocols can be quite cumbersome, capricious and expensive compared to staining/washing protocols used with organic dyes.

- **Stochastic optical reconstruction microscopy (STORM)**. STORM and PALM are essentially the same technique, however STORM is performed with photoswitchable

organic dyes instead of fluorescent proteins. There is a large variety of photoswitchable dyes with multiple photoswitching mechanisms available (Fig. 1.2.1.6). A frequently used approach, direct STORM (dSTORM) utilizes *blinking*, the natural stochastic transitions of fluorophores into a non-emissive triplet state, which can be modulated by adding oxidation and/or reduction agents in the solution (*Linde et al., 2011; Rust et al., 2006*).

The advantage of STORM lies in the wide variety of available dyes and labeling approaches, allowing for a lot of flexibility in the experimental design.

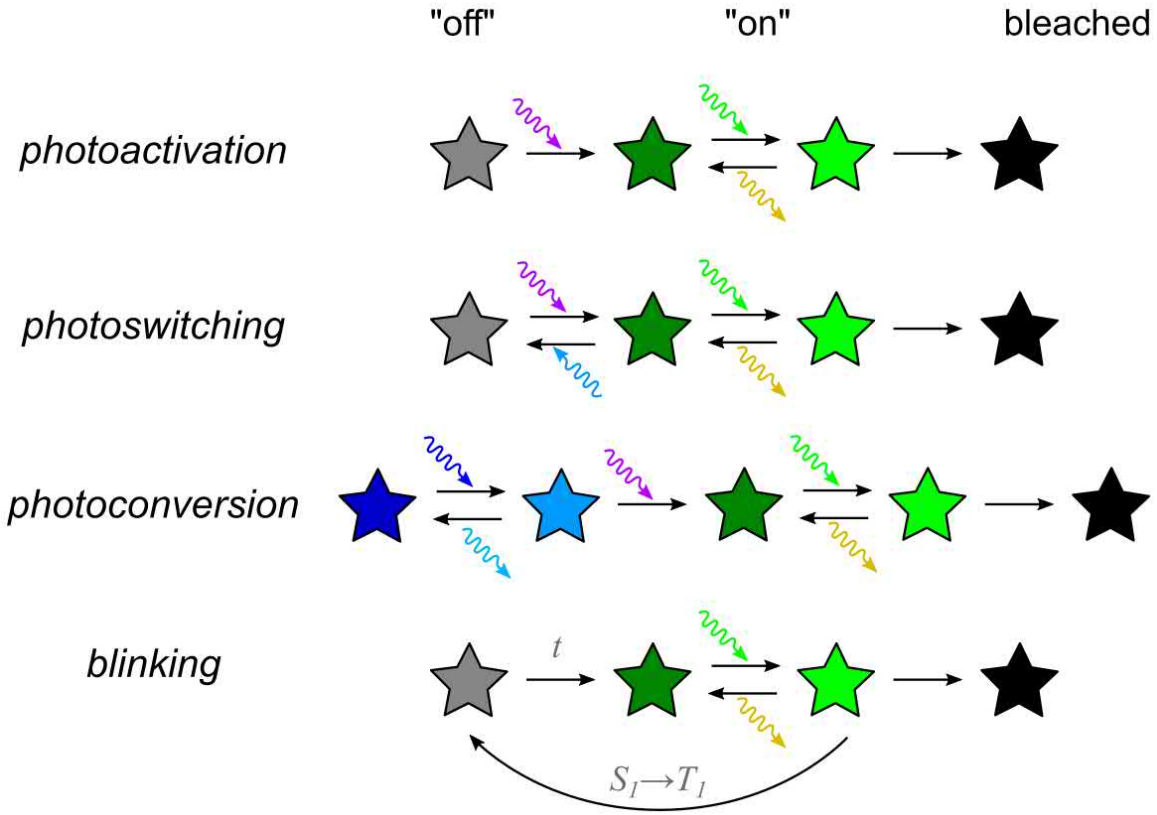

Fig. 1.2.1.6. Examples of mechanisms of dye switching for STORM. In photoactivation, the dye can be irreversibly changed to a fluorescent form by absorbing high-energy light. Photoswitching is the same process, however it can be reversible. In photoconversion, the "off" state is also fluorescent, but with different excitation and emission wavelengths compared to "on" state. In blinking, the dye spontaneously undergoes transition from excited singlet state to a long-lived intermediate non-fluorescent triplet state, and eventually returns to ground state over time. The rate of blinking can be changed by controlling the excitation

intensity and adding reduction/oxidation reagents in the system.

- **Point Accumulation for Imaging in Nanoscale Topography (PAINT)**. In PAINT, special organic fluorophores (*fluorogenic probes*) are used that bind to their targets selectively yet reversibly, and exhibit fluorescence only upon binding to the target. This leads to sporadic, transient fluorescence events in the sample, yielding temporal separation required for SMLM (Fig. 1.2.1.7) (*Sharonov and Hochstrasser, 2006*).

  PAINT is the easiest of the approaches for temporal-separated SMLM, and is the most straightforward to set up and troubleshoot. The disadvantage of PAINT is the requirement for reversible binding, limiting selectivity for certain biological targets.

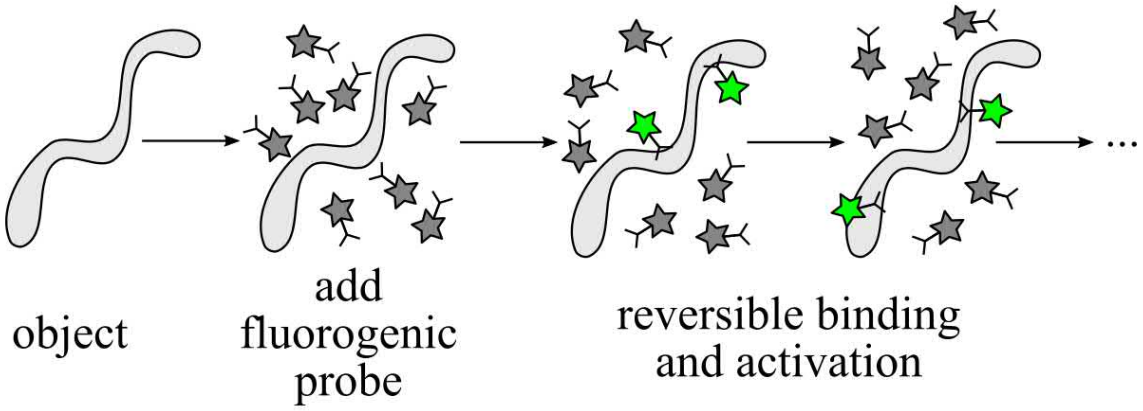

Fig. 1.2.1.7. Principle of PAINT. The fluorogenic probes are added to the object and diffuse around it, reversibly binding to it. The fluorogenic probe becomes fluorescent only upon binding, thus only a few probes are fluorescent at any given moment.

Frequently, SMLM requires resolving fluorophores in three dimensions (3D). For this, the experimental setup can be modified by implementing elements that change the PSF of detected emission. A simplest way to do this is by adding a cylindrical lens in the detection pathway, which induces *astigmatism*, a type of optical aberration where rays propagating in perpendicular planes have different foci. If the original PSF was a circular spot, the resulting PSF will be elliptical, elongated horizontally or vertically dependent on the emitter's position relative to the focal plane (Fig. 1.2.1.8) (*Huang et al., 2008b*). Its ellipticity contains quantitative information about the distance from the focal plane. Advanced techniques for 3D

SMLM use special phase masks that reshape the PSF to maximize the range of distances, precision and accuracy of such measurements (Fig. 1.2.1.9) (*Sahl and Moerner, 2013*).

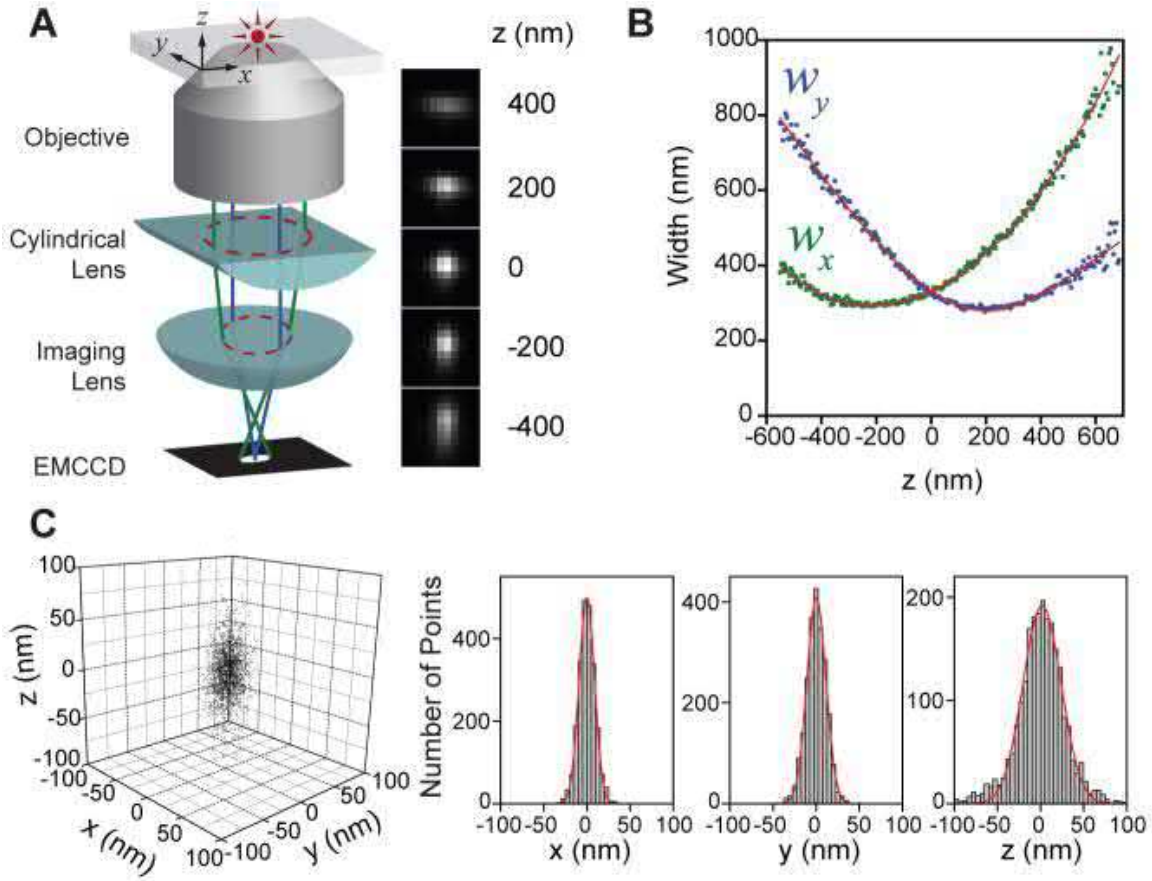

Fig. 1.2.1.8. Three-dimensional fluorophore localization via an astigmatic collection pathway. A: The collection pathway of the microscope includes a cylindrical lens. This forms an elliptically shaped PSF with ellipticity that depends on the axial (z) position of the fluorophore. B: Calibration curves obtained by imaging immobilized fluorophores on a flat surface with a known offset from the surface plane. w_x and w_y correspond to lateral width of the elliptical Gaussian-fitted spot. C: Localization distribution for individual molecules with the astigmatic setup. Note that axial resolution is lower than the lateral resolution. Image adapted from (Huang et al., 2008b).

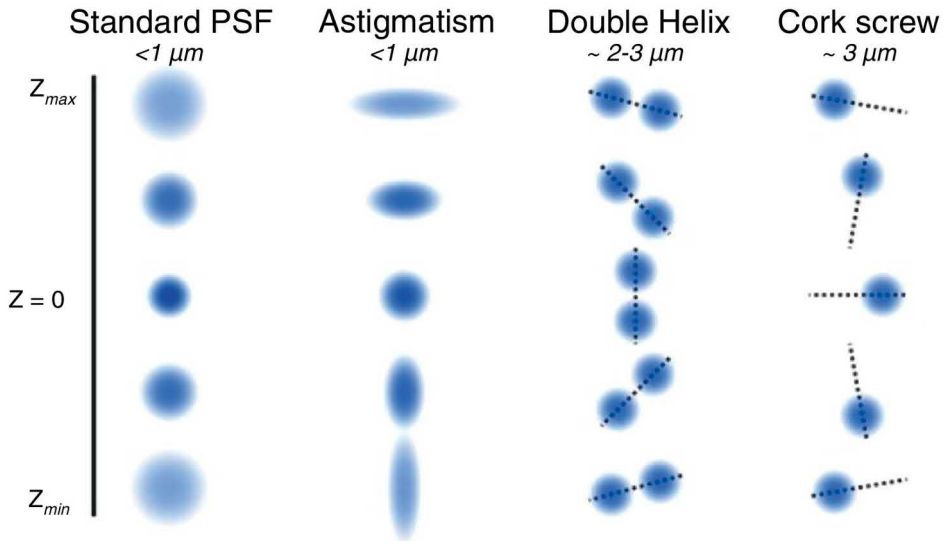

Fig. 1.2.1.9. Comparison of typical PSFs for 3D localization microscopy. Image adapted from (Sahl and Moerner, 2013).

An important parameter in SMLM is *localization error,* which describes the estimated average deviation of the position of the detected fluorophore from its actual position ("ground truth"). This parameter is sometimes also called localization accuracy or localization precision. For the simple case of a circular Gaussian PSF fitted by the least-squares method, the squared localization error can be calculated as (*Mortensen et al., 2010*):

$$\sigma_{LS}^2 = \frac{s^2 + a^2/12}{N}\left(\frac{16}{9} + \frac{8\pi\left(s^2 + a^2/12\right)b}{Na^2}\right) \qquad \textit{(Eq. 1.2.1.1)}$$

where N is the number of detected emitter photons, s the standard deviation of the fitted 2D Gaussian peak, a the pixel size, and b the photon background (approaching zero in a well-isolated system).

To summarize, SMLM allows precise localization of individual molecules in the sample, often with localization error as little as ~20-30 nm. Experiments involving SMLM include localization and colocalization of proteins and nucleic acids in cells, investigation of geometry of protein complexes, etc (Fig. 1.2.1.10) (*Huang et al., 2008a; Löschberger et al., 2012; Xu et al., 2012*). The majority of experiments is done with fixed samples due to low

readout times; however, in recent years there have been multiple advancements in protocol adaptation to live cell imaging (Fig. 1.2.1.11). Since its inception, SMLM became one of the best methods for investigating the structure and topology of cells and organelles, allowing unsurpassed imaging resolution and contrast, while using relatively simple experimental setups.

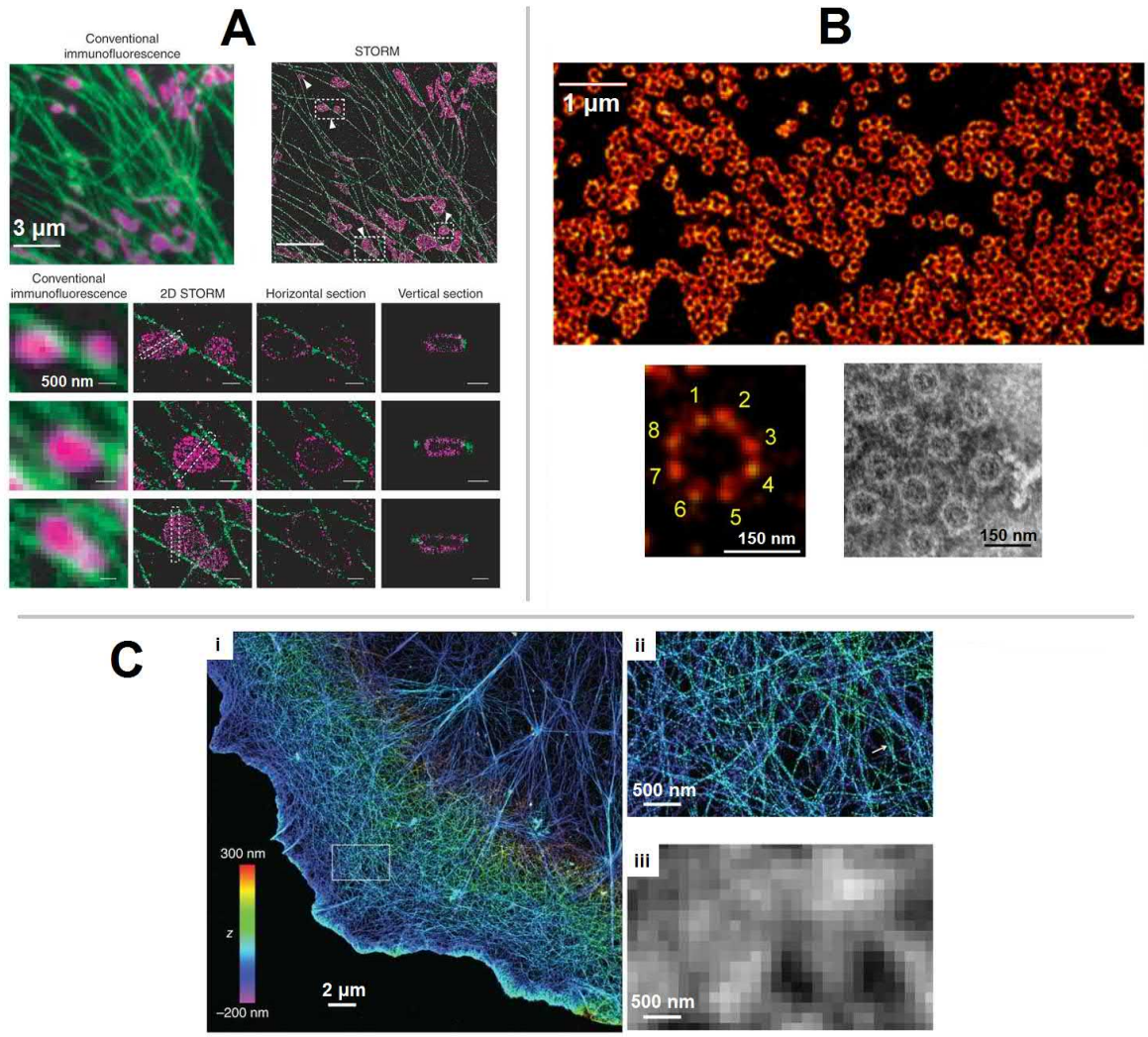

Fig. 1.2.1.10. Examples of SMLM applications. A: Comparison of conventional wide-field fluorescence and STORM images of mitochondria (magenta) and microtubules (green) (Huang et al., 2008a). B: dSTORM images of gp210 membrane protein in African clawed frog oocytes, and comparison of resolution and contrast with electron microscopy of the same sample (Löschberger et al., 2012). C: (i) Full-cell imaging of actin cytoskeleton with dual-

objective 3D STORM. (ii) Close-up of boxed region. (iii) Conventional wide-field image of the boxed region (Xu et al., 2012). Images adapted from the respective references.

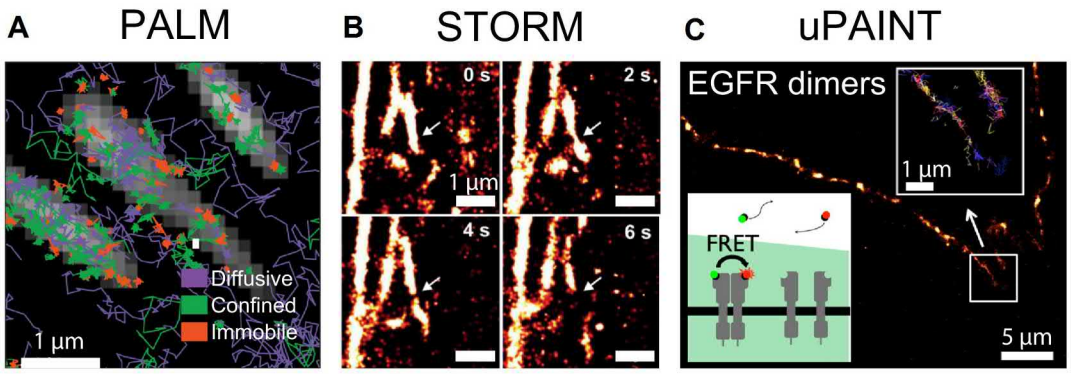

Fig. 1.2.1.11. Examples of live-cell SMLM applications. A: numerous single trajectories of β3-integrin fused with mEOS2, obtained on a single MEF cell with PALM, revealing that β3-integrin undergoes slower free-diffusion inside focal adhesions (gray) than outside (Rossier et al., 2012). B: spatial dynamics of cortical actin skeleton stained with Lifeact-HaloTag/ATTO655 (Wilmes et al., 2012). C: live cell super-resolution imaging of membrane epidermal growth factor receptor (EGFR) dimers based on single-molecule fluorescence resonance energy transfer induced by fluorescent ligand activation. Inset shows referential cell-edge localization of EGFR dimers (Winckler et al., 2013). Image and references adapted from (Godin et al., 2014).

1.2.2. Single-molecule Förster Resonance Energy Transfer (smFRET)

Förster Resonance Energy Transfer (FRET) is a type of nonradiative energy transfer between two fluorophores. The excited fluorophore giving the energy is called a *donor*, and the receiving one is called an *acceptor*. For FRET, three conditions are necessary (Fig. 1.2.2.1) (*Förster, 1948; Lakowicz, 2011*):

1. The energies of donor emission and acceptor absorption must match.
2. Donor and acceptor must be at a close distance to each other, typically <10 nm.
3. Donor and acceptor must be at a proper angle relative to each other. *Transition dipoles* are defined as the difference in dipole moment vectors between ground and excited

state. For FRET, the transition dipoles of donor and acceptor must be non-perpendicular, achieving maximum efficiency in parallel orientation.

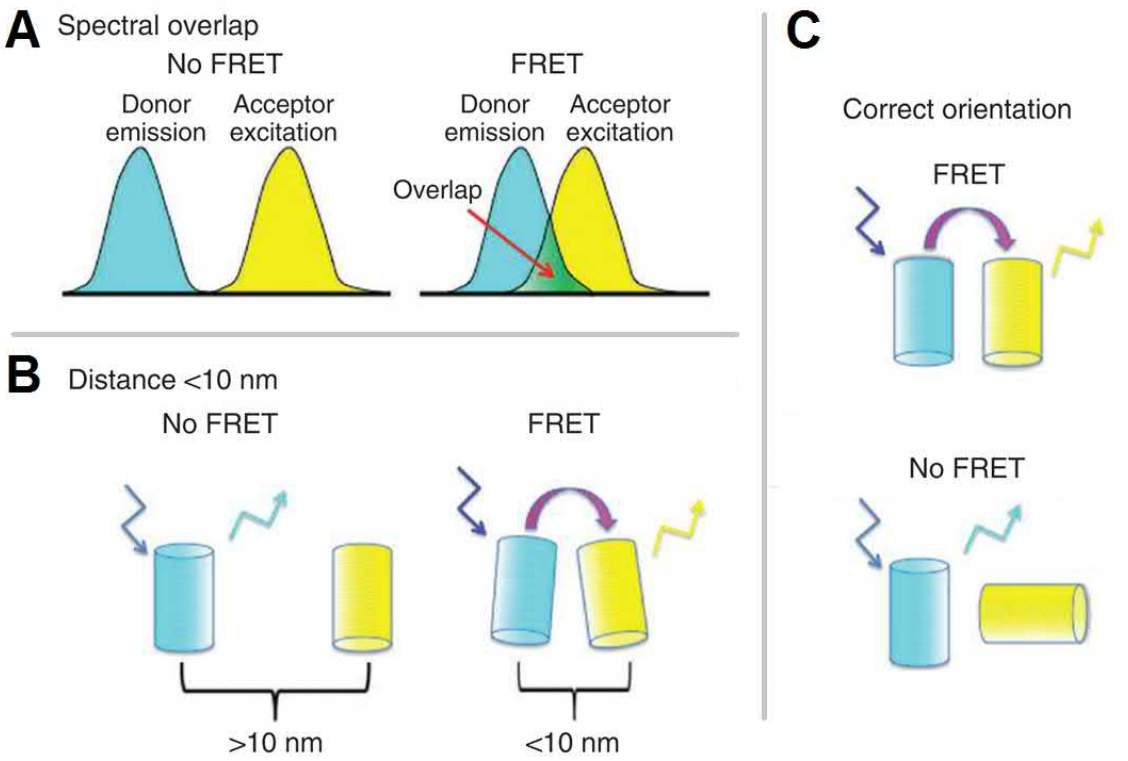

Fig. 1.2.2.1. Conditions necessary for FRET between a donor and an acceptor fluorophore. Image adapted from (Broussard et al., 2013).

Those stringent conditions make FRET a valuable phenomenon for probing short-distance interactions in biological samples. For this, the donor and acceptor are attached to the interacting biomolecules, or two sites on the same molecule in case of intramolecular interactions and conformation changes. From the ratio of donor and acceptor emission, the FRET efficiency is calculated, and the distance between the fluorophores can be extracted, providing information about the binding process or conformational changes (Fig. 1.2.2.2).

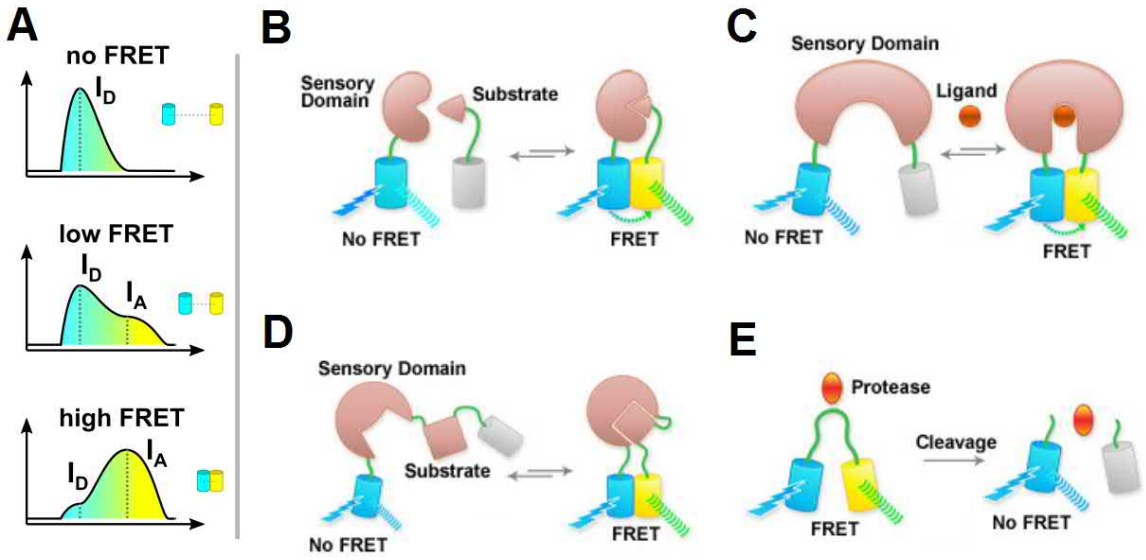

Fig. 1.2.2.2. Using FRET to measure short intra- and intermolecular distances. A: as the distance between fluorophores decreases, the ratio of donor to acceptor fluorescence intensity lowers. B: Classical FRET sensing scheme for binding between two biomolecules. Binding brings fluorophores closer, increasing FRET efficiency. C: FRET sensing scheme for conformational changes within a biomolecule. Upon binding, fluorophores can come closer or farther from each other, changing the FRET efficiency. D: FRET sensing scheme for two biomolecules with a tether for precise stoichiometry. This approach gives more control over the experiment. E: FRET scheme for probing enzymatic activity. When the biomolecule keeping donor and acceptor together gets cleaved, they can diffuse apart, lowering the FRET efficiency. Image adapted from Carl Zeiss AG website.

Quantitatively, FRET efficiency (E) is defined as the quantum yield of energy transfer transition, i.e. the ratio of the energy transfer rate to the total relaxation rate of the donor:

$$E = \frac{k_{\mathrm{ET}}}{k_f + k_{\mathrm{ET}} + \sum k_i} \qquad \textit{(Eq. 1.2.2.1)}$$

where k_{ET} is the energy transfer rate, k_f is the rate of fluorescence, and k_i are the rates of the various non-radiative relaxation process.

FRET efficiency is strongly dependent on the distance between donor and acceptor:

$$E = \frac{1}{1 + (r/R_0)^6} \qquad \textit{(Eq. 1.2.2.2)}$$

where r is the distance between donor and acceptor and R_0 is the Förster distance, which is defined as the distance at which the FRET efficiency is equal to 50%.

In turn, the Förster distance depends on multiple parameters:

$$R_0{}^6 = \frac{2.07}{128\,\pi^5\,N_A}\,\frac{\kappa^2\,Q_D}{n^4}\int F_{\mathrm{D}}(\lambda)\,\epsilon_{\mathrm{A}}(\lambda)\,\lambda^4\,d\lambda \qquad \textit{(Eq. 1.2.2.3)}$$

where N_A is Avogadro's number, κ^2 is the transition dipole orientation factor (averaging to 2/3 for freely rotating dipoles), Q_D is the donor quantum yield, n is the refractive index of the medium around the fluorophores, F_D is the donor fluorescence spectrum (normalized to an area of 1), ε_A is the acceptor extinction spectrum, and λ is wavelength. The latter integral term is frequently called an *overlap integral.*

While being a powerful tool for probing binding interactions, classical FRET experiments performed on a spectrofluorimeter yield information only on the averaged behavior of a vast quantity of individual molecules. This is still very useful, but a number of information about the system is not retrieved, especially concerning the binding dynamics, possible intermediate binding states, and intra-population deviations. Fortunately, FRET experiments can be performed in a different way to extract such information.

In single-molecule FRET (smFRET) experiments, FRET is observed on individual molecules in microscopy conditions (Fig. 1.2.2.3A) (*Blanchard et al., 2004; Juette et al., 2014*). A typical smFRET experiment is performed as a continuous fluorescence wide-field videomicroscopy with TIRF excitation, with the donor-labeled binding partner immobilized on the surface. The surface is continuously illuminated to excite the donors. The emissions of the donor and the acceptor are observed simultaneously via multichannel detection. From the tracks of their luminescence, the FRET efficiency can be calculated. Usually dozens or even

hundreds of donor-acceptor pairs are being observed simultaneously, which allows to quickly build up the statistics necessary for extracting the information about the system.

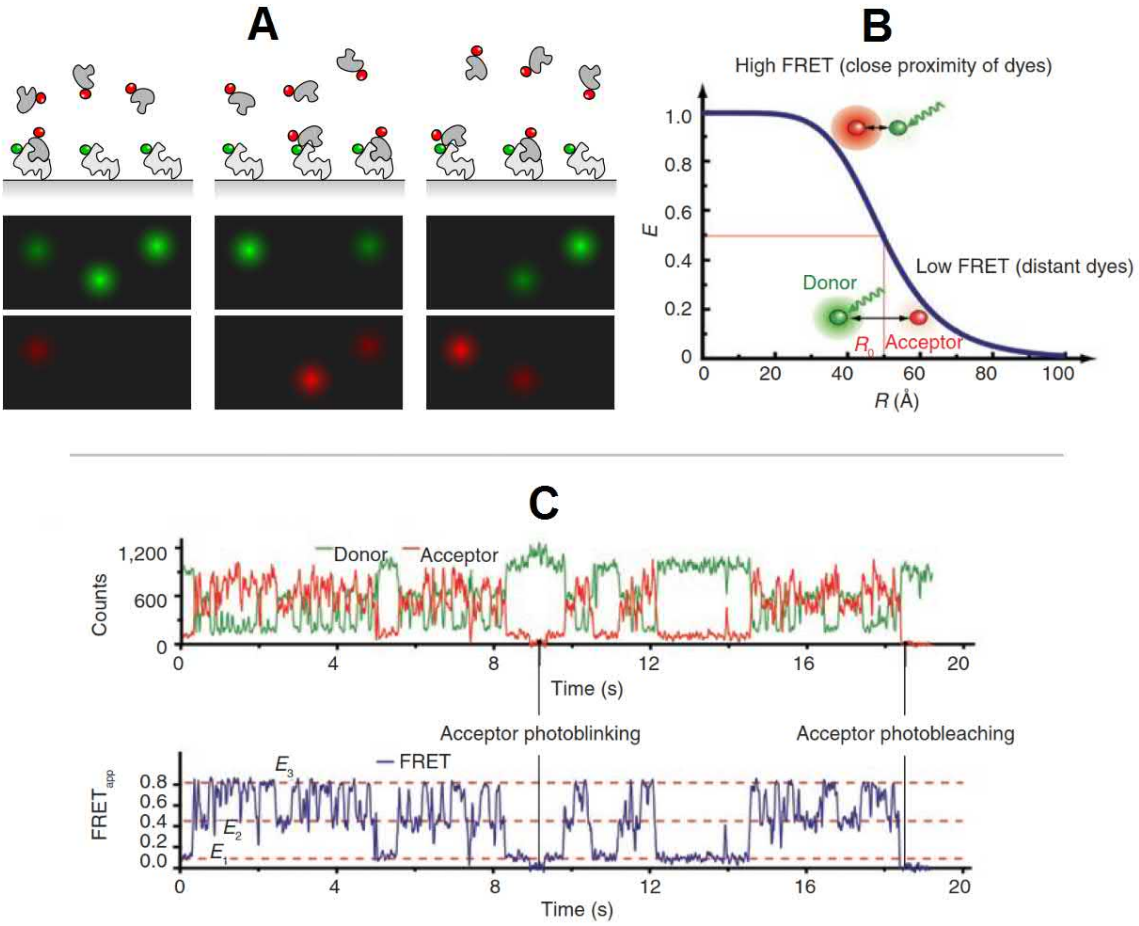

Fig. 1.2.2.3. smFRET principle. A: Biomolecules with donor fluorophores are fixed on a surface. The acceptor-marked molecules are floating in the solution, and can bind to their immobilized partners on the surface, potentially in multiple binding modes (two modes in this case). Excited donors can either emit or transfer their energy to the acceptor fluorophore if it is in close vicinity. Multichannel wide-field microscopy allows to observe the donor and acceptor fluorescence. B: proximity of the dyes determines FRET efficiency and the ratio of donor to acceptor fluorescence upon donor excitation. C: by continuously monitoring a single spot, a trace of donor and acceptor luminescence in time can be found. From this, FRET efficiency in time can be calculated, and be used to quantify the interfluorophore distance. In this case the experiment yields information about two distinct binding modes, which would be hidden or averaged out in a bulk FRET experiment. Image adapted from (Roy et al., 2008).

A typical track of smFRET luminescence is shown on Fig. 1.2.2.3C. As the donor and acceptor come in close proximity, acceptor fluorescence increases, and donor fluorescence decreases (Fig. 1.2.2.3B). During the process, the donor and/or acceptor fluorophore may blink (occupy a non-emissive triplet state) and temporarily stop being fluorescent. After some time, typically after 10^4-10^6 absorption-emission cycles (*Vaughan et al., 2012*), the donor and/or acceptor fluorophore become photobleached and incapable of further fluorescence.

A modification of smFRET called *alternating laser excitation* (ALEX) involves quick intermittent switching of excitation mode from donor excitation to acceptor excitation (*Kapanidis et al., 2004*). This allows to precisely monitor donor-acceptor stoichiometry and distinguish events where multiple acceptor-labeled molecules bind to the same donor-labeled molecule.

The advantage of smFRET experiments over conventional FRET is the possibility to extract information about the kinetics and dynamics of binding and/or conformational changes that is normally unavailable in ensemble experiments due to ensemble averaging effect. smFRET can be also extended to multiple fluorophores, e.g. cascading FRET from a donor to an acceptor that itself can serve as a donor for another acceptor, competitive FRET from a single donor to multiple acceptors, etc (*Ha, 2008*).

The main caveats of smFRET are its high demands in fluorophore photostability and uniform luminescence, difficulty of data interpretation in case of multiple binding modes, and low SNR due to collection of light from individual fluorophores.

In biology, smFRET is one of the most powerful techniques for elucidation of kinetics and dynamics of protein and nucleic acid binding. Examples include probing the dynamic behavior of neurotransmitter symporters (*Zhao et al., 2010*), simultaneously probing multiple distances within a protein-nucleic acid complex (*Uphoff et al., 2010*), monitoring protein folding and nucleic acid bending in real time (*Pirchi et al., 2011; Vafabakhsh and Ha, 2012*), etc (Fig. 1.2.2.4).

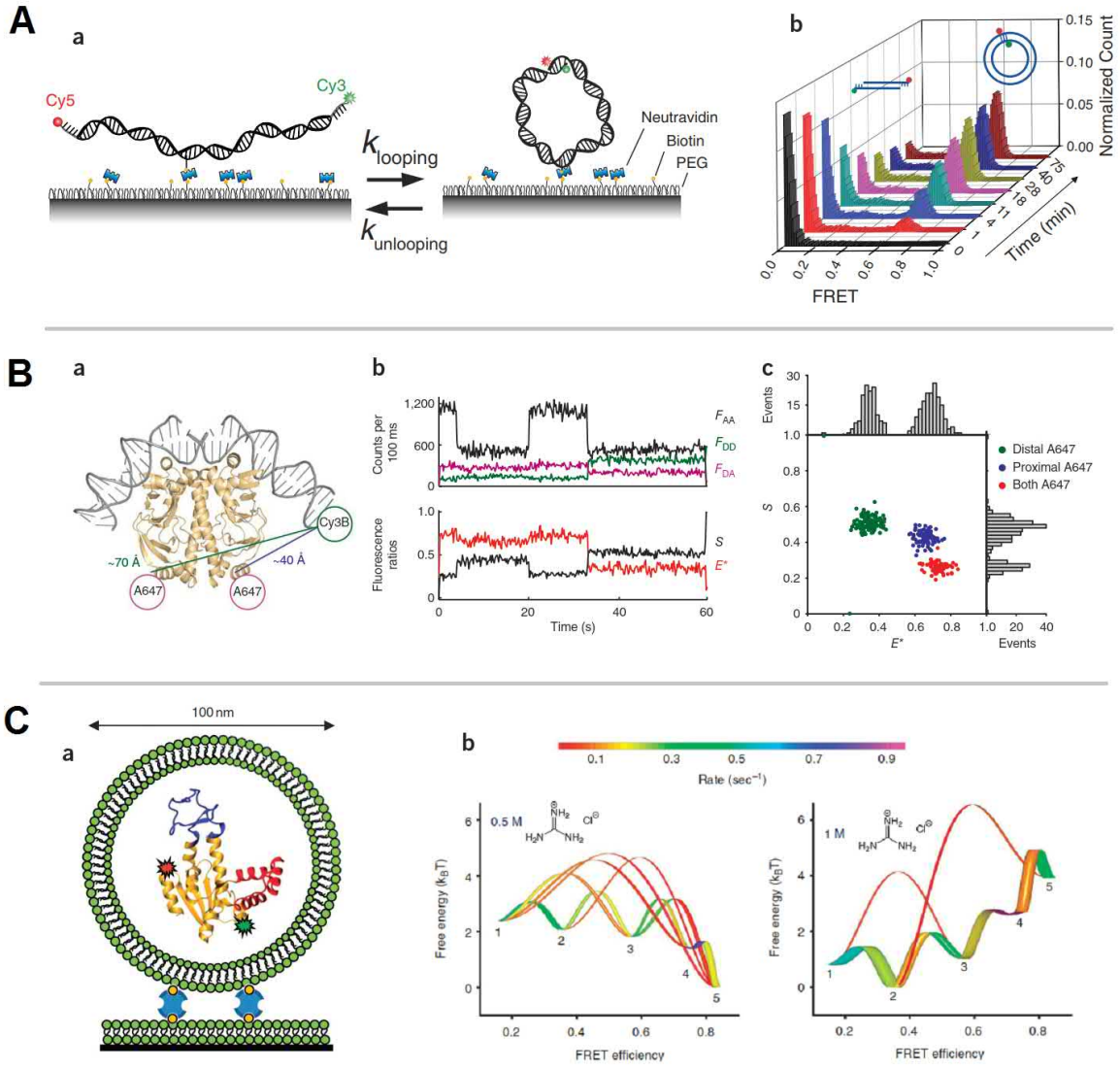

Fig. 1.2.2.4. Examples of smFRET applications. A: (a) A short (91 bp) DNA duplex with complementary "sticky ends" is bound to a glass surface via a biotin-avidin linkage. It can reversibly form a strained circular chain. (b) Performing sequential smFRET experiments with different time lags shows a gradual increase in FRET efficiency in the population. Starting from a population with all chains unwrapped, more and more individual duplexes eventually wrap into a circular chain (Vafabakhsh and Ha, 2012). B: (a) Protein-nucleic acid complex monitored via ALEX, with two acceptors bound to the protein and one donor bound to the nucleic acid. The acceptor dye, Alexa 647, is photoswitchable, temporarily going into dark state upon direct excitation. This permits to temporarily "switch off" one of the acceptors during imaging. (b) During ALEX, the fluorescence of the donor and acceptor can

be detected with sequential donor excitation and direct acceptor excitation. This allows to monitor both the FRET efficiency and the ratio of donor to acceptor fluorophore active at the current moment. (c) Plots of FRET efficiency vs stoichiometry for collected ALEX traces. Several states are observed, corresponding to FRET with either of the dyes, or both, yielding information on two distances inside the complex using one acceptor type (Uphoff et al., 2010). C: (a) A protein labeled by two dyes is confined inside a vesicle bound to a glass surface, and the smFRET experiment is performed. (b) In the presence of guanidinium chloride (a chaotropic agent) the protein has several distinct folding states, with reversible transitions between each other, characterized by their energy barriers and transition rates. By changing the concentration of the chaotropic agent, the folding landscape significantly morphs (Pirchi et al., 2011). Images are adapted from appropriate references.

1.2.3. Single-particle tracking (SPT)

If a videomicroscope is sufficiently fast and sensitive, the movement of individual molecules can be observed, and the trajectories of their movement can be reconstructed afterwards by localizing the positions of the molecules in each frame. This method is called *single-particle tracking* (SPT). SPT provides valuable information on the diffusion and transport behaviors in living cells, and also gives insights on the size of different biomolecule complexes, both stable and transient (*Manzo and Garcia-Parajo, 2015*).

SPT experiments are typically performed with two techniques: wide-field fluorescence videomicroscopy and wide-field scattering videomicroscopy with gold nanoparticles. Another approach called single-particle orbit tracking can be also used, where the particle is followed by rapidly moving the focus of a confocal microscope around it and following the fluctuations in the emission response. In this chapter, the wide-field fluorescence approach is discussed as it remains the most popular approach due to its relatively low cost and ease of setting up.

As native fluorescence of biomolecules is usually very inefficient, SPT is typically performed with labels. In context of SPT, they are typically called *reporters* and are comprised of a conjugate of a fluorophore (usually an organic dye or a quantum dot) and a specificity module (antibody, protein, ligand for a receptor) that selectively binds to the target. Typical sizes of specificity modules are 5 nm for streptavidin, 5-10 nm for antibodies, and 2-

4 nm for nanobodies and aptamer (*Manzo and Garcia-Parajo, 2015*). In the case of fluorescent proteins, specificity is already intrinsically imparted by the cells expressing the protein of interest with the fluorescent protein.

An SPT experiment consists of several steps (Fig. 1.2.3.1):

1. **Acquisition:** the sample is labeled and the video is taken. Depending on the interaction being visualised and the stability of the reporters, imaging can take from several seconds to tens of minutes. A balance between exposure time, reasonable SNR and illumination power has to be found: long exposure leads to loss of time resolution and motion blur, while low SNR leads to higher localization error and worse spatial resolution. High SNR can be combined with short exposure if high illumination intensity is used, but this approach suffers from excessive fluorophore blinking, fast photobleaching, and sometimes even absorptive sample heating.
2. **Pre-processing:** videos with sample drift have to be corrected to avoid mixing the trajectory information with the drift. Ideally, this is avoided by stabilized microscopy setups. However, strategies for drift correction exist, which can be based solely on image information or on locating multiple bright immobilized fluorophores in the sample (*reference markers*). During this step, background correction can be performed as well.
3. **Spot localization:** all frames of the video are treated by spot detection algorithms and the fluorophores are localized in each frame. The algorithms for spot detection that are used for SPT are usually the same as the ones used for SMLM (centroid location, Gaussian fitting, etc.) (*Chenouard et al., 2014*). Stricter thresholds on spot detection give more reliable localization of particles, but may lead to false negatives: frames in which the particle is clearly present, yet not recognized. Conversely, relaxed thresholds will lead to detection of phantom "particles" in the noise.
4. **Tracking (linking trajectories):** the spots from successive frames belonging to the same fluorophore are linked to form a full trajectory. Multiple linking approaches exist, each with its advantages and caveats (*Chenouard et al., 2014*). A simplest linking algorithm is finding the nearest neighbours in successive frames. Low labeling density makes linking more reliable, as there is a lower probability of fluorophores passing close by each other. However, this approach yields a smaller amount of

trajectories per image, requiring multiple experiment repeats to extract sufficient information about the system under investigation.

5. **Post-processing:** overlapping trajectories can be broken in several separate ones; short trajectories that are detected on a small amount of frames can be discarded to avoid polluting the data with information from unreliably detected particles. To compensate for blinking, trajectories can be linked together by interpolating the particle position in frames where the particle is absent.

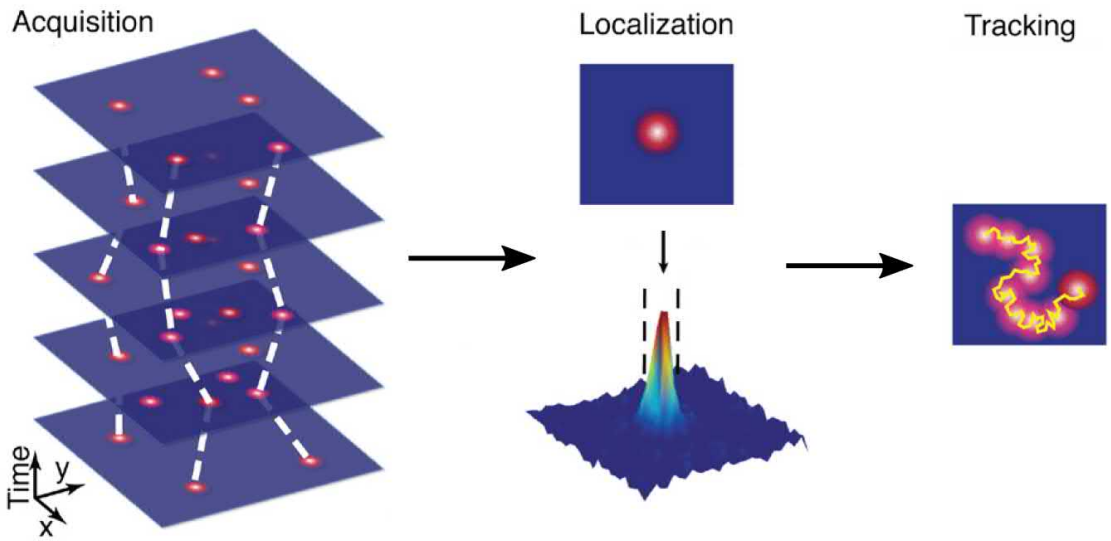

Fig. 1.2.3.1. Principle of SPT. A sequence of images is taken, typically with multiple fluorophores in the field of view. Afterwards, the positions of fluorophores can be localized in individual frames, provided their spots are well-separated. Next, the positions of the same fluorophores in successive frames are linked together to reconstruct the trajectory of the fluorophore, which contains information about the movement of the target to which the fluorophore is attached. Image adapted from (Manzo and Garcia-Parajo, 2015).

The obtained trajectories contain information about the nature of the movement of the molecules under investigation. The simplest and most widely used approach is the analysis of *mean square displacement* (MSD) in the trajectory.

$MSD_{\Delta t}$ is characterized as the mean of the square of the distance that particle travels during Δt frames. From the theory of Brownian motion, a linear relationship between MSD and the diffusion coefficient D can be derived (*Michalet, 2010; Saxton, 1994*):

$$MSD_{\Delta t} = 2\, n\, D\, \Delta t \qquad \textit{(Eq. 1.2.3.1)}$$

, where n is the amount of dimensions in which the particle moves. In biological samples, n is usually 2 (for membrane components) or 3 (for freely diffusing components, e.g. in cytosol).

By fitting the $MSD_{\Delta t}$-Δt curve with a line, one can then extract the diffusion coefficient, which in turn depends on the size and the shape of the diffusing biomolecule. (Fig. 1.2.3.2A)

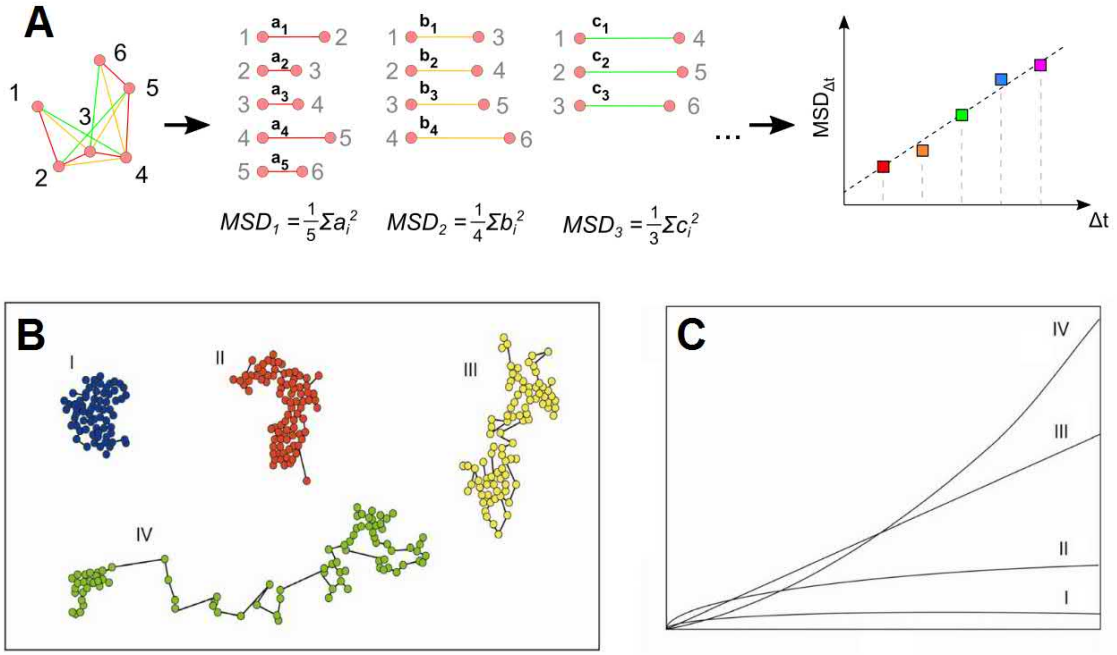

Fig. 1.2.3.2. MSD analysis and typical movement regimes. A: For a trajectory, each MSD value for different time lag Δt corresponds to the mean square distance which the particle traveled during this time lag. MSD is calculated sequentially for all time lags in the trajectory. The $MSD_{\Delta t}$-Δt dependence contains information about the type of diffusion the particle is undergoing. B: Trajectories corresponding to typical movement regimes: (i) confined, (ii) restricted, (iii) free (Brownian), (iv) directed. C: idealized MSD curves for types of movement in B. Image adapted from (Martin-Fernandez and Clarke, 2012).

This relationship is linear for the case when the motion is truly Brownian (Fig. 1.2.3.2B(iii)), which is not always the case in biological systems, where diffusion is frequently *anomalous*.

Consider the case of a straight line motion. In this case, the MSD relationship depends only on the speed of the particle, v, and shows a quadratic Δt dependence:

$$MSD_{\Delta t} = v^2 \Delta t^2 \qquad \textit{(Eq. 1.2.3.2)}$$

In biological systems, directed motion (e.g. transport of vesicles along cytoskeleton) is frequently a mixture of Brownian and directional motion (Fig. 1.2.3.2B(iv)):

$$MSD_{\Delta t} = 2\, n\, D\, \Delta t + v^2 \Delta t^2 \qquad \textit{(Eq. 1.2.3.3)}$$

For the case of restricted diffusion, there is a variety of possible dependencies, depending on the nature of the restriction (*Saxton, 1994*). For example, a particle can be confined inside an immobile vesicle of relatively large size, allowing seemingly Brownian diffusion restricted in a fixed volume (Fig. 1.2.3.2B(i)). The ultimate asymptote for restricted diffusion is the case of a completely immobile particle, in which case $MSD_{\Delta t}$ remains zero for all values of Δt.

However, in practice, single particle imaging always has a localization error. This means that even a perfectly immobile particle will exhibit some degree of phantom "movement" due to imperfections in the microscopy setup and the fundamental limits on the information content of collected photons. Similarly, the observed trajectory of a moving particle contains both valuable information about the random movement and useless noise of "phantom" movement. In terms of MSD, this usually leads to a vertical offset in the MSD curve. For two cases (Brownian movement and immobile particle) this offset depends on the localization error, σ, and the exposure time t_E (*Michalet, 2010*):

$$offset = 4\sigma^2 - (4/3)\, Dt_E \qquad \textit{(Eq. 1.2.3.4)}$$

In biology, SPT is typically used for the investigation of cell membrane dynamics and organization (*Kusumi et al., 2014*), transport and signaling processes in cells (*Bálint et al., 2013*), virus internalization (*Arhel et al., 2006*), etc (*Manzo and Garcia-Parajo, 2015*) (Fig.

1.2.3.3). Experiments that are closely related to SPT include flow cytometry (*Han et al., 2016*) and investigation of taxis and kinesis of cells (*Mitchison and Cramer, 1996*).

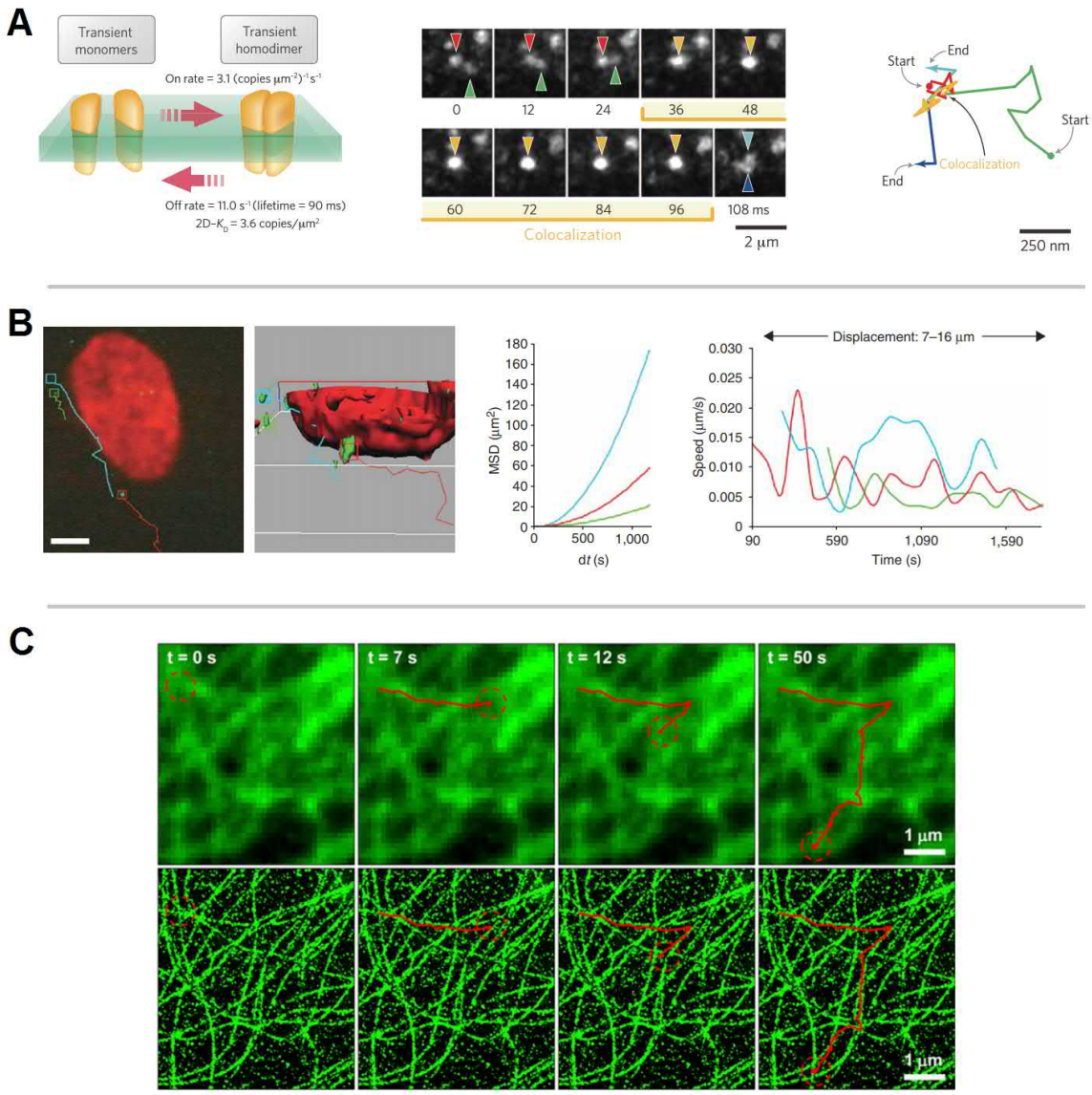

Fig. 1.2.3.3. Examples of SPT applications. A: SPT of FPR receptors marked with a dye-conjugated ligand in live cells. Spots corresponding to the receptor show movement with occasional long periods of colocalization which imply transient dimerization of receptors. From the tracks, the rate constants of reversible dimerization can be extracted (Kusumi et al., 2014). B: 3D SPT of HIV-1 (green spots) complexes in close proximity to a HeLa cell nucleus (red blob). MSD analysis shows upward-curved, almost parabolic tracks, indicating highly directed movement. Diffusion speed analysis shows periodic acceleration bursts,

consistent with transport along actin filaments (Arhel et al., 2006). C: Correlation of SPT of lysosomes (red) with subsequent STORM of microtubules (green). Additional resolution provided by STORM reveals sudden changes of trajectory on microtubule intersections (*Bálint et al., 2013*)*. Images adapted from respective references.*

1.2.4. Overview of luminophores used for the SMM

Imaging individual molecules is not a straightforward task, and it highly depends on the performance of utilised fluorophores. Fluorescence microscopy can be performed with light-emitting structures whose luminescence is based not only on fluorescence, but also on other photoluminescence phenomena; thus the more general appropriate term would be *luminophores*. Some requirements and desirable characteristics for luminophores are general for fluorescence microscopy, and some are specific for the SMM:

- **Brightness:** while there are multiple definitions for it, typically brightness is referred to as the product of absorption coefficient, luminescence quantum yield and the quantity of individual light-emitting elements per luminophore:

  $$B = n \varepsilon \Phi \qquad \textit{(Eq. 1.2.3.4)}$$

  Higher brightness allows to collect more photons per image from the luminophore, yielding more information about its position or other properties, e.g. spectral response.

- **Luminescence wavelength:** as the size of PSF is proportional to the wavelength, luminophores with shorter emission wavelengths concentrate the light in a smaller area, allowing more precise localization. However, in case of fluorescence this requires using an even shorter excitation wavelength, inducing autofluorescence in the sample, lowering the SNR and increasing background.

- **Photostability:** it is almost always a desirable characteristic, as higher photostability allows to collect more total photons from a luminophore. In SMLM, this allows to lower the localization error. In smFRET, higher photostability allows to collect more information from each individual luminophore, yielding more reliable statistics. In SPT, photostability allows to collect longer tracks, relaxing the upper time limit on processes under investigation.

- **Blinking:** for SMLM, blinking can be a desired characteristic, or even the basis of the method in case of dSTORM. Blinking is typically characterized by the ratio of time that the fluorophore spends in emissive and non-emissive states (*on-off ratio*). However, SPT and smFRET suffer from blinking, as it obscures the response of the molecules, lowers the amount of information that can be extracted from a single luminophore and complicates data treatment.
- **Size:** if the combined size of the luminophore and its targeting moiety is too large, it will affect the properties of the target to which it is attached. This can lead to lower the binding specificity, as a larger surface leads to a higher probability of non-specific binding. In smFRET, large luminophore size can lead to steric hindrances, changes in local hydrophobicity and/or electric charge, all of which will bias the experiment, frequently in unpredictable ways. In SPT, a substantial reporter size lowers the observed diffusion coefficient by increasing drag forces, and also may introduce non-specific interactions.

Generally, luminophores do not perform well in relation to all of these characteristics at the same time. Thus a compromise between the parameters has to be found. Here, a comparison of conventional luminophores and their strengths and weaknesses is provided. A brief overview is shown on Fig. 1.2.4.1.

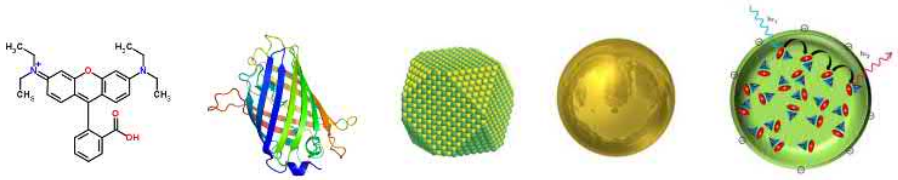

	organic dyes	fluorescent proteins	quantum dots	gold NPs	dye-loaded NPs
brightness	★★	★★	★★★	★★★	☆☆☆☆
size	☆☆☆☆	★★★	★★★	★	★★
photostability	★	★	★★	☆☆☆☆	★★
blinking	★	★	★	☆☆☆☆	★★
protocol simplicity and reliability	★★★	★	★★	★★	★★
instrumental requirements	★★★	★★★	★★★	★	★★★

Fig. 1.2.4.1. Comparison of luminophores for SMM applications, ranked by performance in appropriate property. In case of blinking, performance is appraised for SPT/smFRET (i.e. lower blinking – better performance). Conversely, for SMLM, the blinking performance should be generally rated as inverse (Cognet et al., 2014; Giepmans et al., 2006).

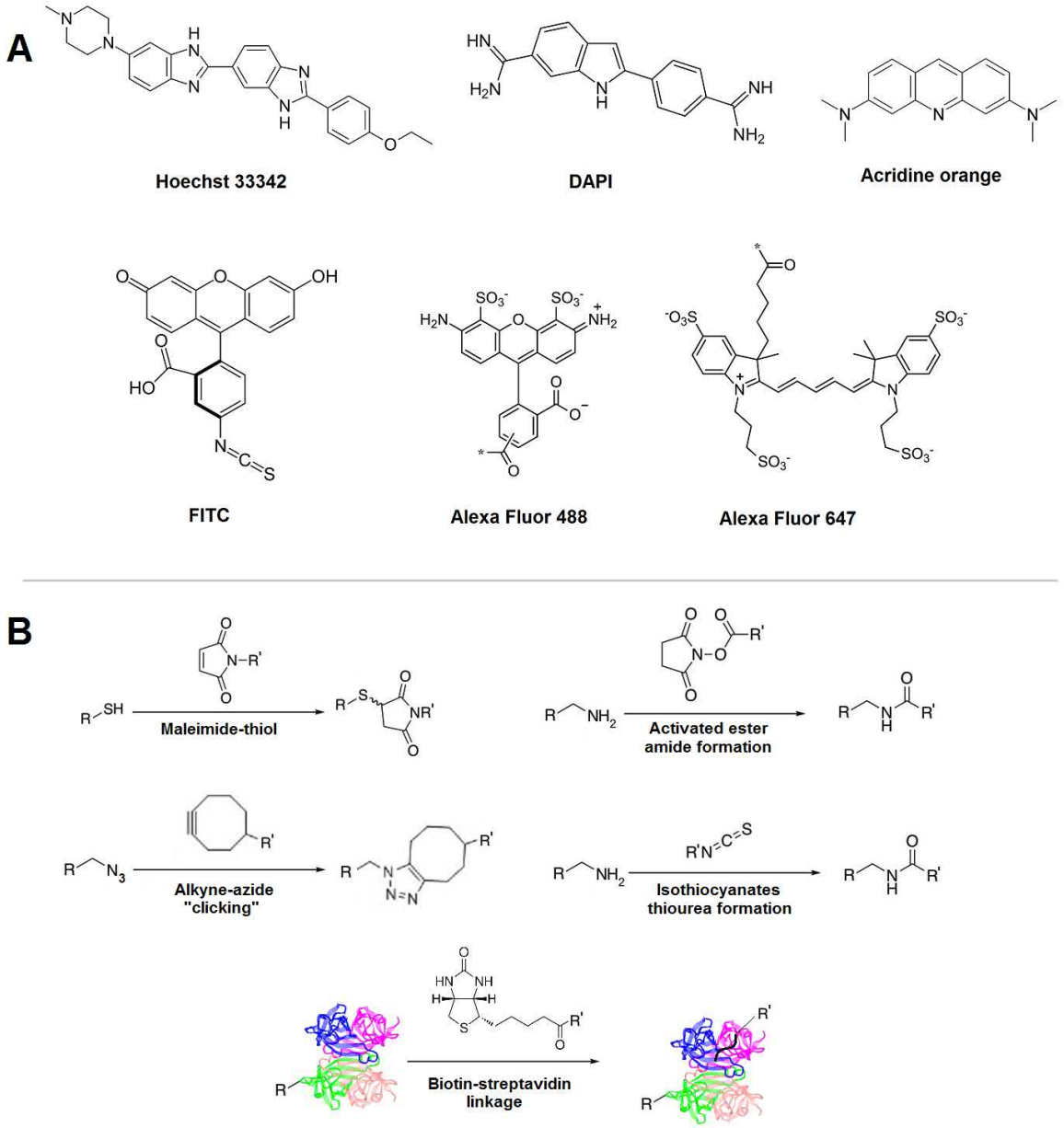

Fig. 1.2.4.1.1. Examples of fluorescent organic dyes and conjugation reactions. A: Organic dyes. Hoechst 33342 and DAPI naturally bind to DNA and can be used for staining cell nuclei without any conjugation. Acridine orange naturally binds to nucleic acids with spectral shift depending on whether it bound to DNA or RNA. FITC and Alexa Fluor dyes are used for protein labeling. B: Conjugation reactions commonly used for biomolecule labeling. "Clicking" and biotin-streptavidin linkage can be used for in vivo labeling.

1.2.4.1. Organic dyes

Organic dyes are most frequently used for SMLM and smFRET, with some examples of SPT applications as well. Typically, the label is constructed through conventional organic chemistry, by covalently attaching the dye to the specificity module. Examples of some organic dyes are provided on Fig. 1.2.4.1.1A. Linking reactions typically employed to this aim are known as *bioconjugation* reactions and include amine-carboxyl coupling (usually via activated esters), azide-alkyne clicking reaction, thiol-maleimide Michael reaction (Fig. 1.2.4.1.1B), isocyanate thiourea formation with amines, biotin-streptavidin non-covalent bond, and some other techniques (*Patterson et al., 2014*). A lot of conjugates and labeling kits suitable for use in SMM are available commercially.

In terms of performance in SMM, the brightness of organic dyes is not high, but usually sufficient for imaging with sensitive cooled CCD cameras. The wavelength choice is quite wide, however due to broad absorption and emission bands it may be difficult to perform SMM with more than three types of dyes at the same time. Low photostability is the bane of the SMM experiments with organic dyes, and imaging with sufficient SNR is usually possible only in short timeframe, <10 min. For smFRET and SPT, blinking is an issue, as the vast majority of organic dyes tends to exhibit substantial blinking, especially at higher excitation intensities. Meanwhile, for stochastic SMLM, controlled blinking is actually a desirable trait. In terms of size, organic dyes are the smallest usable luminophores and thus usually the least likely to perturb the behavior of the target. Small size also allows to better label “crowded” areas of the sample.

1.2.4.2. Fluorescent proteins

In context of SMM, fluorescent proteins generally have a similar performance to organic dyes. Essentially, they consist of an organic fluorophore confined in a protein barrel that shields it from quenching by other molecules, and also keeps its conformation fixed, enhancing its quantum yield (Fig. 1.2.4.2.1A) (*Cranfill et al., 2016; Ormö et al., 1996; Tsien, 1998*). Typically, the label is constructed endogenously in transfected cells, where the protein of interest is expressed with an attached fluorescent protein. To target nucleic acids, a recently developed approach uses fluorophores that exhibit very dim fluorescence, but show highly enhanced fluorescence upon binding with specific RNA aptamers (*fluorogenic dyes*). The overall structure of the complex highly resembles fluorescent proteins. An aptamer combined

with a nucleic acid strand that is complementary to the target sequence can be produced. After transfection, the cells start the transcription of the target RNA with an attached aptamer. In presence of the fluorogenic dye, individual target RNAs can be tracked (Fig. 1.2.4.2.1C) (*Dolgosheina et al., 2014; Huang et al., 2014*).

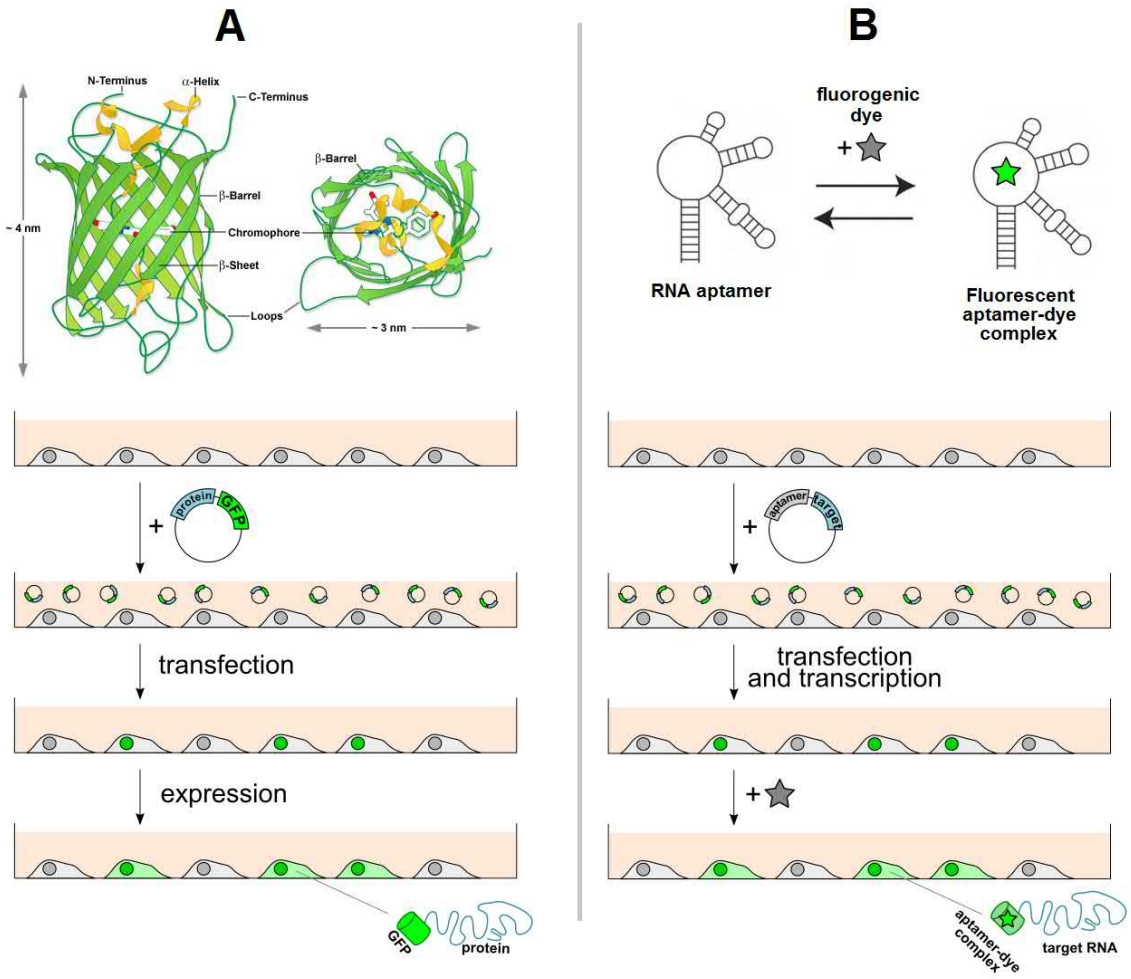

Fig. 1.2.4.2.1. Fluorescent proteins and aptamer-fluorogenic dye complexes. A: 3D Structure of GFP and scheme of a typical experiment involving fluorescent proteins. Cells are transfected with plasmids that contain consecutive sequences corresponding to GFP and the target protein. The protein is expressed with attached GFP, highlighting its location in cell (in this case in cytosol). B: Certain RNA aptamers can confine a fluorogenic dye, forming an aptamer-dye complex and enhancing the dye's fluorescence by several orders of magnitude. This can be used for RNA labeling: cells are transfected with plasmids that contain consecutive sequences corresponding to the aptamer and the targeted RNA. After transcription, incubation of cells with the fluorogenic dye will yield fluorescent aptamer-dye

complexes, highlighting the RNA's location in cell (in this case in cytosol).

Fluorescent protein brightness, blinking and photostability are quite similar to organic dyes. The choice of excitation and emission wavelengths is more constrained, although in recent years the spectral range of fluorescent proteins has been considerably widened (*Cranfill et al., 2016*). The size of fluorescent proteins is typically ~5 nm in diameter. This may significantly affect the diffusion and activity of smaller peptides in cytosol, but is usually not an issue for labeling bigger proteins or membrane components. Aptamer-fluorogenic dye complexes exhibit very similar properties in regards to imaging.

1.2.4.3. Quantum dots

Quantum dots (QDs) are small semiconductor crystals, usually from 2 to 20 nm in diameter. Ordinarily, semiconductors have two distinct energy bands – *valence band*, comprised of multiple energy levels filled with electrons, and *conduction band*, with unoccupied levels. In QDs, due to their small size of and the small amount of atoms in the crystal, the energy levels are discrete. As a result, QDs exhibit a defined bandgap that is wider than in the bulk material. The width of the bandgap in QDs depends on their size, shape and composition (Fig. 1.2.4.3.1). For the aforementioned size range, typical QDs have a bandgap energy that corresponds to the energy of photons in the visible region. Upon absorption of light, an electron-hole pair can be formed. Unlike in bulk material, the electron-hole pair is confined in space, preventing its dissociation and facilitating recombination with photon emission (photoluminescence) (*Michalet et al., 2005*).

To construct a reporter, surface modification of QDs is required, and depends on the used material. For chalcogenide materials (metal sulfides, selenides, tellurides) typically used to construct QDs, biological molecules may be attached directly through strong bonds formed by thiol groups with the chalcogenide surface. Other approaches include covering the particle by surfactants or biological membrane mimics, silica shells and polymer coatings. For the purposes of surface modification to impart functionality on the particle, active groups can be added during or after the particle coating (*Sperling and Parak, 2010*).

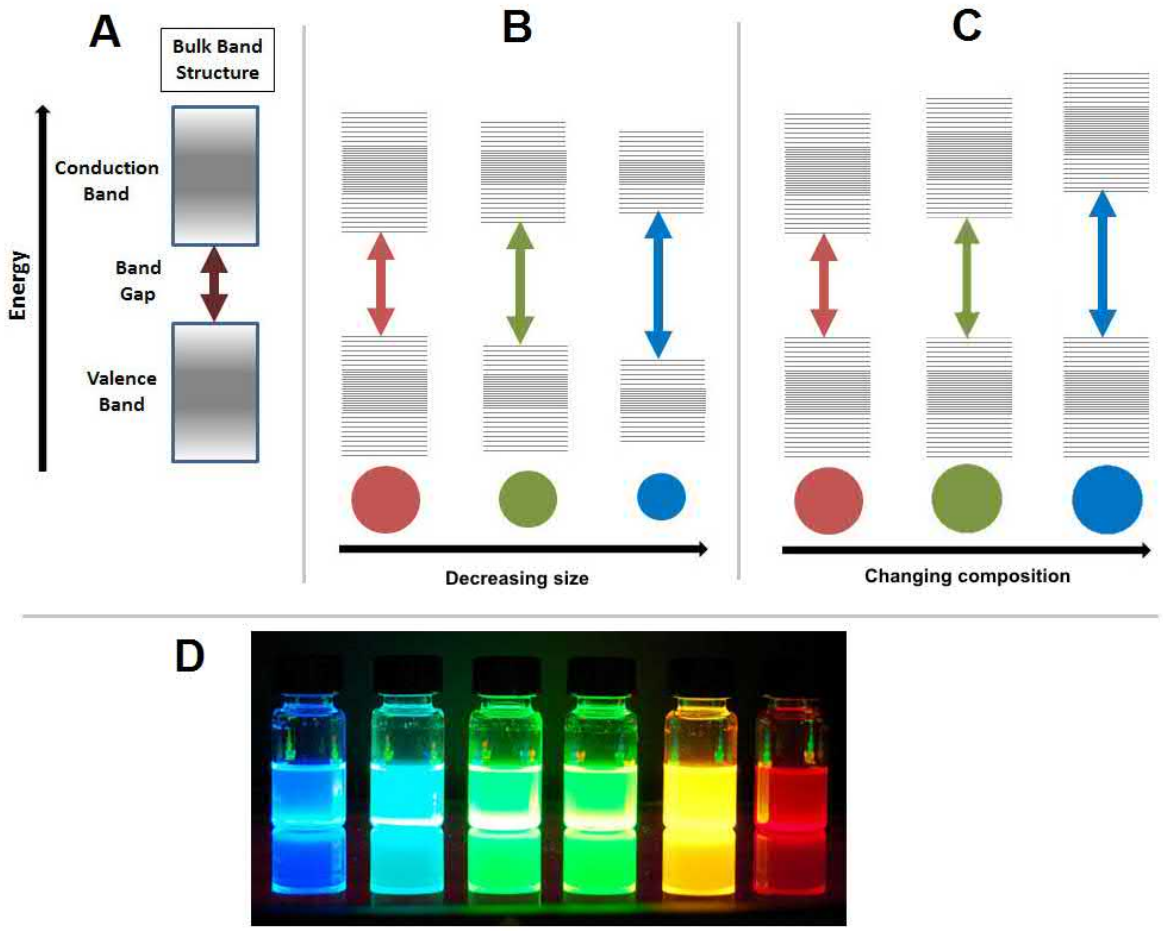

Fig. 1.2.4.3.1. Quantum dots. A: semiconductor band structure. B: if a sufficiently small semiconductor particle is prepared, the energy levels become discrete, widening the bandgap. Smaller particles possess a wider bandgap. C: By modifying the QD composition, the bandgap can be changed in QDs of constant size. D: Photoluminescence of multiple QD dispersions of same size and different compositions under UV excitation. Images are adapted from Merck KGaA.

QDs are usually brighter than organic dyes, and can be engineered to have various emission spectra. QDs have size-dependent tunable emission with relatively narrow bands (usually with ~50 nm half-maximum band width). However, their absorption spectra are quite different compared to organic dyes; they all exhibit high absorption in UV that gradually falls in the visible range and includes one or several additional local maxima in that region. Thus,

spectral separation of QDs through excitation filtering is not straightforward, and sometimes can be impossible.

Photostability of quantum dots is higher than for organic dyes, although they still eventually photobleach. There are multiple mechanisms suggested for QD photobleaching, most of which involve charge separation and chemical reactions on their surface (*Lee and Osborne, 2009*). Recent efforts suggest that forming protective shells around the QD helps to counter photobleaching (*Mahler et al., 2008; Sark et al., 2002*). Overall, in typical SMM conditions QDs can emit for ~10-20 minutes before bleaching.

Typically, QDs show extensive blinking that also depends on excitation intensity. The mechanisms for blinking are not entirely clear, but seem to involve particle charging and formation of trions (electron-hole-electron or hole-electron-hole systems). This can be a detriment for SPT; however, special low-blinking QDs are being developed for this aim (*Mahler et al., 2008; Sark et al., 2002*).

In size, QDs are slightly larger than fluorescent proteins. QDs and other nanoparticles frequently exhibit non-specific binding, especially in live cell conditions, and usually require passivating coatings to reduce this effect.

Overall, their properties make QDs a popular choice for SPT and smFRET, rivaling organic dyes in usefulness (; *Pinaud et al., 2010*).

1.2.4.4. Gold nanoparticles

While not directly related to fluorescence microscopy, SPT with gold nanoparticles (GNPs) in scattering (also known as *dark-field*) mode has to be mentioned due to its high popularity in SPT experiments.

In dark-field imaging, the sample is illuminated with a focused beam with a ring profile. Some light is transmitted through the sample, and some light is scattered. The objective is positioned at a position which permits collection of scattered light, while the transmitted light falls outside the objective aperture. The end result is a dark image with bright regions that correspond to the regions of the sample with high scattering power (Fig. 1.2.4.4.1). Afterwards, the data treatment for SPT is the same as for videos taken on a fluorescence microscope.

GNPs exhibit high scattering cross-sections. For comparison, a GNP 80 nm in diameter scatters light in water as efficiently as a 300 nm polystyrene nanosphere (*Jain et al., 2006*). For small (<100 nm) gold nanoparticles, the scattering cross-sections depends on the sixth power of particle radius. This means that their scattering properties rapidly fall off as the particle gets smaller. Because of this, the bottom limit for reporter size in dark-field microscopy with GNPs tends to be ~20-40 nm (*Sperling et al., 2008*).

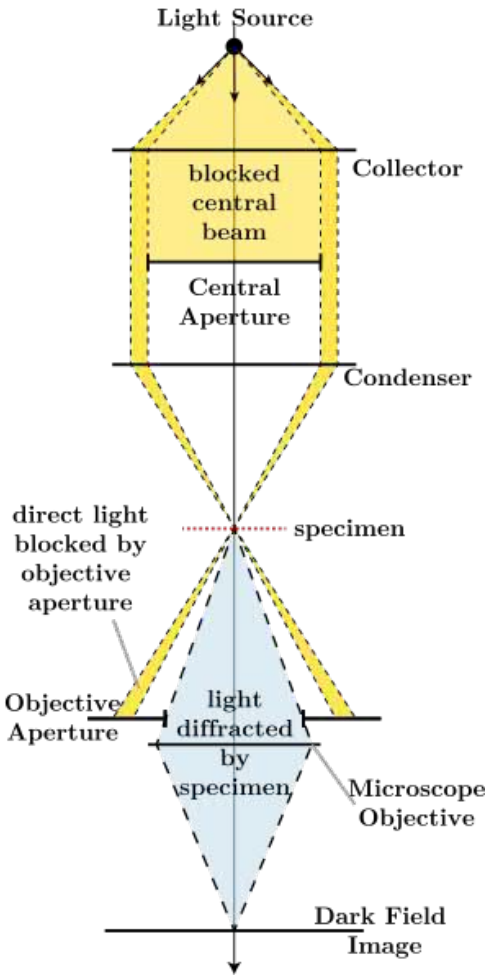

Fig. 1.2.4.4.1. Dark-field imaging. Image adapted from Wikimedia Foundation.

GNPs do not stop scattering light even when exposed to extremely high illumination intensities, and their scattering is constant over short and long timescales. Thus, dark-field imaging with GNPs allows robust tracking with very high imaging frequencies, up to several kHz (*Fujiwara et al., 2002; Kusumi et al., 2014, 1993*). Moreover, light scattering by

biological objects is usually much lower than scattering of typical GNPs, leading to high SNR. The major disadvantages of tracking with GNPs include their large size, high potential for non-specific binding to proteins, and the need of a dedicated well-calibrated setup for dark-field imaging.

1.2.4.5. Dye-loaded nanoparticles

A simple method to increase the brightness of a fluorophore is to confine several smaller fluorophores in a small volume. This idea is the basis for the burgeoning field of imaging with dye-loaded, dye-grafted and conjugated polymer nanoparticles, in which the dyes are trapped inside a nanoparticle, grafted on its surface, or conjugated in a chain to form a giant fluorophore, respectively (Fig. 1.2.4.5.1) (*Braeken et al., 2017; Montalti et al., 2014; Reisch and Klymchenko, 2016*).

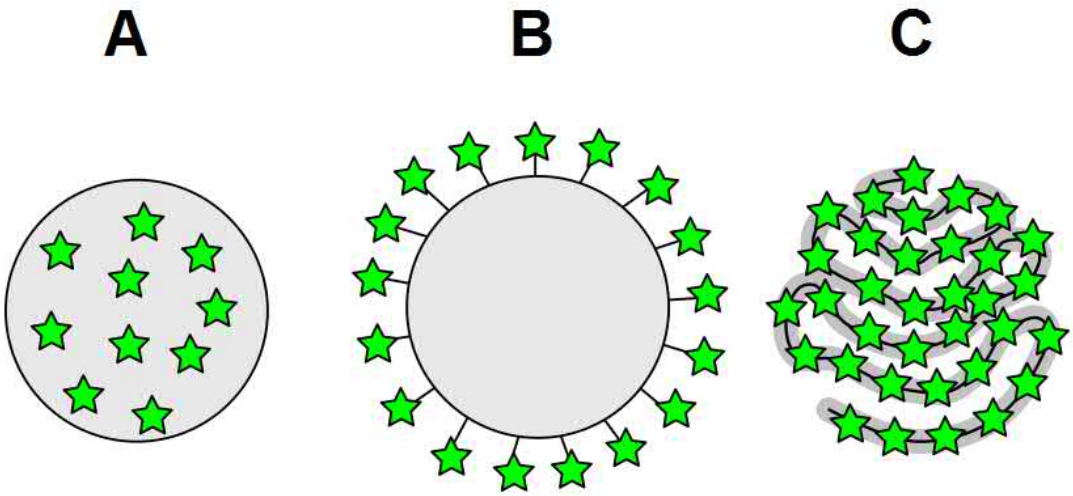

Fig. 1.2.4.5.1. Dye nanoparticles. A: Dye-loaded nanoparticles incorporate dyes during nanoparticle formation. For this, dyes can be either trapped in a lipid micelle or wrapped with an inert polymer. B: Dye-grafted nanoparticles are prepared by chemical reactions of dyes with nanoparticle surface. Typically this approach is used for silica and polymer nanoparticles. C: Fluorescent conjugated polymers have multiple dyes with conjugated electronic systems, forming a giant fluorophore. Similarly to semiconductors, the fluorophore has a bandgap that depends on the polymer composition and chain length.

Usually, bringing organic dyes close together leads to quenching of their fluorescence. However, if the dyes are properly oriented or have specific structures, this effect can be countered. Certain dyes even exhibit an inverse phenomenon, increasing their fluorescence in close proximity to each other, which is known as *aggregation-induced emission* (AIE) (*Mei et al., 2015*).

As dye-loaded nanoparticles are much brighter than a single organic dye, they are of potential interest for SMM and especially SPT, with a few prototypes already presented in the literature (*Kilin et al., 2014; Reisch and Klymchenko, 2016; Yu et al., 2009*). Their main advantage is the substantial improvement in brightness compared to individual dyes, leading to enhanced performance in single-particle imaging conditions (particles of 30 nm diameter can be 10-100 times brighter than an individual quantum dot). However, at high loadings dye-loaded nanoparticles can exhibit strong blinking due to cooperativity effects (*Reisch et al., 2017, 2014*). While certain types of dye-loaded nanoparticles shield the dyes from external influence, they are nevertheless prone to photobleaching. Moreover, similarly to other nanoparticles, a major caveat is ensuring their specificity and selectivity of binding.

1.2.5. Limitations of SMM

After overviewing the single-molecule microscopy techniques and the performance of luminophores, it is evident that SMM has a lot of room for improvement in regards to the used luminophores, each of which having substantial problems associated with it.

Keeping these limits in mind, one could then imagine an ideal luminophore for SMM that should exhibit the following characteristics:

- **High SNR** in the experiments employing the luminophore in single-particle imaging conditions, which can be achieved through increasing brightness and/or reducing the non-specific light collection (e.g. autofluorescence). High SNR can be afterwards traded off for resolving nuanced details of dynamical processes in smFRET, lowering the readout time for tracking fast processes in SPT and smFRET, reducing localization error in SMLM and SPT, or reducing the instrumental setup costs through using cheaper optics and cameras.

- **No blinking** for reliable data collection in smFRET and SPT, or **controlled blinking** for stochastic SMLM.
- **No bleaching** for long-timescale smFRET and SPT in order to achieve better localization in SMLM.
- **Simple instrumental setup**, compatible with commercially available fluorescence microscopes, requiring little to no changes.
- **Small size**, comparable with the size of typical specificity modules (antibodies, aptamers and other targeting groups).

Such a set of parameters is currently unachievable by any of the luminophores conventionally used for SMM. However, during the last decade, a particular novel luminophore has been actively investigated for a variety of applications including biological imaging, with a number of properties that make it a very good candidate for SMM applications. This luminophore is called *upconverting nanoparticles*, or UCNPs.

Part 3. Upconverting nanoparticles (UCNPs).

1.3.1. Terminology

The most common definition of upconversion, which will be used in this work, is "sequential absorption of low-energy photons through one or more intermediate non-virtual excited states with subsequent emission of a high-energy photon from a high excited state". In literature, there is still some inconsistency related to the definition of upconversion, as some sources generalize it to be defined as any process yielding a high-energy photon from multiple low-energy photons, including completely different processes like *second-harmonic generation* (SHG) and *two-photon absorption* (TPA), which proceed through virtual intermediate states.

As the luminescence wavelength of upconverting materials is by definition shorter than the absorption wavelength, a commonly used term referring to upconversion is "anti-Stokes emission", referring to the opposite behavior compared to Stokes shift in fluorescence.

1.3.2. Principles of upconversion

There are multiple ways to achieve upconversion in materials. In this chapter, the mechanisms that allow highly efficient upconversion are presented (a more in-depth review of those is provided in *Joubert, 1999*).

1.3.2.1. Triplet-triplet annihilation (TTA)

Triplet-triplet annihilation (TTA) occurs when two (usually identical) dye molecules are both in their long-lived intermediate triplet state. TTA involves transition of one of the dyes to a ground singlet state and transition of another dye to an excited singlet state, which afterwards can emit light via conventional fluorescence (Fig. 1.3.2.1A). For such a transition to be spin-permitted, the electron systems of the molecules have to overlap, so TTA happens only when the interacting molecules are at a short distance, ca. <1-2 nm.

TTA can be observed in concentrated solutions of dyes under pulsed excitation and was originally named "delayed fluorescence", as it has emission identical to fluorescence (with transition from S_1 to S_0 state) and can be observed some microseconds after an excitation

pulse. The delay is caused by the time it takes for two diffusing molecules in the long-lived triplet state to encounter each other (*Parker and Hatchard, 1962*).

To make TTA efficient, it is necessary to keep two dyes close to each other and make them both occupy a triplet state as much as possible. For this, the efficient approach is utilizing another dye, called a *sensitizer*, which is tailored to have a high absorption and high rate of intersystem crossing. After absorbing light, the sensitizer can absorb light and perform *triplet-triplet energy transfer* (TTET), returning to the ground state and forcing the TTA-capable dye (called an *emitter*) into the triplet state. This is known as *sensitized TTA* (Fig. 1.3.2.1B).

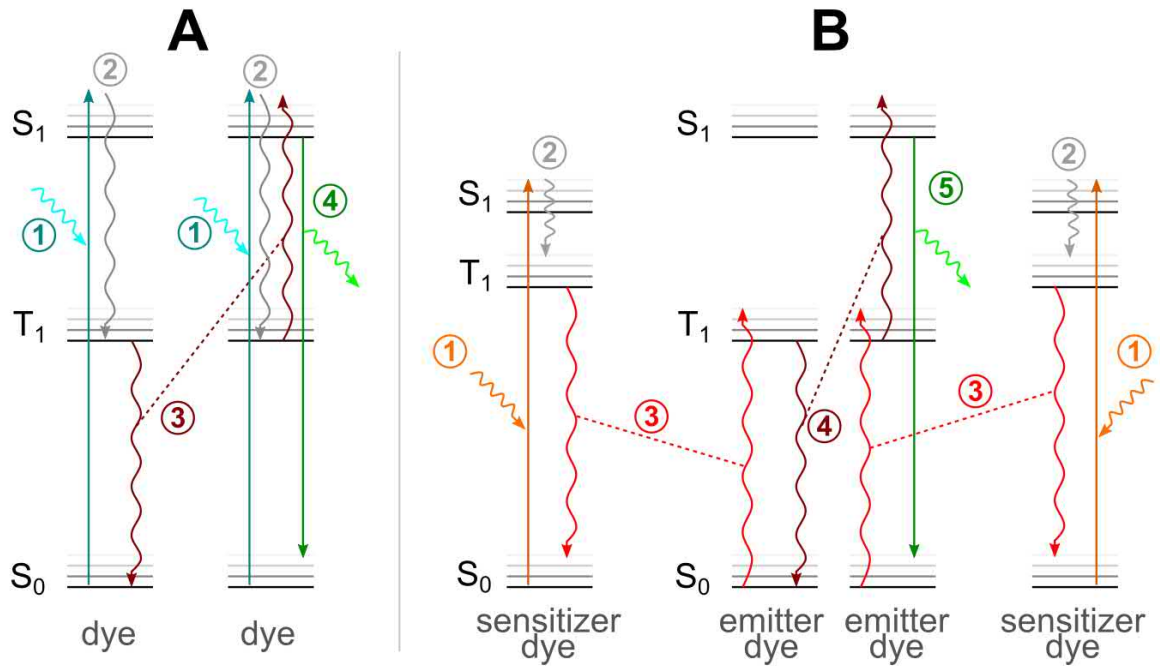

Fig. 1.3.2.1. TTA and sensitized TTA. A: (1) Two dyes absorb high-energy photons and go to an excited singlet state. (2) Both dyes relax to a long-lived triplet state. (3) Dyes perform triplet-triplet annihilation, which puts one dye to ground state and one dye to excited singlet state. (4) The excited dye emits a low-energy photon. B: (1) Two sensitizer dyes absorb low-energy photons. (2) Sensitizer dyes efficiently transition to long-lived triplet state. (3) Sensitizer dyes perform TTET to emitter dyes, exciting the emitters to a triplet state. (4) Emitters perform TTA. (5) The excited emitter emits a high-energy photon.

In practice, TTA with organic dyes can have remarkably high quantum yields, sometimes approaching the theoretical limit of 50% (*Zhao et al., 2011*). Unlike two-photon absorption that requires short excitation pulses of extremely high intensity, TTA can be performed with cheap continuous-wave diode lasers. The anti-Stokes shift is usually in range of ca. 0.5 eV (100-200 nm depending on the part of the spectrum), with occasional higher values being reported for specifically tailored systems (*Huang et al., 2017*). The main caveat of TTA is the rapid drop in efficiency in presence of ambient oxygen and/or oxidation/reduction agents, which is a significant hurdle for applying TTA in biological systems. Also, the photostability of TTA systems is usually quite low, due to high chemical reactivity of the dyes in long-lived excited states (*Dzebo et al., 2017*).

1.3.2.2. Excited state absorption (ESA)

The ions of d- and f-elements frequently have multiple intermediate states. In lanthanide ions in particular those intermediate states are frequently very long-lived, since the transitions between them are symmetry-forbidden. By sequentially absorbing light at one or multiple wavelengths with appropriate energy, the ion can be excited to progressively higher excited states, from which it can emit. This upconversion mechanism is called *excited state absorption*, or ESA (Fig. 1.3.2.2A).

However, because these transitions are usually symmetry-forbidden, the absorption cross-sections corresponding to those transitions are quite low compared to organic dyes or metal complexes. Thus, upconversion through ESA requires high excitation intensity, albeit much lower compared to two-photon absorption.

1.3.2.3. Energy transfer upconversion (ETU)

To make ESA more efficient, the ions can be excited through energy transfer instead of using direct absorption, in an approach similar to sensitized TTA. For this, one or multiple *sensitizer* ions can be put in close proximity to the *emitter* (also known as *activator*) ion. Sensitizers can efficiently transfer their excitation energy to emitter to sequentially pump it into a high excited state. This process is known as *energy transfer upconversion* (ETU) (Fig. 1.3.2.2B).

Efficient ETU requires multiple conditions to be satisfied:

- Sensitizers and emitters have to be close to each other for efficient energy transfer.
- Sensitizers have to be chosen to have appropriate transition energies resonant with the emitter ion's transitions, to be able to perform energy transfer.
- Sensitizers have to have high extinction coefficients.
- Both emitter and sensitizer ions should have long-lived excited states, to facilitate energy transfer and upconversion.
- The non-radiative relaxation pathways have to be minimized.

The most common systems to perform ETU are based on lanthanide-doped inorganic matrix materials (e.g. fluoride or oxide crystals). The typical sensitizer ion is Yb^{3+}, which has strong absorption at 980 nm. The commonly used emitter ions include Er^{3+}, Tm^{3+}, Ho^{3+} and some others.

ETU typically has lower quantum yields than TTA. However, its energy conversion efficiency is usually quite high, translating to large anti-Stokes shifts of 1 eV or more. Also, ETU can happen with acceptable efficiency in three- or even four-photon upconversion. Due to the usage of inorganic materials, ETU systems are usually extremely photostable. The major caveat of employing ETU in biological context is significant quenching by water via non-radiative transitions, lowering the upconversion quantum yield.

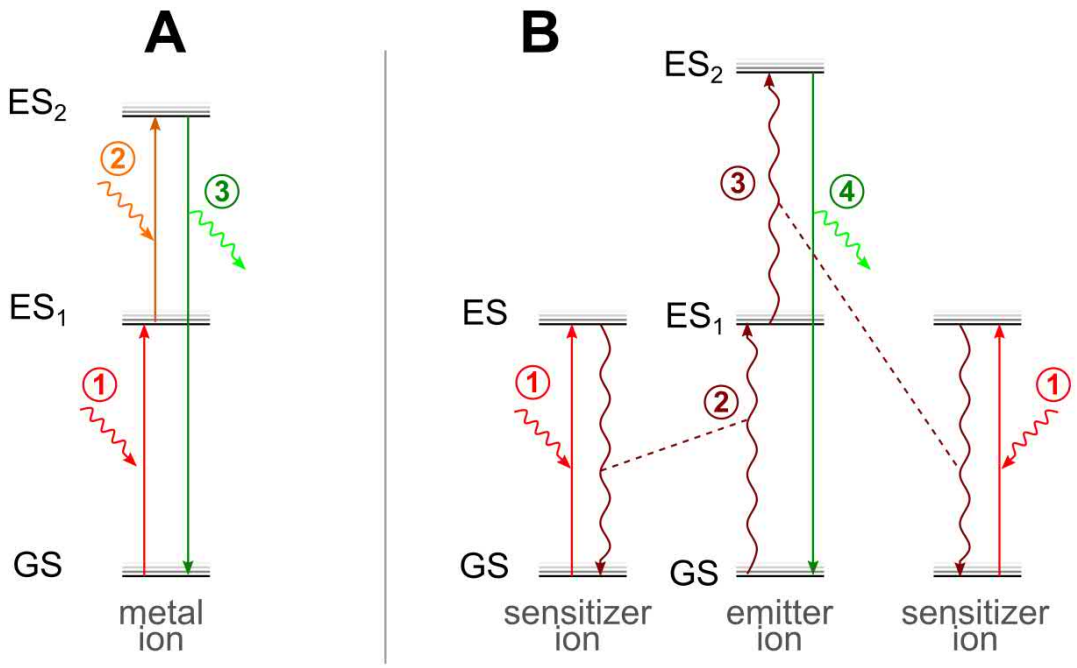

Fig. 1.3.2.2. ESA and ETU. A: (1) A metal ion absorbs a low-energy photon and goes to a long-lived intermediate excited state. (2) From this state, the ion can absorb another photon of the same or different energy to go to high excited state. (3) The excited ion emits a high-energy photon. B: (1) Two sensitizer ions absorb low-energy photons. (2) One of the sensitizer ions transfers its energy to the emitter ion, exciting it to a long-lived intermediate excited state. (3) Another sensitizer ion transfers its energy to the emitter ion, exciting it to a high excited state. (4) The emitter ion emits a high-energy photon.

1.3.2.4. Photon avalanche (PA)

Photon avalanche (PA) is a unique mechanism that bears similarities to both ESA and ETU. In its simplest form, two ions of the same type are located close to each other, and both ions are capable of very efficient absorption if they are in an intermediate excited state. One spontaneously transitions to an intermediate state, either via non-resonant absorption or even via thermal population. From this intermediate excited state, it can perform ESA to transition to a high excited state. Afterwards, it can either dissipate energy in heat, perform radiative relaxation (thus achieving upconversion), or efficiently transfer its energy to the second ion, returning to intermediate state and forcing the second ion to occupy the intermediate state as

well, in a process known as *cross-relaxation*. In the latter case, the net result is two ions in the intermediate state. They both can then efficiently absorb light and transition to a high excited state. Now, if there are two more ions of the same type in close vicinity, the two ions in high excited state can transfer their energy to them. This now yields four ions in intermediate state. Continuing this process, the population of ions in intermediate state continues to increase exponentially (hence the comparison to an avalanche), occasionally losing energy into heat or releasing it as high-energy photons, thus achieving upconversion. Fig. 1.3.2.3 illustrates the process.

There are several conditions required for PA:

- The ions must have a high absorption cross-section in intermediate state and capable of cross-relaxation.
- The ions must be in sufficiently close proximity to enable efficient cross-relaxation.
- Excitation intensity needs to be sufficiently high, so that cross-relaxation overcomes the spontaneous relaxation of the intermediate state.
- The intermediate state should be long-lived so that the excited state absorption and cross-relaxation are efficient.

Over time, PA process eventually reaches a steady state due to the saturation of the intermediate excited state and equilibration of excitation and relaxation transitions.

The advantage of PA upconversion is that the excitation light has to be resonant with only one transition, between intermediate and high excited state, while the ground state-intermediate state transition can be induced by non-resonant absorption or thermal population. PA, however, is a relatively rare phenomenon, that happens only with certain ions in specific conditions (an example is presented in *Levy et al. 2016*).

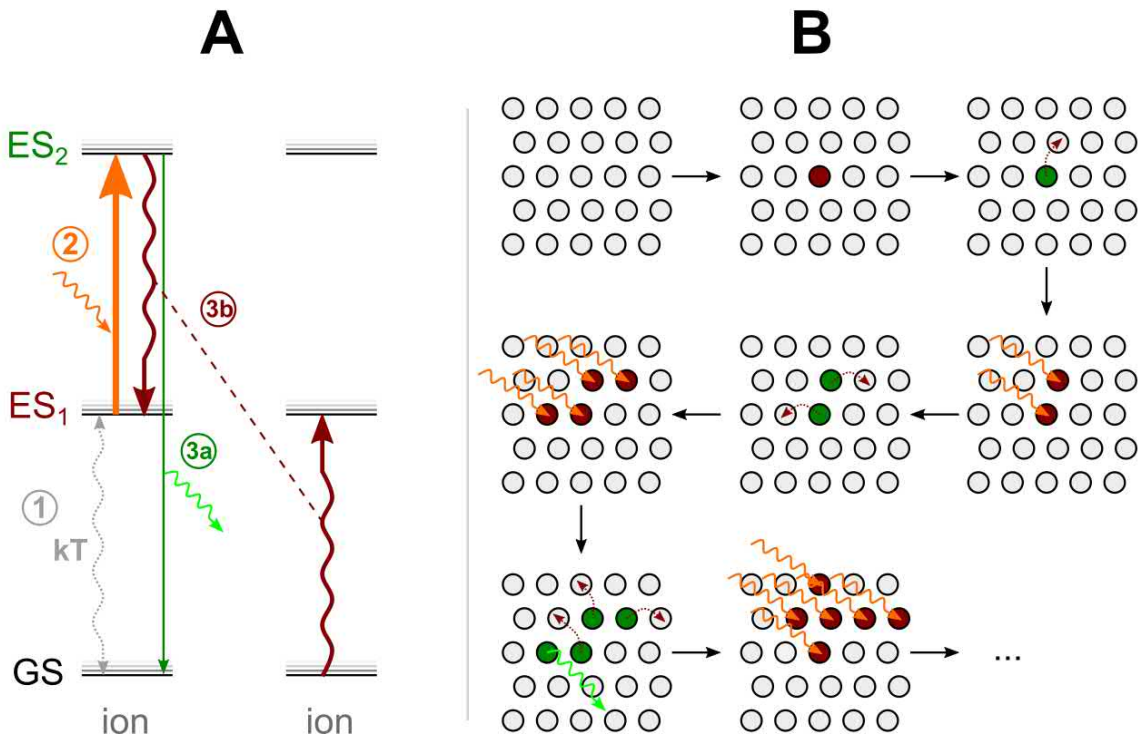

Fig. 1.3.2.3. PA upconversion. A: (1) an ion is spontaneously excited to an intermediate state, e.g. through thermal population. (2) the ion can efficiently absorb a low-energy photon and transition to a high excited state. From this state, it can either emit light (3a) or efficiently transfer energy to another ion of the same type (3b). B: With steady intense illumination, the excitation can spread through multiple ions located close to each other, requiring only one spontaneously excited ion to initiate the process. Occasionally, the ions can emit high-energy photons instead of performing energy transfer.

For applications in biology, upconversion holds a lot of promise. In tissue experiments, the long-wave excitation light in red or infrared region can penetrate the tissues much deeper, as they absorb and scatter much less. The large anti-Stokes shift is not exhibited by any biological materials, so the problem of autofluorescence in imaging can be entirely circumvented. Also, red and infrared light can be used at high intensities without cell damage, unlike blue or UV light (*Wolbarsht, 1971*). Certain inorganic materials with extreme photostability can exhibit upconversion, potentially permitting uninterrupted long-term experiments. Unlike TPA, upconversion does not require expensive short-pulsed laser sources and can be induced by cheap continuous-wave laser diodes.

To harness the mechanisms of upconversion for usage as a luminophore in biological context, the materials capable of upconversion can be constructed into *upconversion nanoparticles* (UCNPs). While the solid-state upconversion itself is not a particularly new phenomenon with examples dating back to 1960s (*Auzel, 2004*), active research on UCNPs has started only in late 2000s (*Heer et al., 2004; Kuningas et al., 2005; Shalav et al., 2005; Wang et al., 2005; Yan and Li, 2005*). Thus, UCNPs are still a novel luminophore with a lot of room for improvement and potential for applications.

Out of the multiple types of UCNPs, the most well-developed UCNPs are inorganic lanthanide UCNPs upconverting via ETU mechanism. They currently exhibit most potential for a variety of applications, especially in biology (*Zhou et al., 2015*). For brevity, all subsequent chapters of this work use "UCNPs" as a shorthand for specifically this type of particles operating via this type of mechanism.

1.3.3. Lanthanide upconverting nanoparticles

1.3.3.1. Structure

There is a large variety of UCNPs engineered for different applications. As an illustrative example, we may consider the spherical β-$NaYF_4$ UCNPs doped with 20% Yb^{3+} and 2% Er^{3+}, which are currently by far the most investigated and most used kind of UCNPs in literature, due to their efficient upconversion. It should be noted that "doping" in this case is not quite a valid term, as in most other fields it usually refers to sub-1% quantities of substituting element, so "mixing" would be more appropriate. However, in UCNP-related literature the "doping" term seems to be dominant, and will be used throughout this work to maintain consistency with the rest of the literature.

The luminescence mechanisms of UCNPs involve a large amount of processes besides ETU and can be intimidating at a glance (Fig. 1.3.3.1A), however recent efforts have allowed to model and sometimes predict these processes to a decent extent (*Anderson et al., 2014; Chan et al., 2015; Hossan et al., 2017; Würth et al., 2018, 2017*).

There are several key parameters in UCNPs which are important for efficient upconversion (Fig. 1.3.3.1B):

- **Sensitizer ions and their concentration** (Yb^{3+} at 20% in the example). Yb^{3+} ions are a common choice for ETU due to to having only one excited state that is within the reach of excitation by low-energy UV, visible, or near-infrared (NIR) light. The transition from the ground state to this excited state corresponds to approximately 980 nm photon wavelength, and is notable for relatively large absorption cross-section. The excited Yb^{3+} ions typically have a long lifetime in the range of 100-1000 μs (*Würth et al., 2017*). This long lifetime and very narrow energy band structure with practically no sublevels allows these ions to efficiently transfer energy to each other, forming a *sensitizer network* in which the energy can quickly migrate throughout the crystal (Fig. 1.3.3.1C). This permits the energy to be efficiently transferred to emitter ions, which quickly deplete the sensitizers around them, allowing far-off excited sensitizers to transfer their energy to depleted ones and transfer even more energy to emitters.

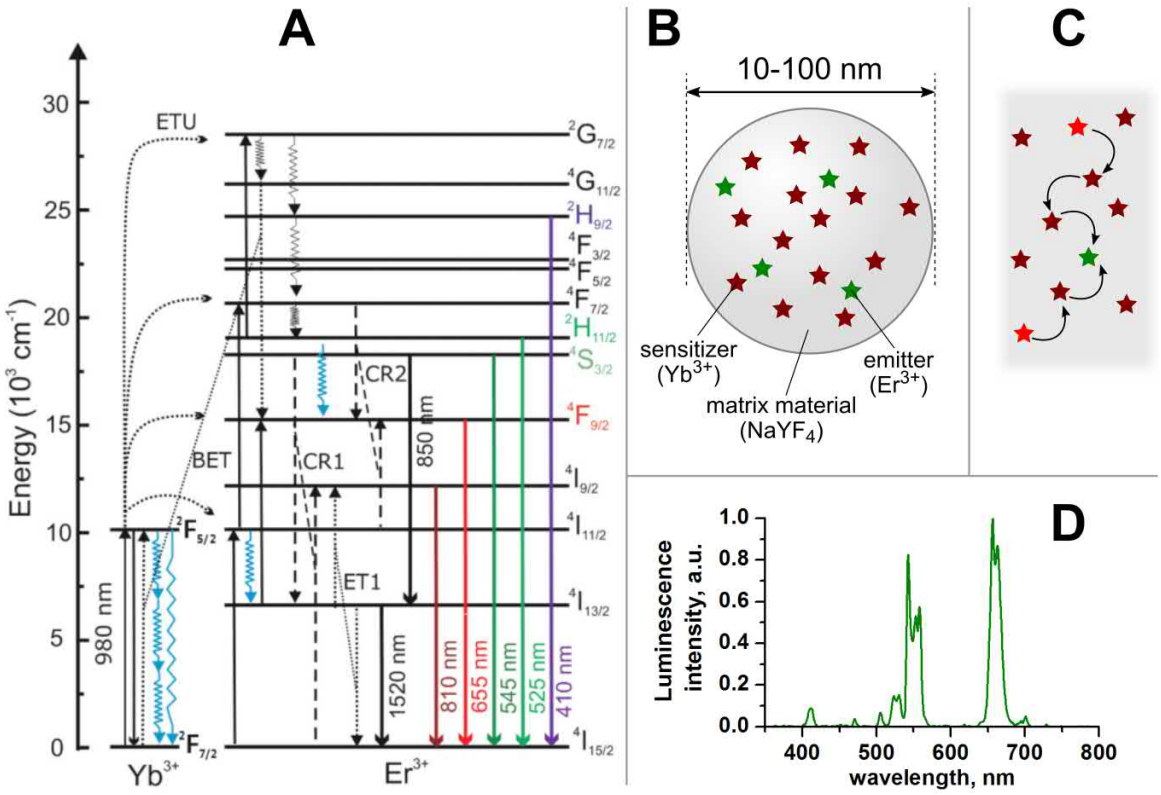

Fig. 1.3.3.1. Typical UCNPs and mechanisms of their luminescence. A: Luminescence mechanism in Yb^{3+}-Er^{3+} system upon excitation at 980 nm and some related processes. BET, CR and ET correspond to back energy transfer, cross-relaxation and energy transfer,

respectively. Blue arrows correspond to relaxation processes associated with quenching by O-H vibrations, e.g. by water. B: structure of a UCNP, with labeled components. C: energy propagation through sensitizer network. Nearby sensitizer ions can exchange energy, eventually transferring it to the emitter to perform upconversion. D: typical luminescence spectrum of a Yb^{3+}-Er^{3+} UCNP dispersion at 980 nm excitation. Image adapted from (*Würth et al., 2017*).

- **Emitter ions and their concentration** (Er^{3+} at 2% in the example). Er^{3+} ions can perform efficient ETU with several bands in visible region, with most intense being the green band at 540 nm and red band at 660 nm (Fig. 1.3.3.1D). Typically emitter ions are used at a low doping proportion due to cross-relaxation processes that reduce the population of high excited states, leading to lower upconversion efficiency. The exception is PA-based UCNPs, where cross-relaxation is actually a beneficial phenomenon. Also, recent evidence suggests that high doping concentrations can be beneficial for applications of ETU-based UCNPs requiring high excitation intensity (e.g. microscopy) (*Gargas et al., 2014; Tian et al., 2018*).
- **Matrix material** (β-$NaYF_4$ in the example). The choice of matrix material is governed by several concerns. First, multiphonon relaxation is one of the main non-radiative relaxation mechanisms for lanthanide ions in inorganic materials, resulting in dissipation of energy into several simultaneous vibrations of the nearby ions in the crystal, which are eventually dissipated into heat. The multiphonon relaxation rate is dominated by the highest-energy phonons in the given crystal structure (*Egorov and Skinner, 1995)*. For a given phonon, the multiphonon relaxation rate associated with it decreases approximately exponentially with the energy gap. Conversely, for a fixed energy gap the relaxation rate exponentially decreases with lower maximum phonon energy. Thus, the material should be chosen to have lowest possible phonon energies. Second, the presence of defects in the bulk material can be both beneficial and detrimental. f-f transitions are partially unforbidden when the local crystal symmetry is distorted, resulting in more efficient upconversion (*Cheng et al., 2012; Wisser et al., 2016*). However, certain defects yield additional relaxation channels via local high-energy vibrations, yielding new non-radiative relaxation channels. This is typically observed in crystalline fluoride and oxide materials. Other concerns for a

matrix material are the ease of preparation and chemical stability, which will be discussed below.

- **Particle surface**. Surface effects are extremely important and can significantly affect the particle emission parameters. Surface defects and certain coordinated ligands can serve as energy sinks by scavenging energy from nearby sensitizers and emitters. There are multiple mechanisms for such effects. For example, in particles constructed with Yb^{3+} as a sensitizer, the whole sensitizer network can quickly get depleted by relaxation via O-H vibrations of ligands close to the surface, lowering the brightness of the UCNPs (Fig. 1.3.3.1A, blue arrows). This can lead to quenching of upconversion by surface-coordinated water molecules (*Arppe et al., 2015*).

- **Particle shape** (spherical in the example). Depending on the synthesis method, UCNPs can be prepared in different shapes. Particles of different shapes have exposed surfaces corresponding to different crystal planes. This can affect the particle luminescence, quenching, strength of ligand attachment, and other parameters (*Shan et al., 2010; Ye et al., 2010*).

- **Particle size.** Size has a direct effect on the brightness of individual UCNPs: lower particle size results in lower amount of active ions per particle. This leads to lower brightness via lower total extinction coefficient and lower amount of individual emitters. Also, smaller particles have larger surface-to-volume ratio which can potentially lead to stronger quenching, further reducing brightness by lowering the upconversion quantum yield. Increasing the size of the particle tends to make its behavior closer to the bulk material, reaching it at particle size of several micrometers (*Boyer and Veggel, 2010; Hossan et al., 2017; Kaiser et al., 2017*).

- **Ion distribution** (uniform in the example). UCNPs can be prepared in a variety of ways, and some allow sequential growing of differently doped shells, resulting in core-shell structures, reminiscent of gobstopper candy. The shells can be doped in a variety of ways. Examples include separating sensitizer and emitter for enhanced upconversion (*Vetrone et al., 2009*), isolating the upconverting composition inside an inert shell to reduce surface quenching (*Gargas et al., 2014*), segregating several sensitizer/activator compositions inside the same particle to make a dual-mode particle with response dependent on excitation wavelength (*Lai et al., 2014*), etc.

All of these parameters are intertwined with each other. For instance, different matrix materials may impart better or worse performance on a given sensitizer/emitter pair. As an another example, certain multilayer ion distributions require a minimum particle size, below which the layers cannot be sufficiently separated due to their intermixing during synthesis. Thus, all of these parameters have to be considered simultaneously when choosing an optimal particle for a given application.

1.3.3.2. Synthesis and matrix materials

Synthesis of inorganic nanoparticles is an actively developing field. Numerous methodologies have been applied to construct metallic, ionic and covalent particles with different size, composition, monodispersity and crystallinity. Quite a lot of mechanisms governing the nanoparticle formation are well-investigated, some are even predictable in quantitative fashion. However, to this day the field remains mostly empirical due to its sensitivity to minute details of the experimental conditions and dependence of the synthesis on a large quantity of parameters, complicating screening for optimal conditions.

Synthesis of lanthanide UCNPs has an advantage of having very similar protocols for very different dopant compositions, due to close ionic radii of lanthanide ions and their similarity in reaction profile.

Typical particle diameters achievable by commonly used methods range from ~10 to 100 nm, although in recent years there have been breakthroughs that allow production of monodisperse sub-10 nm particles (*Gargas et al., 2014; Li et al., 2017; Ostrowski et al., 2012; Ryu et al., 2010*).

Particle geometries can depend on the method, but generally are spherical or approximately spherical. Similar to microcrystals, nanocrystals frequently have preference for exposing particular crystal planes to the outer environment due to lower surface energy, giving the particles a slightly angular appearance.

The following methodologies are typically employed to synthesize UCNPs (*DaCosta et al., 2014*):

- **Thermal decomposition**, which involves decomposing organic lanthanide salts (e.g. oleates) and matrix material precursors at high temperatures in a high-boiling non-polar solvent in presence of surfactants, usually in inert atmosphere. The control over

temperature, heating/cooling rate, reaction time, reagent and surfactant concentration allows to achieve uniform nucleation and slow growth of nanoparticles. This also helps to achieve high UCNP crystallinity. Additionally, core-shell geometries can be produced by adding precursor or small sacrificial nanoparticles at appropriate time during the reaction (*Gainer and Romanowski, 2014; Haase and Schäfer, 2011*). Multiple variations of the method exist, differing mostly in the choice of the reagents and the temperature regime.

Thermal decomposition is one of the most popular and consistent methods of UCNP production which allows to prepare highly crystalline monodisperse particles with low amount of defects and good control over their size. Typically, UCNPs produced by thermal decomposition range from ~5 to >100 nm in diameter. The key disadvantage of the method is the requirement of precise and consistent temperature control, which can affect reproducibility. To overcome this problem, two approaches exist: preparation of particles in large batches (*Wilhelm et al., 2015*) and process automation (*Chan, 2015; Chan et al., 2010*).

- **Coprecipitation**, in which the UCNPs are prepared via rapid mixing of solutions of lanthanide salts and/or complexes with the dissolved matrix materials in the conditions forcing the precipitation of the material. Formation of nanoparticles can be achieved in certain ranges of concentration, mixing speed and mixture polarity.

  Despite being by far the easiest and most straightforward method, it typically produces UCNPs of relatively low quality in regards to upconversion. This drawback can be partially amended by annealing the particles after synthesis.

- **Solvothermal synthesis**. One of the oldest methods to produce crystals of inorganic materials, the method entails taking a suspension of inorganic microcrystals to high temperatures and pressures in an autoclave, typically in aqueous conditions. The precursor microcrystals are formed by mixing lanthanide salts with an appropriate counterion, e.g. ammonium fluoride. Above the critical point of the solvent, the mixture forms a single phase, in which nanoparticles slowly form over time if an appropriate temperature/pressure regime is used.

  The largest advantage of this method is its potential for scalability and the usage of "green" reagents, utilizing only solutions of inorganic salts as the main precursor. The

disadvantages include high particle polydispersity, low crystallinity and lower control over the reaction compared to other methods.

Numerous other less popular ways to produce UCNPs exist, ranging from classic methods like milling and sol-gel processing to unconventional approaches like microwave-assisted heating and gas phase flame synthesis (*Gainer and Romanowski, 2014*).

1.3.3.3. Luminescence properties and doping strategies

The cornerstone element of UCNP optical response is the choice of sensitizer and emitter. Fig. 1.3.3.3.1 shows the energy levels of trivalent lanthanide ions in a $LaCl_3$ lattice. As can be seen from the image, lanthanide ions possess significantly more distinct states compared to organic dyes or transition metal complexes. This, coupled with the fact that a lot of transitions between these states can have comparable rates, makes ETU upconversion a highly nonlinear and sometimes quite unpredictable process. Moreover, the rates can also depend on the local crystal field, and other processes like ion cross-relaxation may appear at higher dopant ion concentrations. Nevertheless, during the development of bulk upconversion materials and later upconversion nanoparticles, certain sensitizer/emitter pairs have been found to produce robust upconversion with relatively high quantum yields. Table 1.3.3.3.2 provides the overview of commonly used sensitizer/emitter pairs, and their absorption/emission wavelengths.

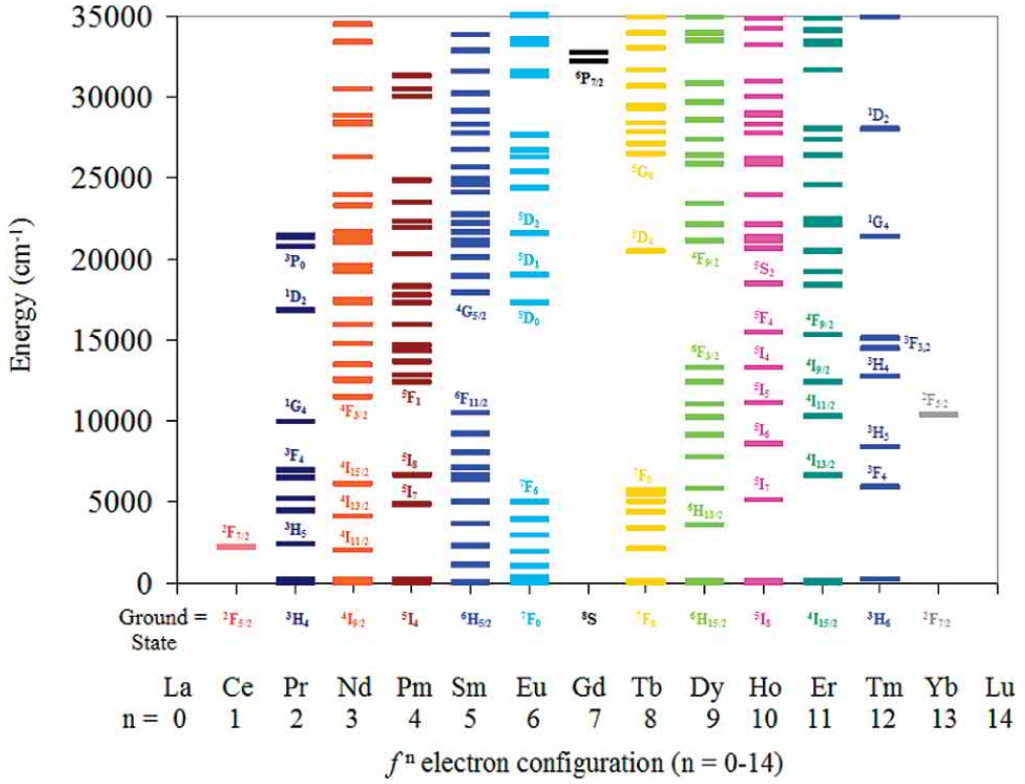

Fig. 1.3.3.3.1. Energy levels of Ln^{3+} in a $LaCl_3$ lattice. Image adapted from (Moore et al., 2009).

Both absorption and emission bands of UCNPs are formed by *f-f* transitions in lanthanide ions. The 4*f* orbitals are shielded from the environment by the filled $5s^2$ and $5p^6$ orbitals. This makes their coupling to electrons of the molecules and ions in their immediate environment very weak, significantly lowering the amount of sublevels for each state. Due to this, lanthanide energy states are very narrow and the energies of the transitions between these states are very consistent in different local environments. This results in narrow absorption and emission bands that are very similar in quite different matrix materials, typically differing in their relative intensity, but not the wavelength (*Wang and Liu, 2014*).

The absorption spectra of UCNPs are dominated by the peak of the sensitizer due to its higher extinction coefficient compared to the emitter. Peaks for commonly used sensitizers are located in NIR region. Occasionally, double-sensitizer systems are used, in which one type of sensitizer transfers the energy to a different one, which then performs ETU with the

emitter. UCNPs can also exhibit some direct absorption by the emitter, usually followed by luminescence at the same wavelength. The direct excitation can be sometimes useful in mechanistic investigations of upconversion behavior, although the extinction coefficients for direct excitation are typically quite low (*Eliseeva and Bünzli, 2010*).

Sensitizer	*Emitter*	λ_{abs}	λ_{em}
Yb^{3+}	Er^{3+}	980 nm	410 nm, 525 nm, **545 nm**, **660 nm**, 810 nm
Yb^{3+}	Tm^{3+}	980 nm	**450 nm**, 470 nm, 650 nm, 695 nm, **800 nm**
Yb^{3+}	Ho^{3+}	980 nm	485 nm, **540 nm**, **645 nm**, 750 nm
Nd^{3+}-Yb^{3+}	Er^{3+} or Tm^{3+} or Ho^{3+}	810 nm, 980 nm	*identical to three previous ones, dependent on the emitter choice*

Table 1.3.3.3.2. Typical dopant compositions for UCNPs. The primary emission peaks are highlighted in bold.

The emission spectra of UCNPs following sensitizer excitation consist of sensitizer and emitter bands. Typically the sensitizer emits with nearly the same energy it was excited with (due to the narrow band structure), while the emitter shows multiple peaks in visible region. Emitters also frequently have luminescence bands with lower energy than that of the excitation, due to *downshifting* processes involving decay of emitters in a high-energy state to a low-energy state with subsequent emission. An example of downshifting is the Er^{3+} luminescence at 1.55 μm after excitation at 980 nm. Downshifting should be not confused with *downconversion* (a.k.a. *quantum cutting*), a process in which a single high-energy photon is transformed by the system to two or more low-energy photons.

The quantum yield of upconversion (UCQY) can be defined in multiple ways. Commonly, the empirical definition is used, in which UCQY is defined as the ratio of the quantity of photons emitted by the emitters in the system to the quantity of photons absorbed by the sensitizers and emitters. By this definition, theoretical maximum UCQY are 50%, 33.3%, 25%, 20%, etc., corresponding respectively to two-, three-, four-, five-, or higher-

order multiphoton upconversion processes. As UCNPs usually possess multiple emission bands, sometimes *partial* quantum yields are defined for individual bands in a similar fashion.

The UCQY depends on the speed of the transitions between the states of lanthanide ions and on a variety of energy transfer processes inside the particle: sensitizer-emitter transfer, emitter cross-relaxation, emitter-sensitizer back-transfer, and some others (*Chan et al., 2012a, 2012b*). Those processes, in turn, depend on a wide variety of parameters: matrix material, particle surface quenching, quenching on defects, dopant concentration, excitation power, pulse shape and length in case of pulsed excitation, etc. Due to strong interconnection between these parameters and difficulties in standardization of experimental setups (especially in relation to excitation intensity), experimental determination of UCQY is not an easy task, as it requires direct determination of UCNP absorption coefficient using infrared spectrophotometers and complicated setups with integrating spheres. Moreover, the experimental UCNP absorption coefficient also has to be corrected for scattering, which can be significant in concentrated nanoparticle dispersions (*Würth et al., 2013*).

In typical UCNPs, UCQY values are usually in the range of 0.1-1%. This is 1-2 orders of magnitude lower than the QY of organic dyes and quantum dots, which can occasionally reach values close to their theoretical maximum of 100%. As a result, the brightness of UCNPs is typically orders of magnitude lower than that of quantum dots, and can be comparable to the brightness of an organic dye. However, the loss of signal-to-noise ratio in UCNP applications due to their low brightness is more than fully compensated by the absence of background luminescence noise even at high excitation intensities, resulting in SNR comparable to other conventional luminophores. Also, due to their extreme photostability, the excitation intensities may be elevated to much higher levels, typically limited only by the sample absorption of light and its speed of heat dissipation. Another advantage is that in biological samples NIR light does not have any significant phototoxic effects besides heating (*Khan et al., 2015*).

The lifetimes of excited states of lanthanides in typical UCNPs are usually at the order of 10 μs to 10 ms, multiple orders of magnitude longer than the nanosecond lifetimes of organic dyes or quantum dots. An example of a decay curve for a UCNP dispersion is provided on Fig. 1.3.3.3.3. Long lifetimes can be both an advantage and a detriment, depending on the application. For instance, time-gated microscopy with long-lifetime

luminophores can be done with very cheap chopper-based experimental setups, while confocal microscopy tends to require much longer readout times due to "streaking" artifacts (*Gainer et al., 2012; Zheng et al., 2016*). The shape of decay curve and the lifetime depend on the interplay of a large quantity of parameters. There are some theoretical models with decent predictive value for calculating UCNP decays and transition rate constants, but they are typically valid only at low excitation intensities (below 100 W/cm^2) (*Hossan et al., 2017*).

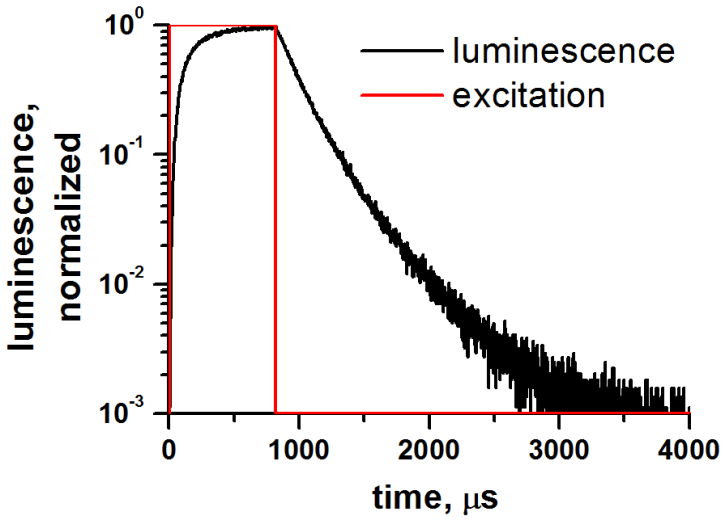

Fig. 1.3.3.3.3. Luminescence decay of a Yb^{3+}-Er^{3+} UCNP dispersion (black line). Decay shape may differ dependent on the excitation pulse length, so boxcar excitation mode (red line) is typically employed to record UCNP decays from a steady state. This is also useful for comparing the information extracted from decays with the spectra, which are typically recorded in a steady state.

UCNPs show unsurpassed photostability, due to absence of irreversible low-activation-energy chemical reactions of lanthanide ions with their environment in their excited states. This puts them at significant advantage compared to organic dyes and quantum dots, which are amenable to photooxidation and photoreduction (*Lee and Osborne, 2009; Resch-Genger et al., 2008*).

As emitters in the vast majority of UCNPs have quite slow emitter-emitter energy transfer, they show mostly independent emission. Because of this, UCNP emission tends to be uniform in time with low variation, as the luminescence of a typical UCNP corresponds to

concurrent luminescence of hundreds and thousands of individual emitters (*Gargas et al., 2014*).

Luminescence properties of UCNPs highly depend on dopant concentration. Sensitizer concentration typically has an optimum in relation to particle brightness. At too low sensitizer concentration, the particle has lower total extinction coefficient, and the probability of two sensitizers being in close proximity to an emitter is also low, leading to inefficient ETU. At too high sensitizer concentration, surface quenching effects can quickly deplete the sensitizer network, leading to higher energy losses despite higher total extinction (*Ma et al., 2017*). Similarly, emitter concentration also has an optimum. At too low emitter concentration, the total quantity of emitters in particle is lower, resulting in lower overall luminescence. At too high emitter concentration, cross-relaxation effects start coming into play, resulting in UC energy loss at lower excitation powers. However, if higher excitation powers are used (e.g. in microscopy conditions), the gain in luminescence due to larger quantity of emitters can overcome the cross-relaxation losses, resulting in higher particle brightness (*Gargas et al., 2014; Tian et al., 2018*).

UCNPs can be constructed from several different materials using layer-by-layer synthesis techniques, which can be used to modulate their luminescence. Usually the layers are made from the same matrix material, but differ in dopant choice and concentration. Some doping strategies of UCNPs are shown on Fig. 1.3.3.3.4. Common strategies include:

- **Doped core, inert shell**. This approach aims to reduce surface quenching effects by increasing the distance between dopant ions and the quenching centers on the particle surface (*Ding et al., 2015; Gargas et al., 2014*). Employing this approach yields higher particle brightness in exchange for slight increase in particle size. Also, because of lower surface quenching, the particle core can be doped more than usually (especially with sensitizers), improving the brightness even further (*Tian et al., 2018*). The disadvantage of this approach is worse particle performance in FRET applications, due to larger distances from emitters to particle surface.
- **Inert core, doped shell**. This approach is inverse to the previous one, and aims to improve particle performance in FRET applications, sacrificing some particle brightness for it (*Bhuckory et al., 2017*).

- **Segregated dopant layers**. For certain UCNP compositions, homogeneous mixture of dopants may have mediocre performance due to introduction of additional undesirable non-radiative relaxation mechanisms. This is especially true for UCNPs doped with more than two dopant types, combining ETU and intra-particle energy transfer to tune their absorption or emission spectra. By isolating incompatible dopants in different regions, this drawback can be eliminated (*Deng et al., 2016; Wang et al., 2011; Zhong et al., 2014*).

- **Segregated full UC compositions**. Different sensitizer/emitter pairs can be isolated in different regions in a same particle, separated with layers of inert matrix material. This approach yields particles with drastically different emission spectra that depend on excitation wavelength (*Lai et al., 2014*).

- **External sensitization**. A promising recent strategy to drastically improve the extinction coefficient of UCNPs involves isolating the sensitizers and emitters in the core of the particle, and doping the shell with sensitizer only. Afterwards, additional sensitizing moieties are grafted to the surface of the particle, typically red and NIR-absorbing organic dyes, which can transfer their excitation energy from the T_1 state to the sensitizer ions. The total energy cascade is external sensitizer – sensitizer – emitter. This approach allows to improve the brightness of UCNPs by 2-4 orders of magnitude, which can be critical for certain applications (*Chen et al., 2015; Garfield et al., 2018; Zou et al., 2012*). However, so far the resulting conjugates show mediocre photostability, especially in the presence of oxygen, where photostability half-life drops to ~1 min.

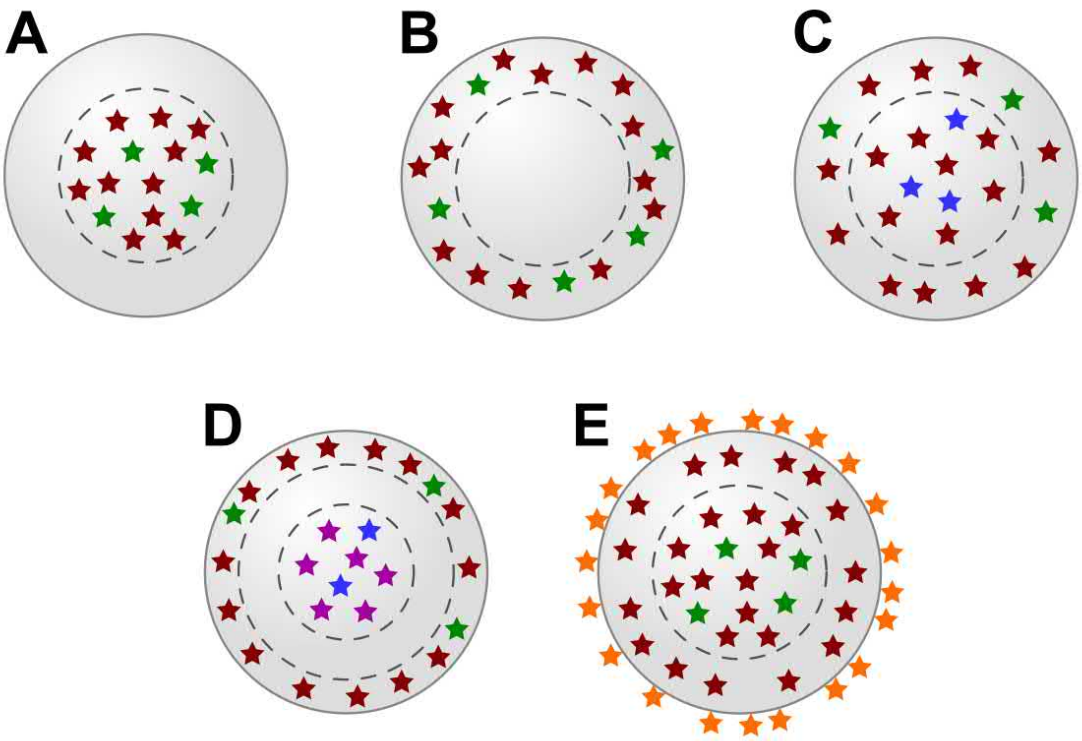

Fig. 1.3.3.3.4. Common UCNP doping strategies. A: doped core, inert shell. B: inert core, doped shell. C: segregated dopant layers. D: segregated full UC compositions. E: external sensitization.

To summarize, upconversion in UCNPs is a highly intricate mechanism that depends on a large set of both internal and external parameters. This is both a boon and a bane for UCNP research, as such behavior presents exceptional possibilities for its modification, at a price of making it difficult to model, predict, and (sometimes) reproduce.

1.3.3.4. Surface modification

Depending on synthesis and purification method, UCNPs may have a variety of ligands on their surface. The most commonly used fluoride-based UCNPs produced via thermal decomposition typically have a layer of fatty acid ions on their surface (commonly oleates), weakly coordinated to positively charged ions on particle surface. Due to high hydrophobicity of this layer, the particles are dispersible only in nonpolar solvents, e.g. hexane or

dichloromethane. While such dispersibility may be passable for certain applications, biological studies typically require the luminophore to be dispersible in aqueous conditions. Frequently there is a need for some potential for further attachment (a.k.a. *grafting* or *decoration*) of biological moieties to the particle surface, e.g. for constructing luminescent labels. To achieve these goals, multiple surface modification processes have been invented. Fig. 1.3.3.4.1 provides an overview of typical approaches, which will be briefly described below. Multiple reviews on the topic exist, providing a more in-depth look (*Muhr et al., 2014; Sedlmeier and Gorris, 2015*).

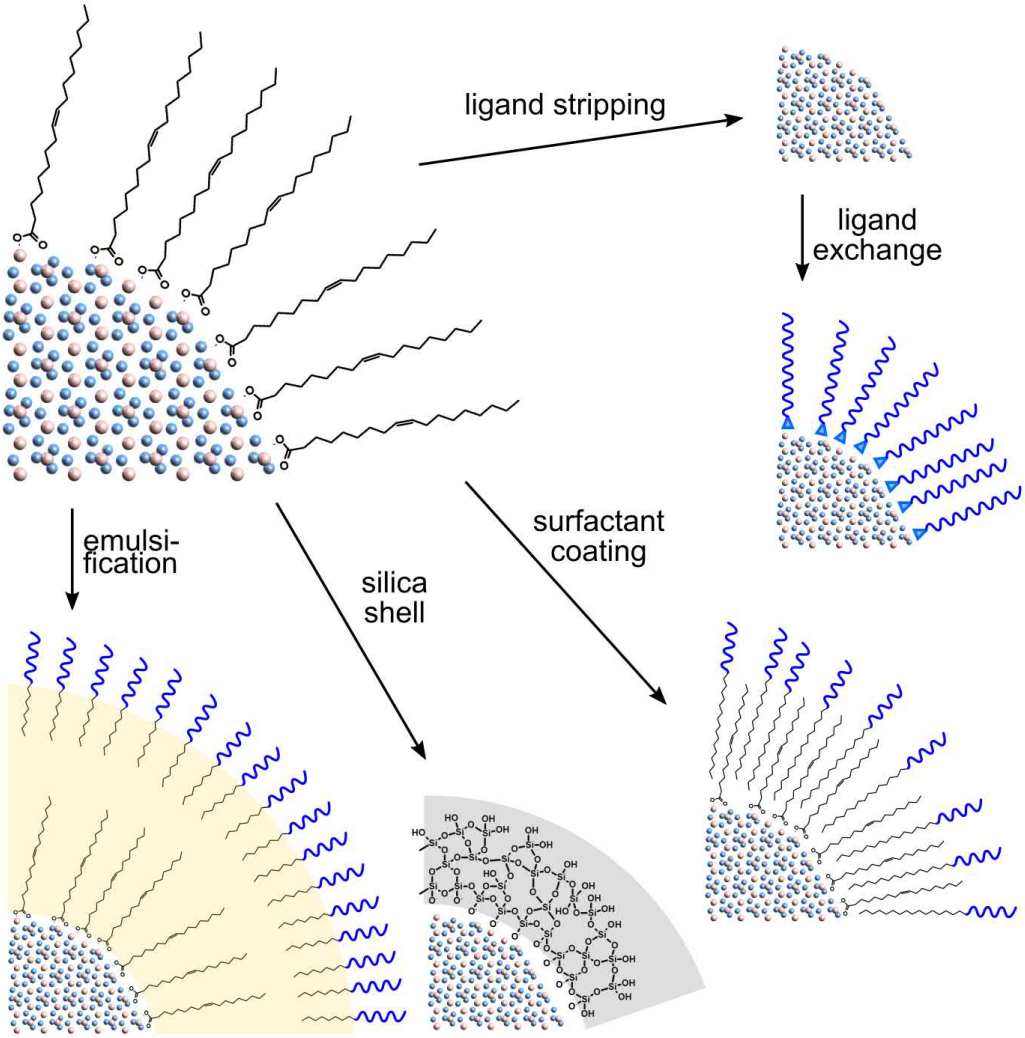

Fig. 1.3.3.4.1. Common strategies for UCNP coating for water dispersibility.

- **Ligand stripping** is the simplest way to render particles hydrophilic. In this process, the hydrophobic ligands are chemically removed from the particle surface. In the most common case which involves surface-bound fatty acids, the particles are treated with strong mineral acid (e.g. HCl), leading to protonation of organic acids and their detachment from the particle surface. Afterwards, the particle surface is hydrophilic, and particle can be dispersed in aqueous environment. This process can sometimes induce particle degradation, so acid precursors such as nitrosonium tetrafluoroborate ($NOBF_4$) can be used for more controlled and gentle ligand stripping (*Dong et al., 2011*). Typically, particles produced by ligand stripping are not very colloidally stable in aqueous dispersions, although dispersions in polar solvents can be stable for years. In case of ionic matrix materials, strong ligand grafting is difficult, quite unlike the covalently modifiable organic dyes or thiol-modifiable chalcogenide QDs.

- **Ligand exchange** is a similar process to ligand stripping, however in this case stripping is followed by particle coating with a hydrophilic ligand. By far the most popular method for UCNP hydrophilisation, ligand exchange protocols combine easy protocols with high subsequent particle colloidal stability (*Sedlmeier and Gorris, 2015; Wilhelm et al., 2015*). Further functionality may be imparted on the particles by mixing in ligands modified with an appropriate recognition moiety, e.g. a protein or a nucleic acid. The main disadvantage of ligand exchange is the detachment of ligands from particle surface if an equilibrium concentration of ligands is not maintained in the dispersion, leading to particle aggregation upon dilution. This can be amended by using polymer ligands, or crosslinking monovalent ligands after coating the particle (*Boyer et al., 2009*).

- **Silica shells** can be grown on the particle using techniques similar to Stöber process (*Hlaváček et al., 2014*). This results in a layer of silica on the surface of particle, which renders the particles hydrophilic. To further enhance colloidal stability, additional groups may be grafted to silica surface during the coating process, or after it. Silica shells are highly modifiable, and a great variety of grafting protocols exist. Silica shells are also quite chemically stable, and are destroyed only via hydrolysis at high pH. The main drawback of the method is partial aggregation of the particles if the growth conditions are not strictly controlled. Even then, slow aggregation over time

limits the shelf life of the particles. Also, silica shells are typically porous, leading to access of water molecules to particle surface, resulting in partial luminescence loss.

- **Surfactant coatings**. Surfactants can form lipid bilayer-like structures with hydrophobic ligands on the surface of UCNPs, making the particle surface hydrophilic without the need to remove the ligands. A modification of the method utilizes cross-linked surfactants also known as *amphiphilic polymers*, which can be kinetically entrapped in the surface layer to form a stable coating that persists on the particle surface (*Wilhelm et al., 2015*). Another modification of the process includes cross-linking of the surfactants after coating, essentially encasing the particle in a thin layer of plastic (*Jiang et al., 2012*). Typically charged polymers are used to further stabilize the particles by introducing interparticle electrostatic repulsion. Surfactant coatings can impart aqueous dispersibility combined with extreme colloidal stability, for years and beyond. Similarly to ligand exchange, the key disadvantage of the method is detachment of surfactants and slow particle aggregation in dispersions that do not contain equilibrium concentration of surfactant. In case of amphiphilic polymer coatings, the disadvantage is the requirement of polymer preparation, as optimal polymers for this goal are not readily commercially available.

- **Nanoparticle entrapment (emulsification)**. A method not commonly used for UCNPs aside from niche applications (*Meruga et al., 2018*), entrapment protocols involve trapping nanoparticles in surfactant-stabilized oil-in-water emulsions, typically with droplet size comparable to UCNP diameter (*nanoemulsions*). The method is usually very fast to perform, and a lot of biocompatible nanoemulsion oil/surfactant pairs exist. The disadvantage of the method is severe UCNP aggregation during the formation of nanoemulsion, and low loading ratio (amount of UCNP-containing droplets relative to total amount of droplets in emulsion).

- **Ligand transformation** involves chemical modification of hydrophobic ligands to render them hydrophilic. An example is permanganate/periodate oxidation of oleic acid to azelaic acid, which has carboxylic groups at both ends (*Naccache et al., 2009*). This method requires strict reaction control to avoid side processes (e.g. MnO_2 formation) that may introduce undesirable hard-to-remove impurities in nanoparticle dispersion.

Attachment of biological moieties to nanoparticle surface can be done either directly during coating process, or after it, using *bioconjugation* techniques. There is a vast variety of different bioconjugation methods for nanoparticles, each with its own advantages and drawbacks. Most of them originate from fields of bioorthogonal chemistry, solid-phase synthesis, protein-drug conjugation, and some others. Multiple well-written reviews provide information on this topic (*Sapsford et al., 2013, 2011; Sperling and Parak, 2010*). The ones highlighted here are commonly used for nanoparticle bioconjugation (Fig. 1.3.3.4.2):

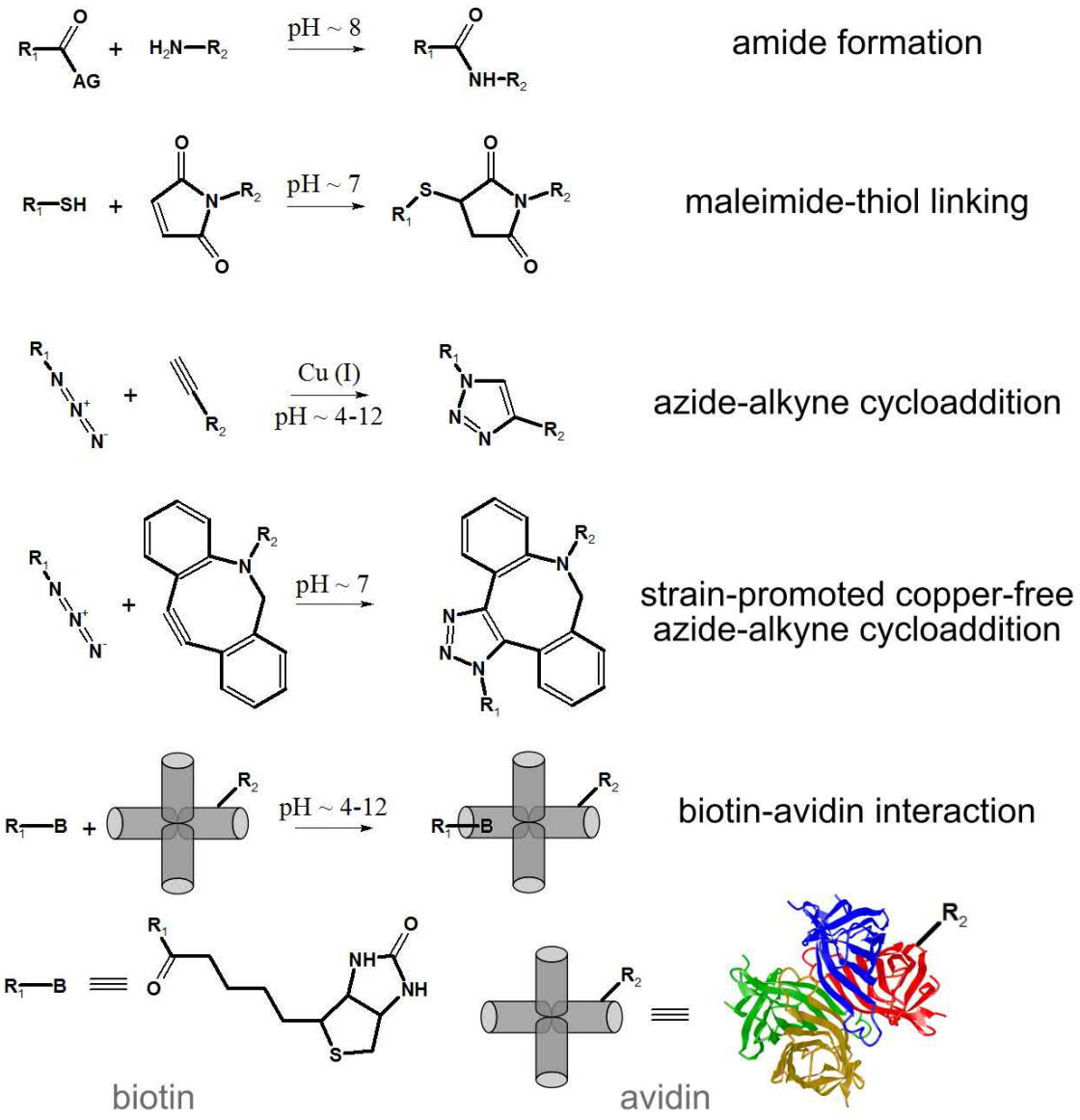

Fig. 1.3.3.3.6. Common strategies for nanoparticle bioconjugation.

- **Amide formation**. A covalent amide bond is produced by a reaction between a primary amine and an activated carboxylic acid ester (or less commonly used anhydride or acyl halide). For grafting, the nanoparticle can be either an amine-bearing or activated acid-bearing partner. For bioconjugation the particle is typically the acid partner, and the amine can be present on a protein lysine side chain, or attached to an appropriately modified nucleic acid. The advantage of amide bonds is their high chemical resistance. In biological conditions, they can be broken down only by certain hydrolase enzymes, and only if the environment around the bond is available for the enzyme attachment. The disadvantage of the method is the requirement for forming an activated carboxylic acid ester on the particle surface, which is achievable in aqueous conditions only by few specific reagents (e.g. EDC/NHS reagent combination). Also, activated esters slowly react with water, requiring to follow the activation immediately with the amide formation.

- **Maleimide-thiol linking**. Maleimide groups react with thiols (sulfhydryls) via a Michael reaction at neutral pH, forming a covalent bond. Typically, maleimide group is tethered to nanoparticle surface, and the thiol is present natively on protein cysteine side chains, or attached chemically to a nucleic acid. Maleimide-thiol linking is one of the most frequently used bioconjugation approaches due to its simplicity. However, the reaction can be capricious: at pH>8, the reaction can proceed with non-protonated amine groups on proteins. Moreover, the reaction is reversible, and products can slowly degrade, especially in presence of other thiols. Maleimide can also hydrolyse in basic buffers, forming non-reactive maleamic acid. For the reaction to proceed quantitatively, reducing agents like hydrophilic phosphines have to be added to reduce disulfide groups that form upon oxidation of the thiol reaction partner by air. Overall, these conditions impose a lot of constraints that may be sometimes incompatible with the particles and their coatings.

- **Azide/alkyne cycloaddition**. A staple of click chemistry methods, formation of triazoles via [3+2] cycloaddition of azides to alkynes is widely used to produce bioconjugates. The reaction can proceed in a variety of conditions and is insensitive to presence of non-marked biomolecules in the dispersion. Classical azide/alkyne cycloaddition requires either high temperature or catalysis by Cu^{+} ions, which are usually generated in situ, e.g. with $CuSO_4$/ascorbate system. For the cases where the

reducing conditions or the presence of copper ions are undesirable, copper-free click chemistry with strained cycloalkynes is used, which can efficiently proceed at room temperature and neutral pH without any catalyst. A wide variety of reagents for making substrates "clickable" are commercially available. The advantage of azide/alkyne cycloaddition is its high selectivity, absence of side reactions, and very simple protocols (in case of copper-free cycloaddition). This allows it to efficiently work even in vivo. The disadvantage is the requirement to install the azide or alkyne functionalities on the biomolecule partner, as neither is available natively.

- **Biotin-avidin interaction**. One of the strongest non-covalent interactions in nature, the binding of biotin (vitamin B_7) to avidin or related proteins (streptavidin, neutravidin) has dissociation constants in the pico- and femtomolar range, approaching the strength of a covalent bond. Avidin and its relative proteins are tetrameric, possessing four binding sites available for four biotins, although mutated variants can be produced with some of the binding sites deactivated. Biotin can be installed on biomolecules either chemically or enzymatically. Avidin can be installed by any of the aforementioned bioconjugation reactions. As avidin is multivalent, there is also a possibility of "sandwich" linking approach, in which both partners are biotinylated and linked through an avidin. The advantage of biotin-avidin linking is the flexibility of attachment and very simple conjugation protocols, consisting of mixing the partners together. Also, biotynilated variants of a variety of proteins are commercially available, as well as kits for biotinylation. The disadvantage of this coupling method is the size of avidin and its variants (ca. 5 nm), making it impractical for FRET applications.

To summarize this subchapter, UCNPs are a luminophore that allows a lot of flexibility regarding its optical performance. They possess unique characteristics that set them apart from conventional luminophores, namely large anti-Stokes shift, narrow emission bands, long lifetimes, high photostability and uniform, non-blinking emission. Of course, they also have their disadvantages (at least for now), which include low brightness compared to other luminophores, more limited surface modification compared to QDs or gold nanoparticles, and excitation spectra restricted by the choice of the sensitizer. Issues inherent to most other

nanoparticles are present as well, namely colloidal instability in high ionic strength dispersions, non-specific binding of biomolecules to the particle surface, occasional protocol irreproducibility, lack of standardization, and problematic production upscaling. Due to the sensitivity of ETU to a large variety of parameters, care should be taken when choosing the synthesis method, composition, surface modification and subsequent conjugation of UCNPs for a given application.

Development of UCNPs and their applications is a very active field, and new insights are gained on a frequent basis. The next subchapter describes some of the fields in which UCNPs are being applied, especially in biological context.

1.3.4. Applications of UCNPs

At the present time, the majority of the research in UCNP applications involves substituting luminophores in existing techniques with UCNPs to gain advantage of their superior performance. Most efforts are concentrated in biological applications, due to their demands for low-background nanoscale luminophores and IR excitation.

1.3.4.1. Biological sensors and assays

Basing sensors on UCNP luminescence has a benefit of eliminating undesirable autofluorescence background. Typically sensing applications involve using UCNPs in following ways:

- **Luminescent label**. In this approach, the particles are grafted with sensing moieties to signal the presence of the analyte. The particle itself is used only as a label, and does not yield any additional information about the system. For this approach, bright UCNPs are preferred.

  The key advantage of UCNPs as labels is higher sensitivity of the assays. High photostability of UCNPs can be also an advantage, allowing long continuous sensing (e.g. for kinetics experiments) with no photodegradation problems.

  The issues in using UCNPs as labels involve lower specificity in certain cases due to non-specific binding, as well as reproducibility, both being common problems in all nanoparticle applications. Aggregation and binding stoichiometry can also influence the assay performance. Employing UCNPs that use Yb^{3+} as a sensitizer also requires

stricter illumination geometry control, as water has a large absorption peak close to 980 nm (ca. ~0.2-0.5 cm^{-1} depending on the wavelength). This can lead to the dependence of signal intensity on the thickness of the aqueous sample.

Examples of the label approach are provided on Fig. 1.3.4.1.1.

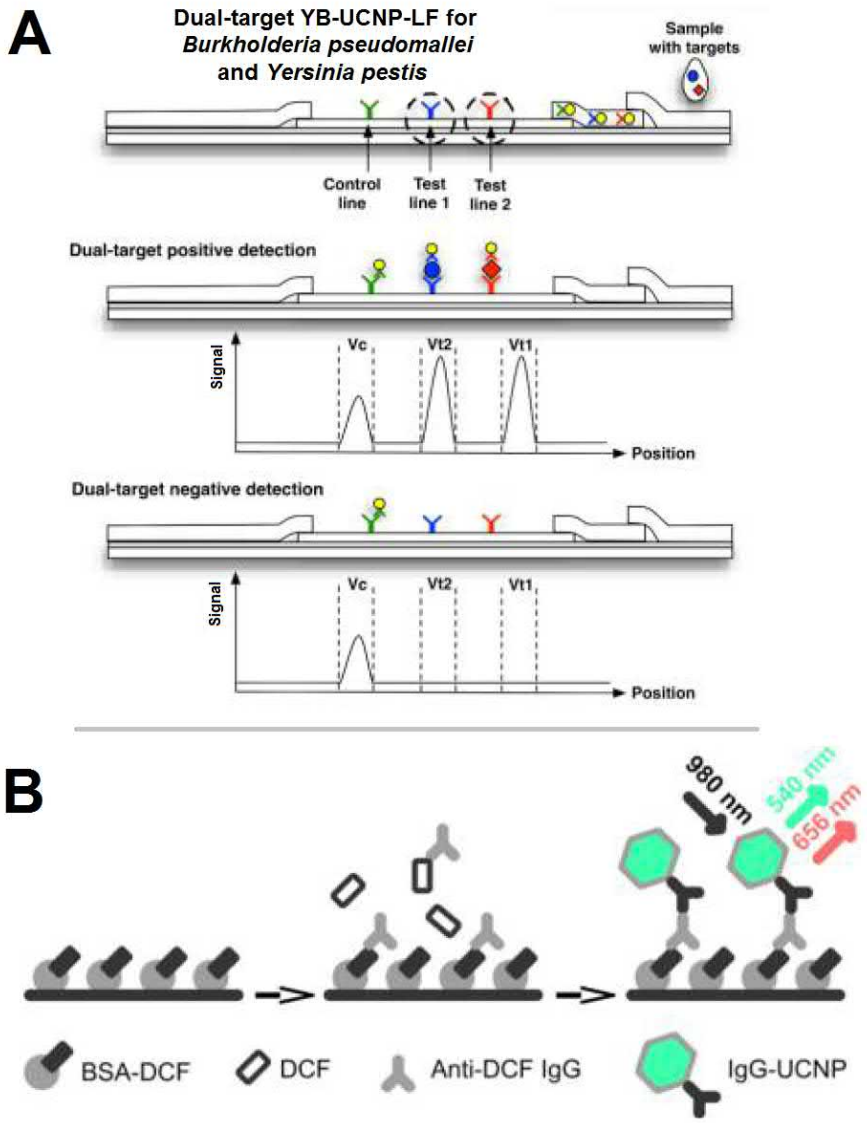

Fig. 1.3.4.1.1. Examples of applying UCNPs as a label element in a bulk assay. A: A lateral flow multi-target heterogeneous immunoassay. Antibody-decorated UCNPs bind to the patterned target, showing luminescence under IR illumination in regions corresponding to the respective targets (Liang et al., 2017). B: A competitive UCNP-linked immunosorbent assay (ULISA) for detection of diclofenac. After washing, luminescence of substrate-bound

UCNPs indicates the presence of the analyte in the initial solution (Hlaváček et al., 2016). Images are adapted from the respective references.

- **Luminescent probe**. In contrast to labels, probes report the changes in their environment (e.g. presence of analyte) by changing the parameters of their luminescence. Signaling parameters include changes in intensity, emission spectrum band shifts or band ratios, and luminescence decay parameters.

  In probing applications, UCNPs are typically used as the integral probe component, the one which changes its luminescence. This is commonly achieved through energy transfer to quencher or acceptor moieties in close proximity to particle. In another probing approach, UCNPs are employed as a nanoantenna, where they are introduced in a fully functional sensing system purely as a means to shift the excitation wavelength into infrared, via energy transfer to the actual sensing element (e.g. a donor in a FRET dye pair). This allows to benefit from the significant reduction of sample autofluorescence, while maintaining the good performance of an already optimized sensing system.

  The major advantage of using UCNPs as probes lies in the removal of sample-caused background, which may be critical in certain applications. As UCNPs exhibit luminescence on several bands, the ratio of luminescence on these bands can serve as an additional signal dimension, allowing construction of robust *ratiometric assays*.

  However, all issues present in applications of UCNPs as labels are also valid for using UCNPs as probes. Aside from those, additional caveats involve the possibility of nonlinear response of the particles due to sensitivity to other elements of the environment, and heterogeneities in binding stoichiometry and particle response. The latter in particular can introduce biases in the data: for instance, a UCNP aggregate in the sample can yield roughly the same amount of signal as the sum of signals of the individual particles that comprise it, however the response of the aggregate is biased due to the internal particles being shielded from the environment by their neighbours. Due to this, UCNP-based sensors require careful calibration in a variety of conditions, to ensure the stability of the sensor's response.

  Examples of the probe approach are provided on Fig. 1.3.4.1.2.

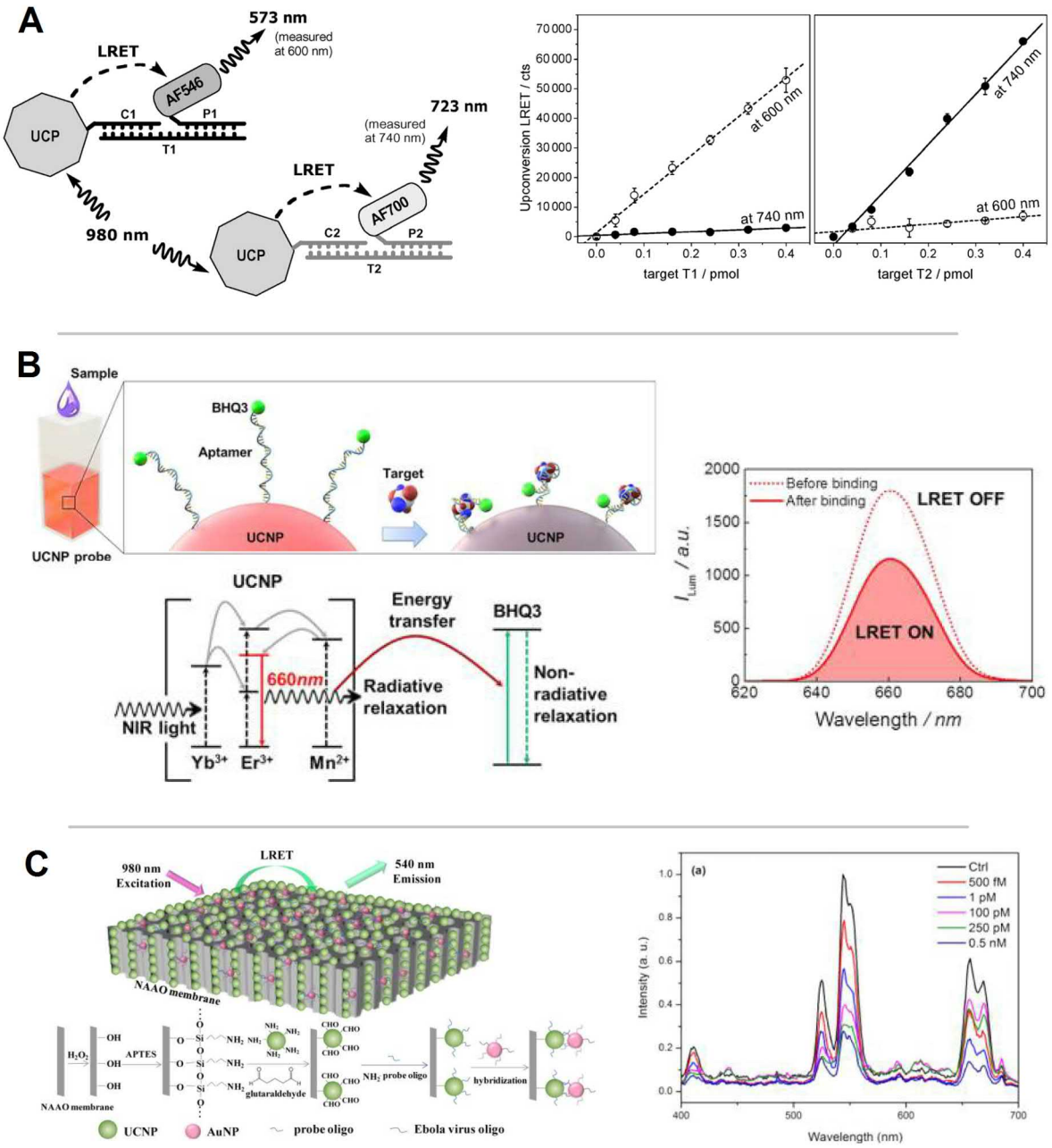

Fig. 1.3.4.1.2. Examples of applying UCNPs as a probe element in a bulk assay A: A dual oligonucleotide hybridization assay. Oligonucleotide-decorated (C) UCNPs are mixed with dye-decorated oligonucleotides (P). If a target (T) is present, it binds C and P together, keeping the dye close to the particle. Upon IR illumination, the particle can perform RET to the dye, which then fluoresces. The UCNP has two luminescence bands, allowing independent detection of two targets at the same time, using two dyes (Rantanen et al., 2009). B: A homogeneous aptamer UCNP assay. UCNPs are decorated with oligonucleotide aptamers

that have a quencher dye on their terminus. Upon binding to the target, the aptamers fold, bringing quenchers close to the particle, resulting in particle-quencher RET and a drop in luminescence (Jo et al., 2018). C: A composite material containing UCNPs decorated with oligonucleotides is washed with the solution of target ebola virus oligonucleotide and with gold nanoparticle dispersion decorated with another oligonucleotide, in an assembly similar to the one described in A. Upon binding, the gold nanoparticles can quench the UCNP luminescence and allow detection of the analyte at low concentrations (Tsang et al., 2016). Images are adapted from the respective references.

1.3.4.2. Photodynamic therapy (PDT) and other tissue applications

In comparison to visible light, NIR light in certain wavelength ranges is much less absorbed and scattered by biological tissues. These wavelength regions are called *NIR biological windows*. Frequently this term is used specifically for the first NIR window with the wavelength range in ~700-1000 nm. Using luminophores with excitation in these ranges – for instance, UCNPs – allows biological tissue imaging and light-induced tissue modification at a much higher sample thickness compared to conventional fluorescence imaging.

One of the techniques of tissue imaging and its light-induced modification that has a lot of medical value is called *photodynamic therapy* (PDT). In the most common varieties of PDT (so-called type I and type II PDT), living tissues are exposed to a *photosensitizer* substance, typically an organic dye that binds to undesired parts of tissue. Upon excitation by light, the photosensitizer can either transfer an electron to the environment, forming a highly reactive hydroxyl radical (type I) or transfer its energy to molecular oxygen (type II), exciting it from the ground triplet state to a metastable excited singlet state, known as *singlet oxygen*. Radical ions and singlet oxygen are extremely chemically reactive, and can irreversibly modify biological molecules in their immediate vicinity, ultimately leading to cell death via a variety of mechanisms (*Bonnett, 2014*) (Fig. 1.3.4.2.1). The agent binding specificity and the illumination pattern allow high degree of control over destruction of undesirable tissue. This makes PDT a very useful non-invasive method of treating a variety of skin conditions and malignant cancers, especially melanomas (*Agostinis et al., 2011; Dolmans et al., 2003*). A variety of modifications of PDT exist, with different phototoxicity mechanisms, agent types, cell type specificities, etc.

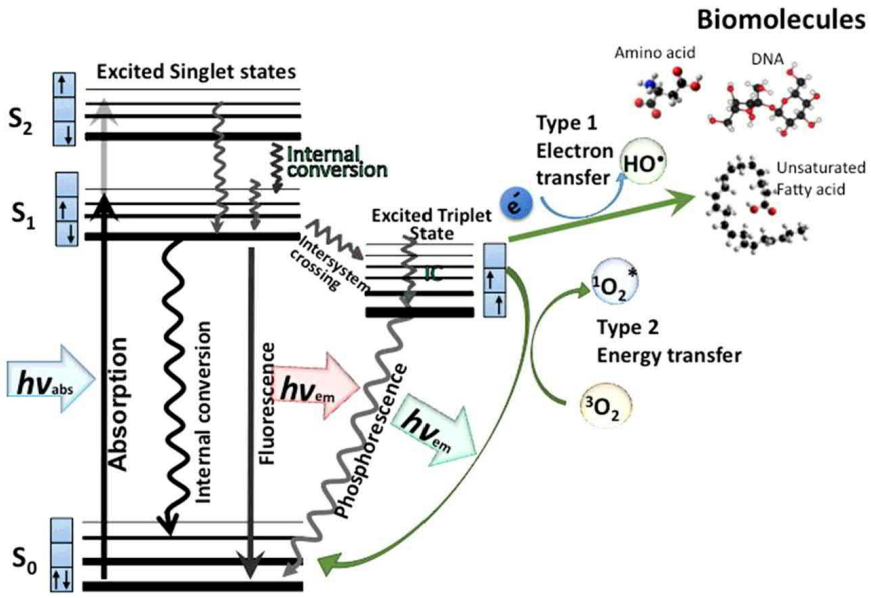

Fig. 1.3.4.2.1. Jablonski diagram for type I and type II photodynamic therapy. Image adapted from (Silva et al., 2015).

A common caveat of PDT is the requirement of excitation via visible light, as most of the efficient photosensitizers typically absorb in visible region. This results in poor tissue penetration and permits only superficial layer treatment (usually ~300 μm depending on the wavelength). To gain tissue penetration depth, alternative PDT agents are being developed with absorption in NIR biological window, however shifting the excitation wavelength often comes with sacrifice in performance.

Employing UCNPs as a nanoantenna in PDT systems allows to excite highly efficient photosensitizers with NIR light, thus improving the overall system performance. Nanoparticle-based PDT agents can be grafted with targeting agents, guiding the active photosensitizer payload towards the targets with higher selectivity. Moreover, UCNPs are known to have low cell and tissue toxicity, especially compared to other types of nanoparticles (*Gnach et al., 2015*).

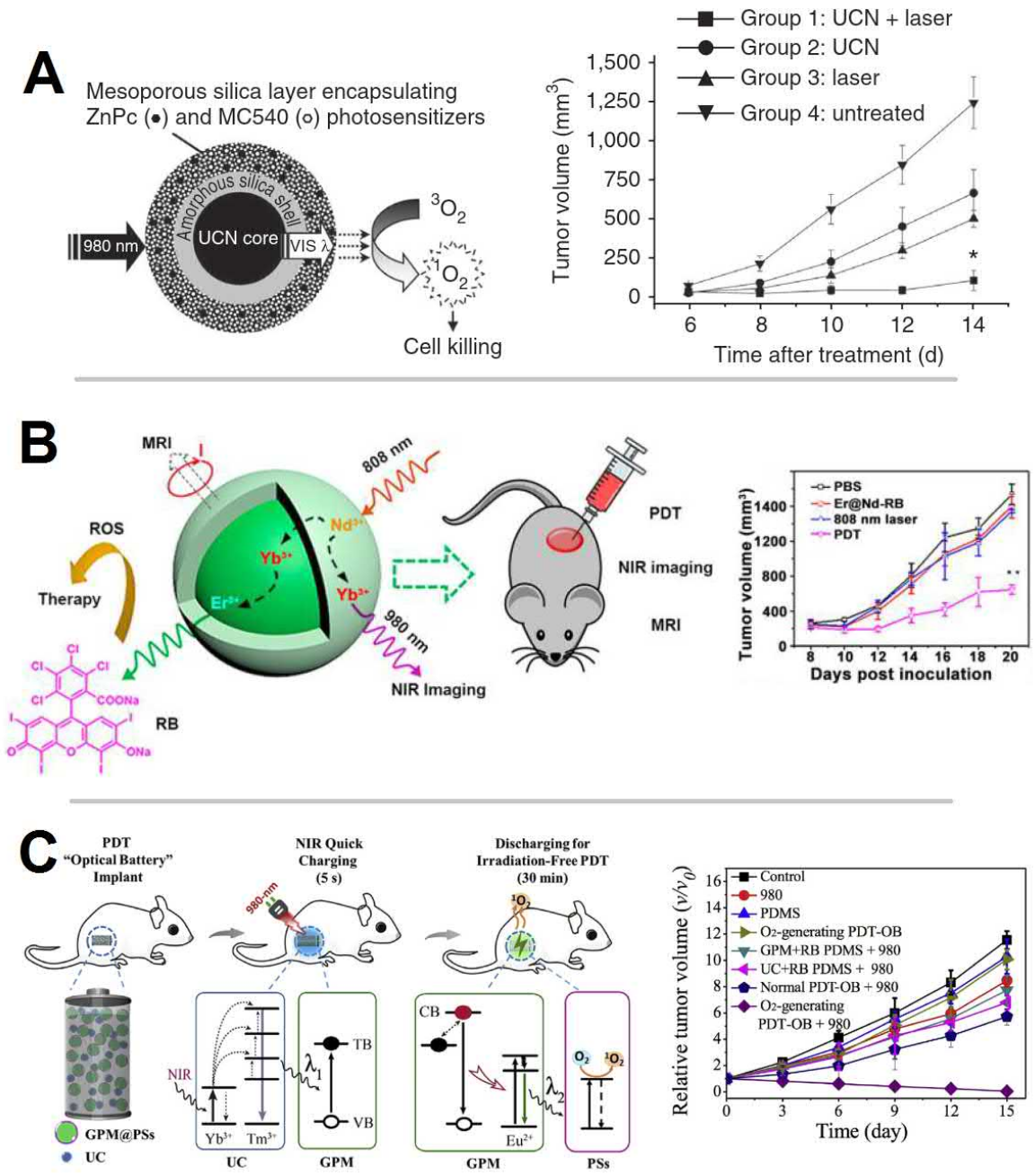

Fig. 1.3.4.2.2. Examples of UCNP applications in PDT. A: A UCNP is decorated with mesoporous silica containing photosensitizer dyes for type II PDT. Upon IR irradiation, the particle generates singlet oxygen (Idris et al., 2012). B: In a similar nanocomposite, certain UCNPs can be used also as a contrast agent for MRI imaging, as well as luminescence imaging upon low-intensity IR irradiation. Additionally, the particles can use Nd-Yb sensitizer system to move the excitation band to 808 nm to counter tissue heating by 980 nm light absorption (Li et al., 2016). C: UCNPs can be used as an antenna element to provide

NIR excitation to persistent luminescence materials, which then transfer the energy to photosensitizers. The composite material containing these elements (called an "optical battery" by the authors) can be implanted on the tumor surface and excited with low-intensity laser pulses to yield consistent singlet oxygen generation for significant amounts of time without tissue heating (Hu et al., 2018). Images are adapted from the respective references.

A large variety of PDT systems based on UCNPs exist. Some examples are presented on Fig. 1.3.4.2.2. One of the frequently investigated approaches involves combining sensor and PDT functionalities in UCNP-based platforms, achieving combined diagnostics and therapy (commonly known as *theranostics*). Some systems combine PDT and other anti-cancer functionalities (photothermal therapy or chemotherapy) in a single UCNP-based platform (*Wang et al., 2013*). In a similar vein, using UCNPs as nanoantennas for drug delivery systems triggered by NIR illumination is also a promising application field (*Yang et al., 2015*).

The major hurdle in applying UCNPs in PDT and other tissue applications is their low extinction coefficient, resulting in a need for higher illumination intensities, using which may cause non-discriminate heat damage of the tissue during therapy. High reproducibility of particle preparation and their homogeneity, as well as multiple characterization methods are required for approval as a therapy. Rapid clearance, an uncommon trait in nanoparticles, is vitally important for PDT, as otherwise the patient would have continuous post-therapy tissue phototoxicity upon exposure to ambient light, which may severely endanger their health. Recent advances in small UCNPs (<10 nm) have potential to improve their clearance profile.

1.3.4.3. Biological microscopy

In cell and tissue imaging, UCNPs offer a lot of immediate advantages due to absence of autofluorescence, extreme photostability and no blinking.

There is a vast variety of experiments involving UCNPs in biological imaging. They can be divided in following categories:

- **Labels and probes**. Some UCNP-based systems used for aforementioned bulk sensing techniques can be also applied as luminophores in microscopy for determining the spatial distribution of the analyte, with a similar set of advantages and caveats as in

bulk assays. Of particular note is higher relevance of particle heterogeneity, the effects of which become more significant when visualizing micro- and nanoscale processes. The particle dispersibility requirements are also more strict, as the particles should be colloidally stable for sufficiently long amounts of time for reliable imaging.

Examples of such UCNP applications are provided on Fig. 1.3.4.3.1.

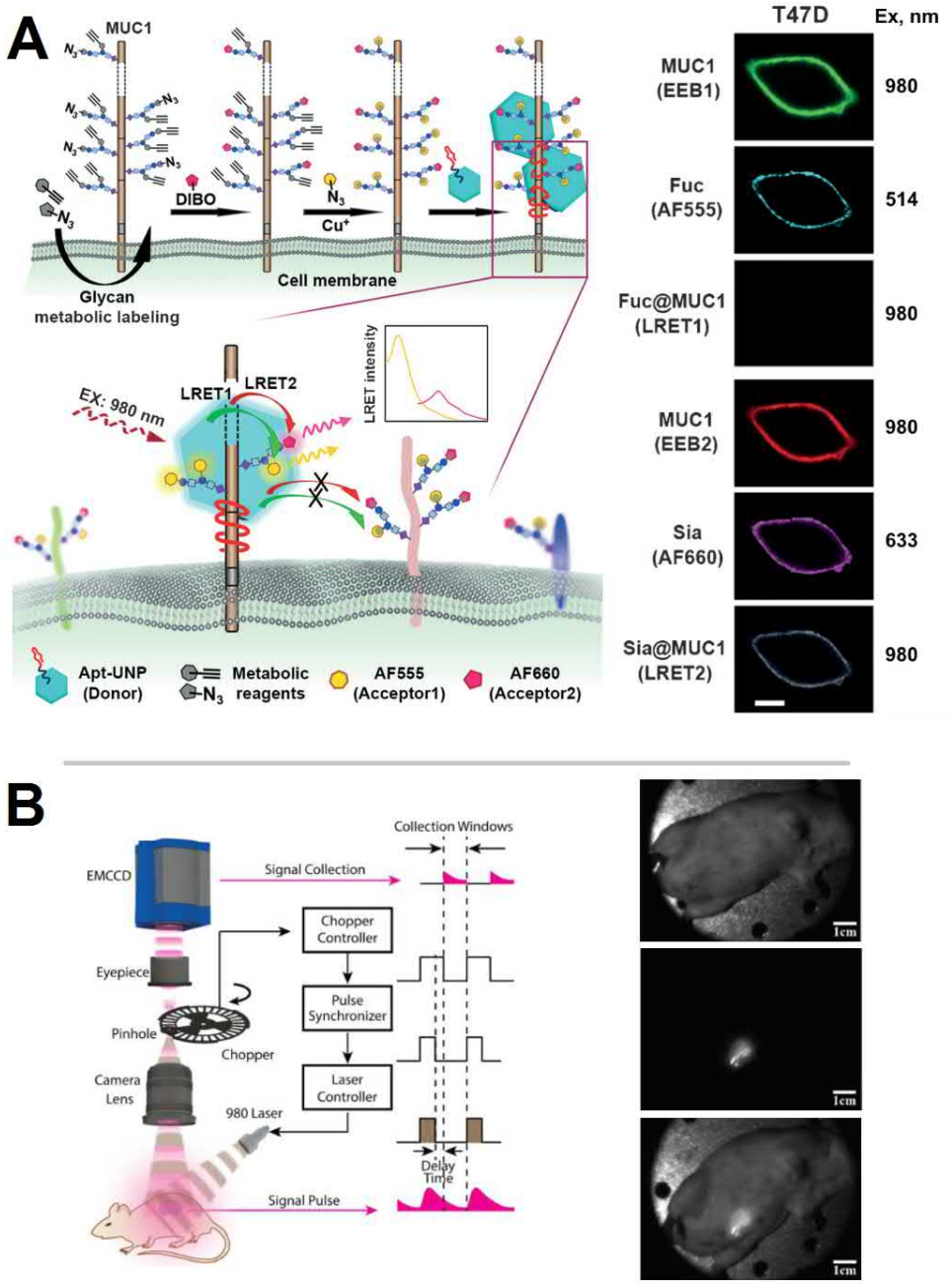

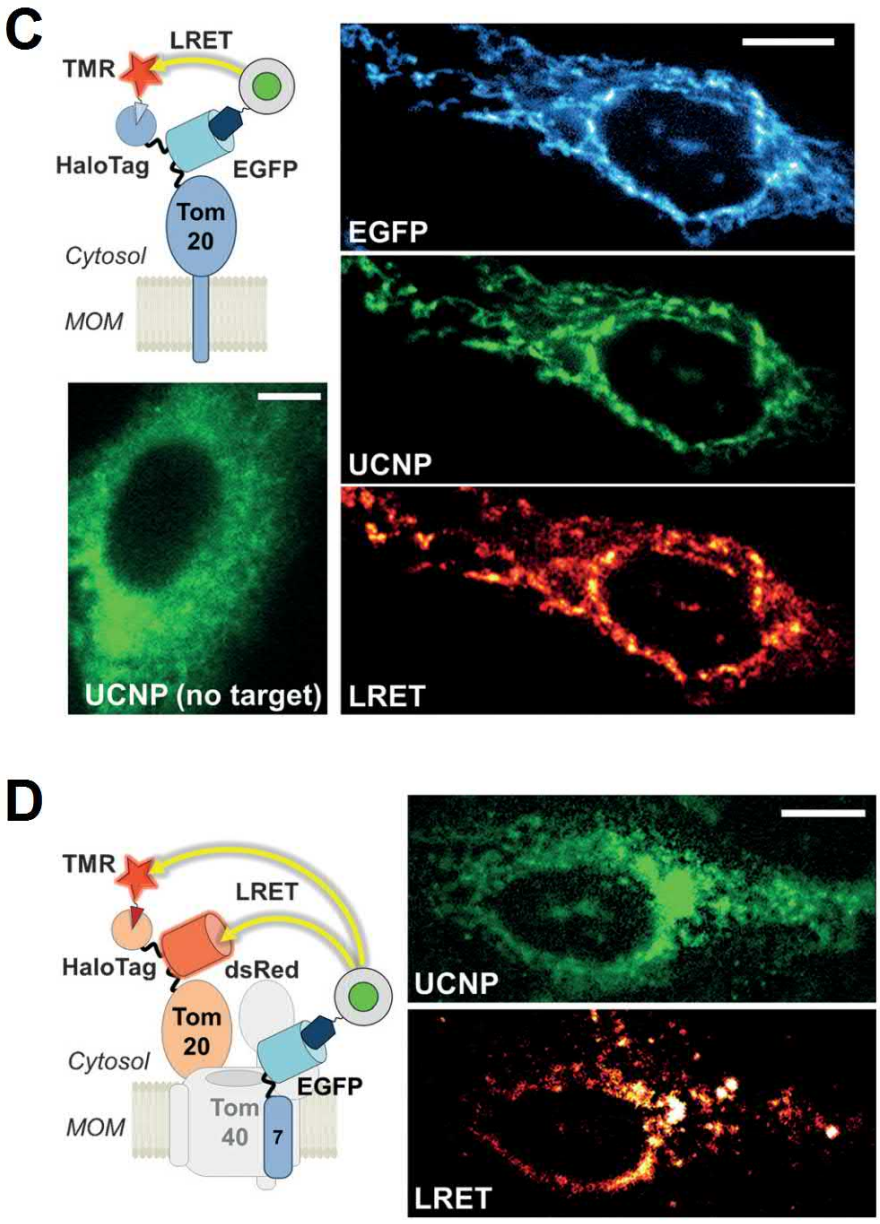

Fig. 1.3.4.3.1. Examples of using UCNPs in biological imaging. A: Different oligosaccharides expressed on cell surface proteins (here - MUC1) can be selectively labeled with acceptor dyes. Binding of a UCNP via protein-recognizing aptamers to these proteins allows to excite these dyes via RET, forming a high-contrast map of proteins labeled with the respective oligosaccharides. Two luminescence channels can be used simultaneously to map two oligosaccharides at the same time (here – Fuc and Sia) and determine if the protein is decorated with them or not. In the provided example only Sia oligosaccharide is present on the probed protein (Wu et al., 2016). Scale bar: 10 µm. B: Due to long luminescence lifetime

of UCNPs, time-gated microscopy can be performed with inexpensive imaging setups to achieve even higher contrast in tissue imaging. Images show a mouse injected with UCNPs under visible light, IR excitation and combined visible/IR excitation (Zheng et al., 2016). C: Cells can be microinjected with nanobody-decorated UCNPs to allow targeted imaging of the proteins inside the cell. Tagging the target protein with a dye capable of performing RET with UCNPs allows to improve the contrast by reduction the influence of non-specific binding. D: This approach can be extended to in vivo protein interaction experiments, in which such dyes are attached to a component of a protein complex, resulting in a high-contrast map of protein interaction inside a cell (Drees et al., 2016). Scale bar: 10 μm. Images are adapted from the respective references.

- **Nanothermometers**. In certain lanthanide ions, e.g. Er^{3+}, there are pairs of emissive states with very similar energies, with energy difference on the order of ~0.01-0.1 eV, roughly equivalent to *kT* energy at room temperature. Excitation of ions into either of these states results in a formation of a metastable thermal equilibrium, in which the ions undergo reversible transitions from one state to another. Emission from either of the states has distinct wavelengths. This results in the dependence of the fine structure of emission spectrum on temperature, and can be exploited for thermometry with high spatial resolution. Experimental design for nanothermometry involves multichannel luminescence imaging on the appropriate wavelengths with post-processing to extract temperature information. Information yielded by nanothermometry is useful for investigation of temperature-dependent processes in biology, including abnormally fast metabolism associated with tumor growth. Also, monitoring temperature with high spatial resolution is beneficial for photothermal therapy, in which cells are destroyed by heat generated from light absorption. Non-biological applications include development of integrated photonic devices and accurate location of microcircuitry defects (*Vetrone et al., 2010*).

  Examples of this application are provided on Fig. 1.3.4.3.2.

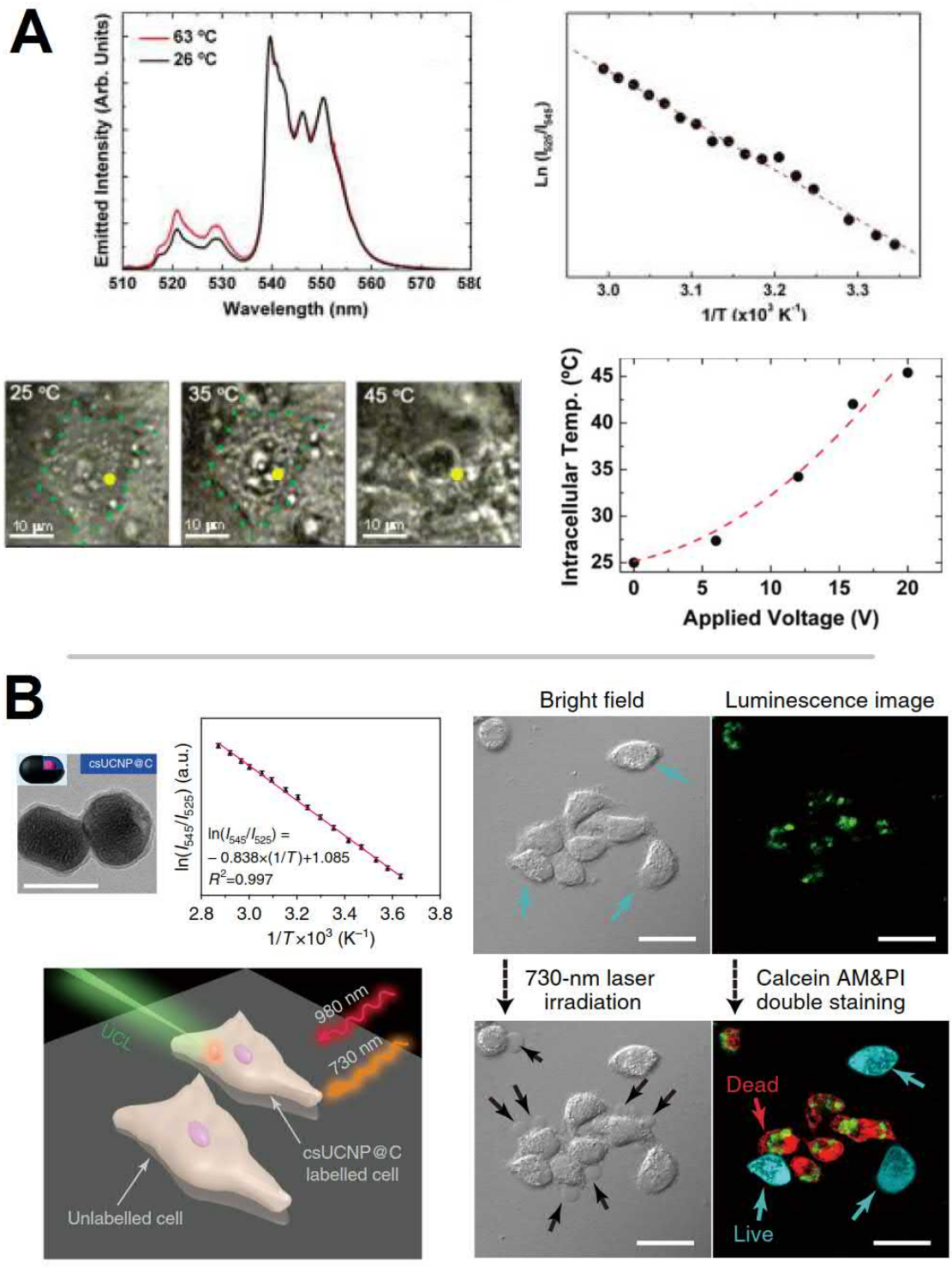

Fig. 1.3.4.3.2. Examples of nanothermometry with UCNPs. A: Fine structure of Er^{3+} UCNP green band depends on temperature, with the band ratio linearly dependent on reciprocal temperature. This is exploited to monitor temperature in cells attached to a heated support.

Increasing the voltage on the heater leads to higher intracellular temperature, which is calculated from UCNP luminescence (Vetrone et al., 2010). B: UCNPs coated with carbon can be used as a photothermal therapy agent with internal temperature reference. Applying a readout beam at 980 nm allows monitoring temperature inside cells, while applying a heating beam at 730 nm heats the particles, leading to cell destruction. Temperature monitoring allows highly selective cell destruction through using minimized amounts of excitation power (Zhu et al., 2016). Images are adapted from the respective references.

- **Multiplexing labels (barcoding)**. As UCNP luminescence is highly customizable by changing the ion concentrations and their distribution throughout the particle, this customizability may be exploited to produce a large set of labels with distinct spectral and/or lifetime response dependent on the particle (so-called *barcodes*). In biological context, this enables the design of assays with simultaneous readout of multiple parameters, with different sensing moieties being bound to different barcodes. Barcoding is also useful in cell sorting applications for encoding-controlled flow cytometry.

  Examples of this application are provided on Fig. 1.3.4.3.3.

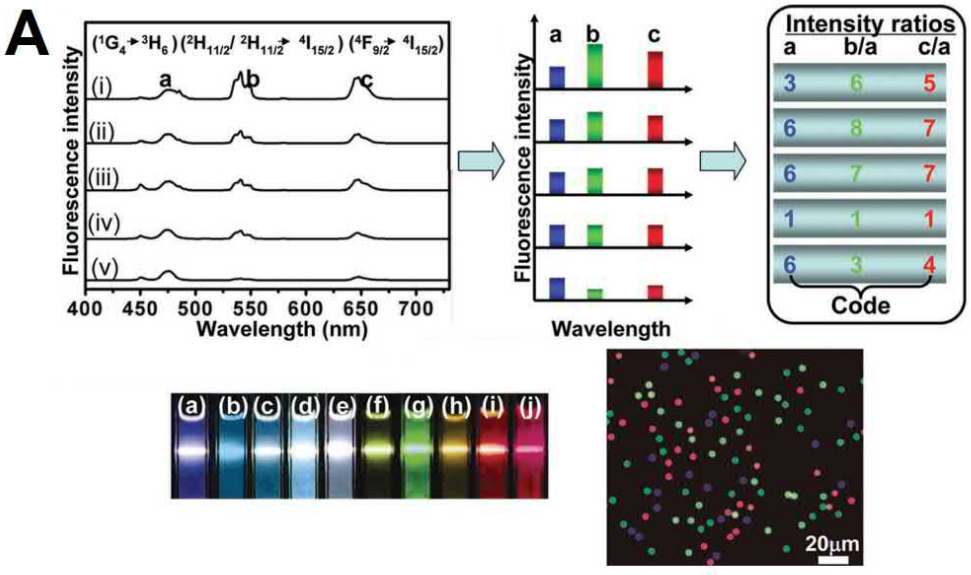

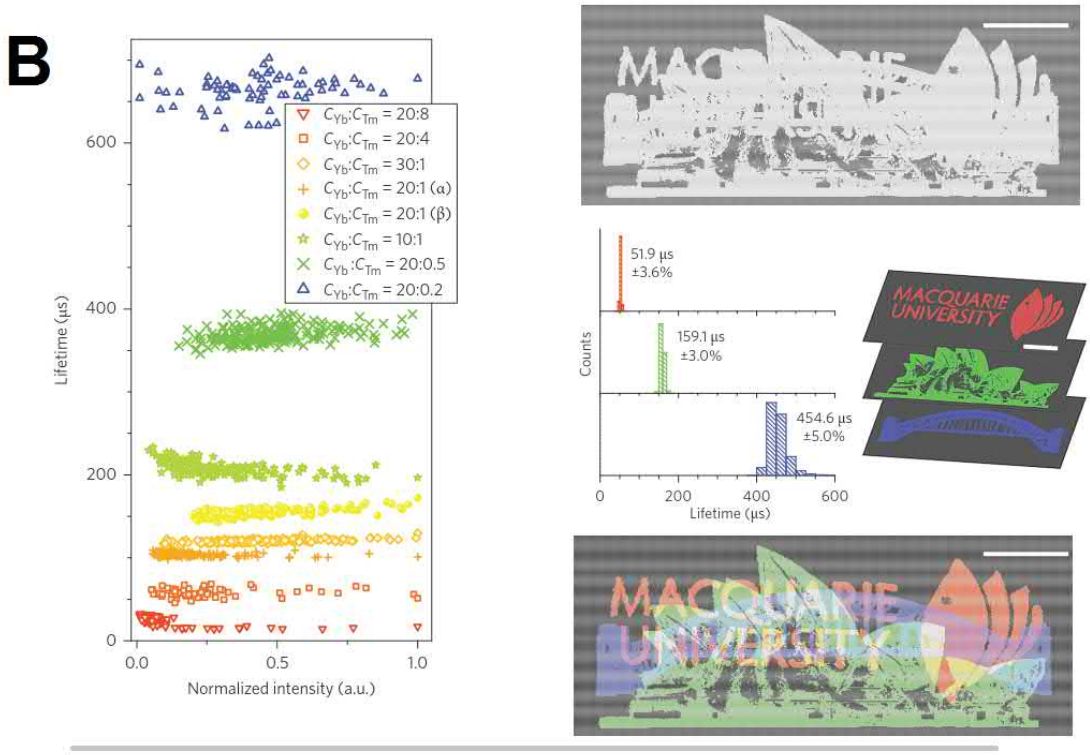

Fig. 1.3.4.3.3. Examples of UCNP-based multiplexing labels. A: Tuning dopant concentrations changes the spectra of UCNPs. If the spectra of UCNPs are sufficiently different, they can be reliably distinguished. For higher intensity in barcoding applications, multiple UCNPs can be embedded in polymer microspheres (Zhang et al., 2011). B: Tuning sensitizer and emitter content yields UCNPs with significantly different luminescence lifetimes. Using time-gated microscopy allows to distinguish different types of UCNP-loaded particles in the same sample (here – patterned microsphere arrays) (Lu et al., 2014). Images are adapted from the respective references.

- **Multimodal imaging labels**. For certain applications in tissue imaging, it may be desirable for a luminophore to be visualizable via multiple imaging modalities, e.g. luminescence with excitation on multiple wavelengths with different emission response, magnetic resonance imaging (MRI), positron emission tomography (PET), X-ray tomography (a.k.a. *computed tomography, CT*), and some others. This approach is occasionally combined with PDT to allow visualization of the particles without their activation.

  UCNPs by definition exhibit luminescence. Due to being a high density inorganic material, they can also absorb X-rays. Doping of UCNPs by paramagnetic ions

(e.g. Gd^{3+}) allows them to become a contrast agent in MRI. Other functionalities may be added by decorating the UCNP surface with imaging contrast materials, or incorporating them into such materials. Combined together, these properties give UCNPs a lot of potential for multimodal imaging.

Examples of this application are provided on Fig. 1.3.4.3.4.

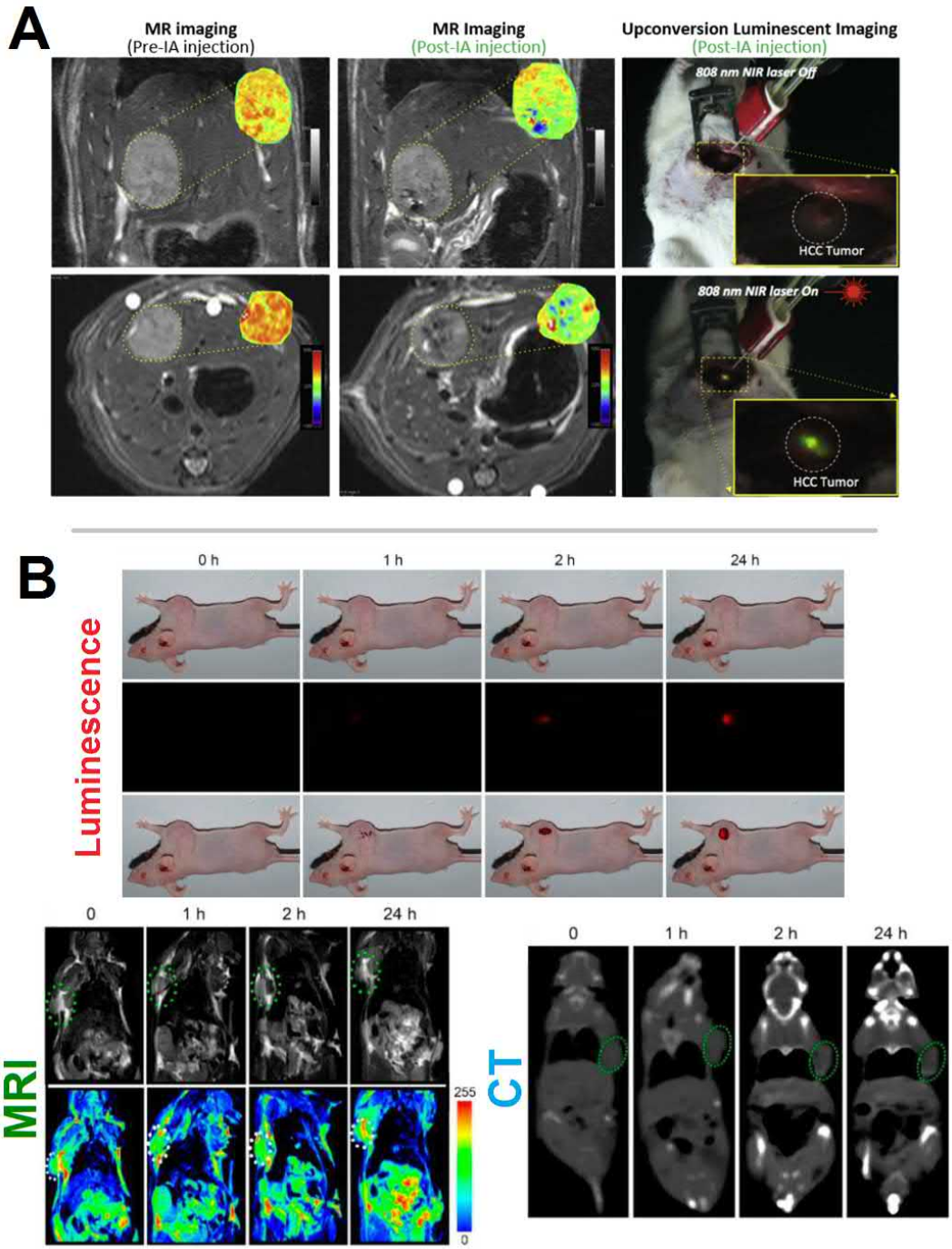

Fig. 1.3.4.3.4. Examples of multimodal imaging labels based on UCNPs. A: Nd^{3+} UCNPs decorated with antibodies allow targeting of tumors for pre-operative MRI and intra-operative guidance through luminescence (Lee et al., 2016). B: UCNPs using Ba_2GdF_7 as a matrix material not only exhibit luminescence, but also work as a contrast agent in X-ray tomography (CT) and MRI (Feng et al., 2017). Images are adapted from the respective references.

- **Cell/tissue control and IR-triggered optogenetics**. As a NIR-absorbing nanoantenna, UCNPs can be used as components of platforms that modulate and control the performance of cells and tissues. The most prominent example of this approach is very recent series of reports on employing UCNPs in low-invasive brain stimulation approach via an optogenetics platform (*S. Chen et al., 2018; Pliss et al., 2017; Shah et al., 2015; X. Wu et al., 2016*).

  Examples of this application are provided on Fig. 1.3.4.3.5.

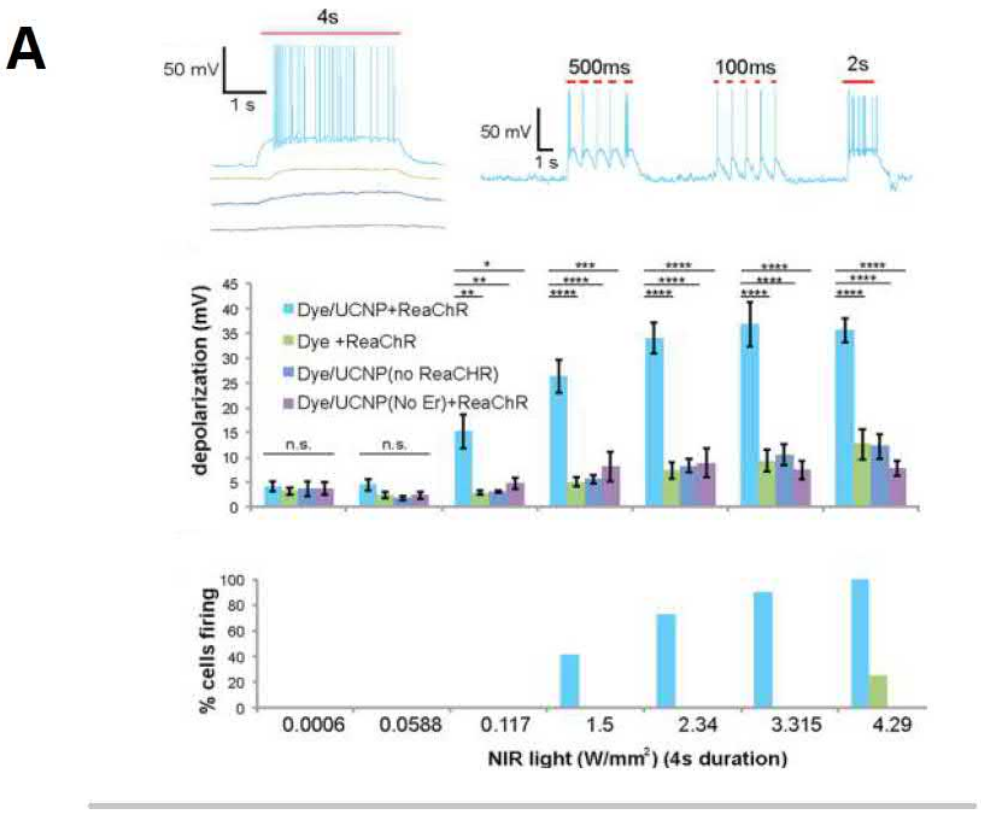

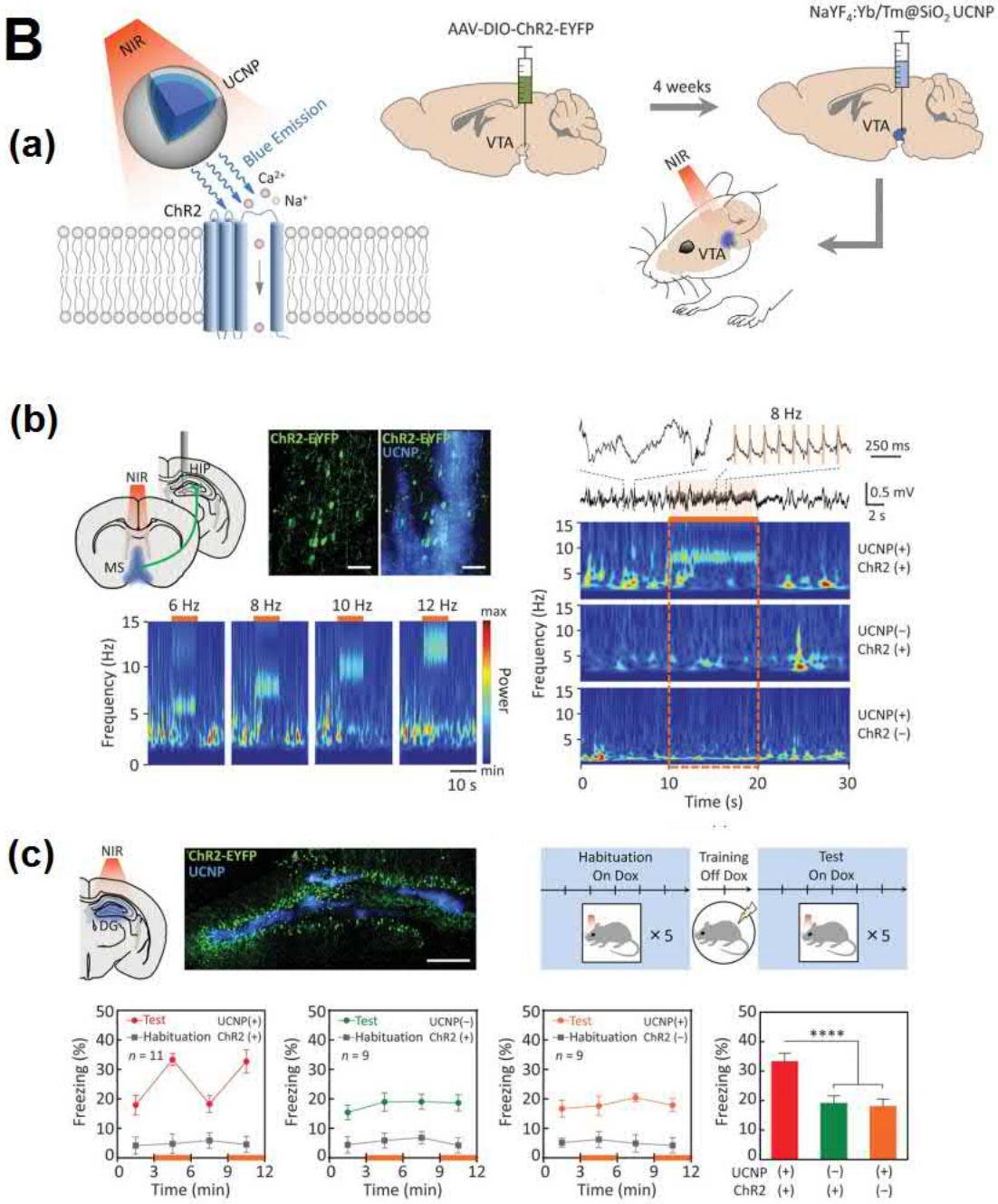

Fig. 1.3.4.3.5. Examples of IR-triggered cell and tissue control. A: Neurons, modified to express light-sensitive ion channels (channelrhodopsins, ChR), are cultured with a fluorescent dye/UCNP conjugate. Illumination with infrared light induces firing (depolarization) of neurons (X. Wu et al., 2016). B: (a) A system similar to that described in A is assembled in live mice, using localized gene therapy. (b) Constructing such system in medium septum (MS) allows IR-controlled induction of theta oscillations, that can be

measured throughout the mouse's brain (e.g. in hippocampal region). (c) Fear-conditioning mice with ChR protein expression activated by removal of doxycycline from diet induces construction of photoactivatable neurons that are specifically involved with the pathways associated with the fear stimulus. After addition of UCNPs into dental gyrus (DG) region, where most of these neurons are located, the fear response can be induced via IR illumination in live awake mice (S. Chen et al., 2018). Images are adapted from the respective references.

Overall, UCNPs hold a lot of potential for biological microscopy. Synthetic techniques that reproducibly yield highly homogeneous and bright UCNPs required for microscopy are a relatively recent advancement (~2012-2014), so the field currently enjoys a lot of progress. Importantly, existing microscopy setups can be easily retrofitted for upconversion, using a cheap infrared diode laser and inexpensive shortpass dichroic mirrors and corresponding filters.

1.3.4.4. Other applications

UCNPs also enjoy an assortment of applications in other fields. Due to them being more niche and less relevant to the topic of this work, most prominent examples will be described here in brief:

- **Anti-counterfeiting**. UCNPs (and upconversion *micro*particles) are proposed as an IR-responsive anti-counterfeiting security marker for documents and currency, similarly to fluorescent inks (*Han et al., 2017; Sangeetha et al., 2013; You et al., 2016, 2015*). This approach can be combined with multiplexed labeling to provide unique particle response combinations that are difficult to reproduce by the forger.
- **High-performance solar panels and concentrators**. A layer of upconversion material can transform low-energy infrared light unusable by silicon solar panels into visible light. This enlarges the useful part of the absorption spectrum of the solar panel, improving the energy collection efficiency (*Meng et al., 2017; Ramasamy and Kim, 2013*).
- **Displays**. Similarly to quantum-dot based displays, tailored UCNPs can be used for tunable RGB and/or white light output with high spatial resolution (*Park et al., 2017*).

- **IR-responsive materials**. UCNPs can be applied as a nanoantenna in a variety of light-responsive elements, wherever NIR excitation is more beneficial compared to visible light. Applications range from NIR-activated photopolymerization 3D printing on microscale (*Rocheva et al., 2018*) to drug delivery and controlled payload release in tissues (*Yang et al., 2015*).

After considering the luminophore-imposed limits of SMM techniques, and the advantages of UCNPs as a luminophore for microscopy, it is clearly apparent that UCNPs are a very promising candidate for single-particle imaging. Indeed, this sentiment has been shared by several research groups around the world. A field still in its infancy, imaging of individual UCNPs currently has only few published proof-of-concept experiments:

- Single-particle imaging has been used as a **quality control** measurement for characterizing UCNPs after synthesis to check the homogeneity of their luminescence on particle-to-particle basis, as well as investigate their luminescence behavior and extract their mechanistic behavior (*Gargas et al., 2014; Kilbane et al., 2016; Tian et al., 2018*).
- Prototypes of **single-particle tracking** with UCNPs have been reported in experiments showing endocytosis of non-decorated UCNPs and their subsequent diffusive movements characteristic of endosome movement along microtubules. No experiments reporting *targeted* single-particle tracking with individual UCNPs have been reported to date (*Nam et al., 2011; Wang et al., 2018*).
- **Super-resolution imaging** in STED-like configuration has been reported in a series of recent articles, as well as one from 2011 that went largely unnoticed until recently (*C.Chen et al., 2018; Kolesov et al., 2011; Liu et al., 2017; Zhan et al., 2017*). UCNPs are advantageous in this application because of their extreme photostability – a very rare virtue in conventional luminophores used for STED.
- To author's best knowledge, no **smFRET** systems based on UCNPs have been assembled to date.

To conclude, SMM with UCNPs as a luminophore is a field ripe with untapped potential for development with immediate applications, especially in biological context. This work is devoted to exploration of this field.

Research objectives.

The subject of this project was defined as **adapting upconversion nanoparticles towards their application in SMM techniques**, with final goal of **building proof-of-concept systems employing UCNPs for SMM**, that show comparable or superior performance to existing SMM methods.

At the outset of the project, a roadmap was devised:

1. For synthesis of the initial particles, our group relied on a collaborator's expertise (research group of Dr. Thomas Hirsch from University of Regensburg). UCNP synthesis is still a developing field with a large number of caveats and, like other nanoparticle synthesis methodologies, requires strict control over a large variety of parameters. Due to this, it commonly has low inter-laboratory reproducibility, where slight equipment mismatches can affect the resulting product significantly, and troubleshooting of protocols can sometimes require local screening of the reaction space, which can take significant amount of time.
2. Afterwards, particle coating methodologies have to be refined to find methods that yield highly monodisperse particles with highly homogeneous luminescence. Unlike in staining or bulk assays, where particle aggregation has to be avoided but oligomerization is usually only a moderate nuisance, in SMM particle oligomerization can be a direct problem due to very different behavior of particle oligomers and aggregates compared to individual particles.
3. The particle performance in SMM conditions has to be estimated, and optimized imaging conditions have to be found, to achieve robust, information-rich experimental design.
4. Simplistic model experiments have to be performed to test the feasibility of SMM with UCNPs, with focus on smFRET and SPT.
5. Based on the more promising model experiments, UCNPs have to be adapted towards their usage in actual smFRET and SPT experiments, and their performance has to be validated and assessed by performing SMM experiments on well-known systems with UCNP as a substitution luminophore.

Chapter 2. Results and discussion.

Part 1. Particle functionalization and characterization.

The initial particles for the project were synthesized by our collaborator group from University of Regensburg led by Dr. Thomas Hirsch.

To ease the comparison of particle performance with the literature sources, we opted for the most well-studied UCNP composition, namely β-$NaYF_4$: 20% Yb^{3+}, 2% Er^{3+}, core-only (homogeneous particles with no core-shell doping). The particles for the project were synthesized in several sizes : 16, 21, and 31 nm in diameter. The particle size was modulated by co-doping with Gd^{3+} (0%, 10% and 20%), which helps to reduce the particle size while keeping the crystallinity and luminescence properties intact (*Damasco et al., 2014*). Examples of particle transmission electron microscopy (TEM) images with particle size histograms and dynamic light scattering (DLS) size distributions are provided on Fig. 2.1.1. The particles are approximately spherical and have a remarkably narrow size distribution. X-ray diffraction spectra (XRD) confirm that particles have highly crystalline β-phase (hexagonal) matrix.

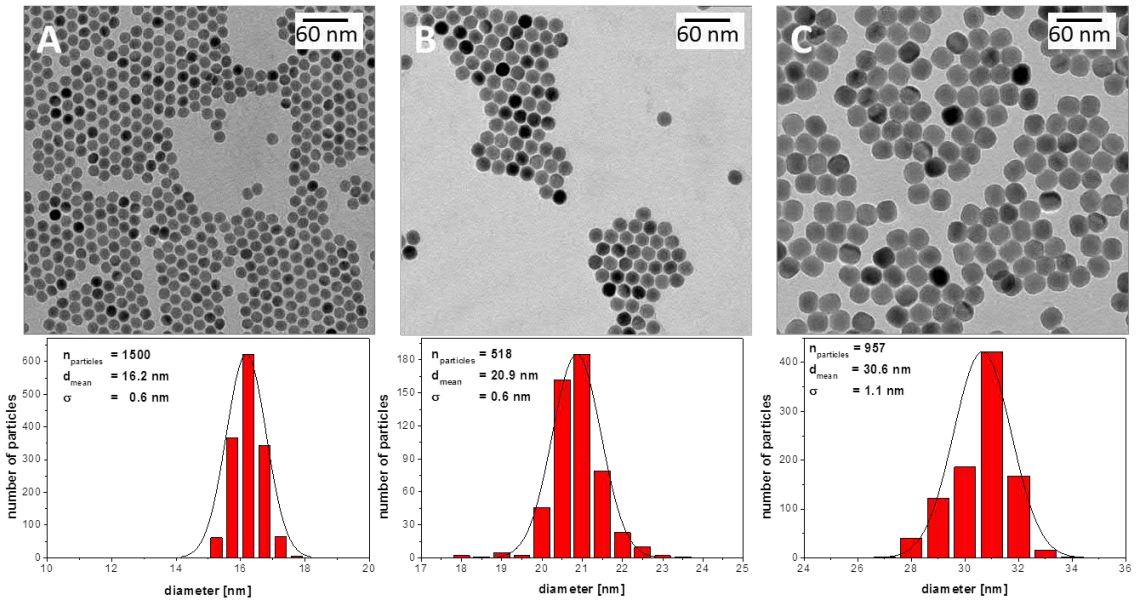

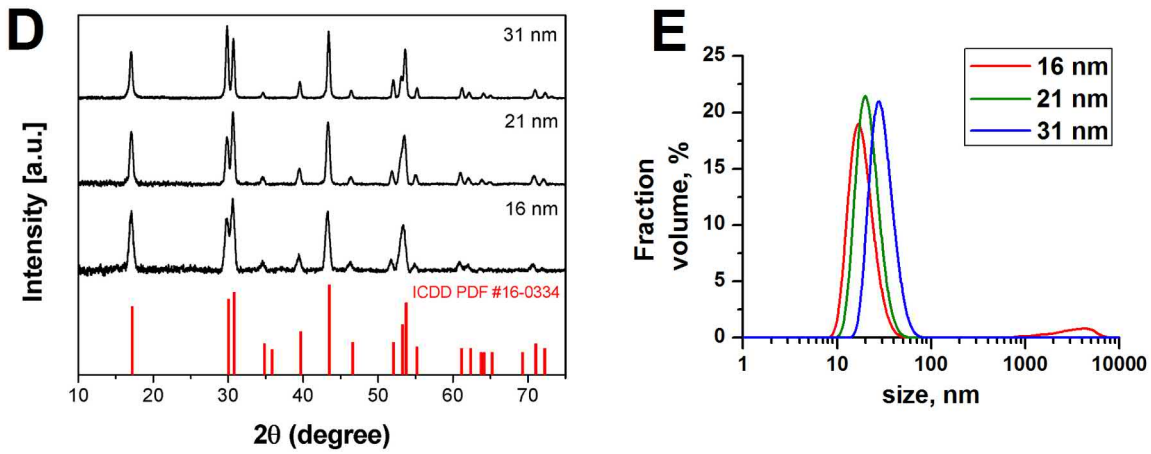

Fig. 2.1.1. Initial particle characterization. A,B,C: TEM images and image-based particle size histograms for 16 nm, 21 nm and 31 nm UCNPs, respectively. D: XRD spectra for UCNPs. E: DLS size distributions of UCNP dispersions in cyclohexane.

Spectra of bulk particle luminescence and their luminescence decays are shown on Fig. 2.1.3. The particles show a behavior typical of Yb^{3+}-Er^{3+} UCNPs. Differences in the spectra and the decay shapes are characteristic of increasing surface quenching as the particle gets smaller (*Arppe et al., 2015; Würth et al., 2018*).

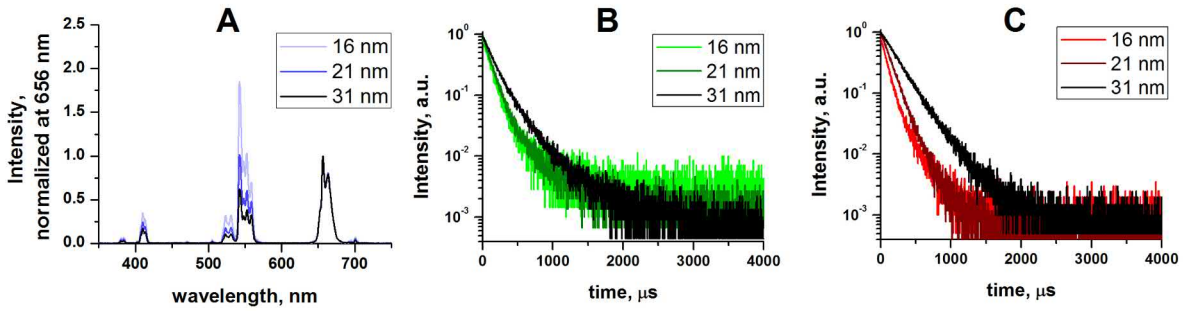

Fig. 2.1.3. Spectra and luminescence decays for oleate-capped UCNPs of 16, 21 and 31 nm diameters, measured in cyclohexane. A: spectra of UCNPs, normalized by the maximum of the red band. B: luminescence decay curves of the green band emission. C: luminescence decay curves of the red band emission. Excitation was performed at 980 nm with a focused beam, using an average excitation power of 6.2 KW/cm^2.

After confirming that the initial material was of sufficient monodispersity to be used as a basis for SMM experiments, the next step was testing different surface coating protocols. The aim is to obtain particles that are dispersible in water, retain high monodispersity and homogeneous luminescence, and show long-term colloidal stability. At that moment, literature reports on particle dispersion in water frequently showed partial particle oligomerization (*Hlaváček et al., 2014; Sedlmeier and Gorris, 2015*). While mostly acceptable for bulk assays, oligomerization can cause severe issues in SMM experiments, where it can induce significant systematic errors and poor assay performance due to large particle-to-particle heterogeneity. It should be also noted that nanoparticle coating and modification protocols are notorious for their poor inter-laboratory reproducibility. Keeping all of this in mind, the following strategy was chosen:

- **Silica shell** coatings were deemed to have low priority for investigation. The main concerns were a large quantity of sensitive parameters in literature protocols, difficulties in subsequent nanoparticle purification, gradual aggregation in storage, and issues in strict control of shell thickness, which is especially needed for smFRET.
- **Surfactant coatings**, specifically **amphiphilic polymers** were assigned the highest priority, due to the reports of exceptional colloidal stability of resulting particles, high potential for surface modification through attachment of active moieties to the polymer, and laboratory's previous experience with the method.
- **Ligand exchange** attracted our attention due to the simplicity of the protocols, large choice of available surface chemistries, and low thickness of the surfactant layer that could aid FRET applications. The main concern about the method was the detachment of ligands upon dilution of the dispersion, as the fluoride matrices from which the bright UCNPs are made do not exhibit any strong interactions with common ligand moieties.
- **Entrapment in nanoemulsion** was not described in UCNP literature at the time. Our interest for this approach was due to the very rapid nanoemulsion formation protocol for certain combinations of non-polar phase and surfactant (*Anton and Vandamme, 2010, 2009*).

We decided to first screen these methods in the order of priority, and then refine the protocol for the one that yielded most promising results “out of the box”.

2.1.1. Amphiphilic polymer coatings

Amphiphilic polymer coatings are widely employed for nanoparticles to make them dispersible in aqueous buffers. The most well-known protocols for coating inorganic nanoparticles were pioneered by Parak group (*Lin et al., 2008; Pellegrino et al., 2004*). Afterwards, multiple groups, including our collaborators, have adapted these protocols to UCNPs (*Jiang et al., 2012; Wilhelm et al., 2015; Wu et al., 2009*).

Typically, amphiphilic polymers can be formed either via polymerizing variously decorated monomers, or via modification of an already formed polymer backbone. (Fig. 2.1.1.1) We opted for the latter approach, as this method allows easy polymer customization, shorter and more reliable protocols and a defined polymer size.

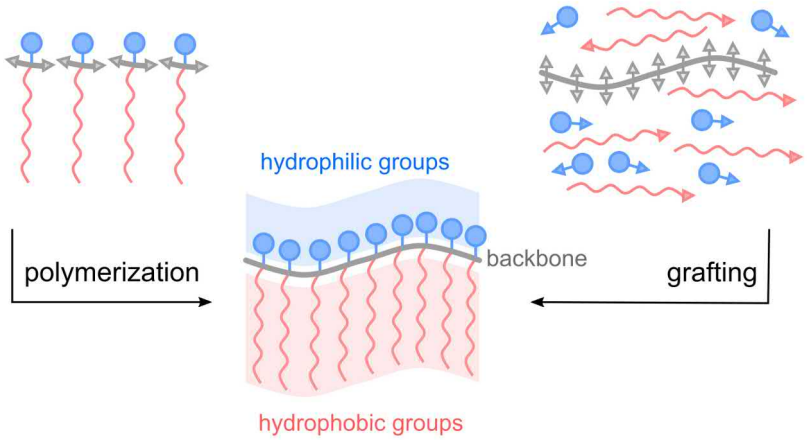

Fig. 2.1.1.1. Strategies for preparation of amphiphilic polymers.

For the polymer synthesis, we used a protocol similar to the one previously described in literature (*Wilhelm et al., 2015*). Briefly, the reaction entails opening of anhydride rings on a commercially available polyanhydride polymer with dodecylamine in the presence of a base, with subsequent hydrolysis to ensure full opening of all rings (Fig. 2.1.1.2A). The obtained polymer has a hydrophilic backbone with carboxylic groups and hydrophobic side chains attached via robust amide bonds (Fig. 2.1.1.2B). We also included a size-exclusion

chromatography purification step to ensure removal of any small-molecule impurities. After the synthesis, the polymer is dispersible in non-polar organic solvents (e.g. chloroform). Importantly, the polymer allows easy attachment of fluorophores, bioorthogonal linkers and other useful moieties during synthesis, by adding an appropriate primary amine during the ring opening step.

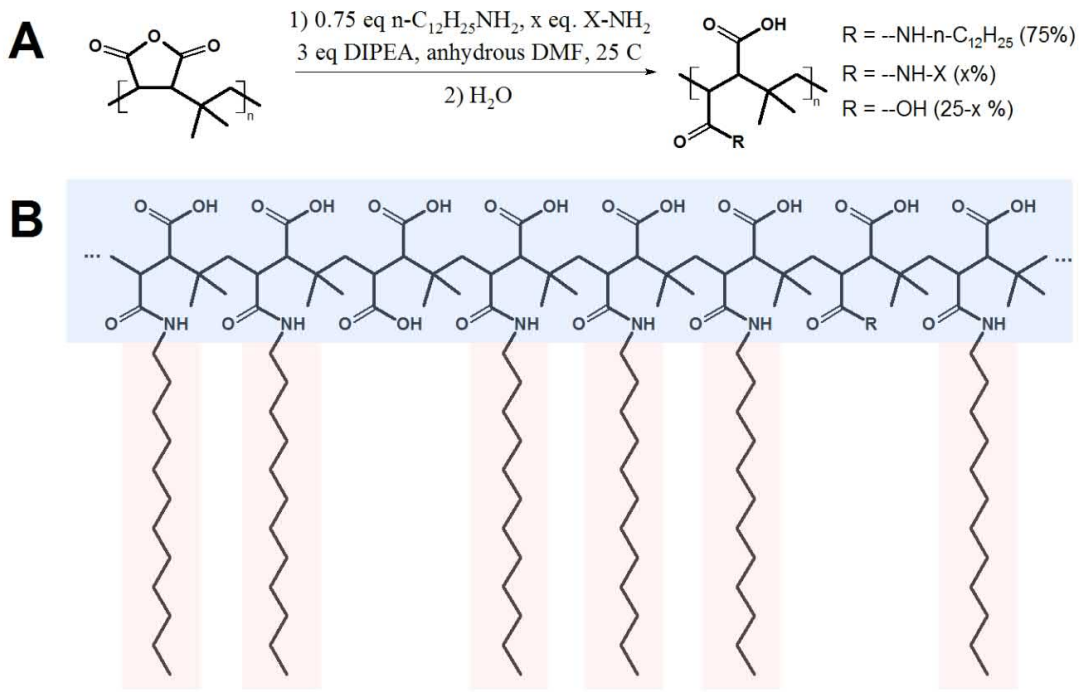

Fig. 2.1.1.2. Amphiphilic polymer synthesis. A: grafting of groups on a polyanhydride backbone through amide group formation. B: example of structure of the formed polymer, with hydrophobic side chains and hydrophilic backbone highlighted.

Afterwards, we performed UCNP coating by the polymer, using aforementioned literature protocols as a basis. The protocol is illustrated on Fig. 2.1.1.3 (full version available in Materials and Methods chapter). Briefly, the UCNPs and the polymer are dispersed together in chloroform (Fig. 2.1.1.3A). Addition of a highly basic aqueous buffer results in polymer residing on the water-chloroform interface, forming large solvent droplets (>1 μm in diameter) (Fig. 2.1.1.3B). Mild heating under a weak vacuum with constant agitation of the dispersion leads to slow evaporation of the chloroform from the mixture. As evaporation of the chloroform reduces the amount of space on the solvent-water interface, the droplets

shrink, forming progressively more rugged surface, and eventually break apart. The mechanism of droplet breaking is not clear, but is likely to be induced by mechanical agitation and electrostatic repulsion of charged carboxyl groups on the particle surface. Evaporation continues until the droplets either contain no solvent at all (thus becoming micelles), or contain one or multiple UCNPs. If a sufficiently high excess of the polymer is used, the resulting droplets will have lower probability to contain multiple UCNPs, ultimately leading to individual particles locked inside a polymer shell (Fig. 2.1.1.3C). At the same time, using an excess of the polymer results in formation of a high quantity of empty polymer micelles, which then need to be separated from the coated UCNPs. Such purification can be performed by centrifugal filtration, size-exclusion chromatography, centrifugal sedimentation with subsequent redispersion, and other nanoparticle purification methods (Fig. 2.1.1.3D).

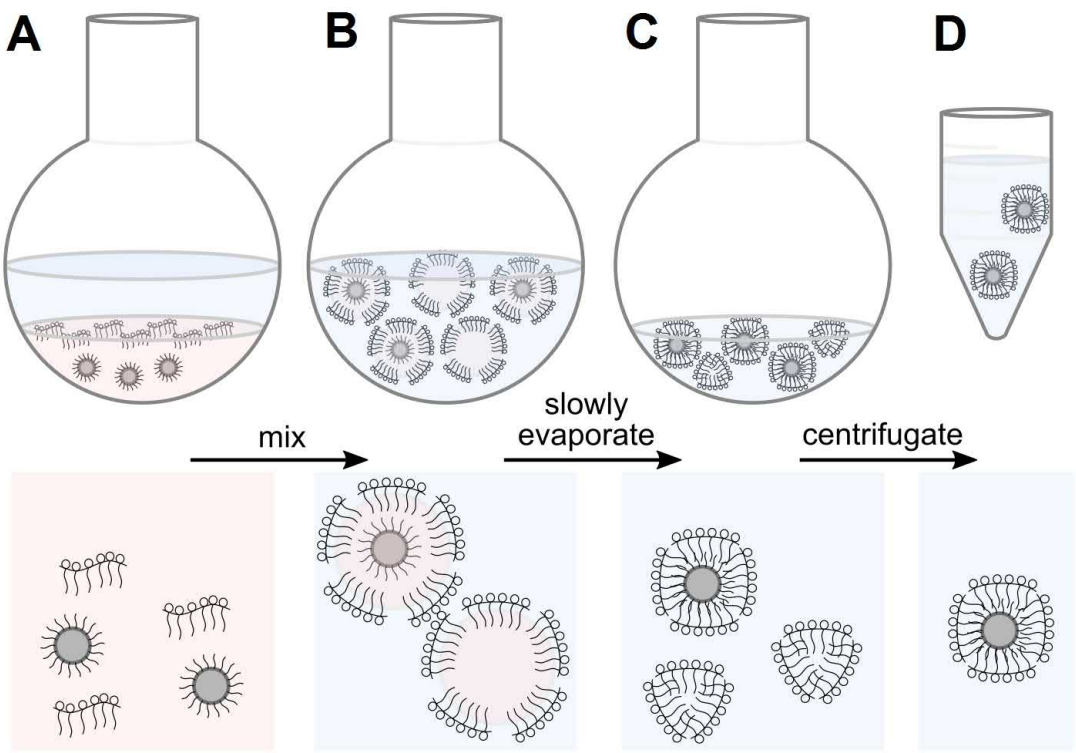

Fig. 2.1.1.3. Coating protocol. A: initial two-phase mixture. Particles remain in chloroform, while the polymer migrates to the interface. B: formation of large solvent droplets via mixing. C: formation of coated particles and polymer micelles. D: separation of particles and micelles.

We tested a variety of conditions for the coating/purification protocol, including changing polymer/UCNP concentration ratio, buffer pH, use of ultrasound to facilitate dispersion of UCNPs, and some other parameters. We eventually succeeded in finding a set of conditions that reliably produced a dispersion containing individual UCNPs locked inside polymer micelles, without substantial oligomerization or aggregation of the particles. We were unable to reproduce literature protocols for separating UCNPs from polymer micelles. However, we found a set of conditions for centrifugal sedimentation/redispersion that yield monodisperse particles with no polymer micelles present after two cycles of purification.

To characterize the particles after synthesis and purification, we performed dynamic light scattering (DLS) measurements, which are commonly used as a fast semi-quantitative method for sizing nanoparticles in bulk dispersions. While it does not allow to precisely resolve the relative concentrations of individual particles and particle oligomers, it can qualitatively signal significant oligomerization or aggregation. Examples of DLS size distributions for particle dispersions with micelles, purified individual particles, and oligomerized/aggregated particle dispersions are provided on Fig. 2.1.1.4.

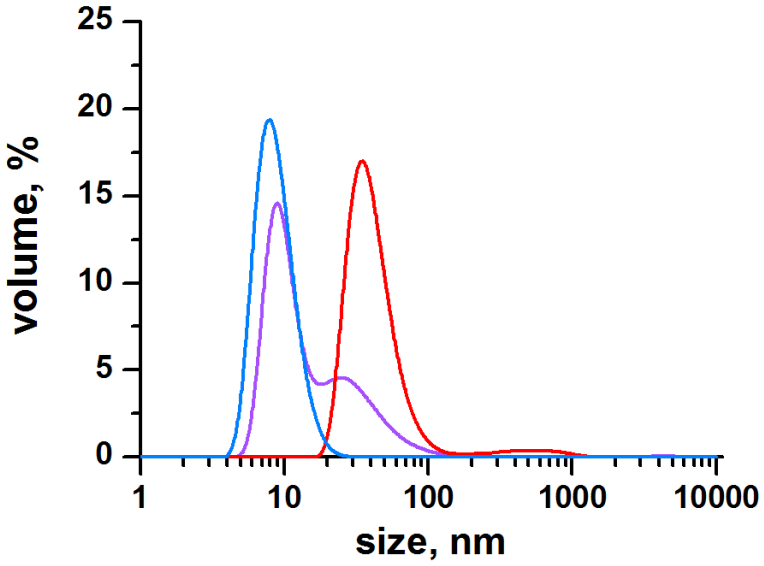

Fig. 2.1.1.4. Examples of DLS size distribution by volume for the dispersions of the polymer-coated particles. Purple: initial sample, containing both UCNPs and polymer micelles. Red: UCNPs purified by centrifugation and redispersion in buffer. Blue: polymer micelles residing in supernatant that was removed after centrifugation.

For SMM experiments, the particles need to be as homogeneous as possible in their size and luminescence. This is required to reliably distinguish individual nanoparticles from oligomers and aggregates based only upon their luminescence intensity, which can be immensely useful for experiments where particle size is not directly accessible (e.g. cell experiments). To assess both parameters at the same time, we performed correlated AFM and wide-field luminescence microscopy. Fig. 2.1.1.5 illustrates the concept of the experiment and an example of obtained images for 31 nm particles. Briefly, a particle dispersion is dried on a surface and then AFM and wide-field microscopy are performed simultaneously or sequentially on a given region of interest of the sample. If the initial concentration of the particles is sufficiently low, they will be separated far apart on the surface, and their luminescence peaks will be at sufficiently large distance from each other to allow their integration for comparing the intensity of luminescence of individual particles.

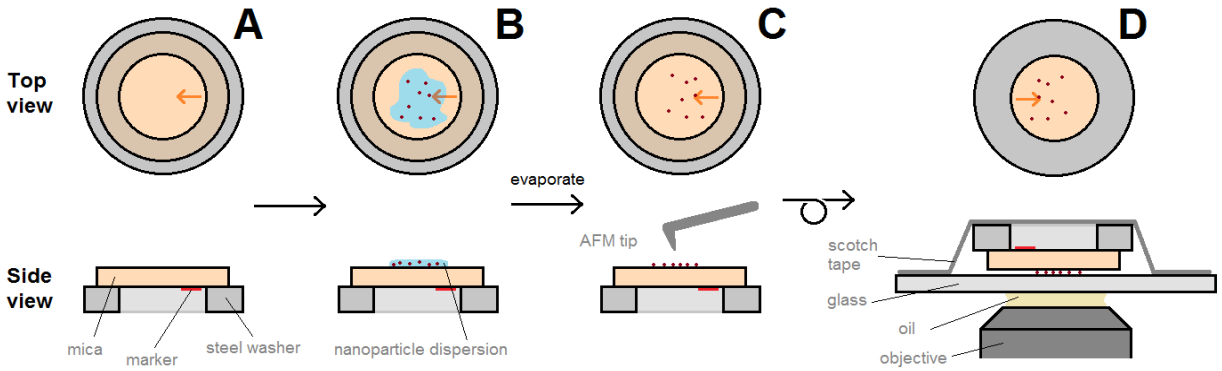

Fig. 2.1.1.5. Sample preparation for correlated AFM/wide-field upconversion luminescence microscopy. A: Initial assembly of mica attached to a steel washer, with a marker on the bottom side (red arrow). B: A drop of nanoparticle dispersion is added. C: After evaporation, AFM is performed on the sample. D: The sample is then inverted, fixed to a glass coverslip and the assembly is fixed on a microscope objective. The marker is located by eye in the bright field mode, and the exact ROI is located with an XY stage. Afterwards, luminescence microscopy is performed.

Fig. 2.1.1.6 shows an example of highly monodisperse sample of polymer-coated UCNPs. The particles show homogeneous luminescence and size (Fig. 2.1.1.6C). As AFM

images are convolved laterally with the shape of the imaging tip, the particle size is estimated from the height dimension, which can be measured very accurately with AFM.

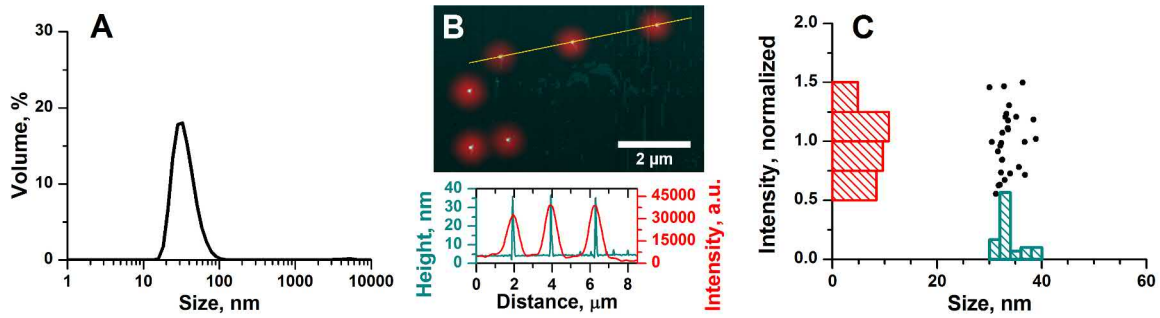

Fig. 2.1.1.6. Purified polymer-coated particles. A: DLS measurement of the water-dispersed UCNPs. B: Top: Region of interest (ROI) of an AFM image of UCNPs dried from an aqueous dispersion and its correlated wide-field upconversion microscopy image in the red channel (shown in red; 660/30 bandpass filter, excitation at 980 nm with intensity of 8 kW/cm2). Bottom: Height and intensity of the three particles highlighted in the top panel. C: Size and relative intensity (black spots) and histograms of these parameters (teal and red) for a sample of 28 particles.

As a side set of experiments, we have also performed synthesis and purification of *zwitterionic* amphiphilic polymers. Similarly to naturally occurring phospholipid membranes, zwitterionic surfactants have a covalently bound pair of positively and negatively charged groups on the hydrophilic end. In aqueous conditions, such polymers have a tendency to form a very dense strongly coordinated water shell around the zwitterionic group. This, combined with the neutral surface charge at physiological pH, allows zwitterionic surfactant micelles to be colloidally stabilized via steric repulsion of their strongly coordinated water shells. This allows them to exhibit aggregation-preventing and nonfouling properties in biological conditions in a way similar to polyethyleneglycol (PEG) grafting, but with a much smaller stabilizing group size (Fig. 2.1.1.7) (*Estephan et al., 2011; García et al., 2014; Schlenoff, 2014*).

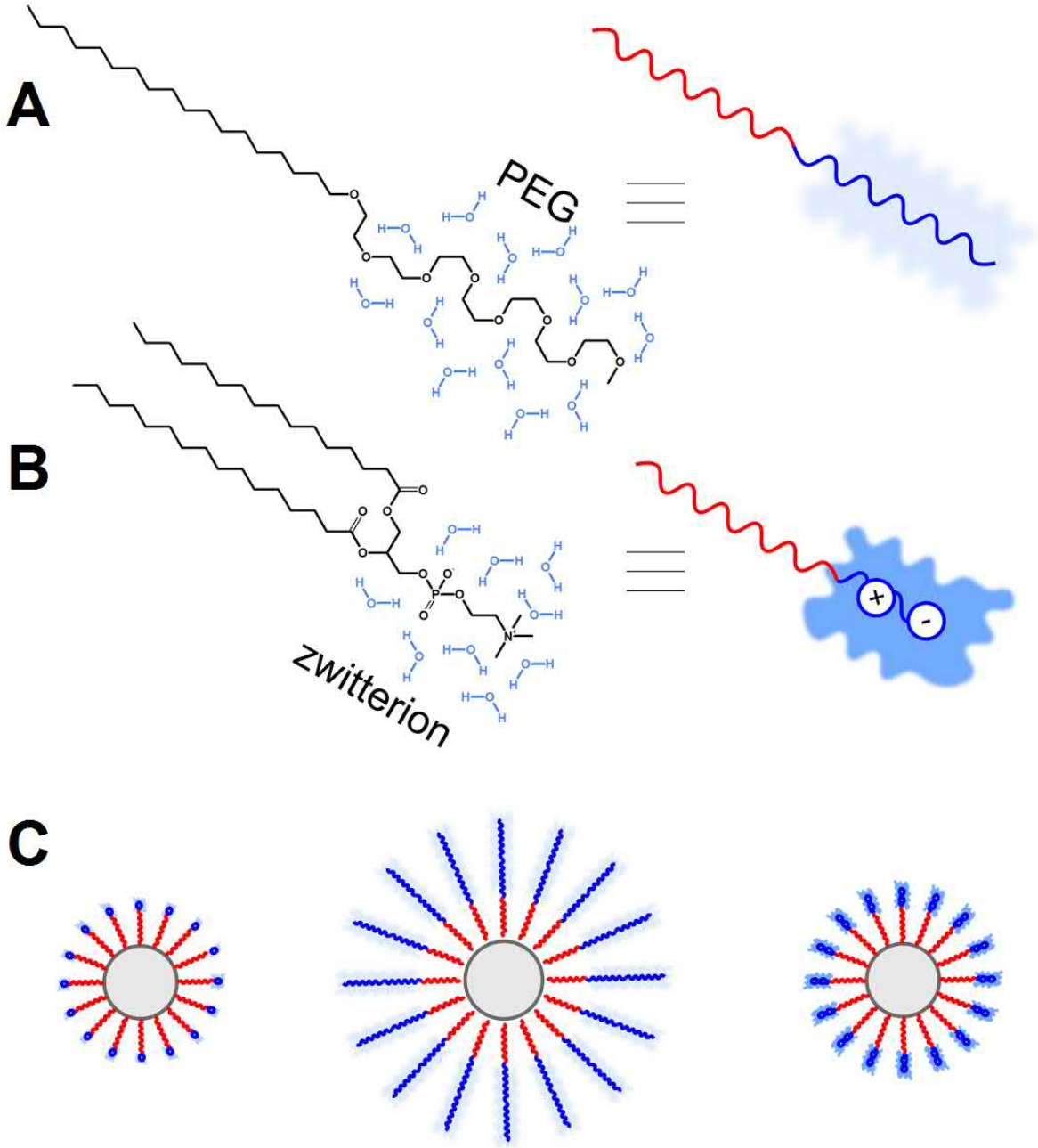

Fig. 2.1.1.7. Steric stabilization by PEGs and zwitterions. A: a surfactant with a PEG chain exposed to aqueous conditions has a moderately coordinated shell of water molecules. B: a zwitterionic surfactant (here: DOPC) has a small shell of strongly coordinated water molecules. C: Comparison of particle sizes for stabilization methods. Single-charge surfactants stabilize particles through electrostatic repulsion, however cease to do so in presence of salts. PEG surfactants stabilize particles through water shell steric repulsion, but require a substantial increase of particle size. Zwitterionic surfactants behave in the same

way, but allow to keep small particle size.

Imparting zwitterionic functionality on amphiphilic polymers, forms compounds known as *amphiphilic polyzwitterions* or *polysoaps*, which have potential applications for stabilizing nanoparticles in aqueous dispersions. Nonfouling properties induced by low net surface charge would allow to protect the particles against nonspecific binding of biomolecules, while thin shell size would be beneficial towards FRET applications that require close distance between the particle and an acceptor moiety. Another beneficial property of zwitterion-coated nanoparticles would be their colloidal stability in physiological buffers that usually have high ionic power, which is an issue with nanoparticles stabilized via electrostatic repulsion.

As there was scarce information in the literature on stabilizing nanoparticles with amphiphilic polyzwitterions, we decided to investigate the feasibility of preparing such compounds and stabilizing UCNPs with them. We have tested several strategies to prepare a zwitterionic polymer, all based on the modification of a polyanhydride backbone with a sulfobetaine-amine. Fig. 2.1.1.8 illustrates the only approach that resulted in significant decoration of the polymer backbone with sulfobetaine moieties. We characterized the polymers by NMR and IR spectra to verify their composition. Due to solubility issues, only one protocol was found to lead to a polymer with a significant quantity of sulfobetaine groups (failed protocols are not presented here but are available upon demand). Unfortunately, coating the UCNPs with this polymer was not successful. Neither of the coating approaches that we tested has yielded anything beyond aggregates of polymer and UCNPs. The likely reason for that was the high thermodynamic stability of polymer films and aggregates obtained during the solvent evaporation step, due to the lack of electrostatic repulsion between individual “head” groups. Another possibility was the insufficient hydrophilicity of the sulfobetaine due to the presence of ethyl groups, hindering the coordination of water molecules. While the subject warrants more investigation, we decided to postpone this side project and instead focus on other dispersion approaches, as well on UCNP applications.

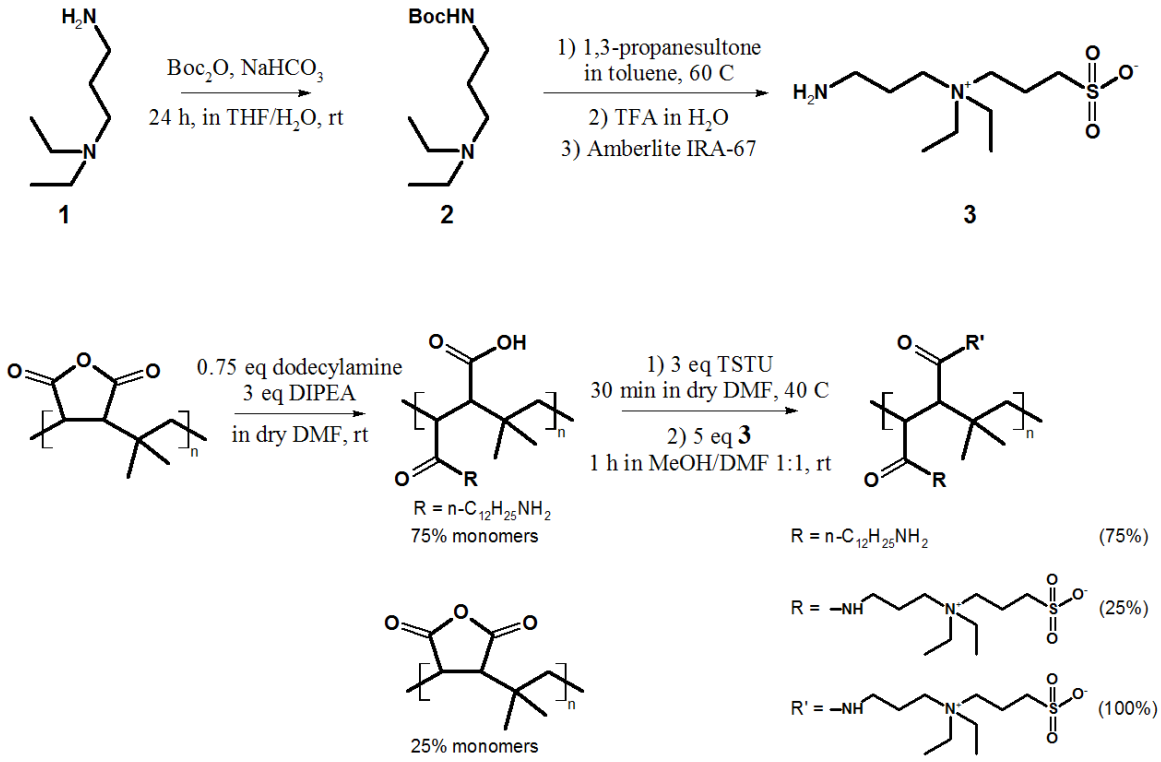

Fig. 2.1.1.8. Synthesis of zwitterionic amphiphilic polymer.

2.1.2. Ligand exchange experiments

We performed a small set of ligand exchange experiments to see if they would yield satisfactory particle quality. For the ligand exchange experiments, we decided to opt for gentle ligand stripping via $NOBF_4$ with simultaneous extraction of the particles into DMF . (*Dong et al., 2011*). DLS of the obtained particle dispersions in DMF showed that no significant aggregation had occurred during ligand stripping and that the particles were colloidally stable over extended periods of time, evidenced by DLS (Fig. 2.1.2.1).

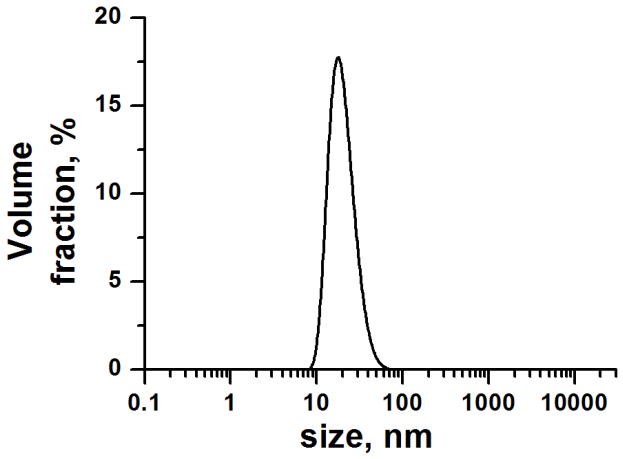

Fig. 2.1.2.1. DLS of 21 nm UCNPs that underwent ligand exchange with $NOBF_4$.

The next step was dispersion of the particles in water with stabilization by surfactant and subsequent purification to remove residual DMF and empty micelles. As a surfactant, we used Tween 20, a neutral surfactant with a branched PEG hydrophilic moiety. The particles remained colloidally stable, but only in the presence of polymer micelles. In the small set of experiments that we performed, we consistently found particle oligomerization and colloidal instability over time to be a problem if the excess surfactant was removed from the dispersion.

2.1.3. Nanoemulsion experiments

Nanoemulsions enjoyed a large amount of attention during the last years, particularly for encapsulating non-polar drugs in oil droplets for drug delivery applications (*Anton and Vandamme, 2010*). Out of the nanoemulsification methods, one method, called *spontaneous emulsification*, is particularly notable for its low experimental setup requirements and possibility to work with fragile substances that would be degraded by conventional emulsification methods like sonication (*Anton and Vandamme, 2009*).

Spontaneous emulsification is based upon making a homogeneous mixture of oil and nonionic surfactant in a certain proportion and then mixing the obtained solution with water or aqueous buffers. Upon mixing, the two-phase system is thermodynamically non-equilibrated and spontaneously follows to the nearest kinetically stable state, resulting in rapid repositioning of surfactant molecules to the oil/water surface. If the surfactant proportion is

sufficiently large, the two phases spontaneously form a large surface area between them, resulting in the formation of nanoemulsion. Afterwards, coalescence of the oil droplets is hindered by the presence of the surfactant at the interface. This leads to nanoemulsions kinetically stable for weeks or months. Successful formation of stable nanoemulsions depends on the surfactant and oil nature, their proportions in the mixture, the temperature at which the mixing is performed, the presence of ions in the aqueous phase, and several other parameters.

If a lipophilic substance is added to the oil/surfactant mixture before forming nanoemulsion, it gets entrapped (encapsulated) inside the emulsion droplets. As UCNPs capped with oleate ions are hydrophobic, they can be potentially entrapped in the droplets, provided that the average droplet size is sufficient to fit a UCNP inside it.

We have performed a broad exploration of possible experimental conditions to find the combinations of oil/surfactant and experimental conditions that would yield reliable loading of UCNPs inside oil droplets. Two relatively successful experiments and some comments are highlighted in Table 2.1.3.1 (full protocol is available in Materials and Methods section). Sadly, no experimental conditions yielded particles with sufficiently long colloidal stability, with the very best showing aggregation and visible sedimentation within 2-3 days.

Nanoemulsion composition and emulsification conditions	**Size by DLS (volume distribution)**	**Comments**
Sample NE42: 55µL Labrafac WL1349, 55µL Solutol HS15, 1.25 mg UCNP 31 nm, 100 µL chloroform (cosolvent for mixing, removed by evaporation before emulsification), emulsification with 25 C water	38 nm	dodecylated amphiphilic polymer used as a co-surfactant; sample shows substantial aggregation over 2 days
Sample NE25: 45µL Suppocire C, 55µL Solutol HS15, 1.25 mg UCNP 31 nm, 50 µL chloroform and 100µL dichloroethane (cosolvents for mixing, removed by evaporation before emulsification), emulsification with 25 C water	34 nm	dichloroethane aids dispersion with high-melting-point oil (Suppocire C); sample shows substantial aggregation overnight

Table 2.1.3.1. Examples of relatively successful nanoemulsification experiment conditions.

We have also performed multi-channel wide-field microscopy and TEM to estimate the loading proportion of UCNPs inside the droplets. For this, the droplets were loaded with

organic dyes together with UCNPs, and afterwards immobilized on glass surface. Excitation with visible light induces dye fluorescence, while IR excitation induces UCNP luminescence. By combining the images, the total amount of droplets and the amount of droplets containing UCNPs could be compared. Fig. 2.1.3.2 illustrates the results. The images suggest that the loading proportion is extremely low, with only few UCNP-loaded droplets among hundreds of empty ones. We tried to separate the particles and droplets using mild centrifugation, reasoning that the major separation-enabling difference between "empty" and UCNP-containing droplets would be their density. Unfortunately, we did not find conditions that allowed sufficient separation of UCNP-containing droplets without inducing their coalescence.

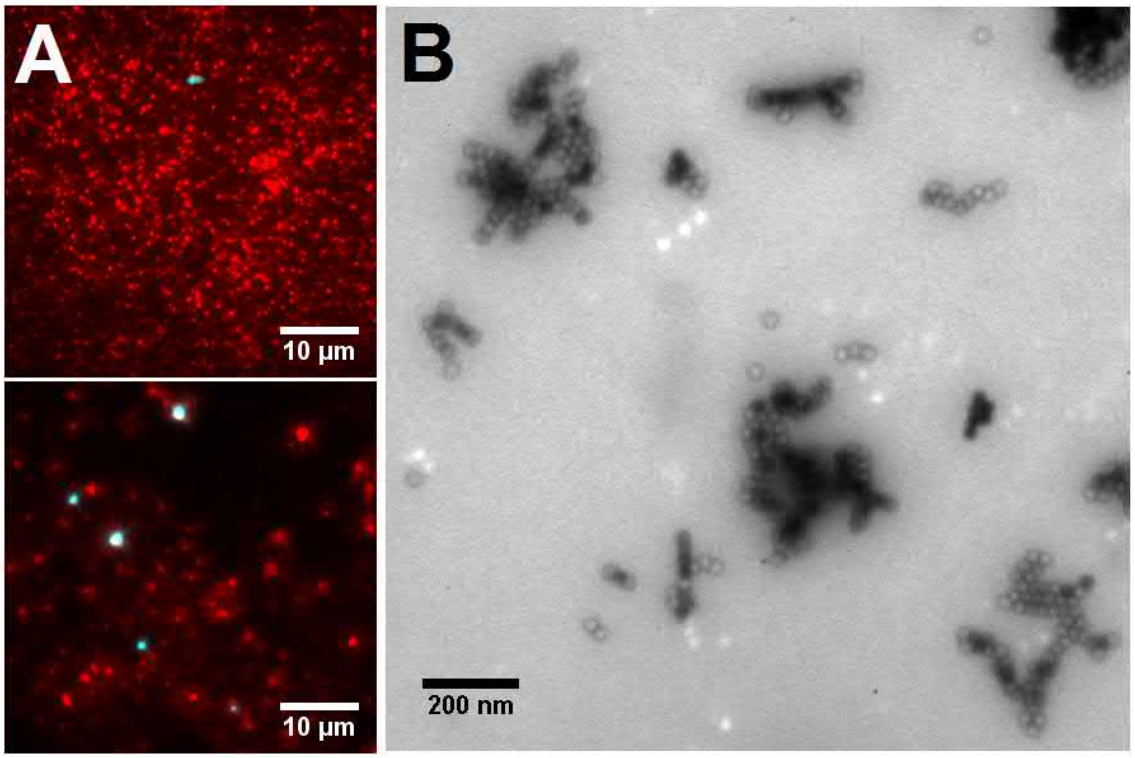

Fig. 2.1.3.2. Nanoemulsion-entrapped UCNP sample. A: two wide-field colocalization microscopy images of UCNPs (cyan) and organic dyes (red) immobilized by drying on glass. "Spreads" around the spots likely correspond to the oil from the emulsion droplets spreading on the surface upon drying. UCNPs are sparsely present and show large spots with high emission, corresponding to aggregates. B: A typical TEM image for the same nanoemulsion sample immobilized by drying on a carbon-coated Formvar TEM grid, using uranyl acetate

staining. Both "empty" nanoemulsion droplets (donuts) and UCNPs (filled circles) are present. Unlike droplets, UCNPs were always found in large clumps, implying they were aggregated before immobilization.

Summing up this chapter, we have found conditions using amphiphilic polymers that allowed hydrophilisation and purification of UCNPs while retaining their monodispersity. Other methods we have tried did not yield satisfactory results for the purposes of applying particles in SMM.

The next step was testing the feasibility of using UCNPs for SMM techniques. We decided to start with smFRET.

Part 2. Estimating applicability of UCNPs to smFRET.

At the beginning of this part of the project, proof-of-concept applications using UCNPs as FRET donors were quite well represented in the literature (*Idris et al., 2012; Lahtinen et al., 2016; Mattsson et al., 2015; Rantanen et al., 2007; Wang et al., 2016*). Meanwhile, we haven't found any example of smFRET experiments based on UCNPs. A particular issue that attracted our attention was the lack of a systematic overview of FRET from UCNPs to organic dyes, especially the quantitative assessment of it. As smFRET is a quantitative technique, employing UCNPs for smFRET requires understanding and predicting UCNP-dye FRET at least at a semi-quantitative level, with the possibility to use this model to find optimal nanoparticle parameters and imaging conditions for reasonable smFRET performance.

In the context of FRET, UCNPs can be considered as a rigid system of independently emitting point donors inside a spherical region, scavenging energy from the volume of the whole sphere, and transferring their energy to individual point acceptors close to the surface of the sphere (Fig. 2.2.1). Qualitatively, we could expect a lower FRET efficiency for larger particles, as they would have a lower total percentage of emitter ions located in vicinity of the organic dye. Meanwhile, increasing the amount of dyes on the nanoparticle surface would increase FRET efficiency due to the larger amount of acceptors scavenging energy from

donors. We thus decided to build a theoretical framework for predicting the efficiency of FRET between UCNPs and organic dyes based on the quantity of dyes and the UCNP size.

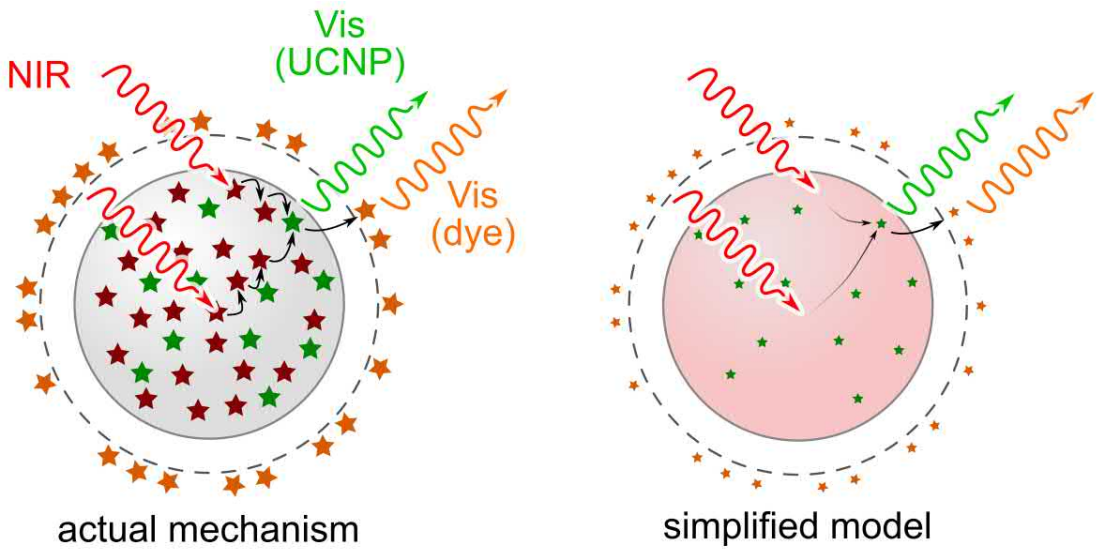

Fig. 2.2.1. Mechanism of FRET from UCNPs to organic dyes and its simplified model. Red and green stars represent sensitizer and emitter ions, respectively. Orange stars represent organic dyes. In the simplified system, the particle absorbs light homogeneously with all its volume, uniformly transferring its energy to the emitter ions, which can then either emit or transfer their energy to the dyes. Both emitter ions and dyes are assumed to be infinitely small.

Considering the complexity of the upconversion processes and quenching pathways in UCNPs, we decided to build a semiempirical theoretical model based on a set of experiments estimating FRET efficiency on particles with different sizes and amounts of dyes on the surface. In regards to the choice of mathematical approach, due the relatively low amount of dyes and emitters, using an analytical integration-based approach could yield inaccurate results. We thus used a simple Monte Carlo model as a basis for theoretical estimation of FRET.

The results are presented in the following research article that we have published in Nanoscale in 2017. We reframed and extended the model to be applicable not only to smFRET, but also to other UCNP-based FRET systems (e.g. FRET-based assays with multiple sensing moieties attached to one particle).

After applying the system to estimate FRET efficiency from an individual UCNP to a single organic dye, we found that obtaining a reasonable FRET efficiency of ~10% would require using particles of sub-10 nm size. We have performed experiments to estimate for individual UCNPs the dependence of their SNR in imaging on their size, using our wide-field microscopy setup and a reasonably slow framerate (25 fps, exposure of 40 ms). Extrapolating this dependence towards nanoparticles of 10 nm in diameter results in a too low SNR to image them on our setup. We thus did not proceed with further smFRET experiments and focused on other applications of UCNPs. Very recent literature (*Tian et al., 2018*) suggests that particles with highly-doped core – inert shell architecture provide reasonable SNR in microscopy even at very small particle sizes. Thus, adapting our theoretical model towards investigating the feasibility of using such particles in smFRET applications could be an interesting direction for future research on the subject.

Publication 1.

Quantitative assessment of energy transfer in upconverting nanoparticles grafted with organic dyes

Nanoscale

PAPER

View Article Online
View Journal | View Issue

Cite this: *Nanoscale*, 2017, **9**, 11994

Quantitative assessment of energy transfer in upconverting nanoparticles grafted with organic dyes†

Oleksii Dukhno, *[a] Frédéric Przybilla,[a] Mayeul Collot, [a] Andrey Klymchenko, [a] Vasyl Pivovarenko, [b] Markus Buchner,[c] Verena Muhr,[c] Thomas Hirsch [c] and Yves Mély *[a]

Upconverting nanoparticles (UCNPs) are luminophores that have been investigated for a multitude of biological applications, notably low-background imaging, high-sensitivity assays, and cancer theranostics. In these applications, they are frequently used as a donor in resonance energy transfer (RET) pairs. However, because of the peculiarity and non-linearity of their luminescence mechanism, their behavior as a RET pair component has been difficult to predict quantitatively, preventing their optimization for subsequent applications. In this article, we assembled UCNP–organic dye RET systems and investigated their luminescence decays and spectra, with varying UCNP sizes and quantities of dyes grafted onto their surface. We observed an increase in RET efficiency with lower particle sizes and higher dye decoration. We also observed several unexpected effects, notably a quenching of UCNP luminescence bands that are not resonant with the absorption of organic dyes. We proposed a semi-empirical Monte Carlo model for predicting the behavior of UCNP-organic dye systems, and validated it by comparison with our experimental data. These findings will be useful for the development of more accurate UCNP-based assays, sensors, and imaging agents, as well as for optimization of UCNP–organic dye RET systems employed in cancer treatment and theranostics.

Received 16th December 2016,
Accepted 16th July 2017

DOI: 10.1039/c6nr09706e

rsc.li/nanoscale

Introduction

Upconverting nanoparticles (UCNPs) have attracted strong interest over the last decade in biological imaging and sensing.[1–4] UCNPs owe their name to the upconversion phenomenon, where high-frequency light is emitted upon sequential absorption of several quanta of low-frequency light. Several systems have been developed for achieving efficient upconversion on a nanometric scale. One of these systems, lanthanide-doped UCNPs, is of particular interest due to the high efficiency of their upconversion, excitation in near-infrared with several narrow luminescence bands in the visible region, and remarkable photostability.[5] Typically, these particles are crystals of an ionic insulating matrix material (*e.g.* β-$NaYF_4$, Y_2O_3 and CaF_2), 10–100 nm in size, which are doped with lanthanide ions.[5] A common and popular example of UCNPs employs two dopant ions performing energy transfer upconversion (ETU). In this process, one of the dopants plays the role of a sensitizer that absorbs low-energy light and then sequentially transfers its excitation energy to an activator (emitter) ion. A typical example of a sensitizer–activator system is the Yb^{3+}–Er^{3+} pair.[6]

Using a luminophore with near-infrared excitation and visible emission allows sidestepping of several critical problems inherent in biological experiments employing conventional fluorescent dyes, namely autofluorescence, excitation light scattering and phototoxicity. As a result, UCNPs can be imaged with an exceptional signal to noise ratio.[1] Another advantage is the possibility of customizing UCNPs for multiplexed imaging. For example, conjugating UCNPs with iron oxide nanoparticles or doping with Gd ions allows their use in magnetic resonance imaging as well as in luminescence microscopy.[7–9]

UCNPs can also be used for constructing resonance energy transfer (RET) systems, where UCNPs act as an IR-absorbing antenna for a conventional fluorophore (*e.g.* organic dye).

[a]*Laboratory of Biophotonics and Pharmacology, UMR 7213 CNRS, University of Strasbourg, 67000 Strasbourg, France. E-mail: oleksii.dukhno@unistra.fr, yves.mely@unistra.fr*
[b]*Faculty of Chemistry, National Taras Shevchenko University of Kyiv, 01033 Kyiv, Ukraine*
[c]*Institute of Analytical Chemistry, Chemo- and Biosensors, University of Regensburg, 93040 Regensburg, Germany*
†Electronic supplementary information (ESI) available. See DOI: 10.1039/c6nr09706e

These systems were used for developing UCNP-based sensors for small molecules, proteins and nucleic acids,[10–16] and IR-responsive drug release systems.[17–20] However, the peculiarities of UCNP photophysics, like the dependence of their quantum yields on excitation intensity[6,21,22] and multiple transitions between several emitting energy levels, make the behavior of the overall RET system challenging to predict quantitatively. Moreover, as the emitter ions in UCNPs are point emitters with low cooperativity due to a large emitter–emitter distance, the behavior of RET systems with UCNPs cannot be predicted from the base case of Förster theory (interaction of two point dipoles). Also, the emitter ions close to the particle surface seem to have lower luminescence yields due to surface quenching effects, which lead to further complications.[21,23] Finally, the field is still in an early stage and methods to construct monodisperse and homogeneous small bright UCNPs required for efficient RET appeared only recently.[23,24]

While there are a number of examples for dye-decorated UCNPs in the literature, they mostly concentrate on proof-of-concept systems and their direct applications.[11,12,16,25–27] In contrast, few efforts were done to thoroughly investigate and optimize the RET behavior in UCNP–dye systems.[28–31] For example, recent work by Ding *et al.*[28] shows the dependence of the relative contribution of RET and reabsorption in dye-decorated UCNPs on the thickness of an inert shell between the active UCNP core and dyes. However, the dependence of RET on the dye density at the UCNP surface was not systematically investigated. In our previous work,[29] we reported the dependence of RET efficiency on particle size with full coverage of the particle surface by dye molecules, with particles dispersed in DMF. To explore the dependency of RET efficiency on dye loading independently of particle size and to move to a more biological context, an alternative method for solubilization and dye decoration is required.

In this context, the objective of this work was to quantitatively predict the RET behavior of water-dispersed UCNPs of various sizes decorated with rhodamine B at different extents. To reach this goal, we have developed a Monte Carlo model for describing RET processes based on an extension of Förster theory to a multiple donor–multiple acceptor system.[32] The model was validated by comparison of the predicted data with experimental RET data obtained on the designed rhodamine B-decorated UCNPs using luminescence lifetimes and spectra. This model will be useful for designing optimized UCNP–dye systems for sensing and theranostics, by predicting the best particle size and composition, as well as the optimal decoration, in respect of the dye properties and coating levels.

Results and discussion

Design of the dye-grafted UCNPs

As the first step, we designed UCNPs decorated with Rhodamine B dyes for providing experimental data to develop a theoretical model. To this end, we selected UCNPs with β-$NaYF_4$ as a matrix, doped with 20% Yb^{3+} and 2% Er^{3+} as sensitizer and activator ions, respectively. This choice of matrix and dopants is one of the most common in UCNP studies, as it produces bright upconversion over a wide power range with well-established synthesis protocols. A simplified scheme of the upconversion mechanism for the Yb–Er UCNPs is provided in Fig. S1.†

Three types of particles with different diameters were prepared: 16.2 ± 0.6 nm particles ($NaYF_4$:20%Yb,2%Er,20%Gd), 20.9 ± 0.6 nm particles ($NaYF_4$:20%Yb,2%Er,10%Gd), and 30.6 ± 1.1 nm particles ($NaYF_4$:20%Yb,2%Er). The particle size and morphology were evaluated by TEM (Fig. 1). A variation in Gd^{3+} doping was used to change the size of the obtained particles while keeping other synthesis conditions constant, as well as to retain high monodispersity for all samples.[33] The X-ray diffraction data confirm a hexagonal crystal structure for all samples (Fig. S2†).

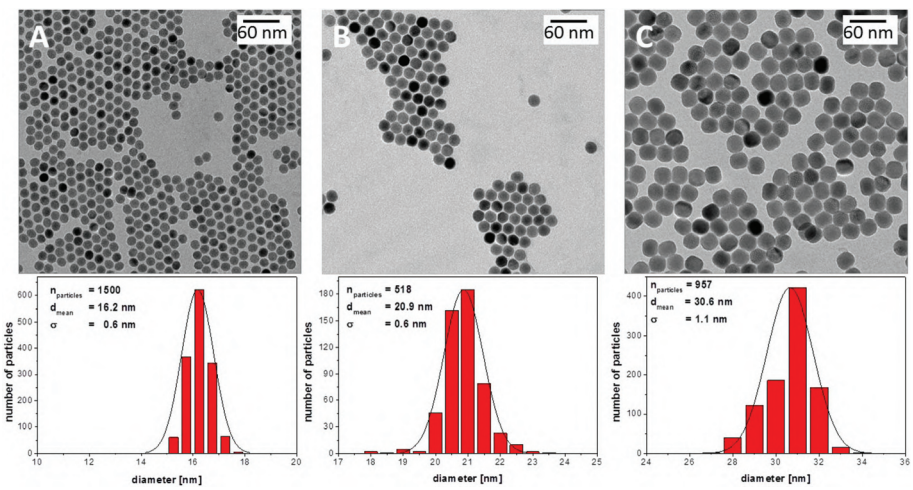

Fig. 1 TEM images of UCNPs. Left-to-right: 16 nm diameter, 21 nm diameter, 31 nm diameter. Top: TEM images, bottom: histograms of the particle size distribution obtained from TEM images.

Two sets of sharp emission bands arising from Er^{3+} transitions are observed in the green and red regions of the visible spectrum of the prepared UCNPs (Fig. 2). For convenience, these luminescence bands are referred to as "green" and "red" bands.

The synthesis produces UCNPs coated with a hydrophobic layer of oleic acid of ~1.1 nm thickness.[34] As the majority of RET systems with UCNPs are developed for applications in biological systems, the UCNPs have to be modified to become water-dispersible. Several methods exist to reach this goal.[35] We chose to coat the hydrophobic UCNPs using an additional layer of poly-isobutylene-*alt*-maleic acid with dodecyl side chains (PMA, Fig. 3), an amphiphilic polyanionic polymer that can form a thin bilayer at the UCNP surface combining the oleic acid chains on the particle surface and the hydrophobic chains of the polymer.[34] This coating permits UCNP suspensions to be colloidally stable in water over extended periods of time and have a high negative zeta-potential (protocol in the ESI,† based on Wilhelm *et al.*[34]). Moreover, PMA coating does not strongly affect particle brightness, which is a common problem for several other UCNP hydrophylisation methods.[34,35]

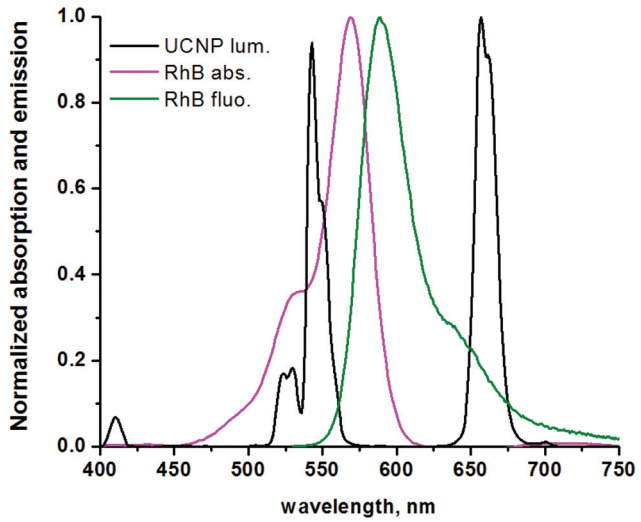

Fig. 2 Luminescence spectrum of polymer-coated water-solubilized 31 nm UCNPs (black), and absorption (pink) and fluorescence (green) spectra of Rhodamine B in water. UCNP luminescence was measured with a 980 nm excitation and 8 kW cm^{-2} power density.

Finally, to construct a RET pair with UCNPs, we selected rhodamine B (RhB) as an organic fluorophore. RhB was modified to contain a side chain with a primary amine, to allow its covalent binding to the UCNP–polymer conjugate (Fig. 3, synthesis protocol and spectra in Fig. S3–S9†). The RhB absorption band overlaps with the UCNP emission band in the green region, so the dye can act as a RET acceptor (Fig. 2). At the same time, the RhB absorption band does not overlap with the red emission band of UCNPs, thus allowing the use of the red band as an internal reference of luminescence intensity. It should be noted that using the red band as an internal reference contains the implicit assumption of the "red" state population not being affected by quenching of other emissive states. While this is a quite serious assumption to make, as is discussed later in this article, this approach is still commonly used in the literature.[36,37] Concerning the luminescence, the RhB emission band is located between the green and red UCNP luminescence bands, which allows separation of the emission of UCNPs and RhB and avoids crosstalk.

The PMA polymers are conjugated with dyes before forming a shell around UCNPs, so that UCNPs of different sizes with the same polymer have the same amount of dyes per unit surface to allow comparison of RET efficiency between particles of different sizes. After conjugation, the absorption spectra of dye-modified PMA are measured to calculate the accurate quantity of dyes grafted per monomer. The comparison of the absorption and fluorescence spectra of RhB dyes and UCNP–PMA–RhB is provided in Fig. S10.†

Twelve samples of UCNP–PMA–RhB particles of three different particle sizes were prepared. The preparation of each sample and the full set of subsequent measurements were performed in triplicate. The samples were classified as **S** (16 nm), **M** (21 nm) and **L** (31 nm), according to their size. The samples were further named **0**, **1**, **2** and **3** to describe that the UCNPs were coated with polymers containing 0%, 0.33%, 1.5% and 6.6% eq. of RhB per monomer (determined from absorption spectra). Therefore, using our nomenclature, the **M2** sample corresponds to 21 nm-diameter UCNPs coated with the polymer containing 1.5% eq. dye per monomer, which corresponds to

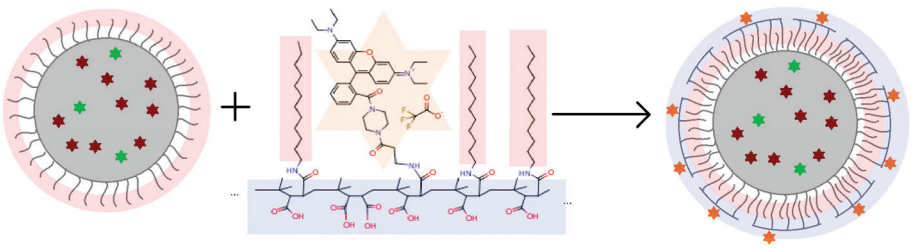

Fig. 3 Scheme of UCNP coating. Left: Initial UCNPs doped with lanthanide ions and coated with oleic acid. Center: Polymer used to disperse UCNPs in water. Hydrophobic parts are highlighted in pink, hydrophilic parts are in blue, and sensitizers, emitters and dyes are symbolized by red, green and orange stars, respectively. Right: Final water-dispersible RhB-labeled UCNPs.

approximately 123 grafted dyes per UCNP (the same calculation for other samples is provided in Table S1†).

To confirm the size of the obtained hydrophilic UCNPs and to check that no aggregation occurs post-coating, we performed DLS measurements. All samples show a peak at their respective sizes, indicating low to no aggregation (Fig. S11–S13†). DLS also shows some smaller particles of about 5–10 nm in diameter, that likely correspond to polymer micelles with no UCNPs inside, as the protocol uses an excess of polymer to ensure complete coating of the UCNPs. As the presence of the dyes bound to polymer micelles may induce "inner filter" effects, all measurements were performed with diluted samples and a setup configuration collecting light only from the focal volume, with a minimized optical path of emission through dispersion, with transmission on green and red bands calculated to be >95% for even the most concentrated samples (see Fig. S20† for the scheme of the setup).

Emission spectra of the dye-grafted UCNPs

The spectra of **M1–M4** dispersions with 980 nm excitation, normalized by the red UCNP band are shown in Fig. 4 (average of normalized curves over 3 measurements). In the absence of RhB, the spectrum of the 21 nm UCNPs is consistent with the spectrum of previously described 21 nm-sized particles, with a green-to-red ratio of about 2.4.[28] As expected from RET theory, an increase in the acceptor dye concentration on the particle surface leads to an increase in the RhB fluorescence band and a drop of the UCNP green band. It should be noted that the drop in the green band in this case is induced by RET, as the inner filter effects would account for a drop of no more than 5% for even the most concentrated sample. On the other hand, the dye band rise is the result of a mixture of RET-induced fluorescence and reabsorption with subsequent reemission. Therefore, in this experiment, quantitative conclusions can be drawn only from the intensities of green and red bands, but not from the dye band. The same behavior can be observed for 16 nm and 31 nm particles (Fig. S14 and S15†).

Comparing the ratio of integrated intensities of the green/red bands in the UCNP–PMA–RhB and UCNP–PMA samples can provide information about the total RET efficiency in the system, using an equation similar to that used for deriving the FRET efficiency from the donor intensity in the donor–acceptor dye pairs (eqn (1)). This approach is typically used to characterize the performance of RET sensors based on UCNPs.[10–12,25,38] It is important to note that this comparison is only valid under the assumption that the red band works as an internal reference not affected by the RET-induced quenching of the UCNP green band.

$$\eta = 1 - \frac{I_{\text{green}}/I_{\text{red}}}{I_{\text{green,no dye}}/I_{\text{red,no dye}}} \quad (1)$$

The calculated RET efficiencies for the tested UCNP–PMA–RhB samples are provided in Fig. 5. Two trends are observed and can be qualitatively (but not quantitatively) explained by the base case of Förster theory. Firstly, smaller particles have higher RET efficiencies due to the larger percentage of emitter ions (RET donors) being in the vicinity of organic dyes (RET acceptors). Secondly, an increasing amount of dyes on the particle surface increases the RET efficiency, due to a higher quantity of acceptors per donor.

Emission decays of the dye-grafted UCNPs

Luminescence decay curves of the particles in solution were recorded using the Time-Correlated Single Photon Counting (TCSPC) technique with a setup coupled to a monochromator in order to investigate the time-resolved decays of the different emission bands. As the optical properties of UCNPs depend on the excitation intensity, both steady-state (spectral) and time-

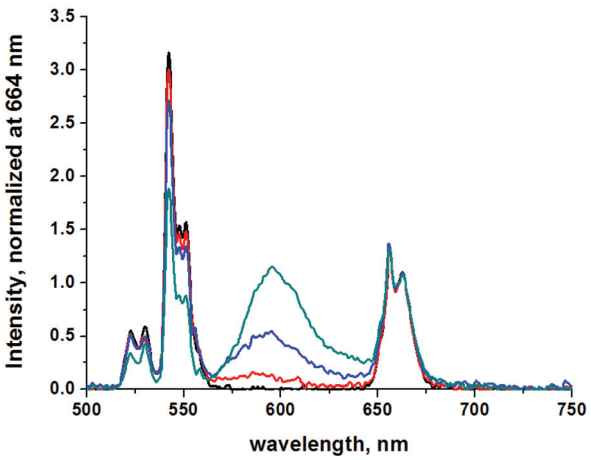

Fig. 4 Spectra of UCNP–PMA–RhB samples **M1–M4** diluted 10× in water, normalized to 664 nm (right shoulder of the red band) to minimize the UCNP/dye crosstalk. The percentage of grafted RhB dyes per monomer is 0% (black), 0.33% (red), 1.5% (blue) and 6.6% (cyan). UCNP luminescence was measured with an excitation at 980 nm and 8 kW cm^{-2} power density, at an approximate concentration of ~0.1 mg mL^{-1}.

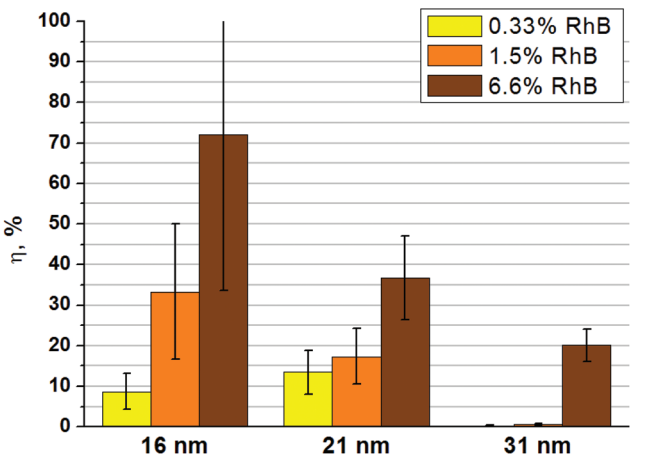

Fig. 5 RET efficiency values for UCNP–PMA–RhB samples based on the intensity ratios of green to red bands, as calculated in eqn (1) (bars correspond to the mean values over three independent measurements, error bars correspond to ±1 standard deviation).

resolved luminescence measurements were performed using the same excitation intensity of 8 kW cm^{-2}.

The decay curves for the green and the red bands of UCNP luminescence for samples **M1–M4** are provided in Fig. 6A and B, respectively. The lifetime values were determined by fitting the decays using multiexponential models by a maximum entropy method (MEM).[39] MEM was chosen to treat the decay curves because it does not require initial assumptions in the fit concerning the number of decay components. This method consistently determines three components for the green-band decays and two components for the red band decays for all particles.

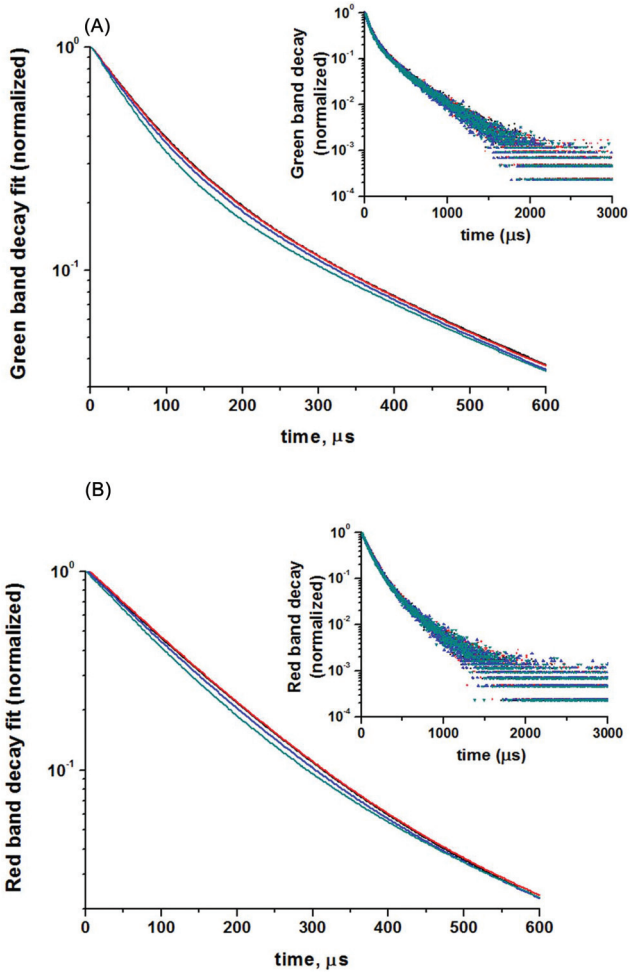

Fig. 6 Luminescence decays of samples **M1–M4** diluted 10× from the initial concentration in water. (A) Normalized green band decay fit and raw data (inset). (B) Normalized red band decay fit and raw data (inset). Excitation was at 980 nm, with 8 kW cm^{-2} power density. Curves are color-coded black, red, blue, and cyan for samples M1–M4, respectively.

For UCNPs coated with PMA without dye (samples **S1**, **M1** and **L1**), the lifetime data (Fig. 6, Fig. S16–S19 and Table S2†) are consistent with those in the literature, with a long component of 100–300 μs and a short component of 50–100 μs.[28] The short lifetime component is commonly assigned to direct Er^{3+} emission, while the longer one may be attributed to an emission after sensitizer-mediated emitter–emitter energy transfer, as has been recently reported by Würth *et al.*[40] When the number of RhB dyes at the surface of UCNPs is increased, not only the green band, but also the red band of UCNPs shows faster decay (Fig. 6), evidencing a strong interconnection between the emissive states of UCNPs. Using the data obtained for UCNP–PMA not coupled to RhB molecules as a reference, we calculated the apparent RET efficiency of the dye-coated UCNPs with the classical equation used for single donor–single acceptor pairs:

$$\eta = 1 - \frac{\tau_{\text{with dye}}}{\tau_{\text{no dye}}} \quad (2)$$

For all samples, the RET efficiencies were calculated from both the short and long lifetime components for both the green and red bands (Fig. 7 and Table S2†).

For RET efficiencies based on the short decay component of the green band (Fig. 7A), the same trends as for spectral measurements were observed (Fig. 5). Indeed, the RET efficiency improved on increasing the dye quantity and decreasing the UCNP size. However, spectral measurements show higher RET efficiency values for UCNPs with a large quantity of dyes. This can be attributed to light reabsorption (inner filter effects), and non-reliability of the red band as an internal reference in spectral measurements, as the lifetime data indicate that the red band is also affected by the RET-induced quenching of the green band.

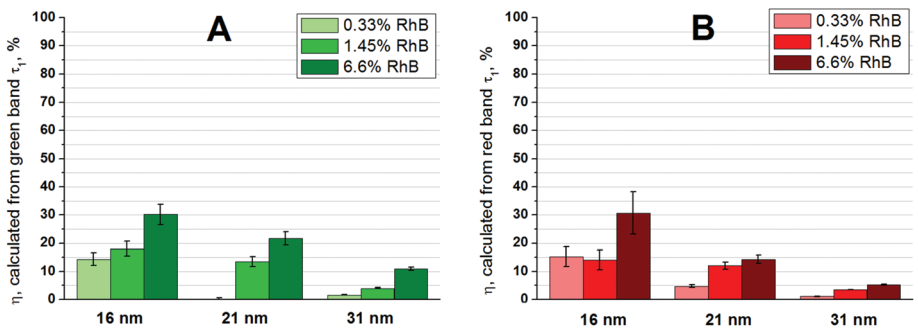

Fig. 7 RET efficiencies, as calculated from UCNP–PMA–RhB decay lifetimes. The RET efficiencies were calculated from eqn (2), using either the short component of the green band (A) or the short component of the red band (B).

In the case of the red band, the short decay component (Fig. 7B) shows a trend similar to the one observed for the green band, indicating that the red band is also affected by the RET-induced quenching of the green band. One can attribute this effect to the red-emissive state being populated partially by non-radiative processes occurring from the green-emissive states, $^2H_{11/2}$ and $^4S_{3/2}$ (Fig. S1†). However, this is thought to occur with a low probability,[41,42] and therefore, the drop in this lifetime component cannot be explained only by the green to red population mechanism. We hypothesize that indirect, higher-order effects may be in play, such as faster depopulation of the green-emissive states reducing the probability of Er^{3+} cross-relaxation with subsequent upconversion to red-emissive states.

Calculating RET from long decay components does not yield any consistent trends (Table S2†).

In the last step, the dye fluorescence upon excitation at 980 nm was investigated. As expected, the dye fluorescence decay is extremely long and roughly follows the UCNP emission decay, as under these conditions, the dye can be excited by RET or reabsorption from UCNPs (Fig. 8). Interestingly, the dye decay is faster than the decay of the green-band emission of UCNPs. Normally one would expect the same decay rate, due to the nearly instantaneous emission of the acceptor after energy transfer or reabsorption. This effect might be explained by considering the division of emitter ions into two populations differing by their distance to the surface, the core emitter ions and the shell emitter ions. The RET-induced dye emission mainly occurs by dye excitation from the shell emitter ions, as only these ones are close enough to the RhB dyes to perform efficient RET. These ions, being quenched by the dyes and other surface quenching effects, should have faster decay rates compared to the core emitter ions. As the dye mirrors the decay of these shell emitter ions, this explains that the dye decay is faster than the overall decay of the green luminescence band of the UCNPs. Quantitative measurements of this effect will require finding a good protocol for removing dyed polymer micelles from solution without inducing UCNP aggregation, and are left as a subject for future work.

Monte Carlo modeling of RET in RhB-grafted UCNPs

The obtained experimental data on the RET behavior of UCNPs allowed us to develop a theoretical model, using the extension of basic Förster theory for multiple donor–multiple acceptor systems *via* a modification of a Monte Carlo algorithm proposed by Corry *et al.*[32] We first modelled the UCNPs as a collection of point donors simulating the Er^{3+} emitter ions with a uniform random distribution inside a sphere. The RhB dyes are simulated by a collection of point acceptors, with a uniform random distribution on the surface of a slightly larger sphere, taking into account the width of the oleic acid-PMA layer on the particle surface, assuming that the dyes are hidden in the hydrophobic layer instead of being exposed to water, due to their hydrophobic nature (Fig. 9).

For calculating the probability of RET events, a table of coefficients for each donor–acceptor pair of the modeled UCNP is built, with each coefficient being equal to the ratio of R_0^6 (Förster radius) to r^6, where r is the donor–acceptor distance. The transfer of energy from Er^{3+} to RhB is assumed to conform to Förster theory, proceeding through dipole–dipole interactions, with R_0 being calculated using eqn (3). The dipole orientation factor, κ^2, is assumed to be equal to 2/3 (isotropic dynamic regime). This assumption is valid because the local reorientation of organic dyes in hydrophobic layers is much faster than the luminescence lifetimes of lanthanide ions.[43] The refractive index of the environment, n, is assumed to be isotropic and equal to 1.48.[44]

An important distinction from regular calculations of the Förster radius is the fact that the donor quantum yield in the absence of an acceptor, Φ_D, does not correspond to the total quantum yield of upconversion in UCNPs. The reason for this is that upconversion is a sequential process with several intermediate states, while FRET occurs only from the final state of

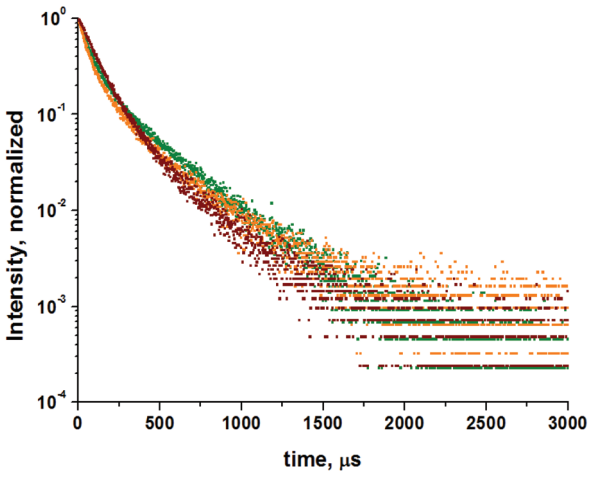

Fig. 8 Comparison of the luminescence decays of the green and red bands with the RhB emission decay for the UCNP–PMA–RhB sample **M2**. Green: green UCNP band. Orange: dye band. Red: red UCNP band.

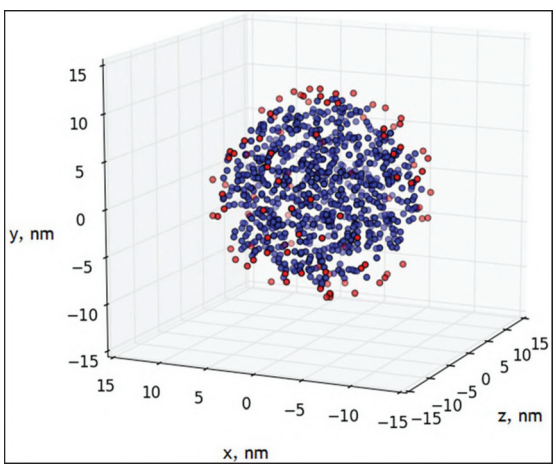

Fig. 9 UCNP–PMA–RhB modeled as an ensemble of point donors ($Er^{3\pm}$ ions, blue points) and point acceptors (RhB dyes, red points).

the system with emitter ions in highly excited states, here the $^2H_{11/2}$ and $^4S_{3/2}$ states of Er^{3+}. As a result, in the context of FRET, the appropriate value of the luminescence quantum yield for the donor, in this case the emitter ion, should be the ratio of its radiative rate constant to the sum of all relaxation constants from the states involved in FRET, also known as the emitter radiative branching ratio (eqn (4)). The exact value of the branching ratio for UCNPs is not given in the literature, but lower and upper bounds can be set. The lower bound value (0.1%) corresponds to the total upconversion quantum yield on the green emission band measured experimentally[45] for 21 nm $NaYF_4$:20%Yb,2%Er UCNPs. The upper bound value (9%) corresponds to the radiative branching ratio for the bulk material, which can be calculated from the literature data.[41]

$$R_0{}^6 = \frac{9000 \ln 10 \Phi_D \kappa^2}{128\pi^5 N n^4} \int_0^\infty f_D(\lambda)\varepsilon_A(\lambda)\lambda^4 d\lambda \quad (3)$$

$$\Phi_D = \frac{k_{\text{rad. green},Er^{3+}}}{k_{\text{rad. green},Er^{3+}} + \sum_{\text{non-rad. green},Er^{3+}}^{k}} \quad (4)$$

To perform the simulation, a sequence of excitation events was generated, the events being uniformly distributed over the total time of simulation and equally likely to occur for each Er^{3+} ion. Each excitation event corresponds to a full process of upconversion from Yb^{3+} ions in the ground state to Er^{3+} in an excited state, ready to emit. The quantity of events depends on the size of the particle, dopant concentration, laser power density, absorption cross-section of Yb^{3+} ions, quantum yield of upconversion and radiative branching ratio of excited Er^{3+}. We assume that a given particle uniformly absorbs light through all its volume. Its total absorption coefficient is thus dependent on the quantity of Yb^{3+} ions. The transfer of excitation energy to Er^{3+} ions is assumed to occur uniformly throughout the particle. This is a reasonable assumption, as Yb^{3+}–Yb^{3+} excitation transfer inside the particle is known to be much faster than the excited state lifetime of Er^{3+} ions.[46] We treat the upconversion process as a "black box" process from the absorption of IR light up to obtaining Er^{3+} in the excited state. This upconversion process is assumed to exhibit an efficiency that is equal to the total green-band upconversion quantum yield of 0.1% measured for non-modified UCNPs of the same composition and size,[45] divided by the green-band radiative branching ratio.

The simulation is performed using the excitation event schedule and sequentially marking donors as "excited". These excited donors are then allowed to emit after a randomly chosen period of time that is dependent on the lifetime of the donor and the energy transfer efficiencies to the acceptors that are not excited at that moment of time. In case the donor is already excited when it receives an excitation event, the event is dismissed as "lost". This allows simulation of the saturation effects in the system and the possible competition between donors to deliver their energy to the same acceptor. A random decision for whether the donor emits by itself or performs RET to an acceptor is made, with probabilities weighted depending on acceptor coefficients for this donor. Finally, after the simulation is finished, the total quantity of RET events is divided by the total quantity of all emissive events, which gives the effective RET efficiency for the system under steady-state conditions (eqn (5)).

$$\eta = \frac{N_{\text{FRET events}}}{N_{\text{FRET events}} + N_{\text{rad. events}}} \quad (5)$$

Because each UCNP has a different geometry of donor ions and acceptor dyes, the effective RET efficiency will be slightly different for each simulated particle. To obtain an average value and to see how much the RET efficiency will differ because of the system geometry, we repeated the simulation multiple times. This emulates the RET behavior of a population of particles, simulating what is observed in spectral and lifetime experiments.

Simulation results and comparison with experimental data

Fig. 10 sums up the results of the Monte Carlo calculations of the RET efficiency for all samples. Three sets of calculations with different Er^{3+} radiative branching ratios were performed. We select branching ratios of (i) 0.1%, a lower limit corresponding to nearly 100% efficient Yb^{3+}–Er^{3+} RET processes, (ii) 9%, an upper limit, corresponding to the branching ratio in the bulk material, and (iii) 1%, a value in between the two previous values.

As expected, the RET efficiency increases with the branching ratio, due to the increase in the Förster radius. Even though the Förster radius is proportional to the sixth root of the radiative branching ratio $\left(\sqrt[6]{\Phi_D}\right)$ and therefore increases only by a factor of 1.44 when the branching ratio increases by a factor of 9, this is enough to increase the RET efficiency by a factor of two or more. This can be explained by the small particle size and the cumulative RET to a large number of dyes. For instance, even if the RET efficiency of a single dye–emitter ion pair is only 1% for an emitter ion in the center of a 21 nm particle, the combined RET to 100 dyes at the surface becomes as large as 63%.

To compare the simulation values with the experimental data, we selected the data with the lower bound branching ratio. Fig. 11 compares the simulation and experimental RET efficiency values for all UCNP–PMA–RhB samples. Overall, we found rather good agreement between the simulation and experimental data, suggesting that the simulation and the assumptions we made are reasonable. The proposed model can thus be used as a tool to predict the RET efficiency of UCNP/dye systems. It can also serve as an indirect method for the determination of the radiative branching ratio, by adjusting this parameter in the model until the model fits the experimental data.

Further improvement of this model to obtain a better match with the experimental data will require to include indirect emitter–emitter transfer. Würth *et al.* experimentally measured the Er^{3+} radiative branching ratio,[40] heterogeneities in the Er^{3+} emitter behavior, and a more detailed modeling of the upconversion process itself.

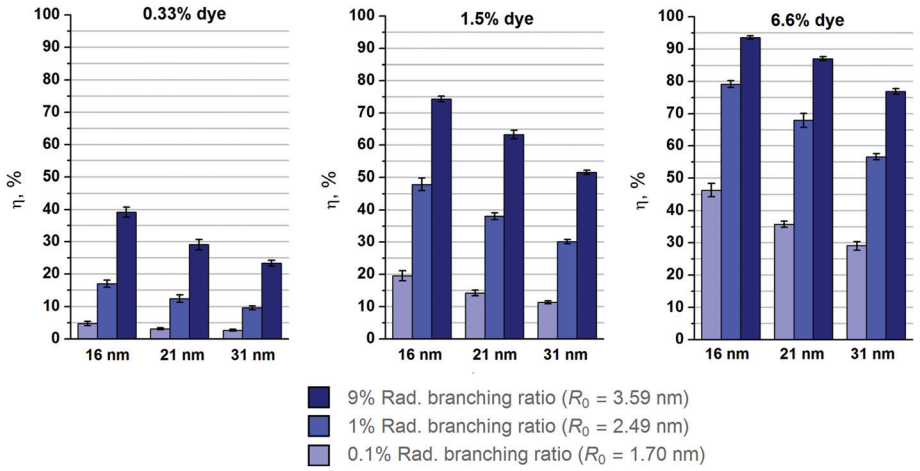

Fig. 10 RET efficiency values obtained by Monte Carlo modeling of all UCNP–PMA–RhB samples, with different green-band radiative branching ratios for Er^{3+} ions (mean values and 1 standard deviation).

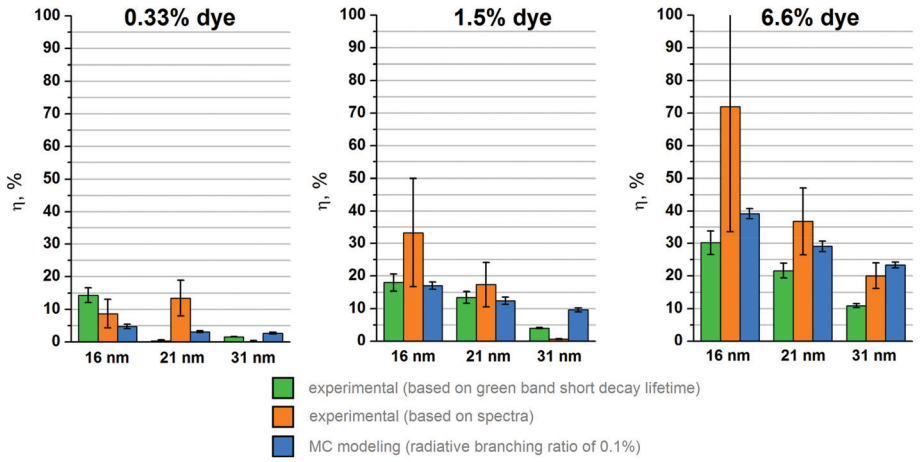

Fig. 11 Comparison of experimental and theoretical RET efficiency values for all samples.

Conclusions

We have performed spectral and lifetime-based measurements, as well as Monte Carlo simulations, to determine the energy transfer efficiency in a set of water soluble UCNPs decorated with organic dyes, mimicking RET-based sensors.

Our results underline the importance of carefully considering the complex behavior of UCNP–organic dyes systems before attributing the spectral/lifetime changes purely to energy transfer events. We showed that the red band of UCNPs with Er^{3+} as an emitter ion is not a reliable internal reference for calculating the energy transfer efficiency based on the changes in the spectra. However, this observation does not invalidate the use of UCNP/dye systems for sensing applications based on the changes in the green/red ratios. Indeed, these systems are usually calibrated to correlate the green/red ratios with known analyte concentrations. The consequence of the indirect quenching of the red band by RET is that any change in the UCNP/dye system or measurement conditions will require to perform a new calibration curve.

Moreover, we found that the luminescence decays of UCNPs decorated with dyes consist at least of two components that showed different behavior on RET. As a result, simplified calculations using the FRET relationships for single donor–single acceptor systems may not provide the exact RET efficiency values. An additional difficulty stems from the dependence of UCNP luminescence lifetimes on the excitation intensity.

The model developed in this study provides a framework for quantitative prediction of the behavior of RET systems based on UCNPs, and is validated by comparison with experimental data. This model is flexible and can be applied to other system geometries. For example, the popular approach used to increase the brightness of RET systems is the use of core–shell UCNPs, which have an optimal shell thickness value – enough to increase particle brightness by reducing solvent/coating quenching effects, but not enough to severely reduce RET to

acceptors on their surface. Experimentally searching the optimal balance between parameters like the UCNP size, core and shell compositions, shell thickness, and choice and quantity of acceptors is a tedious and time-consuming task, which can be considerably sped up by employing computational models to predict the optimal parameter set. As more data on the parameters of the upconversion process become known, the model described herein can be improved to account for processes that have been neglected. The model will be useful in the future design of UCNP-based systems, including sensors, imaging probes and photodynamic therapy agents.

Experimental section

Materials and synthesis

Reagents and solvents were bought from Sigma-Aldrich and used without further purification. UCNPs were synthesized as previously described.[34] The synthesis of the PMA polymer used to coat the UCNPs and the synthesis of Rhodamine-NH_2, the Rhodamine B derivative used to decorate the UCNPs are described in the ESI.†

XRD patterns

The XRD patterns were recorded on a Huber Guinier G670 diffractometer (http://www.xhuber.de) with a Cu-Kα source (λ = 1.54060 Å).

DLS measurements

The DLS measurements were performed to characterize the size of the coated and dye-loaded UCNPs. DLS measurements were performed in Brand plastic cuvettes (lot #759015) on a Malvern Zetasizer instrument. Correlation curves for each sample were accumulated 3 times. Treatment parameters are normal resolution and size distribution by volume.

TEM images

The TEM images were acquired using a 120 kV Philips CM12 microscope on carbon coated copper grids and were analysed using ImageJ and Origin.

Luminescence spectrometry

Luminescence spectrometry for UCNP solutions was performed in quartz cuvettes. Excitation at 980 nm was provided by a continuous-wave laser coupled to a single mode fiber with a maximum output of 350 mW (Qphotonics, QFBGLD-980-350). Excitation light was focused in the cuvette using a lens of 100 mm focal distance. Excitation power inside the cuvette was calculated to be 8 kW cm^{-2}. The emission was collected using a fiber spectrometer (Avaspec ULS3648). The scattered/reemitted laser light was removed using a low pass filter (Semrock, E700SP). The scheme of the setup is provided in Fig. S20.†

Time-resolved luminescence measurements

Lifetime measurements of UCNPs shared the same excitation path as the spectral measurements but the output power of the laser diode was controlled by an external analog modulation generated by a National Instruments multifunction board (PCIe 6361). During lifetime measurements, the laser output power followed a 250 Hz square wave waveform with a 30% duty cycle. The emission was collected using a monochromator (Jobin Yvon HC10IR). The single-photon events were detected using an avalanche photodiode (Excelitas SPCM-AQRH-16) and recorded on a time-correlated single photon counting board SPC-830 (Becker-Hickl GmbH).

Monte Carlo simulation algorithm

The algorithm is based on the algorithm described by Corry *et al.*[32] It was adapted to dye-loaded UCNPs. The algorithm works with the following steps:

1. Generate coordinates in three dimensions for point donors (emitter ions) and point acceptors (organic dyes). Construct the matrix of RET transfer probability coefficients for each pair of donors and acceptors. Calculate the number of excitation events during the simulation (dependent on the excitation power, size of the nanoparticle, concentration and absorption cross-section of sensitizer ions, quantum yield of upconversion). Uniformly randomly position excitation events at the timescale of simulation, assign a target donor to each event, and arrange them chronologically. Initialize counters for radiative emission events and RET events.

2. Move to the next excitation event. Flag any donors that should have emitted by the time of the event as "non-excited". If the current target donor is flagged as "non-excited", change it to "excited", otherwise reject this event and move to the next one. Calculate the apparent lifetime of the donor using the transfer probability coefficients for each non-excited acceptor. Assign a random relaxation time to the donor, weighted to an exponential decay distribution.

3. The donor can relax non-radiatively, radiatively, or transfer its excitation to one of the non-excited acceptors. Using the transfer probability coefficients, roll a weighted random number to determine the outcome of the situation, and increase the respective event counter. If the situation results in RET, roll another weighted random number to choose which of the available acceptors will receive the excitation. Flag this acceptor as "excited" and assign a random relaxation time to this acceptor, weighted to an exponential decay distribution.

4. Repeat steps 2 and 3 until the excitation event schedule is exhausted.

5. The total number of events when the acceptor successfully received excitation is divided by the total number of emissive events, resulting in total RET efficiency.

6. Steps 1–5 are repeated several times, to obtain RET efficiency for different possible geometries of the system, and an average RET efficiency for the system is calculated.

The algorithm was implemented in Python 3.4.3. The simulations were performed with parameters gathered from the literature[45,47] or determined experimentally.

Conflicts of interest

There are no conflicts of interest to declare.

Acknowledgements

This work was supported by the ANR-11-LABX-0058-NIE within the Investissement d'Avenir program ANR-10-IDEX-0002-02 and COST CM 1403 "The European upconversion network". O. Dukhno was supported by an Eiffel fellowship (Campus France) and a fellowship from the French Ministère de la Recherche.

References

1 Y. I. Park, K. T. Lee, Y. D. Suh and T. Hyeon, *Chem. Soc. Rev.*, 2015, **44**, 1302–1317.
2 C. Wang, X. Li and F. Zhang, *Analyst*, 2016, **141**, 3601–3620.
3 B. Zhou, B. Shi, D. Jin and X. Liu, *Nat. Nanotechnol.*, 2015, **10**, 924–936.
4 G. Chen, H. Qiu, P. N. Prasad and X. Chen, *Chem. Rev.*, 2014, **114**, 5161–5214.
5 M. Haase and H. Schäfer, *Angew. Chem., Int. Ed.*, 2011, **50**, 5808–5829.
6 N. Menyuk, K. Dwight and J. W. Pierce, *Appl. Phys. Lett.*, 1972, **21**, 159–161.
7 X. Zhu, J. Zhou, M. Chen, M. Shi, W. Feng and F. Li, *Biomaterials*, 2012, **33**, 4618–4627.
8 F. C. J. M. van Veggel, C. Dong, N. J. J. Johnson and J. Pichaandi, *Nanoscale*, 2012, **4**, 7309–7321.
9 G. K. Das, N. J. J. Johnson, J. Cramen, B. Blasiak, P. Latta, B. Tomanek and F. C. J. M. van Veggel, *J. Phys. Chem. Lett.*, 2012, **3**, 524–529.
10 P. Zhang, S. Rogelj, K. Nguyen and D. Wheeler, *J. Am. Chem. Soc.*, 2006, **128**, 12410–12411.
11 L. Wang, R. Yan, Z. Huo, L. Wang, J. Zeng, J. Bao, X. Wang, Q. Peng and Y. Li, *Angew. Chem., Int. Ed.*, 2005, **44**, 6054–6057.
12 T. Rantanen, M.-L. Järvenpää, J. Vuojola, R. Arppe, K. Kuningas and T. Soukka, *Analyst*, 2009, **134**, 1713–1716.
13 S. Lahtinen, Q. Wang and T. Soukka, *Anal. Chem.*, 2016, **88**, 653–658.
14 R. Wei, Z. Wei, L. Sun, J. Z. Zhang, J. Liu, X. Ge and L. Shi, *ACS Appl. Mater. Interfaces*, 2016, **8**, 400–410.
15 S. Xu, B. Dong, D. Zhou, Z. Yin, S. Cui, W. Xu, B. Chen and H. Song, *Sci. Rep.*, 2016, **6**, 23406.
16 E.-J. Jo, H. Mun and M.-G. Kim, *Anal. Chem.*, 2016, **88**, 2742–2746.
17 B. Yan, J.-C. Boyer, N. R. Branda and Y. Zhao, *J. Am. Chem. Soc.*, 2011, **133**, 19714–19717.
18 J. Liu, W. Bu, L. Pan and J. Shi, *Angew. Chem., Int. Ed.*, 2013, **52**, 4375–4379.
19 H. Wang, R. Han, L. Yang, J. Shi, Z. Liu, Y. Hu, Y. Wang, S. Liu and Y. Gan, *ACS Appl. Mater. Interfaces*, 2016, **8**, 4416–4423.
20 H. Liu, Y. Fu, Y. Li, Z. Ren, X. Li, G. Han and C. Mao, *Langmuir*, 2016, **32**, 9083–9090.
21 Y. Wang, L. Tu, J. Zhao, Y. Sun, X. Kong and H. Zhang, *J. Phys. Chem. C*, 2009, **113**, 7164–7169.
22 S. Fischer, B. Fröhlich, K. W. Krämer and J. C. Goldschmidt, *J. Phys. Chem. C*, 2014, **118**, 30106–30114.
23 D. J. Gargas, E. M. Chan, A. D. Ostrowski, S. Aloni, M. V. P. Altoe, E. S. Barnard, B. Sanii, J. J. Urban, D. J. Milliron, B. E. Cohen and P. J. Schuck, *Nat. Nanotechnol.*, 2014, **9**, 300–305.
24 A. D. Ostrowski, E. M. Chan, D. J. Gargas, E. M. Katz, G. Han, P. J. Schuck, D. J. Milliron and B. E. Cohen, *ACS Nano*, 2012, **6**, 2686–2692.
25 T. Rantanen, H. Päkkilä, L. Jämsen, K. Kuningas, T. Ukonaho, T. Lövgren and T. Soukka, *Anal. Chem.*, 2007, **79**, 6312–6318.
26 F. Vetrone, R. Naccache, C. G. Morgan and J. A. Capobianco, *Nanoscale*, 2010, **2**, 1185–1189.
27 L. Cheng, K. Yang, M. Shao, S.-T. Lee and Z. Liu, *J. Phys. Chem. C*, 2011, **115**, 2686–2692.
28 Y. Ding, F. Wu, Y. Zhang, X. Liu, E. M. L. D. de Jong, T. Gregorkiewicz, X. Hong, Y. Liu, M. C. G. Aalders, W. J. Buma and H. Zhang, *J. Phys. Chem. Lett.*, 2015, **6**, 2518–2523.
29 V. Muhr, C. Würth, M. Kraft, M. Buchner, A. J. Baeumner, U. Resch-Genger and T. Hirsch, *Anal. Chem.*, 2017, **89**, 4868–4874.
30 W. Shao, G. Chen, A. Kuzmin, H. L. Kutscher, A. Pliss, T. Y. Ohulchanskyy and P. N. Prasad, *J. Am. Chem. Soc.*, 2016, **138**, 16192–16195.
31 C. Drees, A. N. Raj, R. Kurre, K. B. Busch, M. Haase and J. Piehler, *Angew. Chem., Int. Ed.*, 2016, **55**, 11668–11672.
32 B. Corry, D. Jayatilaka and P. Rigby, *Biophys. J.*, 2005, **89**, 3822–3836.
33 J. A. Damasco, G. Chen, W. Shao, H. Ågren, H. Huang, W. Song, J. F. Lovell and P. N. Prasad, *ACS Appl. Mater. Interfaces*, 2014, **6**, 13884–13893.
34 S. Wilhelm, M. Kaiser, C. Würth, J. Heiland, C. Carrillo-Carrion, V. Muhr, O. S. Wolfbeis, W. J. Parak, U. Resch-Genger and T. Hirsch, *Nanoscale*, 2015, **7**, 1403–1410.
35 A. Sedlmeier and H. H. Gorris, *Chem. Soc. Rev.*, 2015, **44**, 1526–1560.
36 J. Ni, C. Shan, B. Li, L. Zhang, H. Ma, Y. Luo and H. Song, *Chem. Commun.*, 2015, **51**, 14054–14056.
37 L. Mattsson, K. D. Wegner, N. Hildebrandt and T. Soukka, *RSC Adv.*, 2015, **5**, 13270–13277.
38 J. Peng, W. Xu, C. L. Teoh, S. Han, B. Kim, A. Samanta, J. C. Er, L. Wang, L. Yuan, X. Liu and Y.-T. Chang, *J. Am. Chem. Soc.*, 2015, **137**, 2336–2342.
39 J.-C. Brochon, *Methods Enzymol.*, 1994, **240**, 262–311.

40 C. Würth, M. Kaiser, S. Wilhelm, B. Grauel, T. Hirsch and U. Resch-Genger, *Nanoscale*, 2017, **9**, 4283–4294.
41 R. B. Anderson, S. J. Smith, P. S. May and M. T. Berry, *J. Phys. Chem. Lett.*, 2014, **5**, 36–42.
42 E. M. Chan, E. S. Levy and B. E. Cohen, *Adv. Mater.*, 2015, **27**, 5753–5761.
43 *Principles of Fluorescence Spectroscopy*, ed. J. R. Lakowicz, Springer, US, 2006, pp. 353–382.
44 A. Shalav, B. S. Richards, T. Trupke, K. W. Krämer and H. U. Güdel, *Appl. Phys. Lett.*, 2005, **86**, 13505.
45 J.-C. Boyer and F. C. J. M. van Veggel, *Nanoscale*, 2010, **2**, 1417–1419.
46 L. Tu, X. Liu, F. Wu and H. Zhang, *Chem. Soc. Rev.*, 2015, **44**, 1331–1345.
47 L. D. DeLoach, S. A. Payne, L. L. Chase, L. K. Smith, W. L. Kway and W. F. Krupke, *IEEE J. Quantum Electron.*, 1993, **29**, 1179–1191.

Supporting information for "Quantitative assessment of energy transfer in upconverting nanoparticles grafted with organic dyes"

Oleksii Dukhno [1], Frédéric Przybilla [1], Mayeul Collot [1], Andrey Klymchenko [1], Vasyl Pivovarenko [2], Markus Buchner [3], Verena Muhr [3], Thomas Hirsch [3], and Yves Mély [1*]*

1) Laboratory of Biophotonics and Pharmacology, UMR 7213 CNRS, University of Strasbourg, 67000 Strasbourg, France
2) Faculty of Chemistry, National Taras Shevchenko University of Kyiv, 01033 Kyiv, Ukraine
3) Institute of Analytical Chemistry, Chemo- and Biosensors, University of Regensburg, 93040 Regensburg, Germany

Contents:

1. Scheme of UCNP upconversion mechanism

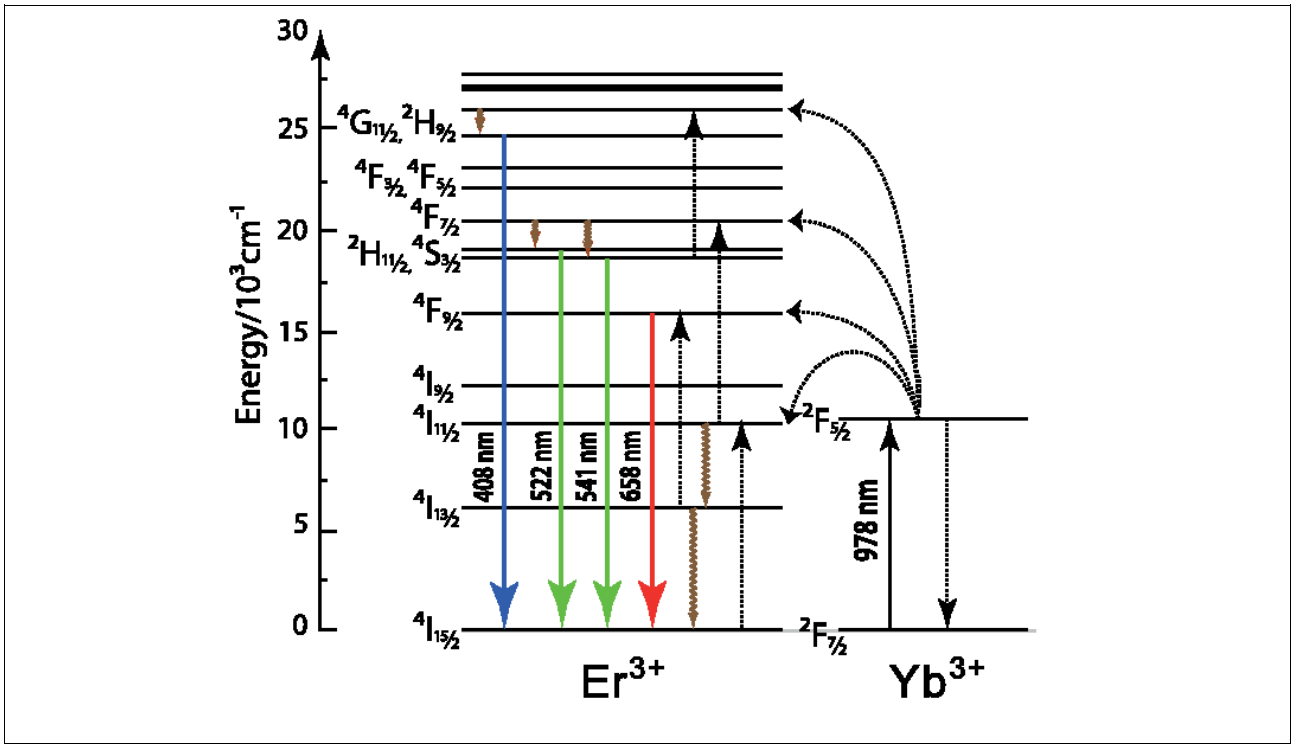

Fig. S1. Simplified upconversion mechanism in Yb-Er UCNPs. Reprinted from Haase and Schafer, 2015.[1]

2. XRD data for raw UCNPs

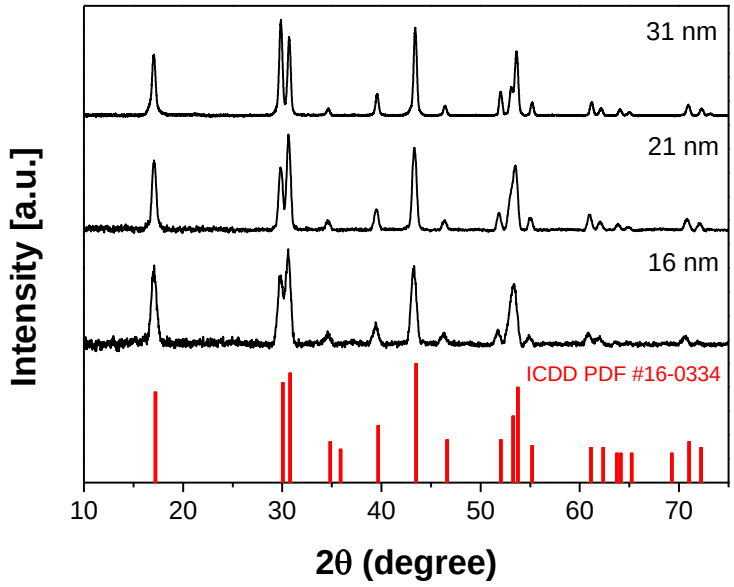

Fig. S2: X-ray diffraction patterns of $NaYF_4$ (20% Yb, 2% Er, 0-20% Gd) nanocrystals with decreasing size from 31 nm to 16 nm (top to bottom) and the corresponding standard pattern of hexagonal phase $NaYF_4$ (red, ICDD PDF #16-0334).

3. Synthesis and spectra of Rhodamine-NH_2

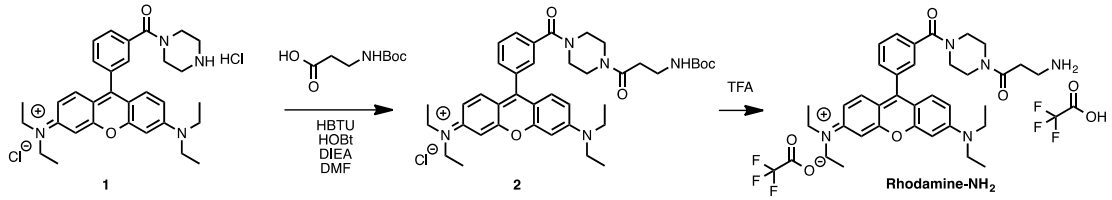

Fig. S3. Scheme of synthesis of Rhodamine-NH_2.

1 was synthesized according to a reported procedure. [2]

Synthesis of **2.** To a solution of **1** (210 mg, 0.360 mmol) in DMF (5 mL) was added N-boc-β-Alanine (72 mg, 0.360 mmol, 1 eq), HOBt (58 mg, 0.360 mmol, 1 eq) and HBTU (145 mg, 0.360 mmol, 1 eq). The solution was stirred under argon and DIEA (188 µL, 1.080 mmol, 3 eq) was added. The mixture was allowed to stir overnight under argon. The solvents were evaporated and the product was extracted with DCM, then washed with water before being dried over $MgSO_4$. The solution was filtered and evaporated. The crude was purified by column chromatography on silica gel (DCM/MeOH : 94/6) to give 250 mg of **2** as dark pink foam (yield= 96%). Rf=0.42 (DCM/MeOH : 96/4). ^{1}H-NMR (400 MHz, $CDCl_3$): 7.60 (m, 2H, H Ar), 7.46 (m, 1H, H Ar),7.24-7.13 (m, 3H, H Ar), 6.95-6.80 (m, 2H, H Ar), 6.72-6.66 (m, 2H, H Ar), 5.20 (m, 1H, NH), 3.59-3.49 (m, 8H, 4 CH_2),3.40-3.25 (m, 10H, 5 CH_2), 2.46 (m, 2H, CH_2), 1.34-1.21 (m, 21H, CH_3 Boc, 4 CH_3). ^{13}C-NMR (100 MHz, $CDCl_3$): 170.7 (CO), 170.3 (CO), 167.7 (CO), 162.5 (C Ar), 157.6 (C Ar), 155.8 (C Ar), 155.6 (C Ar), 135.0 (C Ar), 131.9 (C Ar), 130.9 (C Ar), 130.2 (C Ar), 130.0 (C Ar), 127.4 (C Ar), 114.3 (C Ar), 114.0 (C Ar), 113.7 (C Ar), 96.4, 46.0 (CH_2 Et), 45.1-44.8 (multiple peaks), 41.6-40.8 (multiple peaks), 38.5, 36.4-36.2, 33.3, 31.3, 28.4 (CH_3 Boc), 12.5 (CH_3 Et). HRMS (ES^+), calcd for $C_{40}H_{52}N_5O_5$ $[M]^+$ 682.3963, found 682.3960.

Synthesis of **Rhodamine-NH_2**. To a solution of **2** (250 mg, 0.348 mmol) in DCM (5 mL) was added TFA (4 mL), the solution was sonicated for 20 s and the solvents were evaporated. The crude was then dissolved in a minimum of DCM and the solution was poured in stirring Et_2O. The solution was filtered to obtain 195 mg of Rhodamine-NH_2 as a deep red solid (yield = 69%). Rf=0.15 (DCM/MeOH : 95/5). The purity was checked by ^{1}H-NMR and LC-HRMS. ^{1}H-NMR (400 MHz, DMSO-d6): 7.76-7.72 (m, 6H, H Ar, NH_3^+), 7.54 (s, 1H, H Ar), 7.18-7.10 (m, 4H, H Ar), 6.96 (s, 2H, H Ar), 3.66 (q, 8H, CH_2 Et), 3.39 (m, 12H, CH_2 pip, CH_2 β-ala), 1,24 (t, 12H, CH_3 Et). HRMS (ES^+), calcd for $C_{35}H_{44}N_5O_3$ $[M+H]^+$ 582.3439, found 582.3434.

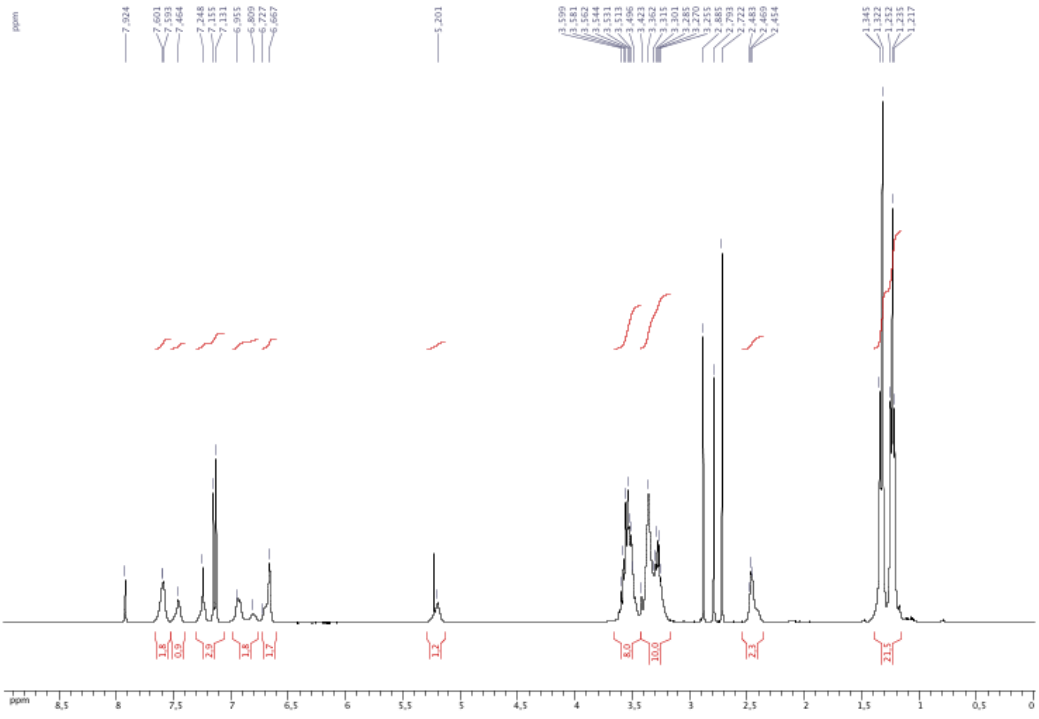

*Fig. S4. ^{1}H NMR spectrum of **2** ($CDCl_3$)*

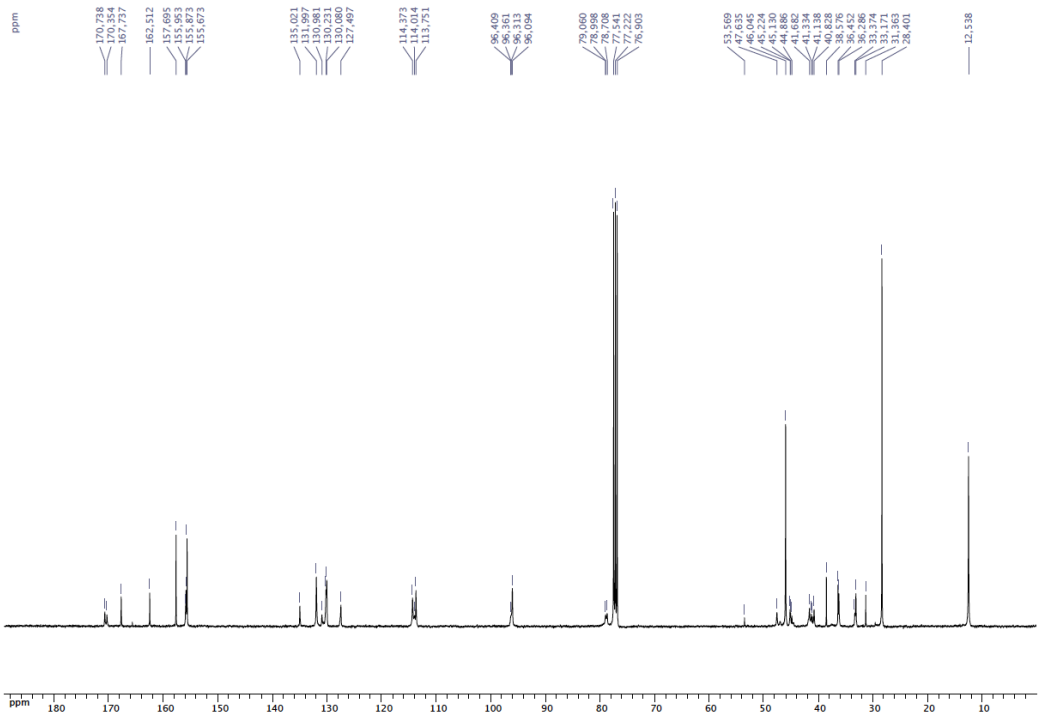

*Fig. S5. ^{13}C NMR spectrum of **2** ($CDCl_3$)*

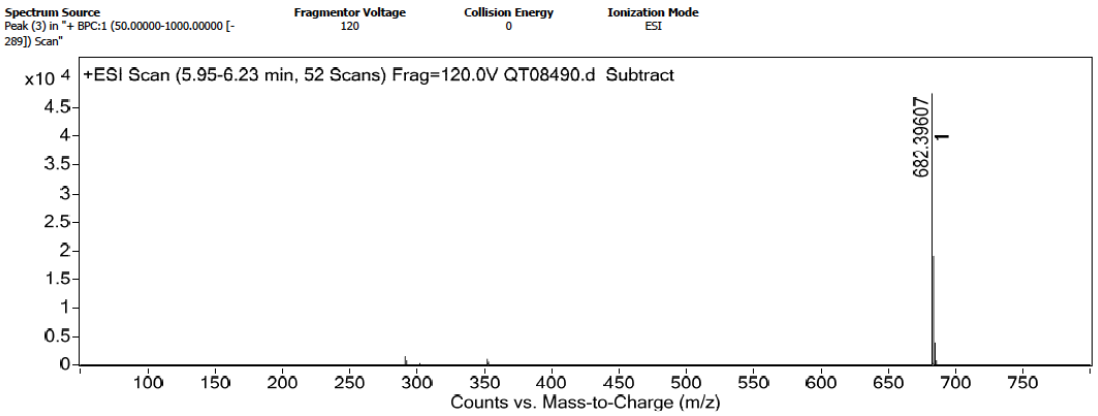

*Fig. S6. HRMS spectrum of **2***

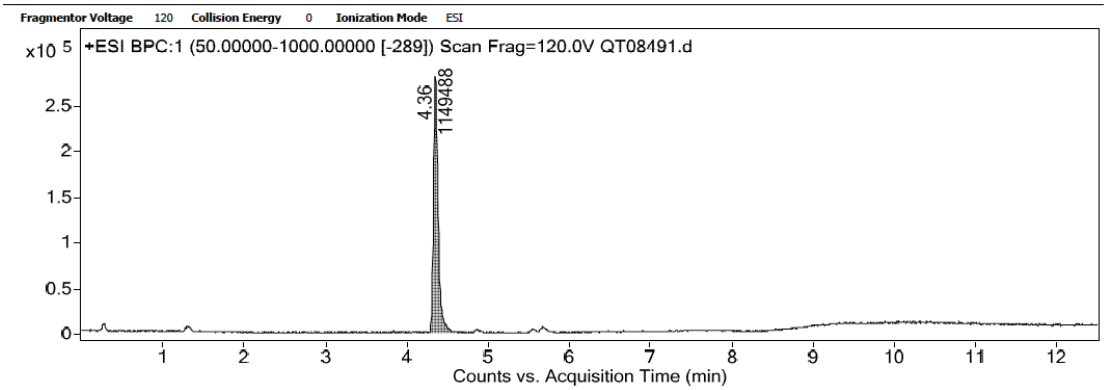

*Fig. S7. Chromatogram of **Rhodamine-NH$_2$** (ACN 0.1% formic acid / Water 0.1% formic acid ; C-18 column)*

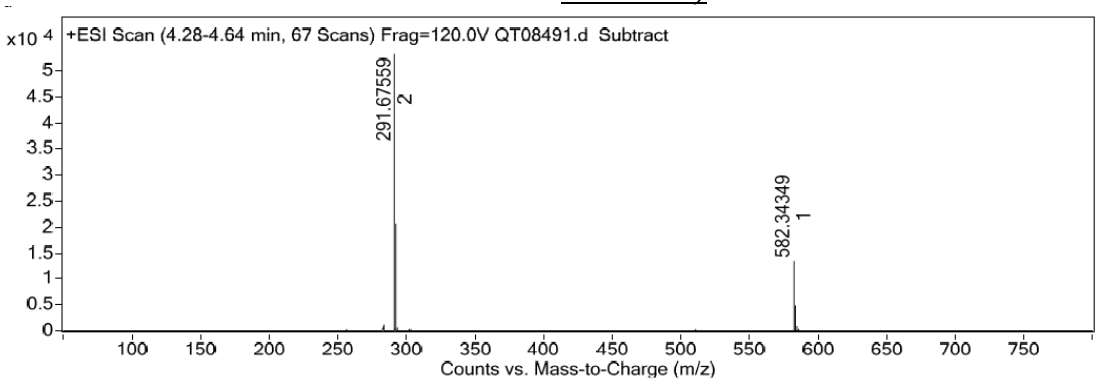

*Fig. S8. HRMS spectrum of **Rhodamine-NH$_2$***

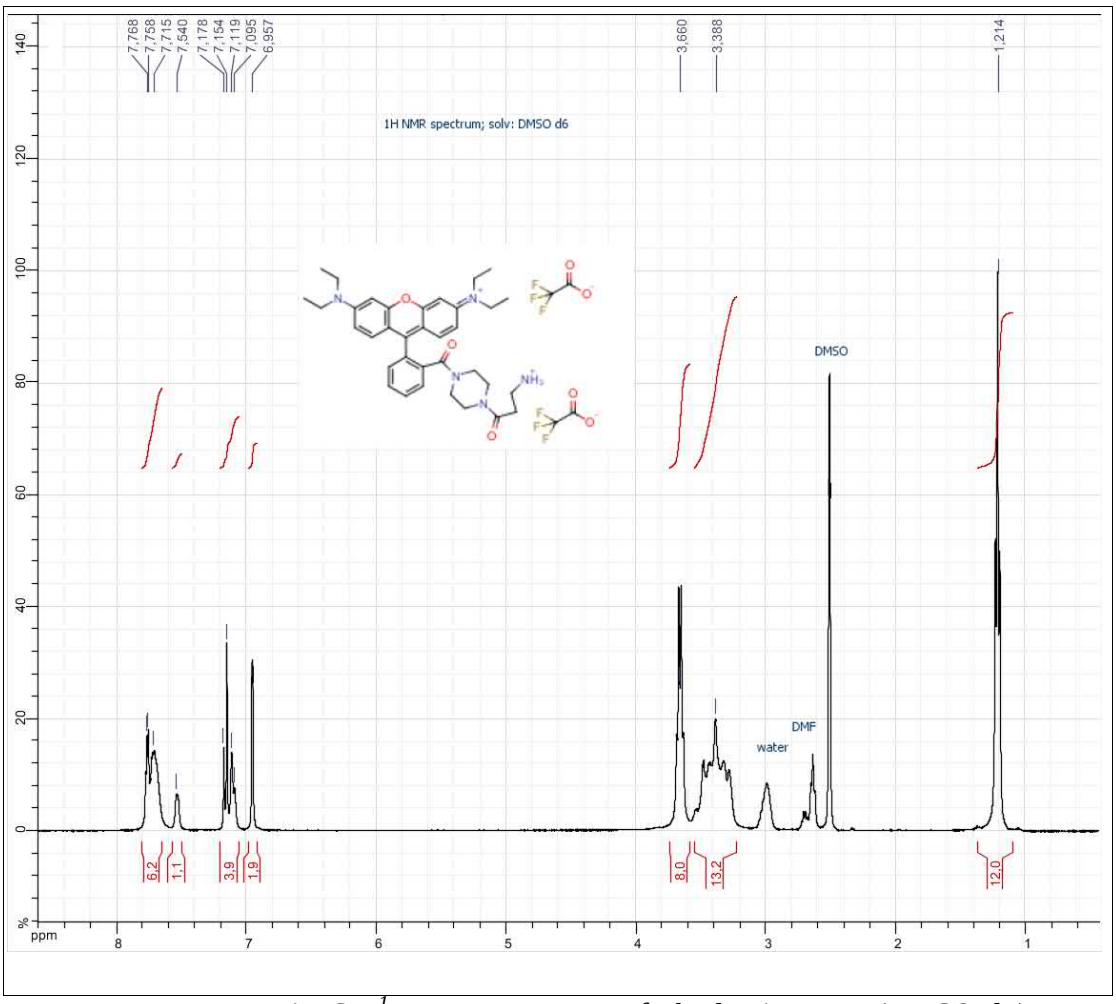

Fig. S9. ^{1}H NMR spectrum of Rhodamine-NH_2 (DMSO-d6)

4. Synthesis of the PMA amphiphilic polymer

In a 10 mL flask with a septum and flushed with argon, 18 mg dodecylamine (97 µmol, 0.75eq) were dissolved in 2 mL anhydrous DMF under magnetic stirring. Diisopropylethylamine (67 µL, 390 µmol, 3eq) was added. 1 mg of piperidyl-beta-alanine-coupled Rhodamine B (1.3 µmol, 0.01 eq) was added. The solution was allowed to stir for 10 min, then 20 mg of poly(isobutylene-alt-maleic anhydride) were added in one portion (130 µmol, 1 eq monomer, avg MW 6000). The vessel was purged with argon a second time, and the reaction mass was stirred at room temperature. After 30 min, a drop of water (approx. 100 eq) was added. The reaction mass was evaporated, redissolved in dichloromethane and purified on LH20 size-exclusion chromatography column (eluent: dichloromethane-methanol 1:1 v/v). Combined elutes were evaporated, and the residue was redissolved in 2.6 mL spectral grade chloroform, corresponding to a theoretical 0.05 M concentration (assuming quantitative yield). This solution was used as a stock for subsequent coating of UCNPs.

5. Polymer coating of UCNPs and calculation of dye quantity per particle

We used a modified version of the protocol from Wilhelm et al., 2015.[3] 0.33 mL of UCNPs with 20.6 nm diameter (5 mg/mL) in cyclohexane were mixed with 0.42 mL 0.05 M PMA solution, sonicated for 1 min at room temperature, and evaporated. The residue was dissolved in 0.75 mL spectral grade chloroform and sonicated for 1 min at room temperature. Then, 1 mL 0.01 M NaOH were added. The mixture was vortexed for 30 s and slowly evaporated on rotavap (high speed of rotation and low vacuum are recommended to avoid bumping), until only aqueous phase remained. Obtained phase was filtered through a Millex GP syringe filter (0.22 µm pore size). The filter was

washed once with 1 mL 0.01 M NaOH. Obtained filtrates were combined.

The quantity of polymer stock solution required for the coating process was calculated using:

$$V_{\text{polymersolution}} = \mathrm{R}_P \pi \frac{\omega_{\text{UCNP}}}{\rho \mathrm{V}_{\text{UCNP}}} d_{\text{eff}}^2 \frac{1}{c_{\text{polymer}}}$$

where R_p is the number of polymer, expressed in monomers, applied per nm^2 of UCNP surface (100 in case of UCNP coated with oleic acid, which is about 5 times in excess compared to the tight fatty chain packing on surface), ω_{UCNP} is the mass concentration of UCNPs (e.g. mg/mL), ρ is the density of UCNPs ($4.21 \cdot 10^{-21}$ g/nm^3), V is the volume of UCNP in nm^3, d_{eff} is the effective diameter of UCNP, which includes the thickness of the oleic acid layer (e.g. for a 20.6 nm diameter the effective diameter is 21.7 nm, because of two 0.55 nm thick layers of oleic acid).

The number of surface dyes per particle can be calculated by:

$$N = \pi(d+2l)^2 * C_{f.ch.} * P$$

where d is the diameter of the particle (nm), l is the thickness of the polymer-oleic acid layer (nm), $C_{f.ch.}$ is the number of fatty chains per nm^2 in the tightly packed monolayer, and P is the percentage of dyes per monomer.
The calculated number of dyes per particle is provided in following table (thickness of oleic acid layer assumed to be 1.1 nm, packing density of fatty chains in monolayer is assumed to be 5 nm^{-2}). It should be noted that this calculation represents the quantity of dyes bound specifically on the surface of UCNPs. Due to excess of polymer being used to ensure proper UCNP coating, some polymer micelles are formed in dispersion. Dyes in polymer micelles are not considered surface-bound to UCNPs and are not accounted for in the calculation.

	dye percentage per monomer			
particle diameter, nm	***quantity of surface-bound dyes per particle after coating process***			
	0%	**0.33%**	**1.5%**	**6.6%**
16	0	17	78	343
21	0	27	123	539
31	0	54	244	1075

	dye:Er^{3+} ratio			
particle diameter, nm	**0%**	**0.33%**	**1.5%**	**6.6%**
16	0	0.043	0.196	0.861
21	0	0.035	0.157	0.692
31	0	0.020	0.093	0.409

Table S1. Calculated dye quantities and dye-Er^{3+} ratios per particle.

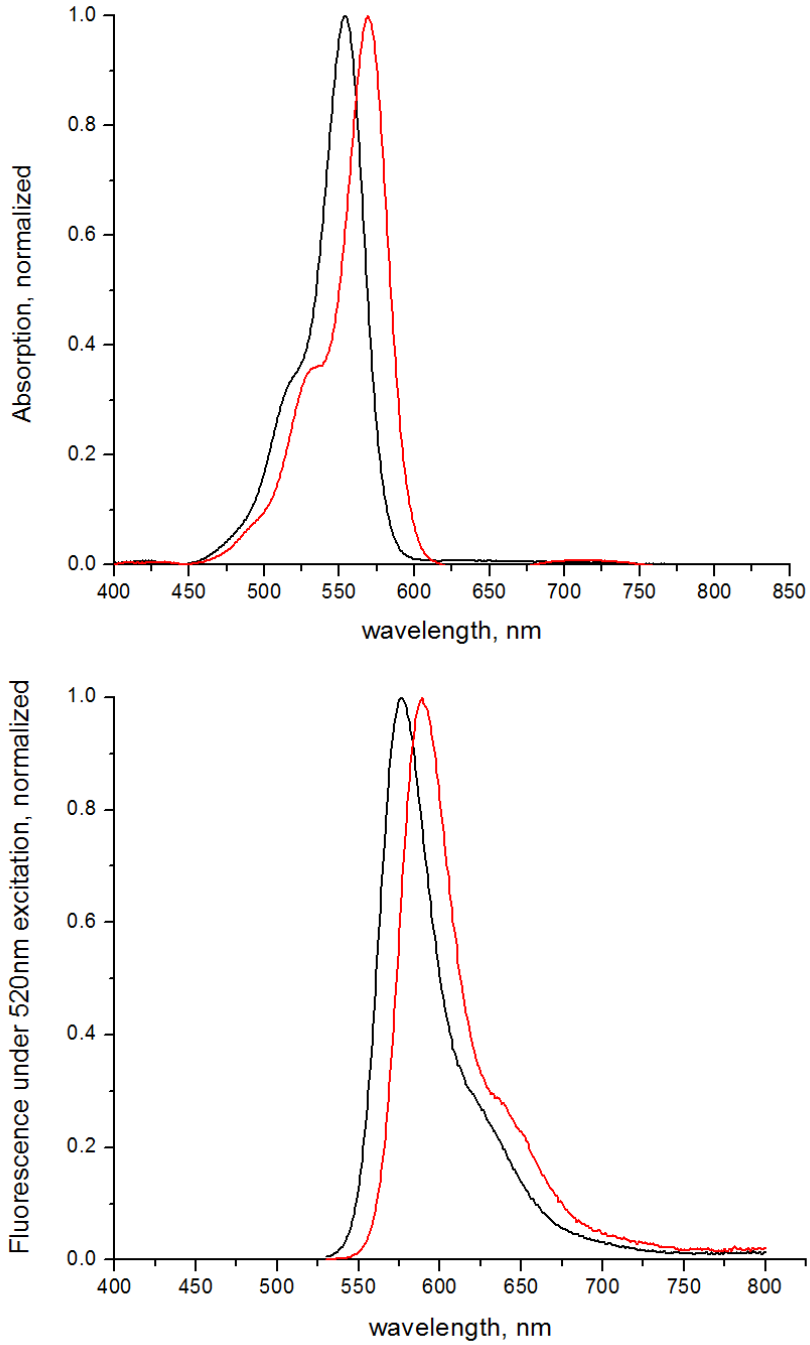

Fig. S10. Normalized absorption and emission spectra of Rhodamine B (black) and UCNP-PMA-RhB conjugates in water (red). Absorption spectra were measured on a Cary 4000 spectrometer. Fluorescence spectra were recorded with a 520 nm excitation wavelength on a Fluoromax-4 spectrofluorimeter.

6. Characterization of the UCNP-PMA-RhB by Dynamic Light Scattering (DLS)

Size distributions have been obtained by "volume" treatment of the correlation curves. This type of treatment was chosen due to overestimation of the percentage of larger particles by "intensity" treatment. All curves and polydispersity indexes (PdI) were calculated as an average of three consecutive measurements. Measurements were done at 298 K. Each curve in figures is an average of 3 measurements of 3 samples of one type. PdI values are given as a mean ± 1 standard deviation. Samples were diluted 10× in mQ water.

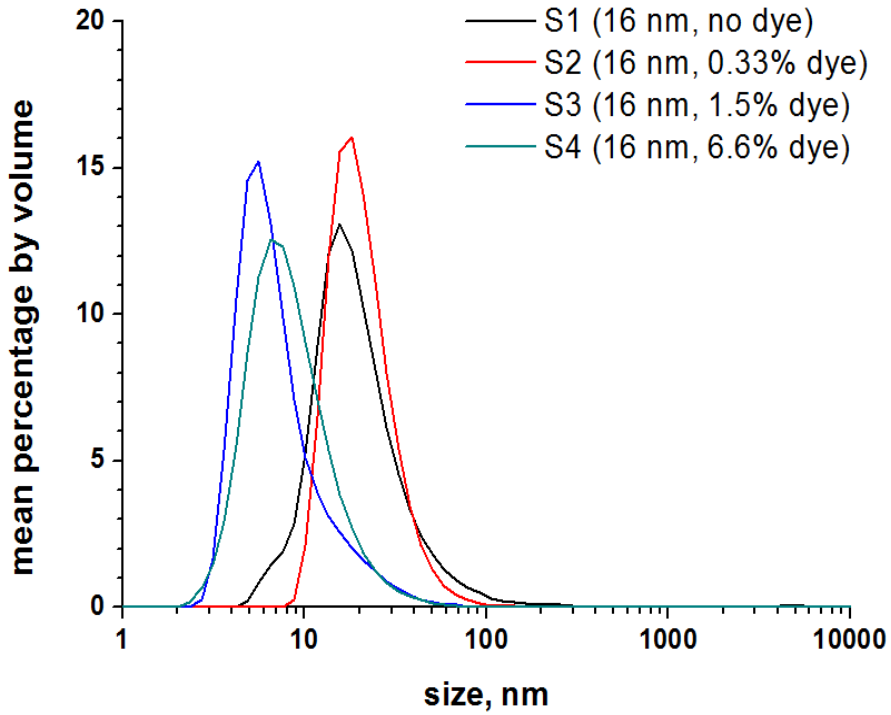

Fig. S11. Mean size distributions for samples S1-S4. PdI are 0.369±0.047, 0.341±0.020, 0.428±0.046, and 0.432±0.033, respectively.

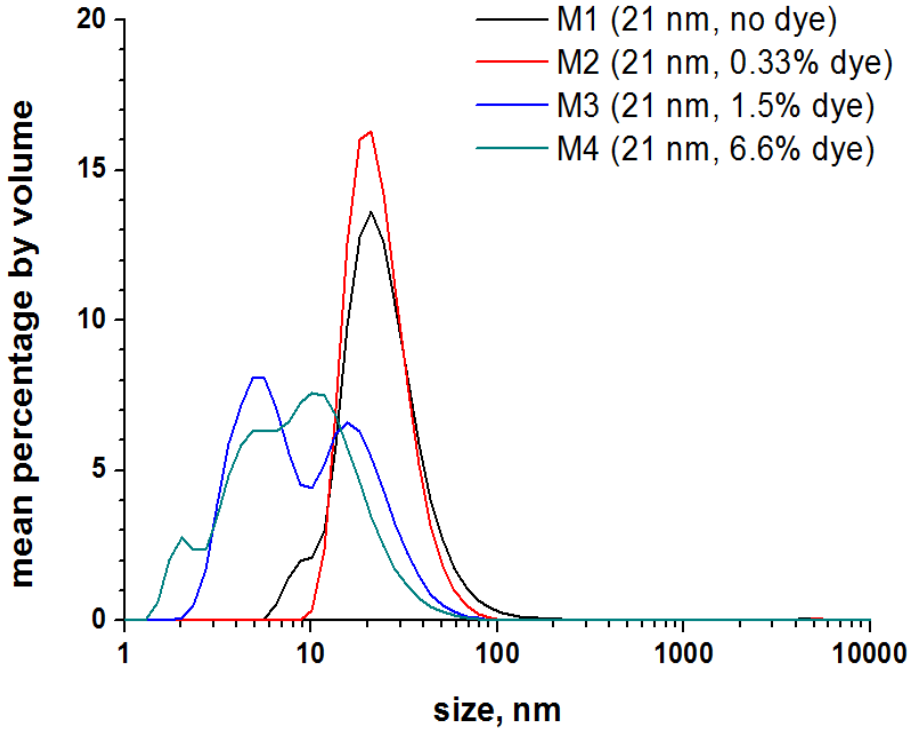

Fig. S12. Mean size distributions for samples M1-M4. PdI are 0.296±0.037, 0.191±0.021, 0.260±0.048, and 0.302±0.034, respectively.

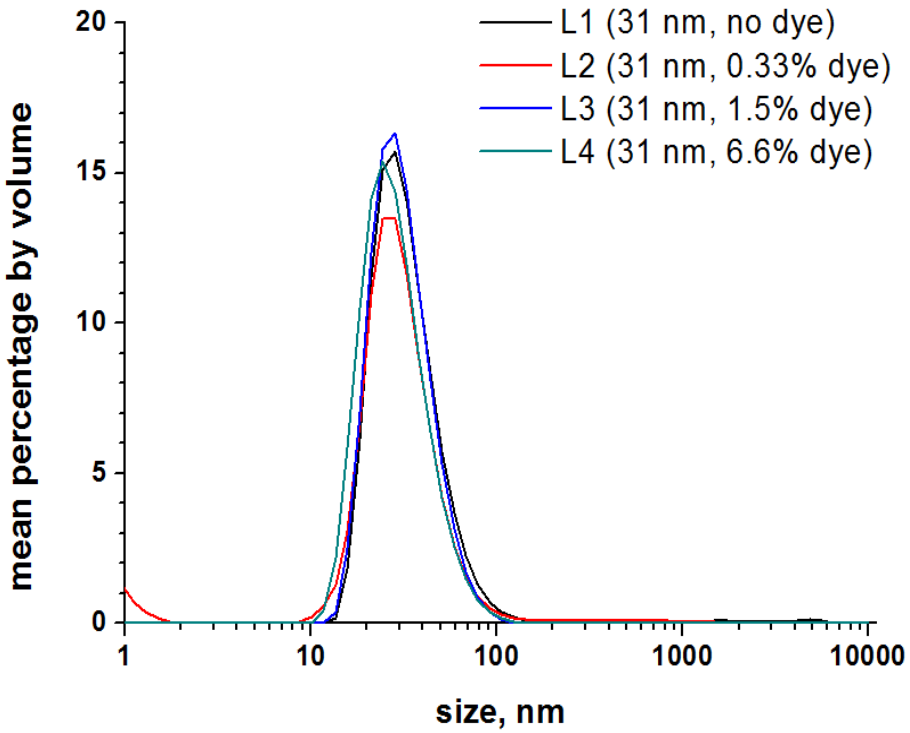

Fig. S13. Mean size distributions for samples L1-L4. PdI are 0.230±0.038, 0.199±0.088, 0.149±0.027, and 0.186±0.032, respectively.

7. Emission spectra of the dye-grafted UCNPs

All spectra were measured in samples diluted 10× in milliQ water, with continuous 980 nm excitation. The position of the beam inside the cuvette was chosen to be as close to the detector as possible, to mitigate any possible inner filter effects (see Figure S20 for details). Each spectrum represents an average of 480 spectra, each with signal accumulation of 5 s. After averaging, the spectra are smoothed (adjacent averaging, 5 points, corresponds to ~1nm spectral resolution), normalized by the intensity at 664 nm (to minimize dye crosstalk), and the bands are integrated to obtain the intensities used in equation 1 (510-565 nm for the green band and 655-680 nm for the red band).

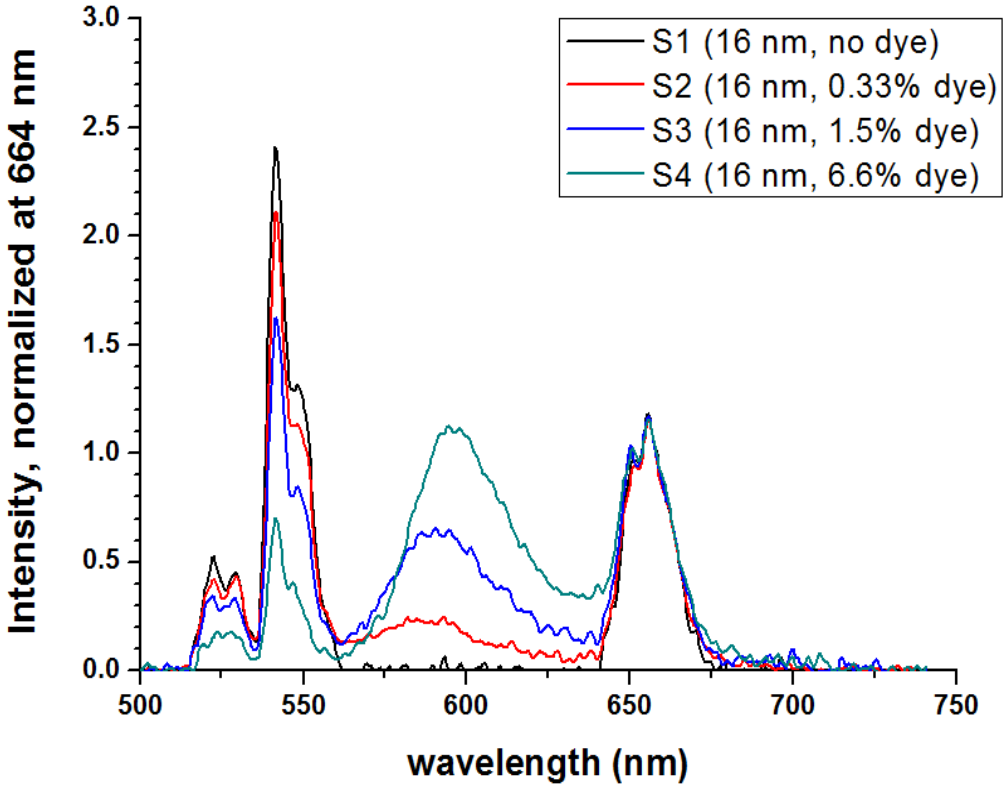

Fig. S14. Mean normalized luminescence spectra of samples S1-S4. Excitation wavelength 980 nm.

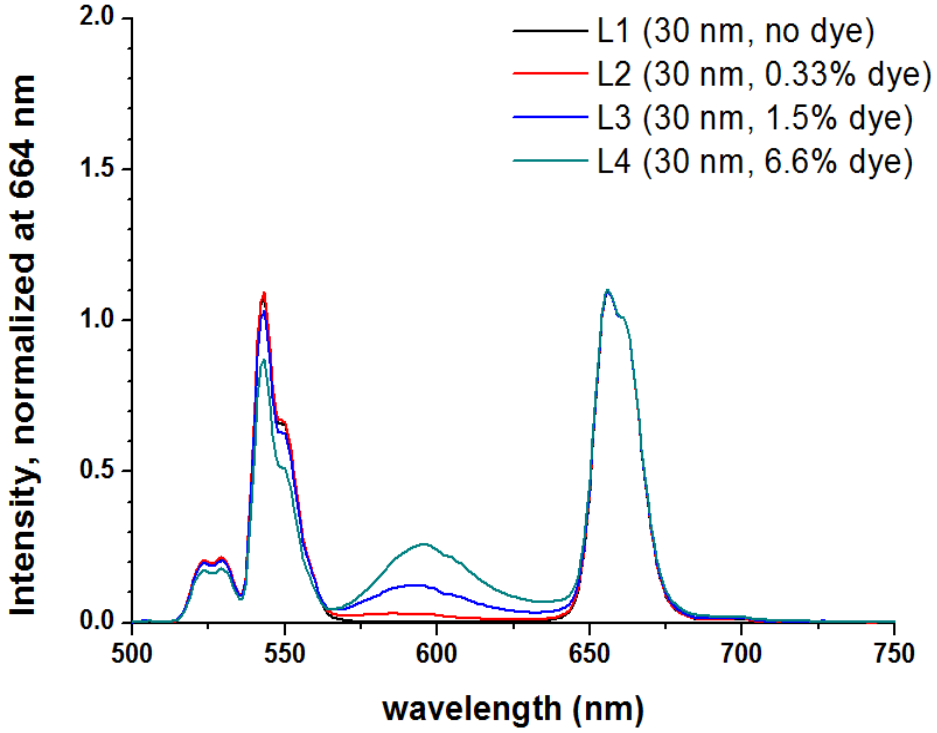

Fig. S15. Mean normalized luminescence spectra of samples L1-L4. Excitation wavelength 980 nm.

8. Emission decays of the dye-grafted UCNPs

All decays were collected to obtain total 2M photons per decay curve (including the truncated rising part). For each sample 5 curves have been collected and independently fitted. Values provided in the table are mean ± 1 standard deviation over 15 decays in total (5 curves x 3 sample repeats).

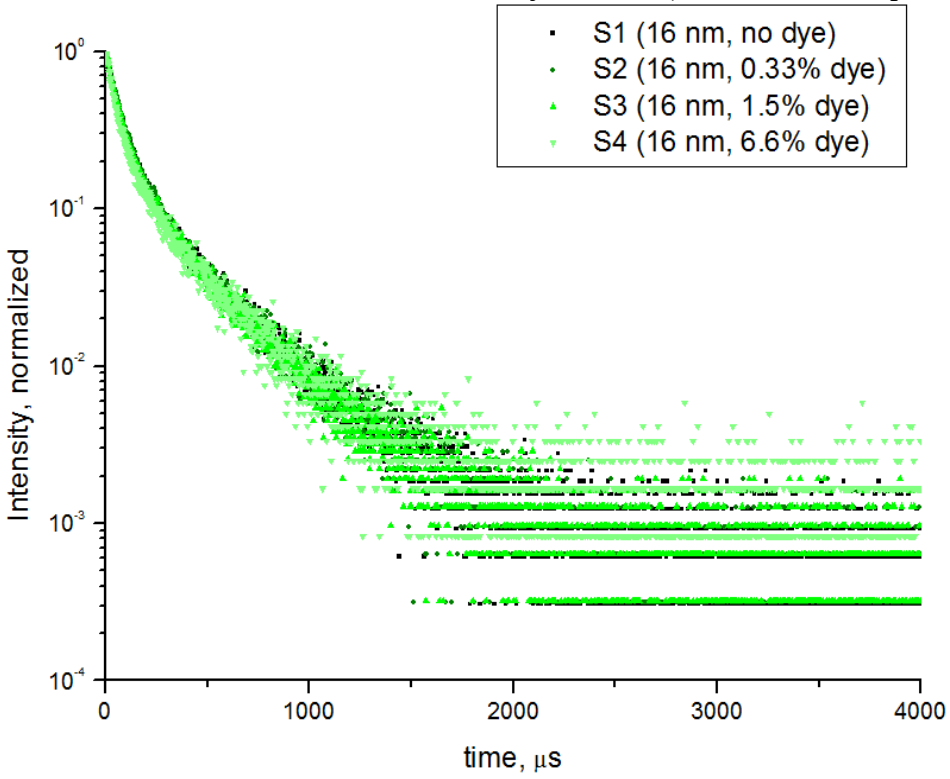

Fig. S16. Examples of normalized decay curves of one batch of samples S1-S4 at 542 nm emission. Excitation wavelength 980 nm.

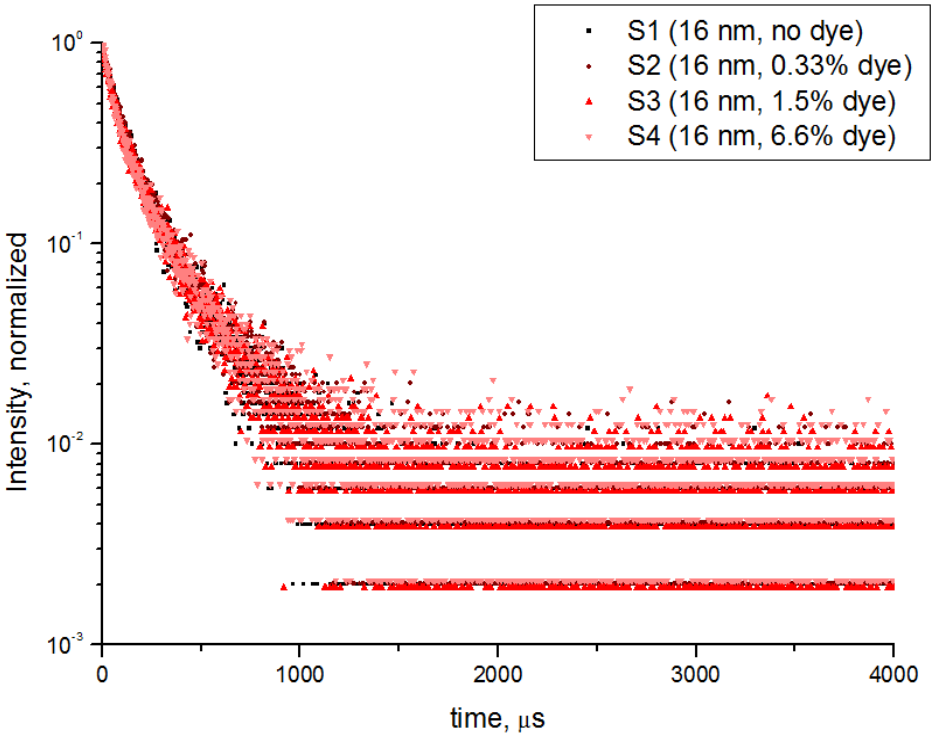

Fig. S17. Examples of normalized decay curves of one batch of samples S1-S4 at 542 nm emission. Excitation wavelength 980 nm.

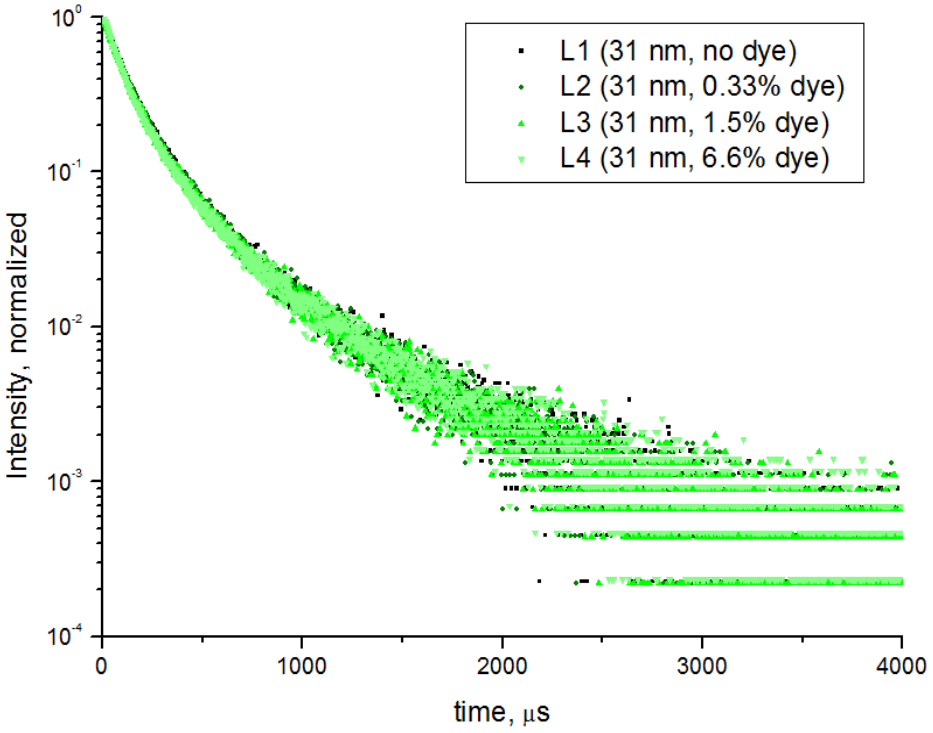

Fig. S18. Examples of normalized decay curves of one batch of samples L1-L4 at 542 nm emission. Excitation wavelength 980 nm.

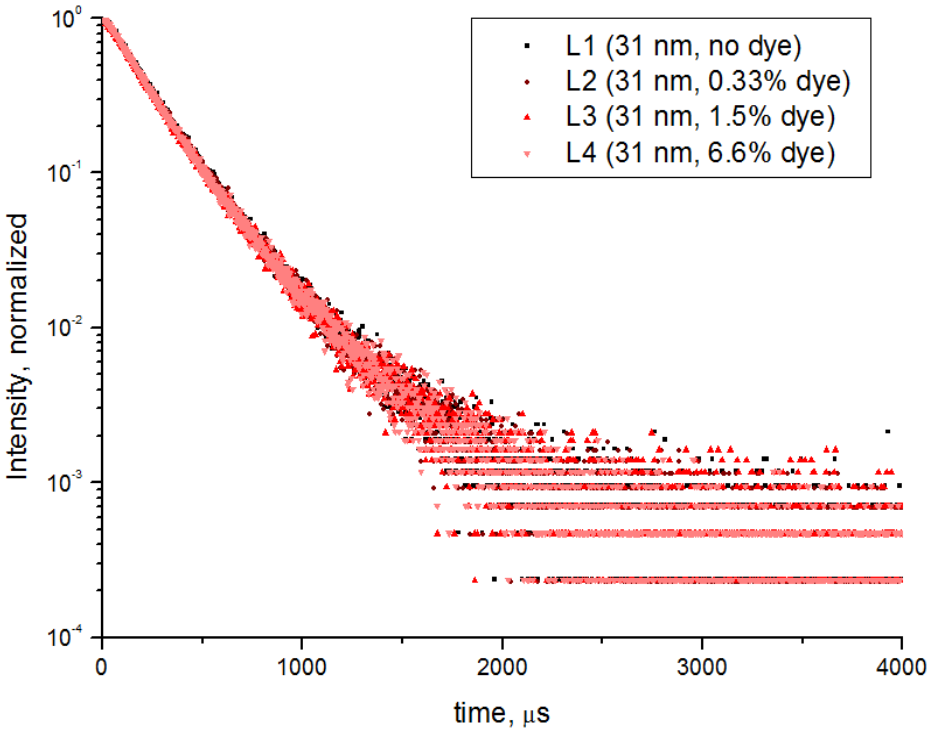

Fig. S19. Examples of normalized decay curves of one batch of samples L1-L4 at 662 nm emission. Excitation wavelength 980 nm.

16 nm diameter

	S1, 542nm	*S2, 542nm*	*S3, 542nm*	*S4, 542nm*
A1	0.68 ± 0.01	0.62 ± 0.08	0.65 ± 0.06	0.68 ± 0.05
t1	60 ± 6	51 ± 6	49 ± 5	42 ± 3
A2	0.20 ± 0.02	0.25 ± 0.06	0.22 ± 0.05	0.20 ± 0.04
t2	149 ± 8	122 ± 22	130 ± 29	134 ± 41
A3	0.12 ± 0.01	0.14 ± 0.03	0.13 ± 0.02	0.12 ± 0.04
t3	364 ± 35	331 ± 26	329 ± 30	348 ± 69
	S1, 662nm	*S2, 662nm*	*S3, 662nm*	*S4, 662nm*
A1	0.57 ± 0.10	0.53 ± 0.04	0.53 ± 0.05	0.57 ± 0.06
t1	76 ± 14	65 ± 9	66 ± 11	53 ± 9
A2	0.43 ± 0.10	0.47 ± 0.04	0.47 ± 0.05	0.43 ± 0.06
t2	236 ± 13	223 ± 15	228 ± 14	224 ± 11
spectral ratio	2.06 ± 0.49	1.88 ± 0.21	1.37 ± 0.15	0.58 ± 0.12

21 nm diameter

	M1, 542nm	*M2, 542nm*	*M3, 542nm*	*M4, 542nm*
A1	0.51 ± 0.08	0.55 ± 0.06	0.49 ± 0.06	0.59 ± 0.03
t1	58 ± 6	58 ± 4	50 ± 4	46 ± 2
A2	0.31 ± 0.08	0.26 ± 0.06	0.31 ± 0.06	0.24 ± 0.03
t2	127 ± 13	131 ± 12	114 ± 10	123 ± 7
A3	0.18 ± 0.01	0.19 ± 0.01	0.20 ± 0.01	0.18 ± 0.01
t3	345 ± 6	329 ± 9	321 ± 6	332 ± 11
	M1, 662nm	*M2, 662nm*	*M3, 662nm*	*M4, 662nm*
A1	0.87 ± 0.02	0.86 ± 0.03	0.85 ± 0.03	0.88 ± 0.02
t1	108 ± 4	103 ± 8	95 ± 7	92 ± 8
A2	0.13 ± 0.02	0.14 ± 0.03	0.15 ± 0.03	0.12 ± 0.03
t2	302 ± 16	297 ± 24	278 ± 23	297 ± 24
spectral ratio	2.35 ± 0.16	2.04 ± 0.63	1.95 ± 0.57	1.49 ± 0.15

30 nm diameter

	L1, 542nm	*L2, 542nm*	*L3, 542nm*	*L4, 542nm*
A1	0.56 ± 0.03	0.56 ± 0.03	0.58 ± 0.03	0.61 ± 0.03
t1	86 ± 4	85 ± 4	83 ± 3	77 ± 3
A2	0.37 ± 0.03	0.37 ± 0.02	0.35 ± 0.03	0.33 ± 0.02
t2	195 ± 9	192 ± 11	193 ± 10	195 ± 10
A3	0.07 ± 0.01	0.07 ± 0.01	0.07 ± 0.01	0.07 ± 0.01
t3	551 ± 19	543 ± 26	539 ± 21	549 ± 15
	L1, 662nm	*L2, 662nm*	*L3, 662nm*	*L4, 662nm*
A1	0.91 ± 0.01	0.91 ± 0.01	0.88 ± 0.02	0.87 ± 0.02
t1	198 ± 5	196 ± 9	191 ± 5	188 ± 6
A2	0.09 ± 0.01	0.09 ± 0.01	0.12 ± 0.02	0.13 ± 0.02
t2	398 ± 19	396 ± 23	371 ± 14	369 ± 16
spectral ratio	1.10 ± 0.03	1.12 ± 0.07	1.09 ± 0.03	0.88 ± 0.07

Table S2. Bi- and triexponential decay fit parameters for all samples. Decay lifetimes are given in μs. Preexponential parameters are unitless. All values are given as a mean ± 1 standard deviation. The choice of the number of components was determined by maximum entropy method. All samples were measured diluted 10x in milliQ water, with 8 kW/cm2 continuous-wave 980 nm excitation.

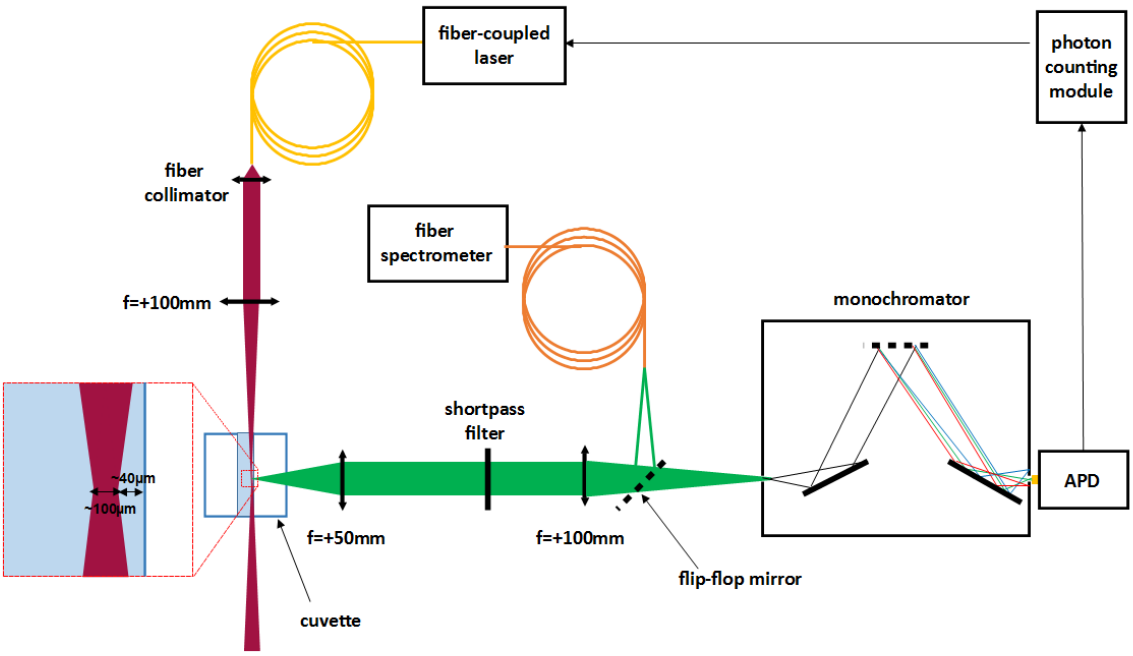

Fig. S20. Setup scheme.

9. References.

(1) Haase, M.; Schäfer, H. Upconverting Nanoparticles. *Angew. Chem. Int. Ed.* **2011**, *50*, 5808–5829., 5808–5829.

(2) Nguyen, T.; Francis, M. B. Practical Synthetic Route to Functionalized Rhodamine Dyes. *Org. Lett.* **2003**, *5*, 3245–3248.

(3) Wilhelm, S.; Kaiser, M.; Würth, C.; Heiland, J.; Carrillo-Carrion, C.; Muhr, V.; Wolfbeis, O. S.; Parak, W. J.; Resch-Genger, U.; Hirsch, T. Water Dispersible Upconverting Nanoparticles: Effects of Surface Modification on Their Luminescence and Colloidal Stability. *Nanoscale* **2015**, *7*, 1403–1410.

Part 3. Refining single-particle microscopy with UCNPs.

For imaging individual UCNPs, we used wide-field microscopy as a main tool. To observe the individual particles, we needed to immobilize them for imaging. The common approach we used involved drying a diluted nanoparticle dispersion. However, as UCNPs exhibit quenching and changes in relative band intensity upon contact with water (*Arppe et al., 2015*), we had to immobilize UCNPs on a surface to observe them in their "native" experimental environment, i.e. keeping aqueous conditions. For this, we chose electrostatic immobilization through depositing a layer of branched polyethyleneimine (PEI) on the glass surface (Fig. 2.3.1). In aqueous buffers at pH values up to ~10, PEI is positively charged, and thus attaches electrostatically to the glass surface, which itself is negatively charged due to silanol group dissociation at pH values of ~2 and above. PEI-coated glass surface is positively charged, thus attracting negatively charged UCNPs coated in amphiphilic polymer. By controlling the concentration of the particle dispersion, the quantity of UCNPs on surface could be modulated. Compared to drying, this approach also has an advantage of avoiding drying-induced aggregation of particles, that results in uneven coating, via what is colloquially known as "coffee stain effect" (*Deegan et al., 1997*).

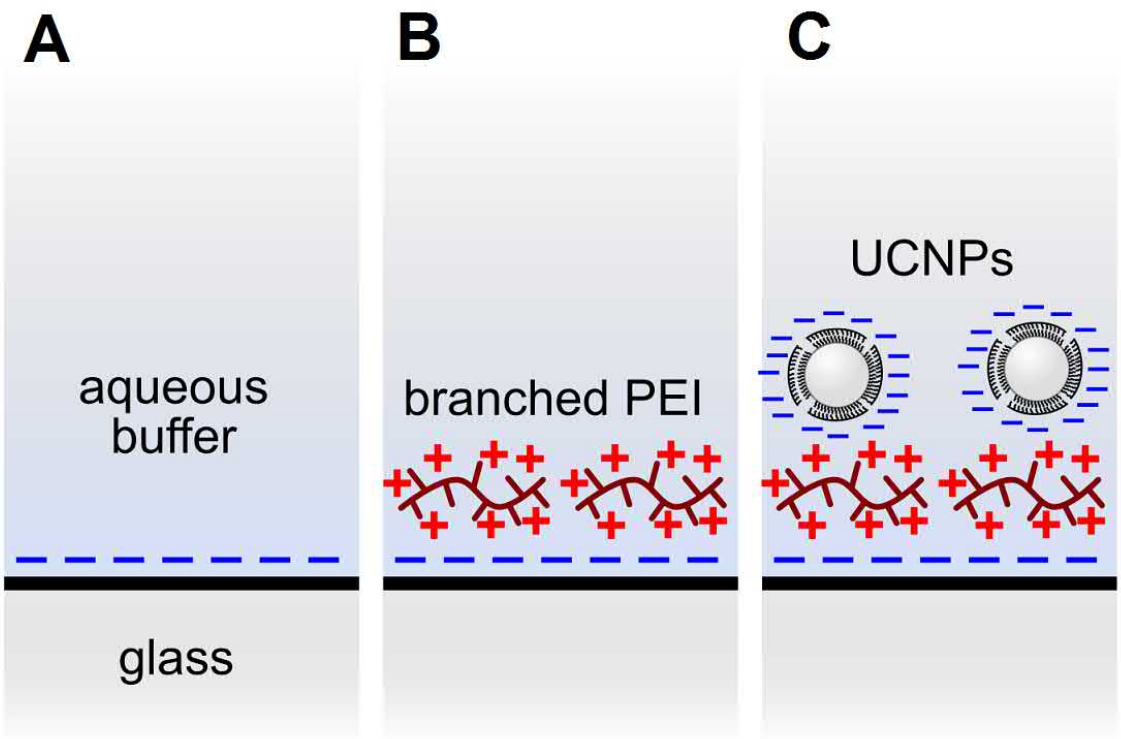

Fig. 2.2.1. Immobilization of UCNPs for wide-field imaging in aqueous conditions.

After depositing UCNPs on glass-polymer surface, we rinsed the surface with an aqueous buffer to increase imaging SNR by removing the freely diffusing particles that increase the background due to out-of-focus luminescence. Our initial experiments used deionized water for this aim. Unexpectedly, we noticed an unusual effect: several minutes after deposition, some particles vanished, and within an hour, most of the particles were absent. We initially attributed this effect to the particles detaching from the surface. However, upon continuous examination of the particles, we observed that all particles lost their luminescence gradually over time, in contrast to the stepwise luminescence loss anticipated for nanoparticle detachment.

Turning towards literature, we noticed several reports in the last years that described gradual luminescence loss in diluted UCNP dispersions due to slow particle dissolution in aqueous buffers (*Lahtinen et al., 2017; Lisjak et al., 2016, 2015; Plohl et al., 2017b, 2017a; Wang et al., 2012*). This phenomenon could potentially have very direct consequences for

UCNP imaging, as imaging is typically done in very diluted UCNP dispersions, in which the dissolution is exacerbated.

However, at that time, there were no reports on the estimation of this effect on a single-particle level. For SMM, keeping the luminophore response stable over time is critical for obtaining sufficient amount of reliable information from the experiment. Moreover, if the particles exhibited heterogeneous loss of luminescence, distinguishing individual particles from oligomers based on their intensity could be problematic. Other potential issues could arise from the possible different response from partially dissolved and intact particles. We decided to systematically investigate this process, and see if the existing strategies to counteract this effect also work on a single-particle level.

The results are presented in the following communication that we have published in Nanoscale in 2018. We noticed extremely high heterogeneity in particle dissolution if the particles were kept in deionized water, with remarkable changes not only in intensity, but also in spectral band ratio. Keeping the particles under relatively high concentrations (1 mM) of sodium fluoride was enough to keep the particle response stable over a time frame of ~20 min.

Following this work, we were quite confident in our ability to image hydrophilic UCNPs in SMM conditions. We decided to focus on single-particle tracking as the most promising SMM application.

Publication 2.

Time-dependent luminescence loss of individual upconversion nanoparticles upon dilution in aqueous solutions

Nanoscale

COMMUNICATION

View Article Online
View Journal | View Issue

Cite this: *Nanoscale*, 2018, **10**, 15904

Received 14th May 2018,
Accepted 30th July 2018

DOI: 10.1039/c8nr03892a

rsc.li/nanoscale

Time-dependent luminescence loss for individual upconversion nanoparticles upon dilution in aqueous solution†

Oleksii Dukhno, *[a] Frédéric Przybilla,[a] Verena Muhr,[b] Markus Buchner,[b] Thomas Hirsch [b] and Yves Mély *[a]

Single-particle luminescence microscopy is a powerful method to extract information on biological systems that is not accessible by ensemble-level methods. Upconversion nanoparticles (UCNPs) are a particularly promising luminophore for single-particle microscopy as they provide stable, non-blinking luminescence and allow the avoidance of biological autofluorescence by their anti-Stokes emission. Recently, ensemble measurements of diluted aqueous dispersions of UCNPs have shown the instability of luminescence over time due to particle dissolution-related effects. This can be especially detrimental for single-particle experiments. However, this effect has never been estimated at the individual particle level. Here, the luminescence response of individual UCNPs under aqueous conditions is investigated by quantitative wide-field microscopy. The particles exhibit a rapid luminescence loss, accompanied by large changes in spectral response, leading to a considerable heterogeneity in their luminescence and band intensity ratio. Moreover, the dissolution-caused intensity loss is not correlated with the initial particle intensity or band ratio, which makes it virtually unpredictable. These effects and the subsequent development of their heterogeneity can be largely slowed down by adding millimolar concentrations of sodium fluoride in buffer. As a consequence, the presented data indicate that microscopy experiments employing UCNPs in an aqueous environment should be performed under conditions that carefully prevent these effects.

Introduction

Lanthanide upconverting nanoparticles (UCNPs) are a family of nanomaterials that exhibit efficient upconversion. Through this property, UCNPs sequentially absorb several quanta of low-energy light with subsequent anti-Stokes emission of a single quantum of high-energy light.[1] Typically, they consist of an inorganic matrix doped with two types of lanthanide ions. The first ion (the *sensitizer*) absorbs light and transfers energy to the second ion (*activator* or *emitter*) in a mechanism known as energy transfer upconversion (ETU). A classic example of an efficient UCNP composition is β-$NaYF_4$:20% Yb,2% Er that absorbs in the infrared region (980 nm) and has several emission lines in the visible region (main emissions at 540 nm and 660 nm).[2,3]

The unique properties of upconversion make UCNPs a promising alternative luminophore for a variety of applications,[4–7] particularly in biology.[5,8–10] As no biological molecule exhibits upconversion, imaging with UCNPs avoids autofluorescence and thus enables tissue and cell imaging applications with a high signal-to-noise ratio. Excitation with infrared light also reduces absorption and scattering effects by the biological sample. Other advantages of UCNPs include virtually no photobleaching and steady luminescence with no blinking.

To date, the brightest UCNPs are made of fluoride-based ionic materials[1,2,11] and have hydrophobic surface ligands after the synthesis (*e.g.* oleic acid). Most biological applications require UCNPs to be dispersible in water and buffers. Therefore, multiple strategies to disperse them in aqueous media have been devised, the most popular being the exchange of surface ligands with hydrophilic ones, or the coating with a silica shell or amphiphilic polymers.[8,12,13]

However, in recent years, there have been several reports on the luminescence loss of water-dispersed UCNPs,[14–20] as a result of nanoparticle dissolution, also known as ion leakage. A basic scheme of the dissolution process is provided in Fig. 1. This dissolution is not significant for the concentrated dispersion of UCNPs in water that can be stable for months, but only appears in diluted dispersions. Indeed, even though fluoride matrix materials typically show a low solubility product constant (*e.g.* 3.98×10^{-19} M^4 for YF_3 [21]), the high dilutions employed for instance in imaging experiments likely shift the equilibrium towards partial or complete particle dissolution, as shown by the theoretical estimation provided in the ESI.†

[a]*Laboratory of Biomaging and Pathologies, UMR 7021 CNRS, University of Strasbourg, 67000 Strasbourg, France. E-mail: oleksii.dukhno@unistra.fr, yves.mely@unistra.fr*
[b]*Institute of Analytical Chemistry, Chemo- and Biosensors, University of Regensburg, 93040 Regensburg, Germany*

†Electronic supplementary information (ESI) available. See DOI: 10.1039/c8nr03892a

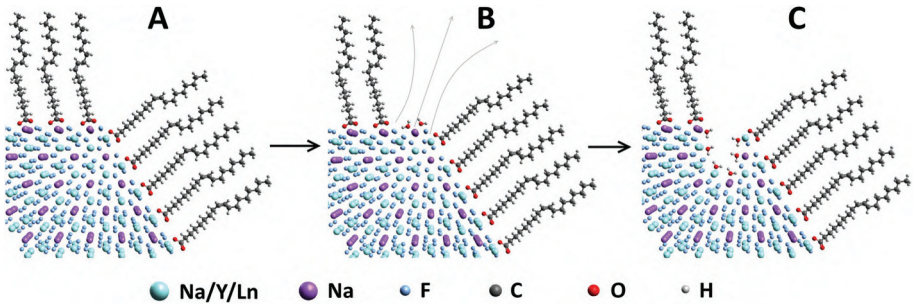

Fig. 1 Schematic representation of dissolution of a doped β-$NaYF_4$ nanocrystal in contact with water (hydrophilizing coating omitted for clarity). A: Intact nanoparticle. B: If an oleic acid ion has desorbed (*e.g.* during the coating process), a vacancy is left and gets occupied by water molecules. C: If the vacancy is in contact with the bulk aqueous phase, dissolution will start from the initial vacancy due to the sub-saturated ion concentration in the bulk aqueous phase.

The reported means to inhibit or prevent dissolution are (a) stabilization of UCNPs by amphiphilic polymers, (b) coating UCNPs with thick shells that are resistant to percolation by water, or (c) adding fluoride ions in the solution to shift the dissolution equilibrium towards the solid phase.[18,20] The dissolution of UCNPs can be a major source of artifacts in biological experiments due to the possibility that it may not be uniform and lead to particles with a large distribution of luminescence properties that vary as a function of time.

To date, all experiments investigating UCNP dissolution in aqueous solutions have been performed in a cuvette to observe the behavior of the ensemble of particles. While this yields general trends in nanoparticle luminescence, its variability at the single-particle level remains hidden. Knowing this variability and the ways to mitigate it would be especially important for quantitative experiments, which are based on observing time- or space-dependent changes in luminescence intensity and/or spectra.

In this work, we monitored in real time the luminescence of individual water-dispersed UCNPs in aqueous solutions in the presence and absence of fluoride ions using a wide-field upconversion microscope. Highly monodisperse UCNPs with homogeneous single-particle luminescence were selected for the experiments. We observed a gradual loss of luminescence for the majority of individual UCNPs. We also noted that this loss was highly heterogeneous at the single-particle level. Moreover, dissolution also affected the ratio of the intensities of the different luminescence bands. We found that these effects can be largely inhibited, but not fully eliminated, by using buffers containing sodium fluoride that shift the dissolution equilibrium back to the solid phase. We believe that our data will be highly useful for the development and application of water-dispersed UCNPs.

Results and discussion

Particle preparation and initial characterization

In this study, the particles composed of β-$NaYF_4$:20% Yb,2% Er are prepared *via* a solvothermal method.[12] Transmission electron microscopy (TEM) and dynamic light scattering (DLS) measurements show that the initial UCNPs have a diameter of 31 nm and are highly monodisperse, with no aggregates (Fig. S1A and B†). X-ray diffraction (XRD) confirms that the UCNP matrix is indeed in the β-phase (Fig. S1C†).

After the synthesis, the initial particles are found to be hydrophobic due to the layer of oleic acid molecules bound to their surface. To disperse these particles in water, we coated them with an amphiphilic polymer, *N*-dodecyl-polyisobutylene-*alt*-maleamic acid (PMA), and purified them by centrifugation, as previously described.[12,22] We chose this coating because it allows the particles to maintain a high monodispersity and partially protects them against dissolution.[18] The luminescence spectrum of the obtained UCNP dispersion recorded with a home-made setup (Fig. S2†) shows fine-structured green and red emission bands at 540 and 660 nm respectively (Fig. S4†), typical of Er^{3+}-doped UCNPs.

The monodispersity of the polymer-coated particles was evidenced by DLS (Fig. 2A), showing a single-peaked distribution with a PDI value of 0.121 and an average diameter of 32 nm. To further confirm their monodispersity and investigate the homogeneity of their luminescence, we performed correlated atomic force microscopy/wide-field upconversion luminescence microscopy of the immobilized UCNPs obtained by drying a diluted dispersion on mica (Fig. 2B; the full image is provided in Fig. S8†). The observed particles have a uniform height of approx. 33 nm and a homogeneous luminescence intensity (Fig. 2C). Moreover, the particles exhibit no correlation between these two parameters.

To further characterize the luminescence of individual UCNPs and check their homogeneity under aqueous conditions, we electrostatically immobilized them on a polyethyleneimine (PEI) layer adsorbed on glass and performed wide-field upconversion microscopy in red and green channels (using 535/50 and 660/30 bandpass filters). A high concentration of NaF (1 mM) was used to prevent the nanoparticle dissolution during their imaging.[20] A 144 × 144 μm region of interest (Fig. 2D) was stitched from a sequence of 49 individual images of 20 × 20 μm (Fig. 2E).[23] Each of the 2968 luminescent spots was fitted with a 2D free-angle elliptic Gaussian func-

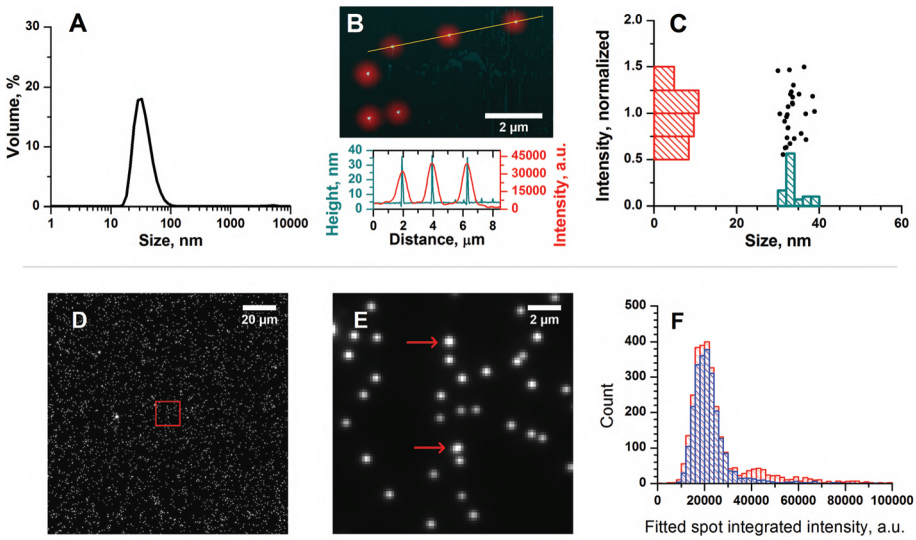

Fig. 2 Characterization of the polymer-coated UCNPs. A: DLS measurement of the water-dispersed UCNPs. B: Top: Region of interest (ROI) of an AFM image of UCNPs dried from an aqueous dispersion and its correlated wide-field upconversion microscopy image in the red channel (shown in red; 660/30 bandpass filter, excitation at 980 nm with an intensity of 8 kW cm^{-2}). Bottom: Height and intensity of the three particles highlighted in the top panel. C: Size and relative intensity (black spots) and histograms of these parameters (teal and red) for a sample of 28 particles. D: Wide-field image of water-dispersed polymer-coated UCNPs adsorbed on a thin layer of PEI and incubated for 5 min with 1 mM NaF. The image shows a 144 × 144 μm ROI in the red channel stitched from 49 (7 × 7) individual wide-field images. Excitation was at 980 nm with an intensity of 8 kW cm^{-2}. The detailed protocol of immobilization is provided in the ESI.† E: 10-fold enlargement of the boxed region in D. Note that some of the spots look larger than the others (highlighted with red arrows). F: Histogram of the integrated intensities of the 2D free-angle elliptic Gaussian spot fits (red) and the same histogram excluding spots that have widths more than 25% larger than the theoretical diffraction limit (blue). The theoretical standard deviation of the Gaussian-approximated PSF for diffraction-limited spots was calculated to be 193 nm for the 660 nm emission.

tion. The histogram of the integrated intensities of the fitted spots shows at least two populations with an approximately 2-fold difference in luminescence intensity, and a small number of higher intensity outliers (Fig. 2F, red). We hypothesized that the brighter subpopulation consists of either UCNP dimers or two single particles that adsorb close to each other. To confirm this, we filtered out the spots that had one or both of their widths 25% higher than the theoretical diffraction limit of the system (Fig. 2F, blue). The abnormal spot size is predominant for the brighter subpopulation, especially for the outliers. As particle dimers would be expected to have the same size as monomers due to the diffraction limit in wide-field imaging, the brighter population of abnormal size is mainly attributed to two single particles adsorbed close to each other. These larger particle spots were subsequently ignored in the analysis of the kinetics of the luminescence loss.

Kinetics of time-dependent luminescence loss

To investigate the kinetics of the luminescence loss for individual nanoparticles, we monitored as a function of time a region of interest containing multiple spots corresponding to single nanoparticles. Briefly, the particles were immobilized on PEI in 1 mM NaF, and then the solution was flushed twice with 1 mM NaF to remove non-adsorbed particles. The images were recorded for 30 min to establish the brightness of the particles before degradation. Then, the solution was flushed thrice with deionized water and images were obtained at different time points. At each time point, the luminescent spots on each individual image were fitted with a 2D free-angle elliptic Gaussian. Particles with close neighbors (<1 μm distance) were removed, and the XY drift was corrected using one of the well-separated particles as a reference.

Comparison of the particles just after flushing with water (Fig. 3A) and after 150 min (Fig. 3B) revealed that the incubation with water led to a time-dependent decrease in intensity and a considerable heterogeneity in particle brightness. This gradual loss of intensity strongly supported the dissolution-related nature of the observed effect. Several particles even disappear from the image, likely as a result of their dissolution to such a degree that their luminescence gets below the detection limit.

To further prove that the observed effects are indeed related to dissolution, we performed combined conductometry/dialysis to directly monitor the ion leakage over time in nanoparticle dispersions. Briefly, an aqueous dispersion of UCNPs was dialysed against deionized water and the conductivity of the dialysate was monitored continuously, periodically replacing the dialysate with deionized water. A gradual increase in conductivity was observed after each replacement, confirming that the ions leave the UCNPs and diffuse through the membrane (Fig. S9B†). In addition, the ion leakage was consistent with the theoretical estimates of ion diffusion through the membrane under our experimental conditions (Fig. S9C†). To exclude the possibility that the intensity loss is related to laser illumination and its associated local heating, we performed

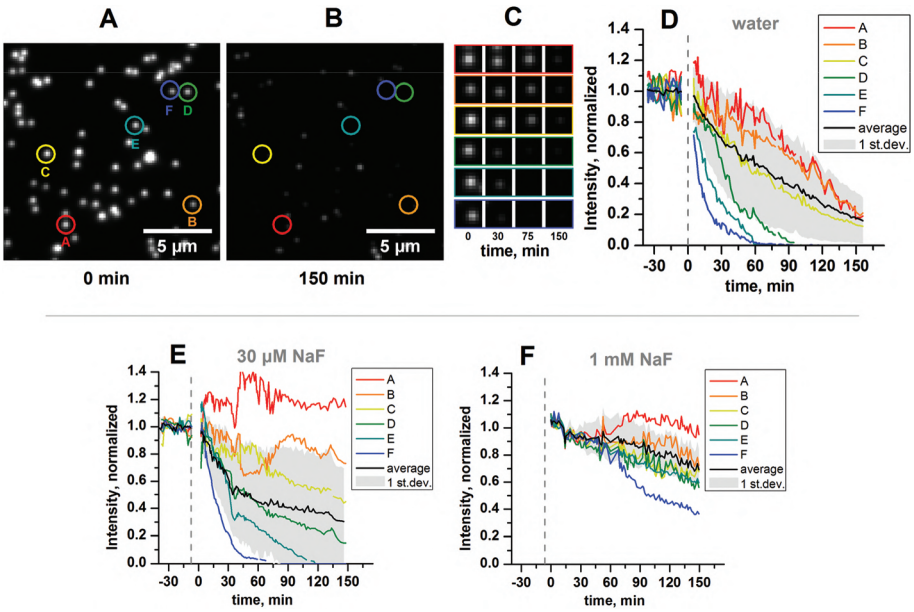

Fig. 3 Time-dependent luminescence loss of individual polymer-coated UCNPs in water and fluoride solutions, as monitored by wide-field upconversion microscopy. A and B: The same ROI with the red emission of UCNPs immediately after washing (A) and after 150 min incubation in deionized water (B), with several particles highlighted. C: Time-dependent intensity changes of the particles highlighted in A and B (1.28 × 1.28 µm). D: Intensity traces for the highlighted particles, normalized to their average intensity during the pre-incubation step (colored lines). The black line corresponds to the average trace for 21 single particles, and the grey area describes the interval corresponding to one standard deviation. E: Traces of normalized red band intensity for particles incubated in 30 µM NaF (colored lines). The black line is the average trace of 15 individual particles, and the grey area depicts the interval corresponding to one standard deviation. F: Traces of normalized red band intensity for particles incubated in 1 mM NaF (colored lines). The black line is the average trace of 20 individual particles and the grey area depicts the interval corresponding to one standard deviation. Wide-field images corresponding to E and F are shown in Fig. S8 and S9.†

large-scale imaging of UCNPs before and after 150 min of incubation with water, without laser illumination during incubation. The images show that the intensity loss occurs to the same extent in continuously illuminated and non-illuminated samples (Fig. 3A, B and Fig. S10A–E†), indicating no influence of illumination on the rate of luminescence loss. Moreover, we found no correlation between the initial particle intensity and the extent of luminescence loss, suggesting that the luminescence loss cannot be reliably predicted based upon the initial particle intensity (Fig. S10F†).

The intensity traces of individual particles showed a high heterogeneity. Examples of individual particles of the same image at different time points and the traces of their integrated intensity, normalized to their initial intensity, are given in Fig. 3C and D. We did not observe any correlation between the initial particle intensity and the rate of intensity loss. The particle intensity decays were found to exhibit different shapes, ranging from exponential-like to practically linear.

There may be several reasons for the heterogeneity of the luminescence loss caused by dissolution. First, no sample is perfectly monodisperse, so the particles probably have slight differences in their surface to volume ratio. Second, as in any crystal, different crystal faces and in particular regions around the defects have different surface energies, resulting in different potential barriers for the ion detachment, leading to the kinetics of dissolution dependent on the crystal face.[20] Third, the porosity and permeability of the surface coating layer may vary from particle to particle. Fourth, the Yb^{3+} ions are known to rapidly transfer energy between each other, forming a cooperative network that allows efficient energy transfer to Er^{3+} ions.[24] The Yb^{3+} quenching by water is non-linear and highly dependent on the amount of Yb^{3+} ions in close contact with water, as they serve as sinks for energy depletion in the whole Yb^{3+} network. A slight variation in the amount of Yb^{3+} in contact with water could thus lead to large differences in the overall quenching efficiency. Fifth, the amount of Er^{3+} exposed to water may vary substantially on a particle-to-particle basis due to its low doping percentage. Those Er^{3+} ions that are quenched by water can deplete the sensitizer network much faster than the emissive Er^{3+} inside the particle and thus contribute substantially to surface quenching.[25]

Therefore, building a theoretical basis for the dependence of the particle intensity upon dissolution would require the inclusion of a number of parameters that are difficult to measure or estimate for individual particles, such as the porosity of the coating layer, the rate of water percolation through it, the distance dependence for water quenching, and the anisotropy of dissolution dependent on the crystal face. Thus, we believe that a purely empirical approach is the most appropriate for such systems.

Countering the luminescence loss with sodium fluoride

To investigate the effect of sodium fluoride on the luminescence loss of individual UCNPs, we recorded the UCNP intensity over time for particles with a final wash in 30 μM NaF and for particles kept continuously in 1 mM NaF without any washing. Examples of intensity traces are provided in Fig. 3E and F, while the raw images are shown in Fig. S11 and S12.†

In 30 μM NaF, the intensity loss clearly slowed down compared to the UCNPs in water, confirming their dissolution-related nature, in line with the data on ensemble measurements.[20] In other words, the addition of sodium fluoride is thought to displace the dissolution equilibrium towards the solid phase, so that the ions remain within the particles and retain the luminescence of the UCNPs. However, heterogeneity appeared to be even greater than that for UCNPs in water, with some outlier particles showing a transient increase in their luminescence. The causes of this increase are unclear, but the observed increase is too high to be attributed to spot fitting artifacts or fluctuations in the excitation power. We hypothesize that it may be caused by a reorganization of the UCNP coating during flushing, which can temporarily reduce the amount of water bound to the surface and thus increase the luminescence intensity. This reorganization could induce a brief increase in intensity, followed by a dissolution-caused intensity decrease. Another possibility is the removal of surface-bound quenchers, again leading to a temporary increase in intensity.

In line with the literature,[20] the luminescence of individual particles was much more stable in the presence of 1 mM NaF than in its absence, though some time-dependent decrease was observed with most particles. At the end of the experiment, a significant intensity heterogeneity can be observed as well. This heterogeneity has implications for any quantitative experiment or assay that assumes a uniform intensity response of UCNPs, either between individual particles or for the same particle at different time points. For instance, a time-dependent change in the luminescence intensity in response to a given agent or property sensed by an UCNP sensor could be difficult to discriminate from the changes related to its dissolution. Distinguishing particles from particle aggregates also becomes more challenging as partially dissolved aggregates could show roughly the same intensity as an intact single particle, while having different size-related properties.

Time-dependent changes in luminescence band ratio

As all of our wide field microscopy experiments were performed in dual-view mode with an image splitter, we simultaneously imaged the red and green emission bands of the particles on the same camera. By fitting the spots in the red and green channels and dividing the red intensity by the green one, a ratiometric signal was produced ("red-to-green ratio", RTGR). Fig. 4 shows the changes in the RTGR parameter for the UCNPs described in Fig. 3. It should be noted that the RTGR values in microscopy measurements slightly differ from those measured in cuvettes (Fig. S13†), as they were measured with slightly different excitation intensities (8 kW cm^{-2} for microscopy and 6.2 kW cm^{-2} for the focused beam in cuvettes). Ample literature evidence suggests that RTGR values nonlinearly depend on the excitation intensity.[26–28]

For the particles in water and 30 μM NaF, the changes in RTGR values with time seem to correlate well with the changes in intensity. Curiously, this effect is opposite to what is normally observed for water quenching, where the increased access of the particle surface to water increases the RTGR values by establishing non-radiative relaxation channels for the green-emissive states of the emitter ion, Er^{3+}.[26,27] However, we believe that other effects may be in play here and explain the observed changes in RTGR values. As the particles dissolve, more and more sensitizers are exposed to water, and the overall amount of energy available in the cooperative sensitizer network becomes lower. This behavior is functionally equivalent to a lowering in the excitation intensity, which decreases the RTGR value (Fig. S14† and ref. 27). It seems that in our particular case, the effect of the sensitizer power loss surpasses the effect of the depopulation of the green state of the emitter, resulting in a net decrease of RTGR. Interestingly, the RTGR for the particles in 1 mM NaF was found to be stable despite the intensity loss (Fig. 4C).

Combined together, these observations have profound implications for applications based on ratiometric measurements, for both microscopy and bulk assays. As each individual particle has a different pattern of dissolution, a quantitative response will unpredictably depend on time and complicate the interpretation of microscopy experiments. Moreover, the intra-population heterogeneity may also nonlinearly affect the response of bulk assays that depend on time, dilution,

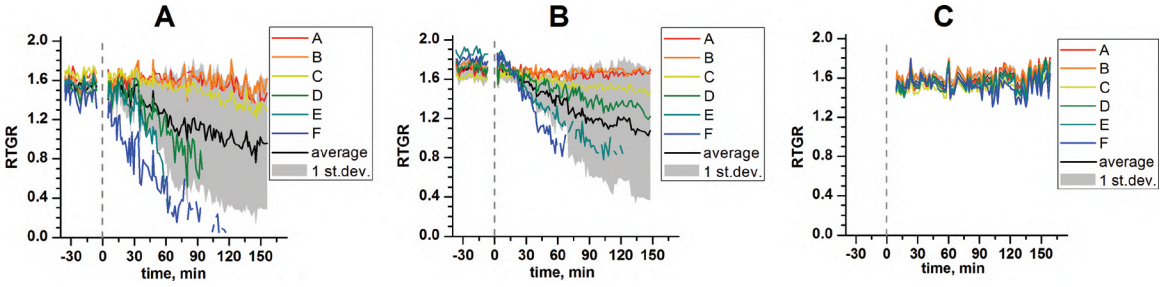

Fig. 4 RTGR curves for individual polymer-coated UCNPs incubated in (A) deionized water, (B) 30 μM NaF and (C) 1 mM NaF (the same particles as the ones shown in Fig. 4, S8 and S9†).

buffer, differences between particle batches, and other dissolution-related conditions.

Conclusions

To conclude, we observed multiple dissolution-related effects in water-dispersed UCNPs that generate considerable heterogeneity over time at the individual particle level both in their luminescence intensity and band intensity ratio. We note that fluoride-containing buffers tend to considerably slow down, but not fully prevent these effects. Moreover, the dissolution-caused intensity loss is not correlated with the initial particle intensity or band ratio, which makes it virtually unpredictable at the single particle level. Thus, quantitative measurements and microscopy experiments employing UCNPs in an aqueous environment should be performed that prevent these effects. For this, several approaches are available: (a) using fluoride buffers to shift the dissolution equilibrium towards the solid phase; (b) using particles with sacrificial shells that shield the particle from water until they are dissolved; (c) using extremely tight coatings that are resistant to percolation by water; (d) using matrix materials that are more resistant to dissolution (*e.g.* oxides).

The gradual particle dissolution implies that UCNPs are biodegradable in aqueous media, provided that their surface coating is degradable as well. This property could be perceived as an advantage over other inorganic nanoparticles (*e.g.* gold or semiconductor quantum dots) of similar sizes, as in principle they should have better clearance. However, dissolution could also cause localized cytotoxicity due to the release of fluoride and lanthanide ions.[29] This should be carefully considered when UCNPs are applied in cell and animal experiments.

Moreover, from our data, it may be advisable to include dissolution stability tests for experiments involving water-dispersed UCNPs in biological applications, as they could be a major source of artifacts.

Experimental section

Full description of experimental methods and any associated references are available in the ESI.†

Conflicts of interest

The authors declare no conflicts of interest.

Acknowledgements

We thank Philippe Carl and Ludovic Richert for help with AFM measurements. This work was supported by the Labex NIE and the COST CM 1403, "The European upconversion network". O. D. was supported by an Eiffel fellowship (Campus France) and a fellowship from the French Ministère de la Recherche.

References

1 M. Haase and H. Schäfer, *Angew. Chem., Int. Ed.*, 2011, **50**, 5808–5829.
2 F. Auzel, *Chem. Rev.*, 2004, **104**, 139–174.
3 S. Heer, K. Kömpe, H.-U. Güdel and M. Haase, *Adv. Mater.*, 2004, **16**, 2102–2105.
4 Y. Liu, Y. Lu, X. Yang, X. Zheng, S. Wen, F. Wang, X. Vidal, J. Zhao, D. Liu, Z. Zhou, C. Ma, J. Zhou, J. A. Piper, P. Xi and D. Jin, *Nature*, 2017, **543**, 229–233.
5 B. Zhou, B. Shi, D. Jin and X. Liu, *Nat. Nanotechnol.*, 2015, **10**, 924–936.
6 C. D. S. Brites, X. Xie, M. L. Debasu, X. Qin, R. Chen, W. Huang, J. Rocha, X. Liu and L. D. Carlos, *Nat. Nanotechnol.*, 2016, **11**, 851–856.
7 X. Liu, Y. Wang, X. Li, Z. Yi, R. Deng, L. Liang, X. Xie, D. T. B. Loong, S. Song, D. Fan, A. H. All, H. Zhang, L. Huang and X. Liu, *Nat. Commun.*, 2017, **8**, 899.
8 A. Sedlmeier and H. H. Gorris, *Chem. Soc. Rev.*, 2015, **44**, 1526–1560.
9 N. M. Idris, M. K. Gnanasammandhan, J. Zhang, P. C. Ho, R. Mahendran and Y. Zhang, *Nat. Med.*, 2012, **18**, 1580–1585.
10 C. Wang, X. Li and F. Zhang, *Analyst*, 2016, **141**, 3601–3620.
11 G. Chen, H. Qiu, P. N. Prasad and X. Chen, *Chem. Rev.*, 2014, **114**, 5161–5214.
12 S. Wilhelm, M. Kaiser, C. Würth, J. Heiland, C. Carrillo-Carrion, V. Muhr, O. S. Wolfbeis, W. J. Parak, U. Resch-Genger and T. Hirsch, *Nanoscale*, 2015, **7**, 1403–1410.
13 V. Muhr, S. Wilhelm, T. Hirsch and O. S. Wolfbeis, *Acc. Chem. Res.*, 2014, **47**, 3481–3493.
14 Y.-F. Wang, L.-D. Sun, J.-W. Xiao, W. Feng, J.-C. Zhou, J. Shen and C.-H. Yan, *Chem. – Eur. J.*, 2012, **18**, 5558–5564.
15 S. Zhang, Z. Jiang, X. Liu, L. Zhou and W. Peng, *Nanoscale*, 2013, **5**, 8146–8155.
16 D. Lisjak, O. Plohl, M. Ponikvar-Svet and B. Majaron, *RSC Adv.*, 2015, **5**, 27393–27397.
17 D. Lisjak, O. Plohl, J. Vidmar, B. Majaron and M. Ponikvar-Svet, *Langmuir*, 2016, **32**, 8222–8229.
18 O. Plohl, S. Kralj, B. Majaron, E. Fröhlich, M. Ponikvar-Svet, D. Makovec and D. Lisjak, *Dalton Trans.*, 2017, **46**, 6975–6984.
19 O. Plohl, M. Kraft, J. Kovač, B. Belec, M. Ponikvar-Svet, C. Würth, D. Lisjak and U. Resch-Genger, *Langmuir*, 2017, **33**, 553–560.
20 S. Lahtinen, A. Lyytikäinen, H. Päkkilä, E. Hömppi, N. Perälä, M. Lastusaari and T. Soukka, *J. Phys. Chem. C*, 2017, **121**, 656–665.

21 T. Mioduski, C. Gumiński and D. Zeng, *J. Phys. Chem. Ref. Data*, 2014, **43**, 013105.
22 O. Dukhno, F. Przybilla, M. Collot, A. Klymchenko, V. Pivovarenko, M. Buchner, V. Muhr, T. Hirsch and Y. Mély, *Nanoscale*, 2017, **9**, 11994–12004.
23 S. Preibisch, S. Saalfeld and P. Tomancak, *Bioinformatics*, 2009, **25**, 1463–1465.
24 A. Nadort, J. Zhao and E. M. Goldys, *Nanoscale*, 2016, **8**, 13099–13130.
25 M. Y. Hossan, A. Hor, Q. Luu, S. J. Smith, P. S. May and M. T. Berry, *J. Phys. Chem. C*, 2017, **121**, 16592–16606.
26 R. Arppe, I. Hyppänen, N. Perälä, R. Peltomaa, M. Kaiser, C. Würth, S. Christ, U. Resch-Genger, M. Schäferling and T. Soukka, *Nanoscale*, 2015, **7**, 11746–11757.
27 C. Würth, M. Kaiser, S. Wilhelm, B. Grauel, T. Hirsch and U. Resch-Genger, *Nanoscale*, 2017, **9**, 4283–4294.
28 D. J. Gargas, E. M. Chan, A. D. Ostrowski, S. Aloni, M. V. P. Altoe, E. S. Barnard, B. Sanii, J. J. Urban, D. J. Milliron, B. E. Cohen and P. J. Schuck, *Nat. Nanotechnol.*, 2014, **9**, 300–305.
29 A. Gnach, T. Lipinski, A. Bednarkiewicz, J. Rybka and J. A. Capobianco, *Chem. Soc. Rev.*, 2015, **44**, 1561–1584.

Supporting information

Time-dependent luminescence loss of individual upconversion nanoparticles upon dilution in aqueous solutions

Oleksii Dukhno[1], Frederic Przybilla[1], Verena Muhr[2], Markus Buchner[2], Thomas Hirsch[2] and Yves Mely[1*]*

1) Laboratory of Biomaging and Pathologies, UMR 7021 CNRS, University of Strasbourg, 67000 Strasbourg, France
2) Institute of Analytical Chemistry, Chemo- and Biosensors, University of Regensburg, 93040 Regensburg, Germany

* *Corresponding authors:* oleksii.dukhno@unistra.fr, yves.mely@unistra.fr

Experimental methods

Materials and synthesis. Reagents and solvents were purchased from Sigma-Aldrich and used without further purification. Water for all experiments was purified with a Merck Millipore Milli-Q system.

Oleate-coated UCNPs were prepared and characterized (Fig. S1) as described in Wilhelm et al. 2015.[1] To render the UCNP hydrophilic and thus, water dispersible, N-dodecyl-polyisobutylene-alt-maleamic acid (PMA) was synthesized and used to coat the UCNPs, as described in Dukhno et al.[2] After coating, the particles were purified by centrifugation (12000 g RCF, 4°C, 1 h) and pellet redispersion in 10 mM NaOH with 1 mM NaF. This treatment was performed twice to ensure removal of empty polymer micelles. Quality control was done by DLS measurements.

XRD patterns were recorded on a Huber Guinier G670 diffractometer with a Kα-Cu source (λ = 1.54060 Å). *TEM images* were acquired with a 120 kV Philips CM12 microscope on carbon-coated copper grids and were analyzed with ImageJ and Origin.

DLS measurements were performed on a Malvern Zetasizer Nano instrument to characterize the size of the polymer-coated UCNPs in Brand plastic cuvettes (lot #759015). Correlation curves for each sample were accumulated 3 times. Treatment parameters were normal resolution and size distribution by volume.

Theoretical estimation of the extent of particle degradation

A typical stock dispersion of water-dispersed UCNPs after synthesis and coating contains ~1 mg/mL of material.[2,3] Knowing the density of β-$NaYF_4$ (4.21 g/cm^3) and the volume of a spherical 30 nm particle (14137 nm^3) we can calculate that the particle concentration is 1.68×10^{13} particles per mL, or ~28 nM. β-$NaYF_4$ unit cell volume is 107 A^3, so a UCNP 30 nm in diameter contains ~132000 unit cells. Knowing the particle concentration and the amount of unit cells per particle, we can estimate the total amount of ions trapped inside the particles, which is 3.7 mM for Na^+, 3.7 mM for Y^{3+}, and 14.8 mM for F^-.

Next, we calculated the concentration of ions in water over saturated $NaYF_4$ and YF_3 from their solubility products.[3,4] The calculation for YF_3 is necessary because its overall solubility is lower than for $NaYF_4$, so the dissolution could potentially proceed through YF_3 as an intermediate.

$$NaYF_4(s) + H_2O \rightleftharpoons Na^+_{aq} + Y^{3+}_{aq} + 4\,F^-_{aq}$$
$$K_s(NaYF_4, pH\ 7) = [Na^+][Y^{3+}][F^-]^4 = 1.6 * 10^{-26}\ M^6$$
$$[Na^+] = 20\,\mu M\ ;\ [Y^{3+}] = 20\,\mu M\ ;\ [F^-] = 80\,\mu M$$

$$YF_3(s) + H_2O \rightleftharpoons Y^{3+}_{aq} + 3\,F^-_{aq}$$
$$K_s(YF_3, pH\ 7) = [Y^{3+}][F^-]^3 = 3.98 * 10^{-19}\ M^4$$
$$[Y^{3+}] = 11\,\mu M\ ;\ [F^-] = 33\,\mu M$$

The saturated concentrations for lanthanide ions are 180-340 times larger than the concentration of ions trapped inside the particles. This implies that in the stock dispersion, the particles only lose ~0.3-0.5% of total material before reaching the solubility equilibrium.
Meanwhile, in single-particle microscopy conditions, particles are typically attached to their target substrates (e.g. coated glass surfaces or cells), with nearly no particles present in dispersion. For a typical single-particle imaging setup with a 100x magnification objective, a good separation of individual particle spots on microscopy image requires approximately 100 particles per region of interest of 20×20 μm^2. For a microscopy well plate with a well surface of 1 cm^2, this corresponds to 25 million particles per well. The wells themselves are filled with 300 μL aqueous buffer. Thus, the *effective* concentration of immobilized particles in microscopy wells is ~140 fM. Again, knowing the particle concentration and the amount of unit cells per particle, the total amount of ions trapped inside the particles can be estimated at 18.5 nM for Na^+, 18.5 nM for Y^{3+}, and 74 nM for F^-. These concentrations are much lower than the concentrations for the saturated solution, meaning that from a thermodynamical standpoint, the particles are expected to dissolve completely. Meanwhile, the kinetics of their dissolution depend on the accessibility of the particle surfaces to the aqueous phase.

Characterization of oleate-capped UCNPs after synthesis

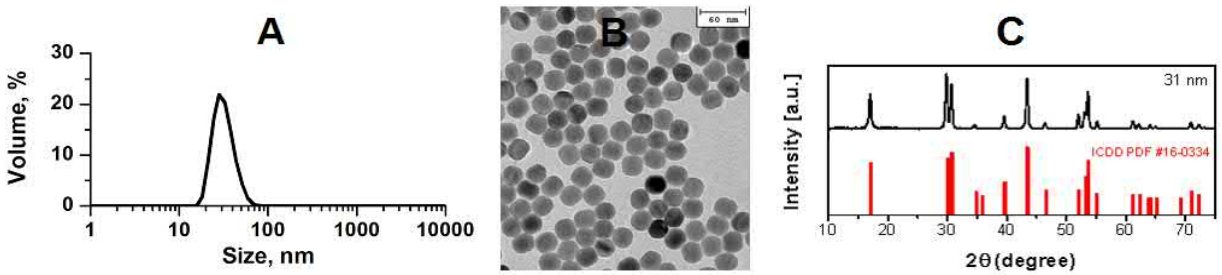

*Figure S1. Characterization of the oleate-capped UCNPs (*β-$NaYF_4$: 20%Yb, 2%Er*) after synthesis. The UCNPs were characterized by A: DLS in cyclohexane. B: TEM and C: XRD. The XRD pattern of the nanocrystals (black) is compared to the corresponding standard pattern of hexagonal phase $NaYF_4$ (red, ICDD PDF #16-0334).*

Cuvette measurements of UCNP dispersions in 1 cm BRAND plastic cuvettes (Cat. No. 7590-15) were performed with a homemade setup (Fig. S2). Excitation at 980 nm was provided by a continuous-wave laser coupled to a single mode fiber with a maximum output of 350 mW (Qphotonics, QFBGLD-980-350). Excitation light was focused in the cuvette by a lens of 100 mm focal distance. Excitation power inside the cuvette was calculated to be 6.2 kW/cm^2 (see below). The scattered/reemitted laser light was removed by a low pass filter (Semrock, E700SP). The emission was collected through a monochromator (Jobin Yvon HC10IR) with an avalanche

photodiode (Excelitas SPCM-AQRH-16). Spectrometry was performed with an identical optical path for excitation, with emission collected by a fiber spectrometer (Avaspec ULS3648).

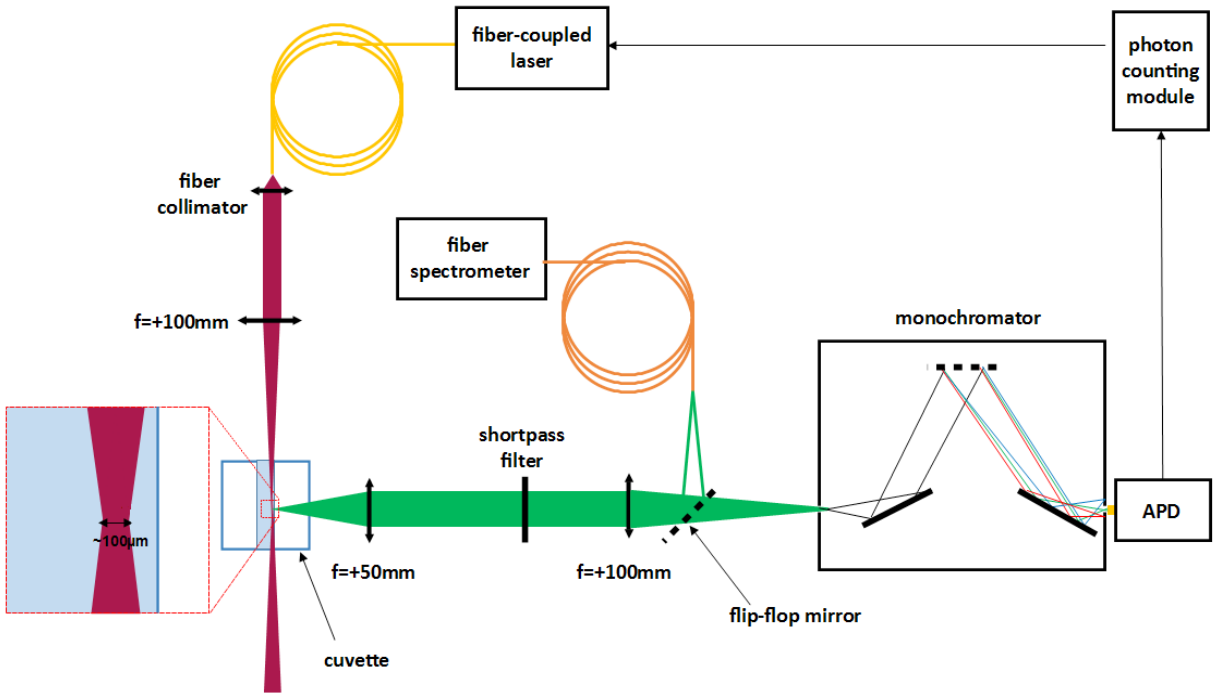

Figure S2. Scheme of the setup for cuvette measurements.

To estimate the excitation intensity within the cuvette, the laser beam intensity profile was experimentally measured inside the cuvette by the knife-edge technique, using a razor blade (~2 mm wide).[5] Briefly, the blade was glued on a thin steel rod, mounted on a two axis micrometer translation stage (Thorlabs PT1A/M), and immersed in the cuvette filled with deionized water. This setup allows to achieve a bidirectional motion, along the beam and vertically (Fig. S3, A). Through the vertical movement, the razorblade progressively occludes the beam and thus, the beam power collected by the detector (Newport 1917R power meter) gets lower. By repeating the measurement at different depths in the cuvette, a full beam blade occlusion profile can be collected (Fig. S3, B), from which the beam geometry can be calculated. For our calculations, the beam geometry was considered to be Gaussian and circular (with no ellipticity). To correct for water absorption, we compared the intensity of the transmitted beam with an empty cuvette and after filling the cuvette with water. We found the water absorption to be non-negligible, at a value of 0.191 cm^{-1}. By knowing the beam geometry and beam attenuation by the medium, the full excitation profile (Fig. S3, C) and thus, the beam waist radius (30.6 µm) and the average excitation intensity in the beam waist (6.2 kW/cm^2) can be estimated. Calculations were performed in Wolfram Mathematica 11.0.

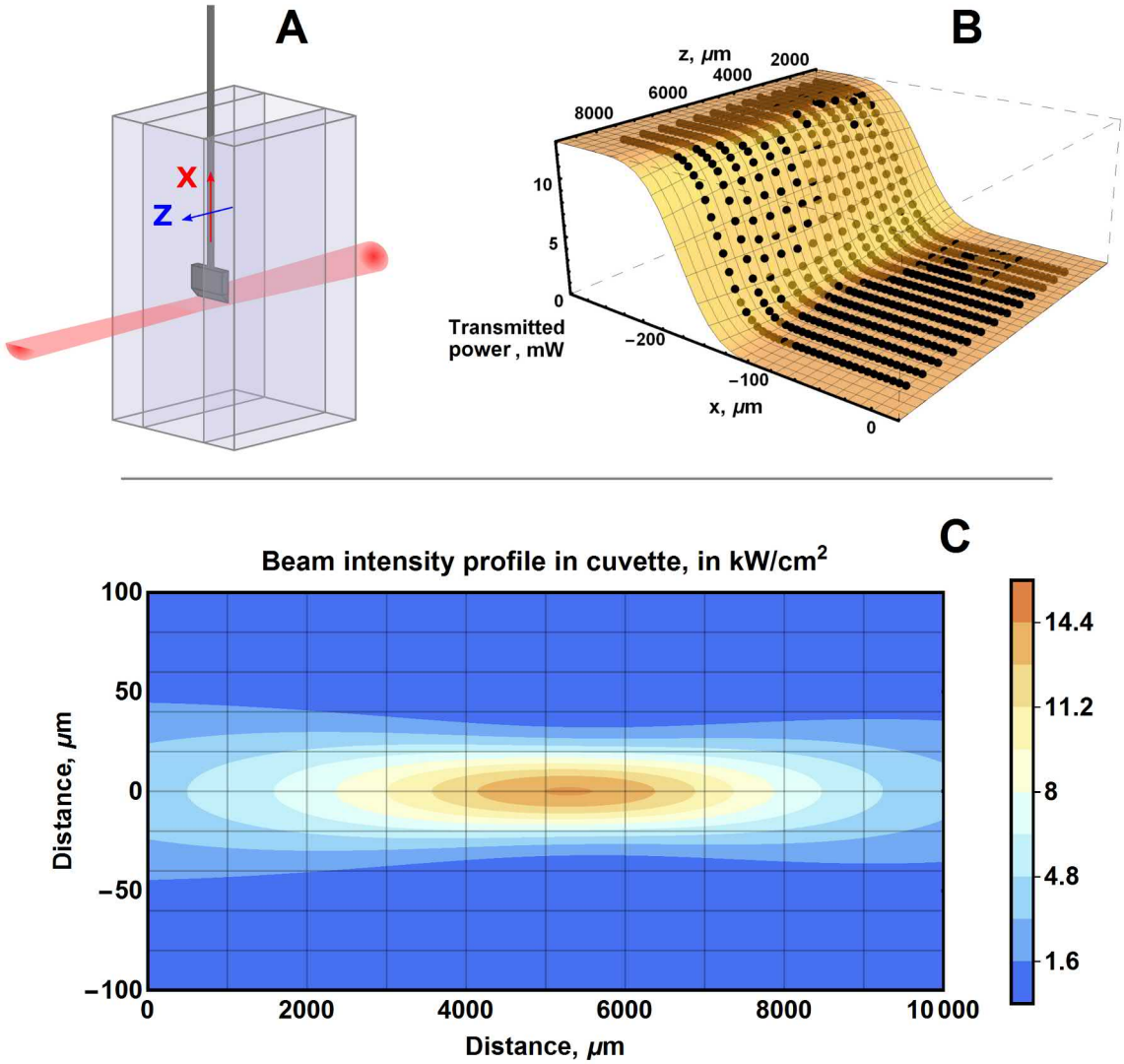

Figure S3. Measurement of the excitation beam intensity profile for the cuvette setup. A: setup for measuring the beam profile. The laser beam is occluded by a movable razor blade, permitting only a part of the beam to go through. B: dependence of the transmitted power on lateral and vertical blade position (black points) and its global fit with the occlusion curve (orange surface). C: obtained beam intensity profile that takes into account water absorption inside the cuvette.

Luminescence spectroscopy of water-dispersed UCNPs

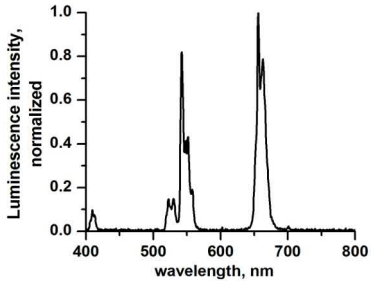

Figure S4. Luminescence spectrum of the stock solution of polymer-coated UCNPs dispersed in 1 mM NaF at an estimated particle concentration of 0.8 mg/mL. The spectrum was measured by

focusing a 980 nm laser beam in a cuvette, with a calculated excitation intensity of 6.2 kW/cm^2.

Microscopy setup and excitation intensity determination

Luminescence imaging of UCNPs was performed on an inverted microscope (Olympus IX71) equipped with a high numerical aperture objective (Olympus, UApo N 100x/1.49 Oil). A 980 nm continuous-wave laser coupled to a single mode fiber with a maximum output of 350 mW (Qphotonics, QFBGLD-980-350) was passed through a longpass filter(Chroma, E780LP) used to excite the UCNPs with an excitation power density of 8 kW/cm^2 in epi illumination. Luminescence emission was separated from the excitation beam by using a short pass dichroic mirror (Chroma, T875spxrxt), while the residual laser light was removed by a low pass filter (Chroma, E700SP). Emission was detected by an electron multiplying CCD camera (Hamamatsu, ImagEM X2 C9100-23B) through an image splitting system for simultaneous dual wavelength imaging (Hamamatsu, W-VIEW GEMINI). This splitting system was used with an appropriate dichroic mirror (Semrock, FF560-FDi01) and band pass filters for green channel (Semrock, FF01-535/50) and red channel (Semrock, FF01-660/30-25). We have calibrated the spectral response of our microscopy setup with an external white light source as a reference and used this calibration for correcting the red to green ratios. Acquisition was fully automated and controlled by scripts within the MicroManager framework.[6] All static images shown in the article were recorded as an averaged stack of 100 images, each with 100 ms exposure time.

Wide-field microscopy images were treated with ImageJ 1.51h as part of the FIJI package. Stitching was performed with the Grid/Collection stitching plugin.[7] Drift correction was done using a homemade script written in ImageJ macro language (available on request). Spot fitting was performed with the Gaussian Fit module of the GDSC SMLM package.[8] Data analysis was performed with homemade scripts written in Python 3.4.3 (available on request).

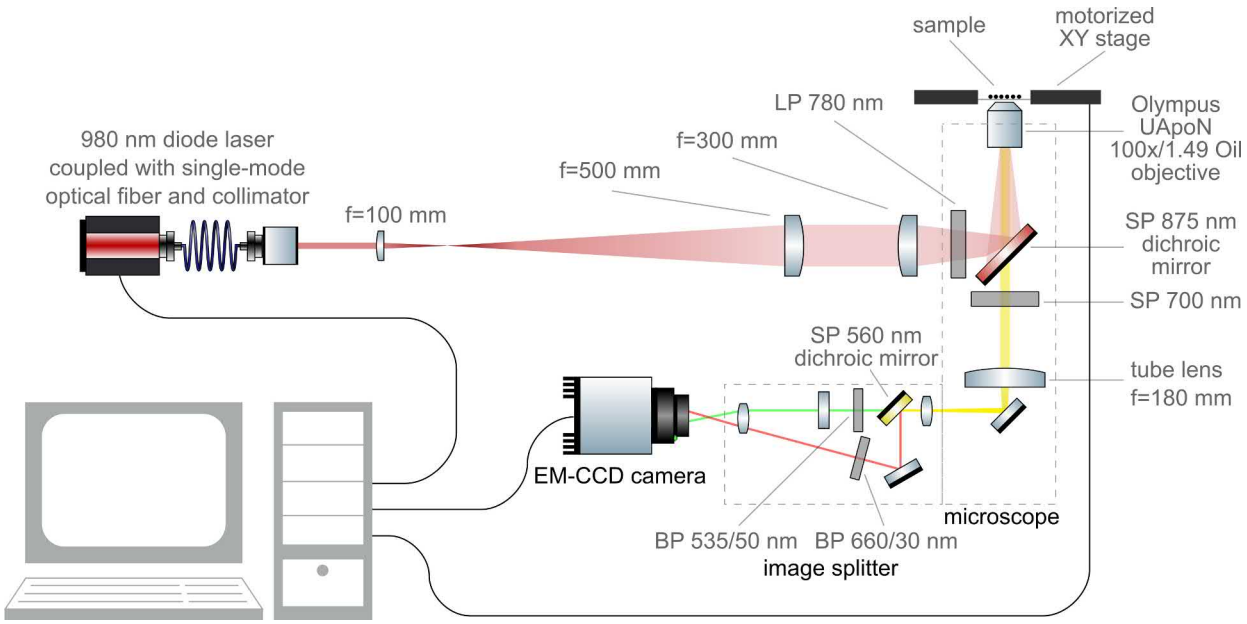

Figure S5. Scheme of the microscopy setup.

To estimate the excitation beam profile in the image plane of our microscopy setup, we imaged oleate-capped UCNPs dried at low density on a glass coverslip. A single UCNP was scanned through the field of view, using the motorized XY stage (Märzhäuser) with a step of 4 µm (Fig. S6, A). The UCNP luminescence was measured as a function of its position, which provides the excitation intensity map (Fig. S6, B). To check the dependence of the UCNP luminescence on the excitation intensity, the UCNP was positioned in the center of the excitation beam and its

luminescence was measured at various laser powers. In the high power regime used in our experiments, the luminescence of the individual UCNP in the red channel was observed to be linearly dependent on the laser power and thus, on the excitation intensity (Fig. S6, C). By fitting the intensity map with a 2D circular gaussian profile (Fig. S6, D), the beam waist radius in the image plane was found to be 28 µm. Knowing the laser power after the objective (96 mW), the average excitation intensity was found to be 8 kW/cm^2 at the center of the beam, where the excitation intensity varied by less than 10% (in a 6.3 µm radius from the beam center). Throughout the paper, we only considered the luminescence of UCNPs positioned in the center of the beam.

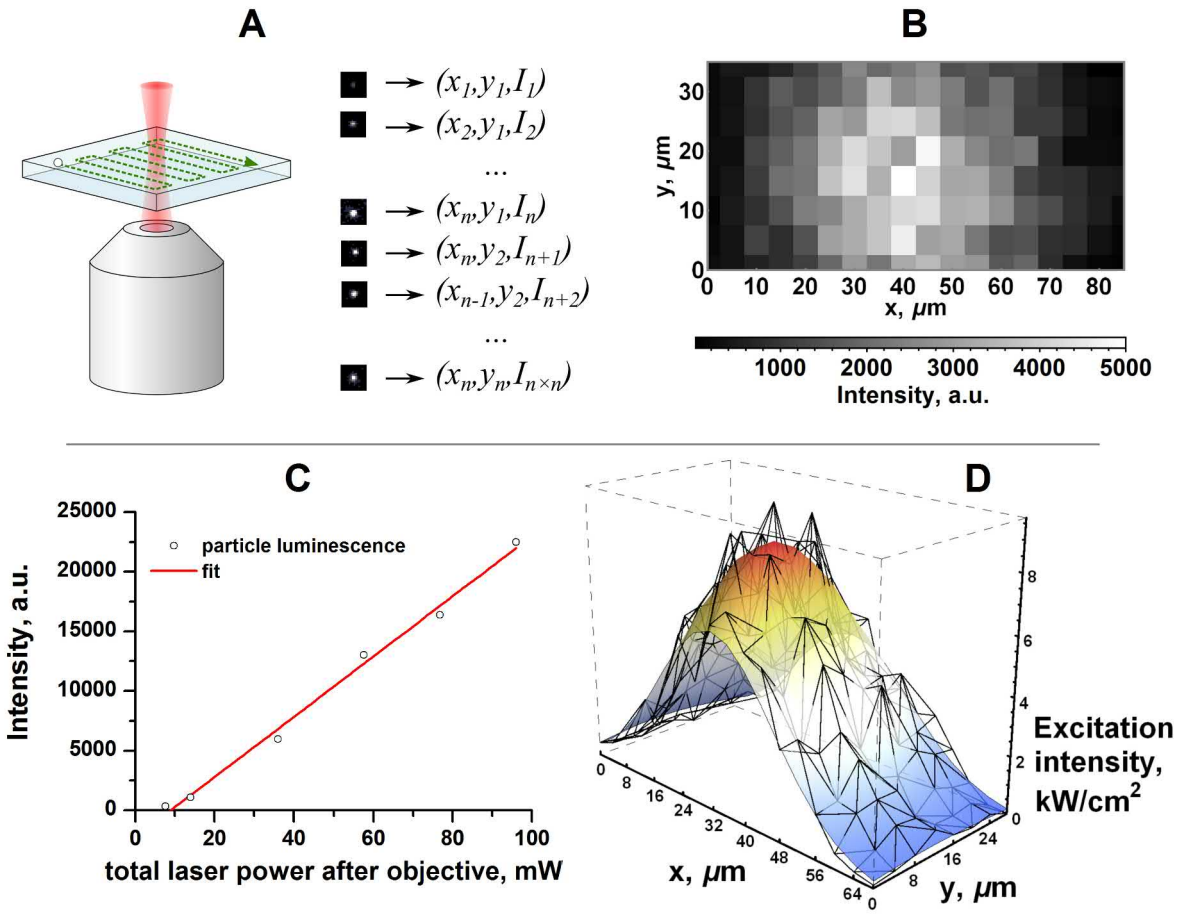

Figure S6. Measurement of the excitation beam intensity profile for the microscopy setup. A: scheme of the mapping experiment. B: excitation intensity map in the field of view. C: excitation power dependency for an immobilized particle. D: excitation beam profile at the maximum laser power.

AFM measurements were performed on a Veeco Nanoscope IIIa MultiMode AFM (Veeco, Santa Barbara, California, United States) in tapping mode, using RTESP7 cantilever probes (silicon, 300 MHz). Raw AFM data were treated with the Gwyddion 2.40 software (automatic mean plane subtraction, then automatic line correction by matching height median).
For correlated atomic force microscopy / wide-field upconversion luminescence microscopy (AFM/Upcon), the particles were 1000-fold diluted in water from stock solution and dried for 1 h in a vacuum chamber on mica glued to a thin steel washer. To ensure a clean flat surface, mica was exfoliated with a scotch tape immediately before the experiment. The bottom side of the mica was marked with a permanent marker (Staedtler permanent Lumocolor, red) to leave a spot clearly visible in bright field microscopy. The position of the scanned region of interest (ROI) relative to the marker spot was noted. Then, the sample was inverted and fixed on a glass coverslip with a

scotch tape. The marker spot was found by illuminating the sample with a white lamp, and the objective was positioned with an XY stage with corresponding offsets relative to the spot, to find the approximate position of the scanned ROI. The precise ROI was located manually afterwards. Fig. S4 illustrates the protocol.
Afterwards, the luminescence images were treated by a landmark-based rigid transformation to match the AFM geometry, using Landmark Correspondences FIJI plugin.[9] The rigid transformation was chosen to retain the spot proportions and inter-spot distances. Landmarks were set manually by the user. An AFM-Upcon image (20x20 µm) of immobilized UCNPs dried on mica is given in Fig. S5.

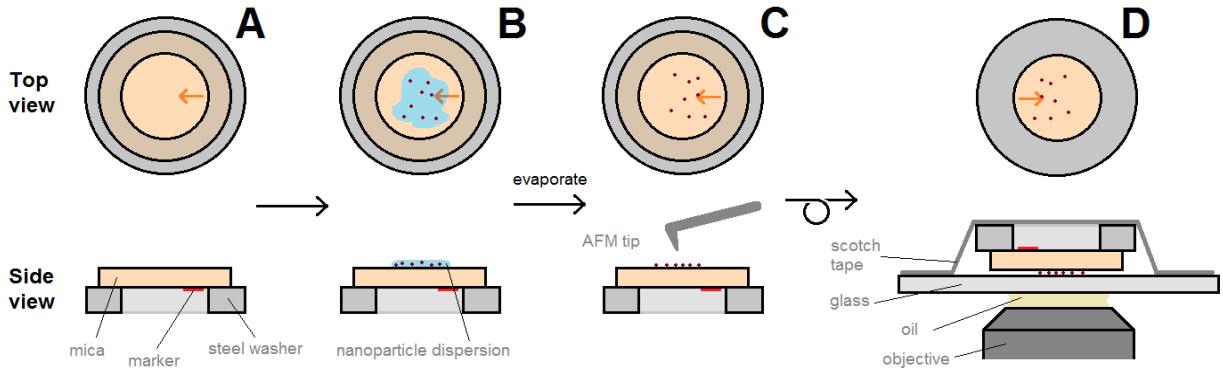

Figure S7. Sample preparation for correlated AFM/ wide-field upconversion luminescence microscopy. A: Initial assembly of mica attached to a steel washer, with a marker on the bottom side (red arrow). B: A drop of nanoparticle dispersion is added. C: After evaporation, AFM is performed on the sample. D: The sample is then inverted and fixed to a glass coverslip. The marker is located by eye in the bright field mode, and the exact ROI is located with an XY stage.

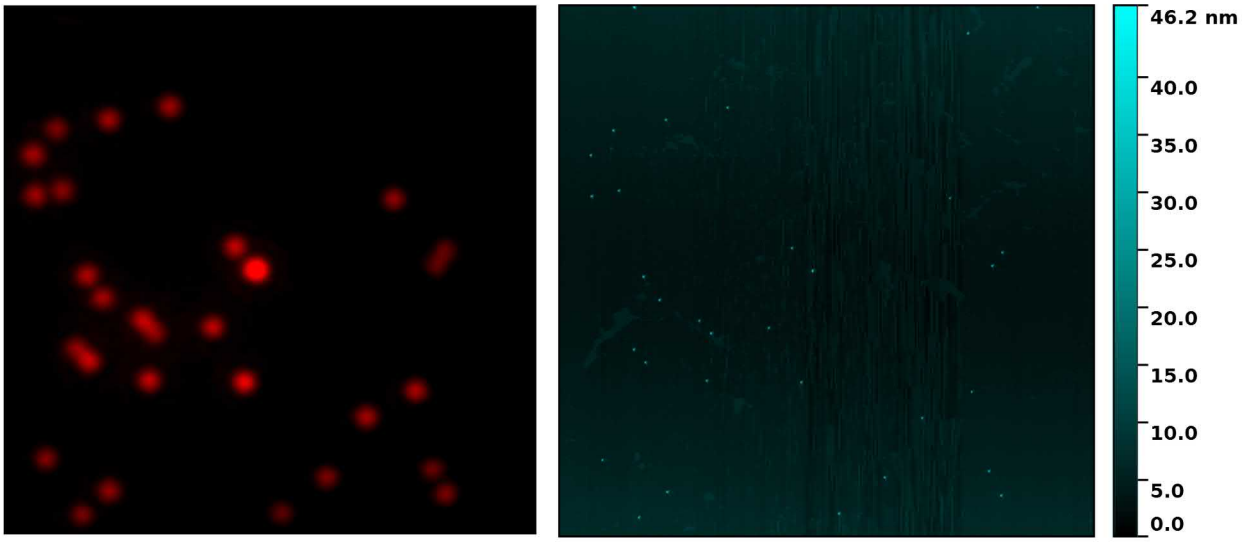

Figure S8. Full AFM-Upcon image (20×20 µm) of immobilized UCNPs dried on mica as described in Fig. S7. Red: luminescence in the red channel. Teal: sample height, as measured by AFM.

Monitoring UCNP dissolution by combined dialysis/conductometry

To directly confirm the UCNP dissolution, we performed combined dialysis/conductometry measurements to monitor the ion leakage from UCNPs in real time. To this aim, 0.4 mL of UCNP stock solution was desalted through an Illustra NAP-5 column (GE) that was equilibrated with deionized water. 0.5 mL of nanoparticle dispersion was collected, diluted to 0.6 mL and closed in a Teflon vessel capped with a SpectraPor RC 3 dialysis membrane (MWCO 3.5 KDa). The vessel was immersed in 3.5 mL deionized water with a platinized conductivity cell (Radiometer CDC 745-9), under continuous stirring. The conductivity of the dialysate was continuously measured by a conductometer (Tacussel CD 6N). After 3-16 h (see below), 1-2 mL of dialysate was replaced with deionized water and the pipetted dialysate was stored. This procedure was repeated 16 times in total.

Before the experiment, all parts of the experimental assembly were thoroughly rinsed and soaked 20 min in deionized water to avoid contamination. This procedure was performed thrice.

Throughout the experiment, the temperature was kept at 22°C. All deionized water used in the experiments was allowed to equilibrate with the atmospheric CO_2 over at least 4 h.

The scheme of the experiment is provided in Fig. S6A. For each dialysate dilution, the solution becomes sub-saturated, lowering the conductivity. Then, UCNP dissolution starts and the solution becomes saturated once more. At a certain point, when all ions escape the UCNPs and only surface coating polymers are left inside the dialysis vessel, slower kinetics of conductivity restoration are expected, as the concentration gradient decreases and dialysis rate drops.

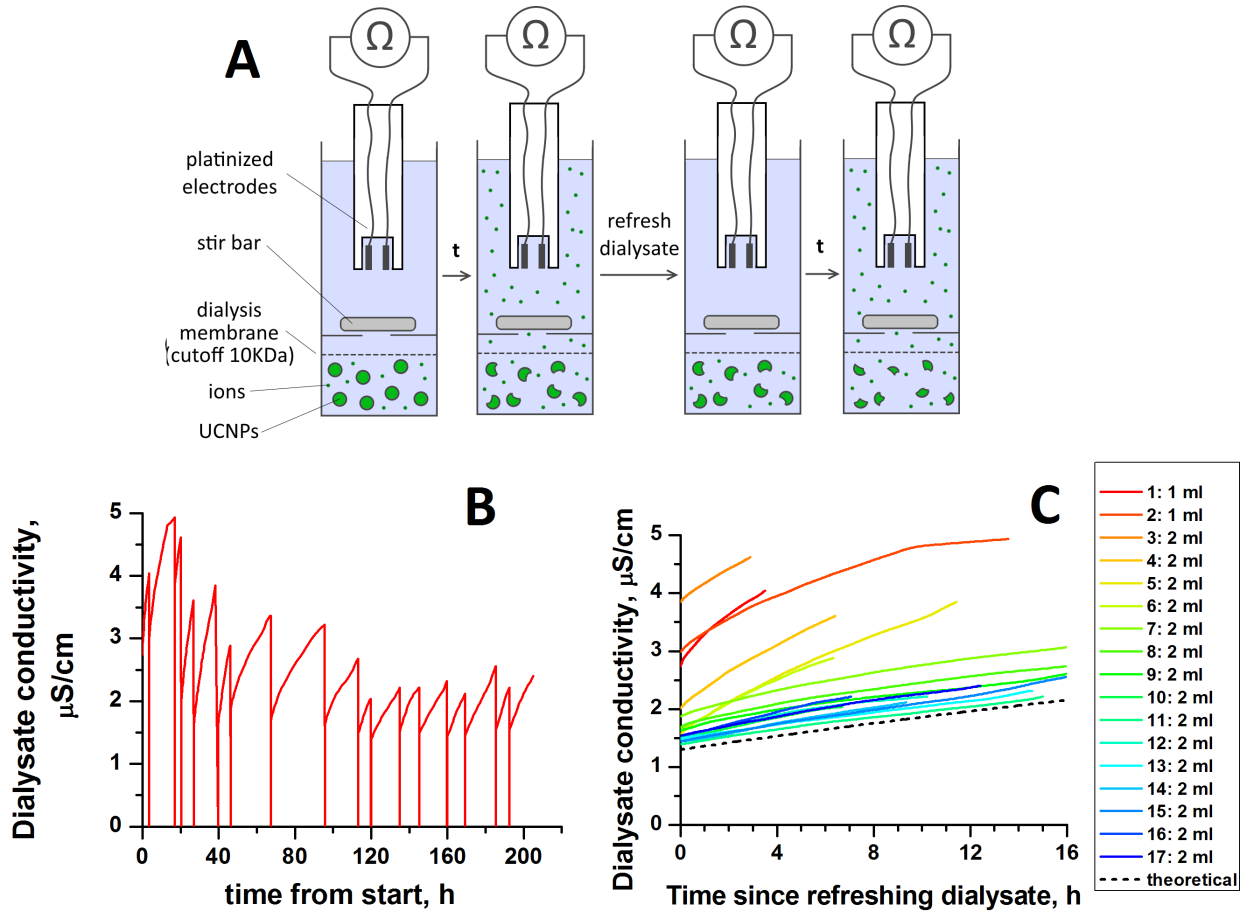

Figure S9. Monitoring UCNP dissolution by combined conductometry/dialysis. A: Schematic representation of the experiment. B: Raw conductivity curves for the full duration of the experiment. At each vertical line, a part of the dialysate was replaced by mQ water. First two cycles have been performed with substitution of 1 mL, the other ones with 2 mL. C: Conductivity restoration curves for each cycle of dialysate refreshing.

The results are shown in Fig. S6B and C. As expected, we observed a drop in conductivity for each dilution, as a result of the solution becoming sub-saturated in UCNP ions. Then, progressive UCNP dissolution restores the solution saturation again. The initial curves show higher conductivities, likely corresponding to the relatively fast diffusion of highly soluble NaF into the dialysate and formation of less soluble YF_3 on particle surfaces exposed to water. The kinetics of conductivity restoration become progressively slower at each dilution. At a certain point, when all ions escape the UCNPs and only surface coating polymers are left inside the dialysis vessel, slower kinetics of conductivity restoration are observed, as the concentration gradient decreases and dialysis rate drops. To confirm that the membrane was intact and no UCNPs escaped the dialysis vessel during the experiment, we also performed upconversion luminescence measurements in cuvette and found no detectable luminescence in any of the collected dialysates. Comparing the luminescence of the dialysis vessel content to the initial stock solution, we found a 36000-fold loss in luminescence intensity, i.e. 99.997% of signal was lost. Overall, these data are a direct proof of ion leakage from UCNPs.

We also performed a theoretical estimation of conductivity restoration. We assumed that after several dialysis cycles, YF_3 is the dominant solid phase at equilibrium, as it has the lowest known solubility product among the solid phases that consist of the combinations of Na^+, Y^{3+}, Yb^{3+}, Er^{3+} and F^-,[4,10] and thus will be the last one to dissolve. We also assumed that hydrated Yb^{3+} and Er^{3+} are equal to Y^{3+} in terms of their mobility and molar conductivity.[11]

Next, we calculated the concentration of ions in water over saturated YF_3 from its solubility product[4]:

$$YF_3(s) + H_2O \rightleftharpoons Y^{3+}_{aq} + 3F^-_{aq}$$

$$pK_s(YF_3) = 18.4;\ K_s(YF_3) = [Y^{3+}][F^-]^3 = 3.98 * 10^{-19};\ 3[Y^{3+}] = [F^-]$$

$$[Y^{3+}] = 11\,\mu M;\ [F^-] = 33\,\mu M$$

Meanwhile, YbF_3 has higher solubility[9]:

$$pK_s(YbF_3) = 16.6;\ [Yb^{3+}] = 31\,\mu M;\ [F^-] = 93\,\mu M$$

This implies that, similar to Na^+, Yb^{3+} ions are removed faster than Y^{3+}.
The influence of ErF_3 can be neglected, as it represents only 2% of lanthanide composition in our UCNPs and has a $pK_s(ErF_3)$=17.5, in between YF_3 and YbF_3.

Next, we calculated the concentration of Y^{3+} and F^- in the dialysate as a function of time. For this, we made following assumptions:
1) The rate limiting step in mass transport at such concentrations is diffusion. The dissolution process is assumed to be faster, even when a large proportion of UCNP surface is shielded by coating. Diffusion is assumed to follow Fick's laws.[12]
2) Solid phase dissolves faster than ion transport occurs, so the ion concentration inside the dialysis vessel is constant, and changes only in the dialysate.
3) Both compartments separated by the membrane are mixed much faster than diffusion occurs. Thus, diffusion *through membrane* is considered to be the rate limiting step.
4) Charge effects and transmembrane potentials arising from the difference in ion concentrations inside and outside of the dialysis vessel are neglected. Both inner and outer solutions are considered

to be neutral, so conservation of charge requires diffusion to be limited by the diffusion of the slowest ion (Y^{3+} with diffusion coefficient of 5.5×10^{-10} m^2/s in water at 298 K [13]). This is a reasonable assumption for such highly diluted solutions.
5) No polymer coating or solid phase is expected to escape through membrane into the dialysate. This is a reasonable assumption, as free polymers tend to assemble in micelles of about 10 nm in size,[2] and the MWCO of membrane is more than 4 times lower than the average mass of individual polymer chains.
6) The dispersion of UCNPs has already reached a dissolution equilibrium at the start of the experiment.
7) The permeability coefficient (K) of regenerated cellulose for small inorganic ions is assumed to be 0.2. Values for the Spectra/Por membrane used in this study are not openly available, but a literature survey for a set of commercially available regenerated cellulose membranes[14] suggests that their permeability for small inorganic ions is very similar.

From these assumptions, we obtained the following system of parameters and differential equations:

$$C(Y^{3+})_{\text{UCNP dispersion}} = 11\ \mu\text{M} = constant$$
$$C(F^{-})_{\text{UCNP dispersion}} = 33\ \mu\text{M} = constant$$
$$\frac{\partial}{\partial t}C(Y^{3+})_{\text{dialysate}} = \frac{KAD}{l}\left(C(Y^{3+})_{\text{UCNP dispersion}} - C(Y^{3+})_{\text{dialysate}}\right)$$
$$\frac{\partial}{\partial t}C(F^{-})_{\text{dialysate}} = \frac{KAD}{l}\left(C(F^{-})_{\text{UCNP dispersion}} - C(F^{-})_{\text{dialysate}}\right)$$
$$K = 0.2;\ A = 1.32\ cm^2;\ D = 5.5 * 10^{-10}\ m^2\ s^{-1};\ l = 1\ mm$$

To calculate the conductivity, we use an infinite dilution approximation, which is reasonable for our concentrations. The conductivity of the dialysate can be expressed from the Kohlrausch law as:

$$G = \sum_i z_i \lambda_i C_i = 3\lambda^{+}(Y^{3+})C(Y^{3+})_{\text{dialysate}} + \lambda^{-}(F^{-})C(F^{-})_{\text{dialysate}}$$

where λ are the ionic conductivityies at infinite dilution for the respective ions at 298 K.

Considering that mQ water is in equilibrium with atmospheric CO_2 (which doesn't substantially influence YF_3 dissolution), we obtain a final expression for conductivity:

$$G = G_{\text{mQ + CO}_2} + 3\lambda^{+}(Y^{3+})C(Y^{3+})_{\text{dialysate}} + \lambda^{-}(F^{-})C(F^{-})_{\text{dialysate}}$$
$$G_{\text{mQ + CO}_2} = 1.5\ \mu S\ cm^{-2}$$

The conductivity of mQ water in equilibrium with atmospheric CO_2 was measured experimentally using the aforementioned setup.

By solving the system of differential equations for the dialysate concentration over time, the theoretical curve for the conductivity dependence over time could be calculated (Fig. S6C). Calculations were performed in Wolfram Mathematica 11.0. Calculation file is available upon request.

Large-ROI microscopy: effect of illumination, correlation of initial intensity and luminescence loss

To confirm that the dissolution of UCNPs does not only happen in the sample volume that is continuously illuminated by the laser, we immobilized UCNPs on PEI in the presence of 1 mM NaF as described above. First, 49 (7×7) individual images of the sample luminescence were taken every 20 μm and stitched into a large ROI. Then, the well was flushed thrice with mQ water and incubated in the dark for 150 min. Finally, the well was flushed thrice with 1 mM NaF and the imaging procedure was repeated.

Raw images are shown on Fig. S7A and B. Images of the highlighted region before and after incubation with water are provided on Fig S7C. Similarly to luminescence homogeneity tests, spots were fitted with free-angle 2D elliptic Gaussian. The intensity histograms were built for all spots and for diffraction-limited spots (Fig. S7D and E).

A total disappearance of the luminescence for most particles and a strong decrease for others were observed. Specifically, from 5458 particle spots (3189 taken as diffraction-limited) only 1342 (990) retained significant luminescence. Taking the luminescence intensity of the disappeared spots as zero, the overall luminescence loss of the sample was found to be 88% (82% for the diffraction-limited spots), similar to the measurements on a small ROI performed under continuous illumination. Thus, we conclude that continuous laser illumination did not affect the dissolution kinetics of our sample and that it occurred in the same way across illuminated and unlit sample regions.

To find out whether the extent of luminescence loss could be predicted from initial particle intensity, we correlated initial particle intensity with its luminescence loss after 150 min in water. This correlation was performed for all particles in the sample (Fig. S7F). We observed virtually no correlation between these parameters, albeit a slight prevalence of high luminescence loss (50 to 100%) was noted for large aggregates. Thus, we conclude that the extent of luminescence loss cannot be reliably predicted from the initial particle intensity.

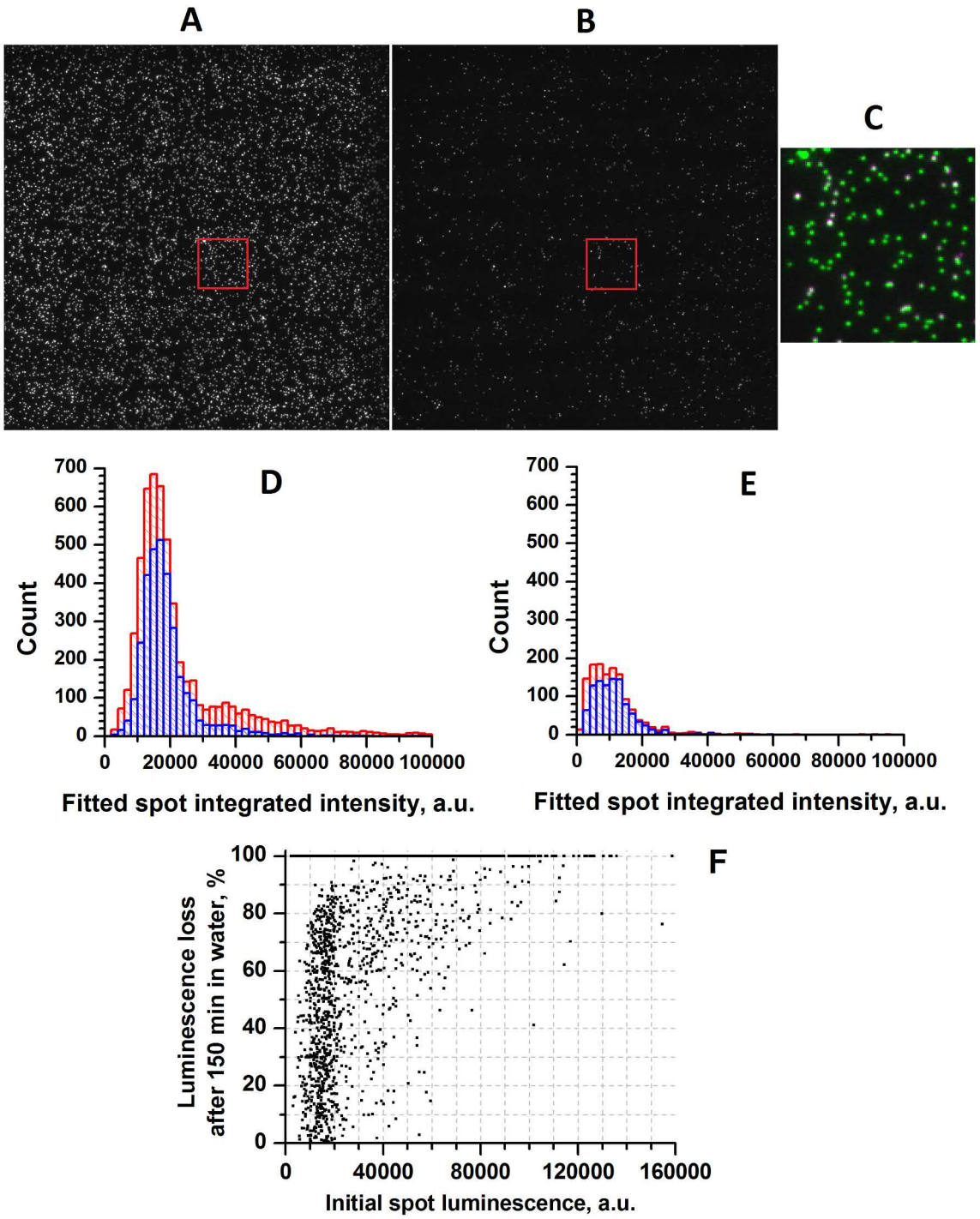

Figure S10. Wide-field imaging and size distribution of water-dispersed polymer-coated UCNPs adsorbed on a thin layer of PEI in 1 mM NaF before and after incubation for 150 min in water. A: 144×144 µm ROI in the red channel, stitched from 49 (7×7) individual wide-field images. Excitation was at 980 nm with an intensity of 8 kW/cm^2. B: Same region imaged after incubation for 150 min in water. C: Overlap of 20×20 µm boxed regions from A (green) and B (magenta). A slight shift in the positions of some particles is commonly observed after multiple flushes. D: Histogram of the integrated intensities of the 2D free-angle elliptic gaussian spot fits from image A (red) and the same histogram excluding spots that have widths more than 25% larger than the theoretical diffraction limit (blue). E: Same for image B. F: Correlation of the extent of luminescence loss and initial particle intensity.

Videomicroscopy of individual polymer-coated UCNPs in aqueous conditions was performed with the aforementioned luminescence imaging setup, using Ibidi µ-Slide 8 well glass bottom plates. First, the wells were filled with 300 µL of 1 mg/mL solution of branched polyethylenimine (PEI, Sigma-Aldrich, lot #408727) in 20 mM Tris buffer, pH 7.2. The wells were incubated for 20 min at room temperature, allowing PEI to electrostatically bind to the glass. Then, the solution was removed by a pipette and washed 2 times with 300 µL of 1 mM aqueous NaF. The stock particle dispersion was 100-fold diluted and added to the well. After 2 min of incubation, the particle dispersion was removed, and the wells with immobilized particles were washed 3 times with 300 µL of 1 mM NaF, before starting the imaging sequence. Images were taken every 30 seconds. As mechanical manipulations (e.g. washing) on the microscope stage induce local strains and movement of the microscopy oil, a focus drift was observed. To compensate, the focus was adjusted manually throughout the experiment to provide a stable diffraction-limited PSF. After 25 min, the buffer was removed from the well and the particles were washed 3 times with 300 µL of deionized water or 30 µM NaF in water. For the 1 mM NaF condition, this step was omitted. After that, the imaging sequence was continued for ~150 min. Frames that gave a consistent change of spot width for all particles were deemed "out of focus" and discarded.
Wide-field videos of UCNP luminescence over time in different conditions are available in the Supporting Information section of the website of the journal (video files labeled "dissolution_1mM_NaF_to_water.avi", "dissolution_1mM_NaF_to_NaF30uM.avi" and "dissolution_1mM_NaF_continuous.avi", corresponding to particle dissolution in water, 30 µM NaF and 1 mM NaF, respectively). Raw uncompressed image stacks in TIFF format are available on request.

Wide-field images of polymer-coated UCNPs in fluoride buffers and magnified individual particles

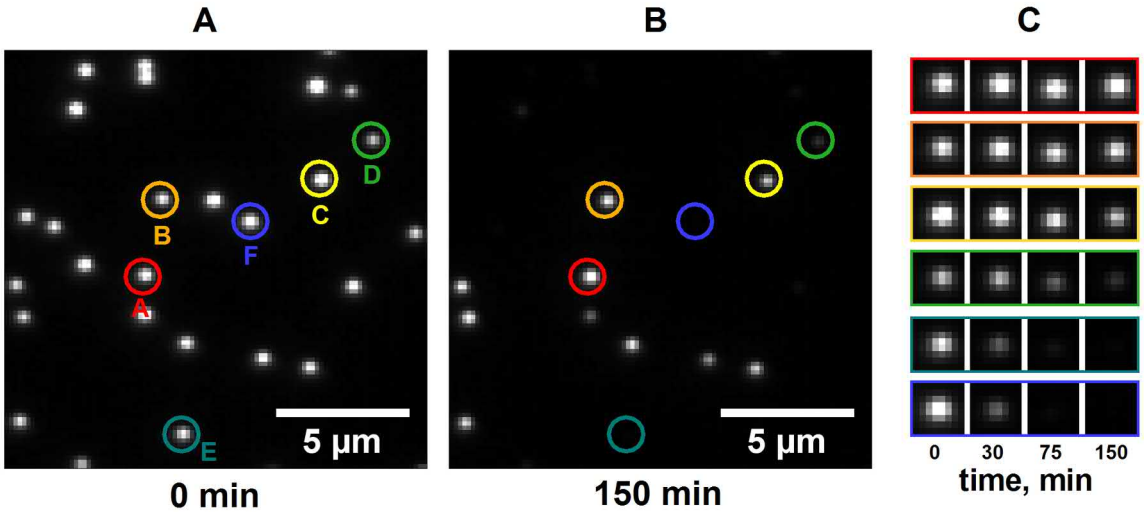

Figure S11. Luminescence over time of individual polymer-coated UCNPs in 30 µM sodium fluoride solution. Wide-field image of polymer-coated UCNPs in the red channel immediately after washing (A) and after 150 min incubation in 30 µM NaF (B), with several particles highlighted. (C) Time-dependent changes of the images of the highlighted particles (1.28×1.28 µm).

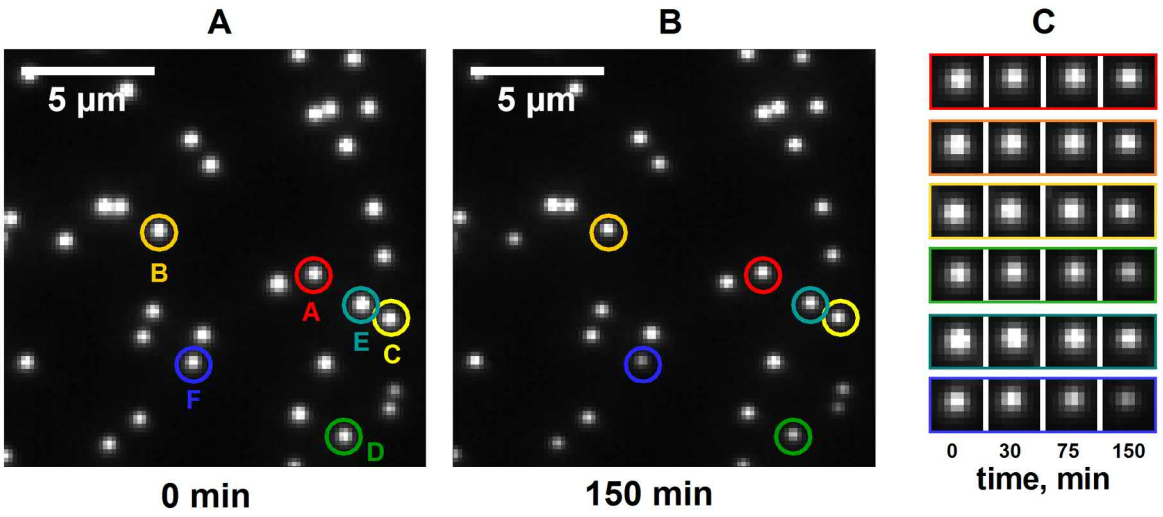

Figure S12. Luminescence over time of individual polymer-coated UCNPs in 1 mM sodium fluoride solution. Wide-field image of polymer-coated UCNPs in the red channel immediately after washing (A) and after 150 min incubation in 1 mM NaF (B), with several particles highlighted. (C) Time-dependent changes of the images of the highlighted particles (1.28×1.28 µm).

Measurements of the changes in UCNP luminescence over time in cuvette

To observe the dissolution-related effects at the ensemble level, we diluted by 100-fold the UCNP dispersions in deionized water, 30 µM NaF or 1 mM NaF, and continuously monitored the photon counts with a sensitive avalanche photodiode, using an integration time of 1 s. The results for the red and green emission intensities and the RTGR are shown in Fig. S10 (each curve is an average of two experiment repeats, smoothed with an 11-point normal-weighted rolling average).

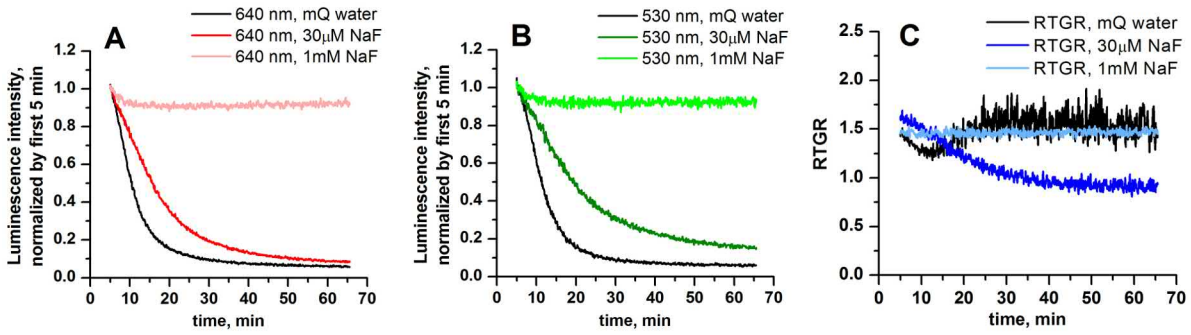

Figure S13. Cuvette measurements of the luminescence changes over time of polymer-coated UCNPs in aqueous solutions. A: red band. B: green band. C: red-to-green ratio.

Excitation intensity dependence of UCNP luminescence in the presence of 1 mM NaF

To investigate how the excitation intensity affects the UCNPs' band ratio, particles were immobilized on PEI in the presence of 1 mM NaF. The single particles in the center of the beam were illuminated with different excitation intensities by adjusting the laser power. To get a robust estimate of the RTGR values, the experiment was repeated 10 times over 30 minutes (Fig. S14, A). Focus drift was corrected by hand throughout the measurement. The particles showed a decrease in the RTGR value which correlated with the decrease in excitation intensity (Fig. S14, B).

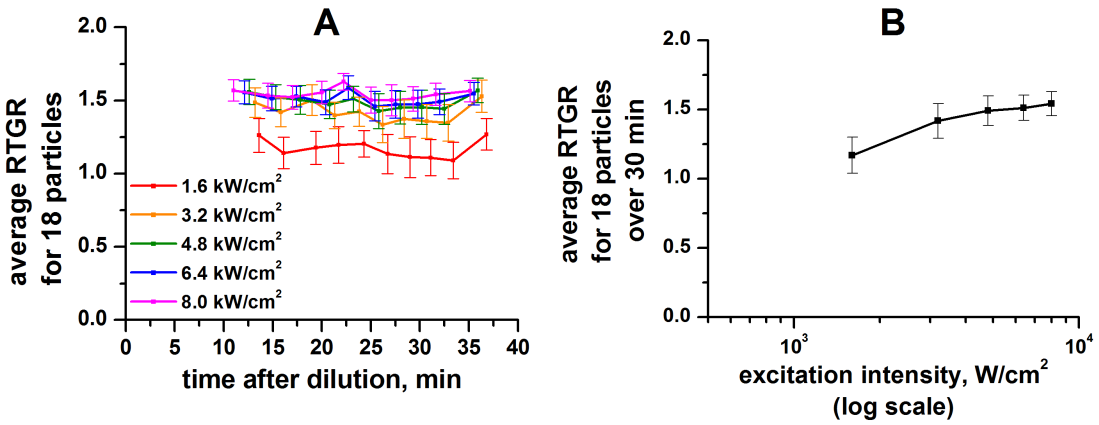

Figure S14. Excitation intensity dependence of UCNP red to green ratio (RTGR). A: Mean (+/- standard deviation) of RTGR values measured for 18 particles under different excitation intensities. Measurements were repeated 10 times over 30 minutes on the same field of view to check the stability over time. B: Average excitation intensity dependence of RTGR values, calculated as an average over 30 minutes.

References

1 S. Wilhelm, M. Kaiser, C. Würth, J. Heiland, C. Carrillo-Carrion, V. Muhr, O. S. Wolfbeis, W. J. Parak, U. Resch-Genger and T. Hirsch, *Nanoscale*, 2015, **7**, 1403–1410.

2 O. Dukhno, F. Przybilla, M. Collot, A. Klymchenko, V. Pivovarenko, M. Buchner, V. Muhr, T. Hirsch and Y. Mély, *Nanoscale*, 2017, **9**, 11994–12004.

3 S. Lahtinen, A. Lyytikäinen, H. Päkkilä, E. Hömppi, N. Perälä, M. Lastusaari and T. Soukka, *J. Phys. Chem. C*, 2017, **121**, 656–665.

4 T. Mioduski, C. Gumiński and D. Zeng, *Journal of Physical and Chemical Reference Data*, 2014, **43**, 013105.

5 Y. Suzaki and A. Tachibana, Applied Optics, 1975, 14, 2809.

6 A. D. Edelstein, M. A. Tsuchida, N. Amodaj, H. Pinkard, R. D. Vale and N. Stuurman, *J Biol Methods*, , DOI:10.14440/jbm.2014.36.

7 S. Preibisch, S. Saalfeld and P. Tomancak, *Bioinformatics*, 2009, **25**, 1463–1465.

8 GDSC ImageJ Plugins : ImageJ : ... : Sussex Centre for Genome Damage and Stability : Lifesci : Schools : Staff : University of Sussex, http://www.sussex.ac.uk/gdsc/intranet/microscopy/imagej/gdsc_plugins, (accessed March 29, 2018).

9 S. Saalfeld, *mpicbg: Fiji module for image transformation and related algorithms*, 2018.

10 T. Mioduski, C. Gumiński and D. Zeng, *Journal of Physical and Chemical Reference Data*, 2015, **44**, 023102.

11 E. Mauerhofer, K. P. Zhernosekov and F. Rösch, *Radiochimica Acta*, 2009, **91**, 473–478.

12 A. Fick, *Journal of Membrane Science*, 1995, **100**, 33–38.

13 A. C. Lasaga, *Kinetic Theory in the Earth Sciences*, Princeton University Press, 2014.

14 C. K. Colton, K. A. Smith, E. W. Merrill and P. C. Farrell, *J. Biomed. Mater. Res.*, 1971, **5**, 459–488.

Part 4. SPT with UCNPs in living cells

Proof of concept 2D and 3D SPT experiments with UCNPs have been described by a few research groups (*Jo et al., 2015; Nam et al., 2011; Wang et al., 2018*). As a model system, the groups used nanoparticle endocytosis and their subsequent transport along the microtubules inside cells. These reports showed that employing UCNPs in SPT has benefits of high SNR and uninterrupted stable luminescence, two features extremely valuable for tracking experiments.

Endosomes are only one of the myriad possible tracking targets in cells. Unfortunately, regular water-dispersed nanoparticles lack specificity for recognition of the vast majority of biological molecules and/or assemblies. Adapting UCNPs towards targeted tracking by attaching targeting modules to their surface would allow them to track any target of interest, similarly to existing experiments with QDs, organic dyes or gold nanoparticles. To our knowledge, targeted tracking with UCNPs has not been done yet. We decided to explore this idea further.

To estimate if UCNPs would yield reasonable information, we decided to perform as a model experiment, the tracking of FcεRI receptors on the surface of murine basophilic cells (line RBL-2H3), using UCNPs decorated with IgE antibody. This system was very well investigated via a variety of methods (including SPT), so that multiple datasets are available to compare with our experiment. As a basis for our experiment, we selected the study by the group of Diane Lidke (*Andrews et al., 2008*), which involved tracking of quantum dots attached to IgE by biotin-streptavidin linkage. We reasoned that out of the possible methods to decorate the particle with biomolecules, biotin-streptavidin linkage is likely one of the simplest, as biotin can be easily attached to the polymer surface, and subsequently connected to a biotinylated IgE with a streptavidin in between (so-called “sandwich” linkage strategy).

Our findings are summarized in the following manuscript, which we aim to publish as soon as we will finish all supporting experiments.

Publication 3.

Targeted membrane receptor tracking with upconversion nanoparticles

Targeted single-particle tracking with upconverting nanoparticles

Oleksii Dukhno[1], Frederic Przybilla[1], Vanille Greiner[1], Julien Godet[1], Lilia Kuzmenko[1], Verena Muhr[2], Markus Buchner[2], Thomas Hirsch[2] and Yves Mely[1*]*

1) Laboratory of Biomaging and Pathologies, UMR 7021 CNRS, University of Strasbourg, 67000 Strasbourg, France
2) Institute of Analytical Chemistry, Chemo- and Biosensors, University of Regensburg, 93040 Regensburg, Germany

** Corresponding authors:* oleksii.dukhno@unistra.fr, yves.mely@unistra.fr

Keywords: upconversion, nanoparticles, single-particle tracking, single-molecule microscopy

Abstract

Single-particle tracking (SPT) is a powerful technique for elucidating the behavior of cell components in real time, especially in regards to microrheology. SPT is based upon labeling the component of interest with a luminophore, such as a fluorescent dye or a light-scattering gold nanoparticle, and visualizing its movement by real-time microscopy, typically in wide-field mode. However, SPT suffers from mediocre performance of luminophores: fluorescent dyes and proteins have low brightness; luminescent quantum dots usually suffer from sporadic switching behavior that interferes with track acquisition and interpretation; and light-scattering gold nanoparticles require custom experimental setups and have a lower limit on particle size for tracking purposes.

In recent years, upconverting nanoparticles (UCNPs) have been shown to be a promising luminophore that enables background-free anti-Stokes luminescence imaging. They are also attractive for SPT applications due to their extreme photostability and steady non-blinking luminescence. Previously, SPT with UCNPs has been shown on nanoparticle endocytosis. However, targeted SPT with UCNPs that specifically bind to biomolecules of interest has not been achieved yet.

In this work, we provided a proof-of-concept experiment of targeted SPT with UCNPs, and show the superior performance of UCNPs in comparison to organic dyes and quantum dots. As a benchmark system for assessing UCNP performance, we tracked FcεRI receptors on the surface of RBL-2H3 cell membranes using UCNP-IgE conjugates, and noted good agreement of our results with literature data. Importantly, the biotin-streptavidin architecture of our system allows easy swapping of targeting elements, allowing the particles to be used towards different targets. Overall, this report lays the groundwork towards practical application of UCNPs in SPT.

Introduction

Single-particle tracking (SPT) is a unique fluorescence microscopy technique that allows direct visualization of the movement of individual molecules and particles. SPT is based on monitoring optically active labels attached to the targets using an optical videomicroscope. If the labels are distributed sufficiently sparsely, they form an image with multiple diffraction-limited *spots*, from which the labels can be precisely localized, with a typical of ~30 nm and down to ~1 nm depending on the setup. Afterwards, label positions over time can be combined into trajectories, colloquially known as *tracks*. Tracks contain information on the movement of the label, which can provide insights on the microrheology of the sample, the preferential areas for target localization, as well as the kinetics and dynamics of target transport in the sample, etc. A variety of methods for

track analysis exist, the most popular one being the mean square displacement (MSD) analysis. **[REF Manzo/Garcia-Parajo 2015]**

SPT is primarily utilized in cell biology, to monitor the diffusion of membrane components and intracellular trafficking of biomolecules and assemblies (e.g. endosomes).**[REF Kusumi 2014 Nat Chem Bio]** Typically, the label is comprised of two elements: the *optically active element*, e.g. a fluorescent molecule, and the *specificity element* (*targeting element*), e.g. antibody or aptamer, which is responsible for the attachment of the label to the desired target. Common implementation of SPT in biology is based on fluorescence microscopy with organic dyes or quantum dots (QDs), and light-scattering microscopy (dark-field microscopy) with gold nanoparticles (GNPs). SPT has very specific demands for labels. The labels must be bright enough to yield sufficient signal-to-noise ratio at exposure times of ~50 ms and less, their luminescence should be long-lived and uninterrupted to yield information-rich well-connected tracks, and they should exhibit minimal non-specific interactions with their environment.

Currently, SPT is limited by the suboptimal performance of the label optical elements that are commonly used. Organic dyes show sporadic photoswitching (*blinking*) and fast photobleaching, leading to short, information-poor tracks. Common QDs are strongly blinking as well. Imaging of organic dyes and QDs is also affected by the autofluorescence of biological samples, especially with excitation in the blue and UV region. Meanwhile, GNPs show sufficient light scattering only at sizes above 40 nm, which can perturb the target's behavior. Imaging with GNPs is limited also by the background resulting from the light scattering by the sample, and lacks the possibility for imaging with multiple spectral channels, as GNPs scatter light at all wavelengths.**[REF Shen/Landes Chem Rev 2017, Clausen/Lagerholm 2011]**

In recent years, new luminophores, called upconverting nanoparticles (UCNPs), have attracted considerable attention from the imaging community in biology.**[REF Zhou Nat Nano 2015]** UCNPs are based on the upconversion phenomenon, consisting in the sequential absorption of several low-energy photons with subsequent emission of a single high-energy photon. This process shares some similarity with two-photon absorption (TPA), but differs from it by its very high efficiency. Typical UCNPs are spherical particles of 10-100 nm in diameter, constructed from an ionic fluoride material that is doped at high concentration with two lanthanide ions, acting as sensitizers and emitters. The sensitizers absorb low-energy photons and sequentially transfer their energy to the emitter ion. As a result, the emitter ion gets excited into an intermediate excited state and then into a high-energy excited state, from which it can emit a high-energy photon. A frequently used UCNP composition is $NaYF_4$: 20% Yb^{3+}, 2% Er^{3+}, in which Yb^{3+} is the sensitizer, absorbing at 980 nm, and Er^{3+} is the emitter, emitting at 540 nm and 660 nm. The UCNP emission can be tuned by the ion composition and doping strategy.**[REF Haase/Schafer 2011]** To render particles compatible with biological conditions, multiple strategies for water dispersibility and surface decoration have been developed.**[REF Sedlmeier/Gorris Chem Soc Rev 2015]**

The key advantage of UCNPs for biological imaging is their capability to emit with a large anti-Stokes shift under excitation from cheap continuous-wave diode lasers. As no biological object exhibits upconversion, imaging with UCNPs benefits immensely from the absence of autofluorescence. UCNPs are also extremely resistant to photobleaching, and the non-cooperative emission of hundreds of individual ions inside the particle ensures stable and non-blinking luminescence.**[REF Gargas 2014 Nat Nano]** These properties make UCNPs particularly attractive optically active elements for SPT labels. Several groups have pioneered 2D and 3D tracking with UCNPs by following endocytosis of nanoparticles as they were gradually uptaken by living cells. **[REF Nam 2011, Jo 2015] [REF Jin's group 2018 article]** Related work used optically trapped upconversion microparticles to measure cell viscosity. **[REF Rodriguez-Sevilla 2016]** In another relevant report, instantaneous ballistic velocity of diffusing UCNPs was measured by using UCNPs with a temperature-sensitive spectral response.**[REF CDS Brites Nat Nano 2016]**

However, to our best knowledge, no *targeted* tracking of UCNPs has been reported so far, and the existing efforts have been limited to the observation of nanoparticle endocytosis. While endocytosis is an important process to be monitored by SPT, particularly in the field of drug delivery, there are multiple other potential targets in which SPT could benefit from the improved label performance provided by UCNPs.
In this study, we provide a framework for constructing and imaging highly homogeneous SPT labels based on UCNPs with an attached targeting moiety. To validate the performance of UCNPs, we performed SPT of FcεRI receptors on the membrane of RBL-2H3 mast cells, using IgE antibody as a targeting element bound to UCNP. This FcεRI receptor/IgE system has been previously investigated by SPT with "conventional" labels **[REF Andrews/Lidke Nat Cell Bio 2008, Ozawa FEBS Letters 1996, Wells PNAS 2009]**, allowing us to compare the performance of our UCNPs. The latter were found superior to other SPT label optical elements, notably in respect to their photostability, steady non-blinking luminescence, and elimination of autofluorescence due to their large anti-Stokes shift. We used a "plug-and-play" biotin-streptavidin label architecture, which allows to rapidly substitute the targeting element by any biotinylated biomolecule. This architecture can be used for the tracking of any target, similarly to SPT with commercially available streptavidin-coated QDs. Our findings underline the potential of UCNPs for SPT, and serve as a basis towards practical autofluorescence-free targeted SPT.

Results and discussion

Based on the ample literature on the design of nanoparticle-based luminescent labels,**[REF Holzinger 2014 Frontiers in Chem, REF Biju 2013 Chem Soc Rev]** we chose a biotin-streptavidin non-covalent linkage as our preferred strategy for constructing our label (Fig. 1). Specifically, we decided to opt for streptavidin-decorated particles and biotinylated targeting elements. Binding of biotin to avidin is one of the strongest non-covalent links in biology. Avidin is a homotetrameric protein with four binding sites for biotin. Streptavidin, a variant of avidin, has improved binding affinity and also high stability against temperature and pH extremes. The high strength of biotin-streptavidin linkage and its stability in biological conditions ensure that the label does not spontaneously disassemble during the experiment. Also, this approach masks the particle surface with protein, providing it with a "built-in" protein corona. This positively impacts the particle performance by mitigating the interactions of the surface charges with the environment and making the non-specific binding profile more predictable, as already shown for similar streptavidin-coated nanoparticles used for SPT.

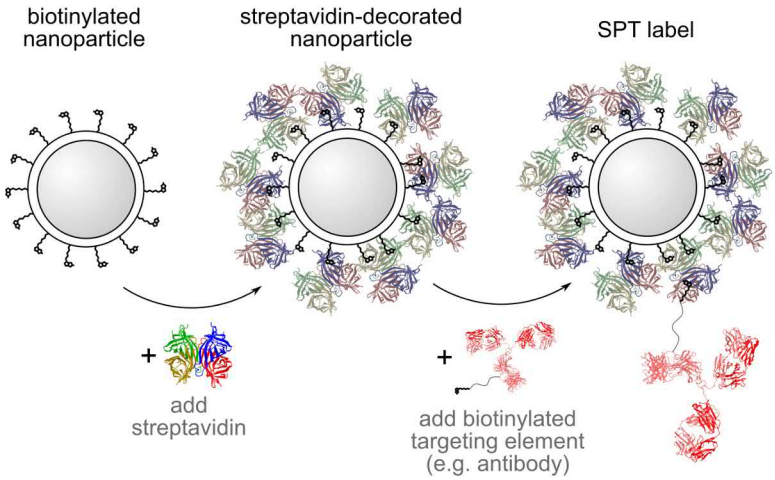

Figure 1. Biotin-streptavidin-biotin strategy for assembling SPT labels (elements not to scale).

To develop our SPT labels, we synthesized homogeneously doped UCNPs of composition $NaYF_4$: 20% Yb, 2% Er UCNPs, 30 nm in diameter. This matrix material and doping composition were chosen due to the well characterized synthesis and properties of these UCNPs. **[REF Wilhelm 2015 Nanoscale]** Also, homogeneous doping simplifies the particle preparation protocol. The particle size was chosen to be sufficiently large for ease of imaging (as bigger particles contain more ions and therefore are brighter) but also sufficiently small to not significantly perturb the diffusion of the target cell membrane receptor. **[REF Mascalchi Soft Matter 2012]** The characterization of the raw UCNPs synthesized for this work is provided on Fig. 2. Full particle characterization is available in Supporting Information (Section A).

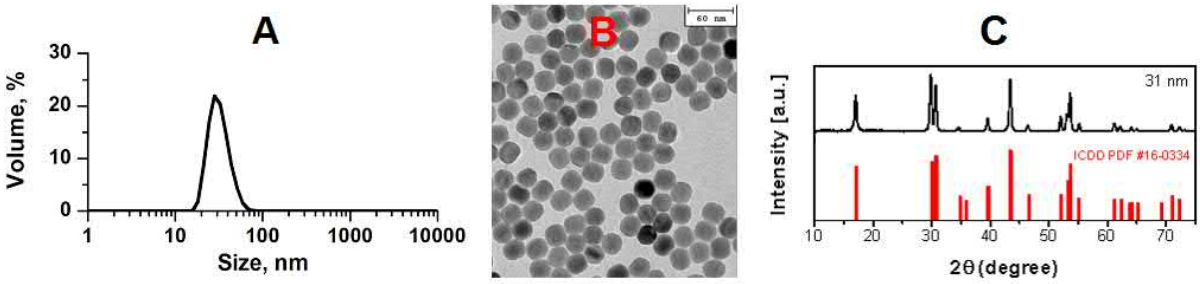

Figure 2. Characterization of raw UCNPs after synthesis. A: Dynamic light scattering (DLS) size distribution of raw UCNP dispersion in cyclohexane. B: Transmission electron microscopy (TEM) of dried diluted UCNP dispersion. C: X-ray diffraction (XRD) spectra of UCNPs and β-$NaYF_4$.

As the initial particles are dispersible only in organic solvents due to a layer of oleic acid on their surface, we coated the particles with a layer of amphiphilic polymer to make them water-dispersible (Fig. 3). Polymer synthesis, characterization, particle coating and purification protocol are provided in Supporting Information (Section B). During synthesis, the polymer was decorated by biotin groups attached to a short PEG spacer. Upon exposure to water, the PEG spacer is strongly hydrated, thus preventing the biotin group from "hiding" inside the hydrophobic layer between the particle and coating surface. The spacer also aids the subsequent formation of the link with streptavidin, ensuring that there is enough space between the UCNP surface and streptavidin so that biotin can fully position itself in the streptavidin binding pocket.

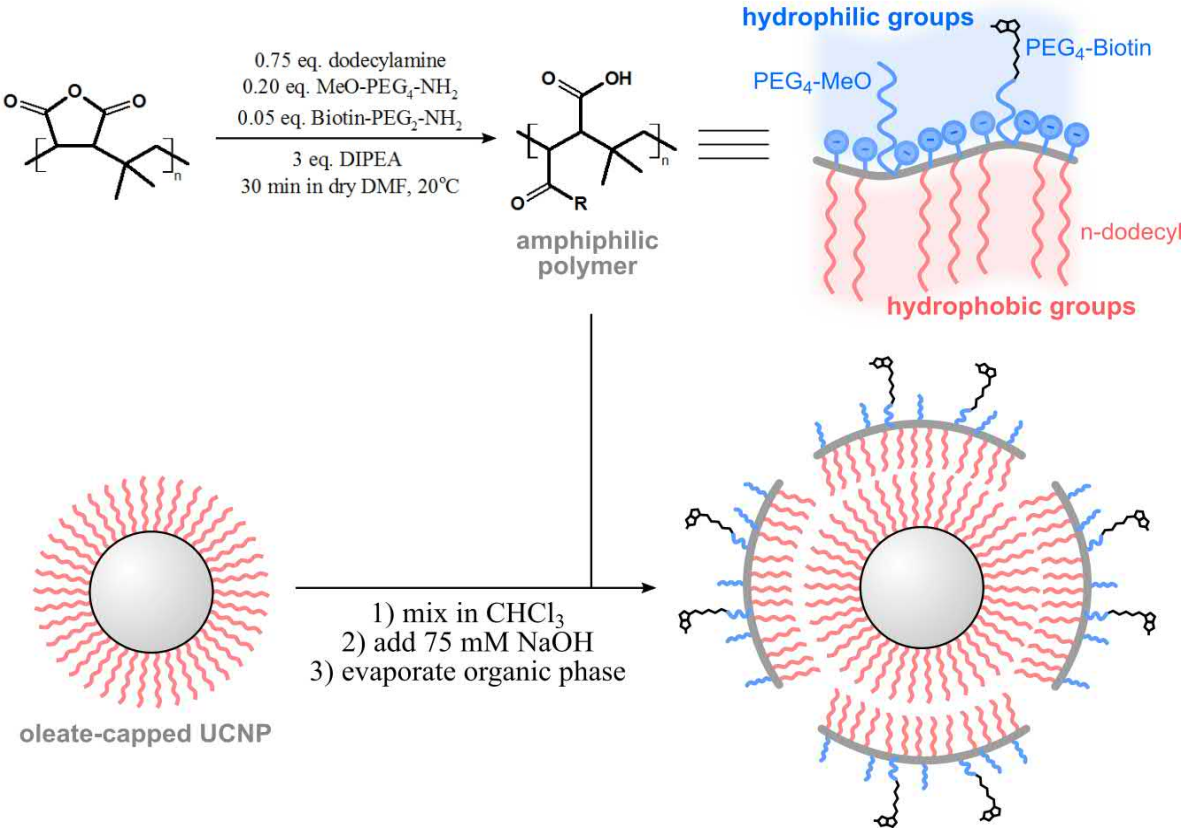

Figure 3. Scheme of biotinylated amphiphilic polymer synthesis and formation of biotinylated particle coating (elements not to scale).

Besides the luminescence properties, there are multiple other required qualities for an SPT label. The most important ones are the label homogeneity in respect both to particle size and luminescence, strong link between the particle and the targeting element, and low non-specific binding. High label homogeneity is required so that individual labels can be clearly distinguished from label oligomers or aggregates based on their luminescence alone, as the diffraction-limited nature of wide-field imaging precludes sizing the nanoparticles based on the spot shape (unless the aggregate is particularly large). To ensure that the coated UCNPs were homogeneous in size, we performed dynamic light scattering (DLS).

Afterwards, the particles were coated with streptavidin and purified by size-exclusion chromatography. Full protocol and particle characterization are available in Supporting Information (Section C). We also confirmed the monodispersity of the particles by comparing their DLS size distributions before and after coating. We noted a slight amount of particle oligomerization, however the vast majority of the particles remained individual (Fig. 4B).

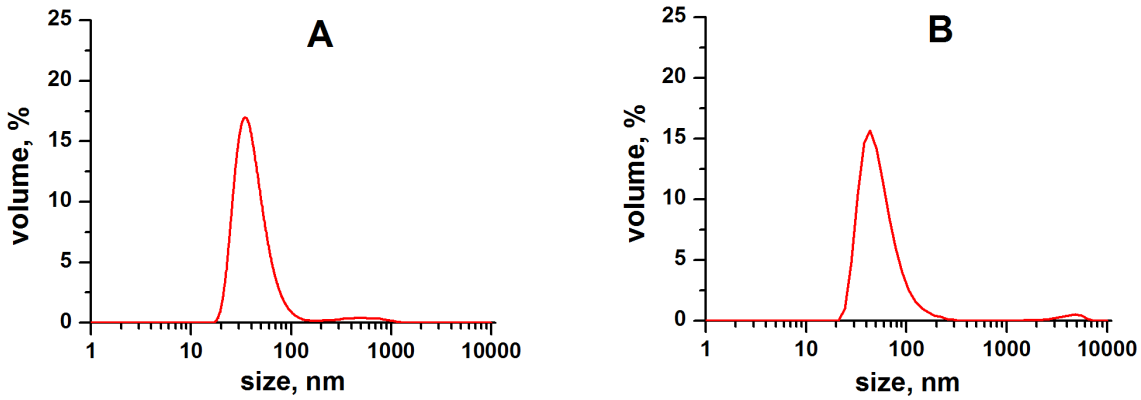

Figure 4. Characterization of polymer-coated and streptavidin- decorated particles. A: DLS curve of polymer-coated particles. B: same for streptavidin-decorated particles.

To confirm that the streptavidin bound to the particle surface had the possibility to connect to multiple biotins, we mixed biotinylated particles with various quantities of streptavidin. Particle aggregation caused by the addition of low amounts of streptavidin confirmed that streptavidin bound to particle surface was afterwards able to bind to another particle and thus, cross-link particles together (Fig. 5).

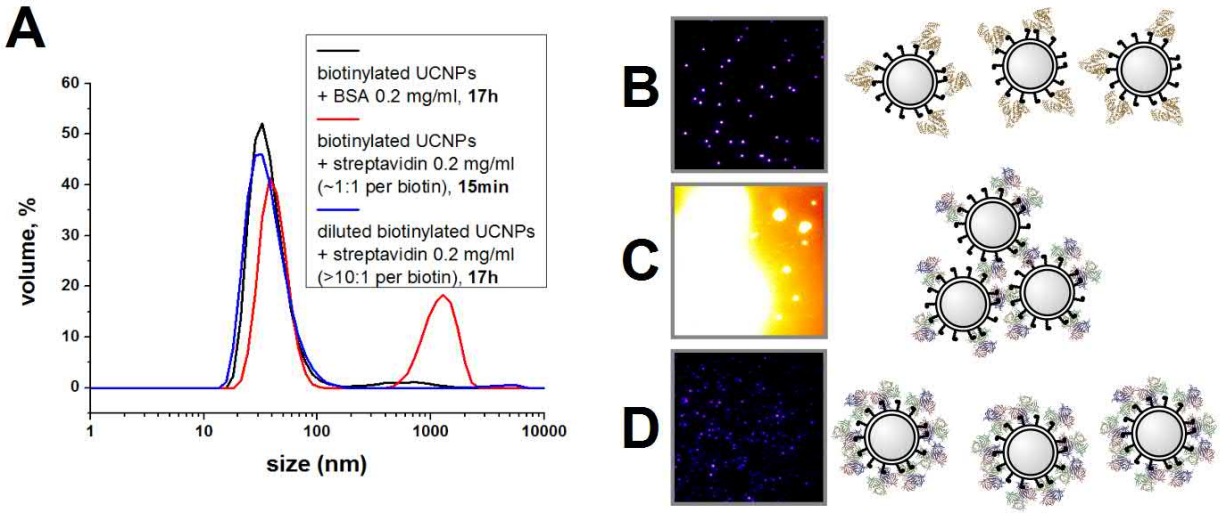

Figure 5. Particle aggregation induced by varying amounts of added streptavidin. A: DLS size distributions for biotinylated UCNPs mixed with bovine serum albumin (BSA) (black), low concentration of streptavidin (red), and large excess of streptavidin (blue). B-D: Wide-field luminescence microscopy for respective samples and cartoon representations of the resulting particles: (B) individual UCNPs with corona of BSA, (C) UCNPs cross-linked with low amount of streptavidin, and (D) individual UCNPs with bound streptavidin.

To assess UCNPs as optical elements of SPT labels, we used them for the tracking of FcεRI receptors on the membrane of RBL-2H3 mast cells, a system that was extensively investigated by SPT with other labels. **[REF Andrews/Lidke Nat Cell Bio 2008, Ozawa FEBS Letters 1996, Wells PNAS 2009]**

Mast cells are immune cells that express on their surface a family of *Fc receptors* that can selectively bind the Fc fragment of antibodies. Upon binding, the antibody retains its selectivity towards its antigen, as this selectivity is governed by the Fab region, which remains accessible to the extracellular space. Cells that possess antibodies bound on their surface are called *primed*. If a multivalent antigen is captured by multiple antibodies on the surface of a primed cell, the receptors can *cross-link*, initiating a cascade of signaling processes inside the cell. This ultimately leads to a process called *degranulation*, in which mast cells expel vesicles (*granules*) filled with a mixture of various inflammation-promoting proteins and chemical compounds (e.g. histamine, cytokines) (Fig. 6). This process is also accompanied by membrane deformations, known as *membrane ruffling*. Overall, degranulation of mast cells plays a central part in mammal allergic response.**[REF Gilfillan Nat Rev 2006]**

Previous SPT studies of labeled FcεRI-IgE complexes showed that they exhibited a partially restricted lateral diffusion in the cell membrane. Upon cross-linking, the receptors formed aggregates, which were much less mobile.**[REF Andrews/Lidke Nat Cell Bio 2008, Ozawa FEBS Letters 1996, Wells PNAS 2009]** As the diffusion behaviors of primed and cross-linked receptors were extensively studied in the literature, we will be able to compare them with our data and thus, assess the performance of UCNP-based labels for SPT.

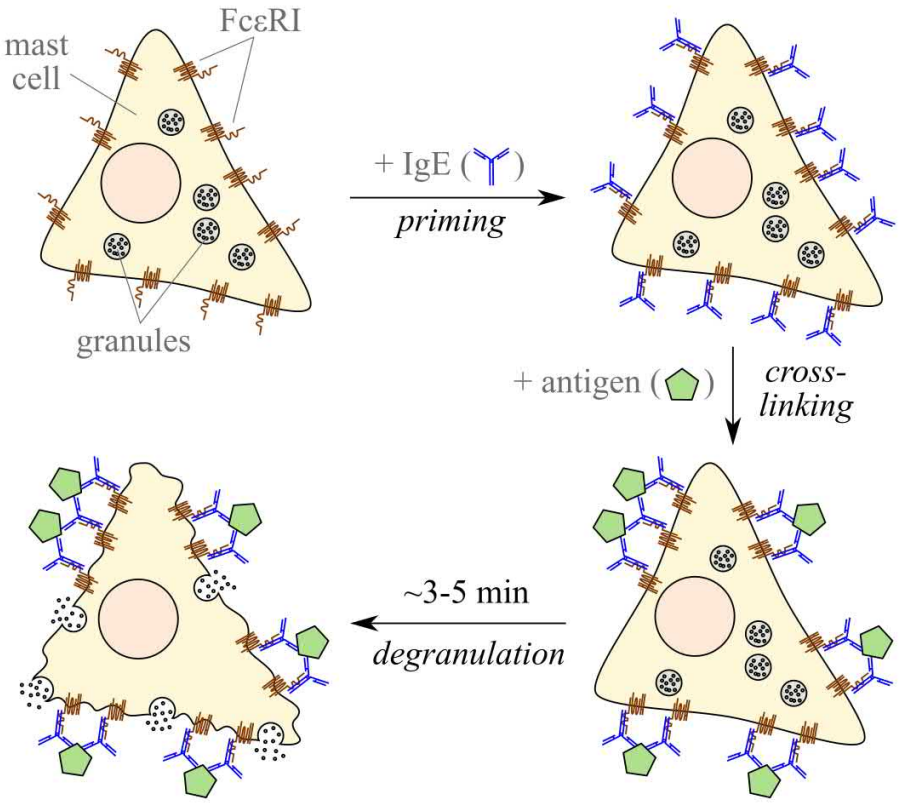

Figure 6. Simplified description of degranulation process in mast cells. Upon priming with IgE followed by receptor-antibody complex cross-linking by a multivalent antigen, cells begin to release granule contents and ruffle the membrane.

To prepare UCNP-IgE conjugates, we biotinylated IgE by a reagent comprised of biotin coupled to a moderately hydrophobic linker with an activated ester on the other end. To minimize the perturbation of the antibody functions, we adjusted the reagent concentrations in such a manner that approximately 2/3 of antibodies were left intact, while ~1/3 would have a single biotin

attached, and a negligible quantity would be labeled with 2 or more biotins. Full protocol and antibody characterization are available in Supporting Information, Section D. The use of a linker induces some space between the antibody and the biotin, ensuring that the biotin can properly position itself in the binding pocket. The linker also provides the UCNP-bound antibody with more conformational freedom for its subsequent binding to the receptor and the antigen.

To ensure that the cells had a preserved degranulation behavior and that our reagents were active, we performed a colorimetric β-hexosaminidase assay, which is widely used to quantify the extent of mast cell degranulation. Briefly, granules of RBL-2H3 cells contain enzymes, including β-hexosaminidase. An appropriate substrate, 4-nitrophenyl N-acetyl-β-D-glucosaminide, can be cleaved by this enzyme, resulting in the release of 4-nitrophenol, which efficiently absorbs light at 405 nm in basic conditions (pH>10). Thus, incubating the supernatant after degranulation with the substrate compound allows to quantify the concentration of the released enzyme, and estimate the extent of degranulation. As antibody, we used IgE, which selectively recognizes dinitrophenyl (DNP), a small chemical group. As a multivalent antigen, we used BSA decorated with multiple DNP groups (DNP-BSA). As DNP is not found natively in RBL cells, common cell media or buffers, this allows to minimize the accidental activation of cells caused by off-target recognition. Degranulation of mast cells was observed upon priming with IgE and cross-linking with DNP-BSA (Figure 7), allowing ~15% of total enzyme content to escape with granules, as observed for degranulating sample (+IgE +DNP-BSA on figure). If cells are not primed, or cross-linking agent is absent, no significant degranulation was observed. This behavior is in line with previous reports on degranulation with the same antibody/antigen pair in appropriate concentrations (100 ng/mL IgE and 50 ng/mL DNP-BSA).**[REF Pandey/Cockroft J Immunol 2004]** Full assay protocol is available in Supporting information, Section E.

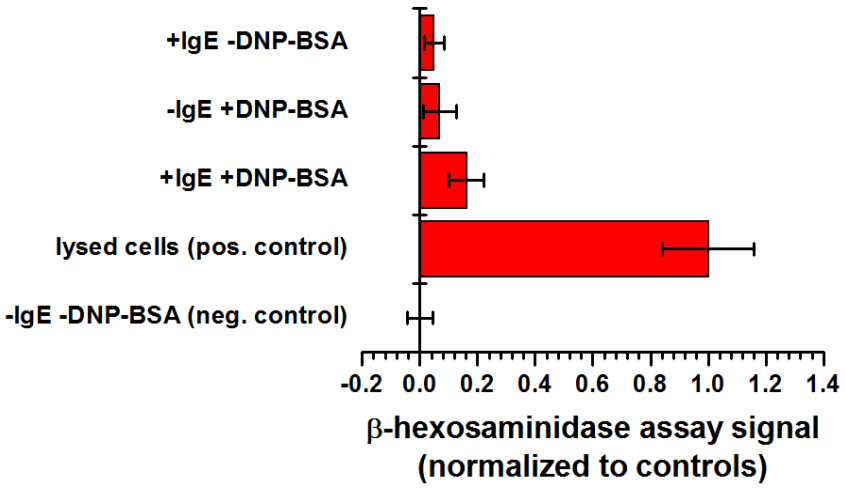

Figure 7. Quantification of degranulation by the β-hexosaminidase assay, as determined by the absorption of released 4-nitrophenol at 405 nm in basic conditions. Values represent the average for 5 experimental repeats; error bars represent 1 standard deviation. Data and standard deviations have been rescaled so that average values of the negative control and to positive control correspond to 0 and 1, respectively. Normalized in this way, the data represents the amount of the released β-hexosaminidase compared to its total quantity in cells. Priming IgE concentration was 100 ng/mL, cross-linking DNP-BSA concentration was 50 ng/mL.

We also performed bright-field phase contrast videomicroscopy to observe the degranulation process. Upon exposure to antibody, most cells did not show any change in morphology (Fig. 8A). In contrast, upon degranulation induction by exposure to the antigen, the vast majority of cells showed rapid changes in morphology. Within 2-3 min, cells were observed to spread, generating a

large number of extensions in all directions, as well as large ruffles on their membrane (Fig. 8B). All morphological observations are consistent with literature data on RBL-2H3 cell degranulation. **[REF Sahara J Histochem/Cytochem 1990, Pandey J Immunol 2004, and Spudich Cell Motility 1994]** We also noted that a minority of cells exhibited a degranulation-like morphological response immediately upon priming by the antibody. Literature suggests this behavior to be induced by the IgE antibodies sourced from our supplier (Sigma-Aldrich, SPE-7 clone).**[REF Bax Sci Rep 2015]**

Fig. 8C shows cells that were not primed with IgE, but exposed to antigen did not show any significant morphological changes after 15 min of exposure to antigen, suggesting that no degranulation took place.

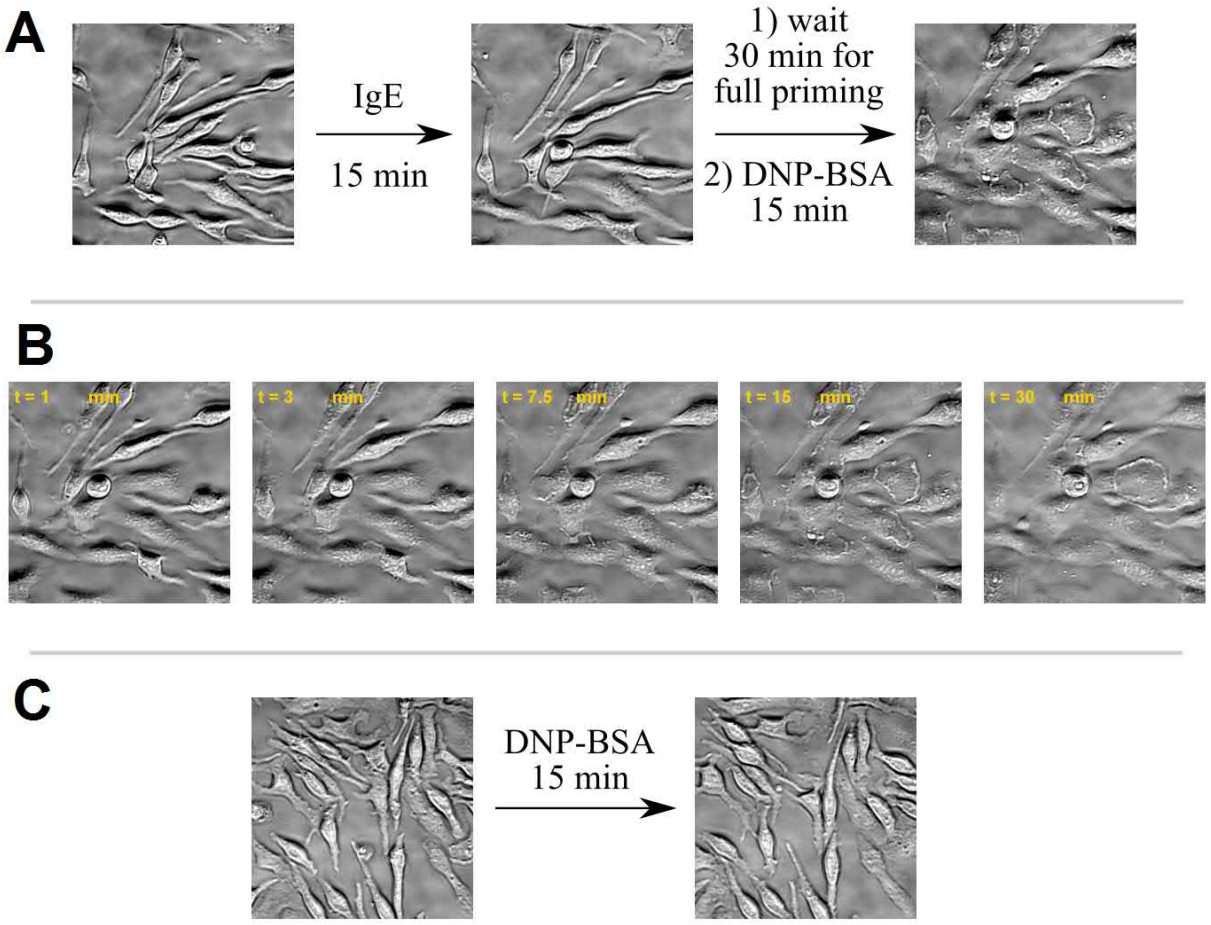

Figure 8. Bright-field phase contrast videomicroscopy of RBL-2H3 cells upon priming with anti-DNP IgE and crosslinking with DNP-BSA. A: Images of cells primed with 100 ng/mL IgE over 30 min. The cells were then activated with 50 ng/mL DNP-BSA. B: Images of the degranulation process in the same sample, taken at 1, 3, 7.5, 15, and 30 min, respectively. Cells rapidly spread on the surface and exhibit characteristic ruffles on the membrane. C: Non-primed sample did not show any marked differences in morphology in the presence of antigen. All images are 160x160 µm.

In a next step, we assembled the label by directly mixing the biotinylated IgE with streptavidin-coated UCNPs, and performed imaging and tracking experiments. Cells were grown in glass-bottom multi-well plates, mounted on the microscope at 37°C, exposed to the label, and imaged in bright-field and wide-field luminescence microscopy mode with 980 nm excitation to visualize UCNPs. To reduce the background luminescence caused by particles out of focus

(inherent in wide-field imaging), we employed total internal reflection (TIRF) excitation geometry. This allows exciting only the particles within ~200 nm from the surface, ensuring that the particles visible on the image are bound either to the glass surface or to the basal surface of the adherent cells. Full experimental conditions and protocol for the tracking experiment are available in Supporting Information, Section F. To validate our microscopy setup and our analysis, we performed tracking of the Brownian diffusion of polymer-coated UCNPs in water-glycerine mixtures of known viscosity. Experiment protocol and results are available in Supporting Information, Section I.

Fig. 9 shows typical cell images during different steps of the experiment. Of note, we observed a rather high degree of non-specific binding of UCNP-IgE labels to the glass surface, resulting in immobile particles and particle aggregates all over the field of view. Videos of cells in wide-field upconversion luminescence mode were taken 5 min after adding UCNP-IgE conjugates and then again 15 min, after adding the antigens. To make sure that cells were showing "native" receptor diffusion behavior, the experiment was performed at 37ºC on a microscope equipped with a heated incubator covering the stage and the objective turret.

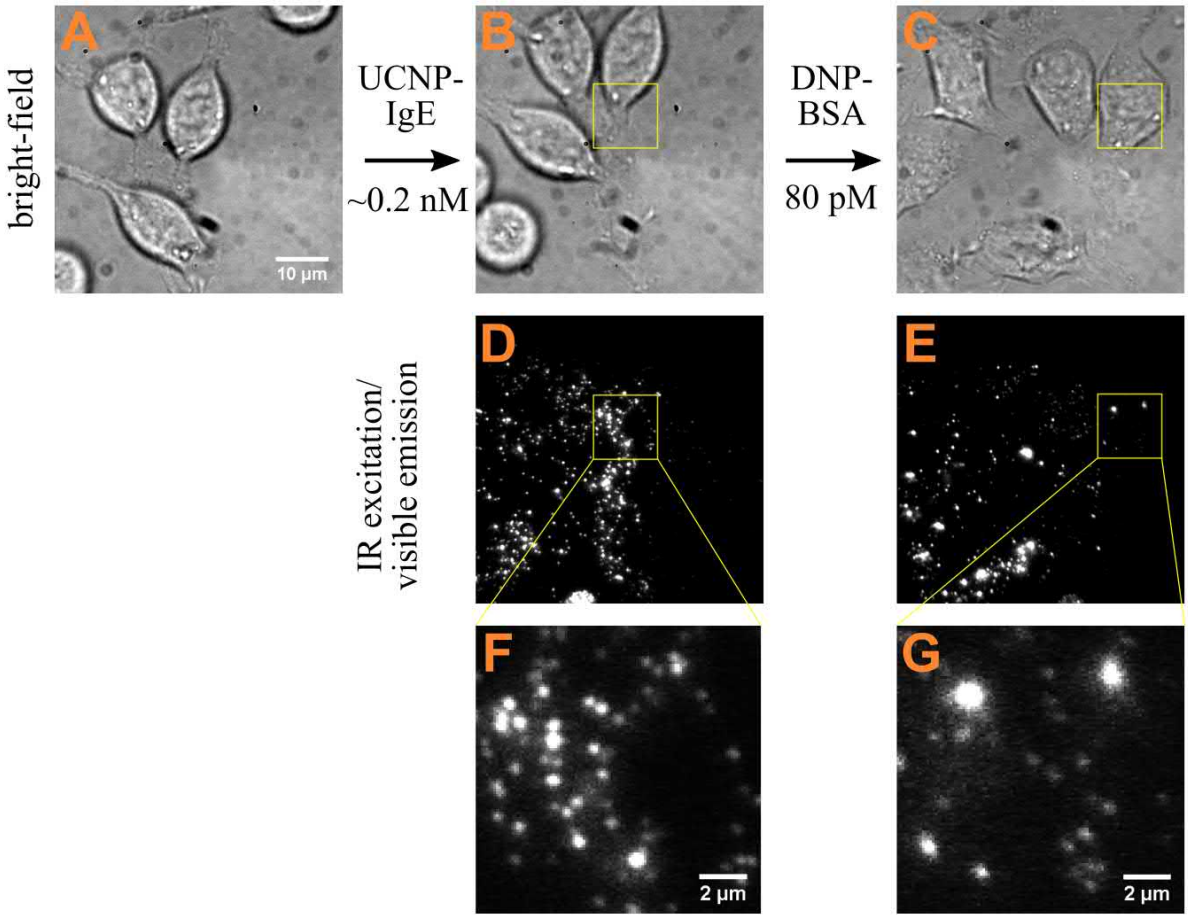

Figure 9. Images of adherent RBL-2H3 cells used for single-particle tracking of UCNP-IgE conjugates on basal cell membranes. A, B, C: Bright-field images of cells before adding UCNP-IgE conjugates, after adding conjugates, and after adding DNP-BSA, respectively. D,E: Wide-field upconversion luminescence images of cells in B and C, respectively. F, G: close-ups of boxed regions in D and E, respectively.

The tracks were analyzed through a mean square displacement (MSD) analysis. Briefly, MSD values are the means of the squares of the particle displacements at positions separated by a given time lag. MSD-time lag dependence contains information about the particle diffusion coefficient and also allows to qualitatively estimate the nature of the movement of the particles: directed (superdiffusive), Brownian, restricted (subdiffusive) or immobile.**[REF Kusumi 1993 Biophys J]** In our case, we used a 2D diffusion model, which is appropriate for receptors moving laterally in the basal cell membrane, and thus, approximately perpendicular to the collection beam. The full protocol for the tracking analysis is available in Supporting Information, Section G. We removed immobile particle tracks from the overall track population, as well as particles with highly directed movement, which are typically associated with nanoparticle endocytosis. To assess the possible heating effects induced by laser illumination, we estimated the heating effects in our microscope configuration based on comparison with literature (Supporting Information, Section J). Our estimation suggested no significant heating effects in our setup that could induce substantial perturbation of the investigated system.

Fig. 10 shows examples of tracks and diffusion coefficient distributions for our experiment. The median diffusion coefficient we obtained for UCNP-IgE-FcεRI complexes before and after adding antigen was 0.046±0.068 (n=459) and 0.024±0.037 $\mu m^2/s$ (n=647), respectively. It is important to note that the distributions of diffusion coefficients are frequently asymmetric and also can be heavily tailed. Because of this, values of diffusion coefficients are given as median value ± interquartile range (IQR). Importantly, these values are close to values reported with quantum dots and organic dyes in similar experimental conditions.**[REF Andrews/Lidke 2008 Nat Cell Bio, Andrews/Lidke 2009 Immunity, Shelby 2013 Biophys J, Spendier 2012 FEBS Letters, Schwartz 2014 ACS Chem Bio]**

Table 1 illustrates the comparison with literature. Overall, our data are in good agreement with previous reports, albeit the movement of the receptors cross-linked by antigen seems to be slightly faster. This may be induced by the rather large size of the UCNP, which reduces the access of the freely diffusing antigen molecules to the receptor-bound antibody, and thus partially inhibits the cross-linking. The diffusion coefficient value is slightly lower, which we associate with the significant size of our UCNPs (~45 nm hydrodynamic diameter). While such particle size is likely not enough to slow down receptor diffusion due to drag forces (diffusion coefficient of the free particle ~15 $\mu m^2/s$), the larger particle surface has more possibility for spurious non-specific interactions with the membrane, which could temporarily hinder the particle movement.

Unlike in experiments with quantum dots and/or organic dyes, our analysis does not require any compensation for blinking, as UCNPs provide uninterrupted tracks with uniform, consistent luminescence, with an average track length of approx. 280 frames for 1000 frame acquisitions. Upon manual inspection, the majority of interruptions in the tracks were found to be caused by the particle going out of focus. Such high track consistency greatly simplifies the data analysis and reduces the risk of erroneously mismatching two particles in close proximity to each other.

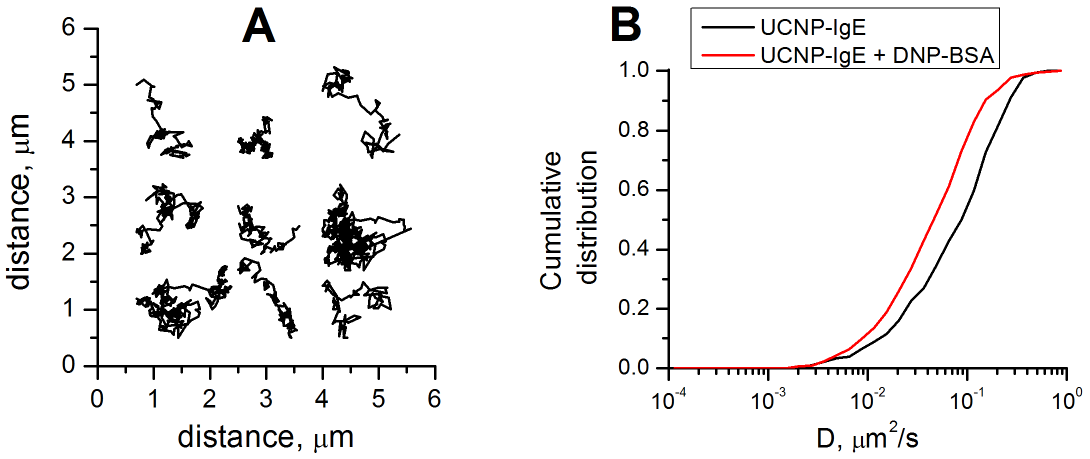

Figure 10. Examples of UCNP-IgE tracks and cumulative histograms of lateral diffusion coefficients of UCNP-IgE-FcεRI complexes obtained from SPT. A: Examples of UCNP-IgE tracks, of 100-900 total points in length, recorded at 33 fps. B: Normalized cumulative histogram of diffusion coefficients for tracks before and after addition of the antigen.

report	**imaging geometry and membrane surface**	**label**	**D, μm²/s (median ± IQR)**	**D, μm²/s (median ± IQR) in the presence of the antigen**	**T, °C**	**exposure time**
Andrews et al., 2009 (Immunity)	unspecified	QD-IgE	0.086±0.075	0.008±0.021	34-36	30 ms
Andrews et al., 2008 (Nat Cell Biol)	epi, apical surface	QD-IgE	0.074±0.065	0.010±0.038	37	30 ms
Andrews et al., 2008 (Nat Cell Biol)	TIRF, basal surface	QD-IgE	0.077±0.065	unspecified	37	30 ms
Shelby et al., 2013 (Biophys J)	TIRF, basal surface	Alexa 647-IgE and Alexa 532-IgE	0.1	0.02	22	33 ms
Spendier et al., 2012 (FEBS Letters)	TIRF, basal surface of a cell in contact with an antigen-containing supported bilayer	Alexa 488-IgE and ATTO 647-IgE	0.041±0.042 or 0.170±0.145, depending on morphology of the contact spot	unspecified	37	50 ms
Schwartz et al., 2014 (ACS Chem Bio)	TIRF, basal surface	FcεRI-MG-FAP	0.15	unspecified	37	50 ms
this report	TIRF, basal surface	UCNP-IgE	0.046±0.068	0.024±0.037	37	30 ms
this report	TIRF, basal surface	Alexa 647-IgE	0.078±0.069	0.051±0.064	37	30 ms

Table 1. Comparison of the values of diffusion coefficients with literature data.

We have also tried to perform SPT with organic dyes to further validate our results. For this, IgE was conjugated with Alexa Fluor 647, an organic dye with far-red emission (to reduce autofluorescence background), high brightness, and reasonable photostability. Details for antibody preparation and experiment conditions are available in Supporting Information, Section H. Overall, we found SPT based on this dye to yield unreliable results due to blinking and bleaching, which precluded us from collecting robust tracks: only ~15% of collected tracks passed the fit quality criteria to be included in diffusion coefficient distribution (in comparison to ~60% for UCNPs, see Supporting Information, Section G for details on track quality criteria).

In regards to brightness, UCNPs were found to be 10-fold brighter than Alexa Fluor 647 organic dyes (~$2*10^4$ vs ~$2*10^3$ camera counts per spot per frame, respectively; organic dye brightness being taken for unbleached dyes at the start of acquisition). The higher brightness of UCNPs improves the reliability of obtained data and can also allow imaging at faster framerates. For UCNPs, the average localization accuracy was calculated to be 50±43 nm from the MSD curve vertical offset and slope.**[REF Michalet 2010 Phys Rev E]** Meanwhile, the localization accuracy for the dye experiments was larger, at 59±47 nm, in line with lower brightness of organic dyes.

As UCNPs are known to be prone to dissolution at high dilutions employed in optical microscopy,**[REF Dukhno et al. 2018 Nanoscale, Lahtinen et al. 2017 J Phys Chem C]** we also performed particle dissolution experiments to confirm that the UCNPs retain their luminescence during the experiment. Description and details are shown in Supporting Information, Section K. Overall, we noted that our particles were resistant towards the dissolution in HBSS, the buffer we employed throughout the measurements.

Conclusions and perspectives

To summarize, we constructed a label for targeted SPT of biological molecules in living cells, incorporating UCNPs as an alternative luminophore. Our protocols allow to produce particles with the high monodispersity that is necessary for SPT applications. Our label shows improved performance in SPT experiments, especially in regards to brightness, photostability, absence of background, and continuous luminescence. The uninterrupted, long tracks allow robust collection of information about the tracked target's behavior, and also simplify data analysis. A significant advantage of our label lies in its easy adaptation towards various targets: the binding specificity of the particles can be changed merely by reacting the particles with a different biotinylated targeting element (e.g. antibody or small-molecule ligand). Biotinylated targeting elements can be easily prepared or purchased from commercial suppliers.

Further improvement in the use of UCNPs for SPT applications may be anticipated by using the smaller and brighter UCNPs optimized specifically for optical microscopy, which have been very recently developed.**[REF Tian/Schuck Nat Comm 2018, Wang Light Sci&App 2018, maybe someone else]** Moreover, due to the gradual increase of background luminescence resulting from internalized UCNPs, a promising future direction for research would be the introduction of controllable luminescence switching mechanisms in UCNP-based SPT labels. This would allow to switch off background-inducing UCNPs and then incubate the cells with a fresh portion of labels to continue robust, high-contrast SPT over extended periods of time.

Supporting information

Section A. Characterization of the raw oleate-capped UCNPs.

Unless otherwise specified, reagents and solvents were bought from Sigma-Aldrich (Merck) and used without further purification.

The XRD patterns were recorded on a Huber Guinier G670 diffractometer with a Cu-Kα source (λ = 1.54060 Å).

DLS measurements were performed in Brand plastic cuvettes (lot #759015) on a Malvern Zetasizer Nano ZSP instrument. Correlation curves for each sample were accumulated 3 times. Curves were treated with the "normal resolution" parameter set. All presented DLS curves represent size distributions by volume.

The luminescence spectrum of the prepared UCNPs and the spectrometry setup are shown on Figure SA1. Spectrometry was performed in 1 cm BRAND plastic cuvettes (Cat. No. 7590-15). Excitation at 980 nm was provided by a continuous-wave laser coupled to a single mode fiber with a maximum output of 350 mW (Qphotonics, QFBGLD-980-350). Excitation light was focused in the cuvette by a lens of 100 mm focal distance. Excitation power inside the cuvette was calculated to be 6.2 kW/cm^2 (for calculation of beam intensity, please refer to the supporting information of our previous article **[REF Dukhno 2018]**). The scattered/reemitted laser light was removed by a short-pass filter (Semrock, E700SP). Spectra were recorded by a fiber spectrometer (Avaspec ULS3648).

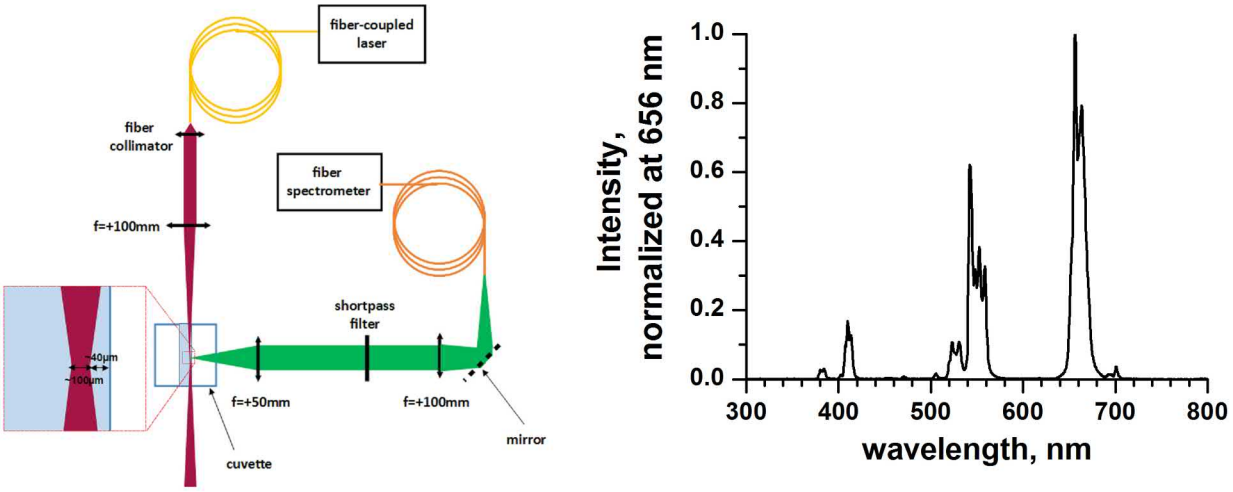

Figure SA1. Homemade spectrometry setup and luminescence spectrum of a dispersion of the raw oleate-capped UCNPs in cyclohexane, with excitation at 980 nm and 6.2 kW/cm^2 average intensity in the collection volume.

Section B. Synthesis and characterization of the biotinylated amphiphilic polymer and coating/purification protocol for UCNPs.

Synthesis of the biotinylated polymer was performed via the following protocol.

In a 10 mL flask with a septum flushed with argon, 31 mg dodecylamine (168 µmol, 0.75 eq), 4.3 mg of biotin-PEG$_2$-amine (11.2 µmol, 0.05 eq, Iris Biotech) and 9.3 mg of methoxy-PEG$_4$-amine (44.7 µmol, 0.2 eq, Iris Biotech) were dissolved in 2 mL anhydrous DMF under magnetic stirring. Diisopropylethylamine (130 µL, 746 µmol, 3.33eq) was added. The solution was stirred for 5 min, then 34.4 mg of poly(isobutylene-alt-maleic anhydride) were added in one portion (224 µmol, 1 eq anhydride per monomer, avg MW 6000). The vessel was purged

with argon a second time, and the reaction mass was stirred at 25ºC for 30 min. Afterwards, a drop of water (approx. 70 eq) was added to hydrolize any leftover unreacted anhydride. The reaction mass was evaporated, redissolved in dichloromethane, filtered through Celite 545 and purified on a LH20 size-exclusion chromatography column (eluent: dichloromethane-methanol 1:1 v/v). The presence of polymer in elutes was followed by drying drops from fractions on a glass coverslip and observing the formation of opaque films upon drying in air. Combined elutes were evaporated. Yield was 55 mg (70%, assuming all carboxyls have formed a salt with DIPEA). The product was redissolved in 3.14 mL spectral grade chloroform, corresponding to a 0.05 M concentration. This solution was used as a stock solution for subsequent coating of UCNPs.

For coating UCNPs, we used a modified version of the protocol of Wilhelm et al., 2015. **[REF Wilhelm 2015]** 165 µL of UCNPs with 31 nm diameter (5 mg/mL) in cyclohexane were mixed with 140 µL 0.05 M polymer dispersion in chloroform, sonicated for 1 min at room temperature, and evaporated. The residue was redispersed in 0.35 mL spectral grade chloroform and sonicated for 1 min at room temperature. Then, 1 mL 10 mM NaOH was added. The mixture was vortexed for 30 s and slowly evaporated on a rotavap (high speed of rotation and low vacuum are recommended to avoid bumping), until only aqueous phase remained. Afterwards, evaporation was continued until ~0.5 mL aqueous phase remained. Obtained phase was filtered through a Millex GP syringe filter (0.22 µm pore size). The filter was washed with 10 mM NaOH into the filtrate to a final combined volume of 1 mL.

The obtained dispersion contained a mixture of UCNPs and empty polymer micelles. For purification, 100 µL of UCNP dispersion were diluted in 900 µL centrifugation buffer (10 mM NaOH + 1 mM NaF), and centrifuged at 4ºC and 12500 g over 1 h. Top 970 µL of the supernatant were carefully removed by pipette to avoid disturbing the UCNP-rich section of the dispersion at the bottom. Afterwards, 970 µL of the centrifugation buffer were added to UCNP dispersion and vortexed for 30 s. The centrifugation was repeated in the same conditions, and the top 970 µL of supernatant were again removed. 70 µL of centrifugation buffer were added to UCNPs, and the dispersion was vortexed for 30 s. The obtained dispersion was used as a stock dispersion of biotinylated UCNPs for the streptavidin decoration step.

To estimate the quantity of biotins per particle, we used the following formula:

$$N_{\text{biotins per particle}} = \phi_{coating}\, \chi_{\text{biotinylation}}\, \pi \left(d_{\text{UCNP}} + 2\, d_{\text{amphiphilic layer}} \right) N_{\text{monomers per nm}^2}$$

where $\varphi_{coating}$ is the percentage of UCNP surface coated by the polymer (~70% for this coating method **[REF Wilhelm 2015]**), $\chi_{biotinylation}$ is the percentage of bound biotins per monomer (here 5%), d_{UCNP} is the UCNP diameter (31 nm), $d_{amphiphilic\ layer}$ is the thickness of the amphiphilic layer (~1 nm for this coating method **[REF Wilhelm 2015]**), $N_{monomers\ per\ nm2}$ is the amount of monomers per area unit of the particle surface (~0.5 nm^{-2} for this coating method **[REF Wilhelm 2015]**). Our calculation leads to **~570 biotins per each UCNP**.

Section C. Preparation and characterization of streptavidin-decorated UCNPs.

For decorating UCNPs with streptavidin, 90 µL of biotinylated UCNP dispersion in a low-protein-binding Eppendorf tube (Eppendorf) was mixed with 9 µL 10 mg/ml BSA in purification buffer (20 mM Tris, 50 mM NaCl, 1 mM NaF) and gently vortexed over 20 s. Then, the mixture was incubated over 30 min at room temperature. This treatment forms a BSA corona weakly bound to the polymer on the surface of the nanoparticles, which is in constant exchange with the bulk BSA proteins in dispersion, with an average protein residing time of ~100 s, based on literature reports. **[REF Röcker/Parak 2009]**

Afterwards, the nanoparticle dispersion was mixed with 9 µL 10 mg/ml streptavidin dispersed in purification buffer. The mixture was immediately gently vortexed. Obtained dispersion was incubated with gentle shaking over 120 min at 37°C. During incubation, BSA molecules occasionally detach from the UCNP surface. Upon this event, the slightly smaller streptavidin molecules can occupy the vacant space on the particle surface and reorient themselves until they bind an available biotin on the particle surface. This results in streptavidin proteins being irreversibly bound to the particle. Over time, more and more BSA proteins are gradually replaced by streptavidin. We stress that this method works only if the BSA corona is introduced before coating UCNPs with streptavidin. We noticed that if the streptavidin is added directly to the "naked" biotinylated nanoparticles, the high concentrations of both particles and streptavidin induce partial oligomerization and aggregation of the sample immediately upon mixing, visible in DLS (data not shown). This effect persists even if a large excess of streptavidin is used.

To remove excess streptavidin from the particle surface, we performed size-exclusion chromatography using a small gravity-fed column filled with 5 ml Sephacryl S300-HR gel (GE Healthcare). After collecting the void volume (~1.5 ml), fractions were collected with 80 µL volume each. DLS of each fraction was measured to confirm the presence of the particles by total scattering count rate on the detector (Fig. SC1, A) and simultaneously assess the presence of proteins (Fig. SC1, B).

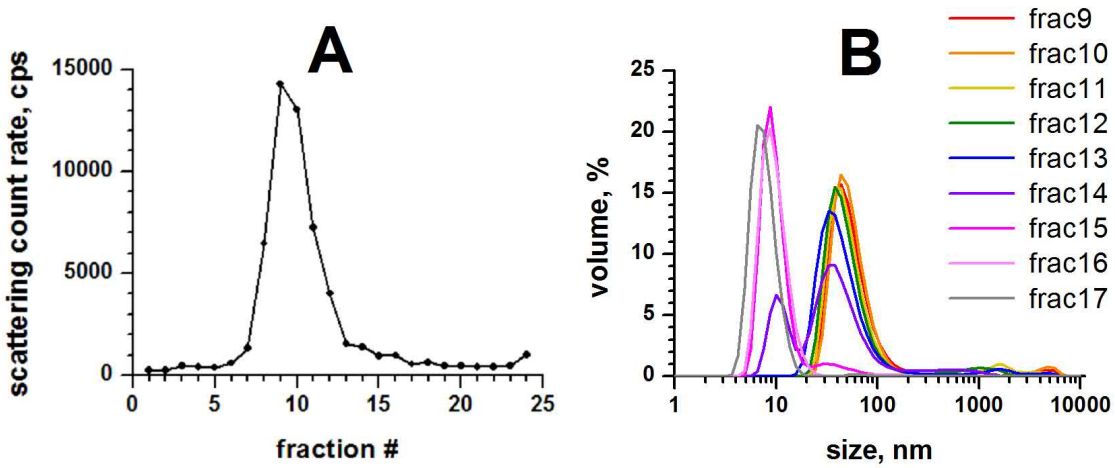

Figure SC1. DLS instrument detector count rate and size distributions for fractions that significantly scattered light. A: scattering count rate for collected fractions. A peak with significant light scattering is clearly visible for fractions 8-12, and a slight "shoulder is present for fractions 13-17. B: DLS volume distributions for respective fractions. Later fractions show a gradual shift in the peak of the calculated volume distribution from ~45 nm, corresponding to individual streptavidin-coated UCNPs, to ~7 nm, corresponding to the diameter of BSA or streptavidin with a ~1 nm thick coordinated water/ion shell.

Assuming a 100% yield during the particle coating step and taking into account the dilution of the particles imposed by purification steps, the estimated concentration of UCNPs in the obtained dispersion was found to be ~3 nM.

To estimate the amount of streptavidin proteins per particle, one has to consider the non-negligible size of the streptavidin protein relative to the UCNP. At first approximation, streptavidin can be assumed to be spherical with 5 nm diameter, based on its structure.**[REF PDB entry 1MK5]** The problem is then reduced to packing spheres of ~5 nm in diameter on a surface of a sphere approximately 33 nm in diameter (to include also the radius). While the exact solution of problems

of this kind is an open mathematical problem, these problems can be easily numerically simulated, or estimated using slightly suboptimal approximate solutions such as phyllotactic coating of surfaces.**[REF Mughal 2011 Phys Rev Lett]**

Fig. SC2 shows an example of packing for our case. The quantity of sterically permitted streptavidins is estimated to be approximately **150 per each UCNP**. This is ~4 times smaller than quantity of permitted biotins per particle, meaning that the reaction is likely to be sterically limited. We note that the actual quantity of streptavidins can be slightly higher or lower, dependent on its actual non-spherical geometry and the streptavidin packing proceeding gradually and in irreversible manner, resulting in possible "holes" between suboptimally packed neighbouring molecules.

The quantity of streptavidin necessary for the reaction is found to be approximately 25 μg/ml (3 nM UCNP concentration * 150 streptavidins per particle * 55 KDa molecular mass). This means that the coating with streptavidin is performed with at least a 37-fold molar excess of streptavidin, suggesting that the particle surface is likely to be fully packed with streptavidin molecules.

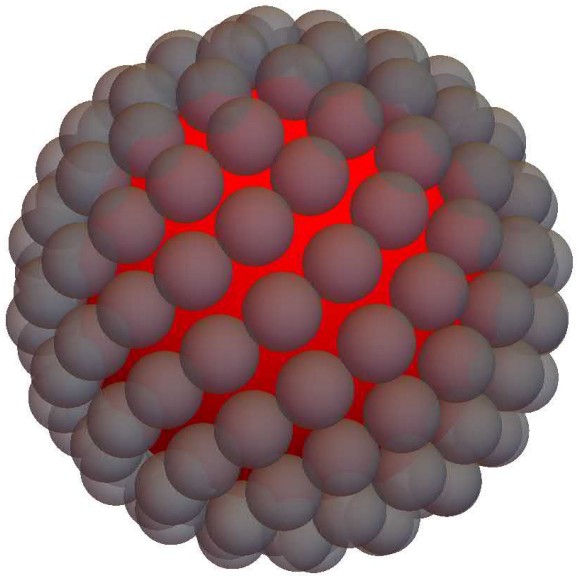

Figure SC2. Approximate geometry of streptavidin packing on a UCNP 33 nm in diameter (31 nm particle diameter + 2 nm added by two thin coating layers). Image conserves the relative scale of the protein molecules and the particle. Calculation and image rendering were performed in Wolfram Mathematica.

Section D. Antibody biotinylation and characterization.

Antibody biotinylation was performed using the Biotin-XX-NHS reagent (Thermo Fisher). "XX" corresponds to a mildly hydrophobic chain that facilitates binding of protein-bound biotin to streptavidin, providing some space between biotin and protein. To biotinylate the antibody, the following protocol was used. 12 μL of 1 mg/mL Anti-DNP IgE (clone SPE-7, Sigma-Aldrich D8406) were exchanged into 1x PBS buffer using a Zeba Micro Spin centrifuge desalting column (Thermo Fisher) following manufacturer's instruction for buffer exchange. This step is required as azide in storage buffer can interfere with the biotinylation reaction. After this step, the total volume of antibody was found to be 18 μL. Next, the biotinylating reagent was dissolved at 58.65 mM concentration in DMSO. 0.27 μL of DMSO solution was added to 1x PBS and vortexed. Immediately after, 18 μL of this solution were mixed with 18 μL of IgE. This corresponded to ~1:3 antibody to biotinylating reagent stoichiometry. The mixture was incubated at room temperature in the dark over 2 h. Afterwards, the mixture was exchanged to 1x PBS on Zeba Micro Spin centrifuge

desalting columns to remove the excess of unreacted reagent. This yields antibody at approx. 0.22 mg/mL concentration, assuming quantitative yield of purification steps and taking into account dilution on all steps.

To estimate the biotinylation extent of the antibody, we performed SDS-PAGE (10% gel) of the biotinylated antibodies in the presence of streptavidin. Before loading, the antibody (4 μL at ~0.22 mg/mL) was denatured by heating at 95ºC over 3 min in reducing loading buffer (using 10% mercaptoethanol as reducing agent). After cooling down, streptavidin was added (6 μL at ~1 mg/mL, purchased from IBA). At room temperature, streptavidin is resistant to denaturation with SDS, and retains activity. This allows to estimate the extent of antibody biotinylation by observing the relative intensity of the bands corresponding to heavy or light chains of antibody, and bands corresponding to complexes of biotinylated heavy or light chains with one, two or multiple streptavidin molecules.

Results are shown on Figure SD1. An increase of the concentration of the biotinylation reagent on the biotinylation step ultimately leads to an increase in heavier bands. We were able to estimate biotinylation only of heavy chains (MW ~70 KDa), as the band of the complex of light chain (~25 KDa) with a single streptavidin has approximately the same molecular weight as the heavy chain (~90 KDa). We tested several antibody to biotinylation reagent stoichiometries, and observed gradual increase in intensity and number of high molecular weight bands corresponding to complexes of antibody heavy chain with one, two or more streptavidins, at molecular weights of ~145 KDa (90+55), ~200 KDa (90+2*55), ~255 KDa (90+3*55), etc. As we wanted the activity of the antibody to be as close to native as possible, we ultimately have chosen the 1:3 stoichiometry described in the aforementioned protocol. Based on the gels, this stoichiometry yields approximately 1 mono-biotinylated antibody per 2 non-biotinylated ones.

We note that this method works only with streptavidin that has a relatively narrow molecular weight distribution. Affinity-purified streptavidin (e.g. the cheaper option from Sigma-Aldrich) has identical activity, but has a wide molecular weight distribution due to its production and purification processes, leading to difficulties in gel interpretation.

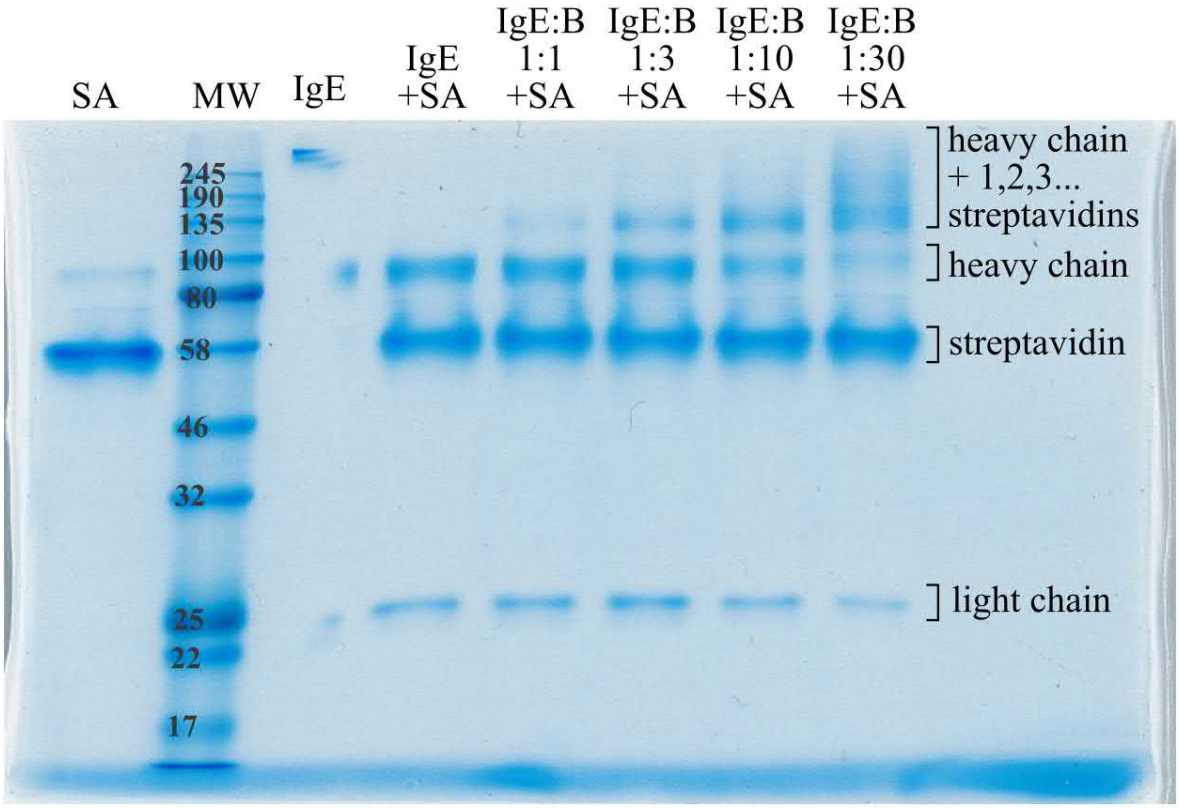

Figure SD1. SDS-PAGE of antibody denatured in reductive conditions, mixed with excess streptavidin. MW reference lane was loaded with Color Prestained Protein Standard, Broad Range (NEB). Unlike the rest of the lanes, pure antibody lane was loaded using non-reducing denaturing conditions. Some reducing reagent from the neighbouring lane has partially denatured the antibody during stacking step, allowing to observe both the non-reduced antibody and antibody reduced into heavy and light chains. Streptavidin lane was deliberately overloaded (10 μg) to monitor the presence of any impurities.

Section E. Cell culture and RBL-2H3 degranulation assay.

RBL-2H3 cells were purchased from ATCC and cultured in complete MEM supplemented with 10% FBS and 1% penicillin/streptomycin at 37ºC in presence of 5% CO_2. Passages were performed every 2-3 days, in confluent or subconfluent cultures (overconfluence was avoided to reduce possible associated adverse effects on cell performance).

Degranulation assay was performed as described in Ortega et al., using 4-Nitrophenyl N-acetyl-β-D-glucosaminide as the substrate. This substrate is cleaved by the hexosaminidase enzyme, forming 4-nitrophenol, the concentration of which can be then measured colorimetrically (absorption at 405 nm).**[REF Ortega 1988 EMBO]** For cell priming with antibodies, IgE was diluted in the culture medium at 100 ng/mL, and cells were primed over 30 min at 37ºC in presence of 5% CO_2. For degranulation, DNP-BSA was diluted in 1x HBSS at 50 ng/mL, and degranulation was allowed to proceed over 30 min. As the released 4-nitrophenol is a pH indicator and absorbs at 405 nm only when in anionic form , it was converted to ionised form by adding 6 μL of 1 M NaOH to the well after adding the stop solution (bringing the solution towards pH 11) to ensure that the assay would yield full signal. Experiment was performed n=5 times in parallel.

Section F. Microscopy setups, tracking experiments, and measurement conditions.

Bright-field phase contrast time lapses were performed on a fully motorized inverted microscope (Leica, FW 4000 with 20x 0.40 N.A. N PlanL Ph1 objective or 40x 0.75 N.A. HCX PL APO Ph2 objective) equipped with a sCMOS Camera (Photometrics, Prime) and controlled by Metamorph 7.8.13.0 (Molecular Device) . An incubator box (Life Imaging System System) allowed temperature, CO2 and humidity control. Samples were prepared in 8 well plates (Ibidi, μ-Slide 8 Well Glass Bottom).

Wide field upconversion-imaging of UCNPs for calibration tracking experiments was performed on an inverted microscope (Olympus, IX71) equipped with a high numerical aperture objective (Olympus, UApo N 100x/1.49 Oil). A 980 nm continuous-wave laser coupled to a single mode fiber with a maximum output of 350 mW (Qphotonics, QFBGLD-980-350) was passed through a longpass filter(Chroma, E780LP) used to excite the UCNPs with a maximum excitation power density of 8 kW/cm2 in epi illumination. Luminescence emission was separated from the excitation beam by using a short pass dichroic mirror (Chroma, T875spxrxt), while the residual laser light was removed by a low pass filter (Chroma, E700SP). Emission was detected by an electron multiplying CCD camera (Hamamatsu, ImagEM X2 C9100-23B) through an image splitting system (Hamamatsu, W-VIEW GEMINI) used in by-pass mode. Acquisition was fully automated and controlled by scripts within the MicroManager framework.

Wide field upconversion-imaging of cells was performed on an inverted microscope (Nikon, Eclipse TiE) equipped with a high numerical aperture objective (Nikon, Plan Apo λ 100x/1.45 Oil). An additional lens inserted in the C-mount side port tube of the microscope was used to obtain a final magnification of 150X corresponding to a pixel size of ~107 nm. A 980 nm continuous-wave laser coupled to a single mode fiber with a maximum output of 350 mW (Qphotonics, QFBGLD-980-350) was coupled to the microscope and allowed to reach excitation power density of 8 kW/cm2 in epi illumination. Luminescence emission was collected by the same objective, separated from the excitation beam by a short pass dichroic mirror (Semrock, FF749-SDi01), while the residual laser light was removed by a low pass filter (Chroma, ET750-SP-2P). Emission was detected by an electron multiplying CCD camera (Hamamatsu, ImagEM C9100-13) through an adaptive optics device (Imagine Optic, MicAO) used to optimize point spread function by minimizing optical aberrations. An incubator box (Okolab) allowed temperature control. Acquisition was fully automated and controlled by scripts within the MicroManager framework. Samples were prepared in 35 mm imaging dish with a glass bottom (Ibidi, μ-Dish 35 mm, high Glass Bottom).

For monitoring degranulation by videomicroscopy, cells were seeded in Ibidi 8-well glass-bottom plates at 30000 cells per plate and cultured in cell medium overnight. Microscopy was performed at 37°C in the presence of 5% CO_2. For cell priming with antibodies, IgE was diluted in culture medium at 100 ng/mL, and cells were primed over 30 min. To induce degranulation, DNP-BSA was diluted in 1x HBSS at 50 ng/mL, and degranulation was monitored over 30 min (same conditions as in degranulation assay). Images were taken every 10 seconds.

For tracking experiments, cells were seeded in round Ibidi glass-bottom plates at 30000 cells per plate and cultured in cell medium overnight. Microscopy was performed at 33 fps (30 ms exposure time) at 37°C with no special atmosphere.

The UCNP-IgE conjugates were prepared 15 min before experiment. For this, the stock dispersion of streptavidin-decorated UCNPs (at approx. 3.3 nM concentration) was mixed with biotinylated IgE mixture (diluted to 3.3 nM biotinylated IgE, corresponding to ~10 nM total IgE concentration). This mixture was incubated at 37°C for 15 min. Immediately before adding the conjugate to the cells, it was mixed with 347 μL 1x HBSS. Assuming a 100% completion of the

reaction during this time frame, the resulting conjugate dispersion contained ~200 pM UCNP-IgE conjugate in 1:1 stoichiometry and ~400 pM free non-biotinylated IgE.

Before imaging, cells were washed 3 times with 1x HBSS. Bright-field microscopy was performed over 5 min with images taken every 5 s to monitor the inert cells' medium-timescale behavior (on the order of minutes) . Cells were observed in 4 different regions of interest (ROIs). ROIs were chosen to contain as many well-separated cells as possible (typically 2-4 cells, due to high magnification). Afterwards, cell buffer was replaced with conjugate dispersion, and bright-field microscopy was continued over 5 min to ensure that the conjugate was not inducing degranulation behavior by itself. Next, illumination was switched to IR mode to visualize UCNPs. Cells were rinsed once with 1x HBSS to remove unbound UCNPs, and videos of 1000 frames each were taken in each of ROIs (overall, this process took approx. 20 min). Afterwards, bright-field microscopy of cells was performed over 2 min to capture the morphology of cells before addition of the antigen. Next, the buffer was replaced by a dilution of DNP-BSA in 1x HBSS at 50 ng/mL. Immediately after, bright-field microscopy images were taken over 15 min every 5 s to capture the degranulation process. Then, illumination was again switched to IR mode, and another set of 1000-frame videos was taken in each of the 4 ROIs, to monitor the diffusion of UCNPs in degranulated cells.

Section G. Analysis of tracking videos.

Videos were treated using the TrackMate framework developed by the group of JY Tinevez. **[REF Tinevez 2016 Methods]** We used the Laplacian of Gaussian (LoG) method for spot detection, with following parameters: quality threshold of 15, spot radius of 3 px (diameter 6 px), no median filtering. Spots were filtered by only detecting spots with total integral intensity of less than 150000. Such filtering allowed us to efficiently eliminate spots corresponding to particle oligomers and aggregates, which have a large hydrodynamic radius and may thus have impeded diffusion as a result.

For linking spots into tracks, we used the Simple Sparse Linear Assignment Problem (LAP) tracking algorithm implemented in TrackMate, with following parameters: maximum frame gap of 1, linking maximum distance of 5 px, gap-closing maximum distance of 6 px. Tracks were filtered using a filter for a minimum track duration of at least 50 frames, to collect robust tracks. Tracks were further filtered by introducing a filter on minimum track displacement (start-to-end distance) of at least 5 px. This filter allowed us to efficiently remove spots corresponding to immobile particles, which are bound to glass surface. Depending on the amount of cells per frame, such treatment typically produces ~80 viable tracks per ROI, of varying length from 50 to ~750 frames in total.

Afterwards, the tracks were analyzed using the TrackMate MATLAB function library. To obtain the diffusion coefficients, the first four points of MSD curves were fitted linearly. This amount of points for fitting is thought to be an informal optimum for determining diffusion coefficients of particles moving in Brownian or restricted mode.**[REF Saxton 1997, REF Kusumi 1993 Biophys J]** The slope of the curve is equivalent to $4D_{2D}$, where D_{2D} is the diffusion coefficient in 2 dimensions.

We also observed that a non-negligible amount of tracks produced highly directed diffusion. Literature suggests this to be linked to endocytosis of nanoparticles and their transport along microtubules, a naturally happening phenomenon with nanoparticles bound to membrane surface. **[REF Zhang/Gao/Bao 2015 ACS Nano, Zhang/Li/Suresh Adv Mater 2009]** Also, a small amount of tracks clearly corresponded to immobile particles that went through the “immobile” filter (e.g. particles that desorbed from glass during the experiment). As we were interested solely in tracks that contained membrane-diffusing particles, we decided to filter out highly directed and immobile tracks. For this, first 50% of points for each track have been fitted with a power law of the form

$MSD(t) = \Gamma t^{\alpha}$, which corresponds to a line in log-log coordinates. When fitted in such way, the α parameter gives information on the nature of track behavior. A very small α corresponds to essentially flat MSD curves associated with immobile particles, α=1 corresponds to particles exhibiting free Brownian diffusion, and α=2 corresponds to particles with ideal directed diffusion (i.e. particle moving in a straight line). As power law fits require high amount of points to yield quantitative information, we used them only for qualitative classification of tracks into three categories: directed, Brownian/restricted, and highly restricted/immobile. For constructing the diffusion coefficient distributions, only tracks with good fit (R^2>0.8) for both linear and power-law fitting were selected. Furthermore, only tracks with 0.6<α<1.2 were taken, which reliably corresponded to particles showing Brownian and restricted motion. We found this simple classifier to be highly reliable, by visual inspection of the populations of tracks that were retained or filtered out.

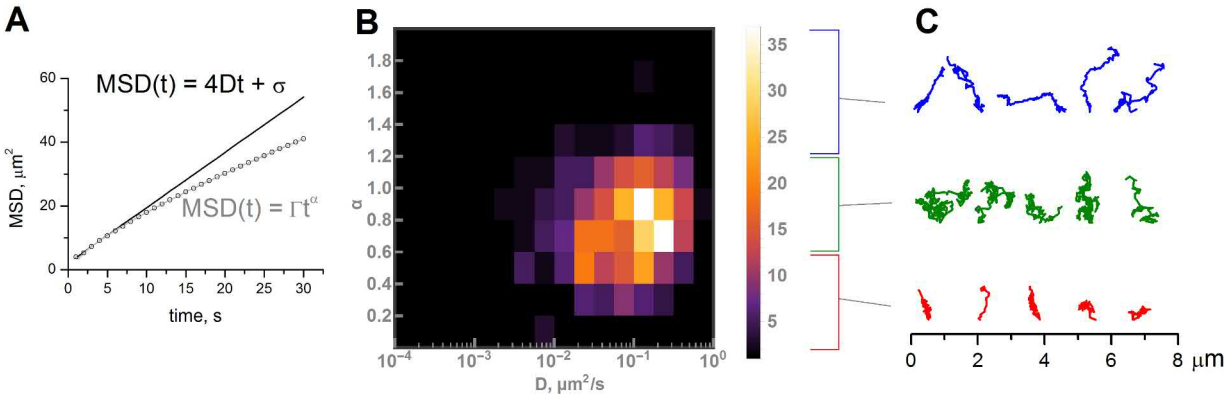

Figure SG1. Track classification for filtering out directed and immobile tracks. A: Idealized MSD curve fitted by a line over first 4 points and by a power law over 50% of the points. B: An example of a 2D histogram of tracks with their diffusion coefficient calculated from linear fit and their α coefficient calculated from power law fit. Color represents the amount of tracks in the corresponding bin. C: examples of tracks falling in different bins.

Section H. Tracking with organic dyes.

The dye-modified antibody was prepared using a literature protocol.**[REF Shelby 2013 Biophysical Journal]** Using absorption spectroscopy, the concentration of the antibody after preparation was found to be 0.4 mg/mL, and the dye modification extent was found to be ~2 dyes per 1 antibody. For imaging, antibody was diluted 1000x to 400 ng/mL concentration.

For tracking analysis, identical parameters as for UCNPs were used.

Section I. Calibration of tracking setup by tracking UCNPs in glycerol-water mixtures.

Polymer-coated UCNPs were typically diluted 100x from stock in different water/glycerol mixtures. For imaging, a drop of the dispersion was mounted between a slide and a cover glass. Acquisition was performed at least 0.5 μm away from the glass surfaces with 100ms/14ms exposure times and 400/1200 Electron-Multiplying (EM) gain with laser excitation in epi configuration with excitation power density of 8 or 1.5 kW/cm^2 (see Section J for more details). Typical videos contained 1500 frames and were analyzed with TrackMate within Fiji **[REF Tinevez Methods 2017]**. The resulting single particle tracks were then imported and treated in Matlab 2017b using the msdanalyzer class **[REF Tarantino/Tinevez J Cell Biol 2014]** and custom scripts. Finally, the diffusion coefficient of the particles in the different mixtures was estimated from the slope of their average mean square displacement curve. As seen on Fig. SI1 experimental results are in good

agreement with the theoretical values expected for Brownian motion. This experiment demonstrates the proof of principle of using UCNPs as labels for tracking targets with diffusion coefficient in the 0.1 $\mu m^2/s$ range. In addition, experiments performed with the two excitation intensities resulted in similar diffusion coefficient values, suggesting that the free diffusion of the particles is not significantly affected by the convection movement induced by the excitation beam. This indicates that in our experimental conditions local heating of the sample by the laser is likely negligible.

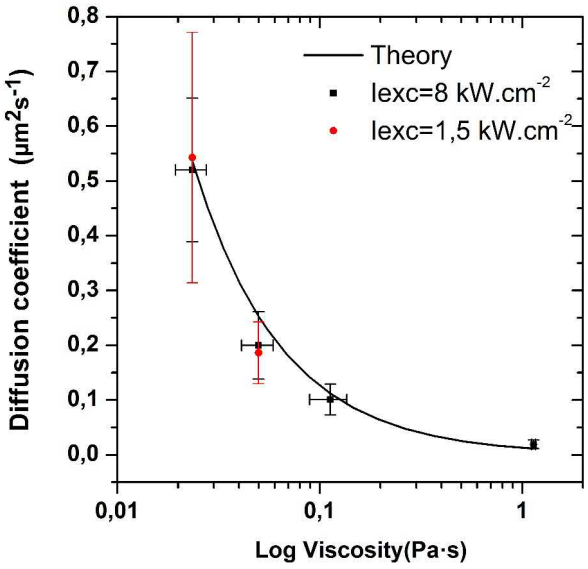

Figure SI1. Diffusion coefficient estimated by analyzing videos of freely diffusing 31 nm core diameter UCNPs coated by amphiphilic polymer (~1 nm thickness) in different water/glycerol mixtures. Theoretical curve corresponds to the diffusion coefficient of a spherical particle of 33 nm diameter as predicted by Einstein's relation.

Section J. Assessment of heating effects.

Literature measurements and theoretical calculations for IR illumination inducing heating in live cell samples in microscopy conditions are mostly well-documented in the fields of patch-clamp measurements of temperature-dependent ion channels, light-induced drug release and optical trapping. A literature source with a similar excitation, microscope and sample configuration reported a ~8ºC maximum steady-state temperature increase in water for ~100 mW incident laser power in a confocal mode.**[REF del Rosal/Jaque 2013 Proc SPIE]** In our case, the same power is spread over a ~3500x larger area, resulting in a much less efficient heating as the intensity gradient is lower and the heated volume has much larger contact area with the rest of the sample. Moreover, experiments in a very similar microscopy configuration with a collimated beam with approximately 20 times higher intensity than in our setup **[REF Wang/Jin 2018 Light Sci App]** have shown no visible adverse effects on the cells.

Section K. UCNP stability against dissolution in buffers.

As we previously observed heterogeneous dissolution of UCNPs in aqueous buffers to be an issue in microscopy,**[REF Dukhno 2018 Nanoscale]** we decided to investigate if the particles were sufficiently stable in 1x HBSS, the buffer employed in our tracking experiments. For this, we performed dissolution stability tests for UCNPs in the same conditions and on the same experimental setup as in our previous article.

Fig. SL1 A,B,C illustrates the normalized red band emission intensity for immobilized individual biotinylated UCNPs that were kept in 1 mM NaF to establish baseline emission intensity, and then were rinsed 3x with milli-Q water, 1 mM NaF, or 1x HBSS, respectively. We note that individual UCNPs are mostly stable in HBSS, showing a very slight decrease in luminescence over 2 h. As the tracking experiments were typically done over 1 h, we consider the dissolution effect to be negligible for the tracking experiments. We also noted long-term inhomogeneity of the intensity of a subpopulation of particles in 1 mM NaF, which is consistent with our previous results. In water, the sample was observed to rapidly dissolve over 25 minutes, after which low particle intensity and low amount of particles on image led to image-based autofocus algorithm being unable to focus on the particles.

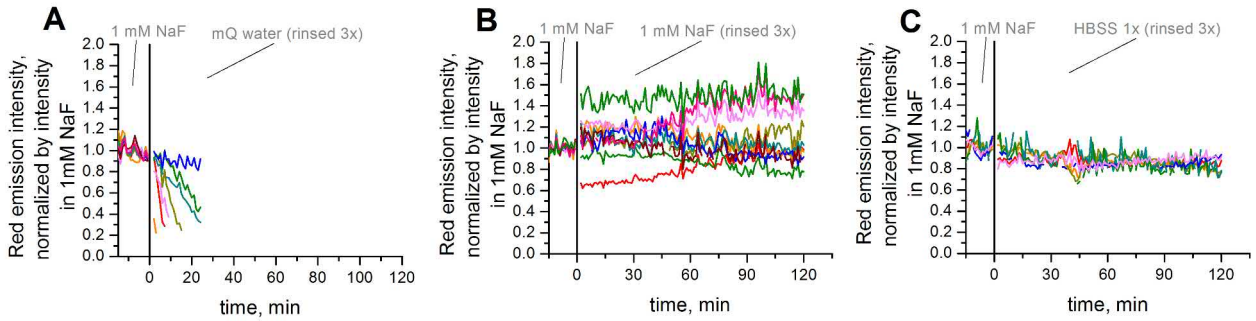

Figure SL1. Dissolution of immobilized biotinylated UCNPs. Each colored curve represents one particle. A: normalized intensity of red band emission of individual UCNPs in 1mM NaF and after rinsing 3x with water. Time of rinsing is set as time = 0. B: same, but rinsed with 1mM NaF. C: same, but rinsed with 1x HBSS.

Chapter 3. Materials and methods.

Note: the vast majority of this information is a duplicate of parts of Supporting Information from the publications shown above, as most of the experiments during the thesis project used the same protocols and instrumental setups.

Part 1. Particle preparation and characterization.

Raw particles for the thesis project were prepared by our collaborators (group of Dr. Thomas Hirsch, University of Regesnburg) using a solvothermal method with the same protocol as described in *Wilhelm et al., 2015*. In total, three samples were used: 16.2±0.6 nm particles (NaYF4: 20%Yb, 2%Er, 20% Gd), 20.9±0.6 nm particles (NaYF4: 20%Yb, 2%Er, 10% Gd), and 31±1 nm particles (NaYF4: 20%Yb, 2%Er). A variation in Gd^{3+} doping was used to change the size of obtained particles while keeping other synthesis conditions constant, as well as to retain high monodispersity for all samples (*Damasco et al., 2014*).

TEM images of raw particles (Fig. 3.1.1) were acquired with a 120 kV Philips CM12 microscope on carbon-coated copper grids and were analyzed with ImageJ and Origin. XRD patterns (Fig. 3.1.2) were recorded on a Huber Guinier G670 diffractometer with a Kα-Cu source (λ = 1.54060 Å).

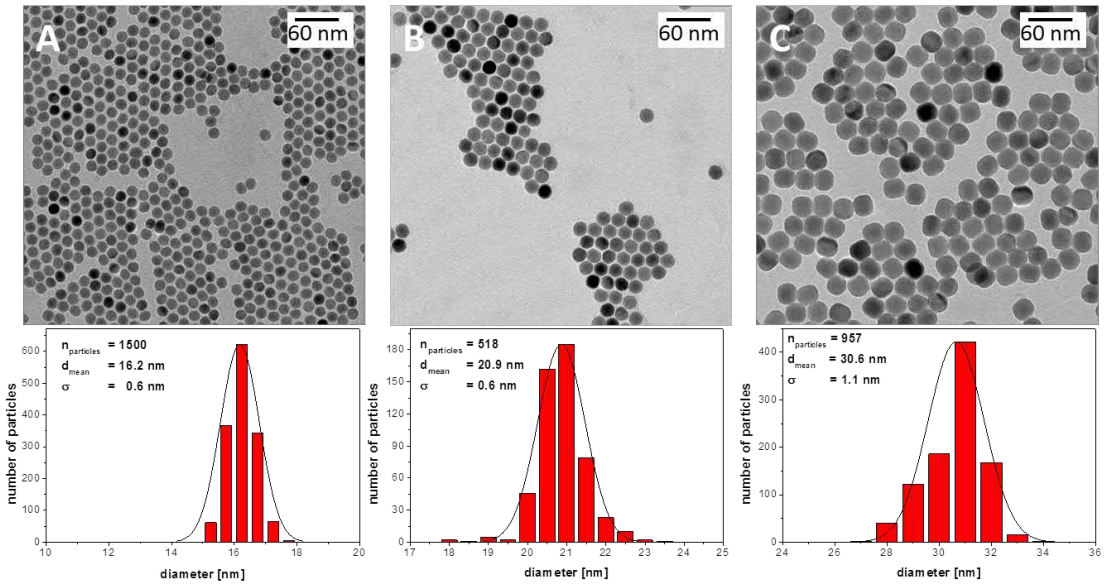

Figure 3.1.1. TEM images of UCNPs. A, B, C: 16 nm diameter, 21 nm diameter, 31 nm diameter. Top: TEM images, bottom: histograms of particle size distribution obtained from TEM images.

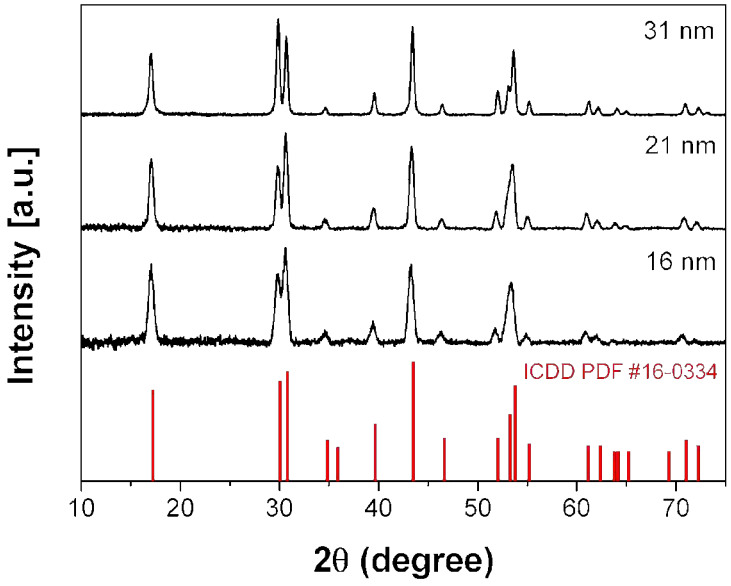

Figure 3.1.2. X-ray diffraction patterns of $NaYF_4$ (20% Yb, 2% Er, 0-20% Gd) nanocrystals with decreasing size from 31 nm to 16 nm (top to bottom) and the corresponding standard

pattern of hexagonal phase $NaYF_4$ (red, ICDD PDF #16-0334).

Part 2. Surface modification of UCNPs.

3.2.1. Preparation of amphiphilic polymers

As the preparation of amphiphilic polymer for particle coating depends on the nature of the desired polymer to be produced, herein an example protocol for preparing 75%-dodecylated, 1% Rhodamine B decorated polymer is presented:

In a 10 mL flask with a septum and flushed with argon, 18 mg dodecylamine (97 μmol, 0.75 eq) were dissolved in 2 mL anhydrous DMF under magnetic stirring. Diisopropylethylamine (67 μL, 390 μmol, 3eq) was added. 1 mg of piperidyl-beta-alanine-coupled Rhodamine B (1.3 μmol, 0.01 eq) was added. The solution was allowed to stir for 10 min, then 20 mg of poly(isobutylene-alt-maleic anhydride) were added in one portion (130 μmol, 1 eq monomer, avg MW 6000). The vessel was purged with argon a second time, and the reaction mass was stirred at room temperature. After 30 min, a drop of water (approx. 100 eq) was added. The reaction mass was evaporated, redissolved in dichloromethane and purified on LH20 size-exclusion chromatography column (eluent: dichloromethane-methanol 1:1 v/v). Combined elutes were evaporated, and the residue was redissolved in 2.6 mL spectral grade chloroform, corresponding to a theoretical 0.05 M equivalent monomer concentration (assuming quantitative yield). This solution was used as a stock for subsequent coating of UCNPs.

Depending on the desired modification of polymer, an appropriate quantity of the modified amine(s) has to be mixed with dodecylamine (e.g. 0.01 eq for 1% modification). Approximately 75% of the polymer anhydrides are required to be reacted with dodecylamine to properly impart amphiphilic functionality.

For zwitterionic polymers, the zwitterionic precursor group was prepared via the following protocol.

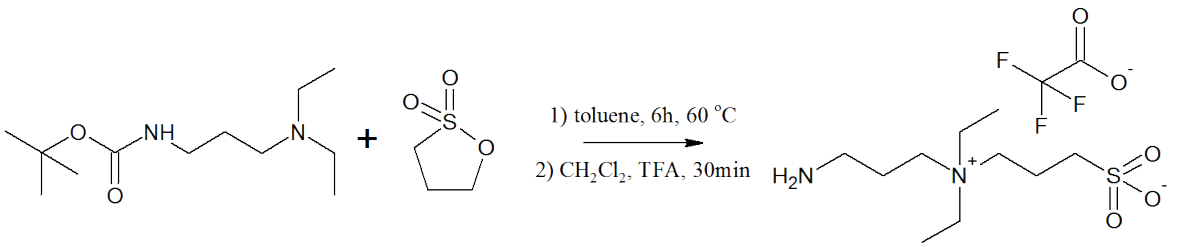

230.35
4.34 mmol (1eq)
1.00 g

122.14
4.77 mmol (1.2eq)
0.58 g

365.39
expected 1.586 g

A solution of tert-butyl 2-(dimethylamino)ethylcarbamate (0.45 g, 1eq) and 1,3-sultone (0.32 g, 1.1eq) in toluene was heated 4 h at 60 °C to form a white solid. After cooling to rt, the solid was collected by filtration and rinsed with hexane (2 x 10 mL). The solid was dissolved in dichloromethane (2 mL) with several drops of acetonitrile to facilitate dissolution, and TFA was dropped in with stirring (2 mL). After 30 min, the reaction mass was concentrated on rotavap (60°C), and dried under vacuum (oil pump). For full deprotection, the compound was boiled in 5 mL water with 1 mL TFA overnight. Rxn mix was evaporated, redissolved in MeOH and stirred 30 min with ~20 mL of Amberlite IRA-67 (pre-washed with water and MeOH). The mixture was filtered, and the filtrate was evaporated and dried with an oil pump to yield transparent yellowish oil. Yield: 0.71 g (50%). The method was adapted from WIPO WO 2011071565 patent, which is described for a similar compound (methyl groups instead of ethyl groups).

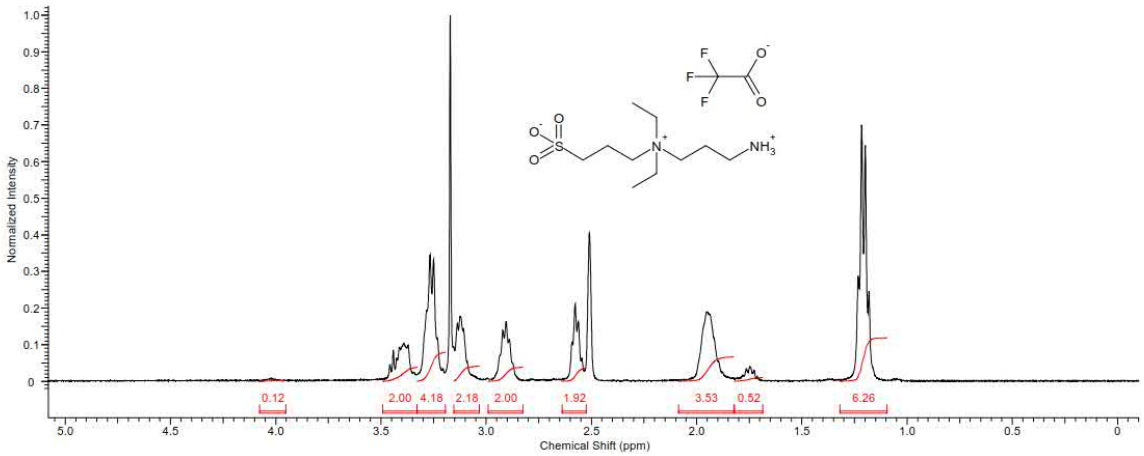

Figure 3.2.1.1. NMR spectrum of the zwitterionic precursor compound. Spectrum was

measured in DMSO-d6 on a Bruker Avance III 400 MHz NMR spectrometer. A drop of TFA was added to the sample to shift the water peak to weak field.

For preparation of the zwitterionic polymer in a flask flushed with argon, 18 mg dodecylamine (0.75 eq, 0.10 mmol), 1 mg piperidyl-beta-alanine-coupled Rhodamine B (1.3 μmol, 0.01 eq), and 100 uL DIPEA (~4.8 eq) were mixed in dry DMF. Poly(isobutylene-alt-maleic anhydride) (20 mg, 0.13 mmol monomer, 1eq) was added in one portion. The reaction flask was purged with argon, and mixed at room temperature for 30 min. Afterwards, 117 mg TSTU (0.39 mmol, 3eq) dissolved in 1 mL dry DMF were added in one portion. The reaction flask was heated to 40°C and allowed to cool down to room temperature over 30 min. Then, 137 mg (0.65 mmol, 5 eq) zwitterionic precursor compound were dissolved in 1 mL MeOH with 1 mL dry DMF and added in one portion. The reaction was mixed for 30 min at room temperature. Polymer was purified on Sephadex LH-20, as described above. Yield was 12 mg (15%). Some product was lost during filtration through Celite before chromatography due to mediocre product solubility in the elution solvent mixture. NMR spectra of the obtained polymer had widened peaks, likely due to formation of aggregates in polar solvents and reverse micelles in apolar solvents (data not shown). The FTIR spectrum of the polymer (Fig. 3.2.1.2) showed intense peaks for the ionized sulfonate groups. Importantly, signals of C=O stretch of carboxylic acid groups at 1700-1720 cm^{-1} were very weak, while the amide group C=O stretch at ~1660 cm^{-1} was very prominent. Overall, this data led us to believe that the degree of amide formation was very high, possibly almost quantitative.

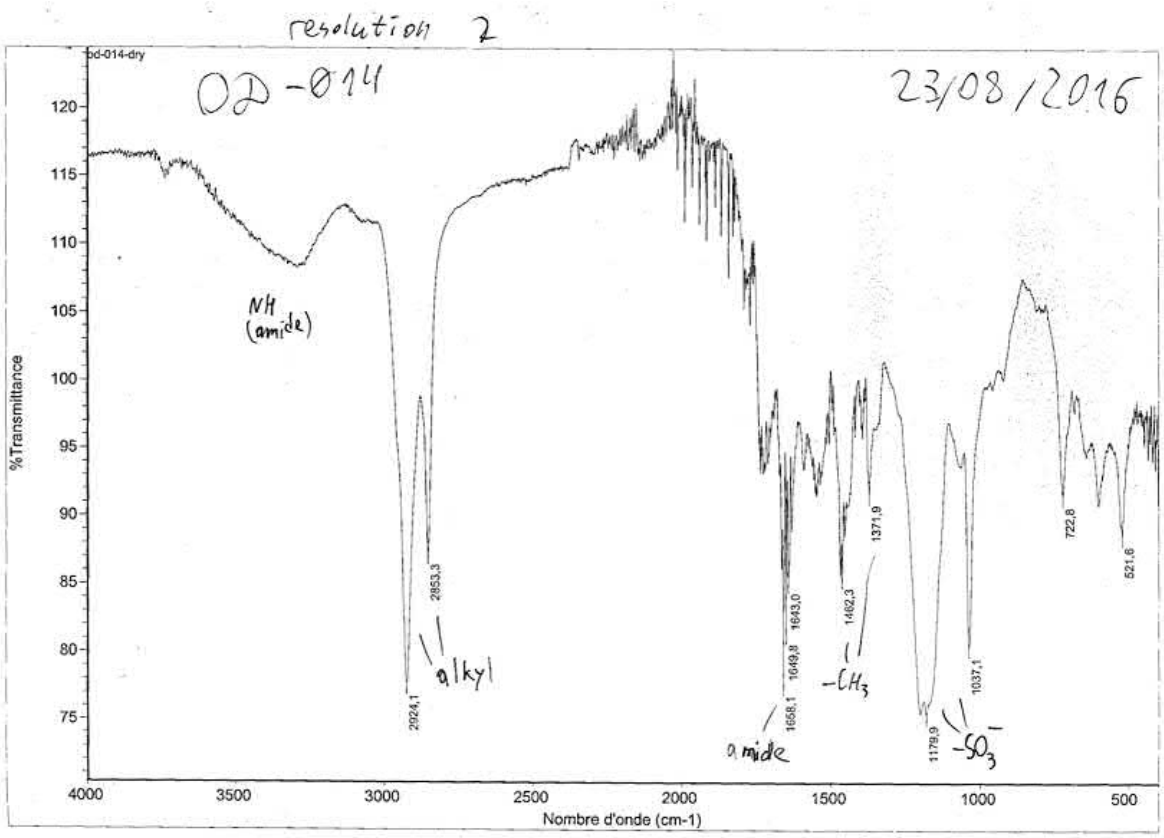

Figure 3.2.1.1. FTIR spectrum of the zwitterionic polymer measured in a compressed thin film using Nicolet 380 FTIR device with Smart-Orbit accessory. Signals of alkyl C-H bonds from dodecyl side chains and backbone, amide N-H bonds from backbone, amide C=O stretch bonds from backbone and S-O stretch bonds from zwitterionic chains are labeled.

3.2.2. Dispersion of UCNPs in water

For coating UCNPs, we used a modified version of the protocol from *Wilhelm et al., 2015*. 165 µL of UCNPs with 31 nm diameter (5 mg/mL) in cyclohexane were mixed with 140 µL 0.05 M polymer dispersion in chloroform, sonicated for 1 min at room temperature, and evaporated. The residue was redispersed in 0.35 mL spectral grade chloroform and sonicated for 1 min at room temperature. Then, 1 mL 10 mM NaOH was added. The mixture was vortexed for 30 s and slowly evaporated on rotavap (high speed of rotation and low vacuum are recommended to avoid bumping), until only aqueous phase remained. Afterwards, evaporation was continued until ~0.5 mL aqueous phase remained. Obtained

phase was filtered through a Millex GP syringe filter (0.22 µm pore size). The filter was washed with 10 mM NaOH into the filtrate to a final combined volume of 1 mL.

The obtained dispersion contained a mixture of UCNPs and empty polymer micelles. For purification, 100 µL of UCNP dispersion were diluted in 900 µL centrifugation buffer (10 mM NaOH + 1 mM NaF), and centrifuged at 4ºC and 12500 g over 1 h. Top 970 µL of the supernatant were carefully removed by pipette to avoid disturbing the UCNP-rich section of the dispersion at the bottom. Afterwards, 970 µL of the centrifugation buffer were added to UCNP dispersion and vortexed for 30 s. The centrifugation was repeated in the same conditions, and the top 970 µL of supernatant were again removed. 70 µL of centrifugation buffer were added to UCNPs, and the dispersion was vortexed for 30 s.

The quantity of polymer stock solution required for the coating process was calculated using the following formula:

$$V_{\text{polymersolution}} = \mathrm{R}_P \pi \frac{\omega_{\text{UCNP}}}{\rho \mathrm{V}_{\text{UCNP}}} d_{\text{eff}}^2 \frac{1}{c_{\text{polymer}}}$$

where R_p is the quantity of polymer, expressed in number of monomers, applied per nm^2 of UCNP surface (100 in case of UCNP coated with oleic acid, which is about 5 times in excess compared to the tight fatty chain packing on surface), ω_{UCNP} is the mass concentration of UCNPs (e.g. mg/mL), ρ is the density of UCNPs ($4.21 \cdot 10^{-21}$ g/nm^3), V is the volume of UCNP in nm^3, d_{eff} is the effective diameter of UCNP, which includes the thickness of the oleic acid layer (e.g. for a 20.6 nm diameter the effective diameter is 21.7 nm, because of two 0.55 nm thick layers of oleic acid).

3.2.3. Preparation of UCNP-dye conjugates

For dye-decorated particles, the dyes were grafted to the polymer during the synthesis, and the particles were coated with dye-grafted polymer.

The number of surface dyes per particle can be calculated by:

$$N = \pi \left(d + 2l \right)^2 C_{f.ch.} P$$

where d is the diameter of the particle (nm), l is the thickness of the polymer-oleic acid layer (nm), $C_{f.ch.}$ is the number of fatty chains per nm^2 in the tightly packed monolayer, and P is the percentage of dyes per monomer.

The calculated number of dyes per particle is provided in following table (thickness of oleic acid layer assumed to be 1.1 nm, packing density of fatty chains in monolayer is assumed to be 5 nm^{-2}). It should be noted that this calculation represents the quantity of dyes bound specifically on the surface of UCNPs. Due to excess of polymer being used to ensure proper UCNP coating, some polymer micelles are formed in dispersion. Dyes in polymer micelles are not considered surface-bound to UCNPs and are not accounted for in the calculation.

	dye percentage per monomer			
particle diameter, nm	***quantity of surface-bound dyes per particle after coating process***			
	0%	**0.33%**	**1.5%**	**6.6%**
16	0	17	78	343
21	0	27	123	539
31	0	54	244	1075

	dye:Er^{3+} ratio			
particle diameter, nm	**0%**	**0.33%**	**1.5%**	**6.6%**
16	0	0.043	0.196	0.861
21	0	0.035	0.157	0.692
31	0	0.020	0.093	0.409

Table 3.2.3.1. Calculated dye quantities and dye-Er^{3+} ratios per particle.

3.2.4. Preparation of UCNP-streptavidin conjugates

The detailed description of the preparation and purification of streptavidin-coated UCNPs is provided in publication 3. Briefly, for decorating UCNPs with streptavidin, 90 µL of biotinylated UCNP dispersion in a low-protein-binding Eppendorf tube (Eppendorf) was mixed with 9 µL 10 mg/ml BSA in purification buffer (20 mM Tris, 50 mM NaCl, 1 mM NaF), mixed with pipette, and gently vortexed over 20 s. Afterwards, the mixture was

incubated over 30 min at room temperature. This treatment forms a BSA corona weakly bound to the polymer on the surface of the nanoparticles, which is in constant exchange with the bulk BSA proteins in dispersion, with average protein residing time of ~100 s, based on literature reports (*Röcker et al., 2009*).

Afterwards, the nanoparticle dispersion was mixed with 9 μL 10 mg/mL streptavidin dispersed in purification buffer. The mixture was immediately gently vortexed. Obtained dispersion was incubated with gentle shaking over 120 min at 37ºC. During incubation, BSA molecules occasionally detach from the UCNP surface. Upon this event, the slightly smaller streptavidin molecules can occupy the vacant space on the particle surface and reorient themselves until they bind an available biotin on the particle surface. This results in streptavidin proteins being irreversibly bound to the particle. Over time, more and more BSA proteins are gradually replaced by streptavidin. We stress that this method works only if the BSA corona is introduced before coating UCNPs with streptavidin. We noticed that if the streptavidin is added directly to the "naked" biotinylated nanoparticles, the high concentrations of both particles and streptavidin induce partial oligomerization and aggregation of the sample immediately upon mixing, visible in DLS (data not shown). This effect persists even if a large excess of streptavidin is used.

To remove excess streptavidin from the particle surface, we performed size-exclusion chromatography using a small gravity-fed column filled with 5 mL Sephacryl S300-HR gel (GE Healthcare). After collecting the void volume (~1.5 mL), fractions were collected with 80 μL volume each. DLS of each fraction was measured to confirm the presence of the particles by total scattering count rate on the detector (Fig. 3.2.4.1, A) and simultaneously assess the presence of proteins (Fig. 3.2.4.1, B).

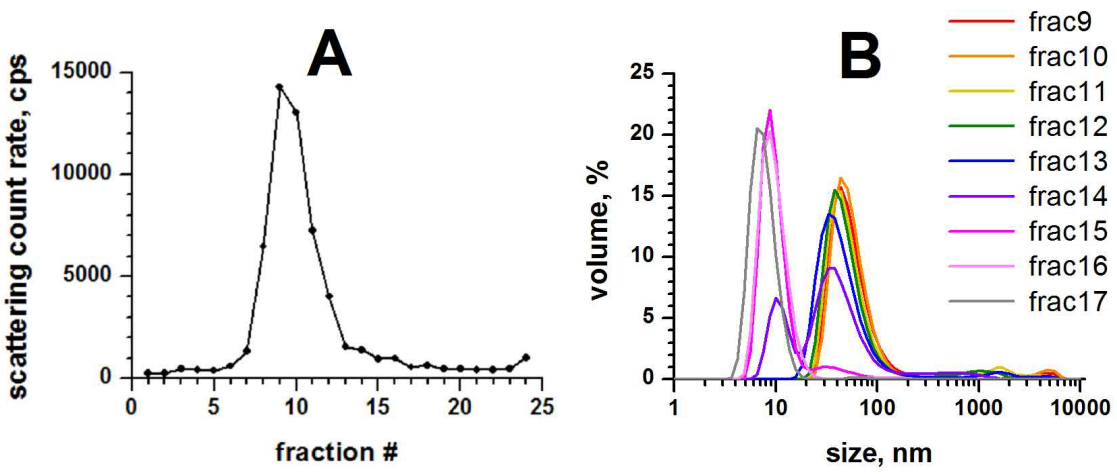

Figure 3.2.4.1. DLS instrument detector count rate and size distributions for fractions that significantly scattered light. A: scattering count rate for collected fractions. A peak corresponding to significant light scattering is clearly visible for fractions 8-12, and a slight "shoulder" is present for fractions 13-17. B: DLS volume distributions for respective fractions. Later fractions show gradual shift in the peak of calculated volume distribution from ~45 nm, corresponding to individual streptavidin-coated UCNPs, to ~7 nm, corresponding to the hydrodynamic diameter of BSA or streptavidin with a ~1 nm thick coordinated water/ion shell.

Assuming a 100% yield during the particle coating step and taking into account the dilution of the particles imposed by purification steps, the estimated concentration of UCNPs in the obtained dispersion was calculated to be ~3 nM.

3.2.5. Preparation of UCNP-streptavidin-antibody conjugates

The UCNP-antibody conjugates were typically prepared 15 min before the experiment that employed them. For this, the stock dispersion of streptavidin-decorated UCNPs (at approx. 3.3 nM concentration) was mixed with biotinylated IgE mixture (diluted to 3.3 nM biotinylated IgE, corresponding to ~10 nM total IgE concentration). This mixture was incubated at 37ºC for 15 min. Immediately before adding the conjugate to the studied system, it was mixed with 347 µL 1x HBSS. Assuming a 100% completion of the reaction during this timeframe, the resulting conjugate dispersion contained ~200 pM UCNP-IgE conjugate in 1:1 stoichiometry.

3.2.6. Nanoemulsion sample preparation

Nanoemulsion sample preparation methods varied slightly from experiment to experiment, depending on which experimental variable was tested to influence the process.

In a typical protocol (for the sample presented in the main text), 250 μL of 31 nm UCNPs (5 mg/mL) in cyclohexane were mixed in a small glass vial with 45 μL molten Suppocire C (BASF), 55 μL Solutol HS15 (BASF), and 0.16 mg of Rhodamine B modified with C_{18} hydrophobic chain (generously provided by Dr. Andrey Klymchenko). 50 μL of chloroform and 100 μL dichloroethane were added to facilitate dispersion. The mixture was heated to 90ºC until no bubbling was observed, then heated 5 min more to ensure full evaporation of solvents. Afterwards, 1 mL of deionized water heated to 90ºC was added in one portion, the vial was rapidly closed and immediately vortexed. The vial was then allowed to cool down to room temperature, and the nanoemulsion was transferred to an Eppendorf plastic tube. Nanoemulsion formation was observed quantitatively by DLS (described below in more detail) and qualitatively by light scattering. In these concentrations, nanoemulsions with droplet size <100 nm are transparent and look yellowish in transmitted light and bluish in reflected light.

Nanoemulsion TEM was performed with a Philips CM12 100Kv electron microscope, equipped with ORIUS 1000 CCD Gatan camera. Samples were diluted and deposited on Formvar carbon-coated grids.

Part 3. Bulk particle characterization methods.

3.3.1. Dynamic light scattering (DLS)

DLS measurements were performed in Brand plastic cuvettes (lot #759015) on a Malvern Zetasizer Nano ZSP instrument. Correlation curves were treated with the "normal resolution" parameter set. All presented DLS curves represent size distribution by volume. Curves represent the mean of size distributions from the three runs. For estimating he scattering signal from the device for the purposes of comparing nanoparticle-containing chromatography fractions, the "derived count rate" was used (which takes into account the attenuator chosen by the device to optimize the measurement conditions).

3.3.2. Zeta potential measurements

Zeta potential measurements were performed in Malvern DTS 1060 cuvettes on a Malvern Zetasizer Nano ZSP instrument, using the default automatically selected instrumental parameters.

3.3.3. Spectroluminometry of UCNP dispersions

Luminometry of diluted UCNP dispersions in 1 cm BRAND plastic cuvettes (Cat. No. 7590-15) was performed with a homemade setup (Fig. 3.3.3.1). Excitation at 980 nm was provided by a continuous-wave laser coupled to a single mode fiber with a maximum output of 350 mW (Qphotonics, QFBGLD-980-350). Excitation light was focused in the cuvette by a lens of 100 mm focal distance. Excitation power inside the cuvette was calculated to be 6.2 kW/cm^2 (see below). The scattered/reemitted laser light was removed by a low pass filter (Semrock, E700SP). The emission was collected through a monochromator (Jobin Yvon HC10IR) with an avalanche photodiode (Excelitas SPCM-AQRH-16). Spectroluminometry was performed with an identical optical path for excitation, with emission collected by a fiber spectrometer (Avaspec ULS3648).

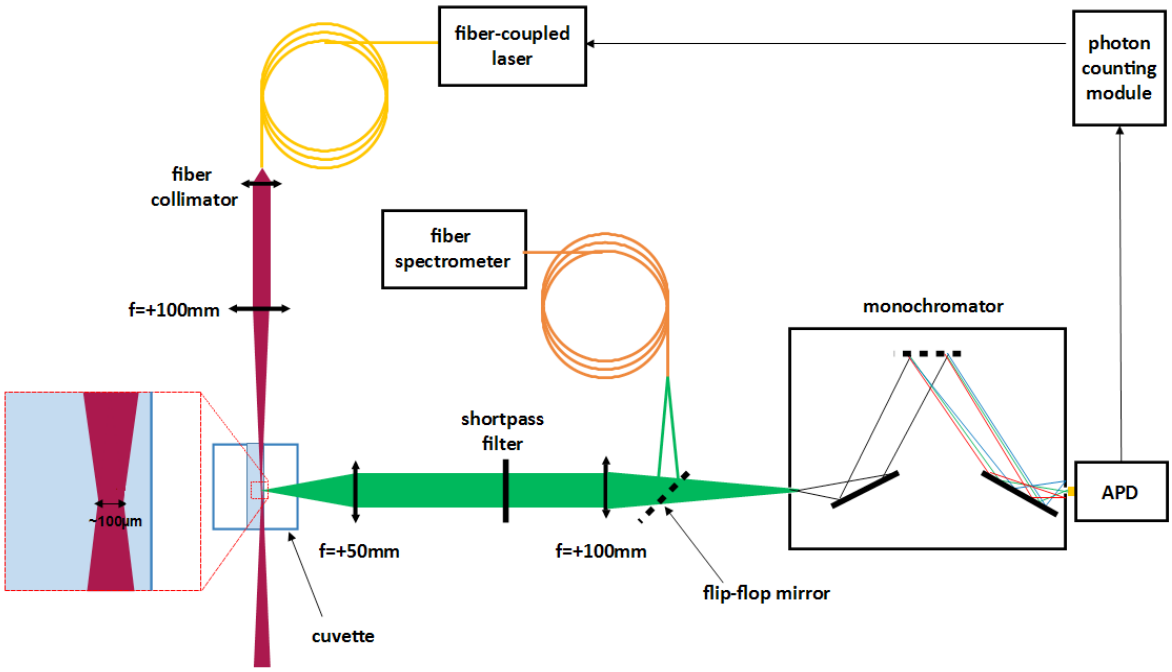

Figure 3.3.3.1. Scheme of the setup for cuvette measurements.

To estimate the excitation intensity within the cuvette, the laser beam intensity profile was experimentally measured inside the cuvette by the knife-edge technique, using a razor blade (~2 mm wide).[5] Briefly, the blade was glued on a thin steel rod, mounted on a two axis micrometer translation stage (Thorlabs PT1A/M), and immersed in the cuvette filled with deionized water. This setup allows to achieve a bidirectional motion, along the beam and vertically (Figure 3.3.3.2, A). Through the vertical movement, the razorblade progressively occludes the beam and thus, the beam power collected by the detector (Newport 1917R power meter) gets lower. By repeating the measurement at different depths in the cuvette, a full beam blade occlusion profile can be collected (Figure 3.3.3.2, B), from which the beam geometry can be calculated. For our calculations, the beam geometry was considered to be Gaussian and circular (with no ellipticity). To correct for water absorption, we compared the intensity of the transmitted beam with an empty cuvette and after filling the cuvette with water. We found the water IR light absorption to be non-negligible, at a value of 0.191 cm^{-1}. By knowing the beam geometry and beam attenuation by the medium, the full excitation profile (Figure 3.3.3.2, C) and thus, the beam waist radius (30.6 μm) and the average excitation intensity in the beam waist (6.2 kW/cm^2) can be estimated. Calculations were performed in Wolfram Mathematica 11.0.

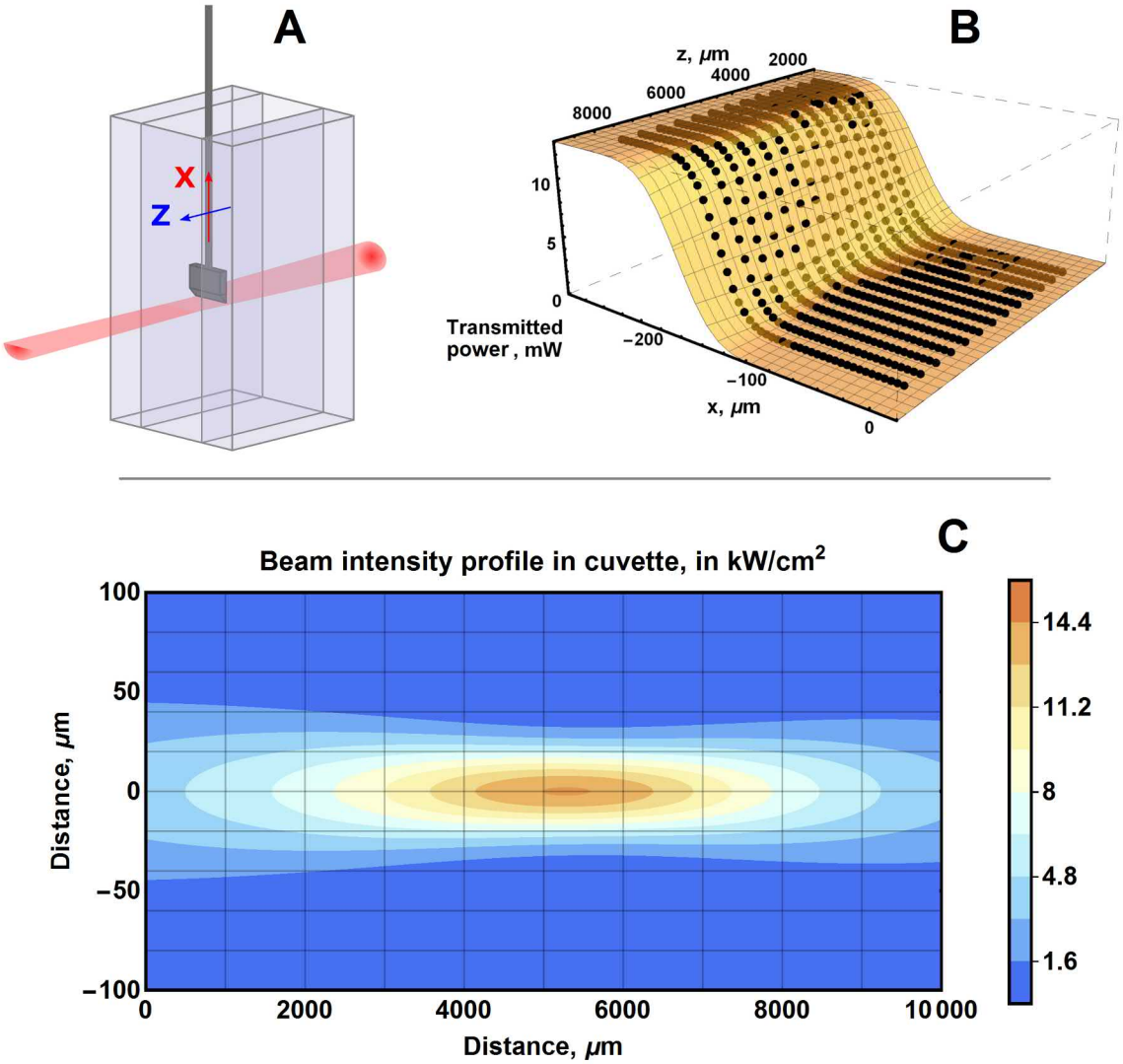

Figure 3.3.3.2. Measurement of the excitation beam intensity profile for the cuvette setup. A: setup for measuring the beam profile. The laser beam is occluded by a movable razor blade, permitting only a part of the beam to go through. B: dependence of the transmitted power on lateral and vertical blade position (black points) and its global fit with the occlusion curve (orange surface). C: obtained beam intensity profile that takes into account water absorption inside the cuvette.

3.3.4. Time-correlated single photon counting (TCSPC) lifetime measurements

Lifetime measurements of UCNPs shared the same excitation path as the spectral measurements, but the output power of the laser diode was controlled by an external analog modulation generated by a National Instruments multifunction board (PCIe 6361). During

lifetime measurements, the laser output power followed a 125 Hz square wave waveform with 15% duty cycle. The emission was collected through a monochromator (Jobin Yvon HC10IR). The single-photon events were detected with an avalanche photodiode (Excelitas SPCM-AQRH-16) and recorded on a time-correlated single photon counting board SPC-830 (Becker-Hickl GmbH). For collecting robust decay curves, at least 2 million photons were collected for each curve, and the photon timings were distributed in 4096 time bins for each 80 ms cycle, for approximately 20 μs per bin. The decay curves were fitted using bi- or tri-exponential fitting models in Origin Pro 8.

Part 4. Microscopy.

3.4.1. Wide-field upconversion microscopy (epi-Upcon)

Luminescence imaging of UCNPs was performed on an inverted microscope (Olympus IX71) equipped with a high numerical aperture objective (Olympus, UApo N 100x/1.49 Oil). A 980 nm continuous-wave laser coupled to a single mode fiber with a maximum output of 350 mW (Qphotonics, QFBGLD-980-350) was passed through a longpass filter (Chroma, E780LP) used to excite the UCNPs with an excitation power density of ~8 kW/cm^2 in epi illumination. Luminescence emission was separated from the excitation beam by using a short pass dichroic mirror (Chroma, T875spxrxt), while the residual laser light was removed by a low pass filter (Chroma, E700SP). Emission was detected by an electron multiplying CCD camera (Hamamatsu, ImagEM X2 C9100-23B) through an image splitting system for simultaneous dual wavelength imaging (Hamamatsu, W-VIEW GEMINI). This splitting system was used with an appropriate dichroic mirror (Semrock, FF560-FDi01) and band pass filters for green channel (Semrock, FF01-535/50) and red channel (Semrock, FF01-660/30-25). We have calibrated the spectral response of our microscopy setup with an external white light source as a reference and used this calibration for correcting the red to green relative emission ratio. Acquisition was fully automated and controlled by scripts within the MicroManager framework.[6] All static images were recorded as an averaged stack of 100 images, each with 100 ms exposure time.

Wide-field microscopy images were treated with ImageJ 1.51h as part of the FIJI package. Stitching was performed with the Grid/Collection stitching plugin (*Preibisch et al.,*

2009). Drift correction was done using a homemade script written in ImageJ macro language. Spot fitting was performed with the Gaussian Fit module of the GDSC SMLM package (*"GDSC ImageJ Plugins : ImageJ : ... : Sussex Centre for Genome Damage and Stability : Lifesci : Schools : Staff : University of Sussex," n.d.)*. Data analysis was performed with homemade scripts written in Python 3.4.3.

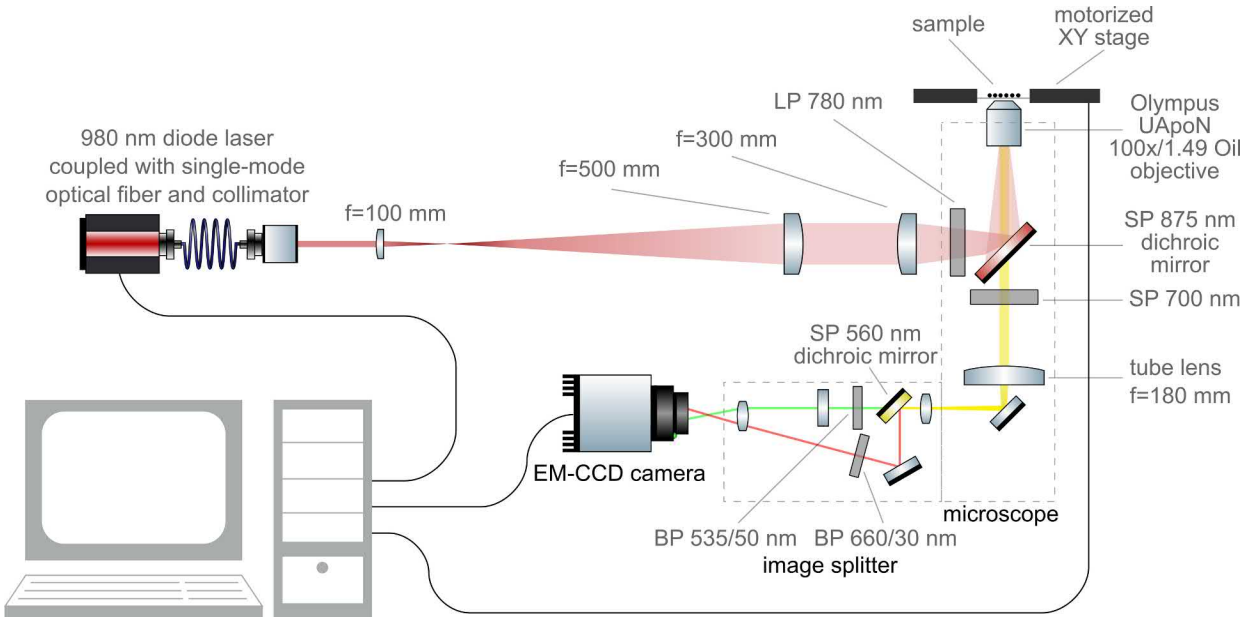

Figure 3.4.1.1. Scheme of the microscopy setup.

To estimate the excitation beam profile in the image plane of our microscopy setup, we imaged oleate-capped UCNPs dried at low density on a glass coverslip. A single UCNP was scanned through the field of view, using the motorized XY stage (Märzhäuser) with a step of 4 µm (Figure 3.4.1.2, A). The UCNP luminescence was measured as a function of its position, which provides the excitation intensity map (Figure 3.4.1.2, B). To check the dependence of the UCNP luminescence on the excitation intensity, the UCNP was positioned in the center of the excitation beam and its luminescence was measured at various laser powers. In the high power regime used in our experiments, the luminescence of the individual UCNPs in the red channel was observed to be linearly dependent on the laser power and thus, on the excitation intensity (Figure 3.4.1.2, C). By fitting the intensity map with a 2D circular gaussian profile (Fig. Figure 3.4.1.2, D), the beam waist radius in the image plane was found to be 28 µm. Knowing the laser power after the objective (96 mW), the average excitation intensity was

found to be 8 kW/cm^2 at the center of the beam, where the excitation intensity varied by less than 10% (in a 6.3 µm radius from the beam center). When treating the data, only the luminescence of UCNPs positioned in the center of the beam was considered.

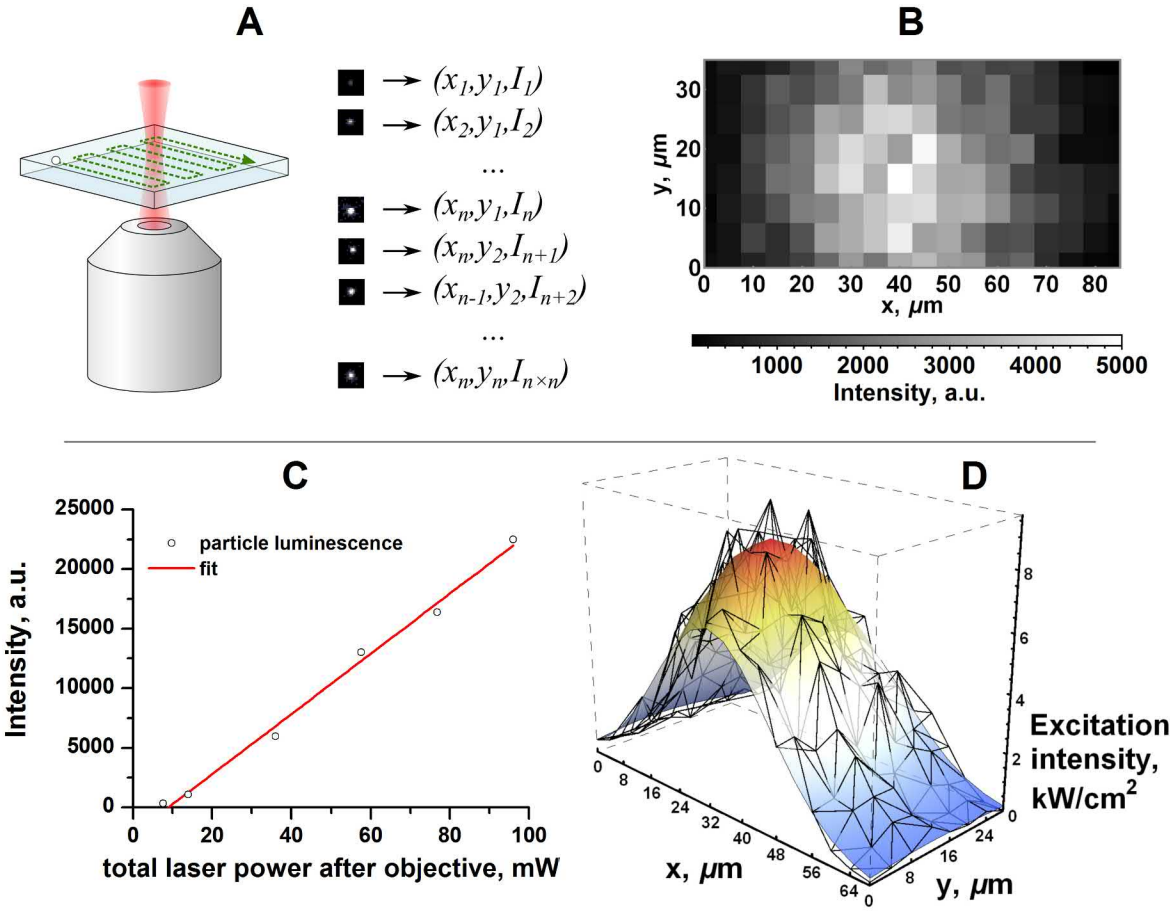

Figure 3.4.1.2. Measurement of the excitation beam intensity profile for the microscopy setup. A: scheme of the mapping experiment. B: excitation intensity map in the field of view. C: excitation power dependency for an immobilized particle. D: excitation beam profile at the maximum laser power.

3.4.2. Total internal reflection upconversion microscopy (TIRF-Upcon)

For TIRF imaging, the setup for epi imaging was realigned by translating the mirror before the entry of the microscope, resulting in the lateral shift of the excitation beam. To confirm that the setup was operating in TIRF mode, the shift of the beam passing through the sample was inspected visually (as the beam gets translated, it exits the sample at progressively

more sharp angle to the horizontally mounted sample). For precise alignment to optimal TIRF mode, the shift was performed with a sample of immobilized UCNPs, to monitor the transient increase in brightness when excitation shifted to TIRF mode. The optimal position was found to be immediately preceding the sudden disappearance of the particles when the beam was translated too far and hit the side of the objective. Realignment back to epi mode was performed by reverse translation of the mirror, returning the beam exiting the sample to perpendicular direction.

3.4.3. Atomic force microscopy (AFM)

AFM measurements were performed on a Veeco Nanoscope IIIa MultiMode AFM (Veeco, Santa Barbara, California, United States) in tapping mode, using RTESP7 cantilever probes (silicon, 300 MHz). Raw AFM data were treated with the Gwyddion 2.40 software (automatic mean plane subtraction, then automatic line correction by matching height median). As no deconvolution with the tip shape was performed, only the height of the sample was used as an estimate of the particle size. Typically, the UCNPs were diluted ~1000x-10000x relative to the stock dispersion to obtain samples with highly separated particles, suitable for correlated AFM/wide-field upconversion measurements.

3.4.4. Correlated AFM/wide-field upconversion microscopy (AFM-Upcon)

For correlated atomic force microscopy / wide-field upconversion luminescence microscopy (AFM/Upcon), the particles were 1000-fold diluted in water from stock solution and dried for 1 h in a vacuum chamber on mica glued to a thin steel washer. To ensure a clean flat surface, mica was exfoliated with a scotch tape immediately before the experiment. The bottom side of the mica was marked with a permanent marker (Staedtler permanent Lumocolor, red) to leave a spot clearly visible in bright field microscopy. The position of the scanned region of interest (ROI) relative to the marker spot was noted. Then, the sample was inverted and fixed on a glass coverslip with a scotch tape. The marker spot was found by illuminating the sample with a white lamp, and the objective was positioned with an XY stage with corresponding offsets relative to the spot, to find the approximate position of the scanned ROI. The precise ROI was located manually afterwards. Fig. 3.4.4.1 illustrates the protocol.

Afterwards, the luminescence images were treated by a landmark-based rigid transformation to match the AFM geometry, using Landmark Correspondences FIJI plugin (*Saalfeld, 2018*). The rigid transformation was chosen to retain the spot proportions and inter-spot distances. Landmarks were set manually by the user.

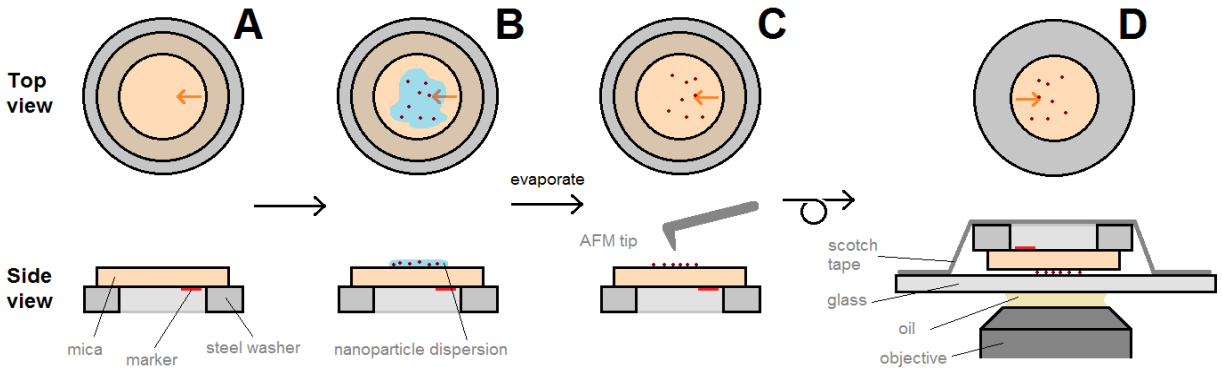

Figure 3.4.4.1. Sample preparation for correlated AFM/ wide-field upconversion luminescence microscopy. A: Initial assembly of mica attached to a steel washer, with a marker on the bottom side (red arrow). B: A drop of nanoparticle dispersion is added. C: After evaporation, AFM is performed on the sample. D: The sample is then inverted and fixed to a glass coverslip. The marker is located by eye in the bright field mode, and the exact ROI is located with an XY stage.

3.4.5. Live cell phase contrast videomicroscopy

Bright-field phase contrast time lapses were performed on a fully motorized inverted microscope (Leica, FW 4000 with 20x 0.40 N.A. N PlanL Ph1 objective or 40x 0.75 N.A. HCX PL APO Ph2 objective) equipped with a sCMOS Camera (Photometrics, Prime) and controlled by Metamorph 7.8.13.0 (Molecular Device). An incubator box (Life Imaging System) allowed temperature, CO_2 and humidity control. Samples were prepared in 8 well plates (Ibidi, µ-Slide 8 Well Glass Bottom). For degranulation videomicroscopy experiments, cells were seeded in Ibidi 8-well glass-bottom plates at 30000 cells per plate and cultured in cell medium overnight. Microscopy was performed at 37°C in the presence of 5% CO_2. For cell priming with antibodies, IgE was diluted in culture medium at 100 ng/mL and cells were primed over 30 min. For degranulation, DNP-BSA was diluted in 1x HBSS at 50 ng/mL, and

degranulation was monitored over 30 min. Images were taken in a time-lapse, every 10 seconds.

Part 5. Biological sample preparation.

3.5.1. Cell culture

RBL-2H3 cells were purchased from ATCC and cultured in complete MEM supplemented with 10% FBS and 1% penicillin/streptomycin at 37ºC in the presence of 5% CO_2 in 5 mL flasks (Nunc EasyFlask, Thermo Scientific). Passages were performed every 2-3 days using 0.25% trypsin/EDTA to detach cells from surface, in confluent or subconfluent cultures (overconfluence was avoided to reduce possible associated adverse effects on cell performance).

3.5.2. Controlled antibody biotinylation

An example protocol for antibody biotinylation using the Biotin-NHS reagent (Thermo Fisher) is given below.

12 µL of 1 mg/mL Anti-DNP IgE (clone SPE-7, Sigma-Aldrich D8406) were exchanged into 1x PBS buffer using a Zeba Micro Spin centrifuge desalting column (Thermo Fisher) following manufacturer's instructions for buffer exchange. This step is required as azide in storage buffer can interfere with the biotinylation reaction. After this step, the total volume of antibody was 18 µL. Next, the biotinylating reagent was dissolved at 58.65 mM concentration in DMSO. 0.27 µL of DMSO solution was added to 1x PBS and vortexed. Immediately after, 18 µL of this solution were mixed with 18 µL of IgE. This corresponded to ~1:3 antibody to biotinylating reagent stoichiometry. The mixture was incubated at room temperature in the dark over 2 h. Then, the mixture was exchanged to 1x PBS on Zeba Micro Spin centrifuge desalting columns to remove the excess of unreacted reagent. This yields antibody at approx. 0.22 mg/mL concentration, assuming quantitative yield of purification steps and taking into account dilution on all steps.

To estimate the biotinylation extent of the antibody, we performed SDS-PAGE (10% gel) of the biotinylated antibodies in the presence of streptavidin. Before loading, the antibody

(4 μL at ~0.22 mg/mL) was denatured by heating at 95ºC over 3 min in reducing loading buffer (using 10% mercaptoethanol as reducing agent). After cooling down, streptavidin was added (6 μL at ~1 mg/mL, purchased from IBA). At room temperature, streptavidin is resistant to denaturation with SDS, and retains activity. This allows to estimate the extent of antibody biotinylation by observing the relative intensity of the bands corresponding to heavy or light chains of antibody, and bands corresponding to complexes of biotinylated heavy or light chains with one, two or multiple streptavidin molecules.

Results are shown on Figure 3.5.2.1. An increase of the concentration of the biotinylation reagent concentration on the biotinylation step ultimately leads to an increase in the heavier bands. We were able to estimate biotinylation only of heavy chains (MW ~70 KDa), as the band of the complex of light chain (~25 KDa) with a single streptavidin has approximately the same molecular weight as the heavy chain (~90 KDa). We tested several antibody to biotinylation reagent stoichiometries, and observed a gradual increase in intensity and number of high molecular weight bands corresponding to complexes of antibody heavy chain with one, two or more streptavidins, at molecular weights of ~145 KDa (90+55), ~200 KDa (90+2*55), ~255 KDa (90+3*55), etc. As we wanted the activity of the antibody to be as close to the native one as possible, we ultimately have chosen the 1:3 stoichiometry described in the aforementioned protocol. Based on the gels, this stoichiometry yields approximately 1 mono-biotinylated antibody per 2 non-biotinylated ones.

We note that this method works only with streptavidin that has a relatively narrow molecular weight distribution. Affinity-purified streptavidin (e.g. the cheaper option from Sigma-Aldrich) has identical activity, but has a wide molecular weight distribution due to its production and purification processes, leading to difficulties in gel interpretation.

.

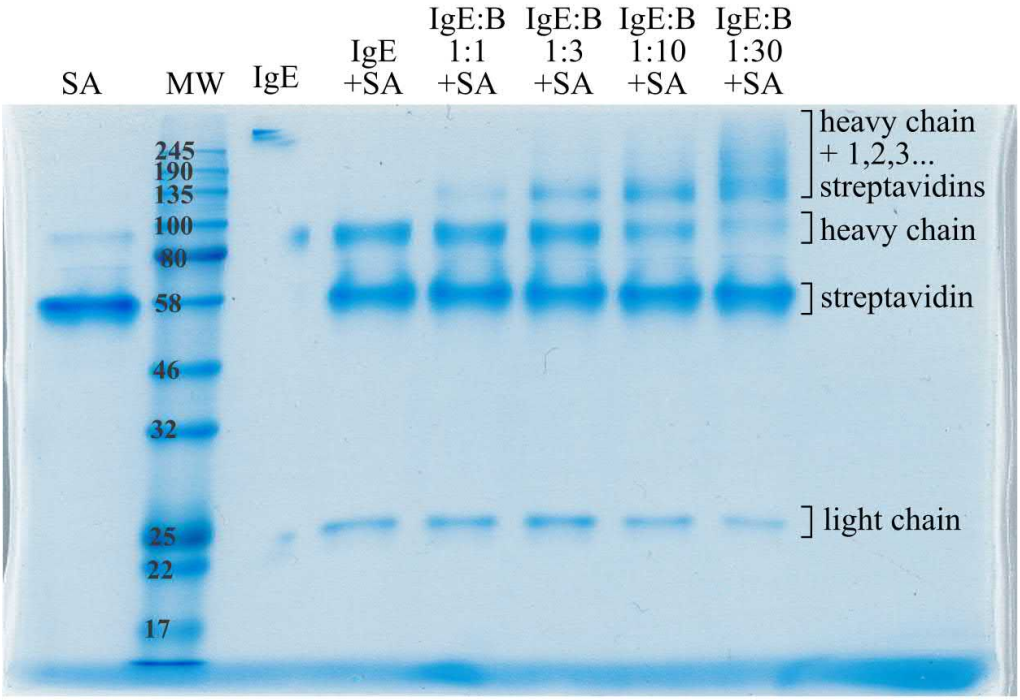

Figure 3.5.2.1. SDS-PAGE of antibody denatured in reductive conditions, mixed with excess streptavidin. MW reference lane was loaded with Color Prestained Protein Standard, Broad Range (NEB). Unlike the rest of the lanes, pure antibody lane was loaded using non-reducing denaturing conditions. Reducing reagent from the neighbouring lane has partially denatured the antibody during the stacking step, allowing to observe both the non-reduced antibody and antibody reduced into heavy and light chains. Streptavidin lane was deliberately overloaded (10 μg) to monitor the presence of any impurities.

Part 6. Calculations, modeling, and data treatment.

Typically, calculations, modeling and data treatment were performed using ImageJ as a part of the FIJI or Micro-Manager packages, Origin Pro 8, Wolfram Mathematica 10.0 and 11.2, Python 3.4.3, MatLab (R2010b or R2016b), LabView, LibreOffice Calc and Microsoft Excel. For single-particle tracking, videos were treated using TrackMate framework developed by group of Jean-Yves Tinevez (*Tinevez et al., 2017*). For preparation of illustrations, the capabilities of the aforementioned programs were used, along with Microsoft Paint, paint.NET and Inkscape. Manuscript preparation was performed in LibreOffice Writer

and Microsoft Word. Due to their considerable size, scripts and code are not presented here, but are available upon request.

Chapter 4. Conclusions and perspectives.

Conclusions

The main objective of this research work was to adapt UCNPs towards single-molecule microscopy to gain advantage of their unique properties. The accent was made on biological applications, as they would benefit the most from the properties of UCNPs. Imaging with UCNPs allows to remove autofluorescence background, which is a common source of issues in conventional fluorescence microscopy in biology. Extreme photostability of UCNPs and the absence of blinking are also notable advantages for microscopy applications.

To this aim, we have perfected protocols for making raw, oleate-capped UCNPs water-dispersible. Our main priority was to retain particle monodispersity, as the homogeneous size of the particles is crucial for SMM applications, where oligomerization and aggregation of particles can induce significant systematic errors in the experiments. We investigated multiple strategies: ligand exchange, nanoemulsion entrapment, amphiphilic polymer coating, and zwitterionic amphiphilic polymers. We found that coating particles with amphiphilic polymers is arguably the best method for adapting them towards SMM due to the high particle monodispersity, colloidal stability, low thickness of the coating, and possibility to decorate the obtained particles with functionality-imparting groups. We added functional groups directly during the polymer synthesis, but we note that the UCNPs can also be decorated after coating. Other strategies for water dispersibility did not yield particles of appreciable quality for SMM.

We have also devised protocols for single-particle imaging of UCNPs and estimated the stability of individual UCNPs in aqueous buffers. We noticed that dissolution-caused damage of UCNPs can induce high heterogeneity in the intensity and spectral response of single particles. We showed that such dissolution-caused effects can be effectively inhibited by employing fluoride buffers during imaging.

We have tried to adapt UCNPs towards smFRET applications. For this aim, we performed systematic experimental assessment of FRET efficiency from UCNPs of various sizes towards organic dyes attached to the particle surface. Based on this data, we have made a semi-empirical Monte Carlo model for prediction of efficiency of FRET from UCNPs to

organic dyes. Ultimately, the efficiencies of FRET from a single UCNP towards a single dye (as in smFRET) were deemed insufficient for smFRET applications, at least for commonly used homogeneously doped Yb-Er UCNPs. Nevertheless, the model has potential for quick estimation of FRET efficiency from UCNPs to multiple dyes, which can be useful in development of other FRET-based applications besides smFRET.

Finally, we adapted UCNPs towards single-particle tracking. For this, the UCNPs were modified with biotin and then streptavidin, yielding streptavidin-decorated particles, allowing easy attachment of biotinylated targeting molecules (antibodies or aptamers). To confirm that the particles had superior performance in SPT, we decorated them with IgE antibodies and performed SPT of FcεRI receptors on the surface of RBL-2H3 cells. This system was well-described in literature specifically with SPT techniques, which allowed us to validate the behavior of our particles by comparing it to the literature data. Overall, we found UCNPs to show uninterrupted long-term emission, exceptional photostability, and low background due to elimination of autofluorescence. All of those properties showed UCNPs to be very promising luminophores for SPT.

In summary, this work is the first extensive exploratory foray of our laboratory into the exciting fields of upconversion nanoparticles and upconversion microscopy. During the work, we have established multiple protocols and gained valuable empirical experience that will serve as a foundation for future work on UCNP applications in biological microscopy.

Perspectives

For dispersing UCNPs in water, the next step for improvement would be expanding the work on zwitterionic polymers, perhaps by using more hydrophilic or oligomeric zwitterions. Keeping the particle surface approximately neutral with a strongly coordinated water shell would be very important to combat non-specific binding to proteins and nucleic acids, both for in vitro and in vivo experiments. Exploring the possibilities of coating UCNPs with a silica shell could also prove fruitful, given its high chemical resistance and well-developed protocols for its modification. Multiple groups have been using this approach for experiments with bulk UCNPs. Devising a method to produce colloidally stable silica-coated UCNPs of high monodispersity would be an important step towards creating UCNPs with a variety of functionalities for microscopy experiments.

For smFRET applications, a crucial improvement of UCNP-dye FRET efficiency would likely involve engineering particles with cooperative emitters. With sufficiently long emitter lifetime, this approach could allow the emitters farther than the Förster distance from the dye to still be able to contribute to FRET, by transferring their energy towards the emitters that are close to the dye. Such particles have been already reported in literature in simple FRET experiments, using homo-FRET between Gd^{3+} ions as the cooperativity mechanism (*Deng et al., 2016; Wang et al., 2011*). However, the potential of such UCNPs towards smFRET experiments has not been investigated yet.

For SPT applications, the streptavidin-grafted particles that we developed can be immediately used towards investigation of cell membrane component behavior via SPT. Unlike organic dyes and quantum dots, the absence of blinking and bleaching with UCNPs allows performing SPT on extremely long timescales, and unlike gold nanoparticles, UCNPs can be made in smaller sizes and can be used in multichannel experiments (e.g. for simultaneous multi-target SPT with several different types of UCNPs). Multichannel experiments can be additionally extended by using UCNPs with dopant-dependent spectral responses, originally developed for multiplexing. By tuning the dopant concentrations, one could produce particles with very distinct spectral signatures with significantly different band structures and band ratios. Ultimately, this approach could allow to perform SPT experiments in which each individual particle has a distinct spectral signature.

All of the above approaches can also be immediately improved and expanded upon by using tailored particles made specifically for microscopy purposes. In recent years, an ample amount of work has been dedicated by multiple research groups around the world towards this aim, for example, through a popular approach of shielding sensitizers against quenching using an inert shell grown on particle surface. The new developed UCNPs have immediate advantages for increasing brightness in SMM. In regards to improving particle brightness, there have been multiple reports on using dyes with a low-energy triplet excited state to efficiently transfer energy to sensitizers inside UCNPs (*Chen et al., 2015; Garfield et al., 2018; Zou et al., 2012*). This approach effectively increases extinction coefficient of UCNPs and hence, their brightness. However, the obtained particles rapidly lose their brightness in biological conditions, as the dye in its excited state is very susceptible towards oxidative

degradation (for example, by ambient oxygen). Entrapping such dyes on the particle surface under a thick impenetrable layer of silica or densely packed polymer could provide them with substantial resistance against photobleaching. The obtained luminophore could combine unprecedented extinction coefficients of dye-loaded nanoparticles with unique properties of UCNPs like high anti-Stokes shift and narrow band structure.

Extending the ideas applied to UCNPs in photodynamic therapy, drug delivery and theranostics, one could imagine making UCNPs with a controllable activated function. Such particles would serve not only as labels, but also as nanoscale *instruments* in SMM. For instance, attaching photocleavable groups to the surface of particles could allow consistent long-term tracking of UCNPs under infrared illumination in cell experiments, observing their localization in different regions of cells (e.g. in late endosomes), and inducing changes in their environment by a flash of focused visible light at the right place in the right moment. Another particularly interesting approach would be using UCNPs with blue or violet emission for controlled IR-activated photopolymerization for nanoscale 3D printing, using FRET from the particle as an efficient highly localized source for initiating the polymerization process (some groundwork towards this application has been laid in *Rocheva et al., 2018*). The on-demand local generation of UV and/or visible excitation by UCNPs also holds potential for optogenetic experiments as well, by attaching UCNPs to photosensitive ion channels introduced in transgenic cells, allowing IR-triggered channel opening behavior (promising examples are shown in *S. Chen et al., 2018; Pliss et al., 2017; Shah et al., 2015; X. Wu et al., 2016*).

Plasmonic effects, particularly absorption and emission enhancement in luminophores close to conductive particles and/or surfaces (e.g. gold nanoparticles) could be another interesting approach towards increasing UCNP brightness in microscopy experiments. Prototype experiments have been already reported in literature, but so far no particularly high brightness enhancement factors have been shown yet. The approach that holds the most promise involves positioning UCNPs on the tip of a gold nanorod of appropriate dimensions that allows both absorption and emission enhancement at the same time, as the nanorod has two appropriate plasmonic resonance frequencies. If a method to reliably assemble this system in an appropriate geometry would be devised, the obtained composite particles would have a formidable improvement in upconversion luminescence, which would be especially useful for microscopy applications.

References

A

Agostinis, P., Berg, K., Cengel, K.A., Foster, T.H., Girotti, A.W., Gollnick, S.O., Hahn, S.M., Hamblin, M.R., Juzeniene, A., Kessel, D., Korbelik, M., Moan, J., Mroz, P., Nowis, D., Piette, J., Wilson, B.C., Golab, J., 2011. Photodynamic therapy of cancer: An update. CA: A Cancer Journal for Clinicians 61, 250–281. https://doi.org/10.3322/caac.20114

Anderson, R.B., Smith, S.J., May, P.S., Berry, M.T., 2014. Revisiting the NIR-to-Visible Upconversion Mechanism in β-NaYF4:Yb3+,Er3+. J. Phys. Chem. Lett. 5, 36–42. https://doi.org/10.1021/jz402366r

Andreiuk, B., Reisch, A., Lindecker, M., Follain, G., Peyriéras, N., Goetz, J.G., Klymchenko, A.S., 2017. Fluorescent Polymer Nanoparticles for Cell Barcoding In Vitro and In Vivo. Small 13, 1701582. https://doi.org/10.1002/smll.201701582

Andrews, N.L., Lidke, K.A., Pfeiffer, J.R., Burns, A.R., Wilson, B.S., Oliver, J.M., Lidke, D.S., 2008. Actin restricts FcεRI diffusion and facilitates antigen-induced receptor immobilization. Nature Cell Biology 10, 955–963. https://doi.org/10.1038/ncb1755

Anton, N., Vandamme, T.F., 2010. Nano-emulsions and Micro-emulsions: Clarifications of the Critical Differences. Pharm Res 28, 978–985. https://doi.org/10.1007/s11095-010-0309-1

Anton, N., Vandamme, T.F., 2009. The universality of low-energy nano-emulsification. International Journal of Pharmaceutics 377, 142–147. https://doi.org/10.1016/j.ijpharm.2009.05.014

Arhel, N., Genovesio, A., Kim, K.-A., Miko, S., Perret, E., Olivo-Marin, J.-C., Shorte, S., Charneau, P., 2006. Quantitative four-dimensional tracking of cytoplasmic and nuclear HIV-1 complexes. Nature Methods 3, 817–824. https://doi.org/10.1038/nmeth928

Arppe, R., Hyppänen, I., Perälä, N., Peltomaa, R., Kaiser, M., Würth, C., Christ, S., Resch-Genger, U., Schäferling, M., Soukka, T., 2015. Quenching of the upconversion luminescence of NaYF4:Yb3+,Er3+ and NaYF4:Yb3+,Tm3+ nanophosphors by water:

the role of the sensitizer Yb3+ in non-radiative relaxation. Nanoscale 7, 11746–11757. https://doi.org/10.1039/C5NR02100F

Ash, E.A., Nicholls, G., 1972. Super-resolution Aperture Scanning Microscope. Nature 237, 510–512. https://doi.org/10.1038/237510a0

Atchison, D.A., Smith, G., 2000. Optics of the Human Eye. Butterworth-Heinemann.

Auzel, F., 2004. Upconversion and Anti-Stokes Processes with f and d Ions in Solids. Chem. Rev. 104, 139–174. https://doi.org/10.1021/cr020357g

Axelrod, D., 2001. Total Internal Reflection Fluorescence Microscopy in Cell Biology. Traffic 2, 764–774. https://doi.org/10.1034/j.1600-0854.2001.21104.x

B

Bálint, Š., Vilanova, I.V., Álvarez, Á.S., Lakadamyali, M., 2013. Correlative live-cell and superresolution microscopy reveals cargo transport dynamics at microtubule intersections. PNAS 110, 3375–3380. https://doi.org/10.1073/pnas.1219206110

Becker, W., 2012. Fluorescence lifetime imaging – techniques and applications. Journal of Microscopy 247, 119–136. https://doi.org/10.1111/j.1365-2818.2012.03618.x

Betzig, E., Patterson, G.H., Sougrat, R., Lindwasser, O.W., Olenych, S., Bonifacino, J.S., Davidson, M.W., Lippincott-Schwartz, J., Hess, H.F., 2006. Imaging Intracellular Fluorescent Proteins at Nanometer Resolution. Science 313, 1642–1645. https://doi.org/10.1126/science.1127344

Bhuckory, S., Hemmer, E., Wu, Y.-T., Yahia‐Ammar, A., Vetrone, F., Hildebrandt, N., 2017. Core or Shell? Er3+ FRET Donors in Upconversion Nanoparticles. European Journal of Inorganic Chemistry 2017, 5186–5195. https://doi.org/10.1002/ejic.201700904

Billinton, N., Knight, A.W., 2001. Seeing the Wood through the Trees: A Review of Techniques for Distinguishing Green Fluorescent Protein from Endogenous Autofluorescence. Analytical Biochemistry 291, 175–197. https://doi.org/10.1006/abio.2000.5006

Blanchard, S.C., Gonzalez Jr, R.L., Kim, H.D., Chu, S., Puglisi, J.D., 2004. tRNA selection and kinetic proofreading in translation. Nature Structural & Molecular Biology 11, 1008–1014. https://doi.org/10.1038/nsmb831

Bobroff, N., 1986. Position measurement with a resolution and noise?limited instrument. Review of Scientific Instruments 57, 1152–1157. https://doi.org/10.1063/1.1138619

Bonnett, R., 2014. Chemical Aspects of Photodynamic Therapy. CRC Press. https://doi.org/10.1201/9781482296952

Boyer, J.C., Johnson, N.J.J., van Veggel, F.C.J.M., 2009. Upconverting Lanthanide-Doped NaYF4−PMMA Polymer Composites Prepared by in Situ Polymerization. Chem. Mater. 21, 2010–2012. https://doi.org/10.1021/cm900756h

Boyer, J.-C., Veggel, F.C.J.M. van, 2010. Absolute quantum yield measurements of colloidal NaYF4: Er3+, Yb3+ upconverting nanoparticles. Nanoscale 2, 1417–1419. https://doi.org/10.1039/C0NR00253D

Braeken, Y., Cheruku, S., Ethirajan, A., Maes, W., 2017. Conjugated Polymer Nanoparticles for Bioimaging. Materials (Basel) 10. https://doi.org/10.3390/ma10121420

Broussard, J.A., Rappaz, B., Webb, D.J., Brown, C.M., 2013. Fluorescence resonance energy transfer microscopy as demonstrated by measuring the activation of the serine/threonine kinase Akt. Nature Protocols 8, 265–281. https://doi.org/10.1038/nprot.2012.147

C

Chan, E.M., 2015. Combinatorial approaches for developing upconverting nanomaterials: high-throughput screening, modeling, and applications. Chem. Soc. Rev. 44, 1653–1679. https://doi.org/10.1039/C4CS00205A

Chan, E.M., Gargas, D.J., Schuck, P.J., Milliron, D.J., 2012a. Concentrating and Recycling Energy in Lanthanide Codopants for Efficient and Spectrally Pure Emission: The Case of NaYF4:Er3+/Tm3+ Upconverting Nanocrystals. J. Phys. Chem. B 116, 10561–10570. https://doi.org/10.1021/jp302401j

Chan, E.M., Han, G., Goldberg, J.D., Gargas, D.J., Ostrowski, A.D., Schuck, P.J., Cohen, B.E., Milliron, D.J., 2012b. Combinatorial Discovery of Lanthanide-Doped Nanocrystals with Spectrally Pure Upconverted Emission. Nano Lett. 12, 3839–3845. https://doi.org/10.1021/nl3017994

Chan, E.M., Levy, E.S., Cohen, B.E., 2015. Rationally Designed Energy Transfer in Upconverting Nanoparticles. Adv. Mater. 27, 5753–5761. https://doi.org/10.1002/adma.201500248

Chan, E.M., Xu, C., Mao, A.W., Han, G., Owen, J.S., Cohen, B.E., Milliron, D.J., 2010. Reproducible, High-Throughput Synthesis of Colloidal Nanocrystals for Optimization in Multidimensional Parameter Space. Nano Lett. 10, 1874–1885. https://doi.org/10.1021/nl100669s

Chen, C., Wang, F., Wen, S., Su, Q.P., Wu, M.C.L., Liu, Y., Wang, B., Li, D., Shan, X., Kianinia, M., Aharonovich, I., Toth, M., Jackson, S.P., Xi, P., Jin, D., 2018. Multi-photon near-infrared emission saturation nanoscopy using upconversion nanoparticles. Nature Communications 9, 3290. https://doi.org/10.1038/s41467-018-05842-w

Chen, G., Damasco, J., Qiu, H., Shao, W., Ohulchanskyy, T.Y., Valiev, R.R., Wu, X., Han, G., Wang, Y., Yang, C., Ågren, H., Prasad, P.N., 2015. Energy-Cascaded Upconversion in an Organic Dye-Sensitized Core/Shell Fluoride Nanocrystal. Nano Lett. 15, 7400–7407. https://doi.org/10.1021/acs.nanolett.5b02830

Chen, S., Weitemier, A.Z., Zeng, X., He, L., Wang, X., Tao, Y., Huang, A.J.Y., Hashimotodani, Y., Kano, M., Iwasaki, H., Parajuli, L.K., Okabe, S., Teh, D.B.L., All, A.H., Tsutsui-Kimura, I., Tanaka, K.F., Liu, X., McHugh, T.J., 2018. Near-infrared deep brain stimulation via upconversion nanoparticle–mediated optogenetics. Science 359, 679–684. https://doi.org/10.1126/science.aaq1144

Cheng, Q., Sui, J., Cai, W., 2012. Enhanced upconversion emission in Yb3+ and Er3+ codoped NaGdF4 nanocrystals by introducing Li+ ions. Nanoscale 4, 779–784. https://doi.org/10.1039/C1NR11365H

Chenouard, N., Smal, I., de Chaumont, F., Maška, M., Sbalzarini, I.F., Gong, Y., Cardinale, J., Carthel, C., Coraluppi, S., Winter, M., Cohen, A.R., Godinez, W.J., Rohr, K., Kalaidzidis, Y., Liang, L., Duncan, J., Shen, H., Xu, Y., Magnusson, K.E.G., Jaldén, J., Blau, H.M., Paul-Gilloteaux, P., Roudot, P., Kervrann, C., Waharte, F., Tinevez, J.-Y., Shorte, S.L., Willemse, J., Celler, K., van Wezel, G.P., Dan, H.-W., Tsai, Y.-S., de Solórzano, C.O., Olivo-Marin, J.-C., Meijering, E., 2014. Objective comparison of particle tracking methods. Nat Meth 11, 281–289. https://doi.org/10.1038/nmeth.2808

Cognet, L., Leduc, C., Lounis, B., 2014. Advances in live-cell single-particle tracking and dynamic super-resolution imaging. Current Opinion in Chemical Biology, Molecular imaging 20, 78–85. https://doi.org/10.1016/j.cbpa.2014.04.015

Combs, C.A., 2010. Fluorescence Microscopy: A Concise Guide to Current Imaging Methods. Curr Protoc Neurosci 0 2, Unit2.1. https://doi.org/10.1002/0471142301.ns0201s50

Cox, I.J., Sheppard, C.J.R., 1986. Information capacity and resolution in an optical system. J. Opt. Soc. Am. A, JOSAA 3, 1152–1158. https://doi.org/10.1364/JOSAA.3.001152

Cranfill, P.J., Sell, B.R., Baird, M.A., Allen, J.R., Lavagnino, Z., Gruiter, H.M. de, Kremers, G.-J., Davidson, M.W., Ustione, A., Piston, D.W., 2016. Quantitative assessment of fluorescent proteins. Nature Methods 13, 557–562. https://doi.org/10.1038/nmeth.3891

Cremer, C., Kaufmann, R., Gunkel, M., Pres, S., Weiland, Y., Müller, P., Ruckelshausen, T., Lemmer, P., Geiger, F., Degenhard, S., Wege, C., Lemmermann, N.A.W., Holtappels, R., Strickfaden, H., Hausmann, M., 2011. Superresolution imaging of biological nanostructures by spectral precision distance microscopy. Biotechnology Journal 6, 1037–1051. https://doi.org/10.1002/biot.201100031

D

DaCosta, M.V., Doughan, S., Han, Y., Krull, U.J., 2014. Lanthanide upconversion nanoparticles and applications in bioassays and bioimaging: A review. Analytica Chimica Acta 832, 1–33. https://doi.org/10.1016/j.aca.2014.04.030

Dahan, M., Lévi, S., Luccardini, C., Rostaing, P., Riveau, B., Triller, A., 2003. Diffusion Dynamics of Glycine Receptors Revealed by Single-Quantum Dot Tracking. Science 302, 442–445. https://doi.org/10.1126/science.1088525

Damasco, J.A., Chen, G., Shao, W., Ågren, H., Huang, H., Song, W., Lovell, J.F., Prasad, P.N., 2014. Size-Tunable and Monodisperse Tm3+/Gd3+-Doped Hexagonal NaYbF4 Nanoparticles with Engineered Efficient Near Infrared-to-Near Infrared Upconversion for In Vivo Imaging. ACS Appl. Mater. Interfaces 6, 13884–13893. https://doi.org/10.1021/am503288d

Deegan, R.D., Bakajin, O., Dupont, T.F., Huber, G., Nagel, S.R., Witten, T.A., 1997. Capillary flow as the cause of ring stains from dried liquid drops. Nature 389, 827–829. https://doi.org/10.1038/39827

Deng, R., Wang, J., Chen, R., Huang, W., Liu, X., 2016. Enabling Förster Resonance Energy Transfer from Large Nanocrystals through Energy Migration. J. Am. Chem. Soc. 138, 15972–15979. https://doi.org/10.1021/jacs.6b09349

Dertinger, T., Colyer, R., Iyer, G., Weiss, S., Enderlein, J., 2009. Fast, background-free, 3D super-resolution optical fluctuation imaging (SOFI). PNAS 106, 22287–22292. https://doi.org/10.1073/pnas.0907866106

Ding, Y., Wu, F., Zhang, Y., Liu, X., de Jong, E.M.L.D., Gregorkiewicz, T., Hong, X., Liu, Y., Aalders, M.C.G., Buma, W.J., Zhang, H., 2015. Interplay between Static and Dynamic Energy Transfer in Biofunctional Upconversion Nanoplatforms. J. Phys. Chem. Lett. 6, 2518–2523. https://doi.org/10.1021/acs.jpclett.5b00999

Dolgosheina, E.V., Jeng, S.C.Y., Panchapakesan, S.S.S., Cojocaru, R., Chen, P.S.K., Wilson, P.D., Hawkins, N., Wiggins, P.A., Unrau, P.J., 2014. RNA Mango Aptamer-Fluorophore: A Bright, High-Affinity Complex for RNA Labeling and Tracking. ACS Chem. Biol. 9, 2412–2420. https://doi.org/10.1021/cb500499x

Dolmans, D.E.J.G.J., Fukumura, D., Jain, R.K., 2003. Photodynamic therapy for cancer. Nature Reviews Cancer 3, 380–387. https://doi.org/10.1038/nrc1071

Dong, A., Ye, X., Chen, J., Kang, Y., Gordon, T., Kikkawa, J.M., Murray, C.B., 2011. A Generalized Ligand-Exchange Strategy Enabling Sequential Surface Functionalization of Colloidal Nanocrystals. J. Am. Chem. Soc. 133, 998–1006. https://doi.org/10.1021/ja108948z

Drees, C., Raj, A.N., Kurre, R., Busch, K.B., Haase, M., Piehler, J., 2016. Engineered Upconversion Nanoparticles for Resolving Protein Interactions inside Living Cells. Angew. Chem. Int. Ed. 55, 11668–11672. https://doi.org/10.1002/anie.201603028

Dzebo, D., Moth-Poulsen, K., Albinsson, B., 2017. Robust triplet–triplet annihilation photon upconversion by efficient oxygen scavenging. Photochem. Photobiol. Sci. 16, 1327–1334. https://doi.org/10.1039/C7PP00201G

E

Egorov, S.A., Skinner, J.L., 1995. On the theory of multiphonon relaxation rates in solids. The Journal of Chemical Physics 103, 1533–1543. https://doi.org/10.1063/1.469775

El Meshri, S.E., Dujardin, D., Godet, J., Richert, L., Boudier, C., Darlix, J.L., Didier, P., Mély, Y., de Rocquigny, H., 2015. Role of the Nucleocapsid Domain in HIV-1 Gag Oligomerization and Trafficking to the Plasma Membrane: A Fluorescence Lifetime Imaging Microscopy Investigation. Journal of Molecular Biology 427, 1480–1494. https://doi.org/10.1016/j.jmb.2015.01.015

Eliseeva, S., Bünzli, J.-C., 2010. Lanthanide luminescence for functional materials and bio-sciences. Chemical Society Reviews 39, 189–227. https://doi.org/10.1039/B905604C

Ermund, A., Schütte, A., Johansson, M.E.V., Gustafsson, J.K., Hansson, G.C., 2013. Studies of mucus in mouse stomach, small intestine, and colon. I. Gastrointestinal mucus layers have different properties depending on location as well as over the Peyer's patches. Am J Physiol Gastrointest Liver Physiol 305, G341–G347. https://doi.org/10.1152/ajpgi.00046.2013

Estephan, Z.G., Schlenoff, P.S., Schlenoff, J.B., 2011. Zwitteration As an Alternative to PEGylation. Langmuir 27, 6794–6800. https://doi.org/10.1021/la200227b

F

Feng, Y., Chen, H., Ma, L., Shao, B., Zhao, S., Wang, Z., You, H., 2017. Surfactant-Free Aqueous Synthesis of Novel Ba2GdF7:Yb3+, Er3+@PEG Upconversion Nanoparticles for in Vivo Trimodality Imaging. ACS Appl. Mater. Interfaces 9, 15096–15102. https://doi.org/10.1021/acsami.7b03411

Förster, T., 1948. Zwischenmolekulare Energiewanderung und Fluoreszenz. Annalen der Physik 437, 55–75. https://doi.org/10.1002/andp.19484370105

Fujiwara, T., Ritchie, K., Murakoshi, H., Jacobson, K., Kusumi, A., 2002. Phospholipids undergo hop diffusion in compartmentalized cell membrane. The Journal of Cell Biology 157, 1071–1082. https://doi.org/10.1083/jcb.200202050

G

Gainer, C.F., Romanowski, M., 2014. A review of synthetic methods for the production of upconverting lanthanide nanoparticles. Journal of Innovative Optical Health Sciences 07, 1330007. https://doi.org/10.1142/S1793545813300073

Gainer, C.F., Utzinger, U., Romanowski, M., 2012. Scanning two-photon microscopy with upconverting lanthanide nanoparticles via Richardson-Lucy deconvolution. JBO 17, 076003. https://doi.org/10.1117/1.JBO.17.7.076003

García, K.P., Zarschler, K., Barbaro, L., Barreto, J.A., O'Malley, W., Spiccia, L., Stephan, H., Graham, B., 2014. Zwitterionic-Coated "Stealth" Nanoparticles for Biomedical Applications: Recent Advances in Countering Biomolecular Corona Formation and Uptake by the Mononuclear Phagocyte System. Small 10, 2516–2529. https://doi.org/10.1002/smll.201303540

Garfield, D.J., Borys, N.J., Hamed, S.M., Torquato, N.A., Tajon, C.A., Tian, B., Shevitski, B., Barnard, E.S., Suh, Y.D., Aloni, S., Neaton, J.B., Chan, E.M., Cohen, B.E., Schuck, P.J., 2018. Enrichment of molecular antenna triplets amplifies upconverting nanoparticle emission. Nature Photonics 12, 402–407. https://doi.org/10.1038/s41566-018-0156-x

Gargas, D.J., Chan, E.M., Ostrowski, A.D., Aloni, S., Altoe, M.V.P., Barnard, E.S., Sanii, B., Urban, J.J., Milliron, D.J., Cohen, B.E., Schuck, P.J., 2014. Engineering bright sub-10-nm upconverting nanocrystals for single-molecule imaging. Nat Nano 9, 300–305. https://doi.org/10.1038/nnano.2014.29

GDSC ImageJ Plugins : ImageJ : ... : Sussex Centre for Genome Damage and Stability : Lifesci : Schools : Staff : University of Sussex [WWW Document], n.d. URL http://www.sussex.ac.uk/gdsc/intranet/microscopy/imagej/gdsc_plugins (accessed 3.29.18).

Giepmans, B.N.G., Adams, S.R., Ellisman, M.H., Tsien, R.Y., 2006. The Fluorescent Toolbox for Assessing Protein Location and Function. Science 312, 217–224. https://doi.org/10.1126/science.1124618

Girsault, A., Lukes, T., Sharipov, A., Geissbuehler, S., Leutenegger, M., Vandenberg, W., Dedecker, P., Hofkens, J., Lasser, T., 2016. SOFI Simulation Tool: A Software Package for Simulating and Testing Super-Resolution Optical Fluctuation Imaging. PLOS ONE 11, e0161602. https://doi.org/10.1371/journal.pone.0161602

Gnach, A., Lipinski, T., Bednarkiewicz, A., Rybka, J., Capobianco, J.A., 2015. Upconverting nanoparticles: assessing the toxicity. Chem. Soc. Rev. 44, 1561–1584. https://doi.org/10.1039/C4CS00177J

Godin, A.G., Lounis, B., Cognet, L., 2014. Super-resolution Microscopy Approaches for Live Cell Imaging. Biophys J 107, 1777–1784. https://doi.org/10.1016/j.bpj.2014.08.028

Göttfert, F., Wurm, C.A., Mueller, V., Berning, S., Cordes, V.C., Honigmann, A., Hell, S.W., 2013. Coaligned Dual-Channel STED Nanoscopy and Molecular Diffusion Analysis at 20 nm Resolution. Biophysical Journal 105, L01–L03. https://doi.org/10.1016/j.bpj.2013.05.029

Gualda, E.J., Pereira, H., Martins, G.G., Gardner, R., Moreno, N., 2017. Three-dimensional imaging flow cytometry through light-sheet fluorescence microscopy. Cytometry Part A 91, 144–151. https://doi.org/10.1002/cyto.a.23046

Gustafsson, M.G.L., Shao, L., Carlton, P.M., Wang, C.J.R., Golubovskaya, I.N., Cande, W.Z., Agard, D.A., Sedat, J.W., 2008. Three-Dimensional Resolution Doubling in Wide-Field Fluorescence Microscopy by Structured Illumination. Biophysical Journal 94, 4957–4970. https://doi.org/10.1529/biophysj.107.120345

H

Haase, M., Schäfer, H., 2011. Upconverting Nanoparticles. Angew. Chem. Int. Ed. 50, 5808–5829. https://doi.org/10.1002/anie.201005159

Han, Y., Gu, Y., Ce Zhang, A., Lo, Y.-H., 2016. Review: imaging technologies for flow cytometry. Lab on a Chip 16, 4639–4647. https://doi.org/10.1039/C6LC01063F

Han, Y., Li, H., Wang, Y., Pan, Y., Huang, L., Song, F., Huang, W., 2017. Upconversion Modulation through Pulsed Laser Excitation for Anti-counterfeiting. Scientific Reports 7, 1320. https://doi.org/10.1038/s41598-017-01611-9

Hecht, E., 2002. Optics. Addison-Wesley.

Heer, S., Kömpe, K., Güdel, H.-U., Haase, M., 2004. Highly Efficient Multicolour Upconversion Emission in Transparent Colloids of Lanthanide-Doped NaYF4 Nanocrystals. Adv. Mater. 16, 2102–2105. https://doi.org/10.1002/adma.200400772

Hell, S.W., Sahl, S.J., Bates, M., Zhuang, X., Heintzmann, R., Booth, M.J., Joerg Bewersdorf, Shtengel, G., Hess, H., Tinnefeld, P., Honigmann, A., Jakobs, S., Ilaria Testa, Cognet, L., Lounis, B., Ewers, H., Davis, S.J., Eggeling, C., David Klenerman, Willig, K.I., Vicidomini, G., Castello, M., Diaspro, A., Cordes, T., 2015. The 2015 super-resolution microscopy roadmap. J. Phys. D: Appl. Phys. 48, 443001. https://doi.org/10.1088/0022-3727/48/44/443001

Hell, S.W., Wichmann, J., 1994. Breaking the diffraction resolution limit by stimulated emission: stimulated-emission-depletion fluorescence microscopy. Opt. Lett., OL 19, 780–782. https://doi.org/10.1364/OL.19.000780

Helmchen, F., Denk, W., 2005. Deep tissue two-photon microscopy. Nature Methods 2, 932–940. https://doi.org/10.1038/nmeth818

Hess, S.T., Girirajan, T.P.K., Mason, M.D., 2006. Ultra-High Resolution Imaging by Fluorescence Photoactivation Localization Microscopy. Biophys J 91, 4258–4272. https://doi.org/10.1529/biophysj.106.091116

Hlaváček, A., Farka, Z., Hübner, M., Horňáková, V., Němeček, D., Niessner, R., Skládal, P., Knopp, D., Gorris, H.H., 2016. Competitive Upconversion-Linked Immunosorbent Assay for the Sensitive Detection of Diclofenac. Anal. Chem. 88, 6011–6017. https://doi.org/10.1021/acs.analchem.6b01083

Hlaváček, A., Sedlmeier, A., Skládal, P., Gorris, H.H., 2014. Electrophoretic Characterization and Purification of Silica-Coated Photon-Upconverting Nanoparticles and Their Bioconjugates. ACS Appl. Mater. Interfaces 6, 6930–6935. https://doi.org/10.1021/am500732y

Hossan, M.Y., Hor, A., Luu, Q., Smith, S.J., May, P.S., Berry, M.T., 2017. Explaining the Nanoscale Effect in the Upconversion Dynamics of β-NaYF4:Yb3+, Er3+ Core and Core–Shell Nanocrystals. J. Phys. Chem. C 121, 16592–16606. https://doi.org/10.1021/acs.jpcc.7b04567

Hu, L., Wang, P., Zhao, M., Liu, L., Zhou, L., Li, B., Albaqami, F.H., El-Toni, A.M., Li, X., Xie, Y., Sun, X., Zhang, F., 2018. Near-infrared rechargeable “optical battery” implant for irradiation-free photodynamic therapy. Biomaterials 163, 154–162. https://doi.org/10.1016/j.biomaterials.2018.02.029

Huang, B., Jones, S.A., Brandenburg, B., Zhuang, X., 2008a. Whole-cell 3D STORM reveals interactions between cellular structures with nanometer-scale resolution. Nature Methods 5, 1047–1052. https://doi.org/10.1038/nmeth.1274

Huang, B., Wang, W., Bates, M., Zhuang, X., 2008b. Three-dimensional Super-resolution Imaging by Stochastic Optical Reconstruction Microscopy. Science 319, 810–813. https://doi.org/10.1126/science.1153529

Huang, H., Suslov, N.B., Li, N.-S., Shelke, S.A., Evans, M.E., Koldobskaya, Y., Rice, P.A., Piccirilli, J.A., 2014. A G-quadruplex–containing RNA activates fluorescence in a GFP-like fluorophore. Nature Chemical Biology 10, 686–691. https://doi.org/10.1038/nchembio.1561

Huang, L., Zhao, Y., Zhang, H., Huang, K., Yang, J., Han, G., 2017. Expanding Anti-Stokes Shifting in Triplet–Triplet Annihilation Upconversion for In Vivo Anticancer Prodrug Activation. Angewandte Chemie International Edition 56, 14400–14404. https://doi.org/10.1002/anie.201704430

I

Idris, N.M., Gnanasammandhan, M.K., Zhang, J., Ho, P.C., Mahendran, R., Zhang, Y., 2012. In vivo photodynamic therapy using upconversion nanoparticles as remote-controlled nanotransducers. Nat Med 18, 1580–1585. https://doi.org/10.1038/nm.2933

J

Jain, P.K., Lee, K.S., El-Sayed, I.H., El-Sayed, M.A., 2006. Calculated Absorption and Scattering Properties of Gold Nanoparticles of Different Size, Shape, and Composition: Applications in Biological Imaging and Biomedicine. J. Phys. Chem. B 110, 7238–7248. https://doi.org/10.1021/jp057170o

Jiang, G., Pichaandi, J., Johnson, N.J.J., Burke, R.D., van Veggel, F.C.J.M., 2012. An Effective Polymer Cross-Linking Strategy To Obtain Stable Dispersions of Upconverting NaYF4 Nanoparticles in Buffers and Biological Growth Media for Biolabeling Applications. Langmuir 28, 3239–3247. https://doi.org/10.1021/la204020m

Jo, E.-J., Byun, J.-Y., Mun, H., Bang, D., Son, J.H., Lee, J.Y., Lee, L.P., Kim, M.-G., 2018. Single-Step LRET Aptasensor for Rapid Mycotoxin Detection. Anal. Chem. 90, 716–722. https://doi.org/10.1021/acs.analchem.7b02368

Jo, H.L., Song, Y.H., Park, J., Jo, E.-J., Goh, Y., Shin, K., Kim, M.-G., Lee, K.T., 2015. Fast and background-free three-dimensional (3D) live-cell imaging with lanthanide-doped upconverting nanoparticles. Nanoscale 7, 19397–19402. https://doi.org/10.1039/C5NR05875A

Johnson, I.D., 2010. Molecular Probes Handbook: A Guide to Fluorescent Probes and Labeling Technologies. Life Technologies Corporation.

Joubert, M.-F., 1999. Photon avalanche upconversion in rare earth laser materials. Optical Materials 11, 181–203. https://doi.org/10.1016/S0925-3467(98)00043-3

Juette, M.F., Terry, D.S., Wasserman, M.R., Zhou, Z., Altman, R.B., Zheng, Q., Blanchard, S.C., 2014. The bright future of single-molecule fluorescence imaging. Current Opinion in Chemical Biology, Molecular imaging 20, 103–111. https://doi.org/10.1016/j.cbpa.2014.05.010

K

Kaiser, M., Würth, C., Kraft, M., Hyppänen, I., Soukka, T., Resch-Genger, U., 2017. Power-dependent upconversion quantum yield of NaYF4:Yb3+,Er3+ nano- and micrometer-sized particles – measurements and simulations. Nanoscale 9, 10051–10058. https://doi.org/10.1039/C7NR02449E

Kapanidis, A.N., Lee, N.K., Laurence, T.A., Doose, S., Margeat, E., Weiss, S., 2004. Fluorescence-aided molecule sorting: Analysis of structure and interactions by alternating-laser excitation of single molecules. Proc Natl Acad Sci U S A 101, 8936–8941. https://doi.org/10.1073/pnas.0401690101

Khan, I., Tang, E., Arany, P., 2015. Molecular pathway of near-infrared laser phototoxicity involves ATF-4 orchestrated ER stress. Scientific Reports 5, 10581. https://doi.org/10.1038/srep10581

Kilbane, J.D., Chan, E.M., Monachon, C., Borys, N.J., Levy, E.S., Pickel, A.D., Urban, J.J., Schuck, P.J., Dames, C., 2016. Far-field optical nanothermometry using individual sub-

50 nm upconverting nanoparticles. Nanoscale 8, 11611–11616. https://doi.org/10.1039/C6NR01479H

Kilin, V.N., Anton, H., Anton, N., Steed, E., Vermot, J., Vandamme, T.F., Mely, Y., Klymchenko, A.S., 2014. Counterion-enhanced cyanine dye loading into lipid nano-droplets for single-particle tracking in zebrafish. Biomaterials 35, 4950–4957. https://doi.org/10.1016/j.biomaterials.2014.02.053

Kolesov, R., Reuter, R., Xia, K., Stöhr, R., Zappe, A., Wrachtrup, J., 2011. Super-resolution upconversion microscopy of praseodymium-doped yttrium aluminum garnet nanoparticles. Phys. Rev. B 84, 153413. https://doi.org/10.1103/PhysRevB.84.153413

Kuningas, K., Rantanen, T., Ukonaho, T., Lövgren, T., Soukka, T., 2005. Homogeneous Assay Technology Based on Upconverting Phosphors. Anal. Chem. 77, 7348–7355. https://doi.org/10.1021/ac0510944

Kusumi, A., Sako, Y., Yamamoto, M., 1993. Confined lateral diffusion of membrane receptors as studied by single particle tracking (nanovid microscopy). Effects of calcium-induced differentiation in cultured epithelial cells. Biophysical Journal 65, 2021–2040. https://doi.org/10.1016/S0006-3495(93)81253-0

Kusumi, A., Tsunoyama, T.A., Hirosawa, K.M., Kasai, R.S., Fujiwara, T.K., 2014. Tracking single molecules at work in living cells. Nat Chem Biol 10, 524–532. https://doi.org/10.1038/nchembio.1558

L

Lahtinen, S., Lyytikäinen, A., Päkkilä, H., Hömppi, E., Perälä, N., Lastusaari, M., Soukka, T., 2017. Disintegration of Hexagonal NaYF4:Yb3+,Er3+ Upconverting Nanoparticles in Aqueous Media: The Role of Fluoride in Solubility Equilibrium. J. Phys. Chem. C 121, 656–665. https://doi.org/10.1021/acs.jpcc.6b09301

Lahtinen, S., Wang, Q., Soukka, T., 2016. Long-Lifetime Luminescent Europium(III) Complex as an Acceptor in an Upconversion Resonance Energy Transfer Based Homogeneous Assay. Anal. Chem. 88, 653–658. https://doi.org/10.1021/acs.analchem.5b02228

Lai, J., Zhang, Y., Pasquale, N., Lee, K.-B., 2014. An Upconversion Nanoparticle with Orthogonal Emissions Using Dual NIR Excitations for Controlled Two-Way Photoswitching. Angewandte Chemie International Edition 53, 14419–14423. https://doi.org/10.1002/anie.201408219

Lakowicz, J.R., 2011. Principles of Fluorescence Spectroscopy. Springer US.

Lee, J., Gordon, A.C., Kim, H., Park, W., Cho, S., Lee, B., Larson, A.C., Rozhkova, E.A., Kim, D.-H., 2016. Targeted multimodal nano-reporters for pre-procedural MRI and intra-operative image-guidance. Biomaterials 109, 69–77. https://doi.org/10.1016/j.biomaterials.2016.09.013

Lee, S.F., Osborne, M.A., 2009. Brightening, Blinking, Bluing and Bleaching in the Life of a Quantum Dot: Friend or Foe? ChemPhysChem 10, 2174–2191. https://doi.org/10.1002/cphc.200900200

Levy, E.S., Tajon, C.A., Bischof, T.S., Iafrati, J., Fernandez-Bravo, A., Garfield, D.J., Chamanzar, M., Maharbiz, M.M., Sohal, V.S., Schuck, P.J., Cohen, B.E., Chan, E.M., 2016. Energy-Looping Nanoparticles: Harnessing Excited-State Absorption for Deep-Tissue Imaging. ACS Nano 10, 8423–8433. https://doi.org/10.1021/acsnano.6b03288

Li, H., Xu, L., Chen, G., 2017. Controlled Synthesis of Monodisperse Hexagonal NaYF4:Yb/Er Nanocrystals with Ultrasmall Size and Enhanced Upconversion Luminescence. Molecules 22, 2113. https://doi.org/10.3390/molecules22122113

Li, Y., Tang, J., Pan, D.-X., Sun, L.-D., Chen, C., Liu, Y., Wang, Y.-F., Shi, S., Yan, C.-H., 2016. A Versatile Imaging and Therapeutic Platform Based on Dual-Band Luminescent Lanthanide Nanoparticles toward Tumor Metastasis Inhibition. ACS Nano 10, 2766–2773. https://doi.org/10.1021/acsnano.5b07873

Liang, Z., Wang, Xiaochen, Zhu, W., Zhang, P., Yang, Y., Sun, C., Zhang, J., Wang, Xinrui, Xu, Z., Zhao, Y., Yang, R., Zhao, S., Zhou, L., 2017. Upconversion Nanocrystals Mediated Lateral-Flow Nanoplatform for in Vitro Detection. ACS Appl. Mater. Interfaces 9, 3497–3504. https://doi.org/10.1021/acsami.6b14906

Lin, C.-A.J., Sperling, R.A., Li, J.K., Yang, T.-Y., Li, P.-Y., Zanella, M., Chang, W.H., Parak, W.J., 2008. Design of an Amphiphilic Polymer for Nanoparticle Coating and Functionalization. Small 4, 334–341. https://doi.org/10.1002/smll.200700654

Linde, S. van de, Löschberger, A., Klein, T., Heidbreder, M., Wolter, S., Heilemann, M., Sauer, M., 2011. Direct stochastic optical reconstruction microscopy with standard fluorescent probes. Nature Protocols 6, 991–1009. https://doi.org/10.1038/nprot.2011.336

Lisjak, D., Plohl, O., Ponikvar-Svet, M., Majaron, B., 2015. Dissolution of upconverting fluoride nanoparticles in aqueous suspensions. RSC Adv. 5, 27393–27397. https://doi.org/10.1039/C5RA00902B

Lisjak, D., Plohl, O., Vidmar, J., Majaron, B., Ponikvar-Svet, M., 2016. Dissolution Mechanism of Upconverting AYF4:Yb,Tm (A = Na or K) Nanoparticles in Aqueous Media. Langmuir 32, 8222–8229. https://doi.org/10.1021/acs.langmuir.6b02675

Liu, Y., Lu, Y., Yang, X., Zheng, X., Wen, S., Wang, F., Vidal, X., Zhao, J., Liu, D., Zhou, Z., Ma, C., Zhou, J., Piper, J.A., Xi, P., Jin, D., 2017. Amplified stimulated emission in upconversion nanoparticles for super-resolution nanoscopy. Nature 543, 229–233. https://doi.org/10.1038/nature21366

Livet, J., Weissman, T.A., Kang, H., Draft, R.W., Lu, J., Bennis, R.A., Sanes, J.R., Lichtman, J.W., 2007. Transgenic strategies for combinatorial expression of fluorescent proteins in the nervous system. Nature 450, 56–62. https://doi.org/10.1038/nature06293

Löschberger, A., Linde, S. van de, Dabauvalle, M.-C., Rieger, B., Heilemann, M., Krohne, G., Sauer, M., 2012. Super-resolution imaging visualizes the eightfold symmetry of gp210 proteins around the nuclear pore complex and resolves the central channel with nanometer resolution. J Cell Sci 125, 570–575. https://doi.org/10.1242/jcs.098822

Lu, Y., Zhao, J., Zhang, R., Liu, Y., Liu, D., Goldys, E.M., Yang, X., Xi, P., Sunna, A., Lu, J., Shi, Y., Leif, R.C., Huo, Y., Shen, J., Piper, J.A., Robinson, J.P., Jin, D., 2014. Tunable lifetime multiplexing using luminescent nanocrystals. Nat Photon 8, 32–36. https://doi.org/10.1038/nphoton.2013.322

M

Ma, C., Xu, X., Wang, F., Zhou, Z., Liu, D., Zhao, J., Guan, M., Lang, C.I., Jin, D., 2017. Optimal Sensitizer Concentration in Single Upconversion Nanocrystals. Nano Lett. 17, 2858–2864. https://doi.org/10.1021/acs.nanolett.6b05331

Mahler, B., Spinicelli, P., Buil, S., Quelin, X., Hermier, J.-P., Dubertret, B., 2008. Towards non-blinking colloidal quantum dots. Nature Materials 7, 659–664. https://doi.org/10.1038/nmat2222

Manzo, C., Garcia-Parajo, M.F., 2015. A review of progress in single particle tracking: from methods to biophysical insights. Rep. Prog. Phys. 78, 124601. https://doi.org/10.1088/0034-4885/78/12/124601

Martin-Fernandez, M.L., Clarke, D.T., 2012. Single Molecule Fluorescence Detection and Tracking in Mammalian Cells: The State-of-the-Art and Future Perspectives. Int J Mol Sci 13, 14742–14765. https://doi.org/10.3390/ijms131114742

Mattsson, L., Wegner, K.D., Hildebrandt, N., Soukka, T., 2015. Upconverting nanoparticle to quantum dot FRET for homogeneous double-nano biosensors. RSC Adv. 5, 13270–13277. https://doi.org/10.1039/C5RA00397K

Mei, J., Leung, N.L.C., Kwok, R.T.K., Lam, J.W.Y., Tang, B.Z., 2015. Aggregation-Induced Emission: Together We Shine, United We Soar! Chem. Rev. 115, 11718–11940. https://doi.org/10.1021/acs.chemrev.5b00263

Meng, F.-L., Wu, J.-J., Zhao, E.-F., Zheng, Y.-Z., Huang, M.-L., Dai, L.-M., Tao, X., Chen, J.-F., 2017. High-efficiency near-infrared enabled planar perovskite solar cells by embedding upconversion nanocrystals. Nanoscale 9, 18535–18545. https://doi.org/10.1039/C7NR05416E

Meruga, J.M., Cross, W.M., Petersen, J.B., May, P.S., Baride, A., Cessac, K., Kellar, J.J., 2018. Stable Inks Containing Upconverting Nanoparticles Based on an Oil-in-Water Nanoemulsion. Langmuir 34, 1535–1541. https://doi.org/10.1021/acs.langmuir.7b03415

Michalet, X., 2010. Mean Square Displacement Analysis of Single-Particle Trajectories with Localization Error: Brownian Motion in Isotropic Medium. Phys Rev E Stat Nonlin Soft Matter Phys 82, 041914.

Michalet, X., Pinaud, F.F., Bentolila, L.A., Tsay, J.M., Doose, S., Li, J.J., Sundaresan, G., Wu, A.M., Gambhir, S.S., Weiss, S., 2005. Quantum Dots for Live Cells, in Vivo Imaging, and Diagnostics. Science 307, 538–544. https://doi.org/10.1126/science.1104274

Mitchison, T.J., Cramer, L.P., 1996. Actin-Based Cell Motility and Cell Locomotion. Cell 84, 371–379. https://doi.org/10.1016/S0092-8674(00)81281-7

Montalti, M., Prodi, L., Rampazzo, E., Zaccheroni, N., 2014. Dye-doped silica nanoparticles as luminescent organized systems for nanomedicine. Chem. Soc. Rev. 43, 4243–4268. https://doi.org/10.1039/C3CS60433K

Moore, E.G., Samuel, A.P.S., Raymond, K.N., 2009. From Antenna to Assay: Lessons Learned in Lanthanide Luminescence. Acc. Chem. Res. 42, 542–552. https://doi.org/10.1021/ar800211j

Mortensen, K.I., Churchman, L.S., Spudich, J.A., Flyvbjerg, H., 2010. Optimized localization analysis for single-molecule tracking and super-resolution microscopy. Nature Methods 7, 377–381. https://doi.org/10.1038/nmeth.1447

Muhr, V., Wilhelm, S., Hirsch, T., Wolfbeis, O.S., 2014. Upconversion Nanoparticles: From Hydrophobic to Hydrophilic Surfaces. Acc. Chem. Res. 47, 3481–3493. https://doi.org/10.1021/ar500253g

Murphy, D.B., 2002. Fundamentals of Light Microscopy and Electronic Imaging. John Wiley & Sons.

Naccache, R., Vetrone, F., Mahalingam, V., Cuccia, L.A., Capobianco, J.A., 2009. Controlled Synthesis and Water Dispersibility of Hexagonal Phase NaGdF4:Ho3+/Yb3+ Nanoparticles. Chem. Mater. 21, 717–723. https://doi.org/10.1021/cm803151y

N

Nam, S.H., Bae, Y.M., Park, Y.I., Kim, J.H., Kim, H.M., Choi, J.S., Lee, K.T., Hyeon, T., Suh, Y.D., 2011. Long-Term Real-Time Tracking of Lanthanide Ion Doped Upconverting Nanoparticles in Living Cells. Angew. Chem. Int. Ed. 50, 6093–6097. https://doi.org/10.1002/anie.201007979

Ntziachristos, V., Ripoll, J., Wang, L.V., Weissleder, R., 2005. Looking and listening to light: the evolution of whole-body photonic imaging. Nature Biotechnology 23, 313–320. https://doi.org/10.1038/nbt1074

O

Ormö, M., Cubitt, A.B., Kallio, K., Gross, L.A., Tsien, R.Y., Remington, S.J., 1996. Crystal Structure of the Aequorea victoria Green Fluorescent Protein. Science 273, 1392–1395. https://doi.org/10.1126/science.273.5280.1392

Ostrowski, A.D., Chan, E.M., Gargas, D.J., Katz, E.M., Han, G., Schuck, P.J., Milliron, D.J., Cohen, B.E., 2012. Controlled Synthesis and Single-Particle Imaging of Bright, Sub-10 nm Lanthanide-Doped Upconverting Nanocrystals. ACS Nano 6, 2686–2692. https://doi.org/10.1021/nn3000737

P

Park, B.J., Hong, A.-R., Park, S., Kyung, K.-U., Lee, K., Jang, H.S., 2017. Flexible transparent displays based on core/shell upconversion nanophosphor-incorporated polymer waveguides. Scientific Reports 7, 45659. https://doi.org/10.1038/srep45659

Park, Y.I., Lee, K.T., Suh, Y.D., Hyeon, T., 2015. Upconverting nanoparticles: a versatile platform for wide-field two-photon microscopy and multi-modal in vivo imaging. Chem. Soc. Rev. 44, 1302–1317. https://doi.org/10.1039/C4CS00173G

Parker, C.A., Hatchard, C.G., 1962. Delayed fluorescence from solutions of anthracene and phenanthrene. Proc. R. Soc. Lond. A 269, 574–584. https://doi.org/10.1098/rspa.1962.0197

Patterson, D.M., Nazarova, L.A., Prescher, J.A., 2014. Finding the Right (Bioorthogonal) Chemistry. ACS Chem. Biol. 9, 592–605. https://doi.org/10.1021/cb400828a

Patterson, G., Davidson, M., Manley, S., Lippincott-Schwartz, J., 2010. Superresolution Imaging using Single-Molecule Localization. Annu Rev Phys Chem 61, 345–367. https://doi.org/10.1146/annurev.physchem.012809.103444

Patterson, G.H., 2009. Fluorescence microscopy below the diffraction limit. Seminars in Cell & Developmental Biology, Imaging in Cell and Developmental Biology 20, 886–893. https://doi.org/10.1016/j.semcdb.2009.08.006

Pellegrino, T., Manna, L., Kudera, S., Liedl, T., Koktysh, D., Rogach, A.L., Keller, S., Rädler, J., Natile, G., Parak, W.J., 2004. Hydrophobic Nanocrystals Coated with an Amphiphilic

Polymer Shell: A General Route to Water Soluble Nanocrystals. Nano Lett. 4, 703–707. https://doi.org/10.1021/nl035172j

Pinaud, F., Clarke, S., Sittner, A., Dahan, M., 2010. Probing cellular events, one quantum dot at a time. Nature Methods 7, 275–285. https://doi.org/10.1038/nmeth.1444

Pirchi, M., Ziv, G., Riven, I., Cohen, S.S., Zohar, N., Barak, Y., Haran, G., 2011. Single-molecule fluorescence spectroscopy maps the folding landscape of a large protein. Nature Communications 2, 493. https://doi.org/10.1038/ncomms1504

Pliss, A., Ohulchanskyy, T.Y., Chen, G., Damasco, J., Bass, C.E., Prasad, P.N., 2017. Subcellular Optogenetics Enacted by Targeted Nanotransformers of Near-Infrared Light. ACS Photonics 4, 806–814. https://doi.org/10.1021/acsphotonics.6b00475

Plohl, O., Kraft, M., Kovač, J., Belec, B., Ponikvar-Svet, M., Würth, C., Lisjak, D., Resch-Genger, U., 2017a. Optically Detected Degradation of NaYF4:Yb,Tm-Based Upconversion Nanoparticles in Phosphate Buffered Saline Solution. Langmuir 33, 553–560. https://doi.org/10.1021/acs.langmuir.6b03907

Plohl, O., Kralj, S., Majaron, B., Fröhlich, E., Ponikvar-Svet, M., Makovec, D., Lisjak, D., 2017b. Amphiphilic coatings for the protection of upconverting nanoparticles against dissolution in aqueous media. Dalton Trans. 46, 6975–6984. https://doi.org/10.1039/C7DT00529F

Preibisch, S., Saalfeld, S., Tomancak, P., 2009. Globally optimal stitching of tiled 3D microscopic image acquisitions. Bioinformatics 25, 1463–1465. https://doi.org/10.1093/bioinformatics/btp184

R

Ramasamy, P., Kim, J., 2013. Combined plasmonic and upconversion rear reflectors for efficient dye-sensitized solar cells. Chem. Commun. 50, 879–881. https://doi.org/10.1039/C3CC47290F

Rantanen, T., Järvenpää, M.-L., Vuojola, J., Arppe, R., Kuningas, K., Soukka, T., 2009. Upconverting phosphors in a dual-parameter LRET-based hybridization assay. Analyst 134, 1713–1716. https://doi.org/10.1039/B901299K

Rantanen, T., Päkkilä, H., Jämsen, L., Kuningas, K., Ukonaho, T., Lövgren, T., Soukka, T., 2007. Tandem Dye Acceptor Used To Enhance Upconversion Fluorescence Resonance Energy Transfer in Homogeneous Assays. Anal. Chem. 79, 6312–6318. https://doi.org/10.1021/ac070376w

Reisch, A., Didier, P., Richert, L., Oncul, S., Arntz, Y., Mély, Y., Klymchenko, A.S., 2014. Collective fluorescence switching of counterion-assembled dyes in polymer nanoparticles. Nature Communications 5, 4089. https://doi.org/10.1038/ncomms5089

Reisch, A., Klymchenko, A.S., 2016. Fluorescent Polymer Nanoparticles Based on Dyes: Seeking Brighter Tools for Bioimaging. Small 12, 1968–1992. https://doi.org/10.1002/smll.201503396

Reisch, A., Trofymchuk, K., Runser, A., Fleith, G., Rawiso, M., Klymchenko, A.S., 2017. Tailoring Fluorescence Brightness and Switching of Nanoparticles through Dye Organization in the Polymer Matrix. ACS Appl. Mater. Interfaces 9, 43030–43042. https://doi.org/10.1021/acsami.7b12292

Resch-Genger, U., Grabolle, M., Cavaliere-Jaricot, S., Nitschke, R., Nann, T., 2008. Quantum dots versus organic dyes as fluorescent labels. Nature Methods 5, 763–775. https://doi.org/10.1038/nmeth.1248

Rocheva, V.V., Koroleva, A.V., Savelyev, A.G., Khaydukov, K.V., Generalova, A.N., Nechaev, A.V., Guller, A.E., Semchishen, V.A., Chichkov, B.N., Khaydukov, E.V., 2018. High-resolution 3D photopolymerization assisted by upconversion nanoparticles for rapid prototyping applications. Scientific Reports 8, 3663. https://doi.org/10.1038/s41598-018-21793-0

Röcker, C., Pötzl, M., Zhang, F., Parak, W.J., Nienhaus, G.U., 2009. A quantitative fluorescence study of protein monolayer formation on colloidal nanoparticles. Nature Nanotechnology 4, 577–580. https://doi.org/10.1038/nnano.2009.195

Rossier, O., Octeau, V., Sibarita, J.-B., Leduc, C., Tessier, B., Nair, D., Gatterdam, V., Destaing, O., Albigès-Rizo, C., Tampé, R., Cognet, L., Choquet, D., Lounis, B., Giannone, G., 2012. Integrins β_1 and β_3 exhibit distinct dynamic nanoscale organizations inside focal adhesions. Nature Cell Biology 14, 1057–1067. https://doi.org/10.1038/ncb2588

Roy, R., Hohng, S., Ha, T., 2008. A practical guide to single-molecule FRET. Nat Meth 5, 507–516. https://doi.org/10.1038/nmeth.1208

Rust, M.J., Bates, M., Zhuang, X., 2006. Sub-diffraction-limit imaging by stochastic optical reconstruction microscopy (STORM). Nature Methods 3, 793–796. https://doi.org/10.1038/nmeth929

Ryu, J., Park, H.-Y., Kim, K., Kim, H., Yoo, J.H., Kang, M., Im, K., Grailhe, R., Song, R., 2010. Facile Synthesis of Ultrasmall and Hexagonal NaGdF4: Yb3+, Er3+ Nanoparticles with Magnetic and Upconversion Imaging Properties. J. Phys. Chem. C 114, 21077–21082. https://doi.org/10.1021/jp107725r

S

Saalfeld, S., 2018. mpicbg: Fiji module for image transformation and related algorithms.

Sahl, S.J., Moerner, W., 2013. Super-resolution fluorescence imaging with single molecules. Current Opinion in Structural Biology, Protein-carbohydrate interactions / Biophysical methods 23, 778–787. https://doi.org/10.1016/j.sbi.2013.07.010

Sangeetha, N.M., Moutet, P., Lagarde, D., Sallen, G., Urbaszek, B., Marie, X., Viau, G., Ressier, L., 2013. 3D assembly of upconverting NaYF4 nanocrystals by AFM nanoxerography: creation of anti-counterfeiting microtags. Nanoscale 5, 9587–9592. https://doi.org/10.1039/C3NR02734A

Sapsford, K.E., Algar, W.R., Berti, L., Gemmill, K.B., Casey, B.J., Oh, E., Stewart, M.H., Medintz, I.L., 2013. Functionalizing Nanoparticles with Biological Molecules: Developing Chemistries that Facilitate Nanotechnology. Chem. Rev. 113, 1904–2074. https://doi.org/10.1021/cr300143v

Sapsford, K.E., Tyner, K.M., Dair, B.J., Deschamps, J.R., Medintz, I.L., 2011. Analyzing Nanomaterial Bioconjugates: A Review of Current and Emerging Purification and Characterization Techniques. Anal. Chem. 83, 4453–4488. https://doi.org/10.1021/ac200853a

Sark, W.G.J.H.M. van, Frederix, P.L.T.M., Bol, A.A., Gerritsen, H.C., Meijerink, A., 2002. Blueing, Bleaching, and Blinking of Single CdSe/ZnS Quantum Dots. ChemPhysChem

3, 871–879. https://doi.org/10.1002/1439-7641(20021018)3:10<871::AID-CPHC871>3.0.CO;2-T

Saxton, M.J., 1994. Anomalous diffusion due to obstacles: a Monte Carlo study. Biophysical Journal 66, 394–401. https://doi.org/10.1016/S0006-3495(94)80789-1

Schlenoff, J.B., 2014. Zwitteration: Coating Surfaces with Zwitterionic Functionality to Reduce Nonspecific Adsorption. Langmuir 30, 9625–9636. https://doi.org/10.1021/la500057j

Schmidt, T., Schutz, G.J., Gruber, H.J., Schindler, H., 1996. Local Stoichiometries Determined by Counting Individual Molecules. Anal. Chem. 68, 4397–4401. https://doi.org/10.1021/ac960710g

Sedlmeier, A., Gorris, H.H., 2015. Surface modification and characterization of photon-upconverting nanoparticles for bioanalytical applications. Chem. Soc. Rev. 44, 1526–1560. https://doi.org/10.1039/C4CS00186A

Sengupta, P., van Engelenburg, S.B., Lippincott-Schwartz, J., 2014. Superresolution Imaging of Biological Systems Using Photoactivated Localization Microscopy. Chem. Rev. 114, 3189–3202. https://doi.org/10.1021/cr400614m

Shah, S., Liu, J.-J., Pasquale, N., Lai, J., McGowan, H., Pang, Z.P., Lee, K.-B., 2015. Hybrid upconversion nanomaterials for optogenetic neuronal control. Nanoscale 7, 16571–16577. https://doi.org/10.1039/C5NR03411F

Shalav, A., Richards, B.S., Trupke, T., Krämer, K.W., Güdel, H.U., 2005. Application of NaYF4:Er3+ up-converting phosphors for enhanced near-infrared silicon solar cell response. Applied Physics Letters 86, 013505. https://doi.org/10.1063/1.1844592

Shan, J., Uddi, M., Wei, R., Yao, N., Ju, Y., 2010. The Hidden Effects of Particle Shape and Criteria for Evaluating the Upconversion Luminescence of the Lanthanide Doped Nanophosphors. J. Phys. Chem. C 114, 2452–2461. https://doi.org/10.1021/jp908976n

Shannon, C.E., 1949a. Communication Theory of Secrecy Systems*. Bell System Technical Journal 28, 656–715. https://doi.org/10.1002/j.1538-7305.1949.tb00928.x

Shannon, C.E., 1949b. Communication in the Presence of Noise. Proceedings of the IRE 37, 10–21. https://doi.org/10.1109/JRPROC.1949.232969

Sharonov, A., Hochstrasser, R.M., 2006. Wide-field subdiffraction imaging by accumulated binding of diffusing probes. PNAS 103, 18911–18916. https://doi.org/10.1073/pnas.0609643104

Shrestha, R.L., Conti, D., Tamura, N., Braun, D., Ramalingam, R.A., Cieslinski, K., Ries, J., Draviam, V.M., 2017. Aurora-B kinase pathway controls the lateral to end-on conversion of kinetochore-microtubule attachments in human cells. Nature Communications 8, 150. https://doi.org/10.1038/s41467-017-00209-z

Silva, Z.S., Bussadori, S.K., Fernandes, K.P.S., Huang, Y.-Y., Hamblin, M.R., 2015. Animal models for photodynamic therapy (PDT). Bioscience Reports 35, e00265. https://doi.org/10.1042/BSR20150188

Sperling, R.A., Gil, P.R., Zhang, F., Zanella, M., Parak, W.J., 2008. Biological applications of gold nanoparticles. Chem. Soc. Rev. 37, 1896–1908. https://doi.org/10.1039/B712170A

Sperling, R.A., Parak, W.J., 2010. Surface modification, functionalization and bioconjugation of colloidal inorganic nanoparticles. Philosophical Transactions of the Royal Society of London A: Mathematical, Physical and Engineering Sciences 368, 1333–1383. https://doi.org/10.1098/rsta.2009.0273

Super-Resolution Tutorial - Education - Advanced Microscopy [WWW Document], n.d. URL https://advanced-microscopy.utah.edu/education/super-res/ (accessed 10.4.18).

Synge, E.H., 1928. A suggested method for extending microscopic resolution into the ultra-microscopic region. The London, Edinburgh, and Dublin Philosophical Magazine and Journal of Science 6, 356–362. https://doi.org/10.1080/14786440808564615

T

Tian, B., Fernandez-Bravo, A., Najafiaghdam, H., Torquato, N.A., Altoe, M.V.P., Teitelboim, A., Tajon, C.A., Tian, Y., Borys, N.J., Barnard, E.S., Anwar, M., Chan, E.M., Schuck, P.J., Cohen, B.E., 2018. Low irradiance multiphoton imaging with alloyed lanthanide nanocrystals. Nature Communications 9, 3082. https://doi.org/10.1038/s41467-018-05577-8

Tinevez, J.-Y., Perry, N., Schindelin, J., Hoopes, G.M., Reynolds, G.D., Laplantine, E., Bednarek, S.Y., Shorte, S.L., Eliceiri, K.W., 2017. TrackMate: An open and extensible

platform for single-particle tracking. Methods, Image Processing for Biologists 115, 80–90. https://doi.org/10.1016/j.ymeth.2016.09.016

Tsang, M.-K., Ye, W., Wang, G., Li, J., Yang, M., Hao, J., 2016. Ultrasensitive Detection of Ebola Virus Oligonucleotide Based on Upconversion Nanoprobe/Nanoporous Membrane System. ACS Nano 10, 598–605. https://doi.org/10.1021/acsnano.5b05622

Tsien, R.Y., 1998. The Green Fluorescent Protein. Annual Review of Biochemistry 67, 509–544. https://doi.org/10.1146/annurev.biochem.67.1.509

U

Uphoff, S., Holden, S.J., Reste, L.L., Periz, J., Linde, S. van de, Heilemann, M., Kapanidis, A.N., 2010. Monitoring multiple distances within a single molecule using switchable FRET. Nature Methods 7, 831–836. https://doi.org/10.1038/nmeth.1502

V

Vafabakhsh, R., Ha, T., 2012. Extreme Bendability of DNA Less than 100 Base Pairs Long Revealed by Single-Molecule Cyclization. Science 337, 1097–1101. https://doi.org/10.1126/science.1224139

Vaughan, J.C., Jia, S., Zhuang, X., 2012. Ultra-bright Photoactivatable Fluorophores Created by Reductive Caging. Nat Methods 9, 1181–1184. https://doi.org/10.1038/nmeth.2214

Vetrone, F., Naccache, R., Mahalingam, V., Morgan, C.G., Capobianco, J.A., 2009. The Active-Core/Active-Shell Approach: A Strategy to Enhance the Upconversion Luminescence in Lanthanide-Doped Nanoparticles. Advanced Functional Materials 19, 2924–2929. https://doi.org/10.1002/adfm.200900234

Vetrone, F., Naccache, R., Zamarrón, A., Juarranz de la Fuente, A., Sanz-Rodríguez, F., Martinez Maestro, L., Martín Rodriguez, E., Jaque, D., García Solé, J., Capobianco, J.A., 2010. Temperature Sensing Using Fluorescent Nanothermometers. ACS Nano 4, 3254–3258. https://doi.org/10.1021/nn100244a

Voie, A.H., Burns, D.H., Spelman, F.A., 1993. Orthogonal-plane fluorescence optical sectioning: Three-dimensional imaging of macroscopic biological specimens. Journal of Microscopy 170, 229–236. https://doi.org/10.1111/j.1365-2818.1993.tb03346.x

W

Wang, F., Deng, R., Wang, J., Wang, Q., Han, Y., Zhu, H., Chen, X., Liu, X., 2011. Tuning upconversion through energy migration in core–shell nanoparticles. Nature Materials 10, 968–973. https://doi.org/10.1038/nmat3149

Wang, F., Liu, X., 2014. Multicolor Tuning of Lanthanide-Doped Nanoparticles by Single Wavelength Excitation. Acc. Chem. Res. 47, 1378–1385. https://doi.org/10.1021/ar5000067

Wang, F., Wen, S., He, H., Wang, B., Zhou, Z., Shimoni, O., Jin, D., 2018. Microscopic inspection and tracking of single upconversion nanoparticles in living cells. Light: Science & Applications 7, 18007. https://doi.org/10.1038/lsa.2018.7

Wang, H., Han, R., Yang, L., Shi, J., Liu, Z., Hu, Y., Wang, Y., Liu, S., Gan, Y., 2016. Design and Synthesis of Core–Shell–Shell Upconversion Nanoparticles for NIR-Induced Drug Release, Photodynamic Therapy, and Cell Imaging. ACS Appl. Mater. Interfaces 8, 4416–4423. https://doi.org/10.1021/acsami.5b11197

Wang, Leyu, Yan, R., Huo, Z., Wang, Lun, Zeng, J., Bao, J., Wang, X., Peng, Q., Li, Y., 2005. Fluorescence Resonant Energy Transfer Biosensor Based on Upconversion-Luminescent Nanoparticles. Angewandte Chemie International Edition 44, 6054–6057. https://doi.org/10.1002/anie.200501907

Wang, Y., Wang, H., Liu, D., Song, S., Wang, X., Zhang, H., 2013. Graphene oxide covalently grafted upconversion nanoparticles for combined NIR mediated imaging and photothermal/photodynamic cancer therapy. Biomaterials 34, 7715–7724. https://doi.org/10.1016/j.biomaterials.2013.06.045

Wang, Y.-F., Sun, L.-D., Xiao, J.-W., Feng, W., Zhou, J.-C., Shen, J., Yan, C.-H., 2012. Rare-Earth Nanoparticles with Enhanced Upconversion Emission and Suppressed Rare-Earth-Ion Leakage. Chem. Eur. J. 18, 5558–5564. https://doi.org/10.1002/chem.201103485

Wilhelm, S., Kaiser, M., Würth, C., Heiland, J., Carrillo-Carrion, C., Muhr, V., Wolfbeis, O.S., Parak, W.J., Resch-Genger, U., Hirsch, T., 2015. Water dispersible upconverting nanoparticles: effects of surface modification on their luminescence and colloidal stability. Nanoscale 7, 1403–1410. https://doi.org/10.1039/C4NR05954A

Wilmes, S., Staufenbiel, M., Lißе, D., Richter, C.P., Beutel, O., Busch, K.B., Hess, S.T., Piehler, J., 2012. Triple-Color Super-Resolution Imaging of Live Cells: Resolving Submicroscopic Receptor Organization in the Plasma Membrane. Angewandte Chemie International Edition 51, 4868–4871. https://doi.org/10.1002/anie.201200853

Winckler, P., Lartigue, L., Giannone, G., Giorgi, F.D., Ichas, F., Sibarita, J.-B., Lounis, B., Cognet, L., 2013. Identification and super-resolution imaging of ligand-activated receptor dimers in live cells. Scientific Reports 3, 2387. https://doi.org/10.1038/srep02387

Wisser, M.D., Fischer, S., Maurer, P.C., Bronstein, N.D., Chu, S., Alivisatos, A.P., Salleo, A., Dionne, J.A., 2016. Enhancing Quantum Yield via Local Symmetry Distortion in Lanthanide-Based Upconverting Nanoparticles. ACS Photonics 3, 1523–1530. https://doi.org/10.1021/acsphotonics.6b00166

Wolbarsht, M., 1971. Laser Applications in Medicine and Biology. Springer US.

Wu, N., Bao, L., Ding, L., Ju, H., 2016. A Single Excitation-Duplexed Imaging Strategy for Profiling Cell Surface Protein-Specific Glycoforms. Angewandte Chemie International Edition 55, 5220–5224. https://doi.org/10.1002/anie.201601233

Wu, S., Han, G., Milliron, D.J., Aloni, S., Altoe, V., Talapin, D.V., Cohen, B.E., Schuck, P.J., 2009. Non-blinking and photostable upconverted luminescence from single lanthanide-doped nanocrystals. PNAS 106, 10917–10921. https://doi.org/10.1073/pnas.0904792106

Wu, X., Zhang, Y., Takle, K., Bilsel, O., Li, Z., Lee, H., Zhang, Z., Li, D., Fan, W., Duan, C., Chan, E.M., Lois, C., Xiang, Y., Han, G., 2016. Dye-Sensitized Core/Active Shell Upconversion Nanoparticles for Optogenetics and Bioimaging Applications. ACS Nano 10, 1060–1066. https://doi.org/10.1021/acsnano.5b06383

Würth, C., Fischer, S., Grauel, B., Alivisatos, A.P., Resch-Genger, U., 2018. Quantum Yields, Surface Quenching, and Passivation Efficiency for Ultrasmall Core/Shell Upconverting Nanoparticles. J. Am. Chem. Soc. 140, 4922–4928. https://doi.org/10.1021/jacs.8b01458

Würth, C., Grabolle, M., Pauli, J., Spieles, M., Resch-Genger, U., 2013. Relative and absolute determination of fluorescence quantum yields of transparent samples. Nat. Protocols 8, 1535–1550. https://doi.org/10.1038/nprot.2013.087

Würth, C., Kaiser, M., Wilhelm, S., Grauel, B., Hirsch, T., Resch-Genger, U., 2017. Excitation power dependent population pathways and absolute quantum yields of upconversion nanoparticles in different solvents. Nanoscale 9, 4283–4294. https://doi.org/10.1039/C7NR00092H

X

Xu, K., Babcock, H.P., Zhuang, X., 2012. Dual-objective STORM reveals three-dimensional filament organization in the actin cytoskeleton. Nature Methods 9, 185–188. https://doi.org/10.1038/nmeth.1841

Y

Yan, R.X., Li, Y.D., 2005. Down/Up Conversion in Ln3+-Doped YF3 Nanocrystals. Adv. Funct. Mater. 15, 763–770. https://doi.org/10.1002/adfm.200305044

Yang, D., Ma, P., Hou, Z., Cheng, Z., Li, C., Lin, J., 2015. Current advances in lanthanide ion (Ln3+)-based upconversion nanomaterials for drug delivery. Chem. Soc. Rev. 44, 1416–1448. https://doi.org/10.1039/C4CS00155A

Yanoff, M., Duker, J.S., 2008. Ophthalmology. Mosby Elsevier.

Ye, X., Collins, J.E., Kang, Y., Chen, J., Chen, D.T.N., Yodh, A.G., Murray, C.B., 2010. Morphologically controlled synthesis of colloidal upconversion nanophosphors and their shape-directed self-assembly. PNAS 107, 22430–22435. https://doi.org/10.1073/pnas.1008958107

You, M., Lin, M., Wang, S., Wang, X., Zhang, G., Hong, Y., Dong, Y., Jin, G., Xu, F., 2016. Three-dimensional quick response code based on inkjet printing of upconversion fluorescent nanoparticles for drug anti-counterfeiting. Nanoscale 8, 10096–10104. https://doi.org/10.1039/C6NR01353H

You, M., Zhong, J., Hong, Y., Duan, Z., Lin, M., Xu, F., 2015. Inkjet printing of upconversion nanoparticles for anti-counterfeit applications. Nanoscale 7, 4423–4431. https://doi.org/10.1039/C4NR06944G

Yu, J., Wu, C., Sahu, S.P., Fernando, L.P., Szymanski, C., McNeill, J., 2009. Nanoscale 3D Tracking with Conjugated Polymer Nanoparticles. J. Am. Chem. Soc. 131, 18410–18414. https://doi.org/10.1021/ja907228q

Z

ZEISS Microscopy Online Campus | Introduction to Superresolution Microscopy [WWW Document], n.d. URL http://zeiss-campus.magnet.fsu.edu/print/superresolution/introduction-print.html (accessed 10.4.18).

Zhan, Q., Liu, H., Wang, B., Wu, Q., Pu, R., Zhou, C., Huang, B., Peng, X., Ågren, H., He, S., 2017. Achieving high-efficiency emission depletion nanoscopy by employing cross relaxation in upconversion nanoparticles. Nature Communications 8, 1058. https://doi.org/10.1038/s41467-017-01141-y

Zhang, F., Shi, Q., Zhang, Y., Shi, Y., Ding, K., Zhao, D., Stucky, G.D., 2011. Fluorescence Upconversion Microbarcodes for Multiplexed Biological Detection: Nucleic Acid Encoding. Adv. Mater. 23, 3775–3779. https://doi.org/10.1002/adma.201101868

Zhang, Z., Kenny, S.J., Hauser, M., Li, W., Xu, K., 2015. Ultrahigh-throughput single-molecule spectroscopy and spectrally resolved super-resolution microscopy. Nature Methods 12, 935–938. https://doi.org/10.1038/nmeth.3528

Zhao, J., Ji, S., Guo, H., 2011. Triplet–triplet annihilation based upconversion: from triplet sensitizers and triplet acceptors to upconversion quantum yields. RSC Advances 1, 937–950. https://doi.org/10.1039/C1RA00469G

Zhao, Y., Terry, D., Shi, L., Weinstein, H., Blanchard, S.C., Javitch, J.A., 2010. Single-molecule dynamics of gating in a neurotransmitter transporter homologue. Nature 465, 188–193. https://doi.org/10.1038/nature09057

Zheng, X., Zhu, X., Lu, Y., Zhao, J., Feng, W., Jia, G., Wang, F., Li, F., Jin, D., 2016. High-Contrast Visualization of Upconversion Luminescence in Mice Using Time-Gating Approach. Anal. Chem. 88, 3449–3454. https://doi.org/10.1021/acs.analchem.5b04626

Zhong, Y., Tian, G., Gu, Z., Yang, Y., Gu, L., Zhao, Y., Ma, Y., Yao, J., 2014. Elimination of Photon Quenching by a Transition Layer to Fabricate a Quenching-Shield Sandwich Structure for 800 nm Excited Upconversion Luminescence of Nd3+-Sensitized Nanoparticles. Advanced Materials 26, 2831–2837. https://doi.org/10.1002/adma.201304903

Zhou, B., Shi, B., Jin, D., Liu, X., 2015. Controlling upconversion nanocrystals for emerging applications. Nat Nano 10, 924–936. https://doi.org/10.1038/nnano.2015.251

Zhu, X., Feng, W., Chang, J., Tan, Y.-W., Li, J., Chen, M., Sun, Y., Li, F., 2016. Temperature-feedback upconversion nanocomposite for accurate photothermal therapy at facile temperature. Nat Commun 7, 10437. https://doi.org/10.1038/ncomms10437

Zimmermann, T., Rietdorf, J., Pepperkok, R., 2003. Spectral imaging and its applications in live cell microscopy. FEBS Letters, Signal Transduction Special Issue 546, 87–92. https://doi.org/10.1016/S0014-5793(03)00521-0

Zou, W., Visser, C., Maduro, J.A., Pshenichnikov, M.S., Hummelen, J.C., 2012. Broadband dye-sensitized upconversion of near-infrared light. Nature Photonics 6, 560–564. https://doi.org/10.1038/nphoton.2012.158

List of publications

Dukhno, O.; Przybilla, F.; Collot, M.; Klymchenko, A.; Pivovarenko, V.; Buchner, M.; Muhr, V.; Hirsch, T.; Mély, Y. Quantitative Assessment of Energy Transfer in Upconverting Nanoparticles Grafted with Organic Dyes. Nanoscale 2017, 9 (33), 11994–12004.

Dukhno, O.; Przybilla, F.; Muhr, V.; Buchner, M.; Hirsch, T.; Mély, Y. Time-dependent luminescence loss for individual upconversion nanoparticles upon dilution in aqueous solutions. Nanoscale 2018, 10 (34), 15904–15910.

Dukhno, O.; Przybilla, F.; Greiner, V.; Kuzmenko, L.; Godet, J.; Muhr, V.; Buchner, M.; Hirsch, T.; Mély, Y. Targeted membrane receptor tracking with upconversion nanoparticles. (*in preparation*)

List of presentations

Dukhno, O.; Przybilla, F.; Arntz, Y.; Collot, M.; Klymchenko, A.; Buchner, M.; Muhr, V.; Hirsch, T.; Mély, Y. Optimizing upconverting nanoparticles for FRET-based assays. Oral presentation at UPCON 2016 international conference, Wroclaw, Poland, 23-27 May 2016.

Dukhno, O.; Przybilla, F.; Arntz, Y.; Collot, M.; Klymchenko, A.; Buchner, M.; Muhr, V.; Hirsch, T.; Mély, Y. Poster presentation at Journees de Campus Illkirch 2016, Illkirch, France, 21-22 April 2016.

Dukhno, O.; Przybilla, F.; Collot, M.; Klymchenko, A.; Pivovarenko, V.; Buchner, M.; Muhr, V.; Hirsch, T.; Mély, Y. Quantitative assessment of energy transfer in upconverting nanoparticles grafted with organic dyes. Poster presentation at 28th International conference on Photochemistry (ICP 2017), Strasbourg, France, 16-21 July 2017.

Dukhno, O.; Przybilla, F.; Collot, M.; Klymchenko, A.; Pivovarenko, V.; Buchner, M.; Muhr, V.; Hirsch, T.; Mély, Y. Quantitative assessment of energy transfer in upconverting nanoparticles grafted with organic dyes. Poster presentation at 15th Conference on Methods and Applications in Fluorescence (MAF 2017), Bruges, Belgium, 10-13 September 2017.

Dukhno, O.; Przybilla, F.; Muhr, V.; Buchner, M.; Hirsch, T.; Mély, Y. Time-dependent luminescence loss of individual upconversion nanoparticles upon dilution in aqueous solutions. Oral presentation at UPCON 2018 international conference, Valencia, Spain, 2-6 April 2018.

Dukhno, O.; Przybilla, F.; Muhr, V.; Buchner, M.; Hirsch, T.; Mély, Y. Time-dependent luminescence loss of individual upconversion nanoparticles upon dilution in aqueous solutions. Oral presentation at Journees de Campus Illkirch 2018, Illkirch, France, 15-16 May 2016. *(best presentation award)*

Resume de these en francais

Chapitre 2. Résultats et discussion.

Partie 1. Fonctionnalisation et caractérisation des particules.

Les particules initiales du projet ont été synthétisées par nos collaborateurs de l'Université de Regensburg, dirigés par le Dr. Thomas Hirsch.

Afin de faciliter la comparaison des performances des particules avec les données publiées, nous avons opté pour la composition de UCNP la plus étudiée, β-$NaYF_4$: 20% Yb^{3+}, 2% Er^{3+} à cœur simple (particules homogènes sans dopage de type cœur-coquille). Les particules du projet ont été synthétisées en plusieurs tailles: diamètres de 16, 21 et 31 nm. La taille des particules a été modulée par co-dopage avec du Gd^{3+} (0%, 10% and 20%), qui permet de réduire la taille des particules tout en préservant les propriétés de cristallinité et de luminescence (*Damasco et al., 2014*). Des exemples d'images de microscopie électronique en transmission (TEM) de particules avec des histogrammes de taille de particules ainsi que des distributions de taille obtenues pour de diffusion dynamique de la lumière (DLS) sont fournis à la Fig. 2.1.1. Les particules sont approximativement sphériques et ont une distribution de taille remarquablement étroite. Les diagrammes de diffraction aux rayons X (XRD) confirment que les particules ont une matrice cristalline en phase β (hexagonale).

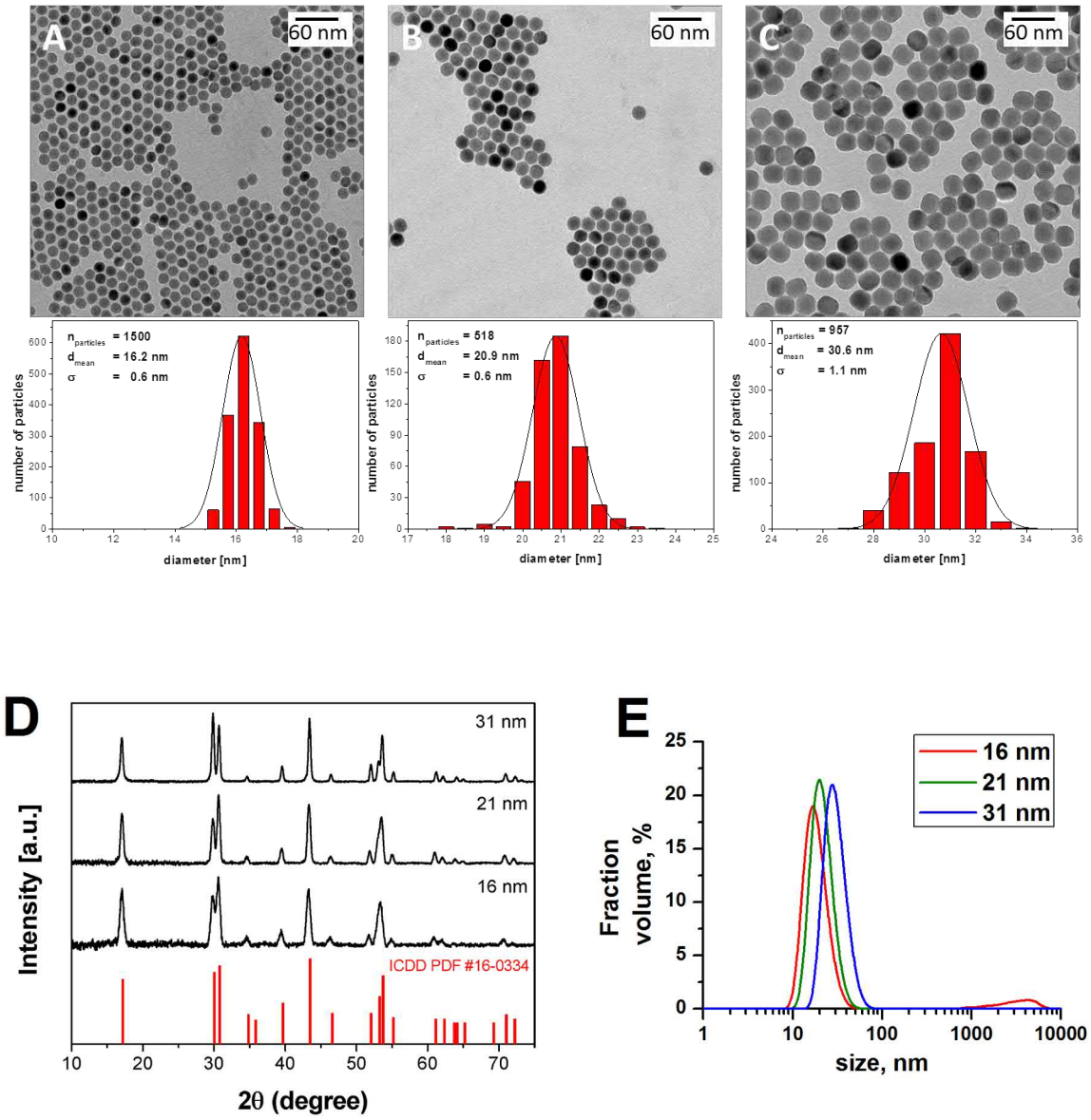

Fig. 2.1.1. Caractérisation initiale des particules. A,B,C: images TEM et histogrammes de taille de particules obtenus par analyse des 'images TEM pour les UCNPs de 16 nm, 21 nm et 31 nm de diamètre, respectivement. D: spectres XRD despoCNPs. E: Distributions de taille obtenues par DLS pour des dispersions d'UCNPs dans du cyclohexane.

Les spectres de luminescence des particules de départ et leurs déclins de luminescence sont représentés dans la Fig. 2.1.3. Ces particules présentent des caractéristiques photo-physiques typique des UCNPs dopées par Yb^{3+}-Er^{3+}. Les différences entre les différents spectres et les différents déclins sont caractéristiques d'une augmentation des effets de

surfaces (notamment quenching) à mesure que le diamètre des particules diminue (*Arppe et al., 2015; Würth et al., 2018*).

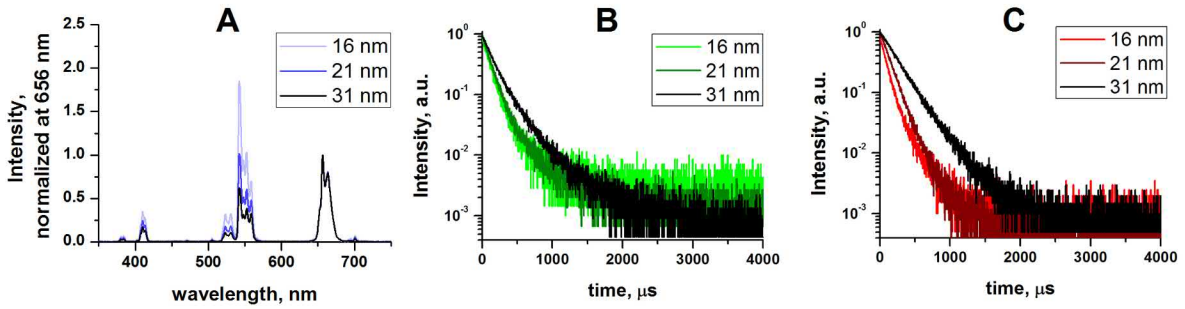

Fig. 2.1.3. Spectres et déclins de luminescence d'UCNPs recouvertes d'acide oléique de 16, 21 et 31 nm de diamètre dispersées dans du cyclohexane. A: spectres d'UCNPs, normalisés au maximum de la bande rouge. B: courbes de déclin de luminescence de la bande verte. C: courbes de déclin de luminescence de la bande rouge. L'excitation a été réalisée à 980 nm avec un faisceau focalisé, en utilisant une intensité d'excitation moyenne de 6.2 KW/cm^2.

Après avoir vérifié que les particules de départ étaient de qualité suffisante pour servir de base aux expériences SMM, l'étape suivante consistait à tester différents protocoles de traitement de surface. L'objectif est d'obtenir des particules dispersables dans l'eau, qui conservent une bonne monodispersité et une luminescence homogène et qui présentent une bonne stabilité dans le temps. A ce moment-là, les données de la littérature concernant la dispersion des particules dans l'eau montraient fréquemment une oligomérisation partielle des particules (*Hlaváček et al., 2014; Sedlmeier and Gorris, 2015*). Bien qu'elle soit généralement acceptable pour les analyses d'ensemble, l'oligomérisation peut poser de graves problèmes dans les expériences SMM, où elle peut induire des erreurs systématiques importantes et une performance médiocre des essais en raison d'une hétérogénéité particule à particule trop importante. Il convient également de noter que les protocoles de revêtement et de modification des nanoparticules sont connus pour leur faible reproductibilité inter-laboratoire. Gardant tout cela à l'esprit, les stratégies suivantes ont attiré notre attention:

- Les revêtements à base de coquille de silice ont été considérés comme peu prioritaires. Les principales préoccupations émanaient du nombre élevé de paramètres critiques présents dans les protocoles de la littérature, des difficultés de purification des

nanoparticules, de l'agrégation progressive lors du stockage et de la difficulté à contrôler finement l'épaisseur de la coquille, paramètre particulièrement important pour le smFRET.

- La plus haute priorité a été attribuée aux revêtements à base de surfactants, en particulier les polymères amphiphiles, en raison de la stabilité colloïdale exceptionnelle des particules produites, de leur fonctionnalisation aisée via simple ajout de groupements réactifs au polymère et de l'expérience antérieure du laboratoire avec cette approche.
- L'échange de ligands a attiré notre attention en raison de la simplicité des protocoles, du vaste choix de modifications chimiques disponibles et de la faible épaisseur de la couche de surfactant qui pourrait faciliter les applications FRET. La principale préoccupation concernant cette méthode concernait le détachement des ligands lors de la dilution de la dispersion, car les matrices à base de fluorure à partir desquelles les UCNPs brillantes sont fabriquées ne présentent pas de fortes interactions avec les ligands qui sont typiquement utilisés.
- L'encapsulation par nanoémulsion des UCNPs n'était pas décrite dans la littérature à ce moment. Notre intérêt pour cette approche était dû à la rapidité et simplicité des protocoles mis en œuvre pour la formation de nanoémulsions pour certaines combinaisons de phase non polaire et de surfactant (*Anton and Vandamme, 2010, 2009*).

Dans un premier temps nous avons décidé d'essayer ces méthodes par ordre de priorité, pour affiner dans un second temps le protocole qui donnait les résultats initiaux les plus prometteurs.

2.1.1. Enrobage à base de polymère amphiphile

Les revêtements à base de polymères amphiphiles sont largement utilisés pour les nanoparticules afin de les rendre dispersables dans des tampons aqueux. Les protocoles les plus connus pour le revêtement de nanoparticules inorganiques ont été mis au point par le groupe de Parak (*Lin et al., 2008; Pellegrino et al., 2004*). Ensuite, plusieurs groupes, y compris nos collaborateurs, ont adapté ces protocoles aux UCNPs (*Jiang et al., 2012; Wilhelm et al., 2015; Wu et al., 2009*).

Typiquement, les polymères amphiphiles peuvent être formés soit par polymérisation de monomères décorés de différentes manières, soit par modification d'un squelette polymère déjà formé (Fig. 2.1.1.1). Nous avons opté pour la seconde approche, car cette méthode permet de modifier facilement le polymère, repose sur des protocoles plus courts et plus fiables et permet d'obtenir un polymère de taille définie.

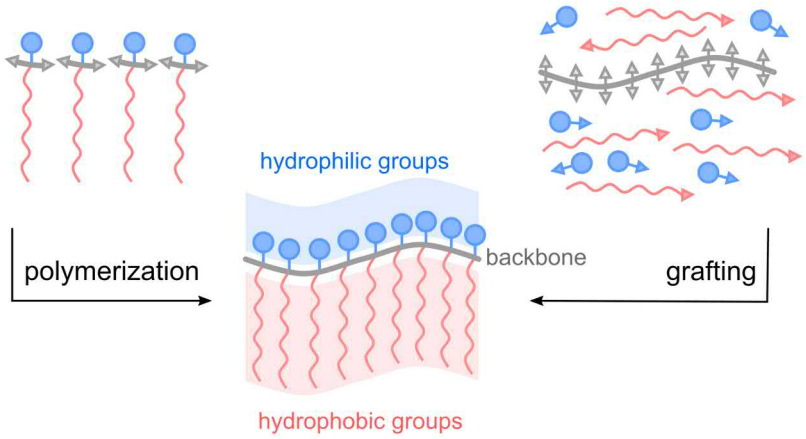

Fig. 2.1.1.1. Stratégies pour la préparation de polymères amphiphiles.

Pour la synthèse du polymère, nous avons utilisé un protocole similaire à celui décrit précédemment dans la littérature (*Wilhelm et al., 2015*). En bref, la réaction implique l'ouverture de cycles anhydrides sur un polymère polyanhydride commercial avec de la dodécylamine en présence d'une base, une hydrolyse ultérieure assure l'ouverture de tous les cycles (Fig. 2.1.1.2A). Le polymère résultant possède un squelette hydrophile avec des groupements carboxyles et des chaînes latérales hydrophobes qui y sont attachées par des liaisons amides robustes (Fig. 2.1.1.2B). Nous avons également inclus une étape de purification par chromatographie d'exclusion stérique pour assurer l'élimination de toutes les impuretés (petites molécules). Après synthèse, le polymère est dispersable dans des solvants organiques non polaires (par exemple le chloroforme). Il est important de noter qu'il est possible d'attacher facilement au polymère des fluorophores, des liens bio-orthogonaux et d'autres fragments utiles pendant la synthèse, simplement en ajoutant une amine primaire appropriée au cours de l'étape d'ouverture de cycles.

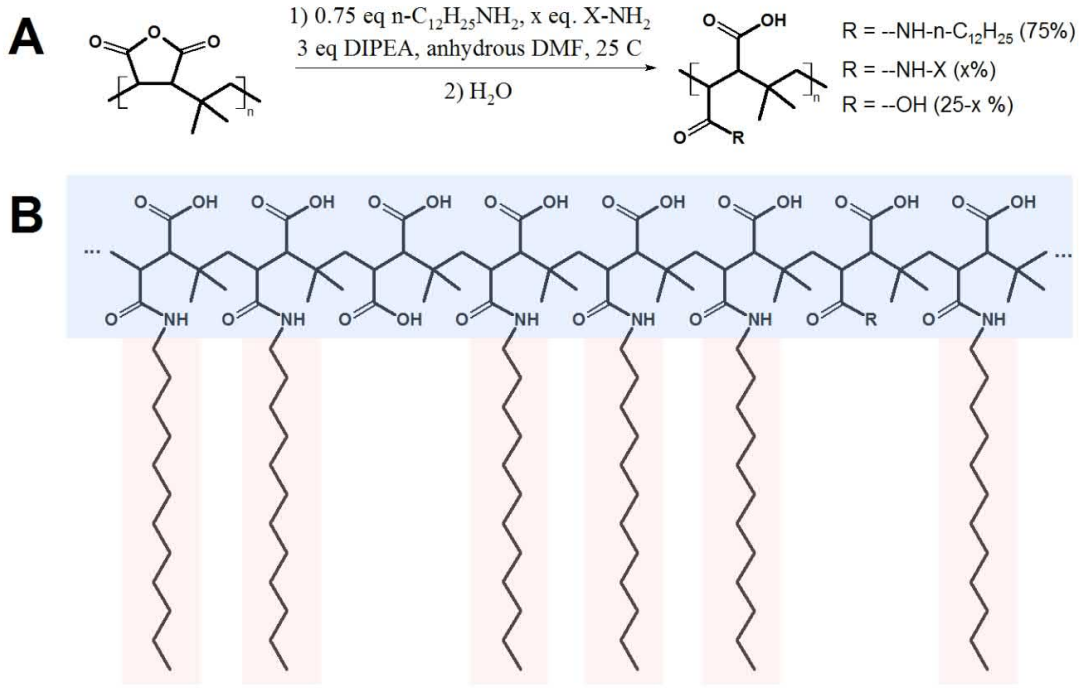

Fig. 2.1.1.2. Synthèse du polymère amphiphile. A: greffage de groupes sur un squelette de polyanhydride par formation de groupes amides. B: exemple de structure de polymère synthétisé, avec les chaînes latérales hydrophobes et le squelette hydrophile mis en évidence.

Ensuite, nous avons enrobé les UCNPs avec le polymère, en utilisant les protocoles de la littérature mentionnés précédemment comme point de départ. Le protocole est illustré à la Fig. 2.1.1.3 (la version complète est disponible dans le chapitre Matériels et Méthodes). En bref, les UCNPs et le polymère sont dispersés ensemble dans du chloroforme (Fig. 2.1.1.3A). L'ajout d'un tampon aqueux très basique amène le polymère à résider à l'interface eau-chloroforme, formant de grosses gouttelettes de solvant (> 1 μm de diamètre) (Fig. 2.1.1.3B). En réchauffant modérément la solution mis sous un faible vide tout en maintenant une agitation constante le chloroforme s'évapore doucement du mélange. Alors que l'évaporation du chloroforme réduit l'espace disponible à l'interface solvant-eau, les gouttelettes se contractent, formant une surface de plus en plus rugueuse, finissant par se séparer. Le mécanisme de rupture des gouttelettes n'est pas clair, mais il est susceptible d'être induit par l'agitation mécanique et la répulsion électrostatique des groupes carboxyles chargés à la surface des particules. L'évaporation se poursuit jusqu'à ce que les gouttelettes ne contiennent plus aucun solvant (devenant ainsi des micelles) ou contiennent une ou plusieurs UCNPs. Si

un excès de polymère suffisamment élevé est utilisé, les gouttelettes résultantes auront une probabilité plus faible de contenir plusieurs UCNPs, ce qui permettra finalement d'obtenir des particules individuelles enrobées par une enveloppe de polymère (Fig. 2.1.1.3C). Néanmoins, l'utilisation d'un excès de polymère entraîne la formation d'une grande quantité de micelles de polymère vides, qui doivent ensuite être séparées des UCNP enrobées. Cette purification peut être effectuée par filtration centrifuge, chromatographie d'exclusion stérique, sédimentation centrifuge avec re-dispersion ultérieure et par d'autres méthodes de purification des nanoparticules (Fig. 2.1.1.3D).

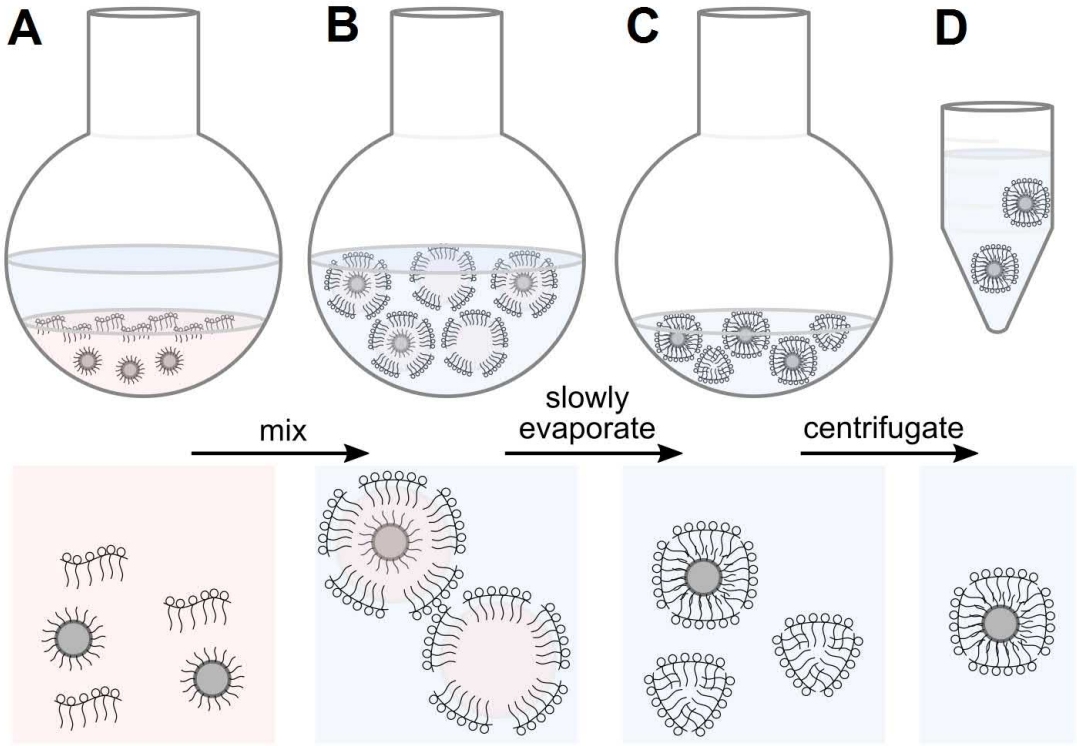

Fig. 2.1.1.3. Protocole d'enrobage. A: mélange initial à deux phases. Les particules restent dans le chloroforme, tandis que le polymère migre vers l'interface. B: formation de grosses gouttelettes de solvant par mélange. C: formation de particules enrobées et de micelles de polymère. D: séparation des particules et des micelles.

Nous avons testé diverses conditions pour le protocole d'enrobage / purification, y compris la modification du rapport de concentration polymère / UCNPs, le pH du tampon, l'utilisation des ultrasons pour faciliter la dispersion des UCNPs et certains autres paramètres.

Nous avons finalement réussi à trouver un ensemble de conditions qui produisaient de manière fiable une dispersion contenant des UCNPs individuels encapsulées dans des micelles de polymère, sans oligomérisation ou agrégation importante des particules. Nous n'avons pas été en mesure de reproduire les protocoles de la littérature pour séparer les UCNP des micelles de polymères. Cependant, nous avons trouvé un ensemble de conditions pour la sédimentation / re-dispersion centrifuge qui donnent des particules monodisperses sans micelles de polymère présents après deux cycles de purification.

Pour caractériser les particules après synthèse et purification, nous avons effectué des mesures de diffusion dynamique de la lumière (DLS), qui sont couramment utilisées comme méthode semi-quantitative pour la caractérisation rapide de dispersion de nanoparticules. Bien que cette méthode ne permette pas d'obtenir précisément les concentrations relatives de particules individuelles et d'oligomères de particules, elle peut signaler qualitativement une oligomérisation ou une agrégation significative. Des exemples de distributions de tailles obtenues par DLS pour des dispersions de particules avec des micelles, des particules individuelles purifiées et des dispersions de particules oligomérisées / agrégées sont fournis à la Fig. 2.1.1.4.

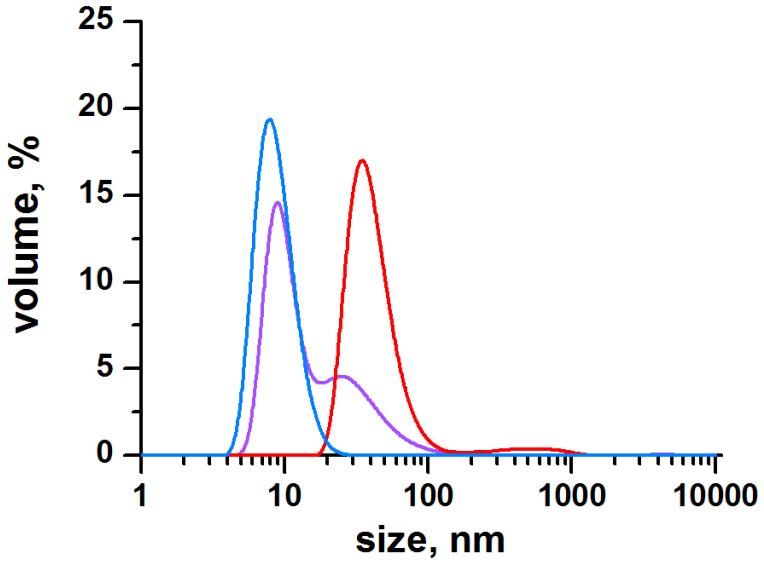

Fig. 2.1.1.4. Exemples de distribution de taille en volume obtenues par DLS pour des dispersions de particules enrobées de polymère. Violet: échantillon initial contenant à la fois des UCNP et des micelles de polymère. Rouge: UCNPs purifiés par centrifugation et redispersion dans un tampon. Bleu: micelles de polymère résidant dans le surnageant qui ont

été éliminés par centrifugation.

Pour les expériences de SMM, la taille et la luminescence des particules doivent être aussi homogènes que possible. Ainsi en se basant uniquement sur leur intensité de luminescence il sera possible de distinguer aisément les nanoparticules individuelles des oligomères et des agrégats, ce qui peut s'avérer extrêmement utile pour des expériences où la taille des particules n'est pas directement accessible (par exemple au cours d'expériences avec des cellules). Pour évaluer les deux paramètres en même temps, nous avons effectué une expérience de microscopie corrélative impliquant de la microscopie AFM et de la microscopie de fluorescence en champ large. La Fig. 2.1.1.5 illustre le concept de l'expérience et présente un exemple d'images obtenues pour des particules de 31 nm. En bref, une dispersion de particules est séchée sur une surface, puis une image AFM et une image de microscopie de fluorescence à champ large sont effectuées simultanément ou séquentiellement sur une région d'intérêt de l'échantillon. Si la concentration initiale des particules est suffisamment faible, elles seront séparées spatialement sur la surface et leurs spots de luminescence seront suffisamment éloignés les uns des autres pour permettre d'intégrer le signal de chaque particules prises individuellement afin de comparer leurs intensités de luminescence.

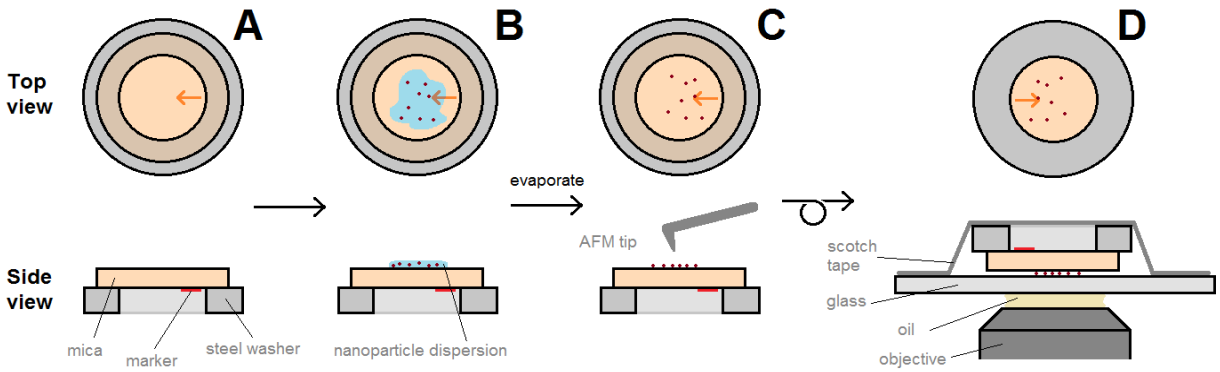

Fig. 2.1.1.5. Préparation des échantillons pour la microscopie corrélative AFM / microscopie de fluorescence en champ large. A: Assemblage initial composé d'un morceau de mica attaché à une rondelle en acier, marqué d'une flèche rouge sur la face du dessous. B: Une goutte de dispersion de nanoparticules est déposée sur le dessus. C: Après évaporation, une image AFM de l'échantillon est effectuée. D: L'échantillon est ensuite inversé, fixé sur une lamelle de verre et monté sur un microscope inversé. La position du marqueur est repérée aux oculaires en champ clair puis la ROI est amenée au centre du champ par un déplacement de la platine XY motorisée. Ensuite, une image de microscopie de fluorescence de la ROI est réalisée.

Pour vérifier que le protocole d'enrobage produisait des particules uniques au lieu d'oligomères, nous avons effectué de la microscopie corrélative AFM / microscopie de luminescence en champ large. La Fig. 2.1.1.6 montre un exemple d'échantillon fortement mono-disperse d'UCNPs enrobées de polymère. Les particules présentent une luminescence et une taille homogènes (Fig. 2.1.1.6C). Comme les images AFM sont convoluées par la forme de la pointe AFM, la taille des particules est estimée à partir de la hauteur, qui peut être mesurée très précisément par AFM.

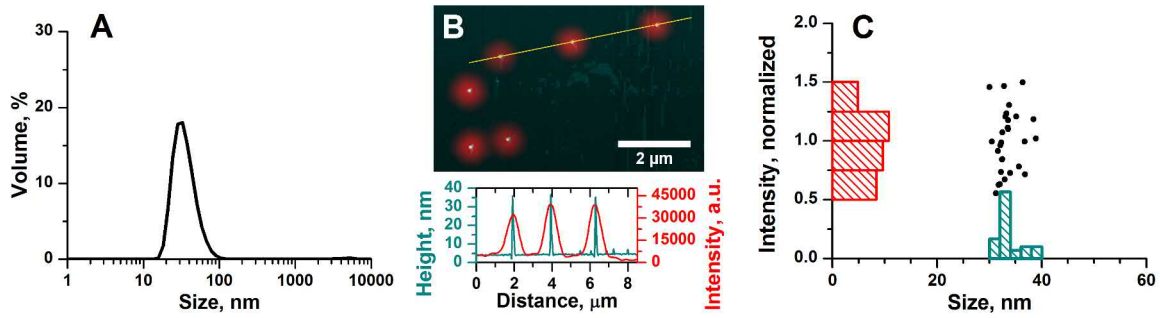

Fig. 2.1.1.6. Particules enrobées de polymère purifiées. A: Mesure DLS des UCNPs dispersés dans l'eau. B: Haut: région d'intérêt (ROI) d'une image AFM d'UCNPs séchés à partir d'une dispersion aqueuse et de son image corrélée de microscopie de luminescence en champ large dans le canal rouge (en rouge; filtre passe-bande 660/30, excitation à 980 nm avec intensité de 8 kW / cm2). En bas: hauteur et intensité des trois particules mises en évidence dans le panneau supérieur. C: Taille et intensité normalisée (points noirs) et histogrammes de ces paramètres (bleu et rouge) pour un échantillon de 28 particules.

En parallèle, nous avons également effectué la synthèse et la purification de polymères amphiphiles zwitterioniques. De la même manière que les membranes naturelles à base de phospholipides, les surfactants zwitterioniques ont une paire de groupements chargés positivement et négativement liés de manière covalente à l'extrémité hydrophile. En milieu aqueux, de tels polymères ont tendance à former une coque très dense et très coordonnée autour du groupe zwitterionique. Ceci, combiné à leur charge de surface neutre à pH physiologique, permet aux micelles à base de surfactants zwitterioniques d'être stabilisés via la répulsion stérique de leurs coquilles d'eau fortement coordonnées. De plus, cela leur permet de présenter des propriétés anti-agrégation et de passiver leur surface dans les conditions biologiques d'une manière similaire à une fonctionnalisation par des groupements polyéthylèneglycol (PEG), mais avec une taille de groupement stabilisant beaucoup plus petite (Fig. 2.1.1.7) (*Estephan et al., 2011; García et al., 2014; Schlenoff, 2014*).

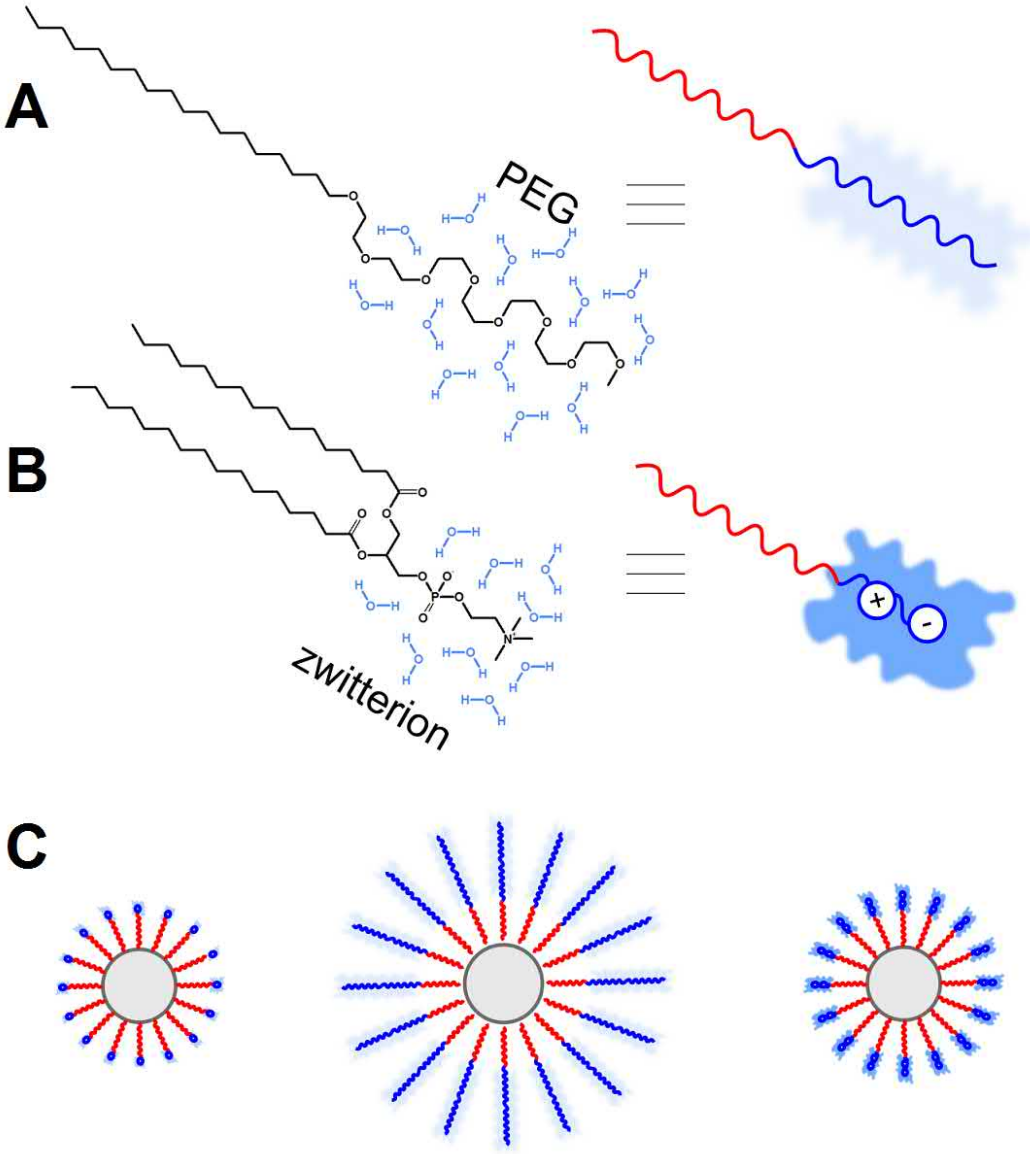

Fig. 2.1.1.7. Stabilisation stérique par PEG et zwitterions. A: un surfactant avec une chaîne de PEG exposée à des conditions aqueuses possède une enveloppe de molécules d'eau modérément coordonnée. B: un surfactant zwitterionique (ici: DOPC) a une petite coquille de molécules d'eau fortement coordonnées. C: Comparaison de la taille des particules pour les différentes méthodes de stabilisation. Les surfactants à charge unique stabilisent les particules par répulsion électrostatique, mais cessent de le faire en présence de sels. Les surfactants PEG stabilisent les particules par la répulsion stérique de l'enveloppe d'eau, mais induisent une augmentation substantielle de la taille des particules. Les tensioactifs zwitterioniques se comportent de la même manière, mais permettent de conserver des

particules de petite taille.

Les polymères amphiphiles portant des groupements zwitterioniques sont connus sous le nom de polyzwitterions amphiphiles ou “polysoaps”. Une de leurs applications potentielles est la stabilisation de nanoparticules dans des dispersions aqueuses. Les propriétés de passivations induites par une faible charge de surface effective permettraient de protéger les particules contre la liaison non spécifique de biomolécules, tandis que la fine épaisseur de l’enveloppe serait bénéfique pour les applications FRET nécessitant une distance réduite entre la particule et l’accepteur. Une autre propriété intéressante des nanoparticules recouvertes de zwitterion serait leur stabilité colloïdale dans des tampons physiologiques qui ont généralement un pouvoir ionique élevé, ce qui pose problème aux nanoparticules stabilisées par répulsion électrostatique.

Comme il existait peu d'informations dans la littérature sur la stabilisation de nanoparticules avec des polyzwitterions amphiphiles, nous avons décidé d'étudier la faisabilité de la préparation de tels composés et de leur utilisation pour stabiliser des UCNPs. Nous avons testé plusieurs stratégies pour préparer un polymère zwitterionique, toutes basées sur la modification d'un squelette polyanhydride avec une sulfobétaïne-amine. La Fig. 2.1.1.8 illustre la seule approche ayant abouti à une décoration significative du squelette polymèrique avec des groupeements sulfobétaïne. Nous avons caractérisé les polymères par RMN et IR afin de vérifier leur composition. En raison de problèmes de solubilité, un seul protocole a permis de préparer un polymère avec une quantité significative de groupes sulfobétaïne (les protocoles qui ont échoués ne sont pas présentés ici mais sont disponibles sur demande). Malheureusement, l’enrobage des UCNP avec ce polymère n'a pas abouti. Aucune des approches que nous avons testées n'a permis de produire autre chose que des agrégats de polymère et d’UCNPs. Une raison probable de cet échec est la grande stabilité thermodynamique des films et des agrégats de polymères obtenus lors de l’évaporation du solvant du fait de l’absence de répulsion électrostatique entre les différents groupements de «tête». Une autre raison possible serait le caractère hydrophile insuffisant de la sulfobétaïne en raison de la présence de groupes éthyle, entravant la coordination des molécules d’eau. Alors que ce sujet mérite plus d'investigation, nous avons décidé de reporter ce projet parallèle et de nous concentrer sur d'autres approches permettant de disperser les UCNPs dans l’eau, ainsi que sur les applications des UCNPs.

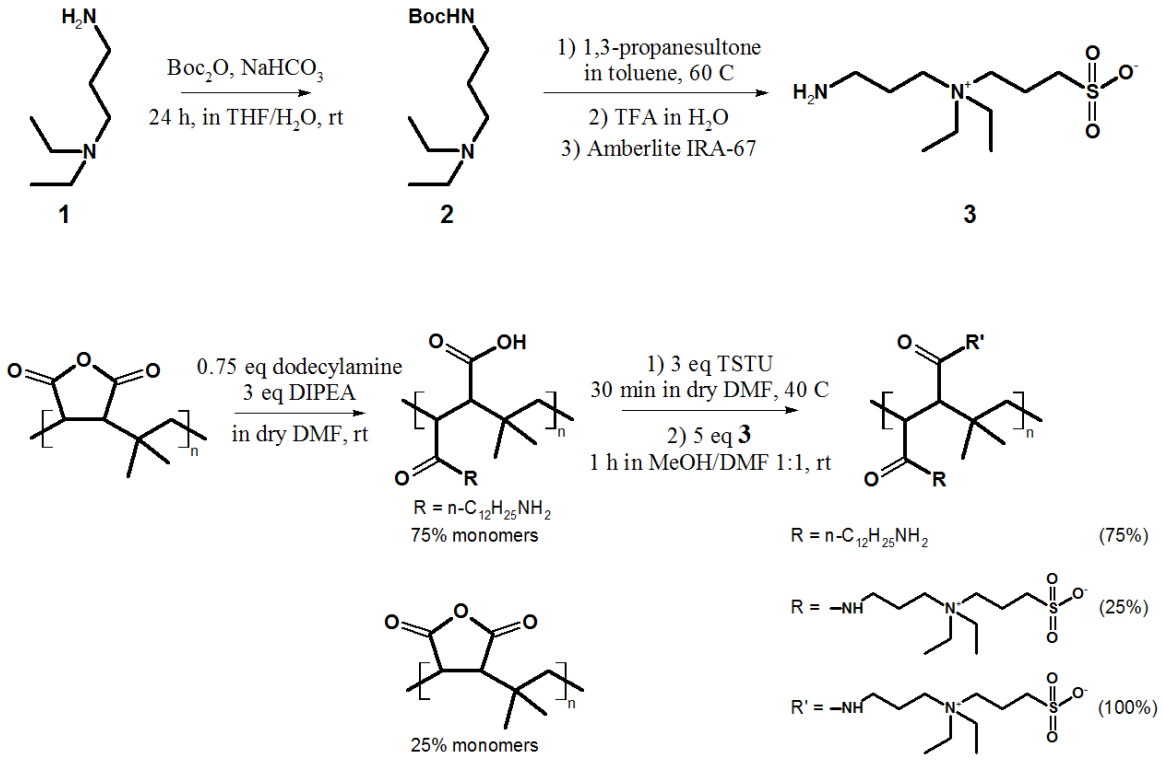

Fig. 2.1.1.8. Synthèse du polymère amphiphile zwitterionique.

2.1.2. Expériences d'échange de ligands

Nous avons effectué une petite série d'expériences d'échange de ligands pour voir si elles permettraient d'obtenir une qualité de particules satisfaisante. Pour les expériences d'échange de ligand, nous avons décidé d'opter pour un décapage doux des UCNPs via $NOBF_4$ avec extraction simultanée des particules dans du DMF (Dong et al., 2011). La DLS des dispersions de particules obtenues dans le DMF a montré qu'aucune agrégation significative ne s'était produite pendant le stripping du ligand et que les particules étaient colloïdalement stables sur des périodes de temps prolongées (Fig. 2.1.2.1).

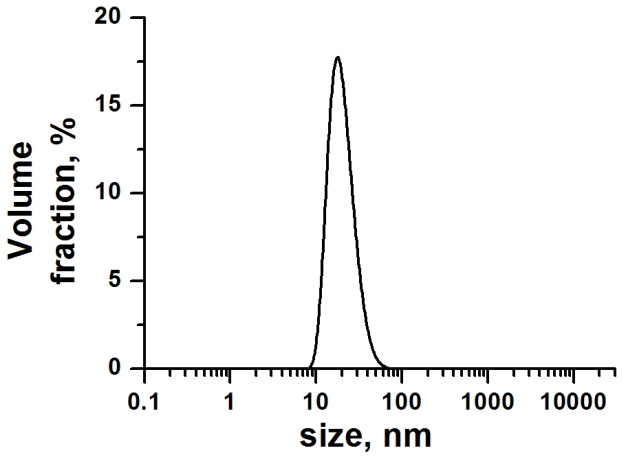

Fig. 2.1.2.1. Distribution de taille obtenue par DLS d'UCNPs de 21 nm ayant subi un échange de ligand avec $NOBF_4$.

L'étape suivante était la dispersion des particules dans l'eau avec stabilisation par un surfactant et purification ultérieure pour éliminer le DMF résiduel et les micelles vides. En tant que surfactant, nous avons utilisé le Tween 20, un surfactant neutre avec un fragment hydrophile de PEG branché. Les particules restent colloïdalement stables, mais uniquement en présence de micelles de polymères. Dans le petit ensemble d'expériences que nous avons effectuées, nous avons systématiquement constaté que l'oligomérisation des particules et l'instabilité colloïdale au fil du temps constituaient un problème si l'excès de surfactant était éliminé de la dispersion.

2.1.3. Encapsulation par nanoemulsion

Les nanoémulsions ont fait l'objet d'une attention accrue au cours des dernières années, en particulier pour l'encapsulation de principes actifs non polaires dans des gouttelettes d'huile destinées à l'administration de médicaments (*Anton and Vandamme, 2010*). Parmi les méthodes de nanoémulsification, une méthode, appelée émulsification spontanée, est particulièrement remarquable en raison de ses faibles exigences expérimentales et de sa possibilité de travailler avec des substances fragiles qui seraient dégradées par des méthodes d'émulsification classiques telles que la sonication (*Anton and Vandamme, 2009*).

L'émulsification spontanée est basée sur la préparation d'un mélange homogène d'huile et de surfactant non ionique dans une certaine proportion, puis le mélange de cette solution avec de l'eau ou un tampon aqueux. Après mélange, ce système à deux phases ne se trouve pas à l'équilibre thermodynamique ce qui entraîne un repositionnement rapide des molécules de surfactant à la surface huile / eau pour rejoindre spontanément l'état stable le plus proche. Si la proportion de surfactant est suffisamment grande, les deux phases forment spontanément une grande surface entre elles, ce qui entraîne la formation de nanoémulsion. Ensuite, la coalescence des gouttelettes d'huile est gênée par la présence du surfactant à l'interface. Cela conduit à des nanoémulsions stables pendant des semaines ou des mois. La formation de nanoémulsions stables dépend de la nature du surfactant et de l'huile, de leurs proportions dans le mélange, de la température à laquelle le mélange est effectué, de la présence d'ions dans la phase aqueuse et de plusieurs autres paramètres.

Si une substance lipophile est ajoutée au mélange huile / surfactant avant de former une nanoémulsion, elle est piégée (encapsulée) à l'intérieur des gouttelettes de l'émulsion. Étant donné que les UCNPs recouvertes d'ions d'oléate sont hydrophobes, elles peuvent éventuellement être piégées dans les gouttelettes, à condition que la taille moyenne des gouttelettes soit suffisante pour contenir une UCNP à l'intérieur.

Nous avons effectué une vaste exploration des conditions expérimentales possibles afin de trouver les combinaisons huile / surfactant et des conditions expérimentales permettant d'obtenir une charge suffisante d'UCNPs dans des gouttelettes d'huile. Le tableau 2.1.3.1 met en avant deux expériences relativement réussies et certains commentaires (le protocole complet est disponible dans la section Matériels et méthodes). Malheureusement, aucune condition expérimentale n'a donné de particules présentant une stabilité colloïdale suffisamment longue, les meilleures présentant une agrégation et une sédimentation visible en l'espace de 2-3 jours.

Nanoemulsion composition and emulsification conditions	**Size by DLS (volume distribution)**	**Comments**
Sample NE42: 55µL Labrafac WL1349, 55µL Solutol HS15, 1.25 mg UCNP 31 nm, 100 µL chloroform (cosolvent for mixing, removed by evaporation before emulsification), emulsification	38 nm	dodecylated amphiphilic polymer used as a co-surfactant; sample shows substantial aggregation over 2 days

with 25 C water		
Sample NE25: 45µL Suppocire C, 55µL Solutol HS15, 1.25 mg UCNP 31 nm, 50 µL chloroform and 100µL dichloroethane (cosolvents for mixing, removed by evaporation before emulsification), emulsification with 25 C water	34 nm	dichloroethane aids dispersion with high-melting-point oil (Suppocire C); sample shows substantial aggregation overnight

Tableau 2.1.3.1. Exemples de conditions expérimentales de nanoémulsification donnant de relativement bon résultats.

Nous avons également étudié les nanoémulsions par microscopie de fluorescence en champ large et par microscopie TEM afin d'estimer la proportion de gouttelettes contenant des UCNPs. Pour cela, les gouttelettes ont été chargées à la fois avec des colorants organiques et des UCNPs, puis immobilisées sur une surface de verre. L'excitation à la lumière visible induit la fluorescence du colorant, tandis que l'excitation IR induit la luminescence des UCNPs. En combinant les images, la quantité totale de gouttelettes et la quantité de gouttelettes contenant des UCNPs ont pu être estimées. La Fig. 2.1.3.2 illustre les résultats. Les images suggèrent que la proportion de gouttelettes contenants des UCNPs est extrêmement faible, avec seulement quelques gouttelettes chargées par des UCNPs parmi des centaines de gouttelettes vides. Nous avons essayé de séparer les goutettes contenant des particules et les gouttelettes vides en utilisant une centrifugation douce, avec l'idée que la différence majeure permettant de les séparer serait leur densité différente. Malheureusement, nous n'avons pas trouvé de conditions permettant une séparation suffisante des gouttelettes contenant des UCNPs sans induire leur coalescence.

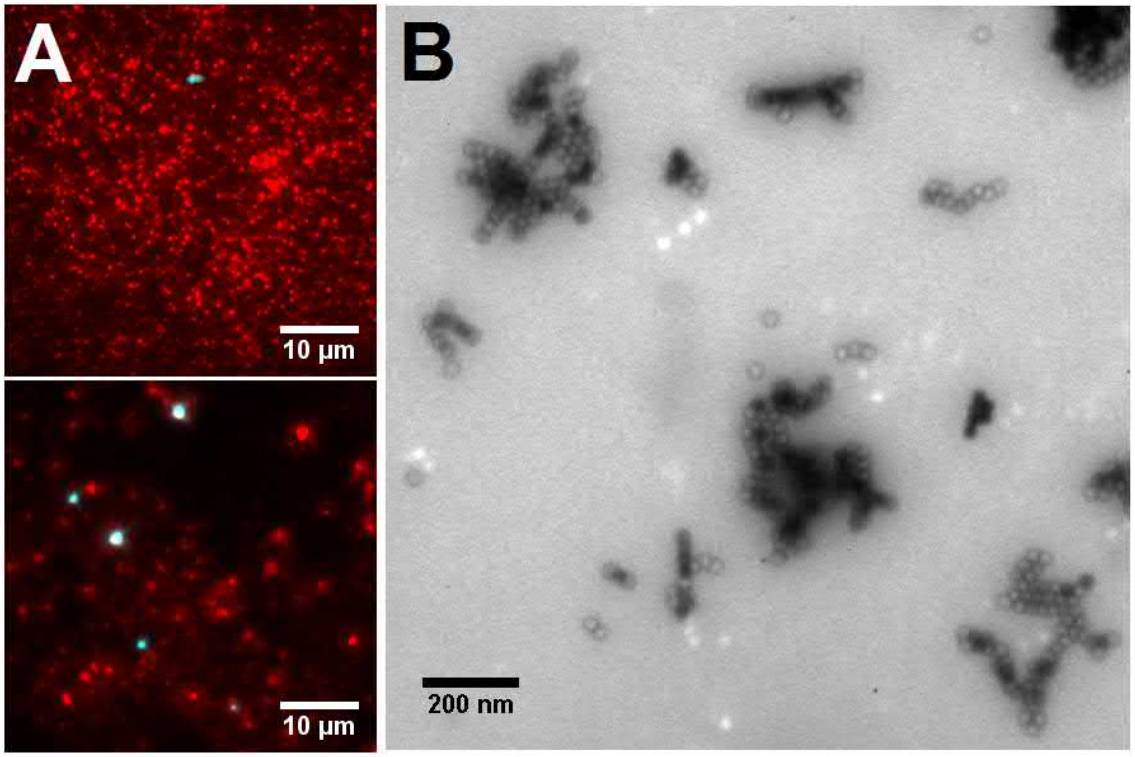

Fig. 2.1.3.2. Encapsulation d'UCNPs par nanoémulsion. A: images de microscopie en champ large d'UCNPs (canal cyan) et de colorants organiques (canal rouge) immobilisés par séchage sur verre. Les «taches» autour des spots de fluorescence correspondent probablement à l'huile des gouttelettes qui s'étale sur la surface du verre lors du séchage. Peu de spots de luminescence sont observées dans le canal des UCNPs et leur large taille et forte émission indique la présence d'agrégats. B: Image TEM typique du même échantillon de nanoémulsion immobilisée par séchage sur une grille TEM recouverte d'un film de Formvar revêtue de carbone, en utilisant une coloration à l'acétate d'uranyle. Des gouttelettes de nanoémulsion «vides» (beignets) et des UCNPs (cercles pleins) sont présents. Contrairement aux gouttelettes vides, les UCNPs sont toujours présentes en larges amas, ce qui implique qu'elles étaient agrégées avant l'immobilisation.

Pour résumer ce chapitre, nous avons trouvé des conditions utilisant des polymères amphiphiles qui permettaient l'hydrophilisation et la purification des UCNPs tout en conservant leur monodispersité. Les autres méthodes que nous avons essayées n'ont pas donné de résultats satisfaisants pour l'application de ces particules en SMM.

L'étape suivante consistait à tester la faisabilité de l'utilisation des UCNP pour les techniques SMM. Nous avons décidé de commencer avec le smFRET.

Partie 2. Estimation de l'applicabilité des UCNPs aux expériences de smFRET.

Au début de cette partie du projet, les preuves de concept d'applications utilisant les UCNPs comme donneurs de FRET étaient assez bien représentées dans la littérature. (*Idris et al., 2012; Lahtinen et al., 2016; Mattsson et al., 2015; Rantanen et al., 2007; Wang et al., 2016*). Néanmoins, nous n'avons trouvé aucun exemple d'expériences de smFRET basées sur les UCNPs. Un problème particulier qui a attiré notre attention était l'absence d'une étude systématique du FRET des UCNPs aux colorants organiques, et plus spécialement son évaluation quantitative. Comme le smFRET est une technique quantitative, utiliser des UCNP pour le smFRET nécessite de comprendre et de pouvoir prévoir le FRET UCNP-fluorophores au moins à un niveau semi-quantitatif, avec la possibilité d'utiliser ce modèle pour trouver les paramètres optimaux pour les nanoparticules et les conditions d'imagerie afin d'obtenir des performances de smFRET raisonnables.

Dans ce contexte de FRET, les UCNP peuvent être considérés comme un système rigide d'émetteurs ponctuels indépendants jouant le rôle de donneurs dans une région sphérique, collectant l'énergie du volume entier de la sphère et la transférant à des accepteurs ponctuels proches de la surface de la sphère (Fig. 2.2.1). Qualitativement, on pourrait s'attendre à une efficacité de FRET plus faible pour les grosses particules, du fait qu'elles présentent un ratio inférieur d'ions émetteurs situés à proximité des colorants organiques de la surface. Dans le même temps, augmenter la quantité de colorants sur la surface des nanoparticules augmenterait l'efficacité du FRET en raison de la quantité plus importante d'accepteurs récupérant l'énergie des donneurs. Nous avons donc décidé de construire un cadre théorique pour prédire l'efficacité du FRET entre les UCNPs et les colorants organiques sur la base de la quantité de colorants et de la taille des UCNPs.

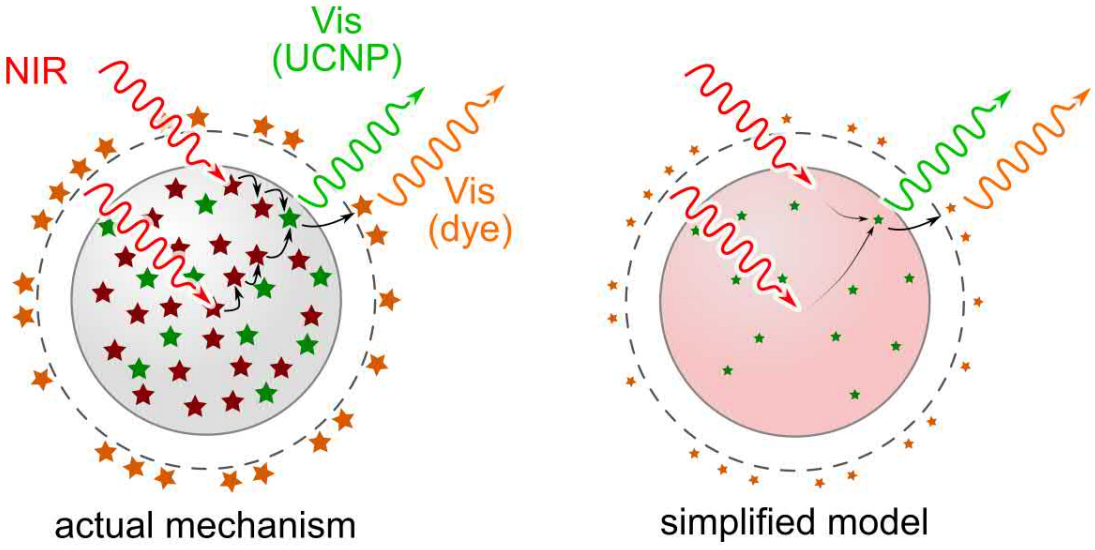

Fig. 2.2.1. Mécanisme du FRET des UCNPs aux colorants organiques et son modèle simplifié. Les étoiles rouges et vertes représentent respectivement les ions absorbeurs et émetteurs. Les étoiles oranges représentent des colorants organiques. Dans le système simplifié, la particule absorbe la lumière de manière homogène avec tout son volume, transférant uniformément son énergie aux ions émetteurs, qui peuvent ensuite émettre ou transférer leur énergie aux colorants. Les ions émetteurs et les colorants sont supposés être infiniment petits.

Compte tenu de la complexité des processus de conversion ascendante et des processus de quenching dans les UCNPs, nous avons décidé de construire un modèle théorique semi-empirique basé sur un ensemble d'expériences évaluant l'efficacité de FRET avec des particules de différentes tailles et présentant différentes quantités de colorants à la surface. En ce qui concerne le choix de l'approche mathématique, en raison de la quantité relativement faible de colorants et d'émetteurs, l'utilisation d'une approche analytique basée sur l'intégration pourrait produire à des résultats inexacts. Aussi, nous avons utilisé un modèle de Monte Carlo pour l'estimation théorique du FRET.

Les résultats sont présentés dans l'article suivant que nous avons publié dans la revue Nanoscale en 2017. Nous avons reformulé et élargi le modèle afin qu'il soit applicable non seulement aux expériences de smFRET, mais également à d'autres systèmes FRET basés sur

les UCNPs (par exemple, des essais basés sur le FRET utilisant des particules avec plusieurs sites de liaisons).

Après avoir utilisé ce modèle pour estimer l'efficacité de FRET d'un UCNP unique à un colorant organique unique, nous avons constaté qu'obtenir une efficacité de FRET raisonnable d'environ 10% nécessiterait l'utilisation de particules d'une taille inférieure à 10 nm. Nous avons effectué des expériences pour estimer pour des UCNPs uniques la dépendance entre le rapport signal sur bruit en imagerie et leur taille, en utilisant notre microscope en champ large avec un taux de rafraichissement relativement lent (25 fps, temps d'exposition de 40 ms). En extrapolant cette dépendance pour des nanoparticules de 10 nm de diamètre nous avons mis en avant que le rapport signal sur bruit serait trop faible pour pouvoir imager ces particules sur notre setup. Nous n'avons donc pas procédé à d'autres expériences de smFRET et nous nous sommes concentrés sur d'autres applications des UCNPs. Une littérature très récente (Tian et al., 2018) suggère que des particules avec un cœur fortement dopé et une coquille inerte fournissent un rapport signal sur bruit raisonnable en microscopie, cela même pour de très petites tailles de particules. Ainsi, l'adaptation de notre modèle théorique à l'étude de la faisabilité de l'utilisation de telles particules pour les applications de smFRET pourrait constituer une voie intéressante pour des recherches futures sur le sujet.

Publication 1.

Quantitative assessment of energy transfer in upconverting nanoparticles grafted with organic dyes

Partie 3. Microscopie de particules uniques avec des UCNPs.

Pour l'imagerie des UCNPs individuelles, nous avons utilisé la microscopie de luminescence en champ large comme outil principal. Pour étudier les particules individuelles, nous devions les immobiliser pour l'imagerie. Nous avons utilisé une approche typique qui consiste à sécher une dispersion de nanoparticules diluée. Cependant, étant donné que l'émission des UCNPs est quenchée et présente des modifications des intensités relatives des différentes bandes d'émission au contact de l'eau (*Arppe et al., 2015*), nous avons dû immobiliser les UCNP sur une surface tout en les conservant dans leur environnement expérimental «natif», c'est-à-dire en les maintenant en condition aqueuse. Pour cela, nous avons choisi une stratégie d'immobilisation basée sur les forces électrostatiques en déposant une couche de polyéthylèneimine branché (PEI) sur la surface du verre (Fig. 2.3.1). Dans les tampons aqueux possédant des valeurs de pH jusqu'à environ 10, le PEI est chargé positivement et se fixe donc électrostatiquement à la surface du verre, laquelle est elle-même chargée négativement en raison de la dissociation des groupements silanol à des valeurs de pH de 2 et plus. La surface de verre recouverte de PEI est chargée positivement, attirant ainsi les UCNPs enrobées de polymères amphiphiles chargés négativement. En contrôlant la concentration de la dispersion de particules, la densité d'UCNPs immobilisées peut être modulée. Par rapport au séchage, cette approche présente également l'avantage d'éviter l'agrégation de particules induite par le séchage, ce qui entraîne un revêtement inégal, via ce que l'on appelle couramment «l'effet rond de café» (*Deegan et al., 1997*).

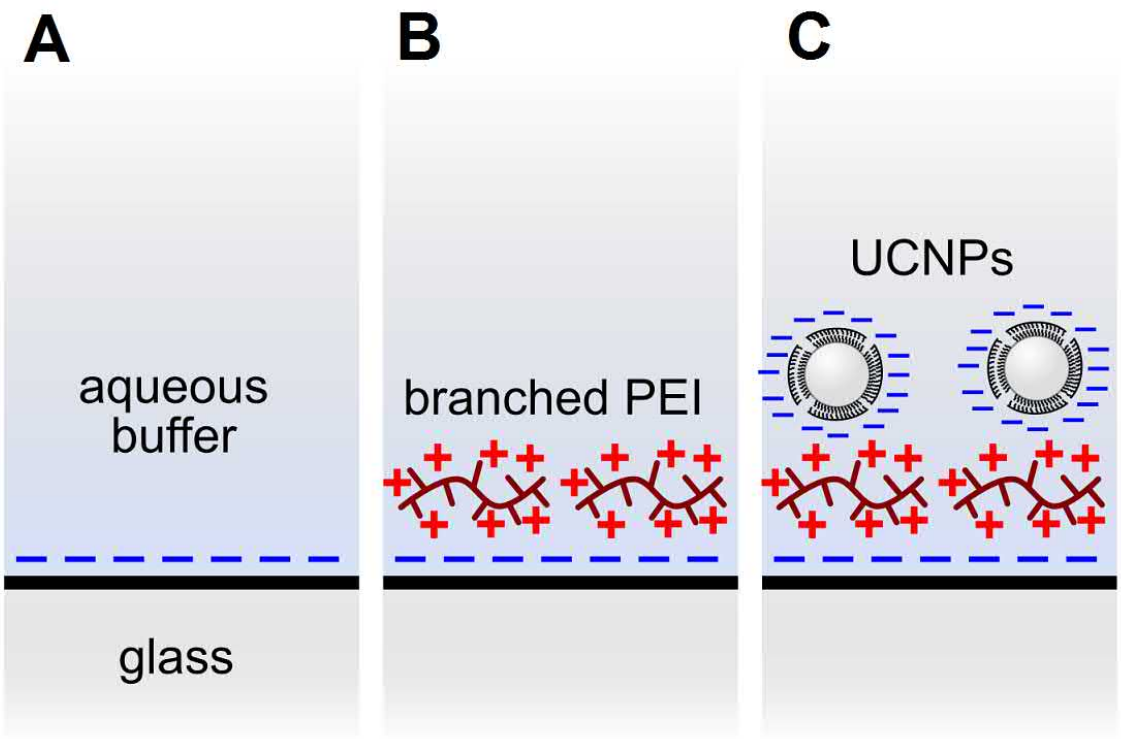

Fig. 2.2.1. Immobilisation des UCNP pour l'imagerie en champ large en condition aqueuse.

Après avoir déposé les UCNPs sur la surface de verre couverte de PEI, nous avons rincé la surface avec un tampon aqueux pour augmenter le RSB des images en éliminant les particules flottantes qui diffusent librement et ainsi augmentent le bruit de fond du fait du signal de luminescence émanant hors du plan focal. Nos premières expériences utilisaient de l'eau déminéralisée pour l'étape de rinçage. De manière inattendue, nous avons constaté un effet inhabituel: plusieurs minutes après le dépôt, le signal de certaines particules disparaissait et dans l'espace d'une heure la plupart des particules étaient absentes. Nous avons initialement attribué cet effet aux particules qui se détachent de la surface. Cependant, en examinant continuellement les particules, nous avons observé que toutes les particules perdaient progressivement leur luminescence au fil du temps, contrairement à la perte de luminescence brutale attendue dans le cas du détachement des nanoparticules.

En se tournant vers littérature, nous avons trouvé plusieurs rapports publiés au cours des dernières années qui décrivaient une perte de luminescence progressive des UCNPs dans les

dispersions diluées en raison de la lente dissolution des particules dans des tampons aqueux (*Lahtinen et al., 2017; Lisjak et al., 2016, 2015; Plohl et al., 2017b, 2017a; Wang et al., 2012*). Ce phénomène pourrait avoir des conséquences directes sur l'imagerie des UCNPs, l'imagerie étant généralement réalisée dans des dispersions d'UCNPs très diluées, dans lesquelles la dissolution est exacerbée.

Cependant, à cette époque, aucun rapport n'estimait cet effet à l'échelle de la particule unique. Pour les méthodes de SMM, maintenir constante la réponse du luminophore dans le temps est essentiel pour obtenir une quantité suffisante d'informations au cours de l'expérience. De plus, si les particules présentaient une perte de luminescence hétérogène, il pourrait être difficile de distinguer les particules individuelles des oligomères en fonction de leur intensité. D'autres problèmes potentiels pourraient découler de la réponse différente des particules partiellement dissoutes et des particules intactes. Nous avons décidé d'étudier systématiquement ce processus et de voir si les stratégies existantes pour contrecarrer cet effet fonctionnent également à l'échelle de la particule unique.

Les résultats sont présentés dans la communication suivante que nous avons publiée dans la revue Nanoscale en 2018. Nous avons constaté une hétérogénéité extrêmement élevée dans la dissolution des particules lorsqu'elles étaient maintenues dans de l'eau déminéralisée, avec des changements remarquables non seulement en intensité, mais aussi dans les rapports de bandes spectrales. Maintenir les particules dans des concentrations relativement élevées (1 mM) de fluorure de sodium était suffisant pour maintenir leur réponse stable sur une période de temps d'environ 20 minutes.

À la suite de ces travaux, nous étions confiant dans notre capacité à pouvoir imager des UCNPs hydrophiles dans des conditions de SMM. Nous avons décidé de nous concentrer sur le suivi de particules uniques en tant qu'application de SMM la plus prometteuse.

Publication 2.

Time-dependent luminescence loss of individual upconversion nanoparticles upon dilution in aqueous solutions

Partie 4. SPT avec des UCNPs sur des cellules vivantes.

Des preuves de concept de l'utilisation des UCNPs pour des expériences de SPT 2D et 3D ont été décrites par quelques groupes de recherche (*Jo et al., 2015; Nam et al., 2011; Wang et al., 2018*). En tant que système modèle, les groupes ont utilisé l'endocytose de nanoparticules et leur transport le long des microtubules à l'intérieur des cellules. Ces études ont montré que l'utilisation des UCNP pour le SPT présente les avantages d'un RSB élevé et d'une luminescence stable et ininterrompue, deux caractéristiques extrêmement utiles pour les expériences de tracking.

Les endosomes ne représentent qu'une cible parmi une myriade de cibles potentielles pour les expériences de SPT sur les cellules. Malheureusement, de base les nanoparticules dispersées dans l'eau manquent de spécificité pour reconnaitre la grande majorité des molécules biologiques et / ou leurs assemblages. Adapter les UCNPs pour le suivi ciblé en fixant des modules de ciblage sur leur surface leur permettrait de suivre toutes les cibles d'intérêt, de la même manière que les expériences existantes utilisant des QDs, des colorants organiques ou des nanoparticules d'or. À notre connaissance, le suivi ciblé avec des UCNPs n'a pas encore été effectué. Nous avons décidé d'explorer cette idée.

Pour estimer si les UCNPs pourrait fournir des informations raisonnables, nous avons décidé de reproduire une expérience modèle, le suivi des récepteurs FcεRI à la surface des cellules basophiles de rats (lignée RBL-2H3), à l'aide d'UCNPs décorées avec des anticorps IgE. Ce système a été très bien étudié via diverses méthodes (y compris le SPT), de sorte que plusieurs jeux de données sont disponibles pour être comparés à notre expérience. Comme base de notre expérience, nous avons sélectionné l'étude du groupe de Diane Lidke (*Andrews et al., 2008*), qui impliquait le suivi de points quantiques attachés aux IgE par une liaison biotine-streptavidine. Nous avons estimé que parmi les méthodes possibles pour décorer les particules avec des biomolécules, la liaison biotine-streptavidine est probablement l'une des plus simples, car la biotine peut être facilement attachée à la surface du polymère, puis connectée à une IgE biotinylée via une streptavidine (stratégie dite en «sandwich»).

Nos conclusions sont résumées dans le manuscrit suivant, que nous souhaitons publier dès que nous aurons terminé toutes les expériences annexes.

Publication 3.

Targeted membrane receptor tracking with upconversion nanoparticles

Chapitre 4. Conclusions et perspectives.

Conclusions

L'objectif principal de ces travaux de recherche était d'adapter les UCNPs à la microscopie de molécule unique pour tirer parti de leurs propriétés optiques uniques. L'accent a été mis sur les applications biologiques, car ce sont elles qui bénéficieraient le plus des propriétés des UCNPs. L'imagerie avec les UCNPs permet de supprimer le fond d'autofluorescence, source commune de problèmes en microscopie de fluorescence conventionnelle en biologie. La photostabilité extrême des UCNP et l'absence de clignotement sont également des avantages notables pour les applications de microscopie.

À cette fin, nous avons mis au point des protocoles permettant de disperser dans l'eau les UCNPs brutes, recouvertes d'acides oléiques. Notre priorité principale était de conserver la monodispersité des particules, car une taille homogène de particules est cruciale pour les applications de SMM, où l'oligomérisation et l'agrégation des particules peuvent induire des erreurs systématiques significatives dans les expériences. Nous avons étudié plusieurs stratégies: échange de ligand, encapsulation dans des nanoémulsions, enrobage par un polymère amphiphile et un polymère amphiphile zwitterionique. Nous avons constaté que l'enrobage des particules par un polymère amphiphile est sans doute le meilleur moyen de les adapter au SMM en raison de la monodispersité élevée des particules, de la grande stabilité colloïdale, de la faible épaisseur du revêtement et de la possibilité de décorer les particules obtenues avec des groupements chimiques en vue de les fonctionnaliser. Nous avons ajouté ces groupes fonctionnels directement lors de la synthèse du polymère, mais nous notons que les UCNPs peuvent également être décorés après leur enrobage. Les autres stratégies pour disperser les UCNPs dans l'eau ne produisaient pas de particules de qualité suffisante pour le SMM.

Nous avons également mis au point des protocoles pour l'imagerie des UCNPs uniques et avons estimé la stabilité des UCNPs uniques dans des tampons aqueux. Nous avons constaté que la dissolution des UCNP peut induire une forte hétérogénéité dans l'intensité et la réponse spectrale des particules uniques. Nous avons montré que ces effets causées par la

dissolution peuvent être efficacement inhibés par l'utilisation de tampons fluorés au cours de l'imagerie.

Nous avons essayé d'adapter les UCNP aux applications de smFRET. Dans ce but, nous avons effectué une évaluation expérimentale systématique de l'efficacité du FRET d'UCNPs de différentes tailles aux colorants organiques fixés à la surface de ces particules. Sur la base de ces données, nous avons élaboré un modèle semi-empirique de Monte Carlo pour la prédiction de l'efficacité du FRET des UCNPs aux colorants organiques. En fin de compte, l' efficacité de FRET d'un UCNP unique à un seul colorant (comme dans le smFRET) a été jugée insuffisante pour les applications smFRET, du moins pour les UCNPs à dopage Yb-Er couramment utilisés. Néanmoins, notre modèle permet d'estimer rapidement l'efficacité du FRET des UCNPs à plusieurs colorants, ce qui peut être utile pour le développement d'applications basées sur le FRET, autres que le smFRET.

Enfin, nous avons adapté les UCNP au suivi de particule unique. Pour cela, les UCNPs ont été modifiés avec de la biotine, puis de la streptavidine, pour donner des particules décorées par de la streptavidine, permettant ainsi la fixation facile de molécules de ciblage biotinylées (anticorps ou aptamères). Pour confirmer que les particules présentaient des performances supérieures en SPT, nous les avons décorées avec des anticorps IgE et avons suivi des récepteurs FcεRI à la surface de cellules RBL-2H3 par SPT. Ce système a été bien décrit dans la littérature avec les techniques SPT, ce qui nous a permis de valider le comportement de nos particules en le comparant aux données de la littérature. Dans l'ensemble, nous avons constaté que les UCNPs présentaient une émission à long terme ininterrompue, une photostabilité exceptionnelle et un faible bruit de fond dû à l'élimination de l'autofluorescence. Toutes ces propriétés ont montré que les UCNP étaient des luminophores très prometteurs pour le SPT.

En résumé, ces travaux constituent la première investigation approfondie de notre laboratoire dans les domaines passionnants des nanoparticules à conversion ascendante. Au cours de ces travaux, nous avons établi de nombreux protocoles et acquis une expérience empirique précieuse qui servira de base aux travaux futurs sur les applications des UCNPs en microscopie des systèmes biologiques.

Perspectives

Pour disperser les UCNP dans l'eau, la prochaine voie d'amélioration consisterait à développer les travaux sur les polymères zwitterioniques, peut-être en utilisant des zwitterions plus hydrophiles ou oligomèriques. Garder la surface de la particule à peu près neutre avec une couche d'eau fortement coordonnée permettrait de lutter efficacement contre la liaison non spécifique des protéines et des acides nucléiques, à la fois pour les expériences in vitro et in vivo. L'exploration des possibilités offertes par un revêtement des UCNP par une coquille en silice pourrait également s'avérer fructueuse, compte tenu de sa grande résistance chimique et de ses protocoles de modification bien développés. Plusieurs groupes ont utilisé cette approche pour des expériences d'ensemble avec des UCNPs. La mise au point d'une méthode permettant de produire des UCNPs recouvertes de silice présentant une monodispersité élevée et colloïdalement stables constituerait une étape importante dans la création d'UCNPs offrant diverses fonctionnalités pour les expériences de microscopie.

Pour les applications de smFRET, une amélioration cruciale de l'efficacité du FRET entre UCNPs et colorants impliquerait vraisemblablement l'utilisation de particules avec des émetteurs coopératifs. Avec une durée de vie de l'émetteur suffisamment longue, cette approche pourrait permettre aux émetteurs les plus éloignés du colorant de continuer à contribuer au FRET en transférant leur énergie aux émetteurs proches du colorant. De telles particules ont déjà été rapportées dans la littérature dans des expériences de FRET simples, utilisant l'homo-FRET entre les ions Gd^{3+} comme mécanisme de coopérativité (*Deng et al., 2016; Wang et al., 2011*). Cependant, le potentiel de telles UCNPs pour les expériences smFRET n'a pas encore été étudié.

Pour les applications de SPT, les particules décorées de streptavidines que nous avons développées peuvent être utilisées immédiatement pour étudier le comportement des composants de la membrane cellulaire via SPT. Contrairement aux colorants organiques et aux points quantiques, l'absence de clignotement et de blanchiment avec les UCNPs permet de réaliser des SPT sur des échelles de temps extrêmement longues. Contrairement aux nanoparticules d'or, les UCNPs peuvent être fabriqués dans des tailles plus petites et peuvent être utilisés dans des expériences multicanaux (par exemple pour le SPT simultané de cibles multiples avec plusieurs types d'UCNPs différents). Les expériences multicanaux peuvent également être étendues en utilisant des UCNP avec des réponses spectrales dépendantes du

dopage, développées à l'origine pour le multiplexage. En ajustant les concentrations de dopants, on pourrait produire des particules avec des signatures spectrales très distinctes avec des structures de bandes et des rapports de bandes très différents. En fin de compte, cette approche pourrait permettre de réaliser des expériences SPT dans lesquelles chaque particule individuelle possède une signature spectrale distincte.

Toutes les approches ci-dessus peuvent également être immédiatement améliorées et développées en utilisant des particules sur mesure spécialement conçues à des fins de microscopie. Ces dernières années, de nombreux groupes de recherche du monde entier ont consacré beaucoup de travail pour réaliser cet objectif, par exemple via une approche populaire consistant à protéger avec une coquille inerte les ions actifs du quenching. Les nouveaux types d'UCNPs développés présentent des avantages immédiats pour les SMM de part l'augmentation de la brillance des particules. Par ailleurs, en ce qui concerne l'amélioration de la brillance des particules, de nombreux rapports décrivent l'utilisation de colorants possédant un état de triplet de basse énergie pour transférer efficacement de l'énergie aux ions absorbeurs présents à l'intérieur des UCNPs (*Chen et al., 2015; Garfield et al., 2018; Zou et al. , 2012*). Cette approche augmente efficacement le coefficient d'extinction des UCNPs et donc leur brillance. Cependant, les particules obtenues perdent rapidement leur brillance dans des conditions biologiques, car le colorant dans son état excité triplet est très sensible à la dégradation par oxydation (par exemple, par l'oxygène ambiant). Le piégeage de tels colorants sur la surface de la particule sous une couche épaisse et impénétrable de silice ou de polymère densément tassé pourrait leur conférer une résistance substantielle au blanchiment optique. Le luminophore obtenu pourrait combiner le coefficient d'extinction sans précédent des nanoparticules chargées de colorant avec des propriétés uniques des UCNP telles qu'un décalage anti-Stokes élevé et une structure de bande étroite.

En élargissant les idées appliquées aux UCNPs en thérapie photodynamique, à l'administration de médicaments et au théranostic, on pourrait imaginer de créer des UCNPs avec une fonction active contrôlable. De telles particules serviraient non seulement d'étiquettes, mais également d'instruments à l'échelle nanométrique dans les SMM. Par exemple, la fixation de groupes photoclivables à la surface de particules pourrait permettre un suivi cohérent à long terme des UCNP sous illumination infrarouge dans des expériences cellulaires, en observant leur localisation dans différentes régions des cellules (par exemple, les endosomes tardifs) et d'induire des modifications de leur environnement par flash de

lumière visible focalisée au bon endroit au bon moment. Une autre approche particulièrement intéressante consisterait à utiliser des UCNP à émission bleue ou violette pour induire la photopolymérisation activée par de l'IR pour l'impression 3D à l'échelle nanométrique, en utilisant le FRET issu de la particule comme source efficace hautement localisée pour l'initiation du processus de polymérisation (des bases ont été posées pour cette application). Rocheva et al., 2018). La génération locale à la demande d'excitations UV et / ou visibles par les UCNPs recèle également un potentiel pour les expériences optogénétiques, en reliant les UCNPs aux canaux ioniques photosensibles introduits dans les cellules transgéniques, permettant l'ouverture de canal déclenché par IR (exemples prometteurs présentés dans *S. Chen et al., 2018; Pliss et al., 2017; Shah et al., 2015; X. Wu et al., 2016*).

Les effets plasmoniques, en particulier l'amélioration de l'absorption et de l'émission de luminophores proches des particules et / ou des surfaces conductrices (par exemple, des nanoparticules d'or), pourraient constituer une autre approche intéressante pour augmenter la brillance des UCNPs dans des expériences de microscopie. Des expériences prototypes ont déjà été rapportées dans la littérature, mais jusqu'à présent, aucun facteur particulièrement élevé d'amélioration de la brillance n'a encore été démontré. L'approche la plus prometteuse consiste à positionner les UCNP sur la pointe d'une nano barreau en or de dimensions appropriées permettant à la fois d'améliorer l'absorption et l'émission, car le nano barreau possède deux fréquences de résonance plasmoniques distinctes. Si une méthode d'assemblage fiable de ce système dans une géométrie appropriée était conçue, les particules composites obtenues présenteraient une amélioration considérable de la brillance de la conversion ascendante, ce qui serait particulièrement utile pour les applications de microscopie.

UNIVERSITÉ DE STRASBOURG

Oleksii DUKHNO

Microscopie de molécules uniques avec des nanoparticules à conversion ascendante

École Doctorale des Sciences de la Vie et de la Santé STRASBOURG

Résumé

La microscopie de molécule unique (single-molecule microscopy, SMM) regroupe un ensemble de techniques pour la biologie moléculaire et cellulaire permettant de visualiser le mouvement de molécules biologiques individuelles. Néanmoins, les techniques SMM imposent de fortes contraintes en ce qui concerne les luminophores utilisés. Récemment, un nouveau luminophore appelé «particule à conversion ascendante» (upconverting nanoparticles, UCNP) a attiré l'attention de la communauté scientifique en raison de son émission efficace de lumière visible après une excitation par de la lumière infrarouge. Cette propriété fait des UCNPs un luminophore très intéressant pour les applications biologiques : l'excitation infrarouge permet d'éliminer l'autofluorescence, généralement associé à une excitation dans la gamme du visible. De plus, la photostabilité extrême des UCNP et l'absence de photoclignottement sont également de précieux atouts pour les expériences SMM.

L'objectif de cette thèse était d'adapter les UCNPs aux applications SMM, avec le but ultime d'exploiter leurs propriétés uniques pour améliorer les performances des expériences SMM. Au cours du projet, les protocoles de dispersion des UCNPs dans des tampons aqueux ont été optimisées pour conserver une bonne monodispersité des particules; l'efficacité des UCNPs dans les expériences de transfert résonant d'énergie en particule unique a été estimée; des protocoles pour l'imagerie d'UCNPs uniques ont été développés; et la preuve de concept de l'utilisation des UCNPs dans des expériences de suivi de molécules uniques à la surface de cellules vivantes a été réalisée. Finalement, ces résultats forment une base solide pour de futures expériences SMM utilisant les UCNPs.

Mots-clés: conversion ascendante, nanoparticules, microscopie de molécule unique, microscopie à luminescence

Résumé en anglais

Single-molecule microscopy (SMM) is a powerful set of techniques for molecular and cell biology that allows visualizing the movement of individual biological molecules, but has strict requirements towards the utilized luminophores. Recently, a new luminophore called upconverting particles (UCNPs) gained attention of the research community due to their efficient emission of visible light upon excitation with infrared light. This property makes UCNPs a valuable luminophore for biological applications due to the elimination of autofluorescence background, commonly associated with regular visible light excitation. Extreme photostability of UCNPs and absence of sporadic photoswitching are also valuable for SMM experiments.

The objective of this thesis was to adapt UCNPs to SMM applications, with the ultimate goal of exploiting their unique properties towards superior performance of SMM experiments. During the project, protocols for dispersing UCNPs in aqueous buffers were streamlined to provide superior particle monodispersity; the efficiency of UCNPs in single-molecule resonance energy transfer experiments was estimated; protocols for single-molecule imaging with UCNPs were developed; and a proof-of-concept system for targeted single-molecule tracking with UCNPs in live cells was demonstrated. Overall, these findings will serve as a foundation towards robust SMM assays based on UCNPs.

Keywords: upconversion, nanoparticles, single-molecule microscopy, luminescence microscopy